UNIVERSITY OF BIRMINGHAM

OXIDATION AND SPALLATION OF AUSTENITIC STAINLESS STEELS FOR ULTRA-SUPERCRITICAL PLANT APPLICATION

Jim Rosser

A thesis submitted to

The University of Birmingham

For the degree of

DOCTOR OF PHILOSOPHY

Department of Metallurgy and Materials

School of Engineering and Physical Sciences

University of Birmingham

March 2014

Abstract

A comprehensive understanding of the steam-side oxidation and spallation properties of austenitic stainless steels is required to enable the use of these materials in ultra-supercritical plant in order to raise efficiency.

Isothermal oxidation of austenitic steels Super 304H, 347H FG and HR3C was performed in laboratory air and deoxygenated flowing steam at atmospheric pressure for oxidation periods of up to 3000 hours and 1300 hours respectively. The oxides on two inner tube surface finishes were characterised – A pickled surface finish, as would be installed in plant (Super 304H, 347H FG, HR3C), and a shot peened surface finish (Super 304H).

Oxidation in flowing deoxygenated steam was found to increase the oxidation rate of austenitic stainless steels compared with oxidation in laboratory air. Pickled Super 304H and 347H FG "18-8" austenitic steels exhibited larger mass gain and oxide thicknesses than 25Cr HR3C in all atmospheres. The inner surface of shot peened Super 304H exhibited dramatically thinner oxides in both air and steam.

The pickled austenitic stainless steels formed a duplex oxide featuring an outer iron rich oxide and inner spinel oxide containing the alloy constituent elements. The outer iron oxide grown in laboratory air was identified as haematite and that in deoxygenated steam, magnetite. At 650 and 700 °C in steam, a protective Cr-Mn spinel formed at the base of the spinel oxide. The parabolic rate constant of this oxide was found to be an order of magnitude larger than that of pure chromia, and hence less protective. The oxidation kinetics of the spinel and outer oxide layers at 650 and 700 °C were found to follow two regimes throughout oxidation. Initially growth of these layers follows an accelerated parabolic regime, until the complete formation of a protective Cr-Mn spinel at the base of the inner spinel oxide. Following this, the growth rate is dramatically reduced. This is caused by reduced cation diffusion through the Cr-Mn layer.

Spallation of the outer oxide of a number of samples occurred following oxidation in ineffectively deoxygenated steam. The presence of 20% or more haematite in the outer oxide was a prerequisite for spallation. The spallation interface was often within the magnetite layer and, occasionally, at the spinel/outer oxide interface.

The study was extended to include oxidation tests in flowing air saturated steam. These were performed to promote spallation of the inner surface oxide on 347H FG. The strain energies within

spalled oxide were calculated and compared to those found in the literature. A value of $\gamma' = 13$ Jm-2 was calculated for the effective fracture energy for the outer oxide on 347H FG, in good agreement with literature values for type-316 austenitic steel. Analysis of the oxide scales revealed that oxide buckling was the most common mode of failure, and that spallation of these oxides satisfies the critical strain energy criterion. Spallation maps for haematite and magnetite growth on 347H FG were constructed, and data was fit, and corresponded to the area at which unstable buckling or wedging was expected, in agreement with the experimental data.

An additional feature of oxidation in air saturated steam was the formation of oxide blisters on the inner surface of 347H FG. These blisters are proposed to nucleate and grow during oxidation, and rupture on cooling.

Acknowledgements

I would like to thank Professor Hugh E. Evans for his continued support and wisdom throughout my period of study, who sadly passed away before this thesis could be completed. I would also like to extend my gratitude to Dr. Christopher Cooper who helped a great deal with the construction of the steam oxidation apparatus and was always on-hand and willing to provide advice and support. My thanks also to Mr. Toby Lant of nPower, for providing support as my industrial supervisor, and providing furnaces for long term oxidation tests.

A special thanks goes to Professor Paul Bowen, for the patience and support he has offered me throughout the project up until the final submission.

I'd like to thank the boys in the office for the great memories, and a special thanks to Dr. Danial Khoshkhou for the late nights in the office and supplying the sleeping bags.

A thanks goes out to my housemates during my PhD – Roohi, Charn, Preet, Pria, Sophie, ADP, Emily, Chris, Bryony, Kate, Joe, Hannah, Meg, Tam, George, Connor, Will, Ash, Milly, Anna, Dave, Maz, Nat, Mum, Dad, Ed, Jen, Shannon, Polly, Sophie, Sam, Danica, Daisy, and Lucy.

A big thanks goes out to my parents, who have supported unconditionally through this project.

Finally, I would like to extend my gratitude to my supervisor Dr. Brian J. Connolly. There is no doubt that without his continued support and determination this would not have been possible.

Table of Contents

Chapter 1 Introduction

This thesis aims to address the limited short-term laboratory data available on the steam-side oxidation of advanced austenitic steel heat exchanger tubes. Super 304H, 347HFG, and HR3C were oxidised in laboratory air and atmospheric steam between 600 and 700 °C, with a view to better understanding oxide growth kinetics and failure mechanisms so as to aid component lifing and material selection.

1.1 Background

Economic and environmental requirements call for ever increasing efficiencies in energy production. In coal fired plants, efficiencies may be increased by increasing the operating parameters (steam temperature and pressure) of the heat recovery steam generator (HRSG), as indicated in Section 2.1.2 of the literature review. In plant, poor material selection has been responsible for large scale failures. However, oxidation of alloys is unavoidable at high temperatures and exacerbated in environments containing water vapour. As construction of new plants that operate at the higher temperatures and pressures defined by ultra-supercritical conditions (>593 °C, 24.1 MPa) continues, and with a vision of pushing conditions into the advanced ultra-supercritical regime (>675 °C), material selection has become an extremely important consideration, necessitating the use of higher chromium ferritic steels for lower temperature regions of the boiler, and high chromium austenitic steels for the hottest parts of the superheater and reheater areas. The need for nickel based alloys will become apparent in the design of advanced ultra-supercritical plants.

Investigations into the oxidation behaviour of pure metals, primitive alloy systems, and engineering steels have gone on for decades, with the current study citing relevant publications from the 1960's. As power plant operating parameters have increased, so have the needs for alloys that can withstand the harsher environments without failure due to mechanical strength or corrosion. As research continues, manufacturers of HRSG alloys have finely tuned chemistry compositions to improve creep strength [1, 2] and oxidation performance at elevated temperatures, sometimes benefiting one property at the detriment to the other [3].

Irrespective of minor element additions, chromium is still acknowledged to have the most influence over oxidation behaviour of steels up to approximately 800 °C (above which alumina and silica oxides begin to offer more effective protection). Alloy selection is important when operating at such high temperatures and pressures, and engineers must balance requirements such as oxidation resistance and creep strength with budgetary constraints.

Figure 1.1 shows how alloy systems have developed through minor element additions [4]. Advanced 18Cr-8Ni austenitic steels such as Super 304H and 347HFG have higher high temperature creep strength than a number of 20-25 wt.%Cr steels. However, minor element additions, such as the addition of niobium to TP310 to create HR3C can provide significant improvement [2]. Nickel based alloys, which have the highest strength and best corrosion resistance, are also the most expensive and therefore avoided where possible.

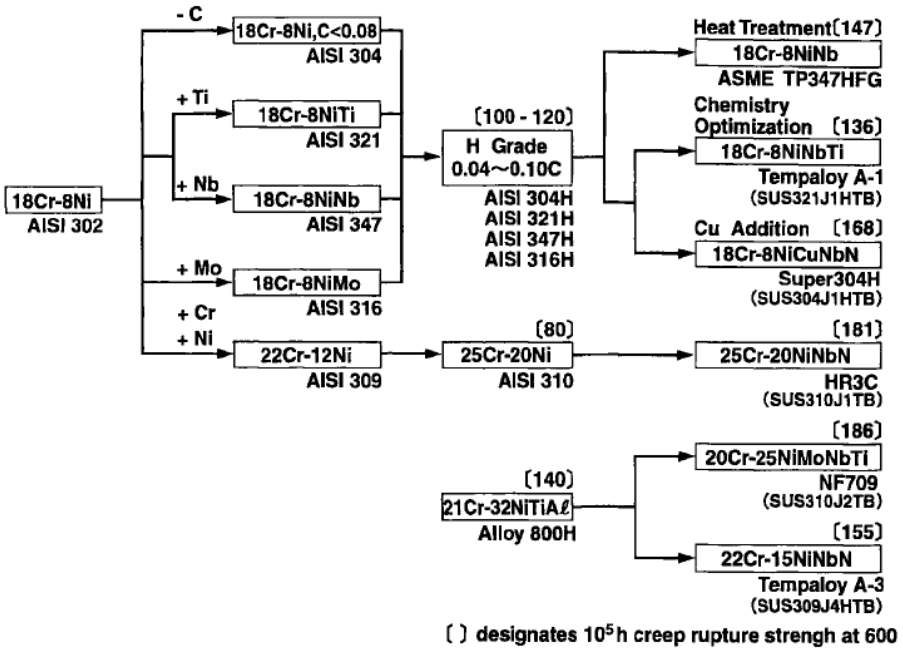

Figure 1.1 – Development of austenitic steels for use in power generation.

This thesis addresses the problems associated with high temperature oxidation of the steam-side of austenitic steels, which cause problems for HRSG systems in the following ways. Oxide scale growth (and therefore metal loss) on both the fire-side and steam-side tube surfaces can cause direct failure of the tube by increasing hoop stress, eventually causing rupture. A problem further exacerbated by local heating due to the insulating effect of the thick oxide scales. The study of oxide growth kinetics is important in predicting mean time before failure when considering design and maintenance of the plant.

Another major contributory factor in plant downtime, and a focus of this thesis, is spallation of steam-side oxide scales, which often occurs during thermal cycling [5]. Spallation contributes to direct tube failure by reducing the thickness of the oxide scale and allowing direct access of the oxidant to the metal surface [6]. However, arguably of greater concern is the damage spallation particles cause downstream, where they collect at tube bends restricting the flow of steam, and erode steam turbine nozzles and blades.

The ideal scenario would be for a singular, thin, adherent oxide film to form quickly, and offer exceptional protection from further oxidation of the underlying alloy. It is these properties that steel manufacturers and researchers strive to achieve through methods such as alloy composition, surface finish modification, and coating technologies. The first two of these variables are investigated in this thesis.

1.2 Research Objectives and Methodology

Scale spallation of austenitic steels in plant is well documented, and spallation mechanisms have been proposed, however, there is an increased need for input data such as scale thickness, spallation interface, oxide phases present and porosity so calculations with increased accuracy can be made on the stresses and strain energies experienced by these oxides. Importantly, the majority of available data is taken from ex-service tubes, and there is very little data available from short term laboratory experiments and from oxidation at temperatures above 600 °C, which becoming increasingly relevant in modern power plants. This research programme focussed on the oxidation and spallation of austenitic steels in air and steam. The programme was designed to generate short term input data that can be used in spallation models to predict the conditions in which spallation of the oxide grown on austenitic steels will occur, in the temperatures range 600 – 700 °C. Oxidation kinetics are also explored, and used to predict scale thicknesses at in-service timescales. The effect of the following parameters were investigated:

- Oxidising temperature
- Alloy type and composition
- Inner tube surface finish
- Oxidation atmosphere

Temperatures of 600, 650 and 700 °C were chosen in atmospheres of laboratory air, deoxygenated flowing steam, and air saturated flowing steam. Austenitic alloys Super 304H, 347HFG and HR3C were chosen for testing in laboratory air and deoxygenated steam, and test samples were cut from tube

sections as would be installed in plant. The inner surfaces of the tubes were pickled and a second tube of Super 304H, with a shot peened inner surface was included in testing for comparison of surface finishes. 347HFG was chosen for testing in flowing air saturated steam to investigate the spallation behaviour of this alloy.

The main objectives of the project were:

- Building and commissioning an atmospheric pressure steam oxidation test facility at the University of Birmingham, to allow for oxidation experiments in flowing steam at the target temperatures;
- Oxidation experiments in laboratory air. Initial screening of austenitic and was undertaken during construction and commissioning of the steam oxidation test facility. These experiments allowed for oxide morphology assessment and determination of oxide kinetics to compare with literature and forthcoming steam oxidation experiments;
- Oxidation experiments in flowing deoxygenated steam. Initial screening of austenitic steels were conducted to determine the morphology of oxides grown in deoxygenated steam, to calculate the kinetics of oxide growth of each oxide layer grown, and to identify any spallation events that might occur;
- Investigation into the effect of oxygen partial pressure on spallation in steam environments. 347HFG was chosen to investigate how increasing the oxidation partial pressure of flowing steam affects the spallation characteristics of the oxide grown on the alloy. Preliminary modelling was undertaken to explore the factors associated with spallation.

The results of this research will be critically reviewed against previous work, and aim to provide valid data to aid oxide growth estimation and spallation modelling for the austenitic steels studied.

1.3 Thesis Structure

The core of the thesis is composed of six chapters. A brief overview of each is given below.

Chapter 2 provides a comprehensive literature review of high temperature oxidation of heat exchanger tubes, and is split into the following four sections:

- Section 2.1 introduces conventional power plant operation and the evolution of plant design and efficiency, which is the driver for the current research programme.

- Section 2.2 provides an overview of oxide formation followed by an overview of oxidation kinetics and critical review of their application by other researchers.
- Section 2.3 reviews the current understanding of ferritic, martensitic, and austenitic steels in both air and steam, and includes proposed mechanisms of oxidation in each environment by different researchers.
- Section 2.4 reviews the development of oxide spallation processes and mechanisms.
- Section 2.5 provides a summary of the current understanding of high temperature oxidation and spallation of austenitic steels. This section also identifies gaps in the research and explains how the current research will address those gaps.

A fundamental introduction to coal-fired power generation, steel metallurgy, and high temperature oxidation can be found in Appendix A.

Chapter 3 describes the materials and experimental methodology used in the research programme. The chapter also presents the evolution of the atmospheric pressure steam oxidation test facility, and explains how each iteration affected the experimental results.

Chapter 4 presents the experimental results, and is split into the following five sections:

- Section 4.1 provides an introduction.
- Section 4.2: examination of pickled (as-received) and shot peened surfaces of each alloy prior to high temperature oxidation.
- Section 4.3: isothermal oxidation in laboratory air of pickled Super 304H, 347HFG, and HR3C, and shot peened Super 304H, was undertaken at 600, 650, and 700 °C for up to 3000 hours. Oxidation kinetics and morphology were reported. Oxidation in laboratory air provided a baseline with which to compare oxidation in atmospheric steam.
- Section 4.4: isothermal oxidation in flowing deoxygenated steam of pickled Super 304H, 347HFG, and HR3C, and shot peened Super 304H was undertaken at 600, 650, and 700 °C for up to 1300 hours. Oxidation kinetics and morphology are reported.
- Section 4.5: investigation into early spallation events. During early development of the steam oxidation facility, spallation was observed on samples of 347HFG and Super 304H after oxidation at 650 and 700 °C. This section analyses the oxide morphology of these early test samples and proposes a reason that spallation was observed after oxidation in seemingly deoxygenated steam.

- Section 4.6: isothermal oxidation in flowing air saturated steam of 347HFG was undertaken at 650 °C for up to 500 hours. The oxidation kinetics, morphology, and spallation behaviour are reported.
- Section 4.7 provides a summary of experimental results.

Chapter 5 discusses the findings of the experiments presented in Chapter 4, and is split into the following sections:

- Section 5.1 explores the oxide morphology observed on each alloy in each environment, and proposes oxidation mechanisms for each.
- Section 5.2 explores oxide growth kinetics, and proposes kinetic regimes for oxidation in both air and flowing steam.
- Section 5.3 explores the spallation behaviour of 347HFG and Super 304H.

Chapter 6 provides the findings and conclusions of the research programme.

Chapter 7 suggests further work based on the findings of the research programme.

Chapter 2 Literature Review

2.1 Fossil Fuel as a Power Source

2.1.1 Introduction

In the UK today 74% of the electricity demand is met by fossil-fuels split between gas-fired (36%) and coal- or oil-fired (38%). Of this, 50% of the electricity comes from steam fired plants [7]. Efficiency of power generation from steam turbines is based on the Rankine cycle and increasing the operating temperature and pressure of a plant increases the efficiency. Current UK coal fired plants run at an efficiency of approximately 37% with high pressure steam outlet operating conditions of 565°C and 17 MPa. Increasing coal fired plant efficiency to 47% is estimated to reduce CO_2 emissions by 22% and save around $16.5 million annually in fuel costs [8]. Increasing the efficiency of plants to the golden target of 60% will have a substantial global impact given that the consumption of China alone predicts for an additional 500 GW of coal-fired capacity by 2030 [9].

Under current generating conditions, however, although cheaper than oil and gas, coal combustion results in higher CO_2 emissions than either of these. The UK government has set a target to cut CO_2 emissions by more than a 3rd between 1990 and 2020. The government is planning that around 50 per cent of the yearly emissions cuts between now and 2020 will be achieved by making the energy mix greener. The government expects 40% of the electricity used in 2020 to come from low carbon sources – 30% from renewables, the rest from nuclear (including new build) and clean coal. Achieving the efficiencies needed for such large reductions in CO_2 output requires the use of USC (ultra-supercritical) steam with operating conditions upwards of 593°C and 24 MPa. The THERMIE research program in Europe has USC targets of 720 °C and 35 MPa, and DoE research in The United States calls for conditions of 760 °C and 37.9 MPa [9]. To reach these temperatures new materials with improved creep strength and oxidation resistance are required. Currently available ferritic steels are able to operate up to 620 °C from a mechanical point of view but their oxidation resistance limits their use to 593 °C [8].

Austenitic stainless steels are considered candidate alloys for boiler tubes, particularly superheater and reheaters, because of their higher strength at the operating conditions considered. Higher strength versions of these materials are proposed for use in the USC plants. Above 700 °C steels with high Cr (>20 wt.%) and Ni (>20 wt.%) content, such as HR3C, and nickel-based super alloys such as Inconol 617 are employed.

This project focuses on characterising the oxide that forms on the candidate austenitic steels 347HFG, Super 304H, and HRC3 under laboratory air and atmospheric steam conditions, in the temperature range 600 – 700 °C.

2.1.2 Power Plant Operation

Steam power is one of the oldest methods of energy production and is responsible for the vast majority of electricity production in the world today. The heat recovery steam generator (HSRG) in a fossil fuelled plant works by transferring heat energy from burning fossil fuel in the boiler to steam pipes that drive turbines to turn electrical generators. The efficiency of fossil fuelled plants has increased steadily through the years and is strongly correlated to the steam parameters (temperature and pressure) within the boiler. Generally plants that operate below 22 MPa are termed subcritical, above 22.1 MPa and between 538 °C and 565 °C supercritical (SC), above 565 °C ultra-supercritical (USC) and those that operate in excess of 675 °C advanced ultra-supercritical (A-USC) [8]. Babcock & Wilcox introduced the first supercritical boiler in 1957 capable of 125 MW and steam parameters of 31.4 MPa and 621 °C with two reheats at 566 °C and 538 °C [10]. Restrictions in achieving favourable steam parameters have largely been a result of material selection [11]. Eddystone 1 was another supercritical plant built in 1960 that was designed to operate with steam conditions of 34.5 MPa and 650/565/565 °C. Mechanical and metallurgical problems forced the plant to run at reduced parameters of 32.4 MPa and 605 °C. A diagram of a supercritical boiler is shown in Figure 2.1.

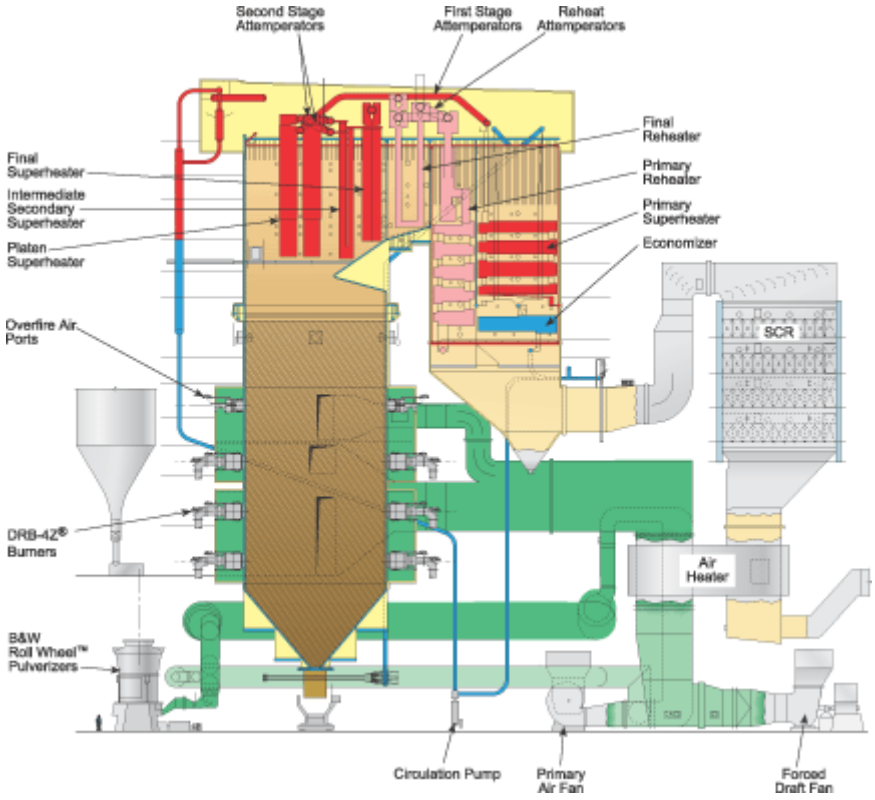

Figure 2.1 – Babcock and Wilcox Supercritical boiler design.

Boilers can be split into two categories; those with a steam drum, and those without [12]. In a steam drum boiler, feed water is pumped to pressure and fed through the economiser to preheat the water to just below the saturation point. Water is then fed into the steam drum at the top of the boiler and mixes well with water from the evaporator tubes to reduce thermal strains. The water leaves the steam drum through downcomer tubes. These are large diameter tubes that carry saturated water to the riser tubes. Variations of this type of boiler are that of natural circulation and assisted circulation. Boilers with natural circulation exploit the density difference between water in the downcomers and steam in the risers to produce continuous circulation between the two. For this reason, downcomer tubes are situated outside the boiler to avoid evaporation of the water that would reduce circulation in the system. Assisted circulation boilers rely on a circulation pump and can generally achieve higher steam pressures. At the base of the furnace, the “mud drum” header collects impurities that are later removed and passes saturated water from the downcomer tubes to the riser tubes. The riser tubes are often dubbed the waterwall and make up the evaporator part of boiler. Here, saturated water partially evaporates and returns to the steam drum. The main purpose of the steam drum is to separate pure steam from any moisture and impurities that would damage the superheater tubes. Any water returns to the waterwall via the downcomers and saturated steam continues to the superheater where it is heated beyond saturation point and on to the turbine section. A diagram of a steam drum boiler with circulation pump is shown in Figure 2.2 (a).

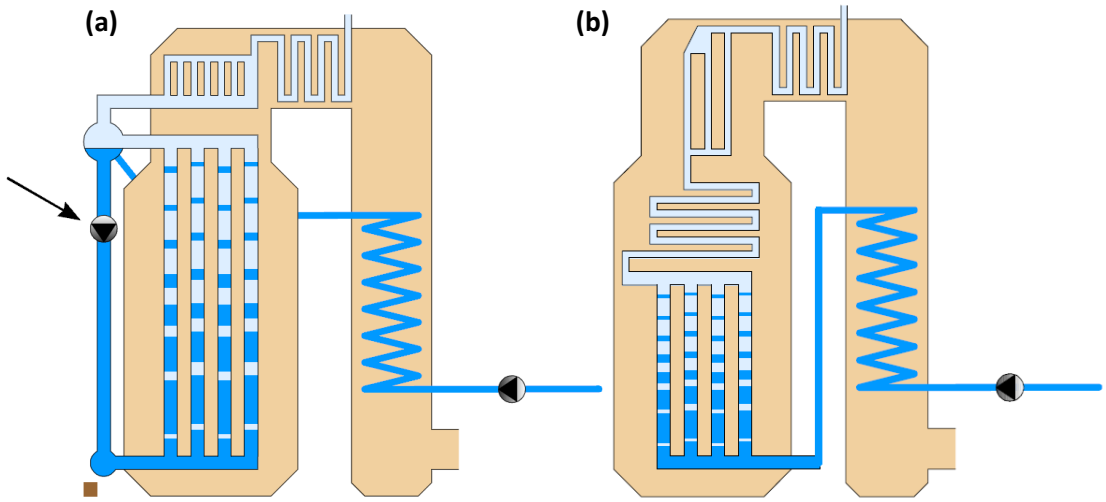

Figure 2.2 – Boiler types. (a) steam drum with circulation pump. (b) Once through Benson type [10].

Once through boilers differ from steam drum boilers in that no circulation of the working fluid takes place [12]. Pressurised feed water is preheated in the economiser and flows into the riser tubes and evaporates. The evaporation can either take place at a fixed point (Sulzer type) that involves a "Sulzer bottle", after which steam is free of water, or variable point (Benson type) where complete evaporation occurs at some point before the superheater section. Once through boilers are also known as universal pressure boilers because they can operate in subcritical or supercritical states. In supercritical boilers evaporation of water into steam does not take place because of the nature of supercritical water. The Sulzer bottle is then redundant in these types of boiler but does not affect supercritical steam production. A diagram of a Benson type once through boiler is shown in Figure 2.2 (b).

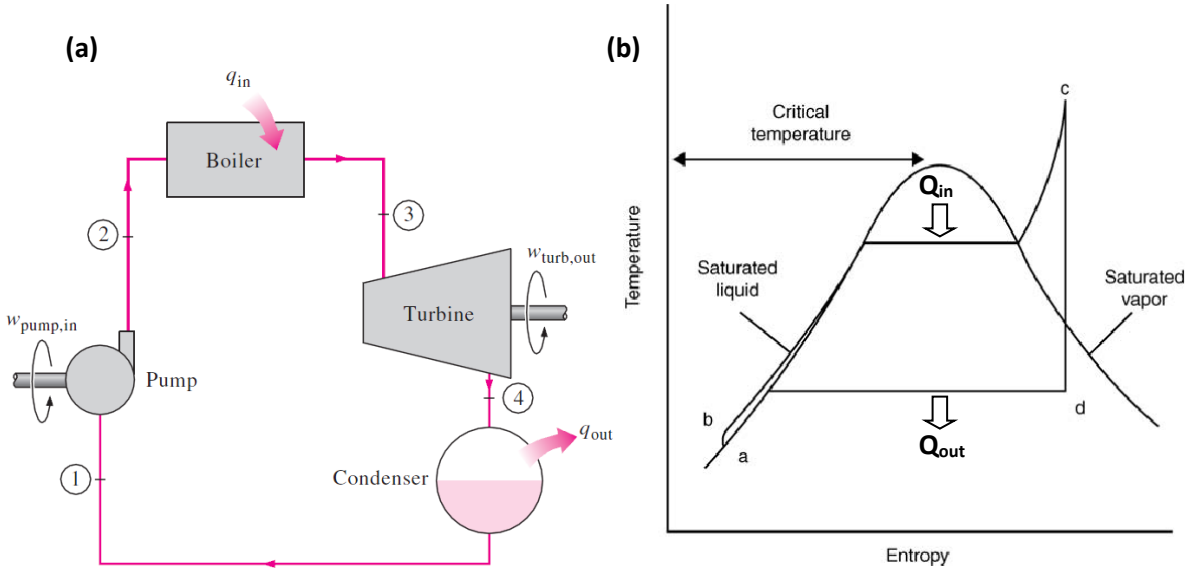

Figure 2.3 – (a) Schematic of the ideal Rankine cycle [13]. (b) T-S diagram of subcritical plant Rankine cycle [14].

The boiler is part of a larger closed cycle heat engine called the Rankine cycle that can be thought of as a practical Carnot cycle for vapour power cycles [13]. A simple schematic of plant components that make up the cycle is shown in Figure 2.3 (a) and the T-S diagram for a subcritical plant Rankine cycle is shown in Figure 2.3 (b). The basic operations involved are as follows:

- a to b (pump) – Saturated water is pumped to pressure (below 22.1 MPa for subcritical plant) from the condenser in an isentropic process;
- b to c (boiler) – Saturated water at boiler pressure is heated at constant pressure to evaporation in the waterwall. Isothermal expansion takes place as the water is vaporised, which is followed by the superheater heating the steam beyond the saturated vapour point to create dry steam;
- c to d (turbine) – Isentropic expansion of dry steam works the turbine shaft and enters the compressor usually as a saturated liquid/vapour mixture;
- d to a (condenser) – Unavailable heat rejection via low temperature sink (cooling tower/river) occurs in an isobaric process. Condensed water travels back to the pump to complete the cycle.

Moisture control is a key aspect of boiler design as any moisture in the dry steam flow from the superheater that enters the turbine will cause erosion of the turbine blades.

In contrast to a subcritical cycle, the concept of supercritical plant design is that the heating cycle is conducted entirely above the critical pressure point of 22 MPa. The heating cycle avoids the isothermal evaporation phase-change associated with a subcritical cycle, enabling a constant increase in temperature, thereby improving efficiency. This is illustrated on the supercritical T-S diagram as step “d to e” (Figure 2.4). Also shown on the figure is a single reheat cycle where expanded steam from the primary turbine is sent back to the boiler to increase in temperature before expanding further in a low pressure turbine. Coal fired plants often have two reheat stages and may be present on both subcritical and supercritical plants.

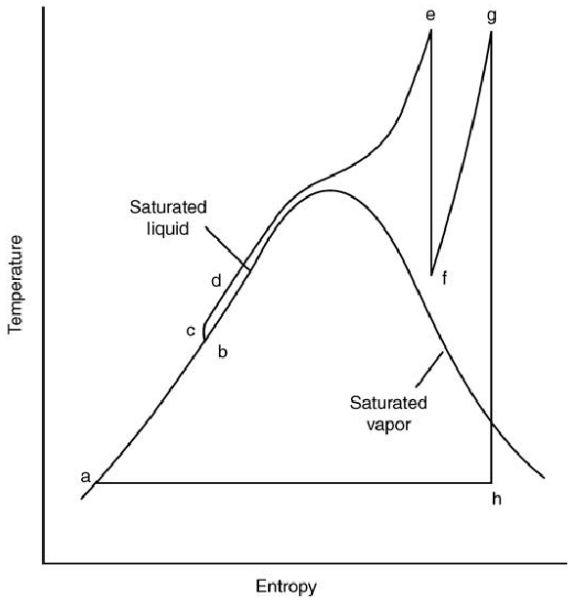

Figure 2.4 – Rankine cycle of a supercritical boiler [14].

The highest theoretical efficiency attainable with a heat engine is given by the Carnot efficiency [13]

$$\eta_{th} = 1 - \frac{Q_{out}}{Q_{in}} \qquad \textbf{(2-1)}$$

where η_{th} is the theoretical efficiency obtained from a reversible heat engine producing work from between a hot reservoir Q_{in} and cold reservoir Q_{out}. Increasing the efficiency requires increasing Q_{in} (increasing live steam temperature) or decreasing Q_{out} (decreasing condenser output temperature and pressure). The latter is restricted by the cooling circuit temperature which is often at a relatively fixed value of around 20 °C. However, this temperature allows for a sufficient drop in pressure to increase the work output of the turbine. To avoid an increase in the moisture content at the final turbine stage, the condenser pressure must be kept above the saturation point, therefore setting a lower limit on condenser pressure. For water at 25 °C this is 3.2 kPa [13]. Most modern condensers work at pressures below atmospheric. Q_{in} is limited by boiler tube oxidation and allowable stress, however, adding reheat cycles increases the mean Q_{in} improving efficiency [10].

Figure 2.3 (b) and Figure 2.4 outline reversible Rankine cycles. In reality, inefficiencies exist at every step of a heat cycle reducing the overall efficiency. These include pressure drops caused by fluid friction in the pipes between the feed water pump and turbine, heat loss to the surroundings at the boiler and turbine stages and inefficiencies in the turbines and feed water pump [13].

2.2 High Temperature Oxidation

2.2.1 Oxide Formation

Oxidation at the surface of metals and alloys causes metal loss at different rates, depending on the oxide that forms. For boiler tubes subject to oxidation at power plant design temperatures (550-750 °C), growth of a complete layer of dense Cr_2O_3 is preferred, because of the low diffusion rate of anions and cations through the oxide. The formation of Cr_2O_3 is dependent on availability of sufficient levels of chromium at the alloy surface. Unfortunately, this is not always the case on lower chromium alloys. This leads to the formation of less protective iron oxides. The following section introduces the common oxides formed on boiler tube steels, and investigates the factors that affect preferential growth of protective oxides such as Cr_2O_3.

2.2.1.1 Iron Oxides

The oxidation properties of iron have been studied extensively because of the abundant use of it as an engineering material. Pure iron forms a multilayered scale consisting of FeO (wustite), Fe_3O_4 (magnetite), Fe_2O_3 (haematite). FeO, the most iron rich oxide, forms at the metal/scale interface and Fe_2O_3, the most oxygen rich oxide, forms at the scale/gas interface [15]. It can be seen from the iron-oxygen phase diagram (Figure 2.5) that FeO is only stable above 570 °C. Below this temperature oxide growth is split between magnetite and haematite depending on the oxygen content. FeO is a p-type metal deficit semi-conductor with a fcc structure whose stoichiometry varies widely over the range $Fe_{0.95}O$ to $Fe_{0.88}O$ at 1000 °C [16]. For this reason, transport through the scale is rapid and FeO is usually found to be the thickest oxide layer. Fe_3O_4 has an inverse spinel structure where Fe^{2+} ions occupy the octahedral sites and half the Fe^{3}+ ions occupy tetrahedral sites. A slight deviation from stoichiometry is found, increasing at high temperatures, and defects are found on both sites. Fe_2O_3 exists in two forms, α-Fe_2O_3 (along with Al_2O_3 and Cr_2O_3) which has a rhombohedral structure and γ-Fe_2O3 which is cubic.

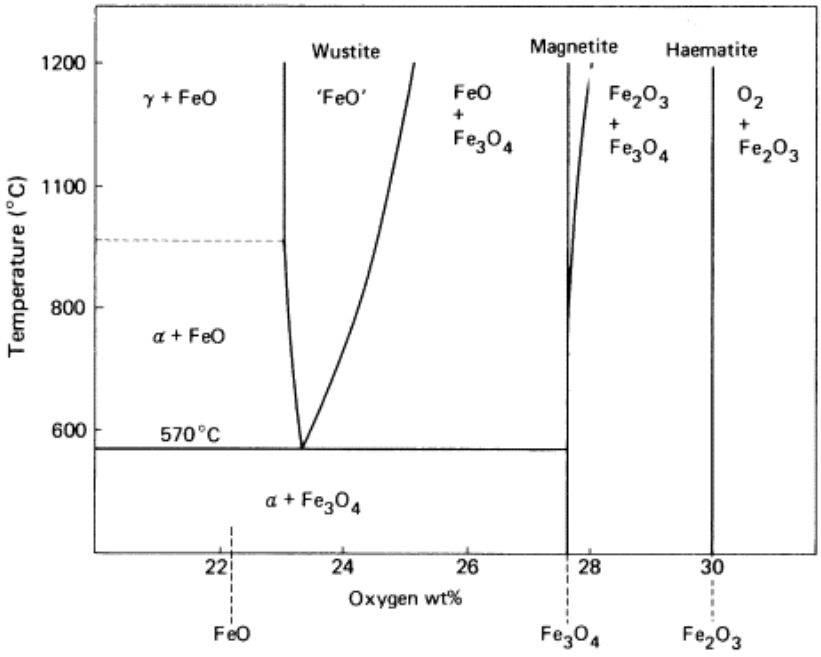

Figure 2.5 – Iron-oxygen phase diagram [17].

2.2.1.2 Chromium Oxide

Chromium forms a single, protective oxide, chromia, Cr_2O_3. There is some discussion of the defect structure of Cr_2O_3. Bevan et. al. measured the conductivity of Cr_2O_3 and deduced the defect structure to be that of a p-type, oxygen excess semi-conductor ., However, others believe it may be p-type or n-type and temperature dependent [18]. Simultaneous diffusion of both anions and cations may result in reaction and formation of oxide within the oxide layer, explaining the compressive growth stresses that develop [19]. Some researchers [20] have found growth of Cr_2O_3 on pure chromium to follow a parabolic law below 900 °C but an increased rate as temperature increases above 1050 °C. The large rate increase above this temperature was attributed to adherence issues and CrO_3 vapourisation. Other researchers [21] have attributed the transition from parabolic to linear kinetics on chromium and Cr_2O_3 FeCr alloys to CrO_3 vapourisation. Although chromia forms a dense and slow growing film, compressive strains lead to spallation [19, 22] and repeated scale loss during cyclic oxidation [23]. Ion diffusion through the oxide lattice cannot explain the growth rates of Cr_2O_3. It is suggested that short circuit diffusion via grain boundaries and possibly micropores may explain the growth rate [24].

2.2.1.3 Aluminium Oxide

Aluminium forms a variety of oxides [25]. The only stable of oxide grown on alloys at high temperature is alpha alumina, α-Al_2O_3. This is a highly stoichiometric amd highly protective oxide. Research has found both anions and cations to be mobile and growth to occur at the metal/scale interface and the scale/gas interface. However, reactive elements such as Y, Hf and Zr appear to decrease outward cation diffusion and depress the kinetics of alumina growth [25, 26]. The use of aluminium is often

restricted to high temperature applications (>900 °C). It is extensively used in jet propulsion engines where temperatures can exceed 2000 °C (although environmental protection is offered in the form of a cool air film and thermal barrier coating reducing the maximum alloy surface temperature to a more manageable ~1000 °C). The use of aluminium as a protective oxide former in boiler tube steels is restricted as the service temperatures are less than is required for α-Al_2O_3 to grow [18].

2.2.2 Factors that Influence High Temperature Oxidation

2.2.2.1 Effects of Grain Refinement on Oxidation

Chromium has been shown to diffuse faster through oxide grain boundaries than the bulk lattice. THis promotes the formation of Cr rich oxides such as Cr_2O_3 where grain boundaries meet the alloy surface. Grain boundary refinement is used by steel manufacturers to increase the oxidation resistance of austenitic steels, and has resulted in the development of fine grained versions of austenitic steels, such as 347HFG and Super 304H. The benefits of grain refinement have been reported by Matsuo et al. [27], who found that the long term oxidation performance of fine grained 347HFG and Super 304H to be far greater than the coarse grained equivalent 347H (Figure 2.6).

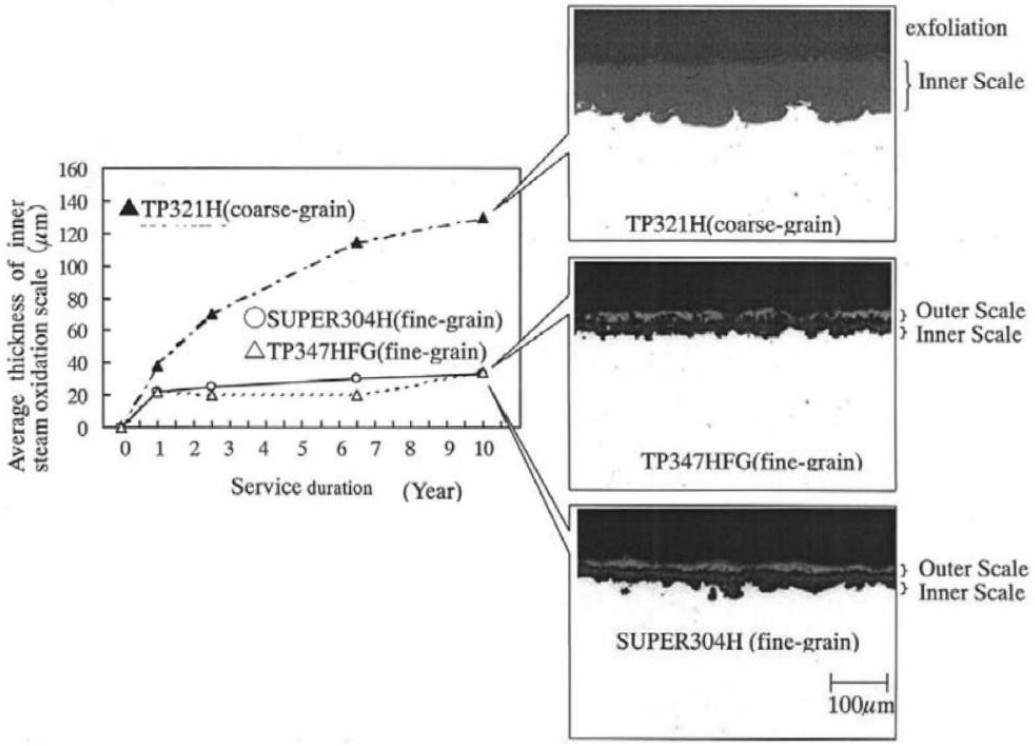

Figure 2.6 – Oxidation kinetics and cross-sectional morphology of coarse and fine-grained steels, after Matsuo et al. [27].

Kim et al. [28, 29] found coarse grained samples to gain more weight than fine grained samples during the oxidation of electro-polished Super 304H for up to 500 hours at 700 °C in air + 20% H_2O.

Grain refinement can also be detrimental to oxidation resistance if the reservoir of available chromium in the bulk alloy is too low to allow for a Cr rich protective oxide to form. On 0-2.25 wt.% Cr ferritic alloys, Trindade et al. found that decreasing the alloy grain size via heat treatment prior to oxidation greatly increased the reported mass gain [30]. The authors attributed the relationship to increased oxygen ion transport through alloy grain boundaries.

2.2.2.2 Effects of Shot Peening

Mechanical shot peening involves firing small ball bearings (shot) at the surface of a material to induce plastic deformation up to a few hundred micrometers below the surface. The resultant layer is put under compression [31]. The process is used advantageously to increase the mechanical life of components susceptible to fatigue and cracking as the surface compression reduces crack initiation and propagation [32]. A drawback of mechanical shot peening is the rough surface left by the shot which is detrimental in terms of crack propagation. Stressing the material prior to shot peening has been shown to reduce crack initiation and propagation [33] by increasing compression near surface and so increases the effect of shot peening. Alternate peening methods exist which aim to tackle drawbacks of mechanical shot peening [34].

In terms of oxidation performance, shot peening has been used to promote the growth of a protective Cr_2O_3 layer and improve oxidation resistance. The dislocation density of the affected zone is increased and therefore there are an increased number of short circuit paths for diffusion near the surface of the metal. Austenitic steels show the most improvement to oxidation resistance and this benefit tends to decrease with decreasing chromium content [17]. The large increase in dislocation density in the fcc structure of austenitic alloys promotes faster diffusion of chromium. Shot peening has also been shown to promote the growth of Mn rich spinel phases above the Cr_2O_3 layer on TP304H and HR3C austenitic steels [35], and additional treatments such as short pre-annealing has been shown to improve the overall oxidation performance on shot peened materials [36].

9-12 wt.% Cr steels benefit from enhanced chromium diffusion but to a lesser extent than austenitic steels. Naraparaju et al. [37] oxidised a 12Cr martensitic steel which had been peened on one side at 750 °C. A chromia film was not observed to grow on either side but a higher Cr concentration was observed in the oxide grown on the shot peened side compared to the non shot peened side. The overall scale thickness was also found to be lower on the shot peened side. On low Cr ferritic steels, a reduction in grain size is detrimental to oxidation [30].

Peng et al. [38] isolated the effect of grain refinement by shot peening by depositing a 30µm nanocrystalline layer of metal of almost identical composition onto the surface of 304 stainless steel.

The deposited layer featured grains approximately 12 nm in diameter in the plane normal to the growth direction to mimic the effect of increased dislocation density in the work hardened zone of a shot peened material. The grain size of 304 stainless steel is approximately 20 µm. It was found that the as received 304 SS experienced breakaway oxidation in wet environments whereas the coated 304 SS followed parabolic kinetics in all environments.

Various studies have observed stress induced martensite formation in the work hardened zone of shot peened materials [17, 39, 40]. Yu et al. found this to occur at mechanical twins whose frequency increased with increasing deposition energy, decreasing ball diameter and proximity to the surface. The increase in hardness measured in the affected zone was attributed to martensitic transformation, high dislocation density and grain refinement. The disarrayed structure of a work hardened material represents an area of high energy and therefore recrystallisation may occur at higher temperatures after extended periods of time reducing the benefit of shot peening [17]. There is evidence that recrystallisation of the work hardened zone occurs after extended durations at temperatures higher than 700 °C, reducing the continued ability of the alloy to form a protective Cr rich oxide [27].

The current study deals primarily with pickled tube whose surface microstructure resembles that of the bulk alloy. However, Super 304H tube with shot peened inner surface is included as a direct comparison of oxidation behaviour.

2.2.2.3 Effects of Surface Preparation on Oxidation

The techniques employed by many researchers are to abrade the surfaces of samples prior to oxidation. This is usually the case when coupons are taken from a larger piece of material and abrasion is required to obtain homogeneity between the surfaces of each sample. As with shot peening, abrasion alters the near surface structure of the material and therefore will likely deviate from the growth kinetics of a “pure”, un-worked surface [41].

Austenitic alloys are particularly sensitive to surface condition. This makes direct comparison of the oxidation behaviour difficult. There are several surface preparation methods researchers might employ, which all produce different levels of deformation in the near-surface substrate. From most deformation to least deformation these are proposed to be: shot peening, coarse grinding, fine grinding, polishing, electro-polishing, pickling. Researchers may introduce an annealing step during or at the end of sample preparation. This is with the aim of normalising grain structure and reducing deformation, such that annealed samples often show oxidation behaviour in the region of polished to pickled samples.

A review of the literature suggests the oxidation resistance generally follows a similar trend (with a shot peened surface being the most oxidation resistant, and a pickled surface being the least). Austenitic steel boiler tubes, which are the focus of the current research, are most commonly used with the inner (steam-side) surface pickled. These alloys generally form duplex oxides – an Fe rich outer oxide, and inner spinel oxide containing the constituent elements of the bulk alloy [42, 43]. In contrast, the oxide grown on shot peened or ground samples is usually a thin protective oxide of either Cr_2O_3, or Cr_2O_3 underneath a slightly less protective spinel such as $FeCr_2O_4$ or $MnCr_2O_4$. The latter was found on finely ground samples of Type 304 alloy oxidised in air at 700 °C for 80 hours by Botella et al. [44]. The authors did observe infrequent Fe rich nodules (similar to what would be seen in early oxidation of the pickled alloy) that took the form $Fe_{2-x}Cr_xO_3$.

Dudziak et al. [45] investigated the effect of surface finish on the oxidation of 347HFG and Super 304H austenitic steels. The authors oxidised as-received (pickled), ground (600 grit), and polished tube section samples at 600 and 700 °C in deoxygenated steam. They observed the pickled samples to exhibit the largest mass gain, followed by polished and then ground. The reduced mass gain on polished and ground samples was attributed to surface deformation, although no cross-sectional analysis was undertaken to substantiate this.

Jansson et al. [46] compared the oxidation resistance of ground and pickled samples on several grades of steel in steam between 500 and 800 °C. The authors reported ground samples to exhibit lower mass gain than pickled samples. However, after extended periods above 700 °C the authors observed inverted behaviour on 18/11 alloys – ground samples recorded a higher mass gain than pickled samples. The authors attributed this change in behaviour to recrystallisation at the alloy surface. No mention was made of chromium volatilisation. However, at 700 and 800 °C volatilisation of chromium in the form of $CrO_2(H_2O)_2$ was likely to be influential on the ground samples, whose initially-formed Cr rich oxide would have been fully exposed to the oxidising environment (see Section 2.3.3.3).

2.2.2.4 Element Depletion

Boiler tube steels rely on a continuous protective oxide film for steamside oxidation protection, ideally Cr_2O_3. This is facilitated by selective oxidation of chromium from within the bulk alloy. However this only occurs if there is sufficiently high chromium concentration to favour formation of Cr_2O_3 over less protective Fe-Cr spinel or iron oxides [47]. Selective oxidation of chromium results in a corresponding depletion of the element in the underlying alloy that tends to expand with time [48]. A concentration gradient will exist that is determined by the diffusion coefficient of chromium in the alloy and the oxidation kinetics. A lower limit of 18.5 wt.% Cr surface concentration has been determined for Cr_2O_3 formation on partially depleted 20Cr25NiNb steel when oxidised at 850 °C [49].

The protective action of Cr_2O_3 growth on alloys that are able to grow the oxide will be threatened if the local surface concentration of chromium is depressed below the critical value., This may occur from localised spallation of the oxide layer, or chromium evaporation (discussed in Section 2.3.3.3). Pitting will occur in these locations [50] and internal oxidation of the alloy will continue to a depth at which the chromium concentration is again high enough to favour growth of a protective film. Experiments on 20Cr25NiNb stainless steel have shown that the local critical chromium concentration for protective layer formation to be approximately 16 wt.% between 750 and 900 °C [50]. Subsequent research indicates that an alloying addition of 18.5 wt.% Cr is required to resist pitting and oxidise under a parabolic regime in dry conditions [49].

Grain size is thought to increase the critical concentration for healing layer formation [51]. This suggests grain boundary diffusion is significant in oxidation protection of high temperature alloys, in agreement with evidence of slower kinetics in fine grained stainless steels compared to coarse grained equivalents [42]. Element depletion is well documented in the research of other workers [52].

Austenitic steels are particularly prone to sensitisation when heat treated between 550 and 900 °C. It has been shown [53] that Cr rich $M_{23}C_6$ carbides precipitate at austenite grain boundaries. This causes chromium depletion and reduces the available surface chromium content to below that required to create a protective film. Researchers therefore avoid annealing in this temperature range during sample preparation [30, 54].

2.2.2.5 Influence of Laboratory Test Factors

The influence of laboratory test procedures on the oxidation of boiler steels has previously been reviewed by Osgerby and Quadakkers [55]. The authors suggest that, with regards to oxidation by a humid carrier gas, the following test parameters may be adjusted in the laboratory:

- ‘Once-through’ or re-circulating steam;
- 100% steam or argon carrier gas;
- Flow rate;
- Pressure;
- Continuous or discontinuous exposure;
- ‘Chemistry’ of water supply; and
- Heat flux.

Of particular interest to the current research is the influence of steam flow rate on oxidation.

Asteman et al. [56] reported that the oxidation kinetics of polished 304L samples increased with increasing water vapour flow rate. The effect was most noticeable at 600 and 700 °C. The authors partially attributed the increase in kinetics to chromium volatilisation in the form of $CrO_2(H_2O)_2$. This was because the effect of flow rate was limited at both 500 °C (where chromium volatilisation is not expected to occur) and 800 °C (where chromium volatilisation was so great that flow rate had less of an influence on oxidation). A following study confirmed a similar behaviour on Type 310 steel. However, the authors noted that Type 310 steel offered slightly better protection than 304L, citing the higher chromium content and lower associated effect of volatilisation [57].

2.2.3 Oxidation Kinetics

The kinetics of oxidation are often difficult to model for many alloys. However, they can be calculated by either monitoring the mass change, or the thickness of each, or all of the oxide layers. Mass change can be monitored in-situ using thermal gravimetric analysis (TGA) rigs, or post oxidation by weighing samples before and after oxidation. Oxidation rates calculated using oxide thicknesses require the sample to be sectioned. The benefit of calculating kinetics in this manner is thickness data from individual layers may be compiled to give the kinetics of each oxide.

An overview of common oxidation rate laws is provided in Appendix A. This section will focus on how oxidation kinetics have been applied in the literature.

Researchers analysing ex-service tubes or long term test loops often assume that the oxidation of austenitic steels follows parabolic kinetics according to:

$$\xi^2 = k_p t + c \qquad \textbf{(2-2)}$$

where k_p is the parabolic rate constant [m^2s^{-1}] and the y-intercept, c, denotes oxide thickness [m^2] at t = 0 s. Figure 2.7 shows parabolic curves fitted to several different grades of austenitic steel oxidised in steam between 620 and 650 °C [58]. The data clearly show the benefit of both high Cr content and grain refinement on oxidation resistance, although it is questionable as to whether the data fit parabolic relationships with a high level of confidence.

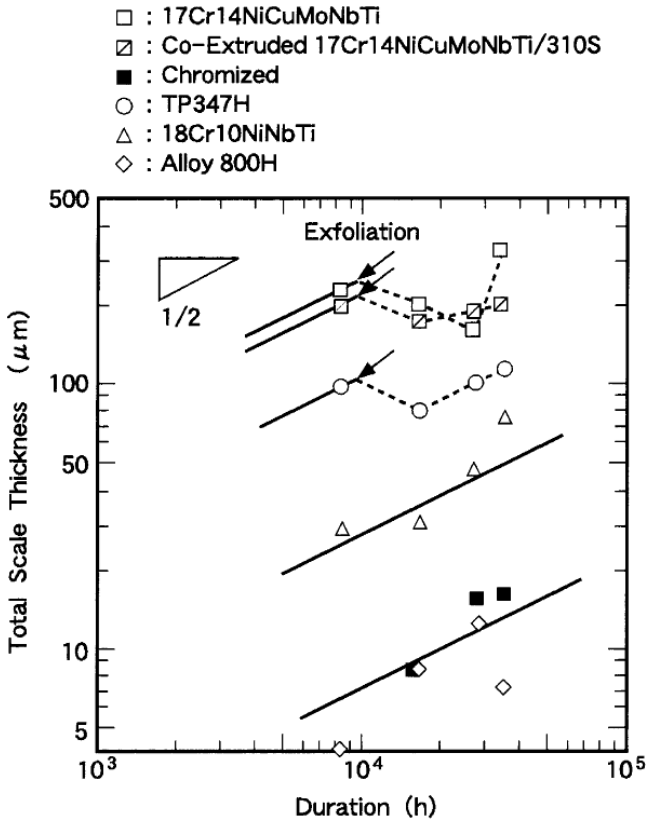

Figure 2.7 – Comparison of coarse grained, fine grained and high Cr austenitics scale growth at 620-650 °C [58].

Assuming parabolic kinetics allows for comparison of the parabolic rate constant with other researchers' data, where a lower k_p value denotes slower oxide growth. k_p values may be compared using an Arrhenius plot of k_p verses $1/T$ according to:

$$k_p = k_0 e^{\left(-Q/RT\right)} \qquad \textbf{(2-3)}$$

where Q is the apparent activation energy, T is temperature K and R is the molar gas constant. Wright and Dooley composed an Arrhenius plot for oxide growth on austenitic steels with less than 20 wt.% Cr [42]. In Figure 2.8, k_p values are derived from mass gain measurements and show a range of between 3 x 10^{-14} and 2 x 10^{-15} $g^2cm^4s^{-1}$ at 650 °C for fine grained steels. The coarse grained austenitics are shown to consistently oxidise at a faster rate than fine grained austenitics.

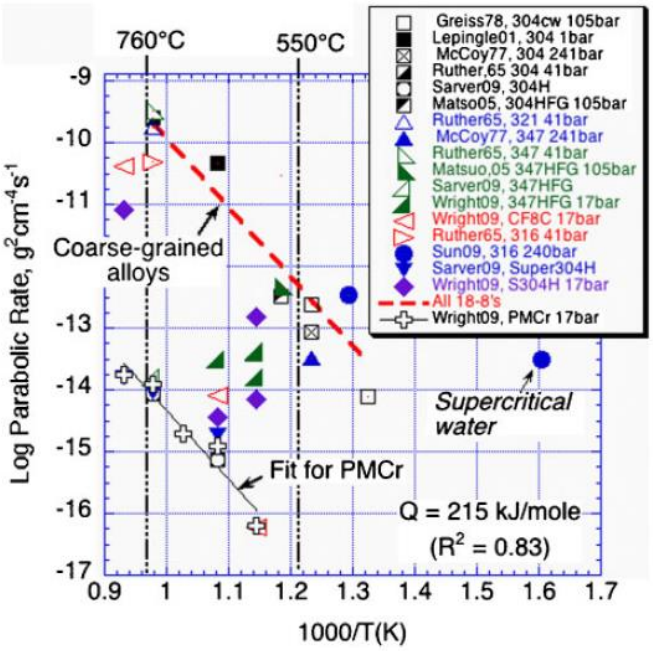

Figure 2.8 – Arrhenius plot of parabolic rate constants for the oxidation of <20 wt.% Cr austenitic steels in steam, after [42].

Otsuka calculated parabolic rate constants for the growth of Cr_2O_3 on 25Cr15Ni in deoxygenated steam for 1000 hours between 500 and 900 °C [59]. Figure 2.9 shows that the oxidation rate increases with temperature.

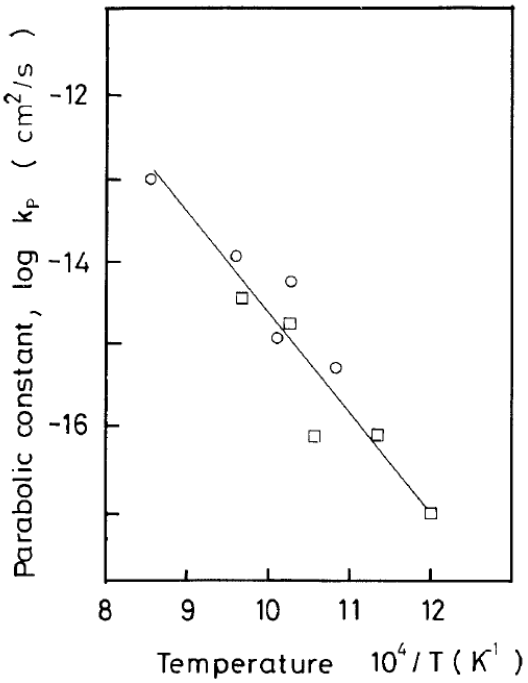

Figure 2.9 – Parabolic rate constants for Cr_2O_3 growth on coarse grained 21and 25 wt.% Cr – 15 wt.% Ni austenitic steels in steam. (□) 21 wt.% Cr, (○) 25 wt.% Cr, after Otsuka et al., [59].

The parabolic rate constants in Figure 2.9 can be compared with those of Cr_2O_3 growth at different temperatures in dry conditions, compiled from several sources by Taylor et al., [60] (Figure 2.10).

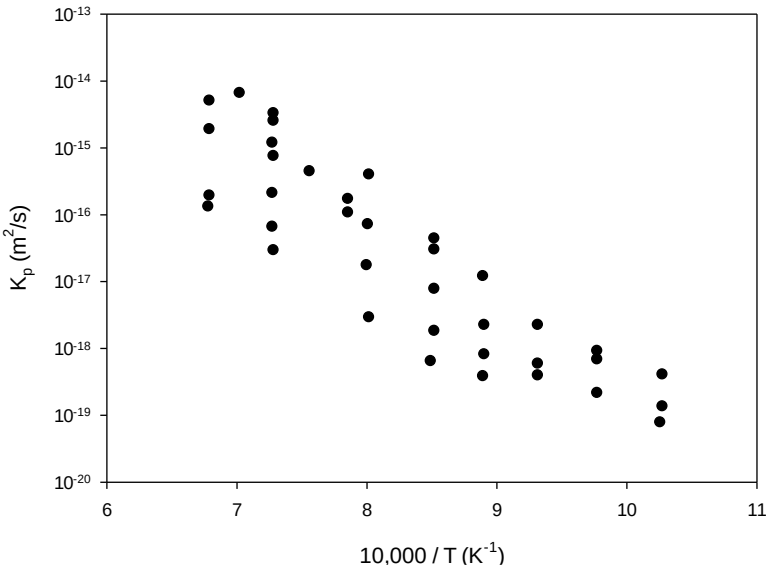

Figure 2.10 – Plot of k_p values of chromia growth on different metals after oxidation in dry atmospheres (●), reproduced after Taylor et al. [60].

The rate constants in Figure 2.9 align well to those in Figure 2.10 at equivalent temperatures (noting the different y-axis units). This is somewhat surprising as it is known that a steam environment accelerates oxide growth [61]. Furthermore, Otsuka et al. used raw weight gain data and converted to thickness for their parabolic rate constant calculations. They also assumed the oxide to be 100% Cr_2O_3, despite the authors stating that the oxide also contained Fe_3O_4. The presence of less protective Fe_3O_4 should reduce values of the parabolic rate constants, as they do not represent 'pure' Cr_2O_3 growth. A limitation of calculating parabolic rate constants from weight gain is that it only provides a representative oxidation rate for total oxide growth on an alloy. Using oxide thickness measurements instead may have allowed the authors to calculate parabolic rate constants for each oxide phase. This would also allow for a more direct comparison with the values in Figure 2.10. Generally however, this is only achievable if each oxide phase is present as a discrete layer.

The activation energy over a given temperature range can be calculated by taken the log of equation (2-4) to give:

$$\ln k_p = \ln k_0 - \frac{Q}{R} \cdot \frac{1}{T} \qquad \textbf{(2-4)}$$

where Q is the apparent activation energy and R is the molar gas constant. The activation energy, Q, is given by the gradient of the linear regression line over a temperature range. It follows that if a change in gradient (and therefore activation energy) is observed above a certain temperature, this would indicate a change in the rate limiting process for the reaction. For example, from cationic diffusion to anionic diffusion. Montgomery and Karlsson calculated a single activation energy for the oxidation of fine grained TP347 in steam. Values of Q = -164 KJmol^{-1} and k_0 = 7.94 x 10^{-7} µm^{2}h^{-1} were calculated over the temperature range 525 – 675 °C [62].

Viswanathan [63] commented on two contrasting studies on the oxidation 0-2%Cr and 9-12%Cr steels: Wright and Pint observed the low Cr alloys to exhibit two distinct activation energies above and below 500 °C and a single activation energy for 9-12%Cr steels over the temperature range studied (290-700 °C). In contrast, Watanabe et al., observed low Cr steels STBA24 and HCM2S (T23) to display a single activation energy over the entire temperature range of 560-700 °C, whereas 9-12Cr alloys NF616 (T92) and HCM12A (T122) exhibited bilinear behaviour above 600 °C (Figure 2.11). It should be noted that the Watanabe et al. study was not conducted below 560 °C and therefore was not able to corroborate the change in activation energy of 0-2%Cr steels below 500 °C, as observed by Wright and Pint.

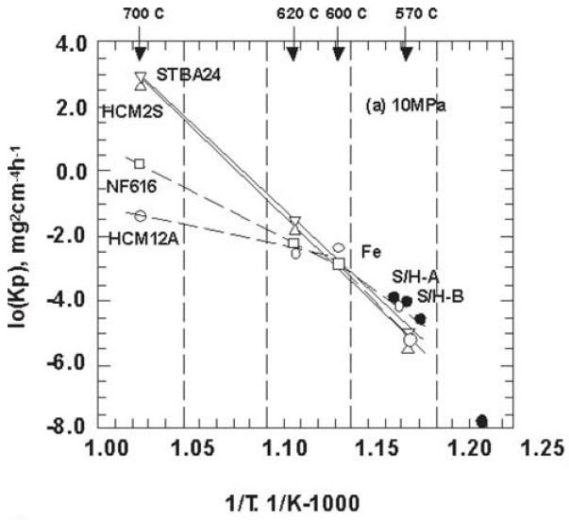

Figure 2.11 – Arrhenius-type plot of k_p values of ferritic steels oxidised in steam at 10 MPa. The figure shows a change in observed activation energy above 600 °C for 9-12%Cr steels, compared with a single activation energy across the entire temperature range for 2.5%Cr steels [63].

An important observation is that both studies assumed parabolic kinetics in the calculation of rate constants. This is common practice for comparison purposes. However, if the raw mass gain data does not fit a parabolic curve with a high level of confidence, the value of k_p may have limited reliability in describing the kinetics. This will have a knock-on effect on the calculation of activation energies. Forcing parabolic kinetics could be one explanation as to why there is a large amount of scatter in the

k_p values for fine grained austenitic steels in Figure 2.8. It should be noted that data were taken from experiments conducted over a range of oxidation times and pressures.

Oxidation kinetics may deviate from parabolic kinetics to sub-parabolic kinetics if the oxidation process is not governed by ion diffusion through the oxide layer. Atkinson et al. [64] observed this to be true for the oxidation of pure nickel between 500 and 800 °C for up to 200 hours. The authors attributed sub-parabolic kinetics to oxide grain growth during oxidation. This effectively reduced the density of grain boundaries (short-circuit diffusion paths), which dominated as the rate controlling process below 1100 °C.

A study relevant to the current research programme was conducted by Dudziak et al. on 347HFG, Super 304H, and HR3C in deoxygenated steam at 600 and 700 °C [45]. The authors reported Super 304H and HR3C to follow parabolic or sub-parabolic kinetics for the experiments carried out on polished, ground, and pickled samples. Unfortunately, the authors did not calculate parabolic rate constants or the order of reaction, n, for the experiments.

Grain size, chromium content, and surface finish are known to influence oxidation kinetics of austenitic steels. A number of studies have reported coarse grained 18/8 austenitics to initially follow parabolic kinetics before assuming a more linear relationship [38, 65].

Kim et al. [29] found the breakdown of Cr_2O_3 into less protective Fe rich oxides to account for a deviation in parabolic kinetics of a coarse grained Cu containing 304 steel at 700 °C in air + 20% H_2O. In contrast, the fine grained version of the steel retained parabolic kinetics in line with those accepted for Cr_2O_3 growth for the full oxidation period of 28 hours. Parabolic rate constants were calculated by the authors for times up to 12 hours This makes comparison to rate constants calculated over much longer durations difficult.

The oxidation rate of fine grained austenitic steels has been reported to transition from an initially faster rate, to a greatly reduced one, following formation of a Cr-rich healing layer at the internal oxidation front [59], [66], [67]. This is significant for laboratory experiments as complete healing layer formation has been observed after a few hundred hours – a time range over which many laboratory experiments are conducted.

Otsuka and Fujikawa reported a drop in oxidation rate because of healing layer formation on 347HFG after the first oxidation interval of 500 hours at 650 °C [68]. Hales acknowledged the oxidation rate reduction effect of a healing layer on the kinetics of 316 steel oxidised in CO_2–2%CO [69]. A similar effect was found on ground samples of AISI oxidised in air at 1000 °C for up to 100 hours. Karimi et al.

[70] reported that a linear kinetic relationship was followed for the first 10 hours followed by a slower parabolic relationship. However, this was attributed to a change in oxide species during the oxidation period.

The formation of a healing layer, and the effect of it on oxidation kinetics suggests that care must be taken when applying a single kinetic regime to a data set from zero time. For example, the sub-parabolic regimes proposed by Dudziak et al. [45] above may correspond to two distinct oxidation regimes, before and after healing layer formation on the pickled alloys. If using rate equations in predictive modelling, fitting a single kinetic regime to a data set that would be more accurately described by more than one kinetic regime may lead to over or under prediction of oxide growth over the extrapolated period.

This was considered by Otsuka et al. [59]. The authors fit a single parabolic regime to Cr_2O_3 growth on HR3C (see Figure 2.9), but no attempt was made to calculate parabolic rate constants for oxide growth on fine grained 18Cr steels. This is because the authors observed a change in oxidation rate because of healing layer formation and concluded that the reaction kinetics could not be represented by a single parabolic rate constant.

Huntz et al. [71] observed polished AISI 304 steel to follow two distinct regimes during oxidation at 900 °C for 50 hours in O_2. The parabolic rate constant for the first stage of growth in Figure 2.12 fits well to the experimental data and was validated by the authors against rate constants calculated for Cr_2O_3 growth and k_p values found in the literature. The second stage, however, produces a less convincing fit to parabolic kinetics, and was assumed without calculation of the order of reaction, n.

A number of researchers have further developed rate equations to more accurately describe either the oxidation rate over a specific time range during the oxidation period [72], or to describe the oxidation kinetics where a change in rate is expected [67, 73]. It has been shown for stainless steel oxidised in CO_2 that misinterpretation of early stage kinetics can result in inaccuracies when extrapolating predicted oxide growth beyond experimental data [74]. Other researchers have calculated kinetics using only the latter stage of the oxidation period to avoid the initial oxidation regime from influencing the calculated rate constants [75]. This section has explored how oxidation kinetics are commonly used in the field of oxidation, and highlighted the need for careful consideration of how well data fits a particular regime.

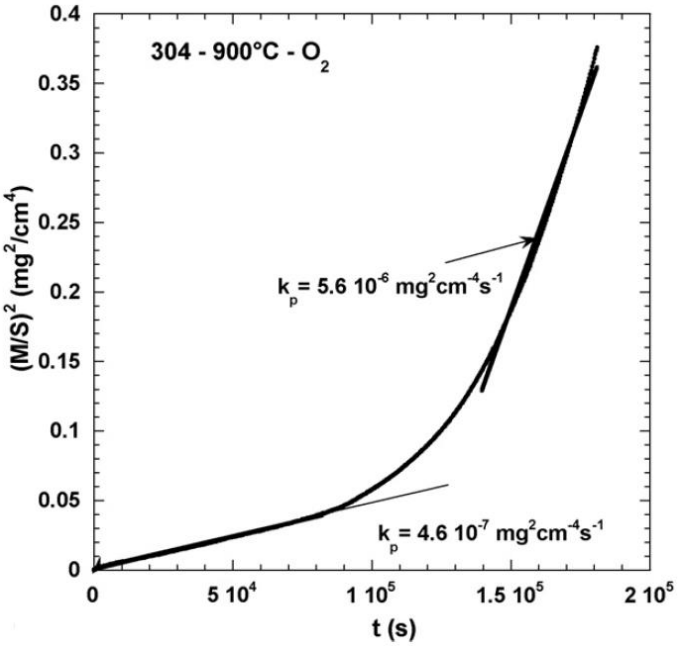

Figure 2.12 – Linear curve fitting to determine the parabolic rate constants for two stages of oxidation of polished AISI 304 samples oxidised in O_2 at 900 °C for 50 hours. The first stage growth appears to fit the experimental data with a higher level of confidence than the second stage growth. After Huntz et al. [71].

2.3 Oxidation Behaviour as a Function of Environment

2.3.1 Introduction

It becomes difficult to predict how alloys containing more than two or three elements will behave in a given oxidising environment. Each element has a different affinity to oxygen and therefore diffusion-based models become complex. Minor element additions may accumulate as metal or oxide at the base of the main scale, or influence the stability of certain phases in the oxide or metal as with the addition of tungsten to P92 martensitic steel over P91 [3]. The issue is compounded when considering the many environments that engineering alloys are exposed to at high temperature, such as air, steam, water vapour, flue gas and CO_2.

High temperature oxidation in steam is characterised by faster oxidation rates than in air, and different, often less protective oxide morphology. Both kinetics and morphology are heavily influenced by alloy composition (and associated crystal structure), grain size, steam parameters (such as pressure and flow rate), and surface finish [40, 55, 76]. The latter of which affects some types of alloy more than others, and has implications on sample preparation during laboratory tests [40].

Specimen geometry is even known to affect oxidation behaviour [77], which is relevant when considering heat exchanger tubes of differing sizes.

Nevertheless, it is generally agreed that the addition of chromium to an alloy has the largest effect on oxidation resistance. An increasing chromium content eventually affords the formation of a complete Cr_2O_3 film at the alloy/oxide interface. The relative ranking of alloys with respect to oxidation resistance is therefore heavily dependant on chromium concentration. Viswanathan proposes the following order from most to least resistant, with grouped alloys exhibiting similar performance: Inconel 740, Alloy 230, HR120 and HR6W (high Ni high Cr), HR3C (high Cr), T347HFG and Super 304H (18Cr8Ni), T91 and T92 (9Cr), and T23 (2.25 Cr) [63].

The following sections review the oxidation behaviour of alloy grades used in coal-fired power generation in air and steam, which are the two environments relevant to the current research. Thermal cycling is known to affect oxide growth and spallation. However, as the current study focuses on isothermal oxidation this is not explored in further detail.

2.3.2 Air

2.3.2.1 Iron-Chromium Alloys

The oxidation of iron-chromium alloys has been reviewed previously [33]. Increasing the chromium content in the binary system, in general, decreases the rate of oxidation over a broad temperature range. In dry conditions, oxidation usually begins with an induction period of varying length depending on composition. This is followed by a period of parabolic or near-parabolic kinetics which may continue or give way to accelerated oxidation depending on temperature and percentage of chromium in the alloy. Scales normally consist of Cr_2O_3 and Fe_2O_3, with a thinner, more uniform and less porous scale favouring higher chromium alloys and lower oxidation temperature [78].

2.3.2.2 Air Oxidation of Low Chromium Ferritic and Martensitic Steels

Ferritic steels, typically those with less than 9%Cr (often 1 ¼ Cr and 2 ¼ Cr) have relatively poor oxidation performance, and are restricted in use to low temperature sections of plant boilers such as waterwalls, although historically also headers [11].

Trindade et. al. [30] found low chromium (<2.5 wt. %) steels oxidised at 550 °C for 72 hours in air to develop an outer scale of Fe_2O_3 at the scale/gas interface and Fe_3O_4 at the outer oxide/spinel interface. The inner scale was reported to consist of a mix of $FeCr_2O_4$ spinel that coexisted with Fe_3O_4. Cr_2O_3 was also identified in some amount. Intergranular oxidation into the substrate via inward oxygen diffusion also occurred.

The compositions of some common ferritic and martensitic steels are listed in Table 2-1.

Table 2.1 – Compositions of some common ferritic and martensitic steels [11].

		Specification		Chemical Composition (wt.%)											
	Steels	**ASME**	**JIS**	**C**	**Si**	**Mn**	**Cr**	**Mo**	**W**	**Co**	**V**	**Nb**	**B**	**N**	**Others**	**Manufacturers**
1-1/4 Cr	T11	T11	…	0.15	0.50	0.45	1.25	0.50	…	…	…	…	…	…	…	…
	NF1H	…	…	0.12	…	…	1.25	1.00	…	…	0.20	0.07	…	…	…	Nippon Steel
2Cr	T22	T22	STBA24	0.12	0.30	0.45	2.25	1.00	…	…	…	…	…	…	…	…
	HCM2S	T23	STBA24J1	0.06	0.20	0.45	2.25	0.10	1.6	…	0.25	0.05	0.003	…	…	Sumitomo
	Tempaloy F-2W	…	…	…	…	…	2.00	0.60	1.0	…	0.25	0.05	…	…	…	NKK
9Cr	T9	T9	STBA26	0.12	0.60	0.45	9.00	1.00	…	…	…	…	…	…	…	Vallourec Mannesman
	HCM9M	…	STBA27	0.07	0.30	0.45	9.00	2.00	…	…	…	…	…	…	…	Sumitomo
	T91	T91	STBA28	0.10	0.40	0.45	9.00	1.00	…	…	0.20	0.08	…	0.05	0.8Ni	Vallourec Mannesman
	E911	…	…	0.12	0.20	0.51	9.00	0.94	0.9	…	0.20	0.06	…	0.06	0.25Ni	Sumitomo
	NF616	T92	STBA29	0.07	0.06	0.45	9.00	0.50	1.8	…	0.20	0.05	0.004	0.06	…	Nippon Steel
12Cr	HT91	(DIN X 20CrMoV121)		0.20	0.40	0.60	12.00	1.00	…	…	0.25	…	…	…	0.5Ni	Vallourec Mannesman
	HT9	(DIN X 20CrMoWV121)		0.20	0.40	0.60	12.00	1.00	0.5	…	0.25	…	…	…	0.5Ni	Vallourec Mannesman
	Tempaloy F12M	…	…	…	…	…	12.00	0.70	0.7	…	…	…	…	…	…	NKK
	HCM12	…	SUS410J2TB	0.10	0.30	0.55	12.00	1.00	1.0	…	0.25	0.05	…	0.03	…	…
	TB12	…	…	0.08	0.05	0.50	12.00	0.50	1.8	…	0.20	0.05	0.300	0.05	0.1Ni	…
	HCM12A	T122	SUS410J3TB	0.11	0.10	0.60	12.00	0.40	2.0	…	0.20	0.05	0.003	0.06	1.0Cu	Sumitomo
	NF12	…	…	0.08	0.20	0.50	11.00	0.20	2.6	2.5	0.20	0.07	0.004	0.05	…	Nippon Steel
	SAVE12	…	…	0.10	0.30	0.20	11.00	…	3.0	3.0	0.20	0.07	…	0.04	0.07Ta	Sumitomo

2.3.2.3 Air Oxidation of Austenitic Steels

For a Cr-Ni-Fe alloy, Cr_2O_3 is the thermodynamically stable binary oxide in air atmospheres, although growth kinetics usually allow the formation of other oxides. Initial oxidation of austenitics appears to be very rapid until a protective layer has built up. This layer is usually high in chromium and is composed of Cr_2O_3 with a small amount of Fe_2O_3, possibly existing as a solid solution. Further oxidation quickly leads to separation into distinct layers [33].

The outer layer on several stainless steels oxidised in air has been reported as Fe_2O_3, mainly on ground or polished samples [30, 56, 70, 71, 79], but also on pickled samples [43, 80]. Tanabe and Imoto [81] analysed the oxides grown on both as-received and polished samples of 316 stainless steel between 600 and 800 °C. They reported thin Cr rich oxides to initially form on polished samples, before iron rich duplex oxide nucleated over the surface, spreading until it gained complete coverage. The authors suggested that once the duplex oxide begins to nucleate, it expands laterally at a rapid rate until the surface is completely covered in iron rich oxide. This was because of faster diffusion of iron ions in iron oxide over chromium ions in chromium oxide. They also suggested that migration of metal ions through the oxide becomes the rate limited step, and parabolic kinetics prevail. Figure 2.13 shows the

nucleation and growth of iron rich oxide of a polished sample. Interestingly, the authors observed iron rich oxide nucleation to be indiscriminate in location on the surface, rather than favouring the centre of grains away from grain boundaries.

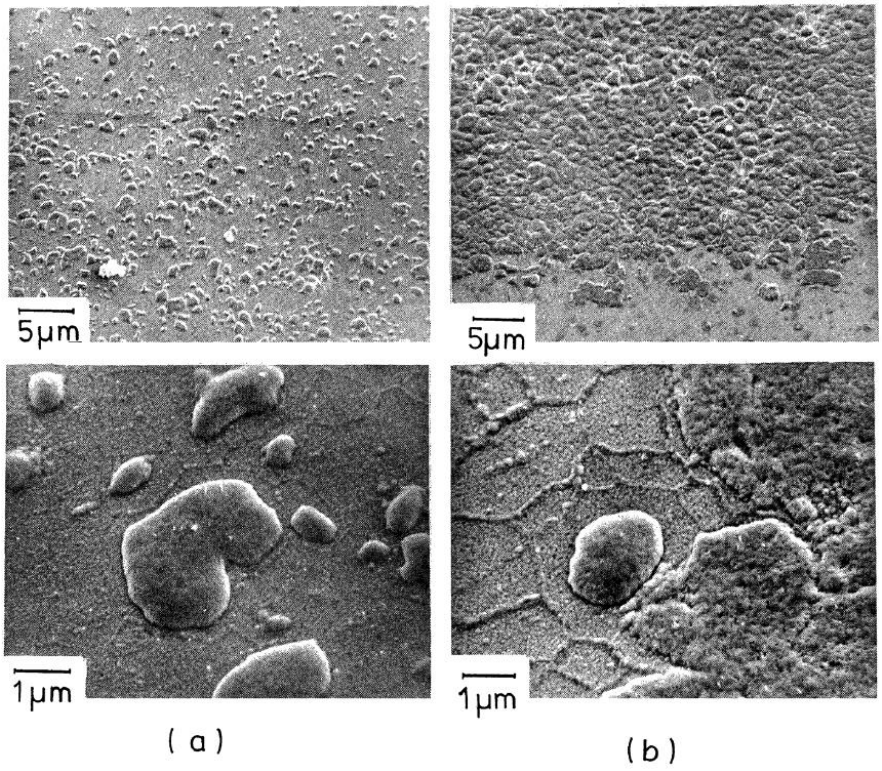

Figure 2.13 – SEM image of (a) nucleation, and (b) growth of iron Fe rich oxide over Cr rich oxide on a polished sample of 316 stainless steel following oxidation in air at 800 °C for 8 hours, after.

In contrast to the polished samples, Tanabe and Imoto observed full coverage of iron rich oxide on as-received samples after as little as 4 hours oxidation. They proposed the mechanism reproduced in Figure 2.14, in which iron rich oxide forms immediately on the as-received sample. This is compared with an initial formation of chromium rich oxide on the polished sample, before outward diffusion of iron ions facilities nucleation and propagation of duplex oxide.

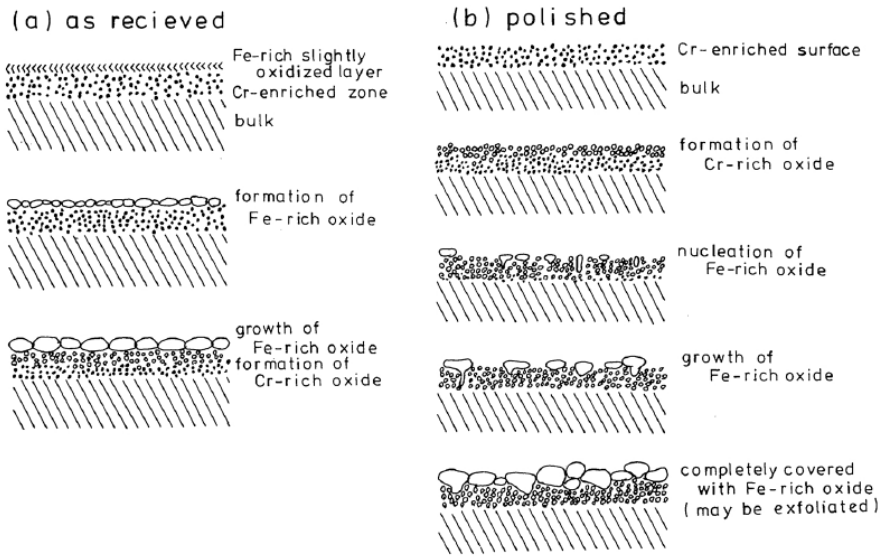

Figure 2.14 – Mechanism proposed by Tanabe and Imoto for oxide growth on as-received and polished samples of 316 stainless steel in air [81].

Simms [82], oxidised Super 304H and 347HFG austenitic steels in air between 600 °C and 700 °C for between 100 and 1000 hours. Super 304H was reported to grow a thin layer of chromium rich oxide dispersed with an increasing number of nodules as oxidation time and temperature were increased. Alloy grain boundaries separated nodules until the extent of coverage led to coalescence and a complete surface scale (after 250 – 500 hours). Nodule composition was reported to consist of an external iron rich oxide and internal iron-chromium spinel, the interface between the inner and outer scale indicating prior grain boundary. Oxide kinetics and morphology was similar for 347HFG. However, nodular growth was less pronounced and a complete surface scale was attained faster.

The inner layer of the duplex oxide that forms on austenitic steels generally contains the constituent elements of the underlying alloy. For the steels of interest in the current project, these are iron, nickel, and chromium, and to a lesser extent, manganese and silicon. Super 304H also contains copper at up to 3 wt.%. Recently, studies have investigated the oxide phases present in this spinel layer. Karimi et al. [70] found the inner oxide that grew on AISI 304 austenitic steel to comprise of the spinels $Mn_{1.5}Cr_{1.5}O_4$ and $FeCr_2O_4$. Cr_2O_3 and SiO_2 were also identified but not as complete layers. Trindade et al. observed Cr_2O_3 and $FeCr_2O_4$ to grow on polished samples of fine grained TP347 at 750 °C [30].

By employing a TEM, Tang et al. [83] were able to use EDX to identify the oxide phases at the alloy/oxide interface of 304L samples oxidised in oxygen at 600 °C. They found the oxide to form a corundum-type oxide of the form $(Cr,Fe,Mn)_2O_3$, and reported nickel to be in metallic form within the oxide scale. The authors were able to identify a corundum-type oxide of the form $(Fe_{1-x}Cr_x)_2O_3$, with varying Fe and Cr ratios at the alloy/oxide interface. Oxide of this type would be less protective than

pure Cr_2O_3. It should be noted that the samples were ground in the Tang study. This would have promoted Cr rich oxide growth. It is likely that if a corundum-type oxide at the alloy/oxide interface forms on pickled 347HFG and Super 304H 300-series austenitic alloys, it would have a higher concentration of Fe. It may also be more localised at grain boundaries and result in a less protective oxide.

Manganese has a similar affinity for oxygen to chromium. In low oxygen partial pressures it has been found in the form of Mn rich oxide at the oxide/gas interface on 316 stainless steel [81], and as Mn rich crystallites on top of Cr_2O_3 on 310 steel oxidised in CO_2 [75]. Silicon oxide has also been found at the alloy/oxide interface, primarily at grain boundary locations, and often as discrete particles rather than a complete layer [43].

There is debate as to the form of nickel in the spinel following oxidation in air. Some researchers reporting it to oxidise, and others reporting it to remain in metallic form [83]. Nickel is less reactive than chromium and iron, and the form of it is probably sensitive to the local equilibrium conditions in any given experiment.

Researchers have also found copper present in both metallic [54], and oxidised [37, 84], form. The copper in Super 304H is also expected to remain in metallic form during oxidation. Swaminathan et al. found copper to exist as fine metallic precipitates in the spinel of a copper containing 304H alloy following oxidation in air at 650 °C for up to 1000 hours [54].

The compositions of some common austenitic steels are listed in Table 2-2.

Table 2.2 – Compositions of some common austenitic stainless steels [11].

	Specification		Chemical Composition (wt.%)											
	ASME	JIS	C	Si	Mn	Ni	Cr	Mo	W	V	Nb	Ti	B	Others
18Cr-8Ni	Tp304H	SUS304HTB	0.08	0.6	1.6	8.0	18.0	…	…	…	…	…	…	…
	Super 304H	SUS304J1HTB	0.10	0.2	0.8	9.0	18.0	…	…	…	0.40	…	…	3.0Cu, 0.1N
	Tp321H	SUS321HTB	0.08	0.6	1.6	10.0	18.0	…	…	…	…	0.50	…	…
	Tempalloy A-1	SUS321J1HTB	0.12	0.6	1.6	10.0	18.0	…	…	…	0.10	0.08	…	…
	TP316H	SUSTP316HTB	0.08	0.6	1.6	12.0	16.0	2.5	…	…	…	…	…	…
	TP347H	SUSTP347HTB	0.08	0.6	1.6	10.0	18.0	…	…	…	0.80	…	…	…
	TP347H FG		0.08	0.6	1.6	10.0	18.0	…	…	…	0.80	…	…	…
15Cr-15Ni	17-14CuMo		0.12	0.5	0.7	14.0	16.0	2.0	…	…	0.40	0.30	0.006	3.0Cu
	Esshete 1250		0.12	0.5	6.0	10.0	15.0	1.0	0.2	1.0	…	0.06	…	…
	Tempalloy A-2		0.12	0.6	1.6	14.0	18.0	1.6	…	…	0.24	0.10	…	…
20Ni-25Cr	TP310	SUS310TB	0.08	0.6	1.6	20.0	25.0	…	…	…	…	…	…	…
	TP310NbN (HR3C)	SUS310J1TB	0.06	0.4	1.2	20.0	25.0	…	…	…	0.45	…	…	0.2N
	NF707*		0.08	0.5	1.0	35.0	21.0	1.5	…	…	0.20	0.10	…	…
	Alloy 800H	NCF800HTB	0.08	0.5	1.2	32.0	21.0	…	…	…	…	0.50	…	0.4Al
	Tempalloy A-3(a)	SUS309J4HTB	0.05	0.4	1.5	15.0	22.0	…	…	…	0.70	…	0.002	0.15N
	NF709(a)	SUS310J2TB	0.15	0.5	1.0	25.0	20.0	1.5	…	…	0.20	0.10	…	…
High Cr-High Ni	SAVE25(a)	SUS25J1HTB	0.10	0.1	1.0	18.0	23.0	…	1.5	…	0.45	…	…	3.0Cu, 0.2N
	CR30A(a)	SUS30J1HTB	0.06	0.3	0.2	50.0	30.0	2.0	…	…	…	0.20	…	0.03Zr
	HR6W(a)	SUS6J1HTB	0.08	0.4	1.2	43.0	23.0	…	6.0	…	0.18	0.08	0.003	…
	Inconel 617	SUS617J1HTB	…	0.4	0.4	54.0	22.0	8.5	…	…	…	…	…	12.5Co, 1.2Al
	Inconel 671(b)	SUS321J1HTB	0.05	…	…	51.5	48.0	…	…	…	…	…	…	…

2.3.3 Steam

2.3.3.1 Mechanisms of Oxidation in Steam

It has been known for many years that the oxidation behaviour of metals in atmospheres containing steam and water vapour differ to those of oxidation in dry atmospheres [85]. In humid atmospheres, several researchers have found lower alloyed steels to follow linear-like kinetics after an initial incubation period [86, 87] and produce scales of different morphology to those grown in dry conditions [88]. Oxidation in humid atmospheres promotes inward oxide growth [88]. Generally, increasing the chromium content of the alloy decreases the oxidation kinetics [88], as in dry atmospheres. Scales grown in humid atmospheres are generally more porous than those grown in dry atmospheres, and direct access of molecular water vapour has been suggested to increase the oxidation rate [89]. Enhanced through-scale cracking as a result of growth stresses during oxidation has been observed on P91 martensitic steel oxidised in water vapour which was thought to increase oxidant transport to underlying chromium depleted subsurface zones [90]. This has also been reported to affect Fe-Cr alloys of various Cr contents [91].

The volatile species $Fe(OH)_2$ has been suggested to account for the increased oxidation rate of P91 [89] and lower Cr steel [88] in atmospheres containing water vapour. Transport of $Fe(OH)_2$ from within

voids in the oxide scale in areas of low pO_2 to areas of higher pO_2 at the outer surface was thought to occur, where it forms mainly Fe_2O_3 [89]. Iron vapour species as a mechanism for oxidation in steam was proposed by Surman and Castle [92], who proposed the rate determining step in the oxidation of iron to be that of cation or anion solid state diffusion, or $Fe(OH)_2$ vapour phase diffusion from the metal/oxide interface to the oxide/gas interface. Volatile chromium species is thought to influence oxidation in humid environments and is considered later.

Fujii and Meussner [86] oxidised a variety of Fe-Cr alloys (0-25Cr) in Ar – 10% water vapour between 700 and 1100 °C. After the establishment of a duplex scale, linear kinetics were assumed for 0-15Cr alloys. They suggested that diffusion through the scale could not account for the increased rate and proposed that a dissociative process, illustrated in Figure 2.15, operates within voids between the outer oxide and spinel layers and that the rate is controlled by reactions at the oxide/gas interface.

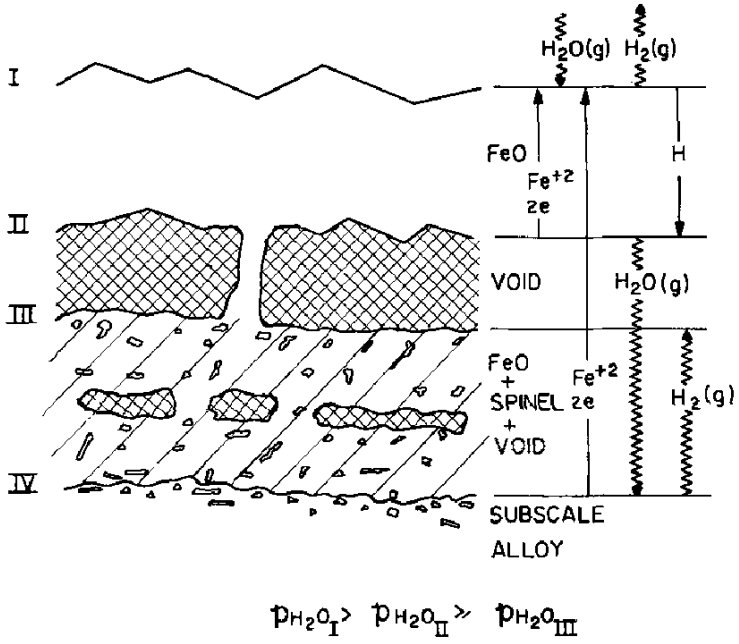

Figure 2.15 – Dissociative mechanism for gaseous species transport across voids after Fujii and Meussner [86].

The following processes were proposed [86]:

At interface I, water vapour is adsorbed and forms new FeO oxide through reaction with Fe^{2+} ions derived from interfaces II and IV, along with defects in the oxide and adsorbed hydrogen. The majority of the hydrogen desorbs back into the gas stream.

$$H_2O_{(gas)} \rightarrow H_2O_{(ads)}$$

$$H_2O_{(ads)} + Fe^{2+} + 2e^- \rightarrow FeO + Fe_{vac} + 2\oplus + H_{2(ads)}$$

$$H_{2(ads)} \rightarrow H_{2(g)}$$

$$H_{2(ads)} \rightarrow 2H^{*}_{(ox)}$$

Here Fe_{vac} is an iron vacancy, $\oplus$ is an electron defect and H^{*} is hydrogen dissolved within the oxide.

At interface II, dissociation of iron oxide makes transitions over the void possible. Oxide ions appear as adsorbed species and the permeating hydrogen permits these to form a carrier gas for oxygen transport through the void.

$$FeO + Fe_{vac} + 2\oplus \rightarrow Fe^{2+} + O^{2-}_{(ads)}$$

$$2H^{*}_{(ox)} \rightarrow H_{2(ads)}$$

$$H_{2(ads)} \rightarrow H_{2(gas)}$$

$$H_{2(ads)} + O^{2-}_{(ads)} \rightarrow H_2O_{(gas)} + 2e^{-}$$

The above reactions permit the formation of FeO at interface I and a similar process is expected at interface III. A small change in the composition of the spinel phase, favouring a higher concentration of iron is expected, such that

$$FeCr_2O_4 + 4FeO \rightarrow 2Fe_2CrO_4 + Fe^{2+} + 2e^{-}$$

Some researchers [91] have found the above mechanism to be unsuitable in explaining the rapid oxidation of alloys with Cr>15% when testing a series of Fe-Cr alloys in O_2 – 10% water vapour between 750 and 900 °C, and suggested an alternative mechanism, where cracks and pores in the protective chromia layer would increase local pO_2 and allow oxidation of iron to form a spinel type oxide. This oxide would be less effective than chromia at reducing the flux of iron outwards through the scale and an iron rich outer oxide would result [93].

Water vapour may have an effect on the defect structure and therefore many oxide systems. As water vapour reacts with the metal oxide it serves as a source of hydrogen which dissolves as protons into the scale. Water vapour may also have an effect on such defect dominated properties as diffusion controlled transport of the reactants through growing scales and high temperature creep [93].

Galerie et al. [94] have compared the effects of oxidation in oxygen and in water vapour focusing on the effect of major point defects and the effect that the acidity of the oxide surface had. Water vapour was considered to enhance the oxidation of metals provided that oxygen was one of the most mobile species in the oxide formed. The solubility of hydrogen was found to be of significance as the metals

most affected by water vapour were those that showed good hydrogen solubility. Hydroxyl species easily cover an oxide surface when exposed to steam and it is the transport of oxygen through the oxide via these hydroxyl species that is the rate determining step of oxidation. There are few oxygen species however. These are formed from OH particles which become disassociated at the O-H bond. For this to occur, the surface must exhibit acidic properties and it has been shown that pure metal species which did not have acidic oxides had a reduced oxidation rate in water vapour. For acidic oxides, Galerie *et al.* have reported that the surface OH decomposition rate was high enough to rule it out as the rate controlling factor for oxidation [94].

2.3.3.2 Oxygen Partial Pressure

As seen previously, for the reaction

$$aM + \frac{b}{2}O_2 \rightarrow M_aO_b$$

the dissociation pressure of the oxide is obtained from the equilibrium constant for this reaction:

$$\ln K_1 = \ln\left[(pO_2)^{b/2}_{dissoc}\right] = -\Delta G_1^0/(2.303RT) \qquad \textbf{(2-5)}$$

where $-\Delta G_1^0$ is the Gibbs free energy for the reaction (Jmol^{-1}), R is the universal gas constant (JK^{-1}mol^{-1}) and the activities of the solid species are assumed to be unity. It follows that the reaction will proceed from left to right if the oxygen partial pressure (pO_2) in the gas, be it air or steam, is higher than the dissociation pressure of the oxide.

In plant, the level of dissolved oxygen in feed water is kept to a minimum to reduce the amount of oxygen available to react with the tube surfaces. Typical values are in the range of 10 ppb dissolved oxygen. If it is assumed that there is no dissolved oxygen in the feed water, the only oxygen available for oxidation comes from dissociation of H_2O molecules at the service temperature via

$$H_2O(g) = H_2(g) + 1/2\, O_2(g) \qquad \textbf{(2-6)}$$

The oxygen partial pressure for steam is then

$$K_{steam} = pO_2^{1/2}\, pH_2/pH_2O \qquad \textbf{(2-7)}$$

where K_{steam} is the equilibrium constant for steam dissociation. The Gibbs free energy change ΔG_1^0 for the reaction is

$$\ln k_{steam} = \ln\left[(pO_2)^{1/2}_{dissoc}\, pH_2/pH_2O\right] = -\Delta G^0_1/(2.303RT) \qquad \textbf{(2-8)}$$

The oxygen partial pressure set by the dissociation of steam may be written as a function of temperature and total pressure, *P*, as follows

$$pO_2 = \left(\frac{K_{steam}}{2}\right)^{\frac{2}{3}} P^{\frac{2}{3}} \qquad \textbf{(2-9)}$$

Using available temperature dependent data, Davies and Dinsdale [95] were able to plot the oxygen partial pressures in equilibrium with steam at a variety of steam pressures against temperature. The data (Figure 2.16) was plotted along with the dissociation pressures of iron oxides (FeO, Fe_3O_4, Fe_2O_3). It can be seen that the partial pressure of oxygen from steam dissociation alone is easily high enough to give stability to each iron oxide at the operating temperatures of modern boilers. It is therefore expected that all of these oxides, along with chromia and oxides of minor elements whose dissociation partial pressure is lower than that of oxygen in steam should be found on steam oxidised boiler steels. The relative thicknesses of each, however, cannot be predicted from knowledge of partial pressures alone. The presence of Fe_2O_3 especially, varies widely and is sometimes not present at all suggesting that equilibrium is not reached at the oxide/gas interface. Wright and Dooley [42] proposed that the absence of Fe_2O_3 in pure steam could be due to changes in the kinetics of water vapour delivery to the surface, causing the effective pO_2 to fall below the dissociation pressure of Fe_2O_3, or changes to the iron ion flux through the scale to the scale/gas interface. Iron ion starvation by a chromium rich protective scale is proposed for ferritic and austenitic steels by Wright and Dooley [96], in a mechanism for oxide spallation which will be discussed later.

An alternative mechanism was propose by Zurek et al. [40], who noticed a change in oxide morphology along the length of the specimen when oxidising a 10Cr steel at 650 °C in flowing argon environments containing 4 and 50% H_2O. They proposed that the most likely reason for this was the evolution of hydrogen gas during oxidation occurring at the front edge of the sample effectively reducing the pO_2 towards the tail edge of the sample to below the dissociation pressure of Fe_2O_3 suppressing its growth towards this edge. Permeation into the substrate of hydrogen has been reported in the work of Nakagawa et al. [32] who oxidised three ferritic steels of differing Cr contents in a steam/air dual environment between 823 and 923 K. They found thicker oxide to grow on the air side of the steel tubes when steam was passed through the cavity, proposing that hydrogen permeation through the substrate via a dissociation mechanism was responsible for the accelerated oxidation rate.

Asteman et al. [56] oxidised polished 304L samples in flowing O_2 + 40% H_2O, and where duplex oxide formed, reported the composition to be that of Fe_2O_3 at both low (10 ml.min^{-1}) and high (1000 ml.min^{-1}) flow rates. This suggests that Fe_2O_3 formation in the outer oxide is less dependant on flow rate in high pO_2 wet atmospheres.

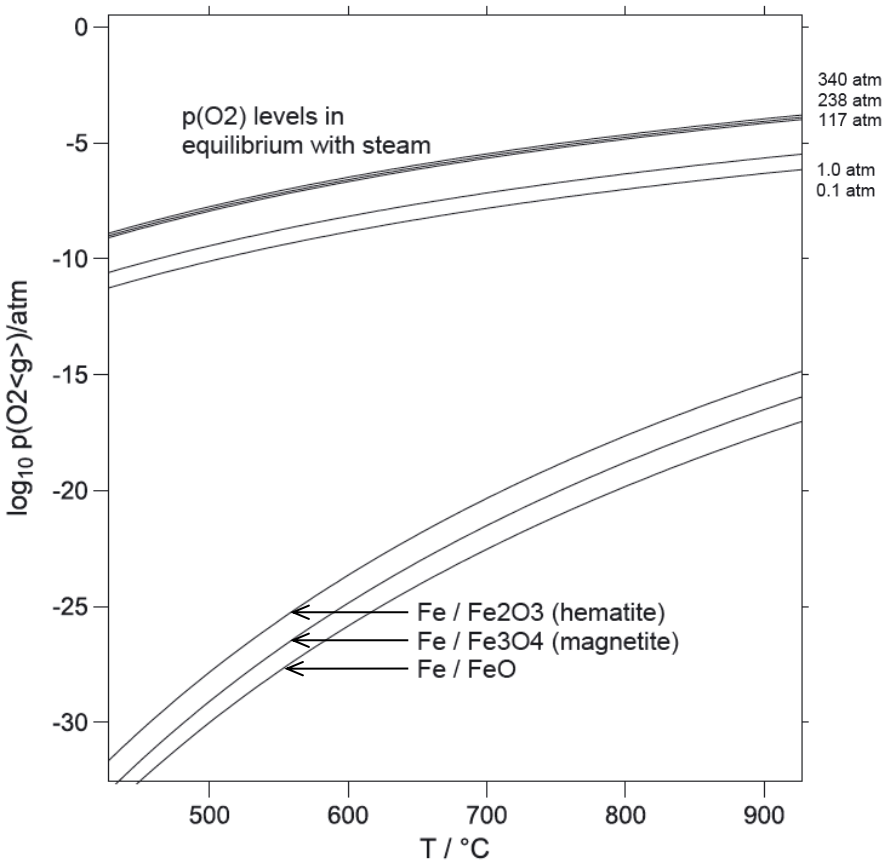

Figure 2.16 – Dissociation pressure of oxygen in steam and iron oxides against temperature [95].

2.3.3.3 Chromium Evaporation

In environments containing water vapour, oxide degradation in the form of chromium volatilisation has been found to occur [97]. For steels that rely on chromium for protection, volatile species in the form of the following equations may occur, as follows

$$^1/_2\, Cr_2O_3(s) + H_2O(g) + {}^3/_4\, O_2(g) = CrO_2(H_2O)_2(g) \qquad \textbf{(2-10)}$$

$$^1/_2\, Cr_2O_3(s) + {}^1/_2\, H_2O(g) + {}^1/_2\, O_2(g) = CrO_2(H_2O)(g) \qquad \textbf{(2-11)}$$

$$^1/_2\, Cr_2O_3(s) + {}^3/_4\, O_2(g) = CrO_3(g) \qquad \textit{(2-12)}$$

$CrO_2(H_2O)_2$ appears to be the dominant volatile species at 873K [97, 98], and probably up until 1173K where $CrO_3(g)$ and $CrO_2(H_2O)(g)$ volatilisation become significant in aqueous environments. Asteman et al. [97, 99] found that chromium volatilisation in O_2 and H_2O atmospheres is strongly dependent on pH_2O and gas flow rate. They found increasing both parameters contributes to the breakdown of protective scales on a number of austenitic steels [57, 100]. For $CrO_2(H_2O)_2$, the vapour pressure for the oxy-hydroxide in a pure steam environment can be expressed as

$$K = \frac{pCrO_2(H_2O)_2}{pO_2^{\frac{3}{4}}\, pH_2O} \qquad \textit{(2-13)}$$

From this, the vapour pressure of $CrO_2(H_2O)_2$ for a variety of conditions (temperature and pressure) can be calculated. Wright and Dooley [42] show that an environment of air and water vapour considerably increases the vapour pressure over that of pure steam estimating that the vapour pressure of $CrO_2(H_2O)_2$ is similar in an air–10% water vapour mix at ambient pressure and pure steam at 240-340 bar.

It should be noted that many of the studies on chromium evaporation were conducted on ground or polished samples, where Cr rich oxides existed at, or near the oxide/gas interface, and thereby being exposed to a relatively high pO_2. For pickled alloys, which grow much thicker duplex scales, any Cr rich oxide that exists does so at the internal oxidation front, where the pO_2 is much lower. The presumption therefore is that chromium evaporation will occur at a much lower rate (if at all) than on polished or ground samples.

2.3.3.4 Steam Oxidation of Ferritic Steels

The term ferritic steel as used here covers both the steels of bcc ferritic structure, typically those with 0-2.25%Cr, and bct (body-centered tetragonal) martensitic structure, typically the 9-12%Cr group of steels. Oxidation properties of these two groups of steels will be treated separately. Martensitic steels with Cr>12% rarely find use in coal-fired boiler applications [11].

Humid atmospheres have an adverse effect on the oxidation of ferritic steels [48]. Below 580 °C, low Cr ferritic steels display parabolic kinetics before breakaway into a more linear regime [34, 101]. The reason for breakaway appears to be scale detachment because of growth strains and the formation of multi-layered scales. The initial slow rate of oxidation may last between several minutes and

hundreds of hours and depends on chromium content [102], with higher chromium content favouring a longer incubation period. At 500 and 550 °C, Lepingle et al. [101] found little difference between the oxidation rates of 2Cr and 9Cr steels, however, 9Cr steels show much better resistance at 600 and 650 °C. This was in agreement with other researchers [63, 93]. 12Cr steels show a significant improvement over 9Cr steels below 600 °C (factor of 1.5-1.7 between T91 and 12Cr in steam at 600 °C [103]) but this is less marked at 650 °C [63]. Parabolic kinetics have been reported for temperatures up to 800 °C for 9-12Cr steels in laboratory studies [63] and in some cases the oxidation rate to be higher at 700 °C than 800 °C attributed to silicon content in the steels. Other researchers [104] have oxidised T91 for up to 10 Kh and reported parabolic kinetics between 600 °C and 700 °C. Overall scale thickness generally increased with temperature apart from at 700 °C where scale thickness was found to be between 600 °C and 625 °C.

The oxidation rate of common 9 Cr steels P91 and P92 has been found to differ in aqueous environments [3, 101, 105]. Between 500 and 650 °C, Lepingle et al. [101] reported thicker oxide growth for P92 oxidised in steam after one year. Mathiazhagan and Khanna [105] found a similar relationship between 600 °C and 700 °C in O_2 + 70% H_2O and suggested that the addition of W to P92, which was found in the inner oxide layer, was responsible for the faster kinetics. This was corroborated two years later by Mogire et al. [3], who reported P92 to grow an oxide 2.5x thicker than that of P91 in flowing steam after 3000 hours at 650 °C. A detailed analysis of the near surface grain structure following oxidation in steam found that in P91 after 3000 hours there had been a phase transformation from martensite to ferrite immediately subjacent to the oxidation front within the alloy. This transformation was absent in P92, where the authors proposed that W-rich particles stabilised the martensitic matrix. A higher volume fraction of grain boundaries and dislocations over P91 led to faster cation and anion diffusion and faster kinetics in P92.

Very low Cr ferritic steels (typically <2%Cr) grow what appears to be a two layered scale between 550 °C and 625 °C, which in fact consists nearly entirely of Fe_3O_4 (Figure 2.17) [106]. A thin layer of FeO containing Cr_2O_3 precipitates may be found at the metal/scale interface, and Fe_2O_3 has been found at the oxide/gas interface in small concentrations at 550 °C [106]. The presence of FeO is temperature and Cr concentration dependent because of the decomposition temperature which varies between approximately 570 °C and 615 °C with increasing chromium content from 0-2.25Cr and so may not be found in the scales of alloys subjected to low oxidation temperatures [63]. Extensive porosity is prevalent in very low Cr ferritics at all oxidising temperatures. At 625 °C pores occur throughout the outer magnetite layer and close to the scale/gas interface. At 550 °C they are

concentrated at the interface between the two magnetite scales, resulting in spallation of this outer layer.

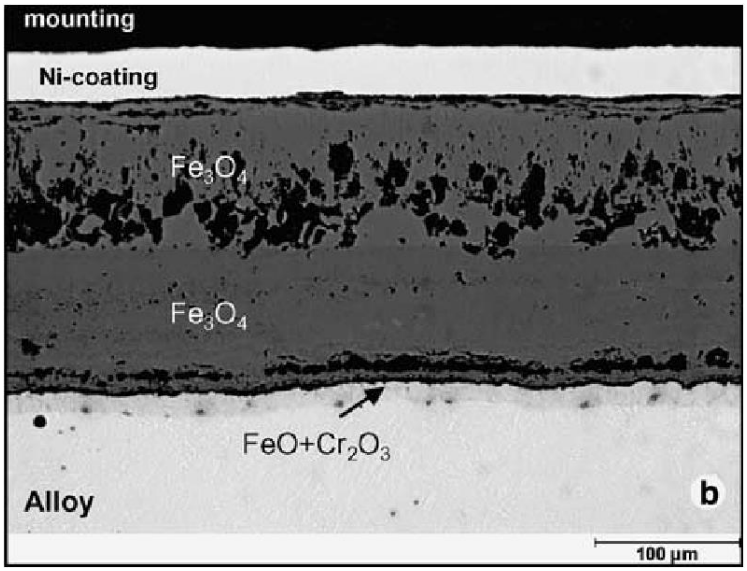

Figure 2.17 – Scale grown on 1 %Cr ferritic steel after exposure to Ar + 50%H_2O at 625°C for 1000 hours [106].

The morphology of low Cr ferritic steels between 2% and 9%Cr after short periods in steam usually show a two layer structure of outer magnetite and inner Fe-Cr spinel [42]. Typical grain structure after plant service consists of the outer magnetite layer being columnar and the spinel, equiaxed, as illustrated in Figure 2.18. The scales usually have equal thickness but with increasing Cr content of the alloy and time the inner scale tends to become thicker than the outer and more enriched in chromium. A third layer, haematite, may grow and form either patches within the magnetite layer near the scale surface or as a connected layer at the scale/gas interface [34]. This layer is usually much thinner than magnetite and spinel layers.

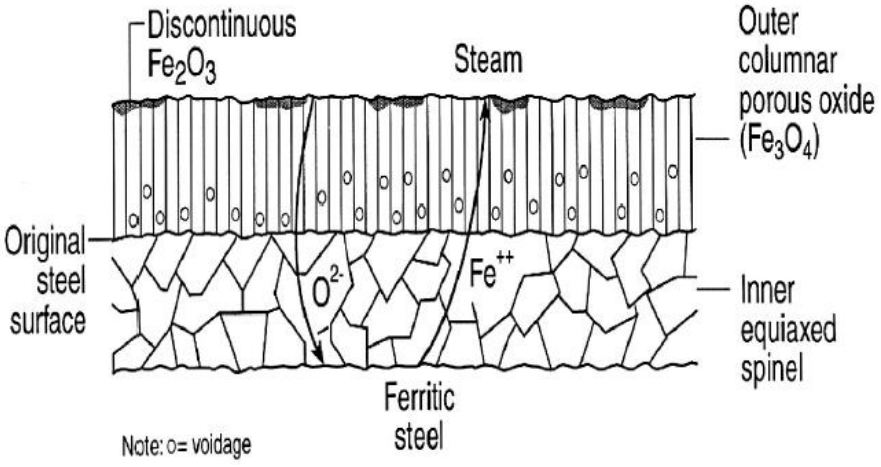

Figure 2.18 – Schematic representation of the grain structure of scale grown on low-Cr ferritic steel post service [107].

Commonly reported on tubes in service, with continued growth, a new, duplex oxide forms beneath the original oxide at the scale/gas interface consisting of magnetite and inner Fe-Cr spinel [34, 42] (on T22 steel the spinel layer has been shown to contain concentrations of Si and Mo [107]). This process will repeat, resulting in an original duplex oxide above multi-layered much thinner laminate layers as shown in Figure 2.19 [107].

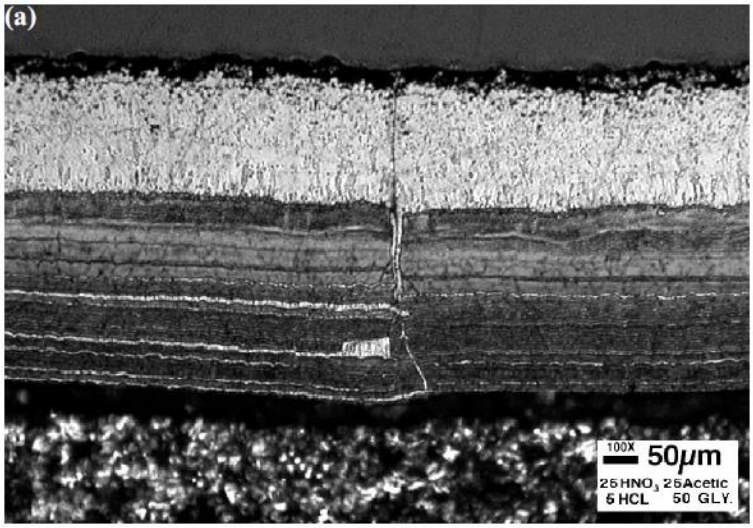

Figure 2.19 – Etched cross section of scale formed on T22 after 263 Kh at 588°C showing multi-layered inner oxide [107].

The morphology of scales grown in steam is similar for most 9-12Cr steels and illustrated for a 9Cr-1Mo steel in Figure 2.20. The composition, from the alloy to the scale/gas interface starts with a depletion of chromium in the alloy subjacent to the inner scale [3, 106] and corresponding iron enrichment. If the oxidation temperature is high enough (>~550 °C) a layer of FeO, thinner than the spinel and outer oxide layers may form at the base of the spinel layer. EBSD/EDX analysis of this area [3] has revealed grain and lath boundaries in this area to be enriched in chromium. If the steel contains strengthening elements such as Mo (P91) or W (P29), these promote the formation of chromium rich oxide stringers in these areas [3]. The inner oxide is composed of $(Fe, Cr)_3O_4$ in a Fe_3O_4 matrix [106] and may exhibit micro porosity [3] and a banded structure, identified for P92 [3] as Cr and Mn rich with W additions. Similar, pronounced banding has been reported on T91 steel after exposure to steam for 48 and 63 Kh [42], and T122 steel after 48 Kh in service at 565 °C [104]. Banding of the inner scale occurs on low Cr steels in a steam environment and oxide grain analysis has revealed a structure of alternating small grain spinel and larger grain magnetite layers in the scale [107]. This is in contrast to the structure of the inner oxide layer of 9Cr alloys, which exhibit homogeneity throughout, indicating the inner scale to be composed purely of Fe_2CrO_4 and $FeCr_2O_4$ spinel [42]. The outer oxide of 9-12Cr steels is often porous and either fully Fe_3O_4 or Fe_3O_4 with Fe_2O_3. The Fe_2O_3 phase is found at the oxide/gas interface either as patches or a complete layer. Fe_2O_3 also accumulates in small amounts

around pores and through thickness cracks in the scale [3]. The grain structure of the outer Fe_3O_4 scale may be a combination of equiaxed and columnar grains [3], depending on the rate of oxidation at the time of growth, columnar grains suggest faster diffusion and oxide growth.

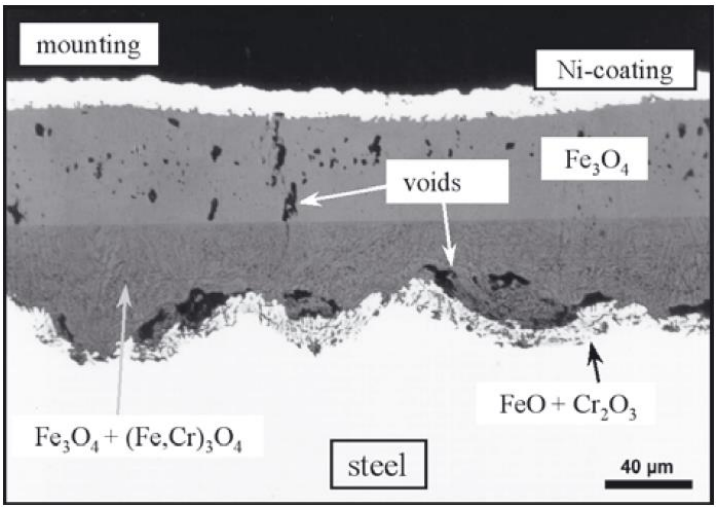

Figure 2.20 – Scale formed on 9Cr-1Mo ferritic steel after oxidation in Ar-50%H_2O at 650 °C for 1000 hours [102].

Porosity in the oxide formed on ferritic steels varies widely depending on alloy type and oxidising conditions and has a strong correlation to spallation on these steels. Spallation occurs most readily when pores congregate parallel to the oxide surface, typically at the interface between spinel and outer oxide or metal/scale interface. When pores are distributed somewhat evenly through an oxide layer, a spallation event is less likely. There are contrasting opinions on the effect of steam pressure on porosity of the scales on ferritic steels. Some researchers report a decrease from 30% to 23% between 1 and 17 bar and others report an increase, or that little (10% over 500-750 °C) variation exists [42]. Low Cr steels oxidised in steam tend to show porosity throughout the original outer layer, with little porosity found in the multi-layered region [106]. Spallation typically occurs at the interface between the layers. However, if porosity is substantial at the metal/scale interface spallation may occur there [34]. When this is the case there is usually a high fraction of haematite in the outer layer, which itself may spall from the underlying magnetite.

Higher alloy steels of around 9-11%Cr show large variation in pore frequency and distribution depending on alloy, oxidising atmosphere, temperature and duration. For these steels, pores tend to be evenly distributed throughout the outer magnetite scale, or congregated along the magnetite/spinel interface [3, 34, 102, 105-107]. Additional porosity may be found in the FeO layer adjacent to the alloy interface. Both this interface and the magnetite/spinel interface are possible decohesion interfaces for these steels [42, 102] as shown in Figure 2.21. Nishimura et al. [104] found scale separation and exfoliation of the outer oxide layer to occur after 10 Kh at 625 °C in steam on the

inner surface of a T91 tube that had been ground but not on a tube that had been oxidised in the as received condition. The authors attributed the exfoliation to a lack of adhesion of the outer layer due to a more even interface compared to the rough as received surface. An ex-service (15 Kh) tube was also tested and scale separation of the outer layer was found as typically found on damaged utility boiler tubes.

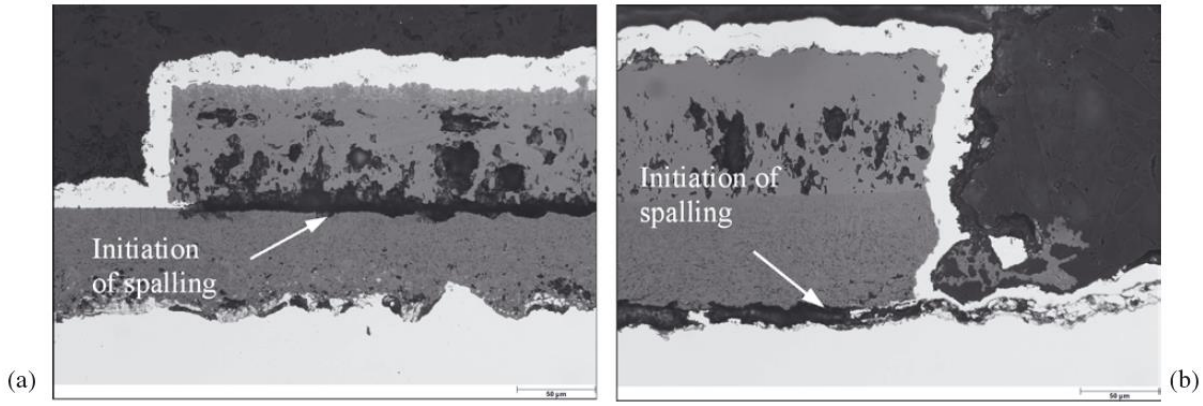

Figure 2.21 – Scale spallation at (a) the spinel/outer oxide interface after 3000 hours and (b) the metal/oxide interface after 1000 hours. Alloy is a 10Cr-1Mo ferritic steel oxidised in Ar-50%H_2O at 625°C [102].

Zurek et al. [40] and Quadakkers et al. [102] proposed the following mechanism, illustrated in Figure 2.22, explaining the growth of pores and spallation on 9-12Cr steels in atmospheres containing water vapour. Initially, an incubation period exists where the scale consists of $(Fe, Cr)_2O_3$ or $(Fe, Cr)_3O_4$ adjacent to the substrate and haematite at the scale surface. The breakdown of this layer results in an increase in the rate of oxidation and the formation of an Fe_3O_4 layer above a layer of Cr_2O_3 precipitates in an FeO matrix. After a while, a gap, formed via vacancy condensation because of rapid Fe_3O_4 formation at the scale/gas interface is formed at the inner/outer scale interface. Scale growth is now largely dependent on mass transport across the gap and as the scale thickens, the increased difficulty of iron ions to diffuse to the outer scale/gas interface reduces the activity of iron at the surface results in the formation of haematite. The authors propose two possible routes for further development of the scale: if isothermal oxidation continues, molecular transport of the oxidant species to the inner oxide surface may allow oxide growth and healing of the gap, thus permitting an increased flux of iron ions to the oxide/gas interface. This reduces haematite back to magnetite resulting in growth similar to that of just after the incubation period, albeit at a slower rate that does not cause large scale vacancy condensation at the inner/outer scale interface. Alternatively, if a thermal cycle is introduced before the gap has healed sufficiently to absorb thermal contraction stresses imposed by the haematite rich layer on cooling, spallation of this outer layer will result. Further exposure at the oxidising temperature will then lead to growth exhibited by the first route, having lost the outer layer. Whether or not a spallation event occurs depends on the oxidation time and consequently,

temperature. At 650 °C healing of the gap was shown to occur at a much faster rate than at 550 °C [40, 102].

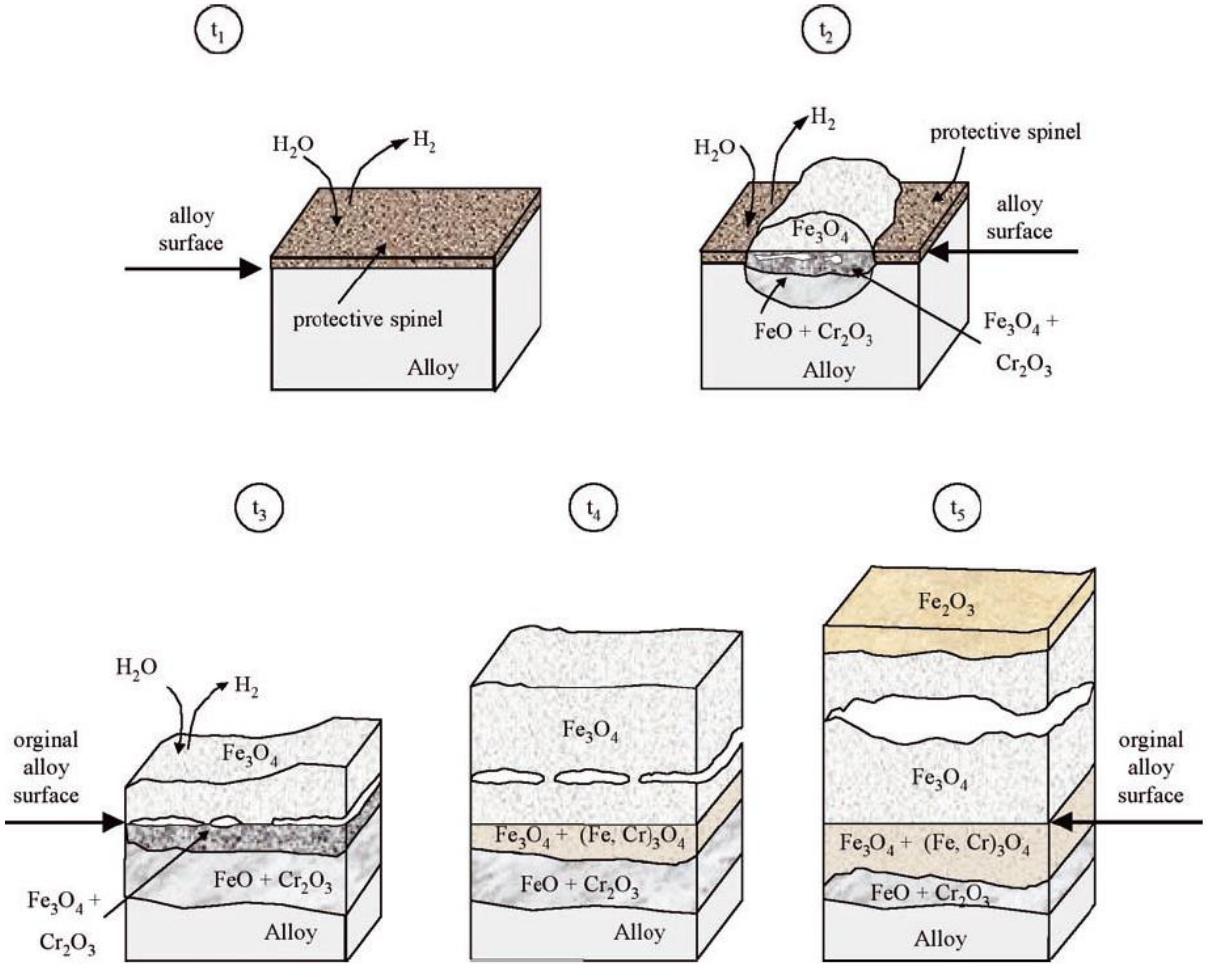

Figure 2.22 – Schematic of oxide growth mechanism on 9-12%Cr ferritic steels in water vapour containing environments. After Zurek et al. [102].

Research into the growth mechanism of ferritic steels in steam have shown that both inward diffusion of oxidant species and outward diffusion of metal cations are responsible for the two layered iron rich outer and inner spinel scale structure grown on these alloys, where the interface between the two is expected to correspond to the original metal surface.

2.3.3.5 Steam Oxidation of Austenitic Steels

All austenitic steels share the same fcc structure and have chromium contents ranging from ~15-35 wt.% Cr. Wright and Dooley [42] split austenitic steels into two groups: those with <20 wt.% Cr and are coarse grained; and, both those with >22 wt.% Cr and <22 wt.% Cr that are fine grained. These groups are defined according to oxidation kinetics and the morphology of oxides formed on each group. However, from both laboratory and service studies it appears that high Cr (>22 wt.% Cr) austenitics consistently show slower kinetics than low Cr, fine grained austenitics as illustrated in

Figure 2.23 [108]. It should be noted that the author only assumed that the data can be described by parabolic kinetics.

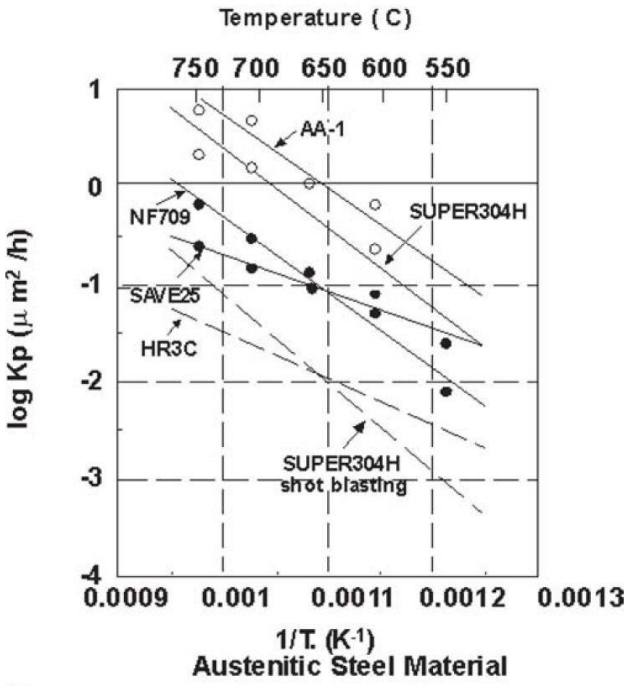

Figure 2.23 – Arrhenius plot of parabolic rate constants for common austenitic alloys after Muramatsu [108].

The morphology of the scale grown on high Cr austenitics differs from that of low Cr fine grained austenitics initially and it is only after long time periods (>1 Kh) that the scales are representative of each other (albeit the scale on high Cr steels will be much thinner). Otsuka et al. [59] found that pickled coarse grained 25Cr15Ni formed a thin oxide scale composed of Cr_2O_3 and Fe_3O_4 all the way up to 900 °C, following oxidation in deoxygenated steam for 1000 hours.

The general trend of increasing chromium content on the oxidation performance of boiler steels is to decrease the oxidation rate. After long time periods (Khrs) austenitic steels tend to parabolic or near parabolic kinetics when oxidised in steam [58, 109]. Atmospheres containing different carrier gases and amounts of H_2O may lead to breakaway after extended periods [100]. Austenitic steels have superior oxidation performance to ferritic steels thanks to the development of more protective chromium rich spinels and possible formation of a thin Cr_2O_3 base layer [42].

The austenite grain size has a large influence on oxidation behaviour and the 18-8 austenitics are further split into coarse grained (TP304, TP347, TP321 = ~90 µm/ASTM ~4) and fine grained (347HFG, Super 304H = ~20 µm/ASTM ~8-9 [110, 111]) variants. Higher Cr austenitics such as HR3C (~90 µm/ASTM ~4 [112, 113]) have grain sizes similar to coarse grained 18-8 austenitics, their increased oxidation resistance is because of their high chromium content. Fine grained 18-8

austenitics consistently show more favourable oxidation kinetics than their coarse grained counterparts and tend to form a complete chromium rich base film, whereas coarse grained steels form an incomplete layer, preferentially over grain boundaries [34]. Wright and Dooley [42] compiled scale thickness data of a variety of coarse and fine grained 300 series austenitics that had seen service and extrapolated the data to give the expected oxide thickness after 40 Kh. The scale thicknesses of TP347H (coarse grain) were factors of 6.4 (550 °C), 5.7 (600 °C) and 4.9 (650 °C) greater than 347HFG (fine grain). Figure 2.24 shows a comparison between coarse and fine grained 300 series austenitics after 6.5 years of service at 571 °C/190 bar compiled by Kan et al. [109].

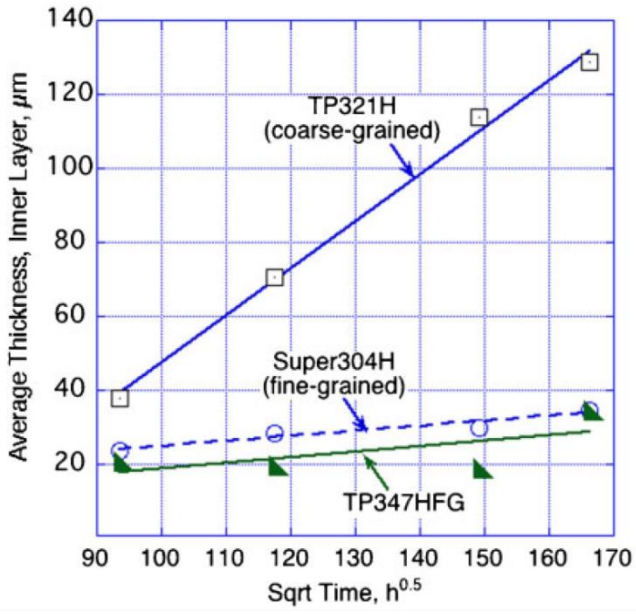

Figure 2.24 – Comparison of inner oxide layer thicknesses between coarse and fine grained austenitic steels after 6.5 years of service at 571°C/190 bar after Kan et al. [109]. Figure after Wright and Dooley [42])

Long term service (up to 57 Kh, 571 °C, 190 bar) of 18-8 austenitic steels has seen these steels follow a parabolic growth rate law [42]. Scale thickness data on 347HFG post service show the oxidation rate of this alloy between 499 and 650 °C (metal temperature) to be largely independent of time between 7,720 and 29,588 hours [111]. After exposure for 57 Kh however, the thickness of the inner scale developed at temperatures lower than 541 °C was reported to be more than twice as thick as those formed at higher temperatures. The authors noted the absence of Cr_2O_3 at the alloy/oxide interface at the lower temperatures, which may have acted as a protective oxide at higher temperatures.

Coarse grained steels TP304, TP347 and TP310 have been reported to follow a parabolic rate law after 1 Kh at 538 °C. Between 482 °C and 538 °C TP304 was reported to obey parabolic kinetics for 5 Kh before assuming linear kinetics [42].

Care must be taken when handling kinetic data of austenitics given the large effect of surface finish on oxidation. It follows that the kinetics of a pickled tube that has seen service or is left in the as-received condition in laboratory tests may exhibit vastly different kinetics to laboratory tests where coupons are machined or grinding/polishing of the surface prior to steam exposure is employed, along with samples that have been shot peened. The variation in kinetics has strong dependence on the depth of deformation in the surface and ultimately the density of dislocations and grain boundaries. Jannson et al. [46] pickled 18-11 and higher alloyed steels. This work showed the general trend of higher weight gain than ground samples oxidised in steam. Cisse et al. [114] found the oxide grown on polished samples of 304L to be a factor of 2 thicker than that grown on precision ground samples when oxidised in 400 °C steam for 500 hours. The recrystallisation zone (the area affected by cold work) extended deeper into the substrate on the ground sample than on the polished sample. Presumably, the polishing process gently removes material from the metal surface without imposing additional cold work into the surface. This reduces the near surface dislocation density and corresponding rate of chromium diffusion. In contrast, Otswald and Grabke [41] show the opposite to be true for a series of ferritics and austenitics at the higher temperature of 600 °C in a variety of oxidising environments. They attribute their findings to the depth of the depletion zone caused by each surface finish. Nevertheless, as discussed in a previous section, the effect of grain refinement [38] and shot peening [35, 36, 115], which are two commonly pursued surface modification techniques. These have proven to be beneficial to the oxidation performance of austenitic boiler steels within the service temperatures they are to be used [42]. Figure 2.25 illustrates the benefit of shot peening on 300 series steels as reported by Yue et al. [35]. The lesser alloyed 18Cr TP304H benefits to a larger extent from the treatment than the 25Cr HR3C. It should be noted that non shot peened samples had been ground and were not oxidised in the pickled state.

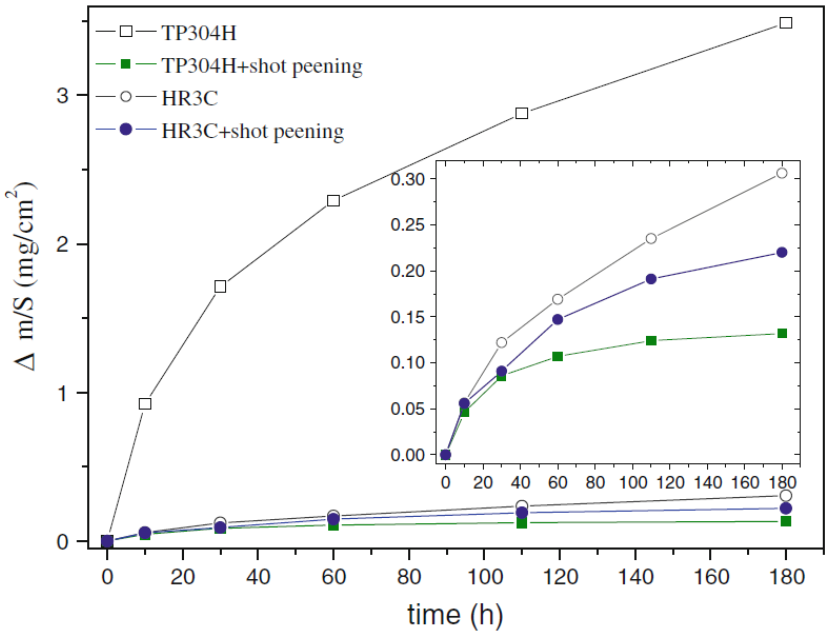

Figure 2.25 – Effect of shot peening on steam oxidation performance of austenitic steels at 650 °C [35].

Coarse grained 300 series austenitics initially form thin, Cr rich films over emerging grain boundaries and Fe rich nodules centred over alloy grains [96]. As time progresses, a double layered oxide is formed of inner Fe-Cr spinel and outer magnetite, possibly with a fraction of haematite [42]. The interface between the inner and outer layers corresponds to the original metal surface [116]. The outer layer is porous and further oxidation leads to pores collecting at the spinel/outer oxide interface, which act to starve the magnetite layer of iron further promoting the decomposition to haematite. The inner and outer scales are of approximately equal thickness, however, the inner layer is non-uniform. Prior austenite grains in the internal oxide are separated by a thin Cr rich oxide or 'healing layer' that, as the oxidation temperature increases above around 600 °C, extends to surround the internal oxidation front on contact with a grain boundary.

The level of protection offered by the healing layer may be insufficient to prevent oxide growth into the next grain, and depends on alloy Cr content, temperature, and oxidation time. On TP347H the healing layer has been shown to contain increased concentrations of manganese and silicon after oxidation in steam at approximately 585-650 °C (metal temperature) for 6 Kh, along with a chromium depletion and corresponding nickel enrichment in the metal directly subjacent to the base layer [96]. The same sample featured a similar Cr (Si, Mn)-rich layer below the inner/outer oxide interface, thought to have grown during the initial stages of oxidation. There was a haematite presence in the outer oxide suggesting the protective inner oxides were reducing the outward flux of iron to the surface. Figure 2.26 shows a typical oxide grown on TP304H along with a schematic of the oxide formed on coarse grained austenitics in steam.

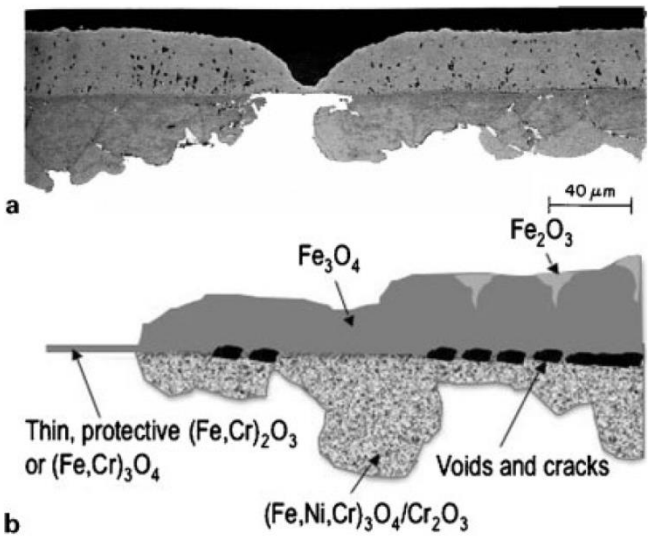

Figure 2.26 – Oxidation of TP304H. (a) Scale after service at 538 °C for 28 Kh in 0.5 MPa steam. (b) schematic of oxide grown [42].

Halvarsson et al. [100], reported a similar morphology of oxide nodules that developed on polished 304 steel coupons after exposure to O_2 + 40% H_2O at 600 °C for 168 hours. Nodules were found to grow from the centre of grains and were surrounded by a Cr-rich protective oxide around grain boundaries. The base layer consisted of protective (Fe, $Cr)_2O_3$. The subjacent alloy was depleted in iron and chromium and enriched in nickel. This depletion/enrichment continued down grain boundaries where present. Cross section analysis of nodules revealed a duplex oxide. The inner of which was enriched along the oxide/metal boundary with chromium and manganese, and silicon at the base. The bulk of the inner zone contained regions of iron/chromium rich oxide in the form of $(Fe,Cr)_3O_4$ spinel and equal concentrations of iron, nickel and chromium, most likely in the form of a Fe-Cr-Ni spinel. The outer oxide within the nodules was iron rich spinel α-$(Fe_{1-x}Cr_x)_2O_3$ type. This is in contrast to the accepted composition of magnetite and/or haematite [34, 42, 96, 115]. However, the authors report the oxide to exhibit variable stoichiometry between the grain centre and boundary, suggesting further oxidation may lead to development of iron oxide.

Fine grained 18-8 austenitics develop similar scales to coarse grained 18-8 austenitics. The main differences being a higher concentration of chromium in the spinel of the fine grained alloy [42] and faster formation of a healing layer that ultimately results in: (a) a thinner overall scale (see Figure 2.24), and (b) faster transformation of magnetite to haematite [96]. The formation of a healing layer depends on temperature and time of exposure. Hansson et al. [80] oxidised 347HFG between 500 and 700 °C in Ar+46%H_2O for 336 hours. A protective base film was absent at 500 °C, present between oxidised grains at 600 °C, and generally uniform at 700 °C. It should be noted however, that the Cr content of the examined steel was 16.9 wt.%. Additional tests were carried out at 600 °C on TP347H FG

containing concentrations of 18.5 and 19.3 wt.%Cr to observe the effects of varying chromium concentration. A thicker base film was observed on the 18.5 wt.%Cr steel and the thickness of the inner layer decreased with increasing chromium content This suggests a healing layer is more readily formed as the chromium concentration is increased. Longer term tests of 347HFG in service [111] (18.5-19.3 wt.% Cr) have shown a Cr rich base film to be present between 515 and 650 °C, albeit with the absence of Cr_2O_3 at the lowest temperatures.

The inner oxide on fine grained austenitics is Fe-Cr-Ni spinel containing concentrations of the materials remaining alloying elements. The spinel is often of the form $(Fe,Mn)Cr_2O_4$ embedded in a metallic Fe-Ni matrix [80]. Hansson et al. show that the spinel becomes essentially a solid layer around grain boundaries with the growth of small amounts of Cr_2O_3 adjacent to the underlying alloy promoted by higher temperatures [111]. In long term tests (>1 Kh) Ni-Fe rich oxide has been found in the outer oxide adjacent to the inner/outer oxide interface [111, 117]. This oxide has been absent during shorter term tests. The oxide scale found on 347HFG after exposure to steam at 670 °C for 11 Kh is shown in Figure 2.27 [96].

Nickel has been reported to exist within the inner oxide in both oxidised and metallic form. Halvarsson et al. [100] reported it to exist in oxidised form on 304L oxidised in O_2+40% H_2O. Hansson et al. [111] reported it to exist in metallic form on 347HFG following long term exposure in a steam test loop. These contrasting findings suggests the oxidation of nickel is particularly sensitive to the partial pressure of oxygen of the carrier gas.

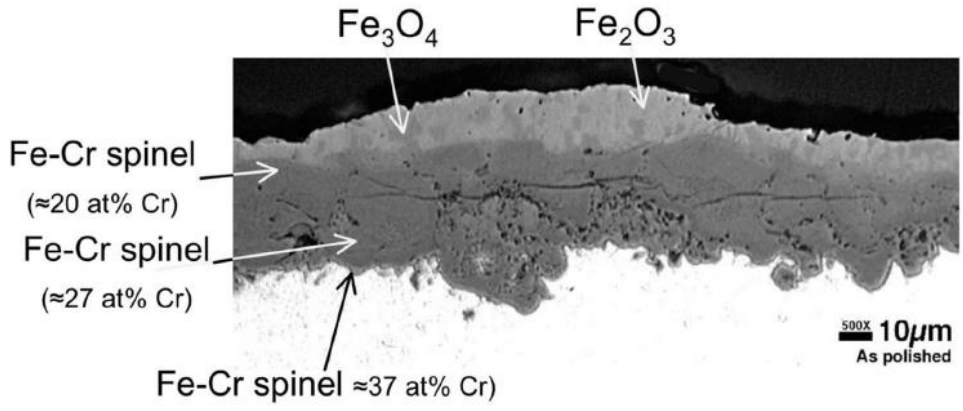

Figure 2.27 – Scale formed on 347HFG after exposure to steam at 670 °C for 11 Kh [96].

A mechanism proposed by Jianmin et al. for the oxidation of 347HFG in steam is illustrated in Figure 2.28. It should be noted that the following mechanism describes the oxidation at 256 bar and an alternative mechanism was proposed based on exposure in the same test loop at 91 bar [118]. Stage 1 involves the formation of a thin, two layer Fe_3O_4/Fe-Cr spinel oxide. This, in fact, occurs following

the decomposition of an initial Cr-rich spinel into oxide nodules [42]. Stage 2 – oxide growth continues unabated in all directions, until close proximity of the oxidation front to a grain boundary causes growth of Cr-rich Fe-Cr spinel here while the bulk grain is oxidised to Fe-Cr-Ni oxide. At this stage a Ni-Fe oxide begins to form in the outer oxide adjacent to the outer/inner oxide interface. Stage 3 – Chromium enrichment at grain boundaries and the enhanced diffusion of chromium in these areas promotes the formation of a healing Fe-Cr spinel layer rich in chromium. Faster diffusion occurs at higher temperatures and a complete layer is formed that thickens with time. If the concentration of chromium is high enough, Cr_2O_3 forms at the metal/oxide interface. Stage 4 – weakening and breakdown of the chromium rich layer leads to breakthrough oxidation of further alloy grains at an accelerated rate, which continues until a consecutive grain boundary is reached. This mechanism is (somewhat) followed by coarse grained 18-8 austenitics, however, the lower grain boundary density means lower overall diffusion of chromium and thicker, less protective scales result. Samples exposed at 91 bar in the same test loop grew healing layers thinner than those found at 256 bar but thicker than those expected on coarse grained 347HFG [118]. The authors make no mention of haematite growth during the analysis of the 347HFG samples the above mechanism is based on. However, research from samples taken from the same superheater testing loop by other workers [111] confirm the presence of varying amounts of haematite in the outer oxide layer.

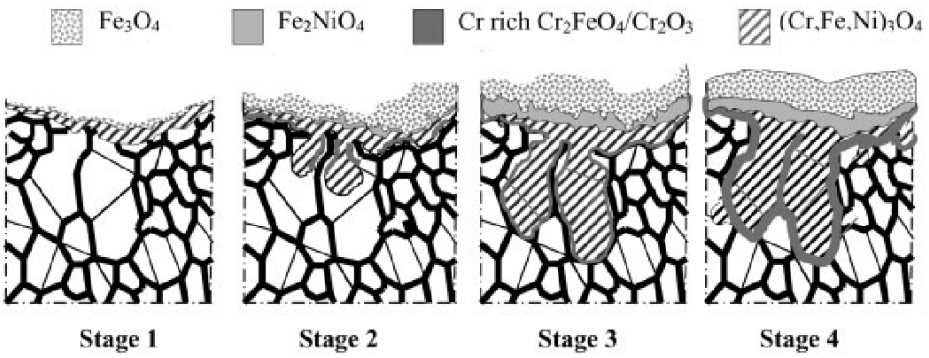

Figure 2.28 – Mechanism for growth of scale on 347HFG in steam [117].

Wright and Dooley address the formation of haematite in the outer layer of 347HFG during steam oxidation and propose a model of the oxidation and spallation of 300 series austenitics, illustrated in Figure 2.29. They suggest haematite formation begins when a complete healing layer has formed around grain boundaries at the oxidation front by reducing the outward flux of iron (stage 3 of the Jianmin et al. mechanism). This also has the consequence of vacancy condensation at the inner/outer oxide interface resulting in porosity here. They propose complete transformation of magnetite to haematite before exfoliation of the entire outer layer occurs, which is initiated on cooling. The authors

base this mechanism on a sample of 347HFG that has seen service at 670 °C for 11 Kh, the outer scale of which has had time to transform almost entirely to haematite.

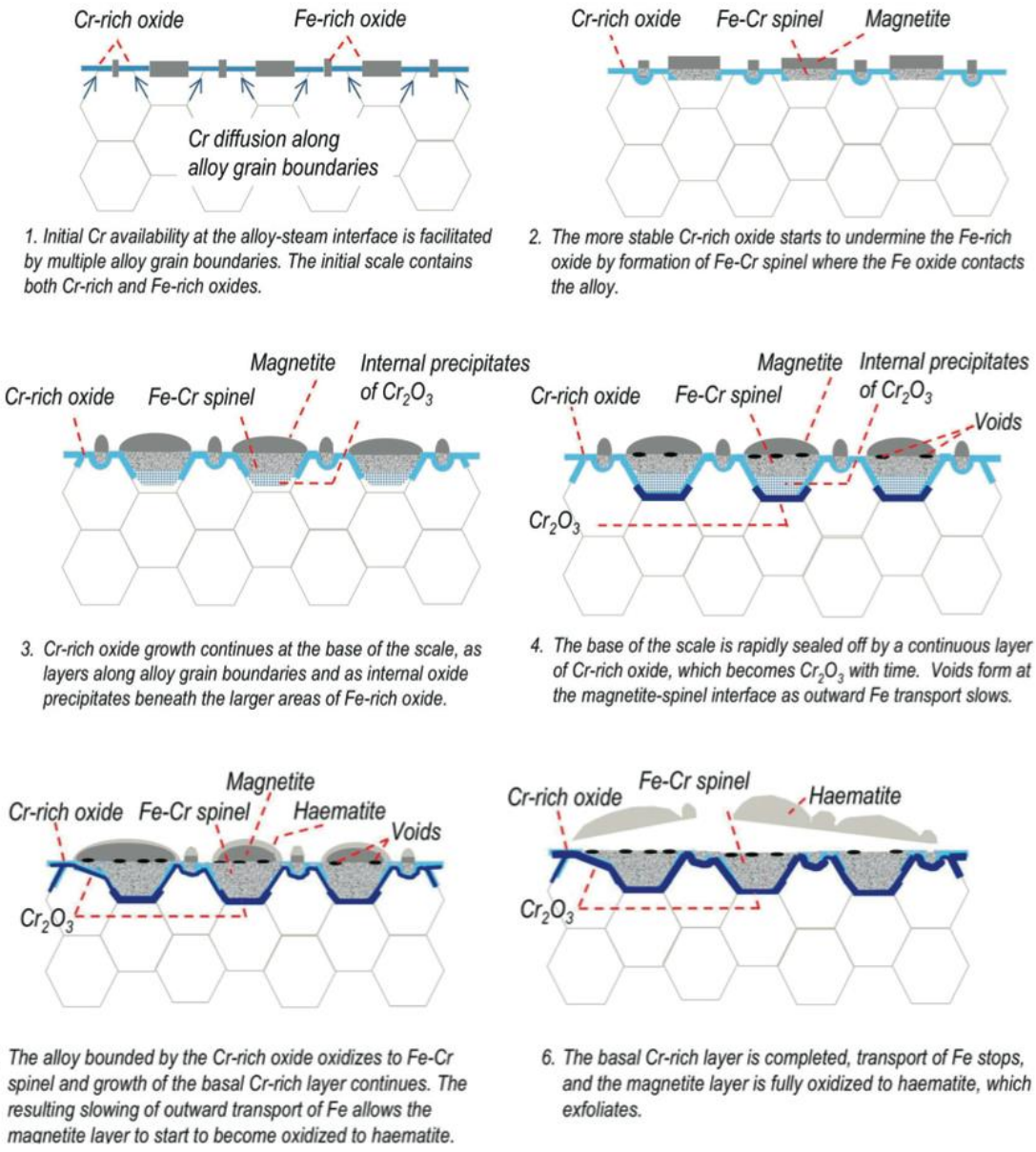

Figure 2.29 – Mechanism for scale development on fine grained 300 series austenitic steels in steam [96].

Wright and Dooley's mechanism does not consider the growth of Ni-Fe oxide in the outer layer (the sample on which it is based does not obviously exhibit a Fe-Ni oxide layer) and so it is unclear if haematite formation would continue into this layer given that it had consumed the entire magnetite layer. To date there have been no observations of Fe-Ni oxide remaining adherent in the case of a spallation event, nor Ni concentrations found in spalled oxide where the outer layer has detached. In addition, scale failure on austenitics usually involves exfoliation of the outer layer [34, 42, 96] as described by Wright and Dooley's mechanism.

2.4 Oxide Stresses and Spallation

2.4.1 Industrial Concerns

The oxidation process, either by sheer scale thickness or through the development of extensive porosity reduces the thermal conductivity through the tube wall increasing the metal temperature and reducing creep life [104]. Tube thinning is a direct result of oxidation and may be accelerated by scale exfoliation, which has the effect of increasing the oxidation rate in areas that have spalled, depending on the decohesion interface [34]. Oxide that spalls and becomes entrained in the steam flow will either collect at lower bends of superheater pendants and lead to steam flow restriction and local overheating failures (this type of failure is widely reported in the UK and Japan [119]) or travel with the steam causing erosion at the turbine stages, as common in the US [119]. Examples of the effects of spalled oxide on superheater tubes and turbine blades can be found in Figure 2.30.

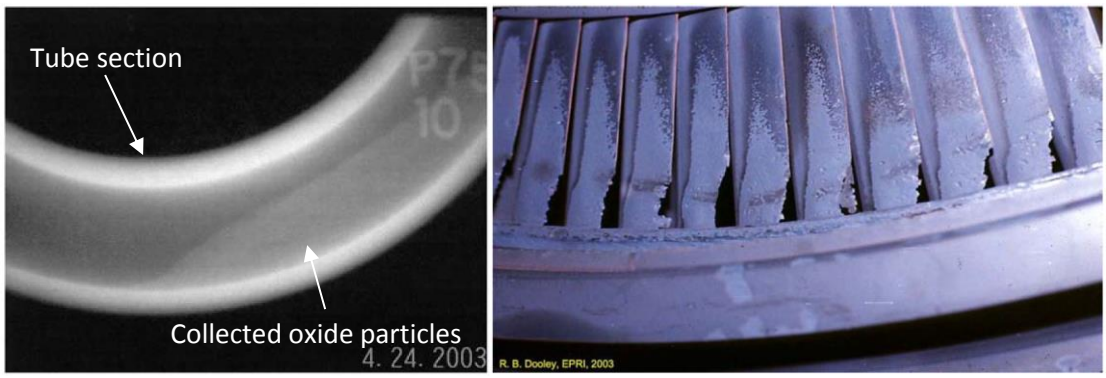

Figure 2.30 – (a) Radiographic image of superheater pendant bend showing spalled oxide accumulation. (b) Erosion of first stage turbine blades caused by spalled oxide [34].

2.4.2 Spallation Experience in Service

Tests in the UK in autoclaves fed from reheat steam at 600 psi have compared spallation properties at different temperatures [119]. At 600 °C extensive spallation was found after 4000 hours on austenitic steels AISI 316, 321, 347 and Esshete 1250. No spallation had occurred on high Cr AISI 310 and Sandvik 12XRN72 or shot peened 316 and 347. These steels tended to form Cr_2O_3 films. No spallation occurred on Incoloy 800 and 9CrMo. At 650 °C spallation to a lesser extent of the same group of alloys occurred after 500 hours and was more extensive after 1500 hours. Other autoclave tests on 316 at 600 °C 600 psi have not reported spallation after 7000 hours, however Fe_2O_3 was absent from the scales which was attributed to hydrogen build up in the rig. Trials on 316 at Cockenzie power station returned mixed results with varying amounts of spallation found on tubes exposed at 552 °C after 8800 hours in pressurised steam.

2.4.3 Stress Generation

It has been known for many years that stresses that build up in the oxide scales of boiler tubes are the cause of spallation. The two main sources of stress are from growth of the oxide and thermal transients, which force the oxide to conform to the expansion or contraction of the alloy and may be compressive or tensile depending on the difference in thermal expansion coefficients between the alloy and oxide. The most common route to spallation in boiler tubes is the compression of oxide scale during plant cool down.

2.4.3.1 Growth Stresses

One of the earliest models attempting to explain growth stresses in oxide layers was developed by Pilling and Bedworth [120]. The model describes the volume change associated with the growth of an oxide purely from oxygen diffusion and the metal lattice. The ratio of the volume of the oxide formed per metal ion to the volume of metal consumed per metal atom is termed the Pilling – Bedworth ratio (PBR):

$$\Phi = \frac{V_{ox}}{V_m} \qquad \textit{(2-14)}$$

where Φ is the Pilling Bedworth ratio and V_{ox} , V_m are the molar volumes of oxide and metal respectively. It predicts that inwardly growing oxides with PBRs greater than unity will grow in compression and oxides with PBRs less than unity will grow in tension. It follows that systems in which an oxide grows under tension will not be able to maintain a protective layer because of constant development of through thickness cracks exposing fresh metal. The strain calculated from the volume change as a result of inward growth of an oxide is [15]

$$\varepsilon_{ox} = \omega \left[(\Phi)^{1/3} - 1 \right] \qquad \textit{(2-15)}$$

where ω is a factor that takes into account stress-reducing processes. The corresponding stress assuming elastic behaviour is then:

$$\sigma_{ox} = \frac{-E_{ox}}{1 - \upsilon_{ox}} \cdot \varepsilon_{ox} \qquad \textit{(2-16)}$$

where $\mathrm{E_{ox}}$ is the elastic modulus of the oxide and $\mathrm{v_{ox}}$ is the Poisson's ratio for the oxide. The Pilling Bedworth ratios for some common oxide/substrate combinations, along with the dominating growth direction, are listed in Table 2.3.

Table 2.3 – PBR values and growth mechanisms for technically important oxide/substrate combinations [120].

System	PBR
FeO/α-Fe	1.68
Fe_3O_4/α-Fe	2.1
Fe_2O_3/α-Fe	2.14
$Fe(Fe, Cr)_2O_4$/Fe-Cr	2.1
$FeCr_2O_4$/Fe-18Cr-8Ni	2.1
Fe_3O_4/FeO	1.2
Fe_2O_3/Fe_3O_4	1.02
Cr_2O_3/Cr	2.07
Cr_2O_3/Fe-25Cr-20Ni	2.1
SiO_2/Si	2.15
Al_2O_3/Al	1.28
NiO/Ni	1.65
CoO/Co	1.86
TiO_2/Ti	1.73

Whereas this model may be used to approximate the stresses generated in scales that grow at the metal/oxide interface from inward anion diffusion, a short fall is that many metal oxides grow via outward cation diffusion. In these cases, the oxide tends to expand in the direction of least resistance e.g. normal to a flat surface, allowing an extent of stress relief. This lends to the approximation that the ratio of oxide thickness, ξ to depth of metal consumed, y is equal to the Pilling-Bedworth ratio [121]:

$$\frac{\xi}{y} = \Phi \qquad \textbf{(2-17)}$$

For the case of unconstrained oxide growth by cation diffusion the mismatch of lattices at the metal/oxide interface would still be expected to generate stress at this interface. However, in favour of keeping to a low energy configuration, the accommodation by intrinsic dislocations is to reduce epitaxial constraints. Stress generation may arise from oxidation within the oxide itself [122]. In this case, Rhines and Wolf [123] propose that in the oxidation of nickel, gaseous oxygen diffuses down grain boundaries and is met by nickel diffusing through the bulk of grains. New oxide is formed within oxide grain boundaries producing lateral compressive stress within the oxide, calculated for Ni/NiO oxidised at 1000 °C to be of the order of 10 MPa. Evidence for lateral oxide growth has been found in the oxidation of pure chromium and high chromium alloys [120]. A schematic diagram of the intrinsic growth mechanism by anion counter diffusion in nickel, after Rhines and Wolf [123] is found in Figure 2.31.

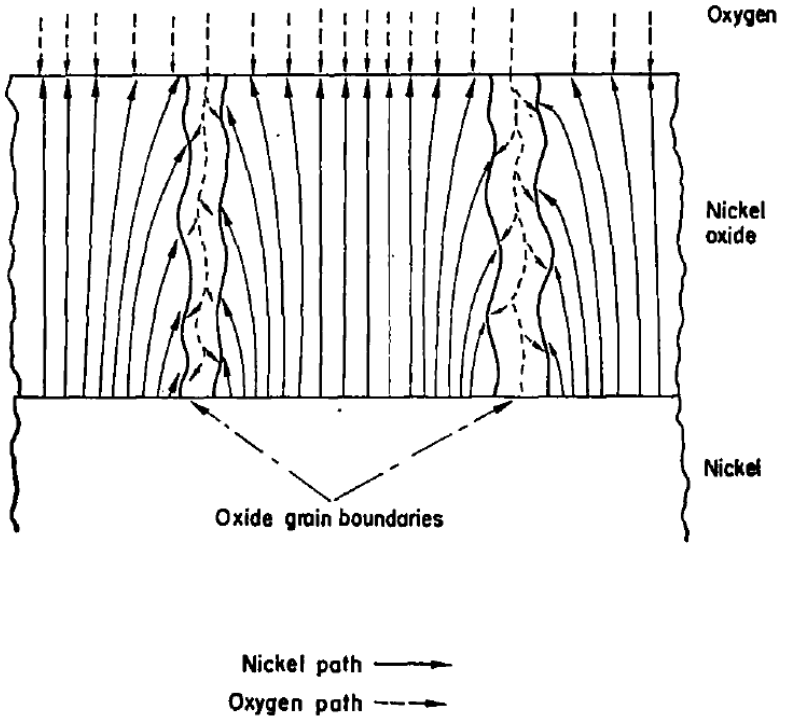

Figure 2.31 – Schematic diagram of a mechanism for oxide growth within grain boundaries via anion counter diffusion in nickel as proposed by Rhines and Wolf [123].

2.4.3.2 Geometrical Stresses

Substrate curvature can have a profound effect on the stresses developed during oxidation. A model proposed by Hancock (described by Evans [121]) considers the stress development on convex and concave surfaces for oxidation via both anion and cation diffusion, Figure 2.32. In (i) and (ii) cation diffusion causes oxide growth at the scale/gas interface and the metal/oxide interface is assumed to retreat. The retreating metal causes a normal tensile stress between oxide and substrate for both convex and concave surfaces. The oxide on convex surfaces will develop radial compressive stresses that may result in either compressive shear failure or tensile failure at the metal/oxide interface. This can lead to the oxide buckling, depending on the strength of the metal/oxide interface. For concave surfaces, tensile radial stresses will lead to through cracking of the oxide at the metal/oxide interface or decohesion of the oxide if this interface is weak. For growth by anion diffusion, as in (iii) and (iv), growth at the metal/oxide interface is compressive. For convex surfaces, as the oxide is pushed away and out from the substrate surface radial tensile stresses form at the oxide/gas interface and the oxide fails via generation of through cracks. On concave surfaces the oxide is formed in compression and so fails via compressive shear.

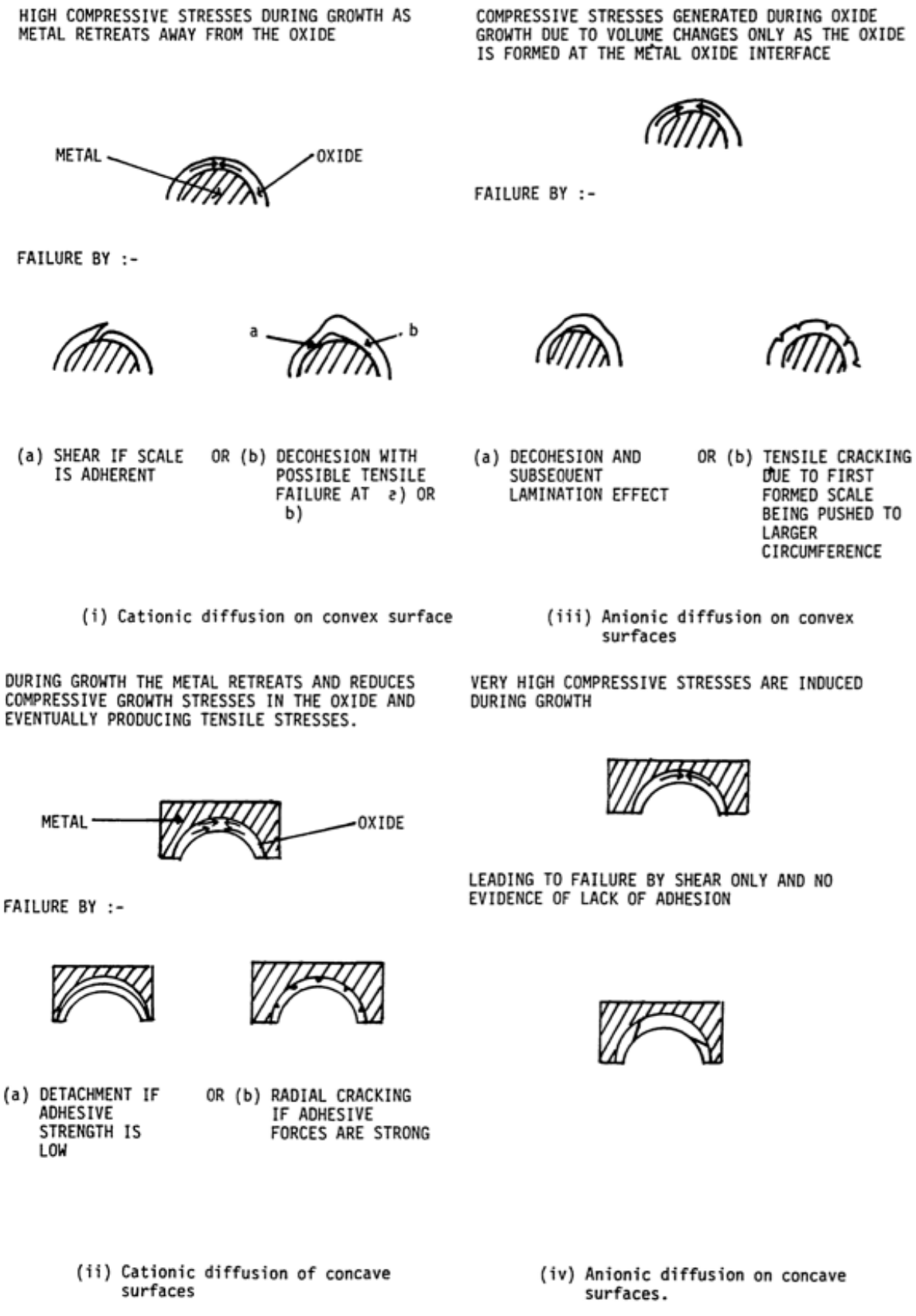

Figure 2.32 – Oxidation and stress development of curved surfaces.

2.4.3.3 Thermal Stresses

The largest source of stress in an oxide is that experienced on cooling (or heating above the oxidation temperature) caused by the mismatch in thermal expansion coefficients between the oxide and substrate.

Tien and Davidson [124] calculated the stress because of a temperature drop for a planar oxide/metal couple where the oxide experiences biaxial stress:

$$\sigma_{ox} = -\frac{E_{ox}\Delta T(\propto_m - \propto_{ox})}{(1-v)\left(1+\frac{E_{ox}h}{E_m\xi}\right)} \qquad \textit{(2-18)}$$

where ξ is the oxide thickness, h is half the specimen thickness, E_{ox} is the Young's modulus of the oxide, ΔT is the temperature change between oxidation temperature and measurement temperature and is positive for cooling, $\propto_m$ and $\propto_{ox}$ are the thermal expansion coefficients of the metal and oxide respectively and v is the Poisson's ratio, assumed to be the same for metal and oxide. Where the thermal expansion coefficient for the metal is larger than that of the oxide, the oxide will be placed in compression and the sign of the stress is negative. The common case for engineering materials is that the substrate thickness, h, is much larger than the oxide thickness, ξ, and Equation (2-18) can be simplified to a thin film approximation:

$$\sigma_{ox} = -\frac{E_{ox}\Delta T(\propto_m - \propto_{ox})}{(1-v)} \qquad \textit{(2-19)}$$

For alloys which grow multi-layered scales the thin film approximation assumes all oxides will be constrained to the dimensions of the alloy substrate and so the above equation can be applied to individual layers in the scale. The "reduced strain" in each oxide layer is [121]:

$$\varepsilon_r = -\frac{\sigma_{ox}(1-v)}{E_{ox}} = -(\propto_m - \propto_{ox})\,\Delta T \qquad \textit{(2-20)}$$

The above equations assume elastic properties for the metal and oxide. However, as will be discussed later, creep effects often act to reduce oxide stresses. These equations also assume that the thermal expansion coefficients and Young's moduli for metal and oxide are independent of temperature, so that generated stresses and strains are proportional to temperature change. Average values often give a reasonable estimation of magnitude and sign of stress. However, certain systems, for example ZrO_2 on Zr and Fe_2O_3 on 9Cr-Mo steel exhibit a change in the sign of $\Delta\propto$ during cooling from different temperatures [125] and so to achieve accuracy in thermal stress calculations integrating the required

parameter over the temperature range of interest is essential. For the strain in an oxide caused by a thermal change this would become [121]:

$$\epsilon_r = -\int_{T_{ox}}^{T} [\alpha_m(T) - \alpha_{ox}(T)]dT \qquad \textbf{(2-21)}$$

where T_{ox} is the oxidation temperature and T is the calculation temperature, usually room temperature. The average thermal expansion coefficients for a number of oxides and alloys are listed in Table 2.4.

Table 2.4 – Average thermal expansion coefficients of some oxides and alloys.

Oxide	α x10^{-6}	Temperature Range °C	Author
Fe_3O_4	10.4	20 – 400	Arkharov et al. [126]
Fe_3O_4	18.6	400 – 700	Arkharov et al. [126]
Fe_3O_4	11.1	700 – 1000	Arkharov et al. [126]
Fe_3O_4	15.4*	25 – 700	Armitt et al. [119]
Fe_3O_4	18.4*	400 – 700	Armitt et al. [119]
Fe_3O_4†	12.5	100 – 400	Rigby et al. [127]
Fe_3O_4†	18.3	100 – 700	Rigby et al. [127]
Fe_3O_4†	17	100 – 1000	Rigby et al. [127]
Fe_3O_4‡	11.5	20 – 400	Sharma [128]
Fe_3O_4‡	16.2	25 – 700	Sharma [128]
Fe_3O_4‡	22.0	400 – 700	Sharma [128]
Fe_2O_3	10.8	100 – 300	Rigby et al. [127]
Fe_2O_3	12.2	100 – 1000	Rigby et al. [127]
Fe_2O_3	11.0 - 14.1	25 – 1000	Gorton et al. [129]
Fe_2O_3	14.9	20 – 900	Tylecote [130]
FeO	15	400 – 800	Robertson et al. [131]
FeO	12.2	100 – 1000	Tylecote [130]
Cr_2O_3	7.3	100 – 1000	Tylecote [130]
Cr_2O_3	8.5	400 – 800	Robertson et al. [131]
Al_2O_3	8.1	400 – 800	Robertson et al. [131]
Fe	15.3	0 – 900	Tylecote [130]
Cr	9.5	0 – 1000	Tylecote [130]
1Cr Mo	12.3 – 17.5	0 – 600	Armitt et al. [119]
2.25Cr 1Mo	11.8 – 16.3	0 – 600	Armitt et al. [119]
9Cr 1Mo	10.1 – 15.1	0 – 600	Armitt et al. [119]
316	17.6 – 19.5	0 – 600	Armitt et al. [119]
Super 304H	17.8	20 – 400	Datasheet [132]
Super 304H	18.6	20 – 700	Datasheet [132]
347HFG	17.8	20 – 400	Datasheet [133]
347HFG	18.7	20 – 700	Datasheet [133]

† - Ore containing quartz and biotite. * - Calculated from curve Fig. 3 -1 in [119]. ‡ - From raw data.

Of practical interest is the thermal expansion of magnetite, which increases linearly up until 400 °C [134]. Above this temperature a steeper gradient is observed until the expansion coefficient reaches a peak at around 570 – 590 °C [126, 127, 129, 134]. The peak is a result of a transformation from inverse spinel structure to a partially ordered one via a cation reordering process [134]. Levy et al. [135] measured the thermal expansion coefficient of magnetite at different pressures and found that under a high vacuum (10^{-6} mbar) the peak at 580 °C was absent and the expansion coefficient followed a roughly linear increase with temperature. The same test conducted in a low vacuum (10^{-4} mbar) displayed the characteristic peak that other researchers had observed [128, 129]. The authors concluded that partial oxidation of samples tested in low vacuum conditions and in previous work [128, 129] had occurred and was responsible for the peak and that the true linear expansion coefficient data was obtained in the high vacuum test. The implication of these findings for boiler steels is that that Fe_3O_4 layer would be expected to grow in compression on both low and high chrome steels. However, that magnetite tends to relieve compressive stresses during cool down [34, 96] and (on a 2.25Cr steel [136]) fail in tension would suggest that the pO_2 conditions in plant are such that historical data for the expansion of magnetite is considered suitable for this system. The thermal expansion coefficients of magnetite measured in oxidising and non-oxidising[1] conditions can be found in Figure 2.33 along with those for haematite, 316 austenitic steel and 9Cr 1Mo steel for comparison.

It can be appreciated from Figure 2.33 that there is a clear peak in the thermal expansion coefficient of magnetite in the conditions in plant. However, scatter exists that needs to be addressed if accurate strain calculations are to be made on oxides containing a significant amount of magnetite.

[1] Levy high vacuum data was fitted to a linear regression line in Figure 2.30.

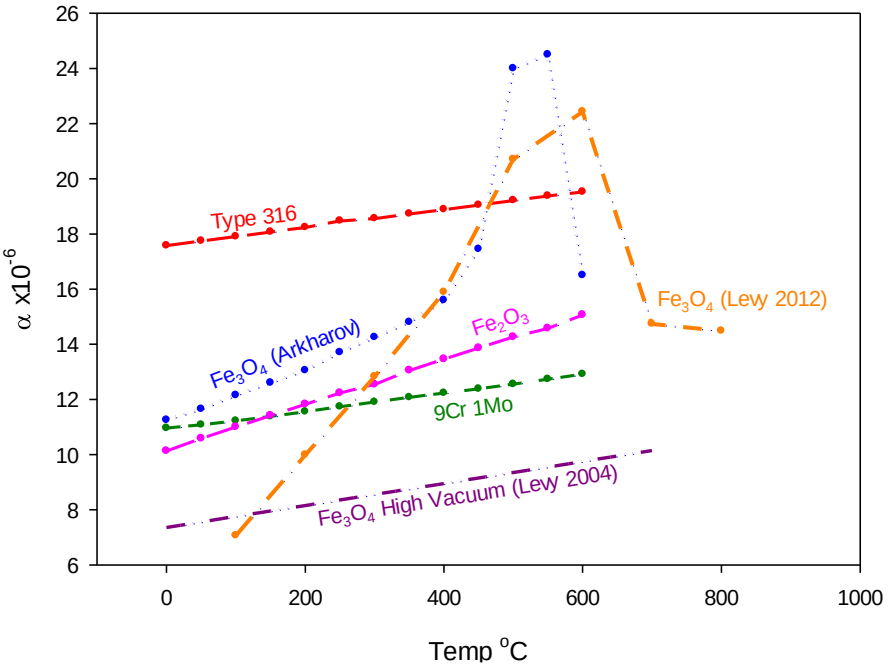

Figure 2.33 – Thermal expansion coefficients of magnetite measured in both oxidising and non-oxidising[1] conditions, along with those for haematite, 316 austenitic steel and 9Cr 1Mo steel [119, 126, 129, 134, 135].

The presence of haematite in the outer scale is thought to contribute significantly to scale adhesion on cooling of boiler steels. Although little quantitative work has been accomplished, there appears to be a correlation between fraction of haematite in the outer layer and quantity of exfoliated scale. Armitt et al. plotted graphs of outer oxide strain after cooling to 25 °C as a function of growth temperature for a series of boiler steels where the oxide was a composite of between 100% magnetite and 100% haematite. Figure 2.34 is one such plot for 9Cr 1Mo steel. The figure shows that increasing the haematite fraction in the outer layer causes the scale to cool in compression, whereas a fully magnetite scale results in a scale in tension on cooling[2]. The possibility for scales both in tension and compression to form on 9Cr steels has been realised by Osgerby [137]. They found the presence of both tensile through thickness cracks and compressive buckling of the outer layer on P92 after exposure to flowing steam for up to 2000 hours at 600 °C. For other steels, such as 18-8 austenitics, any fraction of haematite would be expected to greatly increase the cooling strain in the outer layer making it easy to understand why spallation occurs in the presence of haematite.

[2] Note that in Figure 2.31 a positive value on the y-axis relates to an oxide in compression rather than tension.

a) b)

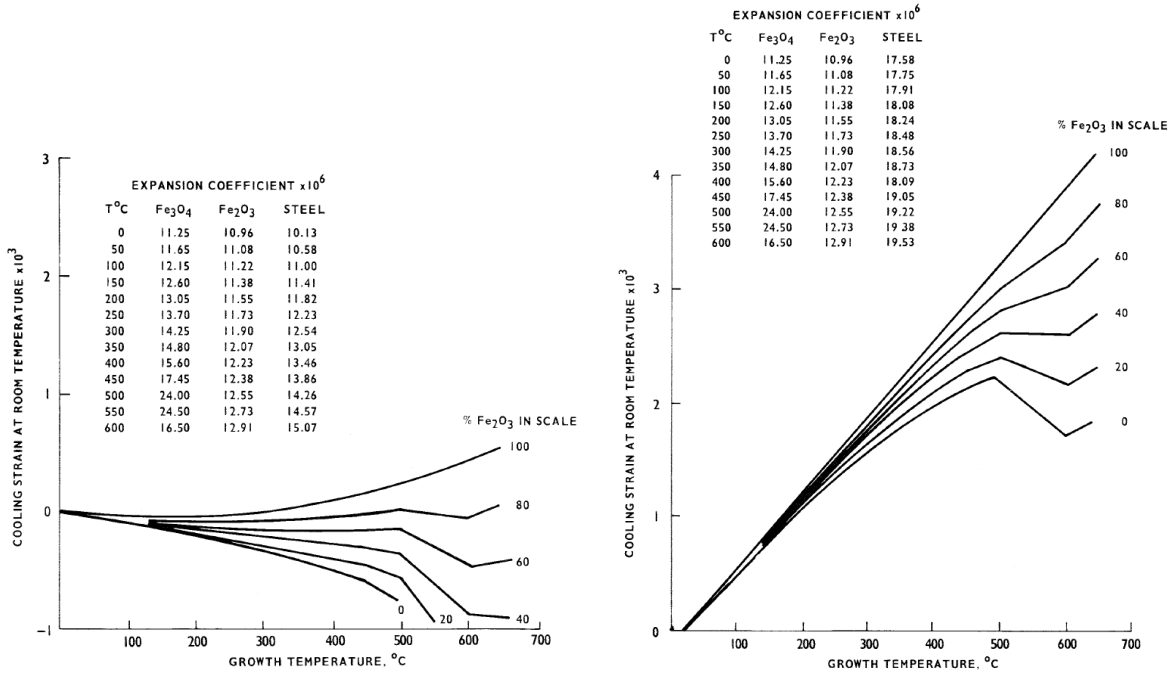

Figure 2.34 – Strain induced on cooling for oxide containing a varying fraction of haematite. (a) 9Cr 1Mo, (b) Type 316. Note that increasing the fraction of haematite causes the scale on 9Cr 1Mo to go into compression [119].

2.4.3.4 Phase Transformation Stresses

It is possible that phase changes within the oxide scale contribute to oxide growth strains [122]. For Fe_2O_3 to Fe_3O_4 growth, the molar volume change would suggest a tensile stress [119], and for Fe_3O_4 to Fe_2O_3, compressive. During the oxidation of boiler tubes both transformations may be expected to occur. An irregular layer of haematite is often present at the scale/gas interface of boiler steels. The presence of this layer after long and short exposures would suggest that, during growth of the outer oxide layer, Fe_2O_3 continually transforms to Fe_3O_4 [137]. However, as the outward cation flux decreases because of protective film formation, suggested by Wright and Dooley [42] for the growth of oxide on austenitic steels in Figure 2.29, Fe_3O_4 may oxidise to Fe_2O_3 resulting in compressive stresses. Unfortunately because of a lack of experimental data, quantitative estimates on strains produced this way are unavailable [119].

The above stress generation mechanisms, along with that of application stresses such as thermal shock and flexural strains [119], contribute to the total oxide stress for the system [138]

$$\sigma_{tot} = \sigma_{gro} + \sigma_{geo} + \sigma_{th} + \sigma_{trans} + \sigma_{app} \qquad \textbf{(2-22)}$$

2.4.3.5 Strain Energy

Neglecting all sources of stress other than that caused by the mismatch of thermal expansion coefficients during temperature transients where $\propto_m > \propto_{ox}$, an oxide grown on a flat specimen will undergo equal biaxial compressive stress on cooling. Considering the "thin film on thick substrate" approximation and assuming elastic conditions, the stored strain energy, W*, within the oxide layer adjacent to the spallation interface after a temperature drop ΔT is [139]:

$$W^* = -(\Delta T)^2 \xi E_{ox} (\propto_m - \propto_{ox})^2 (1 - v_{ox}) \qquad \textit{(2-23)}$$

Evans [140] highlighted two configurations which result in different strain energies. The first envisions an alumina layer of 5 µm on a FeCrAlY steel substrate subject to a 800 °C temperature drop and is an example of how large the strain energy in thin layers can be, giving a W* value of 60 Jm^{-2}. The second is an example of how the strain energy equation can be applied to multiple thin layers on a thick substrate by calculating W* for the commonly grown Fe_2O_3 and Fe_3O_4 layers on 9Cr1Mo steel. Values of 100 µm thickness per oxide layer, a Young's modulus of the oxide of 220 GPa, a temperature drop of 475 °C and thermal expansion coefficients from Armitt et al. [119] are used to obtain approximately 1 Jm^{-2} and 9 Jm^{-2} respectively. Note that W* is always a positive quantity and so cannot be used to identify whether a layer is in tension or compression. In the above case Fe_2O_3 is 85 MPa in compression and Fe_3O_4 230 MPa in tension. Importantly, as highlighted by Evans [140], only small changes in the values of expansion coefficients are needed to potentially alter the sign of stress and so care must be taken when choosing such values from available literature. The example uses values listed in the 1978 EPRI report by Armitt et al. [119], which sourced values from several researchers' findings [126, 127, 129].

2.4.4 Stress Relief

Thermal transients are responsible for producing the largest stresses in steamside oxide layers and so major scale fracture and exfoliation in plant occurs during the boiler cooling cycle. Failure originates from weak spots in the scale such as pores and defects that cracks generate from, which then follows a mechanism for stress relief. The following section outlines mechanisms for stress relief for oxides in tension or compression as a result of a change in temperature.

2.4.4.1 Failure in Tension

Oxide fracture and spallation because of tension is a rare occurrence during cool down and more likely to proceed by heating the metal above its oxidation temperature. Consider elastic deformation where the rapid application of strain allows creep effects to be neglected such that the only form of stress

relief is through fracture of the oxide layer. This is a reasonable assumption for boiler steels where service temperatures do not reach that where creep in the oxide layer is likely to affect stress relief [121]. A through-scale tensile crack will nucleate from a pre-existing surface defect which are numerous in scales. Propagation of the crack will occur at a critical stress, normal to the crack growth direction:

$$\sigma_c = \frac{K_{1c}}{f(\pi\bar{a})^{1/2}} \qquad \textbf{(2-24)}$$

where f is a factor of around unity determined by the nature of the defect, $2\bar{a}$ is the size of the defect. In fact, oxides tend to be porous in nature and multiple defects are likely to contribute to scale failure. $\bar{a}$ is a composite of mechanically interacting defects as defined by Hancock and Nicholls [141]. K_{1c} is the critical stress intensity factor, which characterises the resistance to crack growth and can be written in terms of the critical energy release rate, G_{1c}, and surface energy for elastic failure, γ_s [121]:

$$G_{1c} = {K_{1c}^2}/{E_{ox}} = 2\gamma_s \qquad \textbf{(2-25)}$$

A crack will continue to propagate while the energy release rate is larger than the critical energy release rate of the oxide:

$$G > G_{1c} \qquad \textbf{(2-26)}$$

The critical fracture strain may then be written in terms of γ_s:

$$\varepsilon_c = \left(\frac{2\gamma_s}{f^2\pi E\bar{a}}\right)^{1/2} \qquad \textbf{(2-27)}$$

For the propagation of a long surface flaw this can be simplified to:

$$\varepsilon_c \approx \left(\frac{2.5\gamma_s}{\xi E}\right)^{1/2} \qquad \textbf{(2-28)}$$

where ξ is the oxide thickness and acts as an upper bound to $\bar{a}$ [131].

It can be seen in Figure 2.35, that the critical stress intensity factor, K_{1c}, increases dramatically at higher temperatures. This is a result of creep effects blunting stresses at crack tips [120]. γ_s is the

surface fracture energy of the oxide, taking into account creep effects and is affected by a large grain size and porosity, both decreasing its value [131].

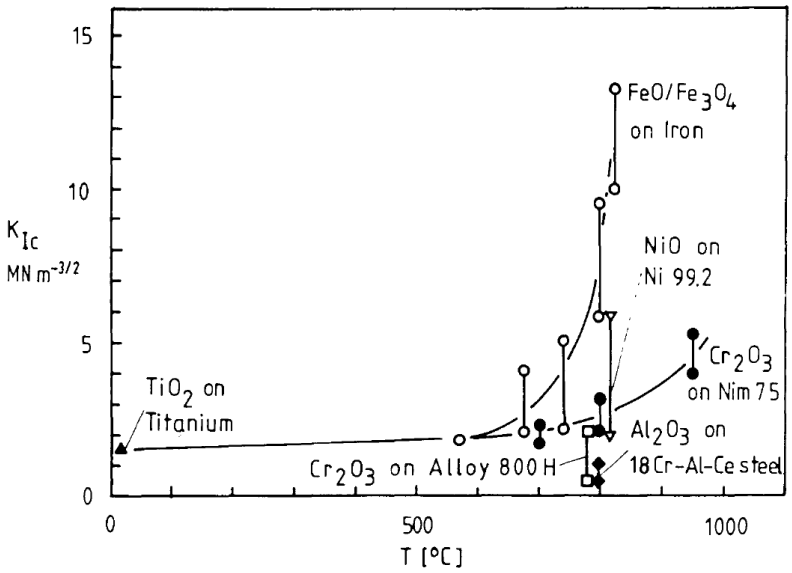

Figure 2.35 – Variation of critical stress intensity factor, K_{1c}, with temperature for some oxides. After Schütze [142].

A through thickness tensile crack will disturb the in-plane stress field adjacent to the crack. A schematic of the stresses present between two cracks is shown in Figure 2.36 (a) [121].

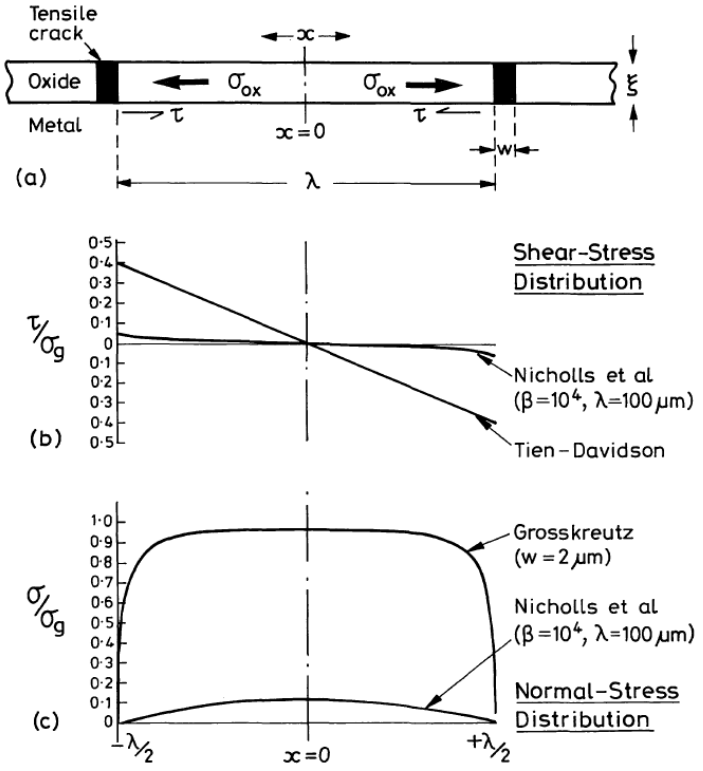

Figure 2.36 – Schematic of in-planes stresses between two tensile cracks [121].

An oxide section between two tensile cracks, as in Figure 2.36 (a), will reduce in length, relaxing the in-plane stress within the oxide layer adjacent to the fracture surface [143]. The exact stress distribution is not known but the in-plane stress will be a maximum furthest away from a crack ($x = 0$ in Figure 2.36) and a minimum at the crack face. Two possible distributions for the in-plane oxide stress are illustrated in Figure 2.36 (c). At the metal/oxide interface, shear stress will develop as the oxide tried to contract. This will be a maximum at the crack tip and reduce to zero at $x = 0$ as in Figure 2.36 (b). At this interface where the shear stress is a maximum, relaxation may occur either by creep deformation of the interface or interfacial cracking. Cracking is expected when the shear stress at the edge of the tensile crack is greater than the interfacial adhesive stress of the metal and oxide as illustrated in Figure 2.37 (a). Tien and Davidson envisage the crack to extend along the metal/oxide interface causing brittle failure and spallation. Alternatively, Evans [144] suggests sliding of the oxide can occur along the metal/oxide interface via the nucleation of voids. If the shear stress is high enough such that these voids grow and coalesce, spallation will result (Figure 2.37 (b)).

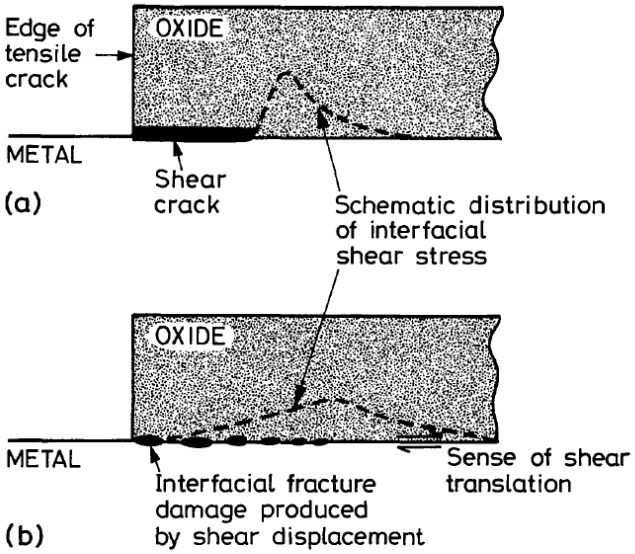

a nucleation and growth of shear crack; *b* interfacial slip and void formation

Figure 2.37 – Relaxation of shear in oxide following a tensile through crack. (a) brittle crack propagation as proposed by Tien and Davidson. (b) relaxation of shear stress via oxide slipping as proposed by Evans [144].

2.4.4.2 Failure in Compression

The spallation of oxide layers from their substrate requires both through thickness cracks and decohesion to occur at whichever interface is spalling. This can be the metal-oxide interface, the interface between two oxide layers or inside a particular oxide. The latter can possibly occur as a result of voids within the oxide layer. The order of which a through thickness crack or decohesion occurs is usually dependent on the oxide thickness and strength of the interface at which decohesion occurs. It follows that this order determines which of two routes proposed by Evans [139] the spallation

mechanism follows. Figure 2.38 schematically illustrates both routes as applied to an oxide grown on a flat substrate. Here, the only source of stress is that applied during cooling, where the thermal expansion coefficient of the oxide is smaller than that of the substrate and so the oxide is put into compression.

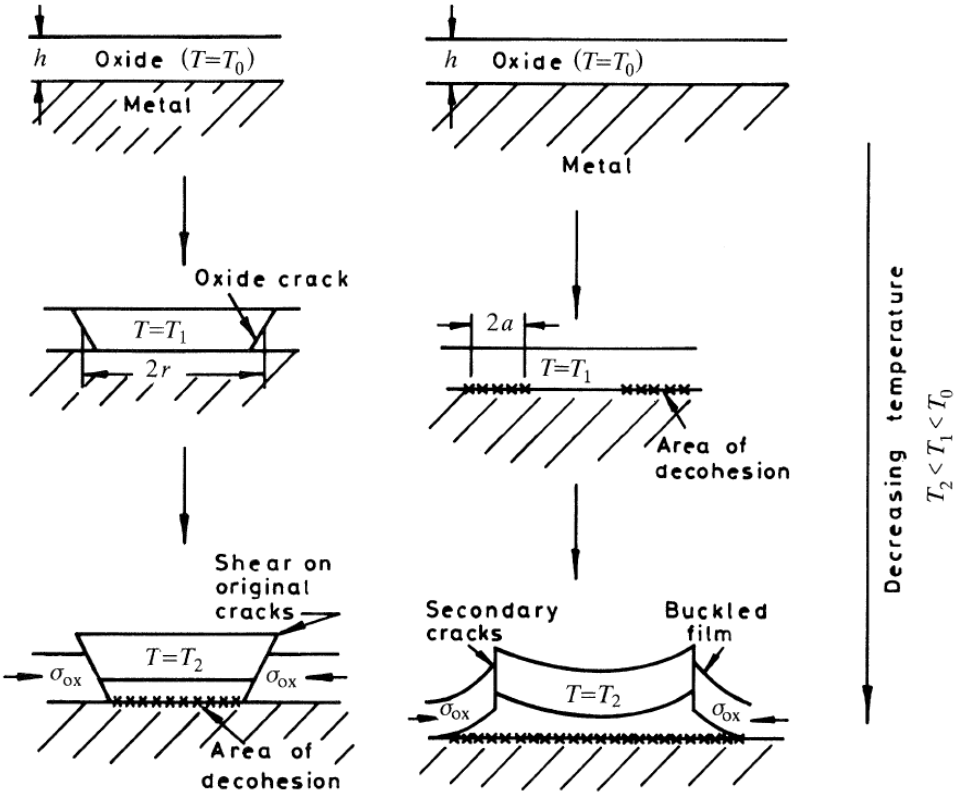

Figure 2.38 – Oxide compressive failure modes by (a) Route I wedging and (b) Route II buckling as proposed by Evans [139].

2.4.4.2.1 Route 1 – Wedging

The wedging process is favoured when the spallation interface has a higher strength to that of the oxide and has not been weakened by void formation. Upon cooling, relaxation occurs through the generation of inclined shear cracks through the oxide layer, providing an amount of stress relief. On continued cooling, the oxide slides over itself to relieve further stress and this exerts a tensile stress at the base of the shear crack between the metal and the portion of oxide to be spalled. As the tensile stress overcomes the strength of the oxide-metal interface, decohesion occurs and a wedge crack initiates and propagates along the spallation interface. Spallation of this type can be recognised by considering the critical strain energy criterion (CSEC), which proposes that spallation will occur when the stored energy per unit interfacial area within the oxide layer, W^*, equates to the shear fracture surface energy per unit interfacial area, γ_F [140]. So, for an interfacial area of decohesion, λ^2, and oxide thickness, ξ, spallation is expected when:

$$\lambda^2 \xi W^* = \lambda^2 \gamma_F \qquad \textbf{(2-29)}$$

Substituting in the equation for strain energy a critical temperature drop to initiate spallation can be obtained:

$$\Delta T_c = \left[\frac{\gamma_F}{\xi E_{ox}(\propto_m - \propto_{ox})^2(1-v)}\right]^{0.5} \qquad \textbf{(2-30)}$$

The above equation implies that as the oxide gets thicker, the temperature drop required to cause spallation decreases. Rearranging the equation it can be seen that for a given practical temperature drop (oxidation to room temperature for example), there will be a critical thickness at which spallation occurs:

$$\xi_c = \frac{\gamma_F}{(\Delta T_{max})^2 E_{ox}(\propto_m - \propto_{ox})^2(1-v)} \qquad \textbf{(2-31)}$$

The applicability of the CSEC has been shown for the growth of chromia on a 20Cr-25Ni-Nb-stabilised steel [139] in which the onset of spallation after isothermal exposure at 1123 K occurred at lower temperature drops as the oxide thickness (calculated from mass gain) increased. A requirement for the CSEC to apply is that stored energy within the oxide particle should be released catastrophically in the spallation of the particle. For this to occur, steady propagation of the interfacial tensile crack is not allowed, instead, instantaneous propagation of an interfacial crack leading to loss of adhesion of the particle should occur at a defined temperature drop. Finite element analysis [125] of wedging spallation behaviour of a 2 µm chromia layer overlaying a 0.1 µm silica interlayer on a 20Cr-25Ni-Nb-stabilised steel has shown that rapid crack propagation is only observed in non-elastic conditions, where creep of the substrate is taken into account, as shown in Figure 2.39 (a).

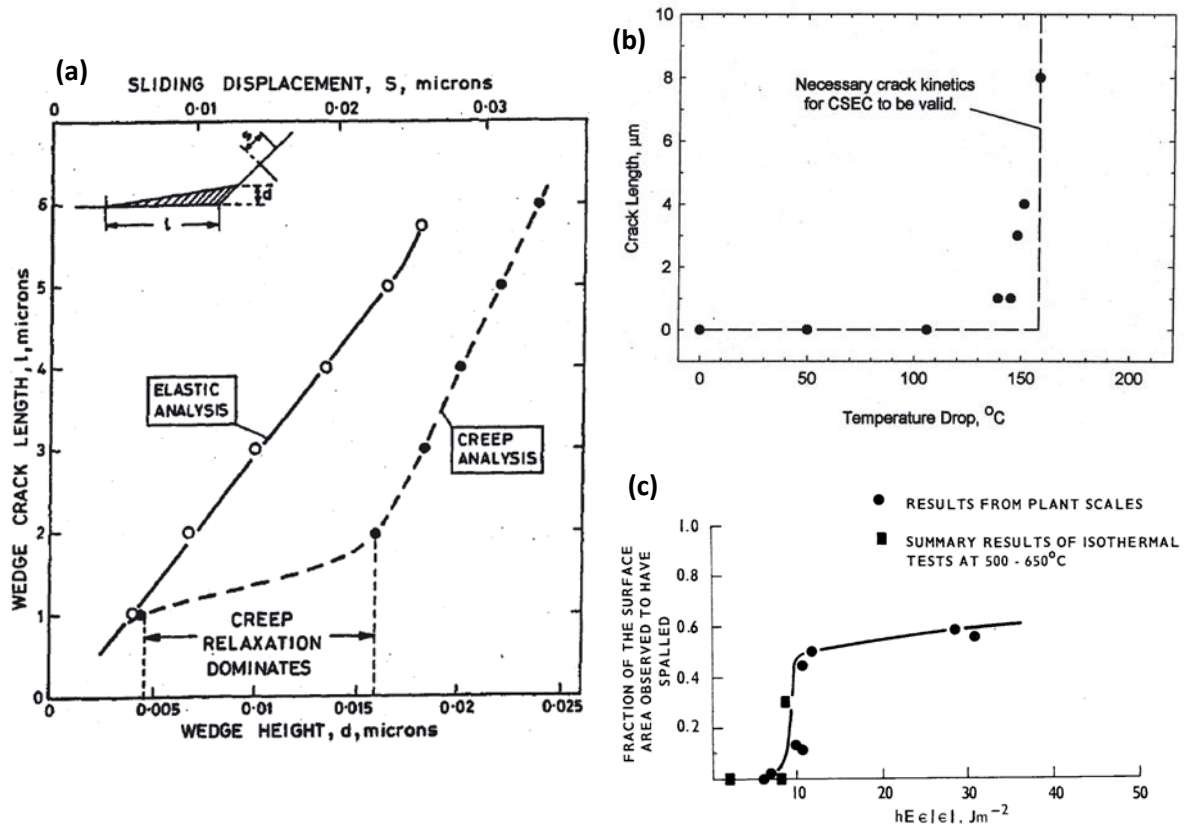

Figure 2.39 – (a) Finite element analysis computation [125] of tensile wedge crack length as a function of height for 2 µm chromia layer overlaying a 0.1 µm silica interlayer on a 20Cr-25Ni-Nb-stabilised steel, illustrating the effect of substrate creep on crack growth rate. (b) Computed critical temperature drop for a 5 µm chromia layer with 0.1 µm silica interlayer on Type 316 steel [140]. (c) Fraction of oxide spalled as a function of stored energy for Type 316 steel [119].

Evans [140] has performed finite element analysis on a 5 µm chromia layer where propagation of the interfacial wedge crack occurs within a 0.1 µm silica interlayer on Type 316 steel and found stress relaxation at the crack tip to occur through a temperature drop of ~150 °C. Catastrophic spallation occurred on further cooling as relaxation processes were unable to prevent wedge crack propagation. The calculated values of crack length with respect to temperature drop, along with required kinetics for application of the CSEC are shown in Figure 2.39 (b). The figure shows that for this system the CSEC is applicable. Plant and laboratory data of spallation of oxide grown on Type 316 steel compiled by Armitt et al. [119] complement the calculations by Evans on Type 316 by showing that the fraction of surface area spalled increases sharply at a critical strain energy, as shown in Figure 2.39 (c). The general conclusion for wedge crack growth is that the CSEC can apply only if creep relaxation is present.

2.4.4.2.2 Route 2 – Buckling

Where the cohesive fracture energy of the oxide exceeds the interfacial fracture strength of the spallation interface, route 2 may be followed. Initially, biaxial compressive stresses in the oxide cause

buckling to occur over an area of decohesion of radius R. On a macroscopic scale this may look like scale rumpling. Enlargement of the buckle requires either the decohesion zone to expand laterally or the buckle to increase in height. In the latter case, tensile stresses will increase in areas of maximum curvature and eventually cause through thickness cracking and release of the oxide particle above the area of decohesion. Assuming elastic conditions, the critical stress to form a buckle over an area of interfacial decohesion of radius R is given by [125]:

$$\sigma_b = \frac{1.22E_{ox}}{(1-v^2)}\left(\frac{\xi}{R}\right)^2 \qquad \textit{(2-32)}$$

and the critical temperature drop:

$$\Delta T_b = \frac{1.22}{\Delta\alpha(1-v^2)}\left(\frac{\xi}{R}\right)^2 \qquad \textit{(2-33)}$$

From the above equation it can be seen that for a given radius of decohesion, the critical temperature drop to produce buckling increases as oxide thickness increases.

2.4.5 Spallation Models

Compilation of accurate spallation models in plant is the goal for research in this area. For this to be realised, a plant operator should be able to input a set of parameters indicating the alloy system, kinetics, steam parameters, cyclic behaviour and exposure duration and obtain data on time and extent of spallation. Ideally, the model would be a computer program that accounts for various sources of stress etc. and outputs a simple estimation of spallation behaviour. So far, attempts at modelling have seen the development of *spallation maps* that predict the failure mode of a given alloy/oxide system.

Spallation maps are separated by boundaries into areas of scale integrity or failure by a particular mechanism and are usually a function of oxide thickness and temperature drop or strain energy. Their usefulness as a predictive tool is limited by the requirement for oxide thickness data. Nevertheless, they are still useful for comparing the failure modes of experimental data. One such map (Figure 2.40) has been compiled by Evans [125]for chromia oxide growth on a 20Cr25NiNb-stabilised steel cooled from an oxidation temperature of 1173 K at a rate of 100 K/h. The map is compiled using equations for the critical temperature drop required to initiate spallation by both buckling and wedging mechanisms and outlines four possible outcomes for the oxide layer on cooling. On the left hand side, buckling will occur where spallation results from tensile through cracks in the oxide around the

parameter of the buckle. Unstable lateral propagation of such buckling is only expected inside the upper region of "wedging or unstable buckling". Dominating the map is failure by wedging. A value of γ_F = 2 Jm^{-2} was chosen for the effective fracture energy. This, in agreement with finite element analysis when allowing for creep of the substrate [125], forms a reasonable lower bound to experimental data of spallation of chromia on the same alloy [139]. The effective fracture energy from the experimental data was deduced to be γ_F = 6 Jm^{-2}. The critical tensile fracture stress of the silicon interlayer was thought to be responsible for the low estimation of ΔT_c in the finite element model, which was chosen to be σ_0 = 300 MPa. Increasing σ_0 to 600 MPa would bring the critical temperature drop for a given oxide thickness in line with the experimental data [125]. Alloy or oxide creep deformation will retard the growth of an interfacial crack on cooling, increasing the effective fracture energy required for spallation. Therefore, alloys with low creep resistance have a high γ_F and are expected to exhibit less spallation. On the spallation map, increasing γ_F will move the wedging boundary to the right increasing the bottom area where little mechanical damage is expected. It follows that as the extent of creep is determined by the cooling rate, increasing this parameter will decrease ΔT_c, shifting the wedging boundary to the left on the spallation map. Buckling is affected by the radius of decohesion, which, for properly designed high temperature alloys should be small, so that buckling is only expected in thin oxides [121]. The boundary in Figure 2.40 was calculated using a radius of *R* = 10 µm, approximately 20 times that of the oxide thickness. Increasing *R* would have the effect of shifting the buckling boundary to the right.

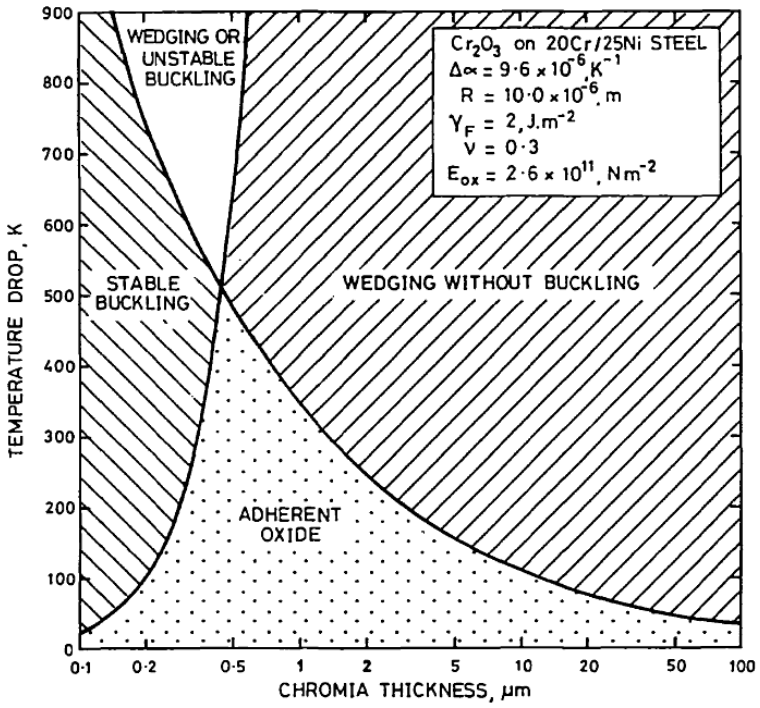

Figure 2.40 – Spallation map for chromia formation on a 20Cr25NiNb-stabilised steel cooled from 1023 K [125].

Robertson and Manning [131] developed a spallation map based on the critical strain of an oxide layer and plotted total elastic strain against oxide thickness using critical strain to failure equations for tensile and compressive failure, to form regions of adherent and exfoliated scale. Tensile:

$$\varepsilon_c = \left(\frac{2.5\gamma_s}{hE}\right)^{1/2} \qquad \textbf{(2-34)}$$

and compressive:

$$\varepsilon_c = \left(\frac{2\gamma_s}{hE}\right)^{1/2} \qquad \textbf{(2-35)}$$

The authors did not quantify the failure boundaries by application of realistic parameter values and so their map remains a highly theoretical one.

An early attempt at mapping spallation was made in EPRI report FP-686 [119]. The map has a similar form to that constructed by Robertson and Manning [131]. Boundaries are plotted of the strain tolerance to failure via the different failure mechanisms exhibited by austenitics (compressive failure) and ferritics (tensile failure). The diagram also includes boundaries for the effect of geometry on compressive strains and the possible regimes associated with tensile failure where features such as through-scale cracking and multi-laminated scales affect adherence.

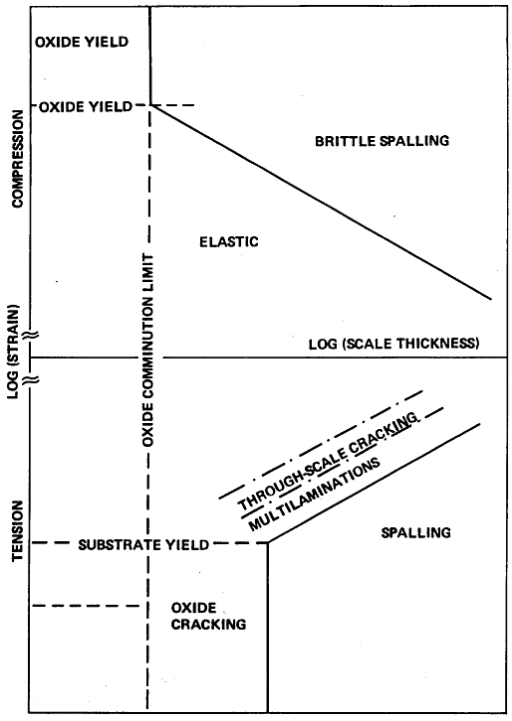

Figure 2.41 – Spallation map of tensile and compressive oxide failure modes after Robertson and Manning [131].

The levels of oxide strain experienced by austenitic steels are often much larger than ferritic steels and that experienced by ferritic steels is usually tensile, unless there is a presence of haematite. It is therefore clear that there is difficulty in obtaining accurate strain data without considering additional parameters. Nevertheless, Dooley et al. [34] calculated the strains on ex-service T22 ferritic and Type 304 austenitic tubes that exhibited exfoliation based on 0% haematite and 20% haematite. The data points, superimposed on the Armitt map in Figure 2.42 (a) shows that the scales grown on Type 304 austenitic steels are in compression and within the domain of expected spallation[3]. The data for T22 ferritic steels are between the boundaries of expected exfoliation and adherent scale introducing an element of discrepancy between the data and calculated boundary conditions. All the scales on the T22 steels had exfoliated. However, it is unclear what percentage of haematite was present in each scale. It is clear from the diagram that the presence of haematite in the oxide of ferritic steels improves scale integrity [34].

Schütze et al. [145] recognised the limitations of the EPRI FP-686 spallation map and used it as a basis for a more comprehensive failure diagram. The updated diagram, shown in Figure 2.43, substitutes oxide thickness on the abscissa for ω_o, the "scale property" parameter that encompasses all the properties of a scale and the effects which arise from operation.

[3] Here again please note that in Figure 2.39 a positive value on the y-axis relates to an oxide in compression rather than tension.

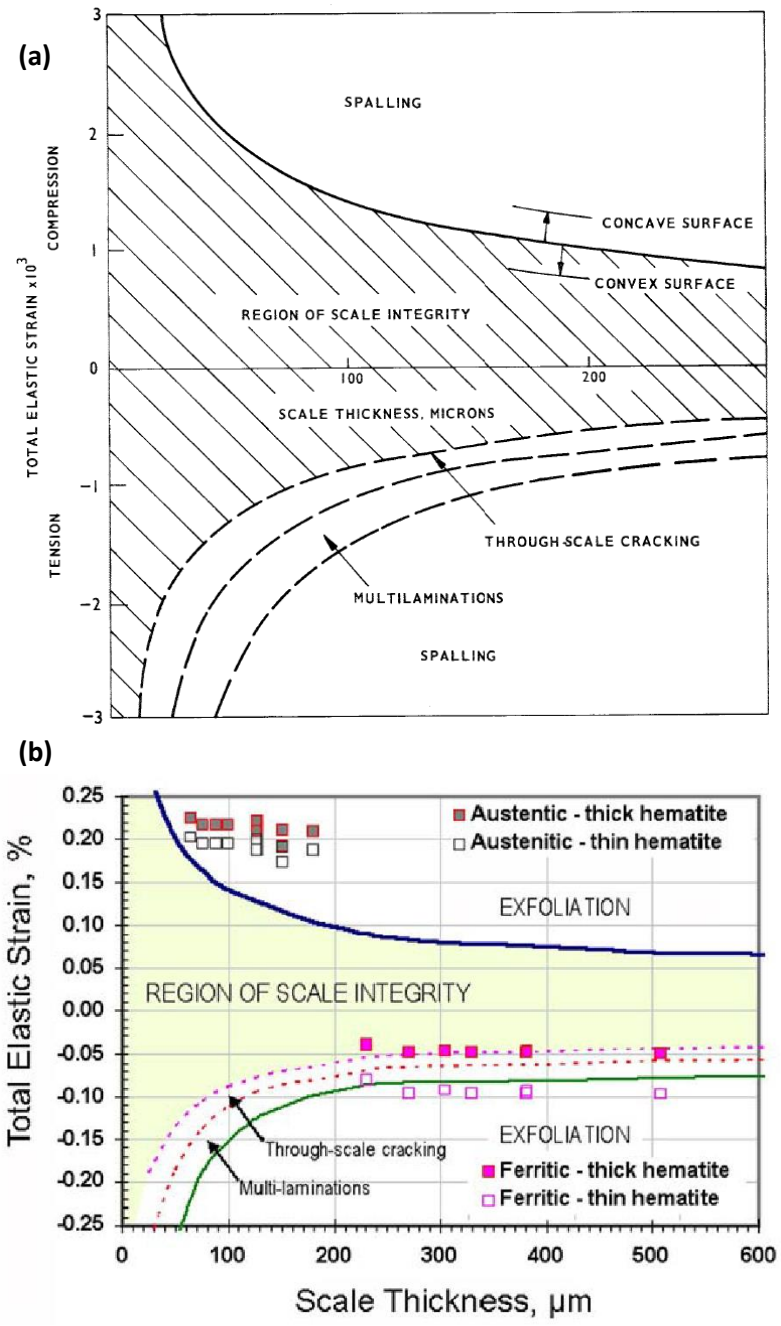

Figure 2.42 – (a) Spallation map in terms of total elastic strain and oxide thickness developed by Armitt et al [119]. (b) Scale thickness data for austenitic and ferritic steels super-imposed on Armitt et al. spallation map [34].

The authors initially consider the parameters that affect the strain on the oxide due to plant operation to give the total strain. This can be compared to the critical strains for the different modes of failure the oxide scale may be subject to (through-scale cracking, delamination, wedging, buckling):

$$\varepsilon = \varepsilon_{ext} + \varepsilon_{therm} + \varepsilon_{grow,int} + \varepsilon_{grow,geo} - \varepsilon_{creep} - \varepsilon_{pseudopl}$$

The different strain terms are as follows:

ε_{ext} – External strains imposed on the oxide via the alloy during operation;

ε_{therm} – Thermal transient strains caused by thermal expansion coefficient mismatch;

$\varepsilon_{grow,int}$ – Intrinsic oxide growth strains;

$\varepsilon_{grow,geo}$ – Growth strains resulting from the geometry of the alloy (concave for steamside of boiler tubes);

ε_{creep} – Creep processes that act to relieve the strain on the system; and

$\varepsilon_{pseudopl}$ – Pseudo plasticity strains that relieve the strain on the system via networks of microcracks that can appear and heal during operation.

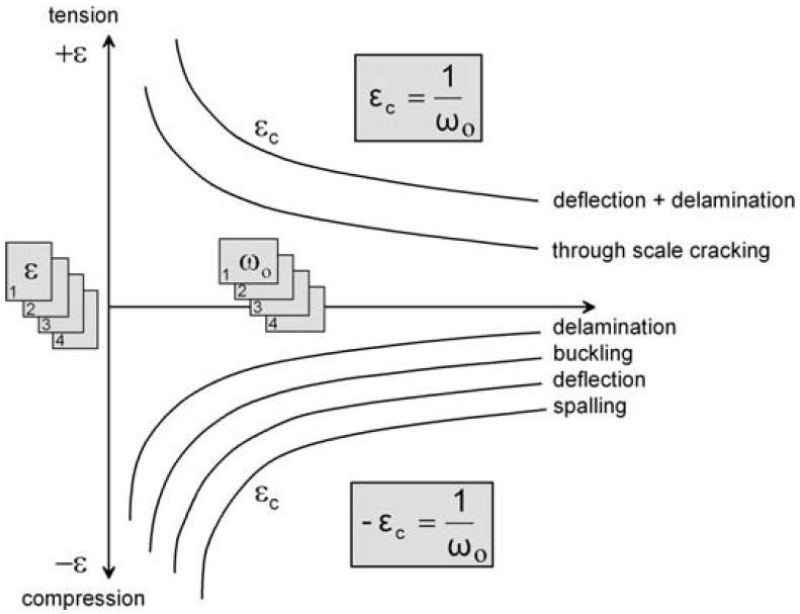

Figure 2.43 – Comprehensive oxide failure diagram as proposed by Schütze et al. [145]

The scale parameter term, ω_o, is related to the critical strain, ε_c, by:

$$|\varepsilon_c| = \frac{1}{\omega_o} \qquad \textbf{(2-36)}$$

and is related to different failure modes:

- Through-scale cracking in tension;
- Continued crack growth in tension via an existing microcrack network;
- Interfacial crack growth initiating at a pre-existing defect, either in tension or compression;
- Scale buckling in compression; and
- Spalling in compression.

The ω_o concept may be used as a foreground diagram and further background "levels" may be added for increased complexity. These levels would involve describing the parameters of each failure mode by separate equations to increase the accuracy of the model. A relevant example of this would be for thermal strains, in which the identified strain equation:

$$\varepsilon_{therm} = -\frac{\Delta T(\alpha_m - \alpha_{ox})}{(1-\nu)} \qquad \textbf{(2-37)}$$

contains sub-parameters (α_m and α_{ox}) that can be described in a further equation as a function of temperature to improve accuracy:

$$\Delta\alpha = \int_{T_{ox}}^{T} [\alpha_m(T) - \alpha_{ox}(T)]dT \qquad \textbf{(2-38)}$$

The parameters associated with ω_o were then categorised as low and high-impact. Low impact parameters are those that are independent of operation history and show little change during high temperature service. These were summarised by $\eta(m)$, characterised by equations relating to each failure mechanism (m). The high impact parameters, those that are influenced by high temperature exposure, are summarised by $\omega(t, m)$, which also takes into account exposure time (t). The critical strain then becomes:

$$\epsilon_c(m) = \frac{\eta(m)}{\omega(t, m)} \qquad \textbf{(2-39)}$$

This approach should provide a more reliable assessment of oxide scale integrity compared to the oxide thickness approach considered by Armitt el al. [119]. However, to benefit fully from the model, a computer program based approach is suggested. Currently, no computer implementations of this model have been developed to accurately predict in service failure mechanisms. It was proposed that the parameter that most influenced the critical strain to scale failure for each failure mechanism was the physical defect size c. A simplified diagram that allows estimation of the critical strain to failure based on the defect size c and low impact parameters η was proposed:

$$\epsilon_c(m) = \frac{\eta(m)}{\sqrt{(c/c_o)}} \qquad \textbf{(2-40)}$$

and shown to provide critical strains in reasonable agreement with the $\eta(m)$, $\omega(t,m)$ approach for a typical oxide grown on low alloy steel. Obtaining accurate data on the physical defect sizes in the oxide scale is still a requirement for this approach, which must be done metallographically post-oxidation.

2.5 Current State of Understanding of Steam Oxidation of Austenitic Steels and Research Focus

In this chapter oxidation mechanisms and behaviour in air and steam were reviewed for three types of steels used in heat recovery steam generators today. In order of least oxidation resistant to most oxidation resistant these were found to be: low-chromium (<5%Cr) ferritics, mid-chromium martensitic ferritic (9-12%Cr), and high-chromium (≥18%Cr) austenitic steels. The current research focuses on the steam oxidation of 347HFG, Super 304H and HR3C austenitic steels.

The reviewed literature can broadly be split into two groups – long term studies conducted on ex-service [96], [58], [109] or in-plant / test loop trials [111], [117], [118], and short term laboratory studies conducted on machined coupons or small sections of installation-ready boiler tubing. Boiler tubes are usually installed with the inner (steamside) surface pickled. Long term studies that analyse pickled tubing provide an accurate reflection of the morphology and long term kinetics of a given alloy. These long term studies have shown 18Cr austenitics to grow a duplex oxide in high temperature steam [96]. 25Cr austenitic steel has been reported to resist internal oxidation, and form an external passivating Cr_2O_3 oxide in steam. The effect of chromium content will be explored in the current project by directly comparing the oxides grown on 18Cr 347HFG and Super 304H with 25Cr HR3C in both air and steam.

Short term laboratory experiments conducted on pickled 18Cr austenitic steel confirm duplex oxide growth, noting healing layer formation at prior austenite grain boundaries. Laboratory studies on pickled alloys are limited [68, 80]. Experiments conducted on ground samples that grew duplex oxide have shown that the outer layer grows by outward cation diffusion and the inner layer by inward anion diffusion [116].

Several analyses on ex-service or test loop tubes report the outer oxide layer to consist of both Fe_3O_4 and Fe_2O_3 following long term oxidation in deoxygenated steam. A mechanism provided by Wright and Dooley [96] proposes that Fe_3O_4 oxidises to Fe_2O_3 following the formation of a Cr-rich healing

layer at the base of the spinel. Laboratory experiments for up to 336 hours on 347HFG suggest that Fe_2O_3 growth is suppressed in low pO_2 environments at 600 °C but forms when the pO_2 of the carrier gas increases. Interestingly, little difference in oxidation rate was observed between high and low pO_2 environments. Oxidation experiments in air, deoxygenated steam, and air saturated steam will be undertaken in the current project to directly compare the effect of oxidation atmosphere and oxygen partial pressure on oxidation behaviour.

Although many short term laboratory studies have been conducted on the oxidation of austenitic steels, they are often conducted on ground or polished samples (in air [35], [30], [44], [54], [146] or steam [76], [57]).This makes direct comparison to pickled alloys difficult. As discussed in Section 2.2.2.3, surface preparation has a large effect on the oxidation of austenitic steels, and a general trend can be deduced from the literature. The surface finishes that show from most to least oxidation resistance are: shot peened>ground>polished>electro-polished>etched>annealed>pickled. A high "resistance" in this context refers to the growth of a thin, Cr-rich protective oxide, rather than a thick duplex oxide as would be expected in plant. Comparisons between ground and pickled samples have been made, and show pickled samples to grow consistently thicker scales [46], [66], [45].

As with shot peening, ground or polished surfaces promote the formation of Cr-rich oxides, which offer more protection than duplex oxide growth found on pickled alloys. Formation of these oxides affect the oxidation kinetics, spallation behaviour and ultimately the lifing characteristics of the alloy. The use of ground coupons in short term laboratory tests can be useful for reproducibility when investigating a particular variable, for example, flow rate. However, the aim of the current research is to investigate the oxidation behaviour of the surface treatments that would be installed in plant, and therefore, much of the existing literature cannot be drawn on for direct comparison. Two steamside surface finishes commonly used in plant will be directly compared in the current project: pickled and shot peened.

Of the three alloys that are the focus of the current research, 347HFG has been the subject of the most research. A number of laboratory studies have investigated the oxidation performance of Super 304H and HR3C [29], [35], [45] (or the similar TP310 grade [57], [79]), but these were conducted primarily on ground or polished samples, and so do not reflect the oxide that would be expected to grow in-service. A study on the effect of shot peening of TP304 (coarse grained) and HR3C confirmed the benefit of shot peening but was compared with ground samples and therefore not illustrating the improvement over the standard pickled finish [35]. Lukaszewicz [76] compared the effect of modifying steam flow rate over samples of 347HFG and Super 304H. The results showed that increasing the steam flow rate increased the oxidation kinetics. These experiments were carried out on ground

samples, although the mechanistic process proposed would suggest they would be applicable to pickled alloys. The steam flow rate has been shown to influence oxidation behaviour of austenitic steels and so flow rate will be monitored and controlled in the current project to reduce the effect of this variable.

Regarding oxidation kinetics in steam, it is common for researchers to assume their data follows parabolic kinetics [108]. This allows for direct comparison of the parabolic rate constant, k_p, with other researchers. Confidence in fit increases with time, as the kinetics of short term experiments may be skewed by an initial period of transient oxidation [72]. Assuming parabolic kinetics has been most successful when applied to high Cr (>20 wt.%) austenitics [42, 59], or shot peened alloys [27, 35], which tend to form Cr-rich protective oxides, rather than thick duplex oxides. Coarse grained austenitics with less than 20 wt.% Cr appear to be susceptible to breakaway oxidation in steam because of insufficient Cr flux to the oxidation interface [38]. Whereas the opposite is true for fine grained austenitics. These oxidise at an initially rapid rate before significantly slowing once the internal oxidation front consumes the first layer of austenite grains and rapid Cr diffusion along grain boundaries facilitates the formation of a Cr-rich healing layer [38, 66]. The latter behaviour is of significant interest to the current project.

Surface finish is known to influence oxidation kinetics [45], and the kinetics reported by many laboratory studies may not be directly applicable to those seen in plant. There is therefore a need for further laboratory data on the oxidation of pickled alloys that is representative of those installed in plant. The current project will address these issues by calculating the reaction order, n, for each alloy, surface finish, and oxidation environment, and determine whether the oxidation behaviour of each alloy can be fit with a high level of confidence to a particular kinetic regime. The oxidation kinetics will be calculated from both mass change and oxide thickness data. The thickness of individual oxide layers will be used to investigate the variation of oxidation kinetics with time.

The literature review has also shown that spallation is favoured when the outer oxide contains an appreciable fraction of haematite. However, few studies were found that compare oxidation in steam atmospheres containing varying amounts of oxygen with the specific aim of comparing the morphology and spallation tendency of the outer oxide. Therefore, this project will conduct oxidation experiments in air, deoxygenated steam, and air saturated steam to compare the effect of oxygen partial pressure on the spallation behaviour of austenitic steels. These experiments will aim to validate proposed mechanisms that have primarily developed from analysis of the oxide grown on ex-service boiler tubes [42].

In summary, the current research will focus on addressing gaps in the literature by investigating:

- The steam oxidation of 347HFG, Super 304H and HR3C austenitic steels;
- The effect of chromium content for the oxides grown on 18Cr 347HFG and Super 304H with 25Cr HR3C in both air and steam;
- The effect of oxidation atmosphere and oxygen partial pressure on oxidation behaviour;
- The effect of pickled and shot peened steamside tube surface finishes commonly used in plant;
- The reaction order for each alloy, surface finish, and oxidation environment, to enable determination the oxidation behaviour to a particular kinetic regime; and
- The effect of oxygen partial pressure on the spallation behaviour of austenitic steels.

Chapter 3 Experimental Procedure

3.1 Introduction

This research programme investigated the oxidation behaviour of the steam-side (inner surface) of austenitic steel HRSG tubing used in conventional power plant applications. All alloys used in this project were in the "as-received" tube form to ensure they would be representative of those installed in plant. Two inner (steamside) surface were investigated – pickled and shot peened, to compare the effect of surface modification on the oxidation behaviour.

Oxidation was primarily conducted in flowing steam at atmospheric pressure. The effect of oxygen partial pressure on oxide morphology and spallation was investigated by conducting experiments in both deoxygenated steam to replicate conditions in plant, and air saturated steam to promote oxide spallation.

A major activity of the research programme was the building and commissioning of an atmospheric steam oxidation facility at the University of Birmingham. This is described in Section 3.4. During commissioning of the facility, oxidation experiments in static laboratory air were carried out to provide a baseline comparison to steam oxidation.

3.2 Materials

All austenitic stainless steels were provided by Sumitomo Metals Japan. The alloys were chosen because of their application in current plants and potential application in higher temperature plants. Super 304H, 347HFG, and HR3C alloys were received with the inner tube surface pickled using an unknown method at Sumitomo Metals. Pickling is a standard preparation process whereby an acid solution is applied to the surface of the steel to remove any high temperature scale that remains from forming and processing the tube. Pickling promotes passivation by slightly etching the surface to remove a thin layer of metal that may be depleted in chromium. A common mixture for stainless steels is a solution of 3 vol % HF and 15 vol % HNO_3. Other workers [46, 59, 66, 68, 80] have used this solution to attain a similar surface finish.

A separate tube of Super 304H with a shot peened inner surface was included to investigate the effects of surface treatment. Specific details of the exact shot peening method were not available. However, the general principle is for shot to be introduced to a high pressure air stream and directed through a rotating nozzle at the surface to be peened, as shown in Figure 3.1.

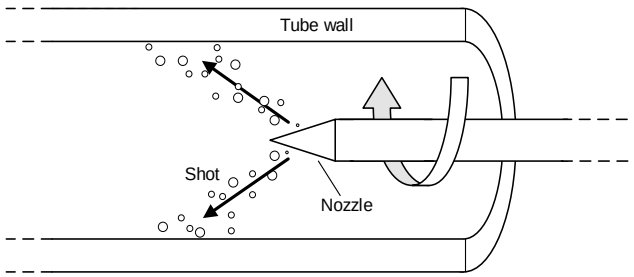

Figure 3.1 – General principle of shot peening process. The nozzle is drawn through the length of the tube.

3.2.1 As-Received Alloys

Macro images of as-received samples cut from each of the austenitic steels can be found in Figure 3.2. Observations of the inner surface finish are provided below.

Super 304H

Super 304H was developed from the ASTM 304H ("H" designating "high" carbon content) standard steel. The "Super" prefix relates to the addition of copper. The addition of copper increases the creep strength of the alloy, increasing the maximum service temperature compared to regular 304H.

As-received Super 304H was characterised by a fairly rough pickled inner tube surface and exhibited an irregular array of grooves running in the axial direction along the tube of approximately 25µm wide and 25µm deep.

The inner tube surface of one of the Super 304H tubes was shot peened at Sumitomo Metals using an unknown method. The shot peened tube had slightly larger dimensions than the pickled Super 304H tube, and so was not simply a section of the same tube that had been subject to the surface treatment. The inner surface of the shot peened tube could be described as glossy.

347HFG

347HFG is a popular standard 18/8 family austenitic stainless steel included in this programme as a baseline to determine how the alloy behaves at temperatures higher than current plant service temperatures. The "FG" suffix stands for "fine grain" to differentiate the alloy from course grained 347H. Note that the differentiation applies only between these two alloys and that the grain size of fine grained 347HFG is similar to Super304H as detailed in Table 1.1.

347HFG had an inner tube surface similar in appearance to batch 2 Super 304H and both HR3C tubes with no obvious defects.

HR3C

HR3C has a higher chromium and nickel content than 347HFG and Super 304H and has a higher maximum service temperature. The appearance of the inner surface was similar to that of 347HFG, without the surface defects present on the pickled Super 304H tube.

Two batches of HR3C were used in testing. Both behaved similarly in oxidising environments and were therefore not differentiated by batch in the results.

3.2.2 Alloy Specifications

Tube dimensions and grain sizes are listed in Table 1.1. The alloy grain sizes are the specific heat ASTM E112 grain sizes reported in the referenced inspection certificates that accompanied the alloys. Grain size measurements were not conducted as part of the research. A second batch of HR3C alloy was received during the programme. The oxidation results were comparable and are not distinguished in the results section. Dimensions of both batches are presented in Table 3.1.

Table 3.1 – Alloy dimensions and grain sizes.

Batch	Alloy	Surface Finish	Outer Diameter (mm)	Wall Thickness (mm)	Grain Size
1	Super 304H	Pickled	42.4	5.6	8.7 [110]
1	Super 304H	Shot Peened	41.3	6.5	7.0*
1	347HFG	Pickled	38.1	4.5	8.8 [110]
1	HR3C	Pickled	45.0	11.1	4.3 [112]
2	HR3C	Pickled	48.0	9.5	3.5 [113]

* - Grain size of heat not given. ASTM grain size specification minimum as given in inspection certificate [110].

Macro images of the as-received alloy samples are presented in Figure 3.2.

The specification average compositions in wt.% and actual compositions according to inspection certificates in both wt.% and at.% can be found in Table 3.2 and Table 3.3. Note that the specification for Super 304H also allows for trace amounts of boron and aluminium to be present.

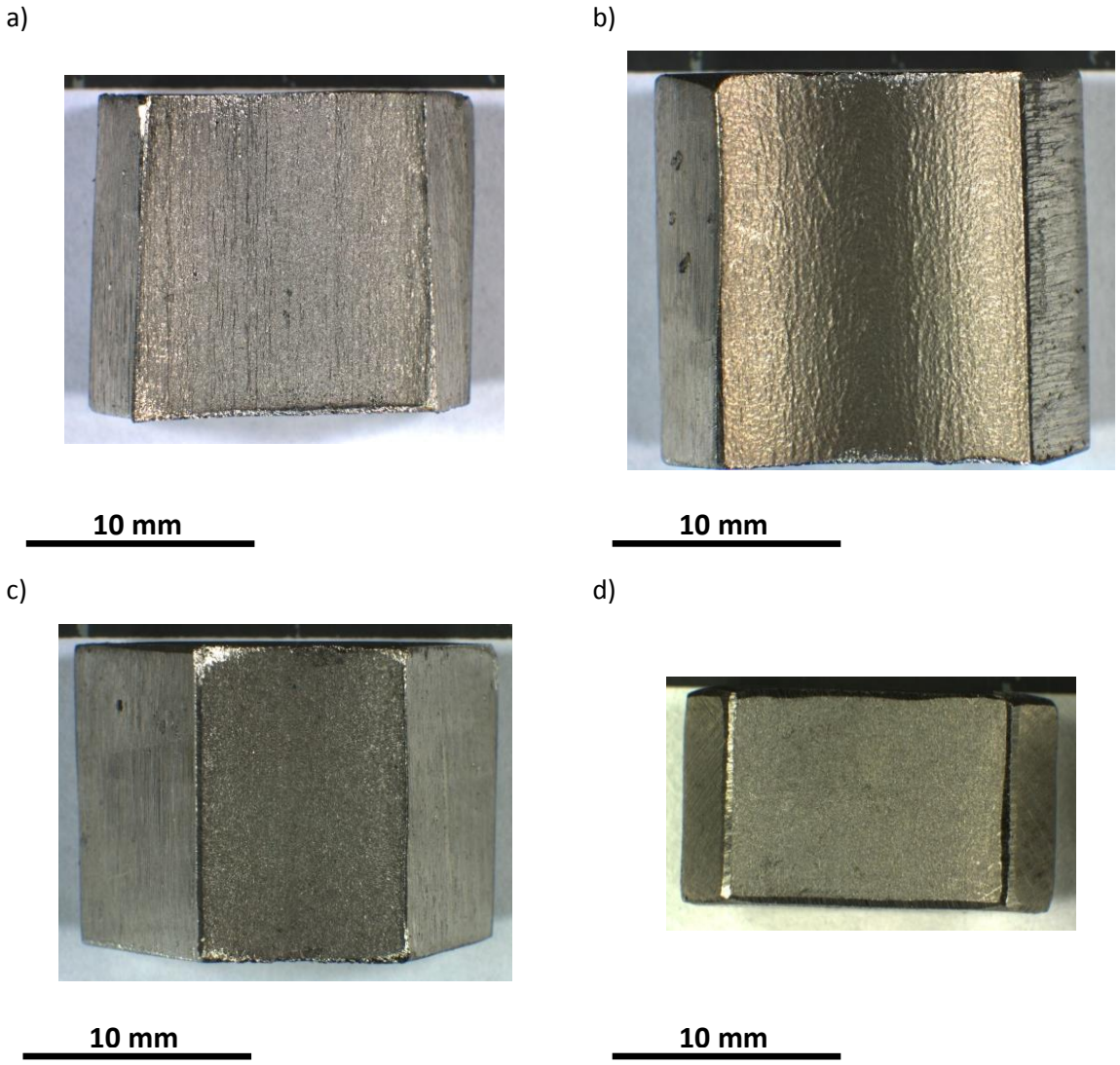

Figure 3.2 – Unoxidised austenitic stainless steel samples as sectioned from tube, showing internal steam-side surface. a) Super 304H, b) shot peened Super 304H, c) HR3C, d) 347HFG.

Table 3.2 – Specification average compositions for all alloys in wt %.

Batch	Alloy	Surface Finish	C	Si	Mn	P	S	Cu	Cr	Ni	Nb	N	CT*	Mo	W	V	Ref
1	Super 304H	Pickled	0.1	0.2	0.5	0.02	0.005	3.0	18.0	9.0	0.45	0.09	-	-	-	-	[110]
1	Super 304H	Shot Peened	0.1	0.2	0.5	0.02	0.005	3.0	18.0	9.0	0.45	0.09	-	-	-	-	[110]
1	347HFG	Pickled	0.1	0.4	1.0	0.015	0.015	-	18.5	11.0	0.50	-	-	-	-	-	[110]
1	HR3C	Pickled	0.1	0.4	1.0	0.015	0.015	-	25.0	20.0	-	0.25	0.4	-	-	-	[112]
2	HR3C	Pickled	0.1	0.4	1.0	0.015	0.015	-	25.0	20.0	0.40	0.25	-	-	-	-	[113]

* - CT: Nb+Ta

Table 3.3 – Actual compositions of austenitic steels as taken from calibration sheets.

Batch	Alloy	Surface Finish	Analysis		C	Si	Mn	P	S	Cu	Cr	Ni	Nb	N	Ref
1	Super 304H	Pickled	Ladle[4]	wt-%	0.09	0.22	0.80	0.033	0.000	2.87	18.40	8.80	0.47	0.11	[110]
				at-%	0.41	0.43	0.80	0.059	0.000	2.49	19.50	8.26	0.28	0.43	
1	Super 304H	Shot Peened	Product[5]	wt-%	0.08	0.22	0.81	0.029	0.001	3.06	18.56	8.86	0.48	0.11	[110]
				at-%	0.37	0.43	0.81	0.052	0.002	2.65	19.68	8.32	0.28	0.43	
1	347HFG	Pickled	Ladle[4]	wt-%	0.09	0.40	1.48	0.026	0.001		18.21	11.34	0.88		[110]
				at-%	0.41	0.79	1.49	0.046	0.002		19.32	10.66	0.52		
1	HR3C	Pickled	Product[5]	wt-%	0.06	0.38	1.14	0.018	0.001		25.10	20.00	0.43	0.24	[112]
				at-%	0.27	0.74	1.14	0.032	0.002		26.41	18.65	0.25	0.94	
2	HR3C	Pickled	Product[5]	wt-%	0.06	0.40	1.12	0.015	0.001		24.93	19.95	0.42	0.26	[113]
				at-%	0.27	0.78	1.11	0.026	0.002		26.22	18.59	0.25	1.01	

[4] Ladle analysis – a chemical analysis representative of a heat of steel, preferably obtained during the pouring of the steel

[5] Product analysis – a chemical analysis of the semi-finished or finished product, usually for the purpose of determining conformance to the specification requirements

3.3 Experimental Methodology

3.3.1 Test Matrix

The aims of the research programme were to investigate the oxidation and spallation behaviour of austenitic steels as a function of environment. The effect of varying the following factors was investigated:

- The effect of oxidising atmosphere was investigated by oxidising samples in laboratory air and flowing deoxygenated steam. Further into the programme oxidation tests were run using air saturated steam to promote oxide spallation and to enable analysis of the conditions for spallation.
- The effect of oxidation temperature was investigated based on current and future steam parameters in super-critical and advanced super-critical plants. Isothermal oxidation was chosen for 600, 650, and 700 °C conditions
- The effect of alloy composition was investigated by selecting two 18/8 alloys (Super 304H and 347H FG) and one 25Cr20Ni alloy (HR3C).
- The effect of surface finish was investigated using as-received tube sections with both pickled (Super 304H, 347H FG, and HR3C) and shot peened (Super 304H) inner surfaces.

Factors such as oxidation cycling, steam flowrate, sample geometry, and sample orientation with respect to steam flow are known to affect oxidation behaviour. These variables were fixed throughout testing so as not to influence outcomes [40, 55, 76].

Oxidation in laboratory air was conducted across the full temperature range. The long term use of box furnaces at an RWE nPower facility enabled test durations of up to 3000 hours (Table 3.4). Results for these experiments are presented in Section 4.3.

Table 3.4 – Test matrix for oxidation in static laboratory air.

Static Laboratory Air		
Alloy	Temperature (°C)	Duration (hours)
Super 304H	600, 650, 700	100 - 3000
Super 304H Shot Peened	600, 650, 700	100 - 3000
347HFG	600, 650, 700	100 - 3000
HR3C	600, 650, 700	100 - 3000

Oxidation in flowing deoxygenated steam was conducted across the full temperature range. The test regime was less structured and limited to approximately 300 hours for the majority of experiments. This was due to the commissioning and periodic upgrading of the steam oxidation facility, as well as a department renovation mid-way through the programme that involved relocating and recommissioning the facility in a different laboratory.

Longer term tests up to 1300 hours at 650 °C were conducted on 347HFG in deoxygenated steam when investigating the spallation behaviour of this alloy. The test matrix for oxidation in deoxygenated steam is shown in Table 3.5. Results for these experiments are presented in Section 4.4.

Table 3.5 – Test matrix for oxidation in flowing deoxygenated steam.

Flowing Deoxygenated Steam		
Alloy	Temperature (°C)	Duration (hours)
Super 304H	600	50 - 280
	650	50 - 170
	700	50 - 250
Super 304H Shot Peened	600	100 - 280
	650	50 - 250
	700	50 - 500
347HFG	600	50 - 100
	650	24 - 1300
	700	24 - 330
HR3C	600	100
	650	50 - 500
	700	50 - 330

In order to promote oxide spallation, the feed-water tank degassing medium was changed from nitrogen to air. Air saturated steam experiments were performed on 347H FG only. This was because the alloy was shown to spall in early steam oxidation tests. Additionally, the inner surface was free from the line defects that were present on the Super 304H tube – a cause for concern with regards to stress concentration and the possibility of interfering with the spallation mechanism. The test matrix for these experiments is shown in Table 3.6 Results are presented in Section 4.6.

Table 3.6 – Test matrix for oxidation in air saturated steam

Flowing Air Saturated Steam		
Alloy	Temperature (°C)	Duration (hours)
347HFG	650	50 - 500

It should be noted that a number of Super 304H and 347HFG samples oxidised in deoxygenated steam exhibited spallation in early deoxygenated steam experiments. This is thought to be because of

ineffective oxygen removal of the feed-water by de-gassing in the early stages of development of the steam oxidation facility. The results of these samples are discussed separately and presented in Section 4.5.

3.3.2 Oxidation Procedure

Specimens were prepared from standard tubes supplied by Sumitomo Metal Industries Ltd. These were cut into sections, each approximately 10mm in length and subsequently sectioned into sixths using an aluminium carbide disc. Sample dimensions indicated in Figure 3.3 were measured using a Fisher Scientific model FB70250 digital micrometer accurate to 0.03 mm. Sample dimensions were used to calculate the sample surface area. This was then used when calculating the mass gain per unit area after sample oxidation. Samples were cleaned in ethanol using an ultrasonic bath for 3 minutes and weighed using a top-pan Sartorius MC1 Research RC210P analytical balance accurate to ±0.000005g. This was calibrated before use, using the internal calibration function.

Samples were placed in an alumina boat in the configuration detailed in Figure 3.4, such that the inner surface of each sample faced upwards and the axial direction of each sample was parallel to that of the direction of steam flow. The alumina boat was then inserted into either a static laboratory air furnace or flowing steam furnace. On removal, boats containing samples were placed onto a heatproof mat and allowed to cool before reweighing to obtain mass gain data. For samples oxidised in steam that spalled, both the weight with, and without collected spall were recorded. For samples oxidised in air saturated steam it was difficult to differentiate between the spalled oxide of different samples, and therefore, only the weight without spall was recorded.

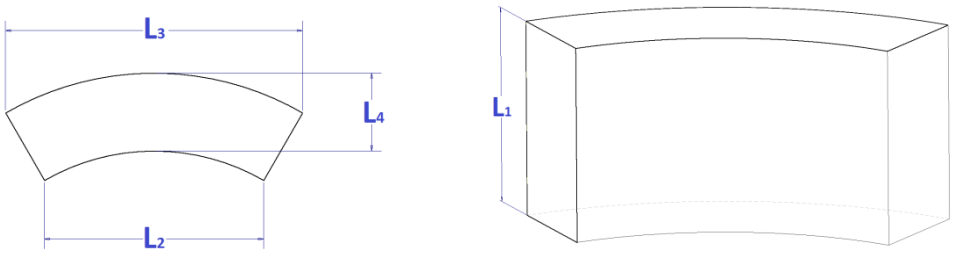

Figure 3.3 – Dimensional measurements taken for calculation of sample surface area.

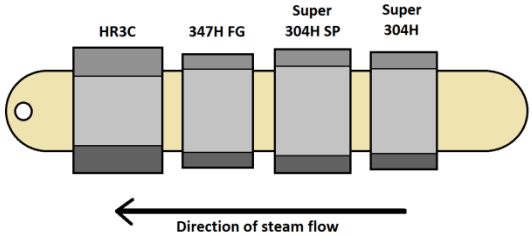

Figure 3.4 – Sample layout in alumina boat. Samples were placed such that the inner surface was facing upwards and steam would flow across the axial direction.

For oxidation in air, samples were placed into an Elite Thermal Systems Ltd model TSH12/50/610-2416CG tube furnace (Figure 3.5) for 100, 250, 500 and 1000 hours. 2000 and 3000 hour experiments were performed in box furnaces at RWE nPower, Swindon. A calibrated N-type thermocouple was used to map the temperature gradient within the worktube where the oxidation temperature could be kept within +/- 5 °C of the target temperature. This ensured optimum placement of test samples. Temperature calibration in the box furnaces was not conducted.

The procedure for oxidation in steam is presented in the following section.

Figure 3.5 – Elite Thermal Systems Ltd model TSH12/50/610-2416CG tube furnace

3.4 Atmospheric Pressure Steam Oxidation Facility

An atmospheric pressure steam oxidation facility was built and commissioned at the University of Birmingham Metallurgy and Materials department in order to perform high temperature oxidation

experiments in flowing steam. The design was originally based upon the concepts embodied at similar facilities developed at the National Physical Laboratory (NPL), Teddington, and underwent several modifications throughout the programme.

The steam oxidation facility will be described below in four discrete stages of development. Experiments were undertaken at each stage of development. These are aligned to sections in the results chapter.

3.4.1 Gas Supply

To replicate the low P_{O_2} steam chemistry in plant, the feed-water tanks were purged with oxygen free nitrogen for at least 24 hours before running oxidation experiments. This length of time was believed (and later confirmed by monitoring oxygen content) to reduce the level of molecular oxygen entrained in the steam flow to below approximately 10 ppb, a level similar to that found in plant and consistent with levels reported in the work of other researchers [3]. A schematic of the gas supply is shown in Figure 3.6.

Two cylinders were used sequentially to enable continuous degassing whilst changing the empty cylinder. The gas stream was split to allow flow control and isolation of each feed-water tank. It was found that a flowrate of between 20 and 30 ml.min^{-1} per tank was sufficient to effectively reduce oxygen content in the feed-water to a satisfactory level within 24 hours. These conditions maintained a positive pressure in the active tank while draining.

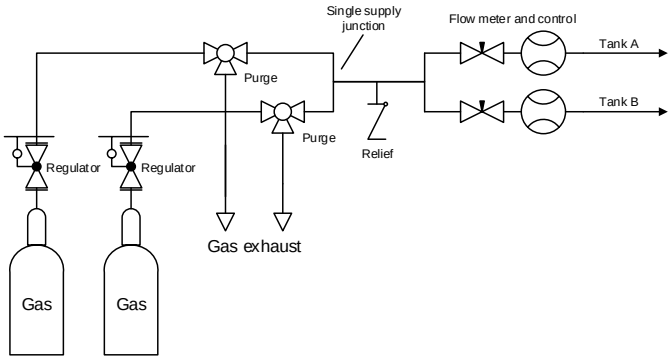

Figure 3.6 – Schematic of the steam oxidation facility gas supply.

The relief valve was originally connected to the worktube inlet of Furnace 1 to allow purging of the worktube prior to starting the steam flow. However, this was later disconnected in favour of continuously flowing steam through the worktube even when experiments were not taking place. The gas supply remained unchanged for the duration of the programme and is represented in the schematics below by the label “Gas supply”.

A photograph of the gas supply is shown in Figure 3.7.

Figure 3.7 – Image of the gas supply apparatus installed.

3.4.2 Stage 1

Initially, the concept was trialled with a single feed-water tank that fed two furnaces, as shown in Figure 3.8. The worktubes were made from Kanthal APM, an alumina forming FeCrAl alloy. This was selected over a chromia forming alloy so as not to contaminate the samples. The schematics for Furnaces 1 and 2 were identical, so only Furnace 1 is shown in the schematics.

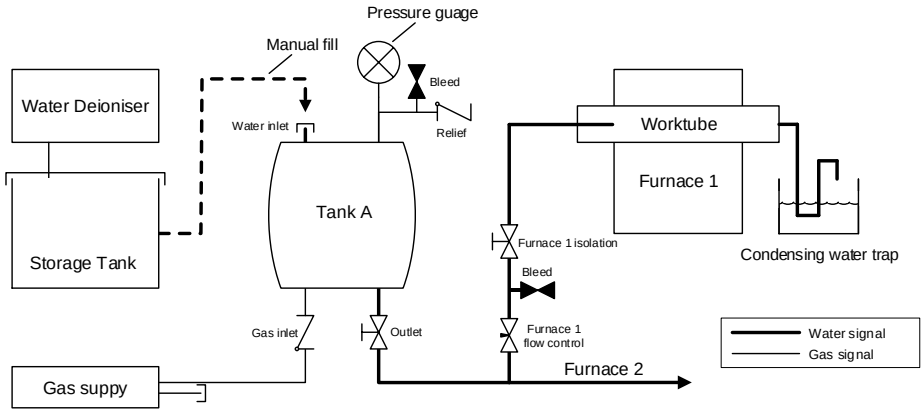

Figure 3.8 – Schematic of Stage 1 steam oxidation facility.

Deionised water was periodically fed into the storage tank to ensure a constant reservoir of water was available to the feed-water tank. Tank A was refilled manually by unscrewing the water inlet cap. To determine the water level in the feed-water tank it was placed on an electronic balance (not shown in the schematics).

Degassing was conducted by purging the work tank with oxygen free nitrogen[6] for at least 24 hours prior to use and throughout drainage in accordance with the procedure followed at NPL. An overhead pressure of approximately 30 KPa was maintained in the feed-water tank. This was controlled by the check relief valve and served two purposes; to oppose oxygen ingress into the tank and to provide overhead pressure that acted as the driving force for feed-water flow into the worktubes when draining.

Draining was initiated by opening the manual outlet control valve. The flow rates to each furnace were calibrated by balancing needle valves on the input to each furnace. Prior to fitting a flowmeter in Stage 3, the bleed valve was used to calculate flow by measuring the volume of water collected in a given time period, with a target flow rate of 5 $ml.min^{-1}$ per worktube. A correlation was found between a drop in feed-water tank water level, a reduction in flow rate, and a temperature drop in the worktube over the samples. This necessitated the need for daily calibration of the needle valves to maintain optimum flow rate. Using this method flow was controlled to between 3 and 6 $ml.min^{-1}$ per worktube.

Exhaust steam was drained via a condensing water trap suspended in a cold reservoir. This restricted oxygen ingress and back-flow of steam into the worktube and acted to prevent a steam hammer from forming. A steam hammer was further suppressed by suspending the worktube at a slight angle to encourage any condensed water to collect at the outlet and not flow back towards the hot spot.

The water trap had to be removed for hot spot temperature readings. A calibrated N-type thermocouple was inserted before performing an experiment to check that the hot spot location and temperature were stable. Temperature measurements were also taken directly before sample removal following test, to record any temperature drift during oxidation.

A photograph of the rear of the facility is shown in Figure 3.9.

[6] For tests that were conducted in a flow of air saturated steam, nitrogen was replaced with BOC air as the degassing medium.

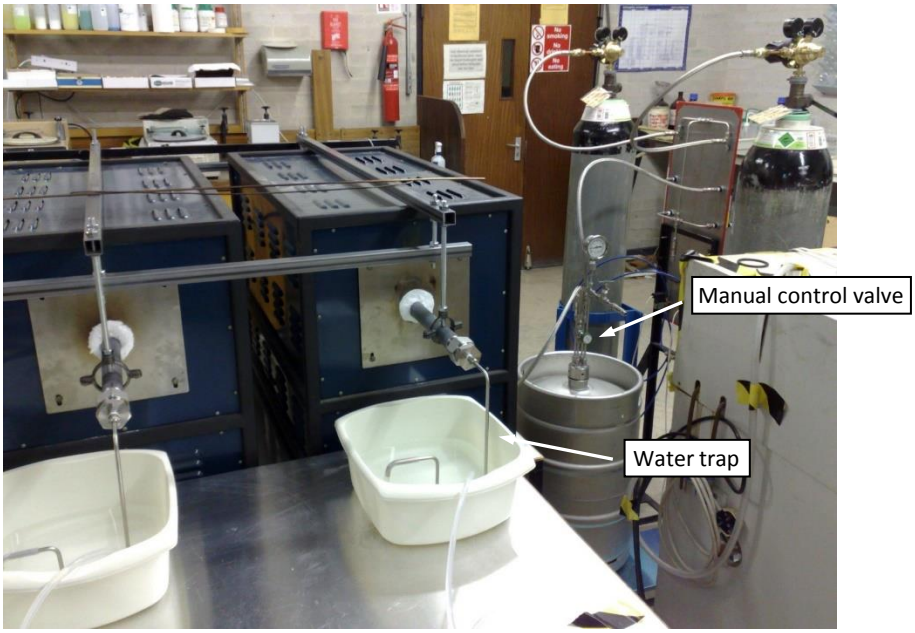

Figure 3.9 – Rear side of the steam oxidation facility at Stage 1 of development.

3.4.3 Stage 2

The facility was upgraded shortly after initial commissioning to Stage 2. A schematic is presented in Figure 3.10. A second feed-water tank was added to allow for switching of tanks when the active tank became fully drained. The feed-water tanks had a usable capacity of approximately 50 L and were switched over every three days. This provided sufficient time for removal of oxygen from the freshly filled tank by degassing. Filling and draining of the tanks was upgraded to electronic control via a control box. A pump fed feed-water directly to the feed-water tank inlets, which were controlled by solenoid valves. The manual outlet control valve was replaced with a pneumatically actuated control valve, which was powered by a small air compressor and controlled by solenoid valves. The outlet control valves were housed directly on the feed-water tanks and so pneumatics were used for safety. All pneumatic and solenoid valves were of the normally off type as a fail-safe to stop the worktube from flooding in the event of a power cut.

A photograph of the front of the facility during Stage 1 and 2 development is shown in Figure 3.11.

A number of samples in early deoxygenated steam tests exhibited spallation during development stages 1 and 2. These were not replicated again throughout deoxygenated steam testing. The results of these isolated samples are presented separately in Section 4.5. It is thought that a combination of opening tank A to the environment for refilling in Stage 1, and not suitably purging the furnace with steam prior to testing contributed to the cause of oxide spallation by raising the pO_2 of the oxidising atmosphere.

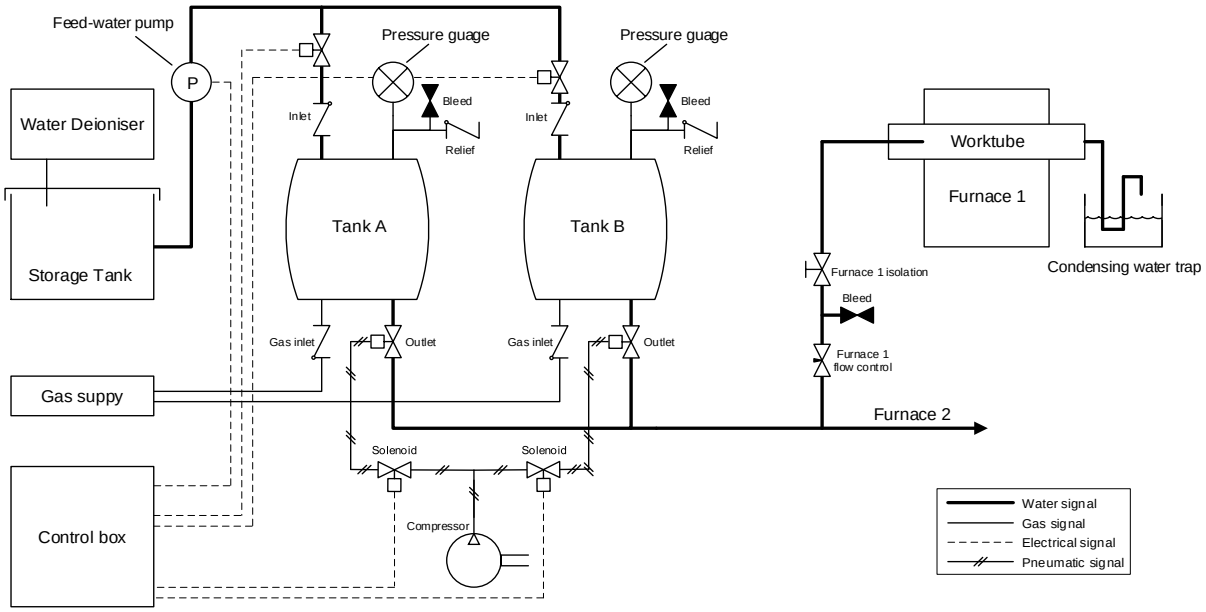

Figure 3.10 – Schematic of Stage 2 steam oxidation facility

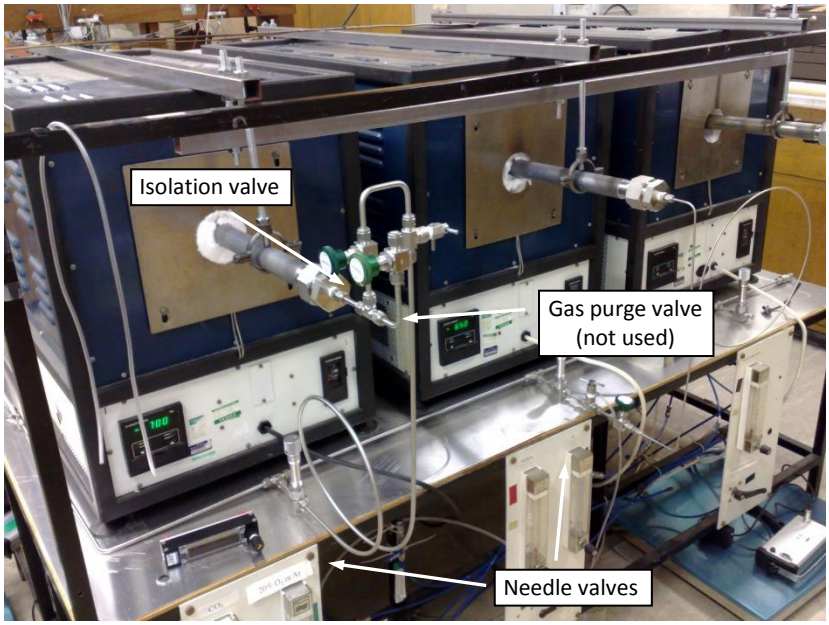

Figure 3.11 – Front view of the steam oxidation facility prior to installing the flowmeter upgrade on the furnace inlet.

3.4.4 Stage 3

Stage 3 (Figure 3.12) saw two upgrades to the facility. A flow meter was fitted at the input to the Furnace 1 worktube. This allowed for in-situ monitoring of feed-water flowrate. The target feed-water flowrate remained at 5 ml.min^{-1} per worktube, however this still required manual calibration. Additionally, the water trap was modified with a T-junction to allow permanent housing of an N-type thermocouple for in-situ temperature monitoring. Both of these upgrades provided greater monitoring and control of temperature and flowrate.

The majority of deoxygenated steam experiments were run on the facility at Stage 3 or Stage 4. The results for these experiments are reported in Section 4.4.

Photographs of the flowmeter and thermocouple upgrades are presented in Figure 3.13.

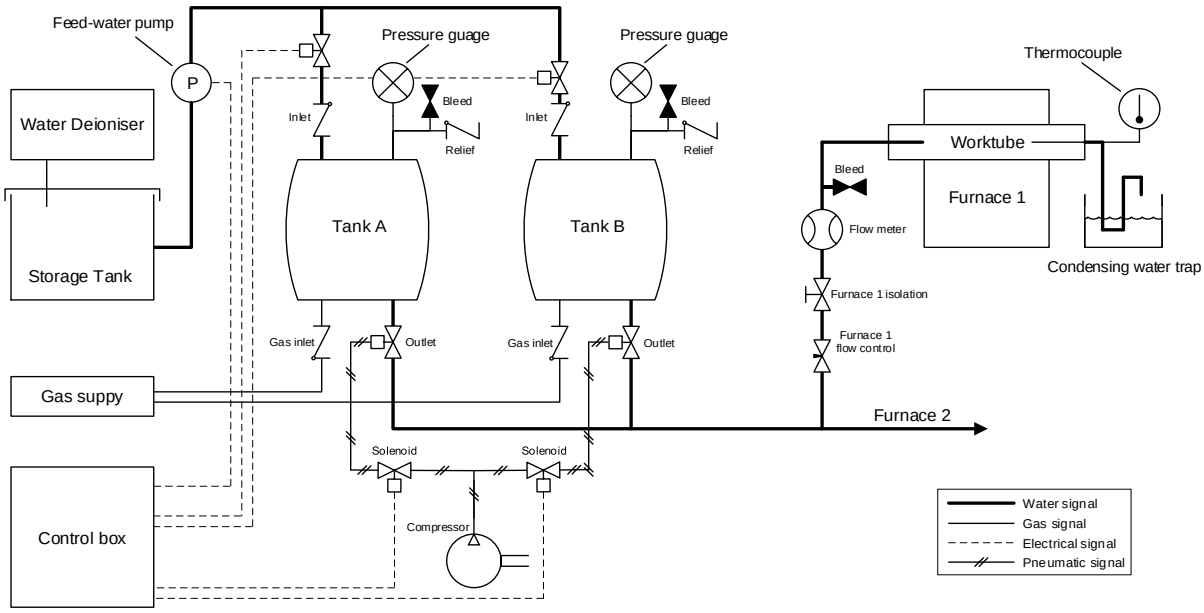

Figure 3.12 – Schematic of Stage 3 steam oxidation facility.

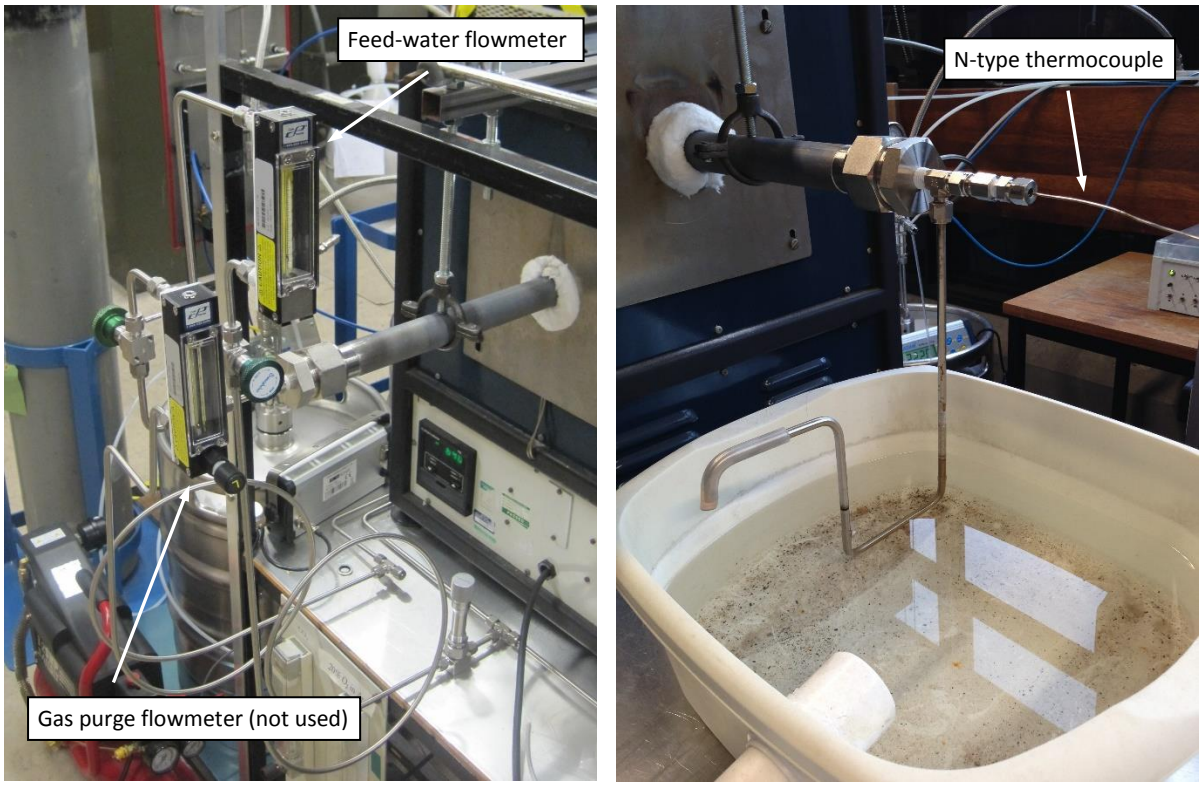

Figure 3.13 – a) flow meter and b) integrated N-type thermocouple upgrades during steam oxidation facility Stage 3 development.

3.4.5 Stage 4

The final upgrades made to the facility during the term of the programme were to improve flowrate control and monitor the level of dissolved molecular oxygen in the feed-water. A schematic of the final stage of development is presented in Figure 3.14.

A Grundfos DDE6/10-B-SS/T/SS-X9772-31AAFG digital dosing pump was installed at the common feed-water outlet to provide a steady flow irrespective of feed-water tank level. The feed-water tank relief check valve was adjusted to reduce the pressure to approximatly15 KPa to accommodate the dosing pump. A check valve positioned forward of the feed pump offered 30 KPa of overhead pressure for the pump to work against to stabilise flow.

Prior to installation of the dosing pump, the furnace hot spot temperature, as measured by the calibrated N-type thermocouple would vary by up to ±15 °C. This is thought to be a result of a variation in steam flow rate as previously stated. The dosing pump provided a steady feed-water flow and worktube hot spot temperatures varied by no more than ±5 °C. Modifying the steam flowrate has been shown to influence the kinetics [76] and morphology [40] of oxide growth in steam. A steady flowrate reduces this effect while also controlling the effects of temperature drifting on oxidation.

A photograph of both the dosing pump and oxygen sensor is shown in Figure 3.15.

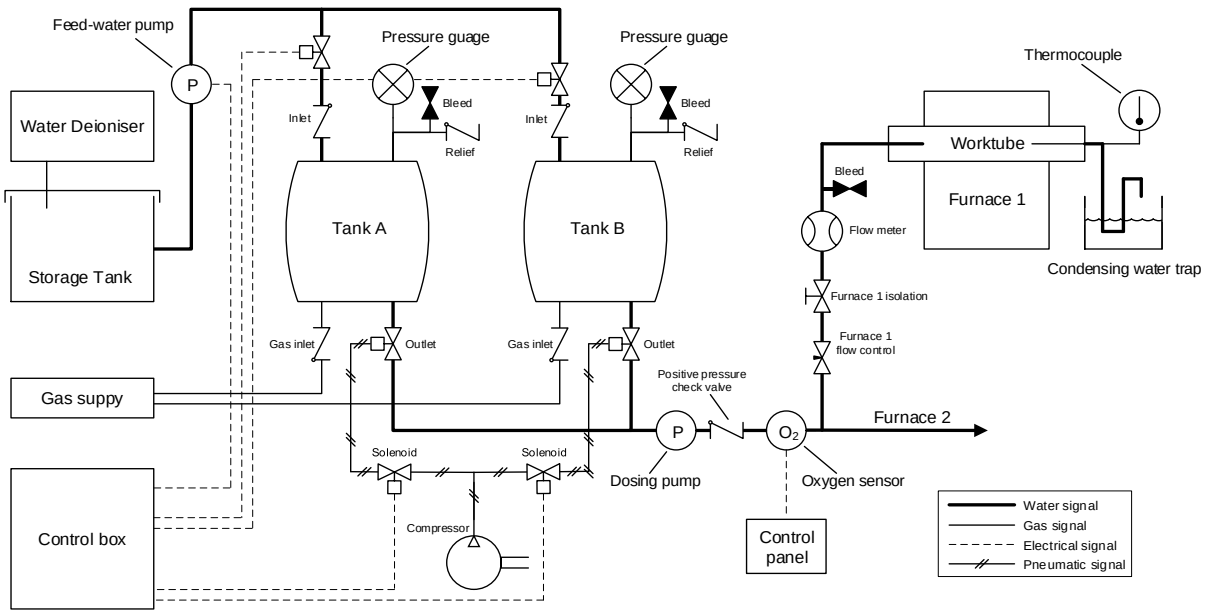

Figure 3.14 – Schematic of Stage 4 steam oxidation facility.

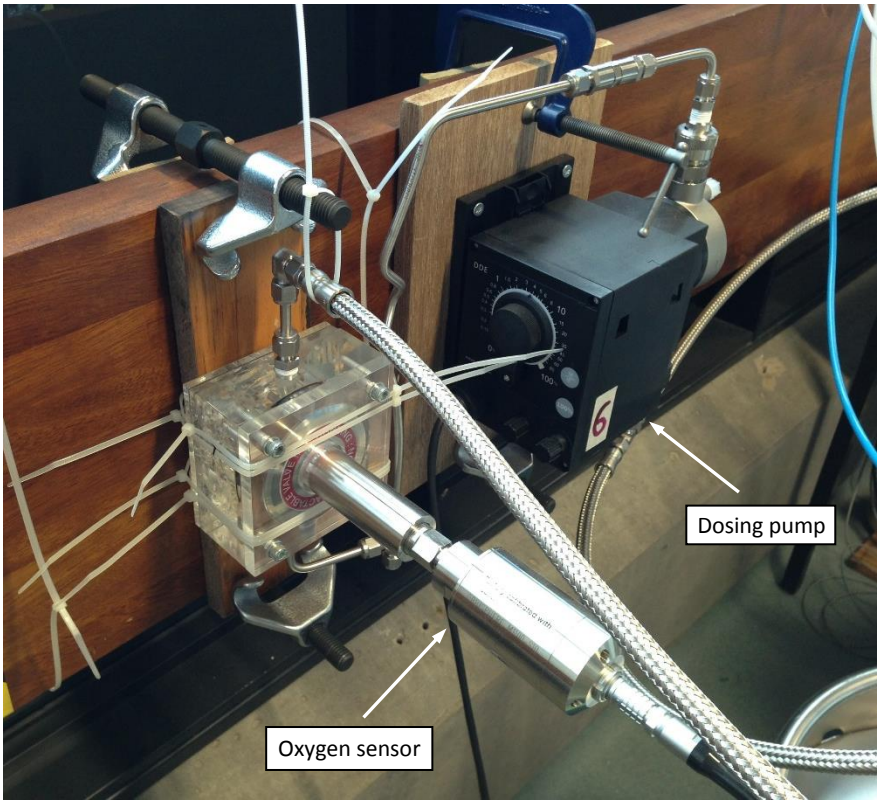

Figure 3.15 – Left, the Hach Orbisphere M1100 oxygen sensor installed in custom housing, and right, the Grundfos digital dosing pump. Both installed during Stage 4 steam facility development.

A Hach Orbisphere 410 controller with M1100 oxygen analyser was installed directly downstream of the dosing pump (Figure 3.15). The probe sensor head was situated in the centre of a 30 mm diameter chamber such that feed-water would flow through the chamber parallel to the probe sensor head ensuring unrestricted flow over the head. The Hach Orbisphere 410 permitted data logging, which was conducted on most deoxygenated steam tests to measure the variation in dissolved oxygen content. It was found that oxygen content remained steady over periods of a few days and varied between 1 and 10 ppb throughout testing, with an average of approximately 5 ppb. The resolution of the M1100 oxygen sensor is ±0.8 ppb. Spikes in the oxygen content occurred after a feed-water tank change. This was likely because of stagnation of flow in connecting pipes and oxygen ingress through seals. These spikes were rarely over 20 ppb and typically lasted for more than a few hours. Figure 3.16 illustrates the typical feed-water oxygen content over a 17 hour period (the maximum logging time permitted) measured after initiating a feed-water tank change. No oxygen content measuring was conducted on the worktube outlets.

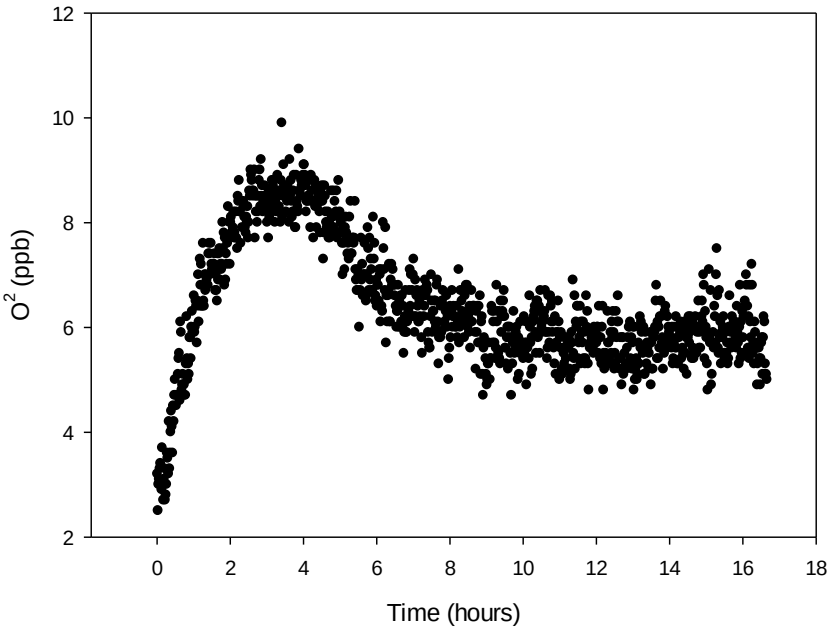

Figure 3.16 – Typical molecular oxygen content of deoxygenated feed-water. Spike indicates work tank change before resuming a steady value of approximately 6 ppb.

A major objective of the research programme was to investigate the spallation behaviour of austenitic steels in steam. To promote spallation, the degassing medium was changed from oxygen free nitrogen to BOC air. This had the effect of increasing the P_{O_2} of the steam. Experiments in air saturated steam were conducted on 347HFG and are presented in Section 4.6. Air saturated steam experiments were conducted after the Stage 4 upgrades were made.

3.4.6 Temperature Logging on Sample Furnace Removal

Critical stress and strain energy calculations required accurate measurement of the temperature at which spallation occurs. Various methods of monitoring the surface temperature of samples removed from the furnace following oxidation were investigated. These included resting the tip of a calibrated N-type thermocouple against the underside of a sample following removal from the furnace, using a non-obtrusive infrared monitor directed at the sample surface, and spot welding thermocouple wire to the inner surface of samples. A large variation in cooling profiles between samples was found with the first method, and large variation in acquisition data from the infrared monitor.

Spot welding K-type thermocouple wire to the inner surface of samples proved the most consistent. Therefore, this method was used to create a cooling profile for 347HFG from which, surface temperatures at a given time could be recorded. Small diameter wire was used to minimise the heat sink effect. The thermocouple was calibrated against a calibrated N-type thermocouple and found to be within ±5 °C agreement with the N-type thermocouple at 650 °C. Samples used to obtain the

cooling profile were oxidised in deoxygenated steam for 100 hours prior to removal and measurement to minimise any differences in insulation effects an oxide layer may have compared to oxidation testing samples.

3.5 Characterisation Techniques

3.5.1 Sample Preparation

Analysis of oxidised specimens was primarily undertaken using SEM analysis of the inner surface cross-section. Macro images were taken of the inner surfaces of samples after post oxidation weighing.

Samples were prepared for cross-section examination in one of two ways. Either they were:

1) vacuum impregnated using a Struers Epofix low shrinkage resin system.

or,

2) sputtered with gold before submerging in "Watt's bath" electrolyte ($NiSO_46H_2O$, $NiCl_26H_2O$ and H_3BO_3) to electroplate the sample with nickel. Electroplated specimens were subsequently vacuum impregnated using the above method.

It was found that electroplating was less effective than direct application of epoxy resin to the specimen surface on specimens that exhibited spallation or buckling. Small cracks and voids between oxide and substrate would not be sufficiently plated. Vacuum impregnation appeared more effective at surrounding all oxide, and so, for specimens that exhibited spallation, direct vacuum impregnation was preferred. Impregnated specimens were sectioned using an aluminium carbide disc or diamond impregnated disc. Sectioned specimens were then ground using SiC paper (400, 800, 1200, 2500 grit) and polished using 3 µm diamond suspension. Final polishing was performed with either neutral or acidic OP-A alumina suspension. Oxide pull-out during the polishing phase was difficult to avoid on specimens that exhibited spallation because of how brittle the oxide was. Polished specimens were ultrasonically cleaned in ethanol to remove dirt and polishing media from open cracks before placing a small amount of resin along the inner surface of the specimen under vacuum in an attempt to secure loose oxide to reduce pull-out.. The specimen was then re-polished. This technique reduced pull-out to some extent but in certain cases oxide pull-out was unavoidable. Samples were sputtered with gold and areas away from those of interest painted with silver to improve conductivity prior to SEM analysis.

3.5.2 Analysis

3.5.2.1 Oxidation Kinetics

The mass gain and oxide thickness of samples oxidised for different times and at different temperatures can provide information on the growth rate and activation energies for oxidation. The difference in mass before and after oxidation was used to calculate the mass gain per unit area according to

$$\Delta m = \frac{(m_a - m_b)}{A} \qquad \textit{(3-1)}$$

where Δm is the mass gain per unit area [mg.cm^{-2}], m_b and m_a are the sample mass [mg] before and after oxidation, respectively, and A is the surface area of the unoxidised sample [cm^{-2}].

Mass gain data was used to find the order of the reaction where

$$\Delta m^n = k_n t + c \qquad \textit{(3-2)}$$

Here, n is the order of the reaction, k_n is the rate constant [(mg.cm^{-2})^n], and the integration constant, c, is the initial mass gain. n was calculated by taking the log of equation (3-2) to reach

$$\ln \Delta m = \ln k_n + \frac{1}{n} \ln t \qquad \textit{(3-3)}$$

k_n is then the y-intercept of the line plotted. An order of reaction greater than 2 relates to a reaction that is sub parabolic. A useful quantity for comparison of oxides that grow in a near parabolic fashion is the parabolic rate constant, k_p. n is selected as 2 and the regression line of a plot of mass gain squared against time is forced through the origin (to represent zero mass gain immediately before inserting into the furnace) such that k_p can be represented as follows

$$\Delta m^2 = k_p t + c \qquad \textit{(3-4)}$$

There are limitations associated with calculating oxidation kinetics using the change in mass gain of an entire sample. The change in mass gain per unit area takes account of oxide growth over the entire sample surface. If a sample of multiple sides has more than one surface finish it will likely to lead to the growth of different types and quantities of oxides (as is the case for austenitic steels), and the mass change per unit area calculation will be skewed and not represent the growth of oxide on a single surface. This is likely to be the case in the current programme as samples are sectioned from as-

received tubing, taking care not to disturb the inner pickled surface. Figure 4.6 in Section 4.2.1 illustrates how the machined surface leads to much thinner oxide growth than the pickled surface of interest. Furthermore, due to the need to preserve the as-received inner surface finish, in-situ mass change monitoring using TGA was an unsuitable method. To more accurately calculate the oxidation kinetics on the inner pickled surface, oxide thickness measurements were taken. Mass change was substituted for oxide thickness in equations (3-2) and (3-4). For a parabolic relationship this gives

$$\xi_i^2 = k_p t + c \qquad \textit{(3-5)}$$

The additional benefit is that the kinetics of individual oxide layers can be calculated if required. ξ_i is therefore either the total oxide thickness, or thickness of a single oxide layer/phase [µm], and c is given in µm^2. One disadvantage of calculating kinetics via oxide thickness measurements is the requirement to section each sample resulting in its destruction. Many samples are then required to cover a suitable time period over which the kinetics are calculated.

The activation energy, Q, can be determined from the rate constants obtained between 600 and 700 °C, according to the Arrhenius equation

$$k_p = k_0 e^{\left(-Q/RT\right)} \qquad \textit{(3-6)}$$

where T is the absolute temperature in K and R is the ideal gas constant. Q is usually given in J.mol^{-1} so R is given as 8.314 J.K^{-1}.mol^{-1}. k_0 is the activation constant. The log of equation (3-6) was taken to give

$$\ln k_p = -\frac{Q}{R} \cdot \frac{1}{T} + \ln k_0 \qquad \textit{(3-7)}$$

plotted in the form $y = mx + c$, and Q was calculated from the gradient, $-Q/R$, where $x = 1/T$.

3.5.2.2 Optical Microscopy

Macro images of samples before and after oxidation were taken using a Zeiss CCD camera and Nikon 60 mm lens.

Optical microscopy was performed using a Zeiss microscope with CCD camera and 50x zoom capability. Images obtained were primarily for distinction between magnetite and haematite oxide phases, which showed no contrast in either backscattered or secondary electron SEM images.

The haematite fraction of the outer oxide layer was measured by imaging the oxide cross-section of samples and calculating the area of light and dark contrast outer oxide in ImageJ software. A representative sample of six or more optical micrographs were selected for each sample. Each micrograph was loaded into ImageJ and the freehand drawing tool was used to outline the full area of the outer oxide. This provided a "total outer oxide area" value in pixels^2. The freehand tool was then used to outline individual areas of either haematite or magnetite (based on contrast difference), the sum of which were subtracted from the total outer oxide area to reach the haematite fraction of the oxide. Automatic identification of each phase was explored, but due to the complexity of the images manual identification was used. Due to the speculative nature of identifying both oxide phases from the micrographs, the error in measurement was considered to be approximately ±10%.

A similar approach was used to determine the fraction of spallation that had occurred on samples that spalled. This time a micrograph of the inner surface of the sample was loaded into ImageJ. The inner surface area was measured, followed by areas of either spalled regions or regions of adherent oxide. Spalled regions could easily be identified by visual analysis, so it is believed error associated with miss-identification was low.

3.5.2.3 Scanning Electron Microscopy

A Jeol 7000F Field Emission Gun (FEG) SEM was used for topological and cross-sectional examination of oxides and substrates. This was controlled using Oxford Instruments INCA software. Both secondary electron and backscatter modes for image acquisition were used. However, it was found that the backscatter mode provided the clearest contrast between oxide layers and substrate and so this method was preferred for imaging and analysis. The majority of analysis was performed using the attached Oxford instruments Energy Dispersive Spectroscopy (EDX) system, which was calibrated with a nickel standard. An accelerating voltage of 20 KeV was used throughout. This corresponded to an interaction volume of approximately 2 μm from the beam impact point. A working distance of 10 mm was used.

Quantitative spot analysis was performed to determine the element concentrations within different oxide layers and underlying alloy. Spot sizes of either 5 or 6 were used with a process time of 5 μs, to achieve a dead time of 30 ±10%.

Qualitative area maps and line scans were obtained to view the distribution of elements at a site of interest. Spot sizes of 6 or 7 were used with a process time of 3 μs. The interaction volume limited the resolution obtainable, which made distinction between scales less than a few microns in thickness difficult. Accurate quantification of light elements such as oxygen is difficult using EDX making it

difficult to differentiate between oxide phases with similar oxygen contents, importantly for this project, Fe_3O_4 (Fe 72.36 wt.%, O 27.64 wt.% / Fe 42.86 at.%, O 57.14 at.%) and Fe_2O_3 (Fe 69.94 wt.%, O 30.06 wt.% / Fe 40.00 at.%, O 60.00 at.%). To distinguish between these oxide phases XRD analysis and optical microscopy was used.

SEM was also used to obtain oxide thickness data using the following method:

1. 10 Back Scatter Electron (BSE) SEM micrographs (20 for HR3C oxidised in air) were recorded at even intervals across the oxide surface. This magnification was selected such that the total oxide layer consumed approximately one third of the micrograph (~one tenth for HR3C and shot peened Super 304H).
2. Micrographs were loaded into ImageJ software and the micrograph scale bar was used to calibrate the scale.
3. For each micrograph 6 straight lines were drawn to measure the oxide, either of the total oxide or of its individual layers resulting in 60 measurements (120 for HR3C oxidised in air) of oxide thickness. The lines were drawn with equal distance between them and measurement was taken in the growth direction. An example of a micrograph with measurement lines can be found in Figure 3.17.
4. ImageJ stored each length measurement in a temporary database automatically converting each line drawn to the correct thickness in µm according to the scale bar calibration.
5. Thickness measurements were copied into an Excel spreadsheet for statistical analysis.

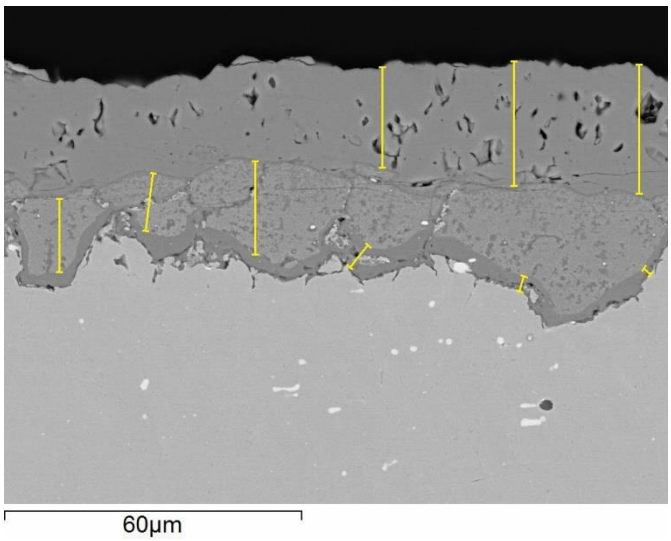

Figure 3.17 – Example of measurements taken to calculate oxide layer thickness from cross section micrograph.

3.5.2.4 X-Ray Diffraction (XRD)

The primary aim of XRD analysis was to determine the presence of haematite and/or magnetite in the outer oxide layer of samples oxidised in air and steam. Analysis was performed on a sample of 347HFG oxidised in laboratory air, and on spalled oxide from Super 304H and 347HFG after oxidation in steam. XRD analysis was also performed on a sample of unoxidised 347HFG to enable identification of peaks generated by the underlying alloy. Spalled oxide from the steam oxidation samples was carefully attached to an adhesive carbon tag, which was secured to a glass slide. The alloy sample from which the oxide had spalled from was not included in the analysis, so peaks caused by the underlying alloy were absent for these scans.

The machine was a PANalytical MPD (Multi-Purpose Diffractometer) using Cu Kα (0.154nm) radiation from a PW3373/00 long fine focus ceramic X-Ray tube at 40 kV and 40mA. The scan range chosen was 10 – 100°. PANalytical Xpert Highscore software was used to remove background signal in the scan and for peak search. To support the software in identifying oxide phases, only those elements identified in the oxide by EDX during SEM cross-sectional analysis were selected. For the sample oxidised in laboratory air this was all of the constituent elements present in the 347HFG alloy. For the spalled oxide samples, only the outer oxide was observed to have spalled, so only Fe and O were selected.

Chapter 4 High Temperature Oxidation and Spallation of Austenitic Steels

4.1 Introduction

This chapter presents the results from isothermal oxidation experiments on samples of 347HFG, Super 304H, shot peened Super 304H and HR3C austenitic steels in laboratory air and flowing steam. Experiments were conducted at 600, 650, and 700 °C. The chapter is structured as follows:

- Section 4.2 reports analysis on the as-received tubes;
- Section 4.3 reports the results of oxidation experiments in laboratory air;
- Section 4.4 reports the results of oxidation experiments in deoxygenated steam, and corresponds to steam oxidation facility development stages 3 and 4 (see Sections 3.4.4 and 3.4.5);
- Section 4.5 reports the results of early oxidation experiments in ineffectively "deoxygenated steam", where samples of 347HFG and Super 304H exhibited spallation. The experiments reported on in this section correspond to steam oxidation facility development stages 1 and 2 (see Sections 3.4.2 and 3.4.3);
- Section 4.6 reports the results of oxidation experiments in flowing air saturated steam. Experiments were conducted on samples of 347HFG at 650 °C with the aim of investigating the spallation behaviour of 18Cr alloys in steam. The experiments reported on in this section correspond to steam oxidation facility development stage 4 (see Section 3.4.5); and
- Section 4.7 provides a summary of the experimental results.

The term "deoxygenated steam" (in parenthesis) refers to, in this project, oxidation tests that were performed early in the development of the steam oxidation facility. A number of these early samples

exhibited spallation and analysis of the oxides indicated that nitrogen purging of the feedwater may not have been effective at reducing pO_2 to the target level of above 10 pbb. Results of these early experiments are presented separately in Section 4.5, and the term “deoxygenated steam” is used to describe feedwater that was ineffectively deoxygenated.

4.2 As Received Austenitic Alloys

The inner surfaces of sectioned samples were examined under SEM to observe the surface finish.

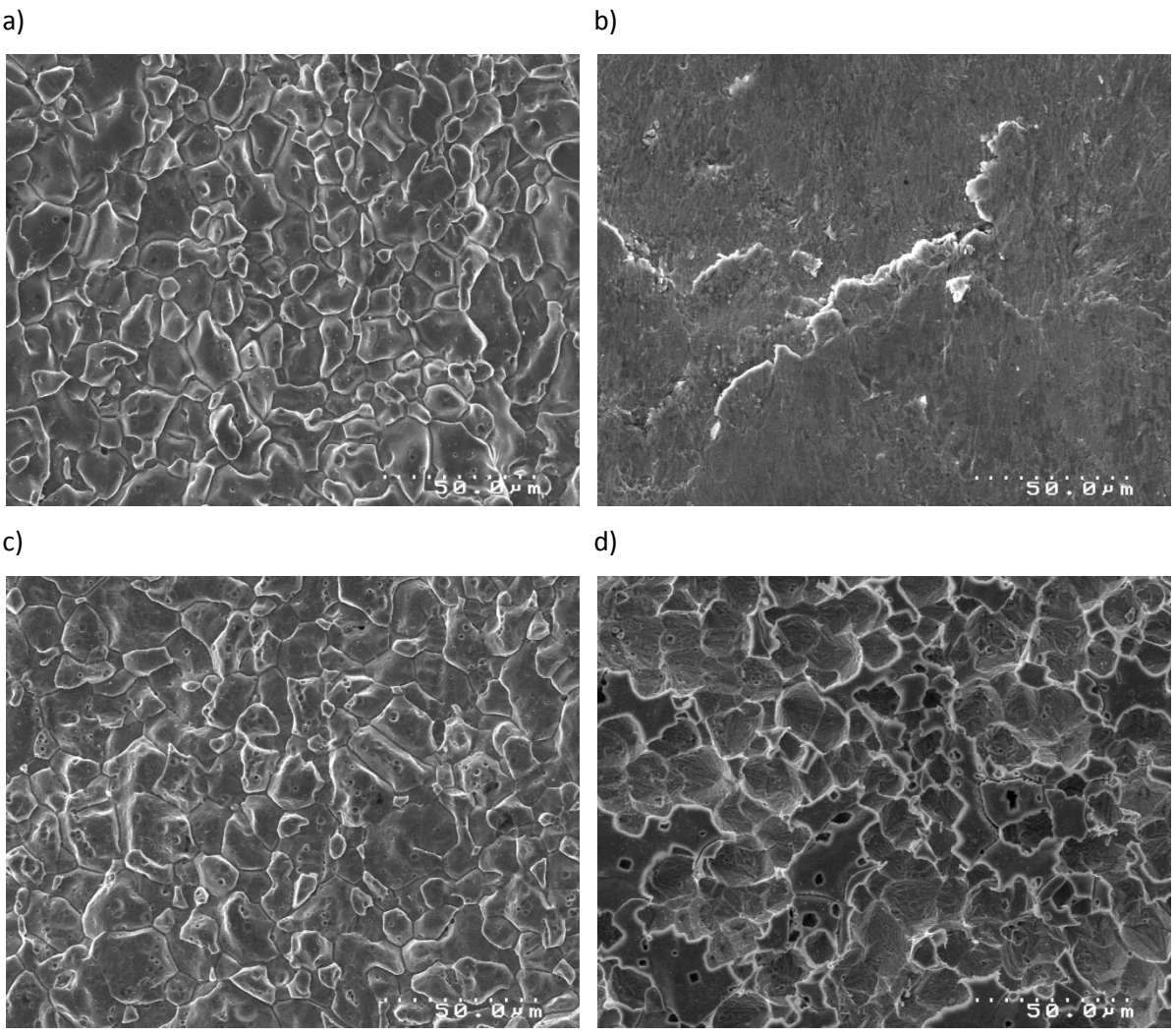

Figure 4.1 – SEI SEM micrographs of inner tube surfaces of as received alloys. a) Super 304H, c) 347HFG and d) HR3C pickled surfaces, and b) Super 304H SP shot peened surface.

Pickling left clearly defined grains on Super 304H and 347HFG alloys. The treatment had a slightly different effect on HR3C. The Super 304H shot peened surface appeared smoother than the pickled tubes. Ridges like the one that run bottom left to top right of Figure 4.1 (b) appear to be have been formed as a result of the impact of the shot.

Line defects were found on the inner surface of Super 304H and Super 304H SP alloys (Figure 4.2). The homogeneity between the surface finish within the defects and over the bulk surface of Super 304H alloy would suggest that they arose prior to pickling, probably during the extrusion process. The shot peening process did not mechanically deform the surface in the vicinity of these defects to such a depth as to effectively remove them from the surface. The resulting surface within these defects remained unaffected, as illustrated in Figure 4.2 c) and d). The effect of oxidation to these areas is addressed in the oxide morphology section.

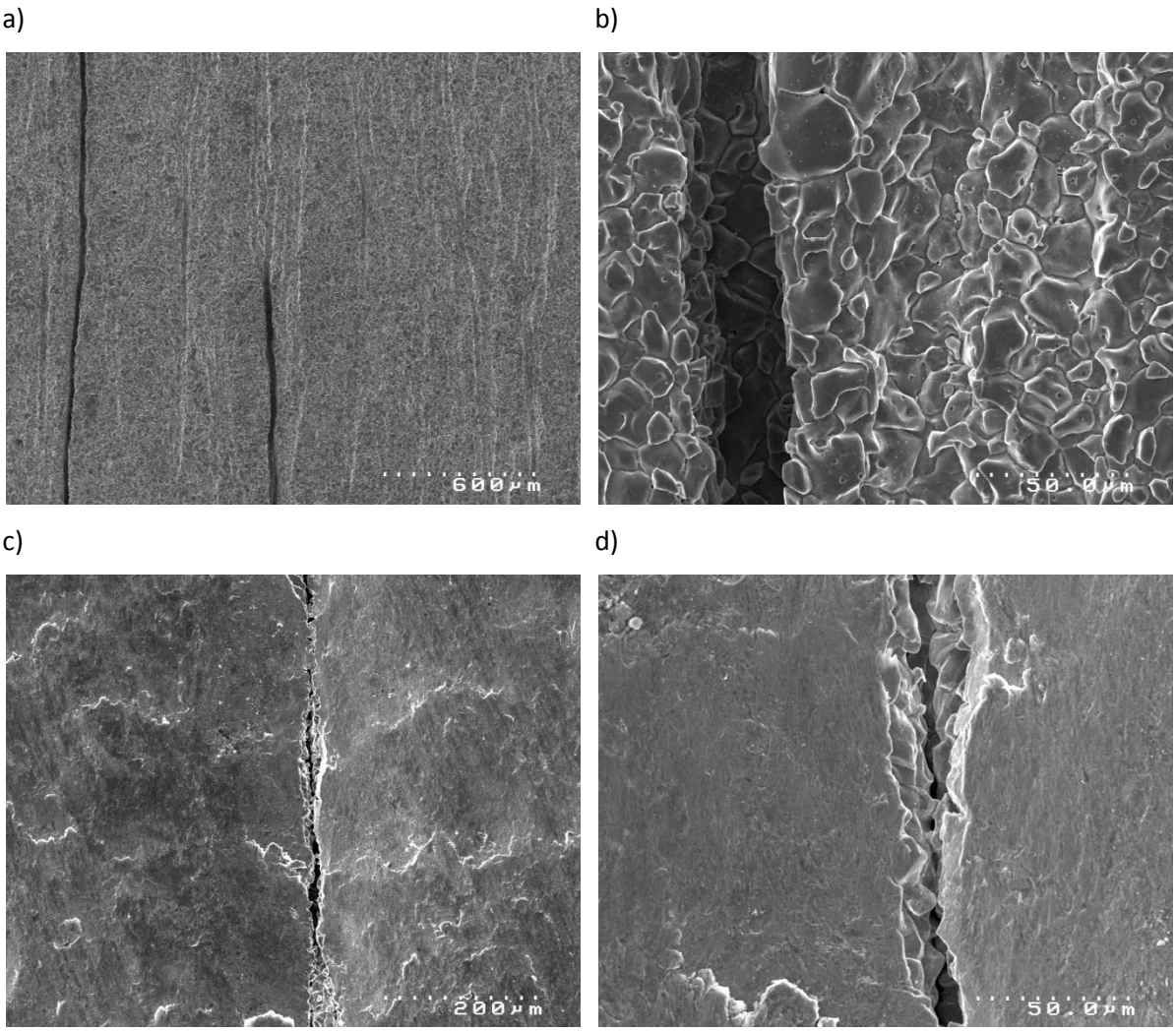

Figure 4.2 – Line defects present on surface of a), b) Super 304H and c), d) Super 304H SP. Areas not representative of bulk surface.

As-received samples were sectioned, polished, and etched to reveal the grain structure. The bulk grain structure for each alloy shown in Figure 4.3. These show the larger bulk grain size of HR3C compared with the fine grained 18Cr-8Ni alloys.

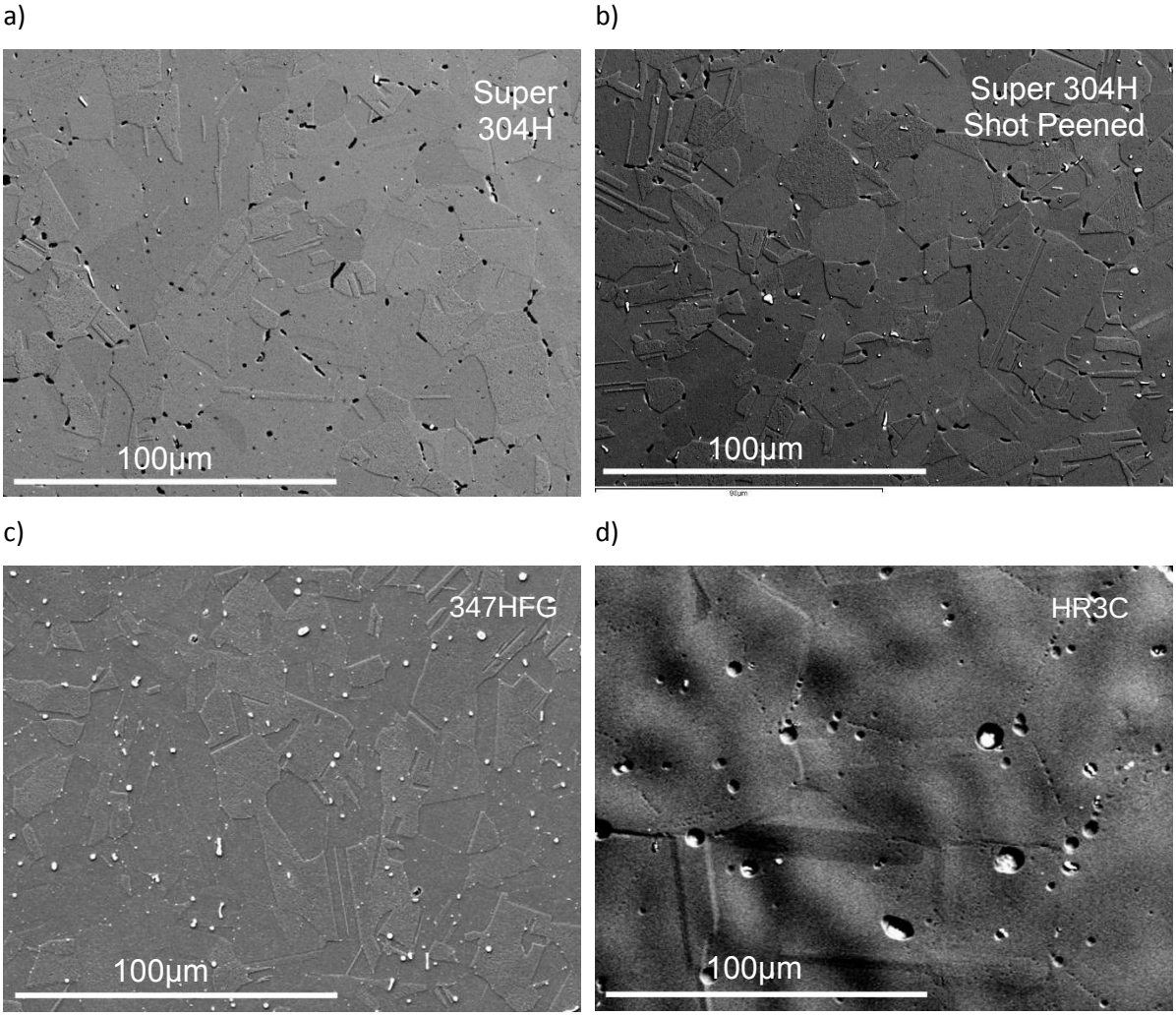

Figure 4.3 – Optical micrograph of alloy cross-sections showing difference in bulk alloy grain size between the 18Cr-8Ni alloys and 25Cr-20Ni HR3C. a) Super 304H, b) Shot peened Super 304H, c) 347HFG, d) HR3C.

Cross-section analysis revealed the effect of shot peening on the near surface grain structure as illustrated in Figure 4.4. Shot peening reduced the surface roughness compared to that of pickled Super 304H. Near surface grains up to a depth of approximately 30 µm were heavily worked by the peening process. Hardness profiles of Super 304H and shot peened Super 304H cross-sections revealed higher hardness in the area of surface deformation in the shot peened Super 304H compared to the near surface region of pickled Super 304H (Figure 4.5).

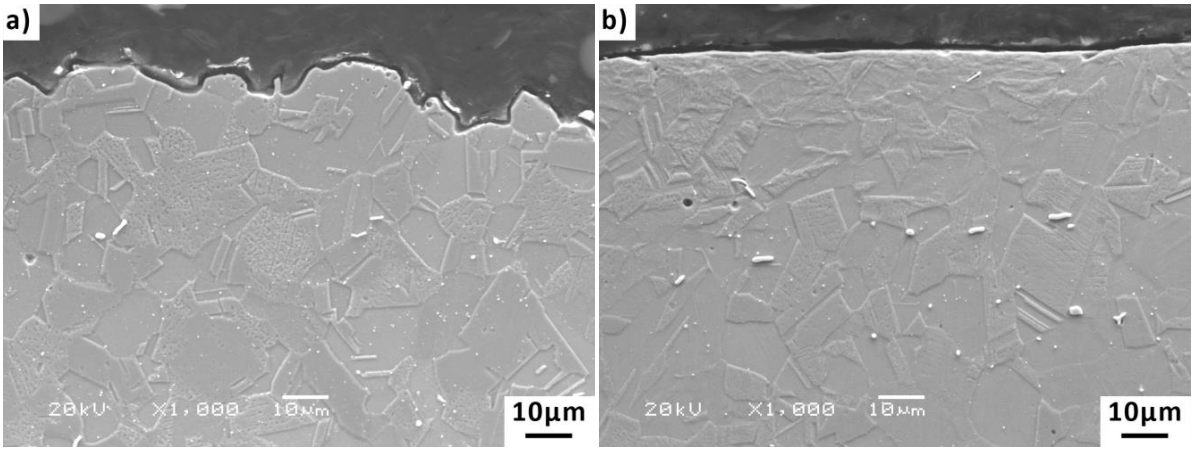

Figure 4.4 – SEI SEM micrographs of etched a) Super 304H and b) Shot peened Super 304H inner-surface cross-sections illustrating worked grains in the shot peened specimen.

The hardness of pickled Super 304H remained constant at around 2.8 GPa to a depth of 300 µm. The hardness of shot peened Super 304H was a factor of 1.6 higher than that of pickled Super 304H at a depth of 25 µm from the surface in cross-section. This decreased with depth from the surface until the bulk hardness of the material was reached at a depth of around 100-150 µm.

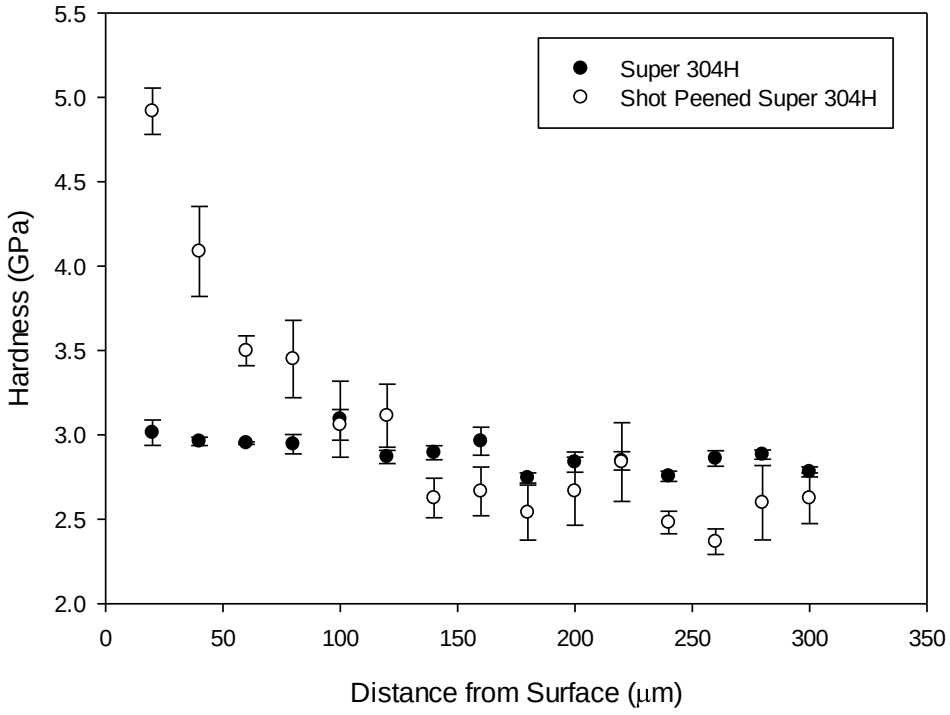

Figure 4.5 – Hardness profile for shot peened and non-shot peened Super 304H. Shot peening increased the hardness of the alloy in the affected area.

4.2.1 Effect of Sample Preparation on the Oxidation of Different Sample Surfaces

The reader is reminded that only the inner (steam-side) surface of the heat exchanger tubes was of interest in the current project. This is an important consideration before presenting the results of oxidation and spallation of austenitic steels in air and steam. Figure 4.6 shows the cross-section of a Super 304H sample, which has been sectioned using a silica circular saw on the side that shows low oxide thickness, inducing cold work into the alloy.

Oxide thickness and morphology are affected by mechanical work. Therefore, the oxide grown on the machined sides of the samples do not give an accurate representation of oxide growth on the inner surface of pickled HRSG tubes. Care was taken throughout testing to avoid knocking, scratching, or modifying the inner surface at any time.

As explained in Section 3.5.2.1, the oxide grown on all surfaces affects the mass change results. This is expected to disproportionately influence the mass change measurements for the shot peened material. This was only treated on the inner surface, leaving the outer tube surface to grow thick oxides.

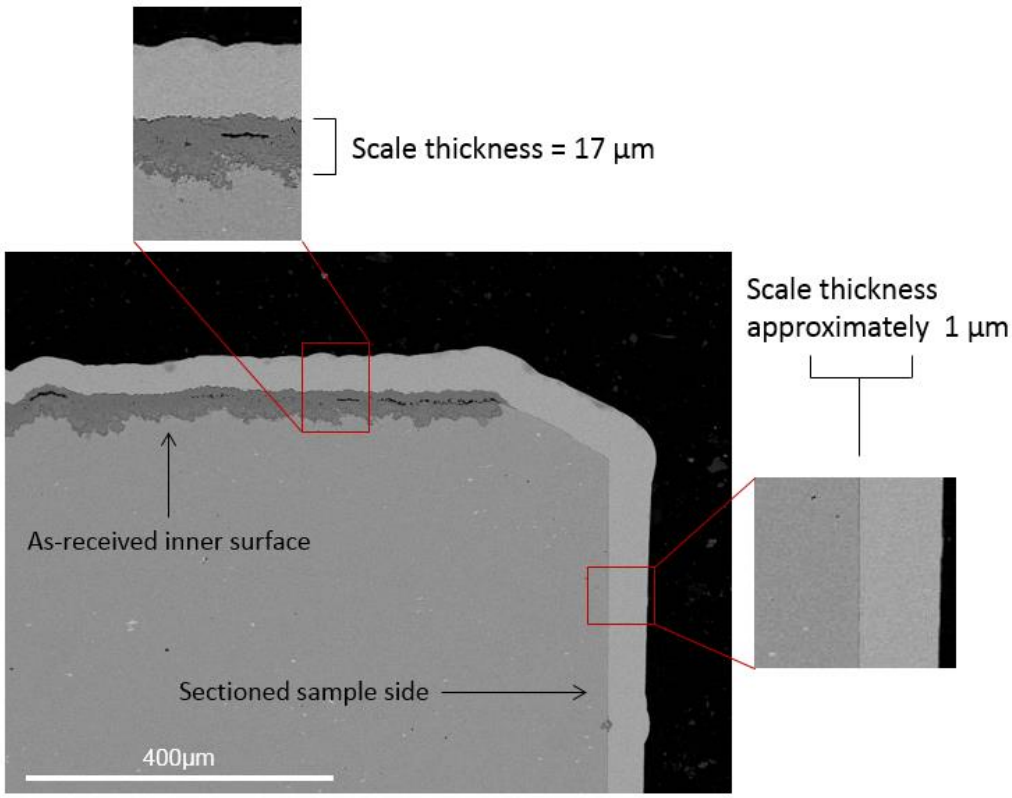

Figure 4.6 – Illustration of the effect of sample preparation on Super 304H oxidised in deoxygenated steam for 250 hours at 700 °C. Mechanical sectioning affected the morphology and thickness of oxide grown on the sides of austenitic steels.

4.3 Oxidation of Austenitic Stainless Steels in Laboratory Air

4.3.1 Oxidation Kinetics after Oxidation in Laboratory Air

Mass gain and oxide thickness measurements are presented in this section and the findings summarised at the end. The oxidation kinetics of air oxidation, calculated from mass gain and oxide thickness, are explored in the discussion chapter. No oxide spallation was observed to occur from any sample oxidised in air.

4.3.1.1 Mass Gain Measurements after Oxidation in Laboratory Air

Mass gain data accounts for oxide grown on all surfaces of the sample. The shot peened Super 304H has only been treated on the inner surface. This must be taken into account during analysis of mass gain data as the different surface finishes (machined sides, shot peened inner and as received outer) will exhibit different kinetics. Therefore, accurate kinetic data for the inner surface of each sample cannot be extracted from sample mass gain alone. Nevertheless, mass gain data is a quick method for obtaining an idea of the oxidation performance of an alloy. Plots of mass gain for austenitic steels exposed to laboratory air are shown for periods up to 3000 hours at 600, 650 and 700 °C in Figures 4.7, 4.8, and 4.9, respectively. An initial observation is that the 25Cr HR3C steel showed lower mass gain, under all test conditions, compared with the 18Cr steels Super 304H and 347HFG. In addition, Super 304H SP recorded a mass gain similar to that of HR3C at all temperatures and durations.

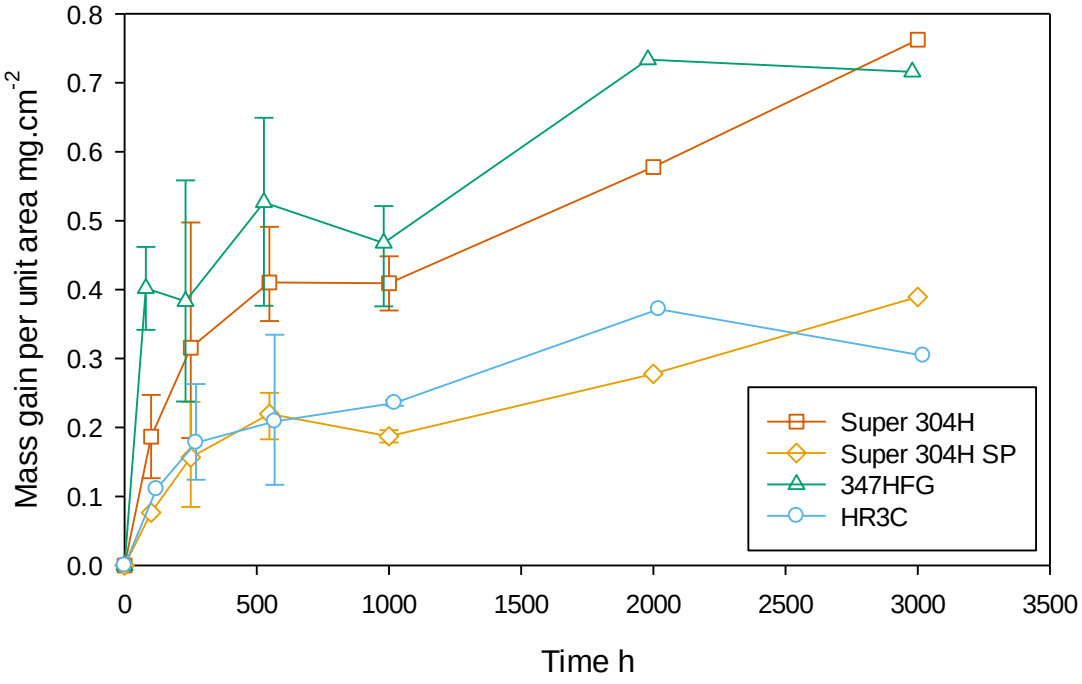

Figure 4.7 – Mass gain data for austenitic steels oxidised in laboratory air at 600 °C. Super 304H and 347HFG show higher mass gain than shot peened Super 304H and HR3C. Error bars show the range where multiple experiments were undertaken. For clarity of illustration, 347HFG and HR3C data points have been offset by 20 hours.

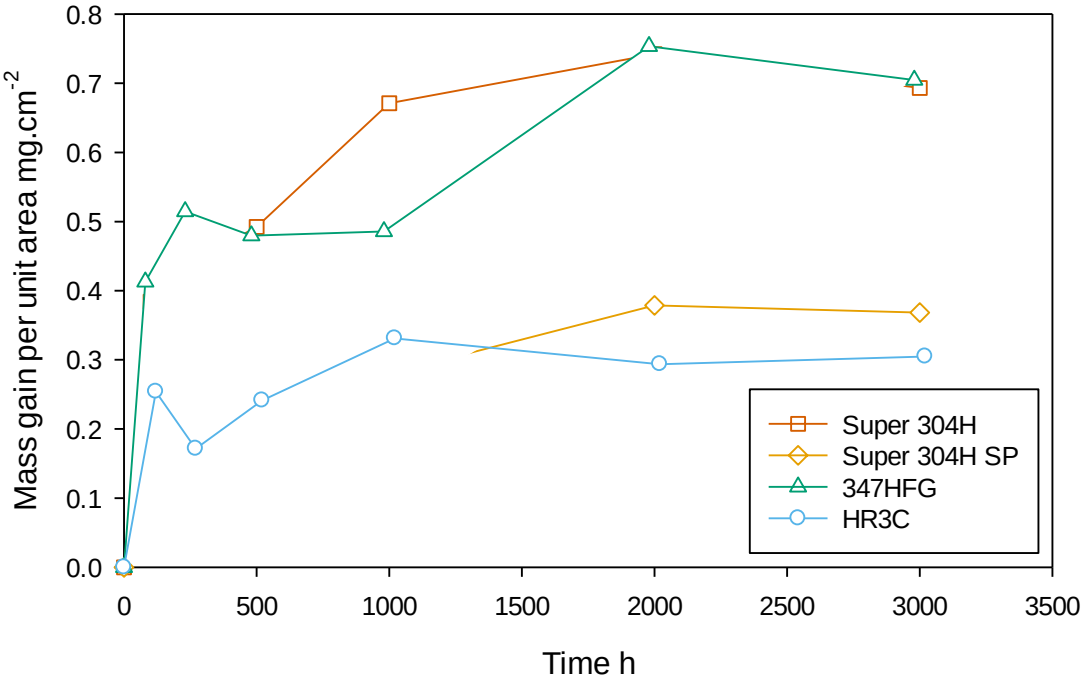

Figure 4.8 – Mass gain data for austenitic steels oxidised in laboratory air at 650 °C. Super 304H and 347HFG show higher mass gain than shot peened Super 304H and HR3C. For clarity of illustration, 347HFG and HR3C data points have been offset by 20 hours.

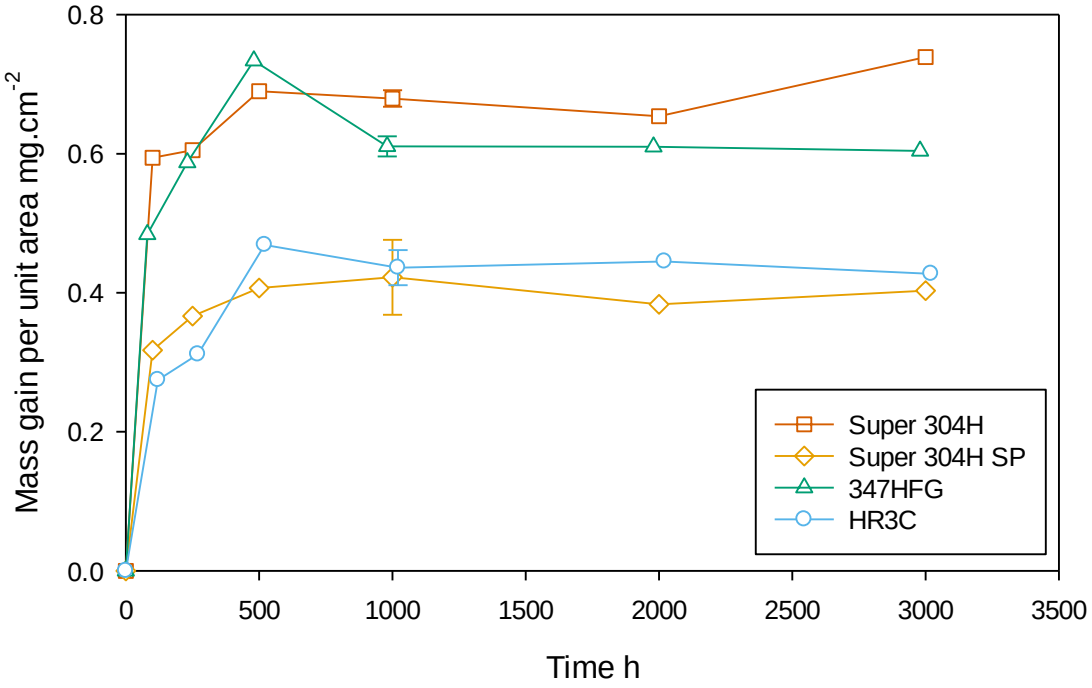

Figure 4.9 – Mass gain data for austenitic steels oxidised in laboratory air at 700 °C. Super 304H and 347HFG show higher mass gain than shot peened Super 304H and HR3C. Error bars show the range where multiple experiments were undertaken. For clarity of illustration, 347HFG and HR3C data points have been offset by 20 hours.

The 18Cr alloys 347HFG and Super 304H recorded a higher mass gain at all temperatures and durations than shot peened Super 304H and 25Cr HR3C. At 600 °C, mass gain increased gradually with a decrease in rate, akin to the parabolic relationships seen in the literature. However, at 700 °C and to a lesser extent 650 °C, an initial rapid rate of growth preceded a notable reduced rate after the first ~100 hours. This was most noticeable for 347HFG and Super 304. At 600 and 650 °C 347HFG exhibited the fastest rate of initial growth, before converging to the mass gain of Super 304H. The cross-sectional micrographs in sections 4.3.2.1.3 (347HFG) and 4.3.2.2.3 (Super 304H) show 347HFG to form a complete thick duplex oxide after as little as 100 hours at 600 °C, compared to Super 304H, in which a mixture of thin protective oxide exists alongside thick duplex oxide nodules at up to 500 hours at 650 °C. The rapid formation of complete duplex oxide coverage on 347HFG could explain the early increase in mass gain.

The oxidation rate of shot peened Super 304H broadly mimicked that of pickled Super 304H, albeit at a consistently lower mass gain. This behaviour is to be expected as they are the same base alloy, and only the inner surface had been shot peened. HR3C was comparable in mass gain to shot peened Super 304H at all temperatures. Given that a thick duplex oxide grew on the outer surface of shot peened Super 304H samples, this would suggest the inner shot peened surface grew a much thinner oxide than the pickled surface of HR3C. This is despite the higher chromium content of HR3C. In fact, the

cross-sectional micrographs in Section 4.3.2.4.3 show a thin protective oxide film on HR3C at all oxidation times, interspersed with larger oxide nodules, similar to the surface of Super 304H after 100 hours.

4.3.1.2 Oxide Thickness Measurements after Oxidation in Laboratory Air

The total oxide thickness of each sample was calculated by taking ten micrographs along the length of the inner surface cross-section, and measuring the total oxide thickness at six locations. This gave 60 total measurements, as outlined in the experimental procedure. The oxide on HR3C was found to be highly nodular, and so 120 thickness measurements were taken to provide a more accurate representation of both the thin protective oxide and larger nodules.

Oxide thickness data for Super 304H SP at 700 °C for up to 2000 hours revealed a thin film of less than 1 µm to be present after all exposures. This highlights the limitation of using mass gain measurements to derive oxidation kinetics from samples that do not have a homogeneous surface finish on all sides.

Difficulty in sample preparation with regards to the extremely thin oxides on the inner surface of Super 304H SP at 600 and 650 °C resulted in inaccurate or unobtainable thickness measurements at these temperatures. Therefore, oxide thickness data was only reported for oxidation at 700 °C.

The mean oxide thicknesses are plotted in Figure 4.10, Figure 4.11 and Figure 4.12. ±1 standard deviation is used for the error bars, assuming a normal distribution. The mean was found to give good representation of the average oxide thicknesses for Super 304H, 347HFG, and shot peened Super 304H. However, the mean disguises the bimodal nature of the oxide grown on HR3C. Although the oxidation rate described by the mean thickness matches the rate recorded by mass gain, the data is poorly described by a normal distribution over the time frame of testing. This is highlighted by the lower error bars, which fall below 0 µm suggesting negative oxide thickness – an impossibility for thickness measurements. They are included to illustrate the point.

Note that oxide thickness measurements were taken for up to 1000 hours at 600 and 650 °C, and for up to 2000 hours at 700 °C.

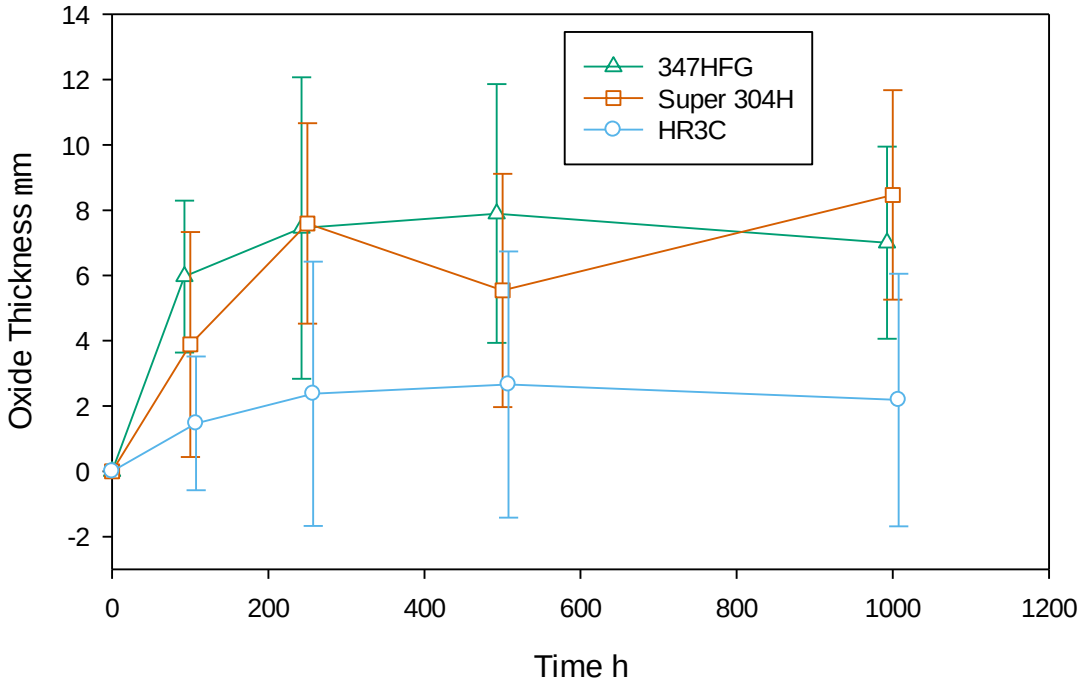

Figure 4.10 – Mean total oxide thickness on the steam side surface of austenitic steels oxidised in laboratory air at 600 °C. The thickness of the oxide grown on shot peened Super 304H was too thin to accurately measure. Error bars are one standard deviation. For clarity of illustration, 347HFG and HR3C data points have been offset by 7.5 hours.

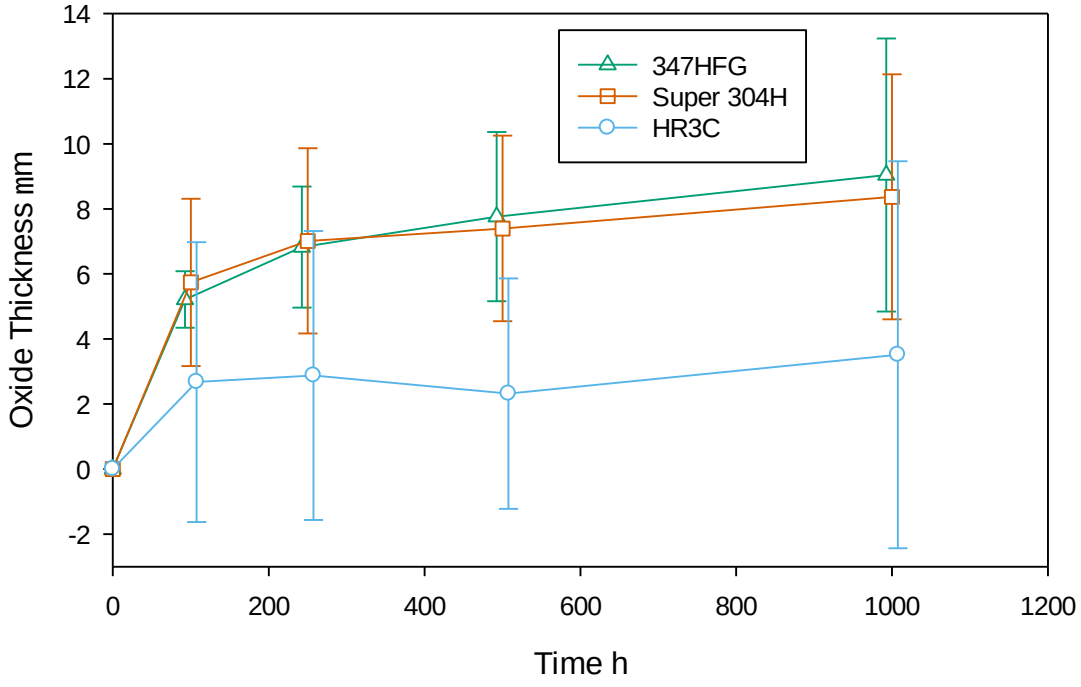

Figure 4.11 – Mean total oxide thickness on the steam side surface of austenitic steels oxidised in laboratory air at 650 °C. The thickness of the oxide grown on shot peened Super 304H was too thin to accurately measure. Error bars are one standard deviation. For clarity of illustration, 347HFG and HR3C data points have been offset by 7.5 hours.

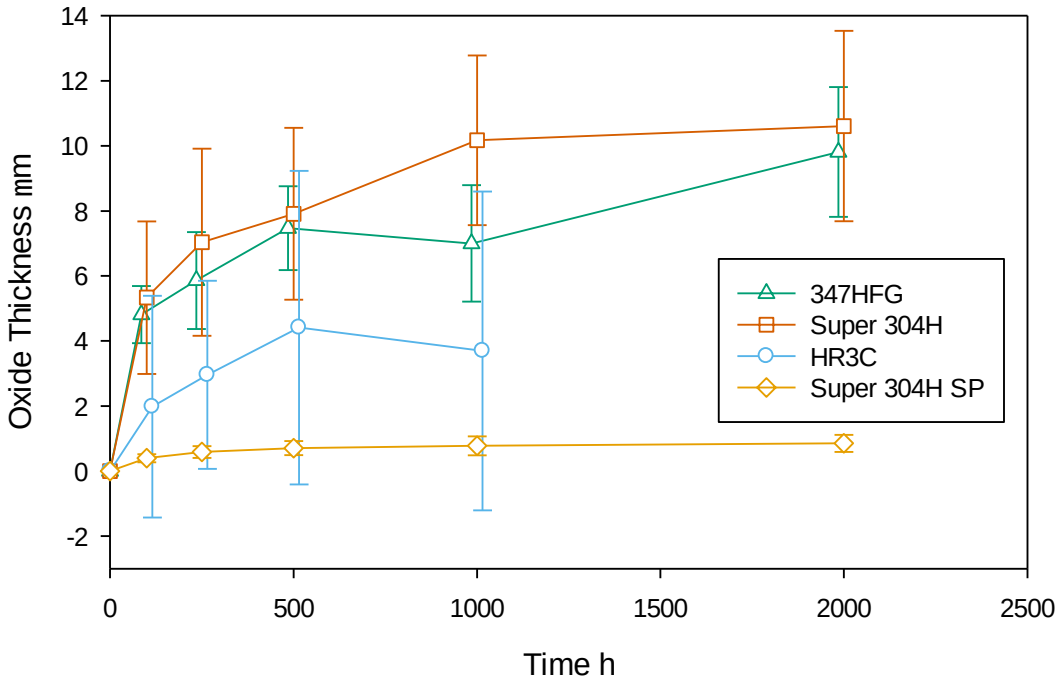

Figure 4.12 – Mean total oxide thickness on the steam side surface of austenitic steels oxidised in laboratory air at 700 °C. Error bars are one standard deviation. For clarity of illustration, 347HFG and HR3C data points have been offset by 15 hours.

The histograms in Figure 4.13 show the distribution of oxide thickness measurements for Super 304H and HR3C for oxidation at 700 °C for 1000 hours. This was the longest test at the highest temperature for which oxide thickness measurements were taken. It therefore represents the conditions at which the most duplex oxide had formed. Super 304H fits a normal distribution well, suggesting (and confirmed by cross-sectional analysis) a complete and relatively uniform layer of duplex oxide had formed on the surface. HR3C on the other hand is heavily skewed with the majority of oxide thickness measurements at the lower end of the scale, representing protective film growth. The mean value of oxide thickness measurements gives disproportionate weight to the few measurements that were taken where oxide nodules had grown.

To illustrate the skewed distribution, the median of the oxide thickness measurements, with upper and lower quartile error bars, are plotted in Figure 4.13. The most obvious difference in comparison to the mean thickness plots is the considerably lower thickness of the HR3C data. These show that the majority of the surface is covered by thin protective oxide. The upper and lower quartile error bars also give more accurate representation of the oxide nodules, and do not fall below 0 µm.

The median plots for Super 304H and 347HFG are comparable to the mean plots at 650 and 700 °C, indicating a relatively unimodal and normal distribution in thickness, i.e. the formation of a complete

duplex oxide layer. At 600 °C the discrepancy between the mean and median for both alloys is a reflection of the nodular nature of the oxide that had grown at this temperature. This was especially true for Super 304H, and agrees with the cross-sectional micrographs in Section 4.3.2.2.3.

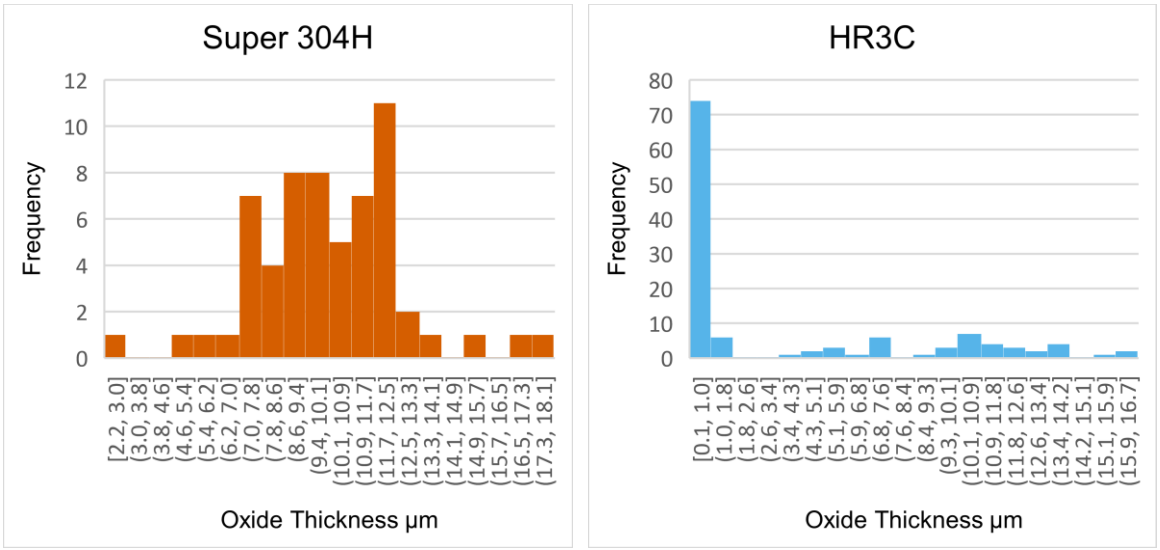

Figure 4.13 – Histograms of oxide thickness measurements for 18Cr Super 304H and 25Cr HR3C after oxidation in laboratory air for 1000 hours at 700 °C, showing skewed distribution in measured oxide thickness on HR3C. Note that 60 thickness measurements were taken for Super 304H and 120 for HR3C.

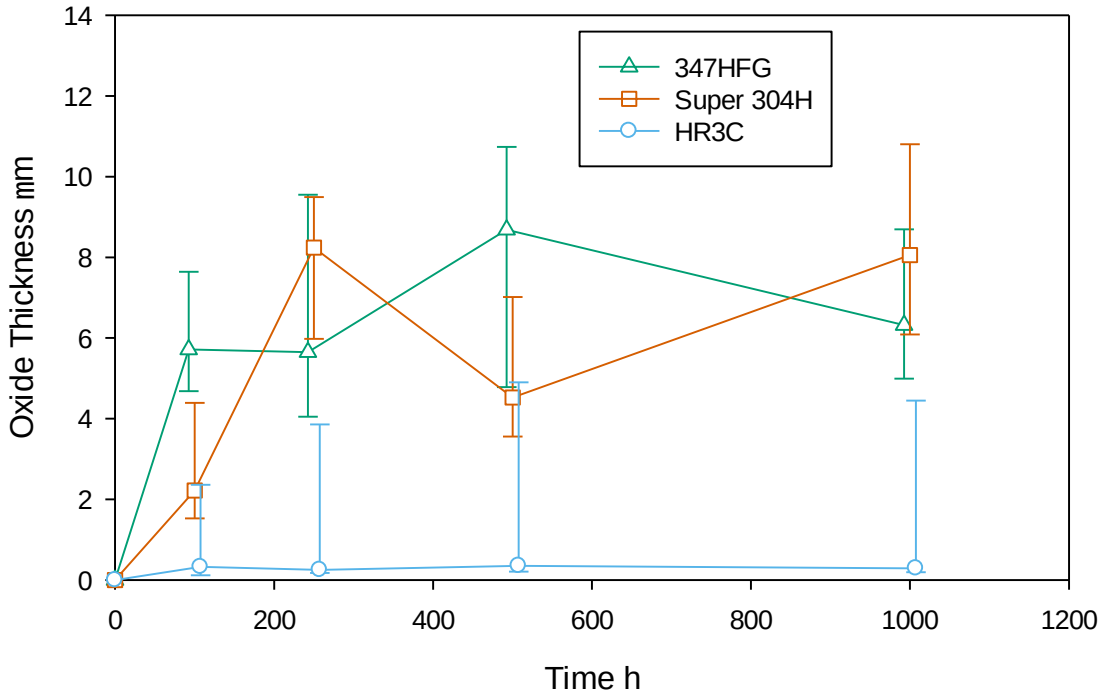

Figure 4.14 – Median total oxide thickness on the steam side surface of austenitic steels oxidised in laboratory air at 600 °C. The thickness of the oxide grown on shot peened Super 304H was too thin to accurately measure. Error bars indicate the 25th and 75th percentiles. For clarity of illustration, 347HFG and HR3C data points have been offset by 7.5 hours.

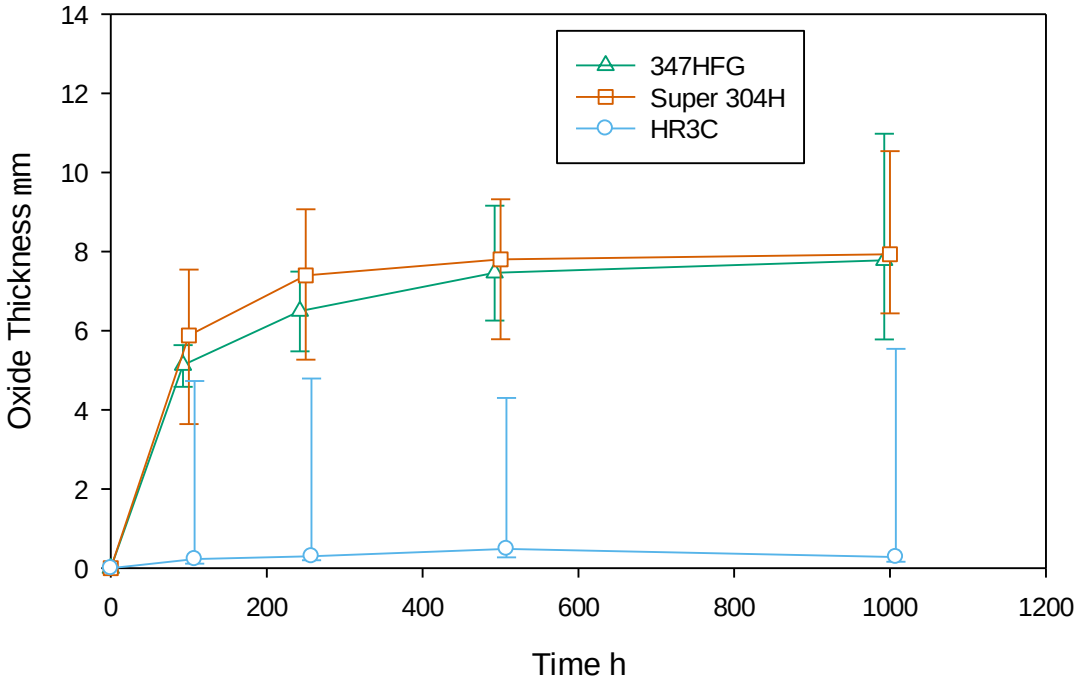

Figure 4.15 – Median total oxide thickness on the steam side surface of austenitic steels oxidised in laboratory air at 650 °C. The thickness of the oxide grown on shot peened Super 304H was too thin to accurately measure. Error bars indicate the 25th and 75th percentiles. For clarity of illustration, 347HFG and HR3C data points have been offset by 7.5 hours.

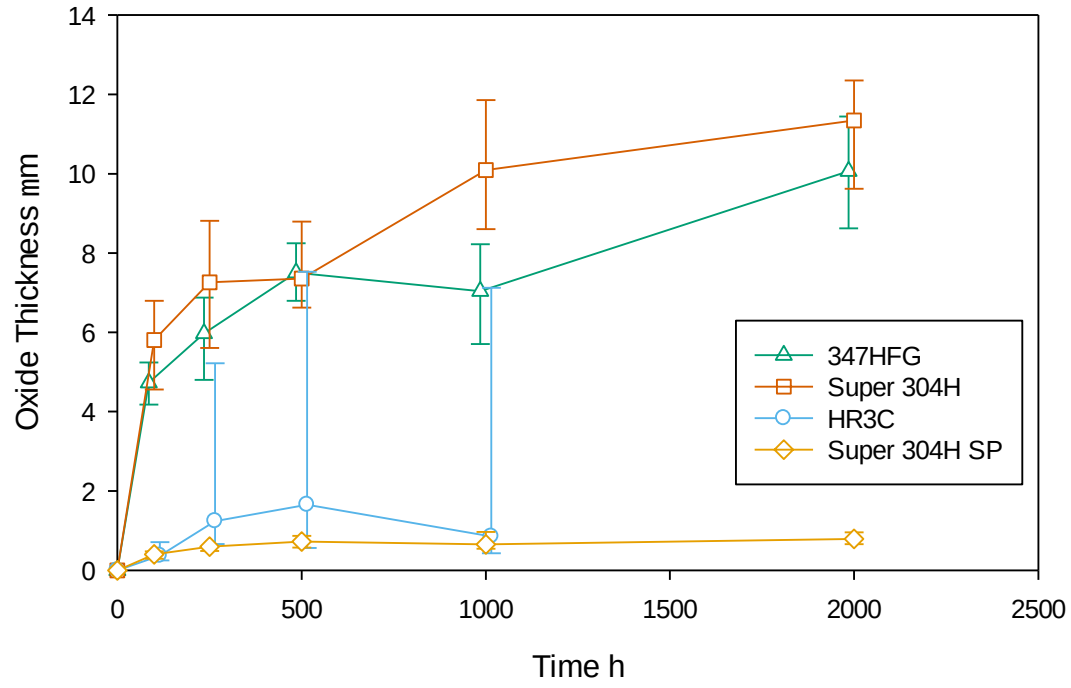

Figure 4.16 – Median total oxide thickness on the steam side surface of austenitic steels oxidised in laboratory air at 700 °C. Error bars indicate the 25th and 75th percentiles. For clarity of illustration, 347HFG and HR3C data points have been offset by 15 hours.

The median and quartile plots in Figure 4.14, Figure 4.15 and Figure 4.16 show that the thin protective oxide grown on HR3C continues to form a high fraction of total oxide after 1000 hours oxidation in air (and is confirmed by the cross-sectional micrographs in Section 4.3.2.4.3). This is in contrast to the thin oxide layer that initially forms on the surface of the pickled surface of 18Cr steels. This oxidises to iron rich duplex oxide after a relatively short period of time, and could be considered a transient oxide.

It is therefore of interest to understand the oxidation kinetics of the protective oxide layer. This was achieved by separating the protective oxide thickness measurements from those that represented nodule oxide growth.

Figure 4.17 shows the distribution of oxide thickness measurements for HR3C at all temperatures, ordered in increasing oxide thickness. To isolate measurements that relate to protective oxide growth only, measurements were only included in the population up to the point at which the distribution rapidly increases in gradient for each sample. It should be noted that this method was somewhat subjective, and the cut-off point was more obvious for some samples (700 °C, 1000 hours) than others (600 °C, 100 hours).

The mean and median of the reduced population was calculated for each sample, and little variation was found. Therefore, the mean protective oxide thicknesses were plotted for each temperature and can be found in Figure 4.18. Also included in the figure are the mean total oxide thicknesses for shot peened Super 304H at 700 °C.

The HR3C protective oxide thicknesses at 600 and 650 °C are similar, suggesting the increase in mass gain at 650 °C is a result of increased nodule growth. This is in agreement with the upper quartile ranges in the median oxide thickness plots. At 700 °C there is a marked increase in protective oxide thickness. There is scatter in the data, but the rate broadly aligns with the oxide grown on shot peened Super 304H at the same temperature, suggesting a similar oxide composition.

The scatter in HR3C is partially attributed to error in the measurement of the sub-micron thick oxide. However, there is significantly more variation in oxide thickness than measured for shot peened Super 304H. Two reasons for this could be: a) HR3C fundamentally grows two types of oxides, and the protective oxide thickness measurements were taken from a larger population, and b) the shot peening treatment on Super 304H is known to introduce a high density of short-circuit diffusion paths. This may allow for even and predictable growth of chromium rich oxide on the shot peened surface, when compared to the coarse grained HR3C.

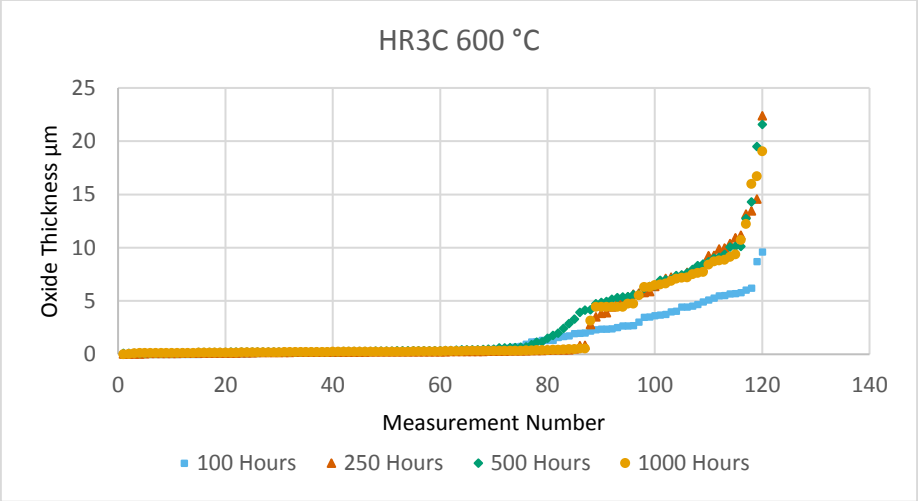

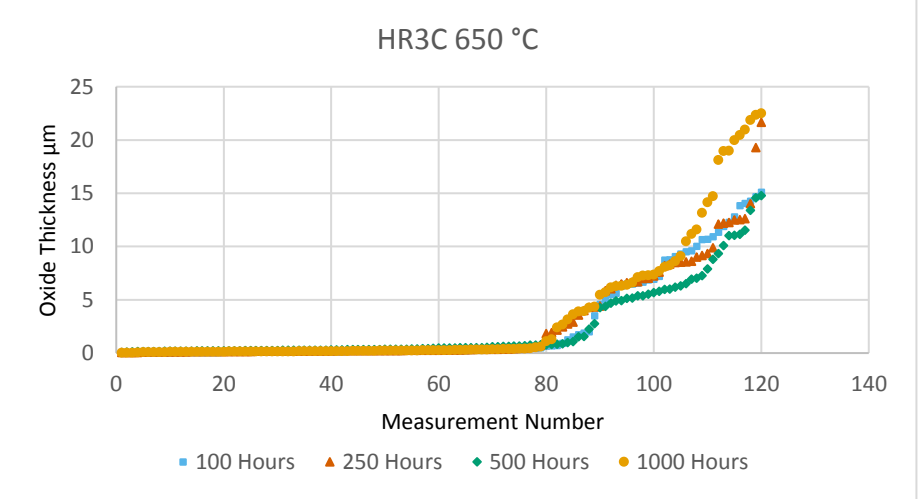

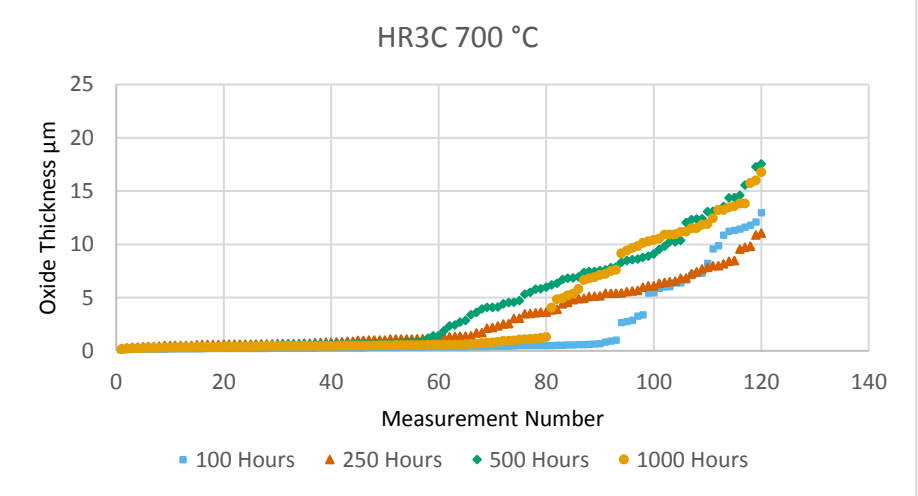

Figure 4.17 – Distribution of oxide thickness measurements for HR3C oxidised in laboratory air.

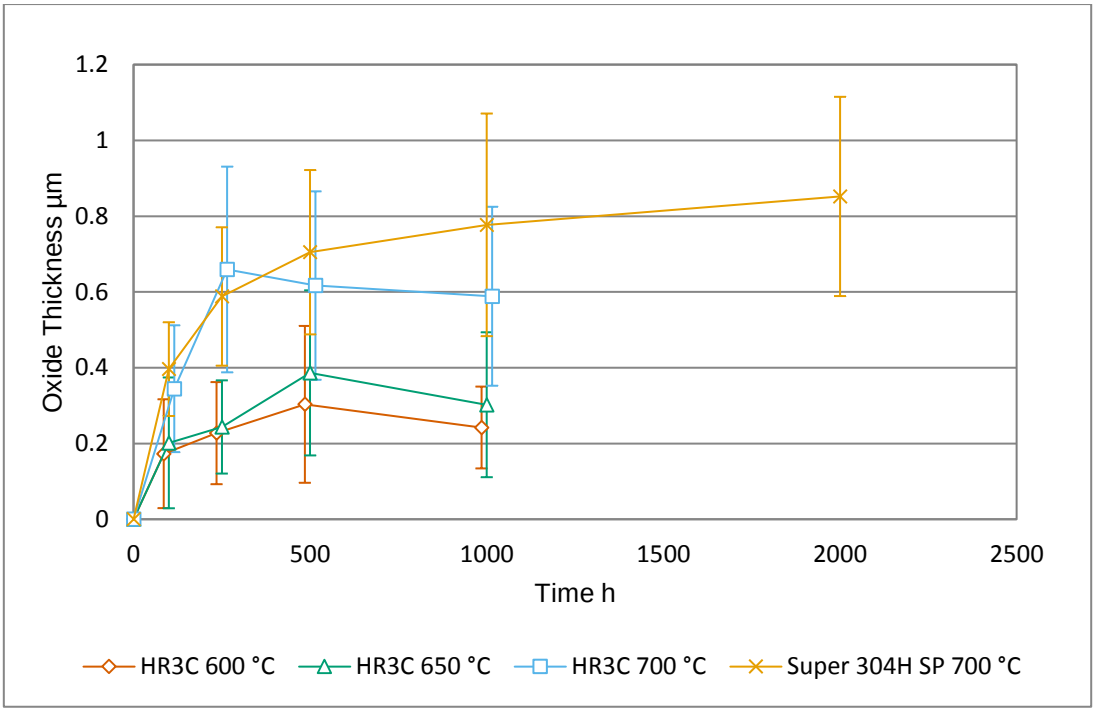

Figure 4.18 – Mean protective oxide thickness data for HR3C oxidised in air at 600, 650, and 700 °C. Included for comparison is mean total oxide thickness for shot peened Super 304H at 700 °C. Error bars are one standard deviation.

4.3.2 Oxide Morphology after Oxidation in Laboratory Air

4.3.2.1 347HFG

4.3.2.1.1 Visual Observations of 347HFG after Oxidation in Laboratory Air

Samples of 347HFG oxidised in laboratory air were typically matt grey in appearance upon removal from the furnace. There was only a small variation in this over the entire oxidation period and temperature range. No observable spallation occurred on any samples. The appearance of the sample surface is shown in Figure 4.19 and Figure 4.20.

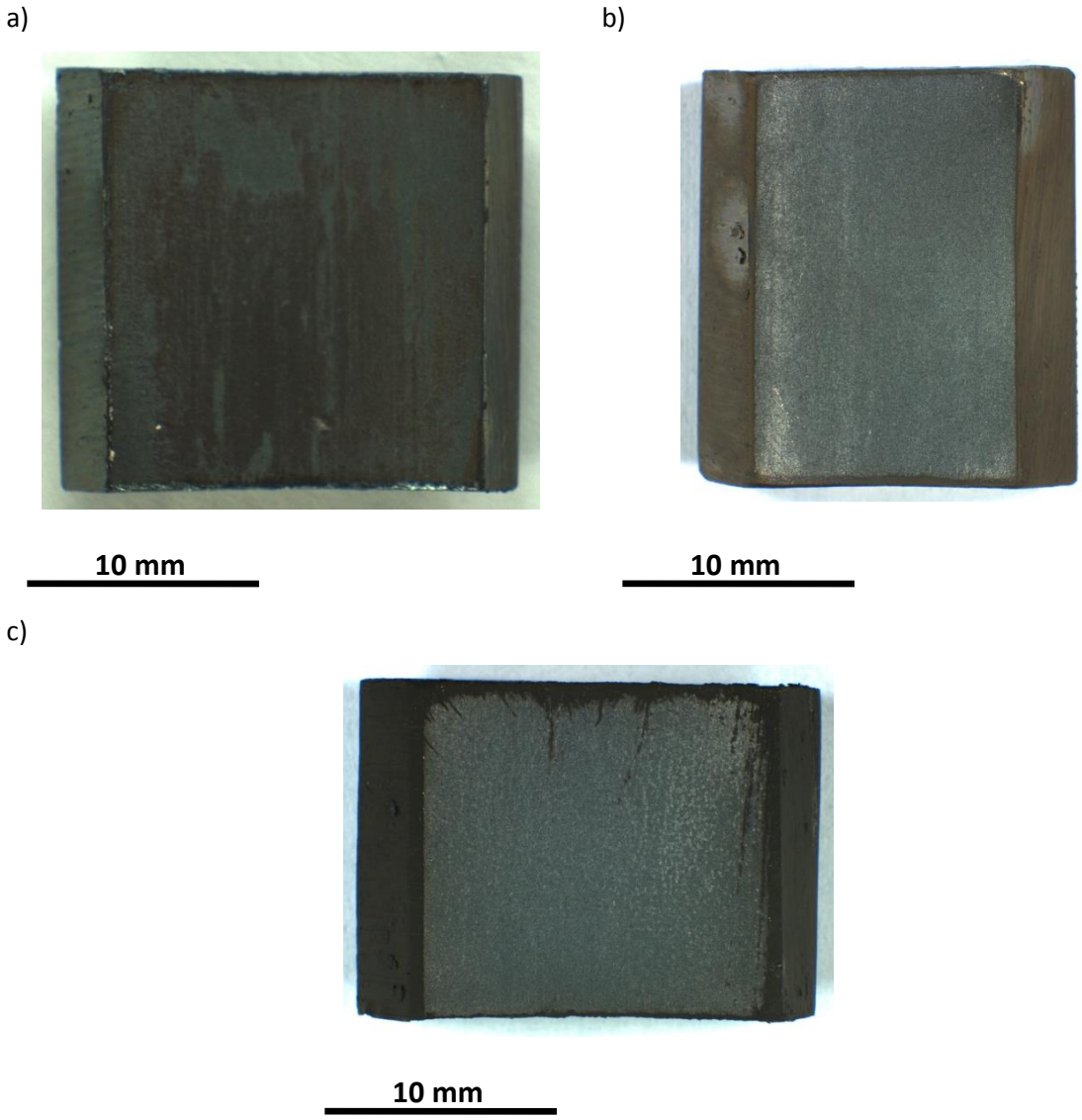

Figure 4.19 – Macro images of air oxidised 347HFG inner surface after 100 hours at a) 600 °C, b) 650 °C, c) 700 °C. The inner surfaces were all matt grey following oxidation.

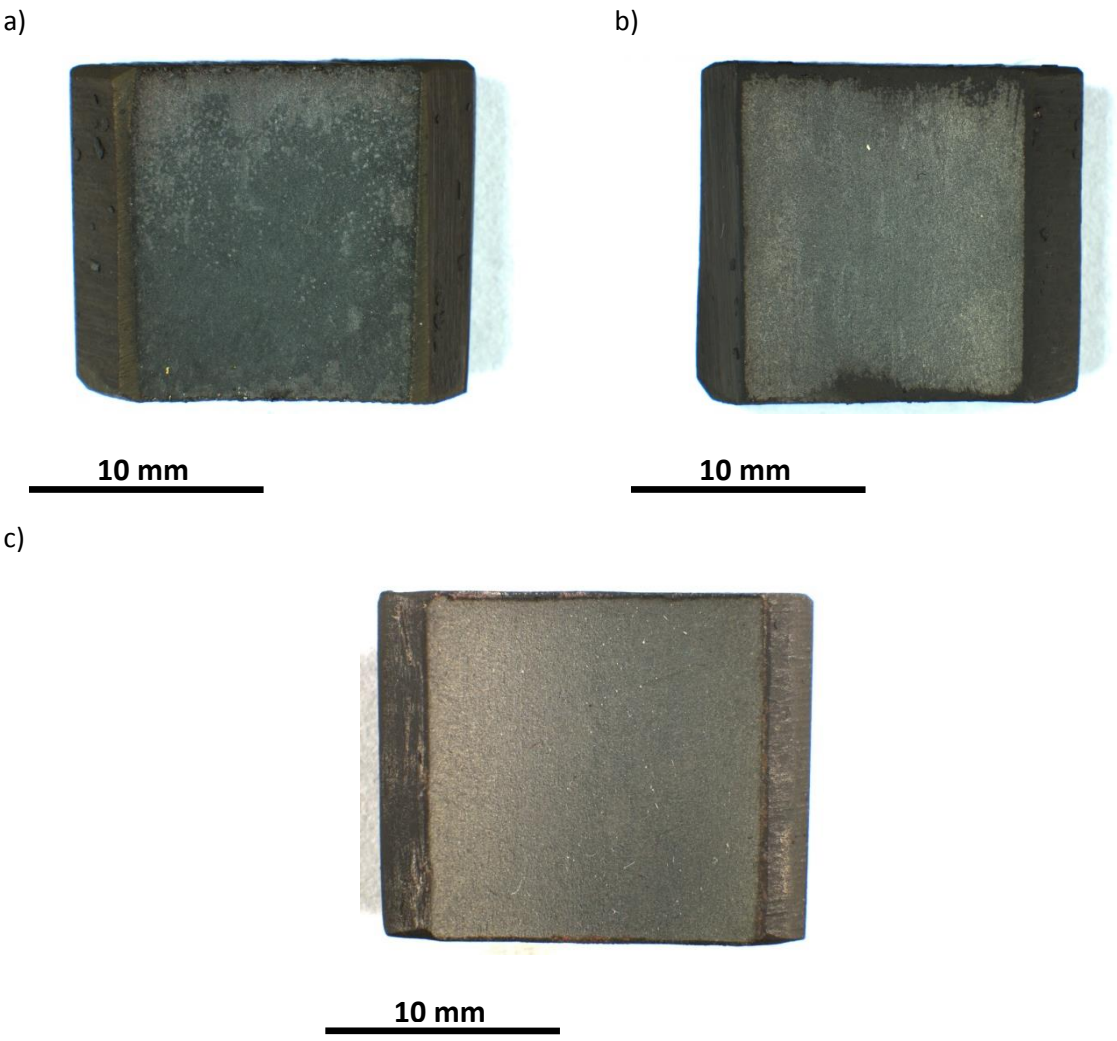

Figure 4.20 – Macro images of air oxidised 347HFG inner surface after 1000 hours at a) 600 °C, b) 650 °C, c) 700 °C. The inner surfaces remained a matt grey colour following oxidation for 1000 hours.

4.3.2.1.2 SEM Surface Analysis of 347HFG after Oxidation in Laboratory Air

SEM images of the inner surface topography of 347HFG revealed oxide with slight porosity in the outer scale, the extent of which increased as oxidation time increased. At 600 °C whiskers formed on the iron rich outer oxide surface at all durations and were more abundant as oxidation time increased as shown by Figure 4.21, Figure 4.22 and Figure 4.23.

a) b)

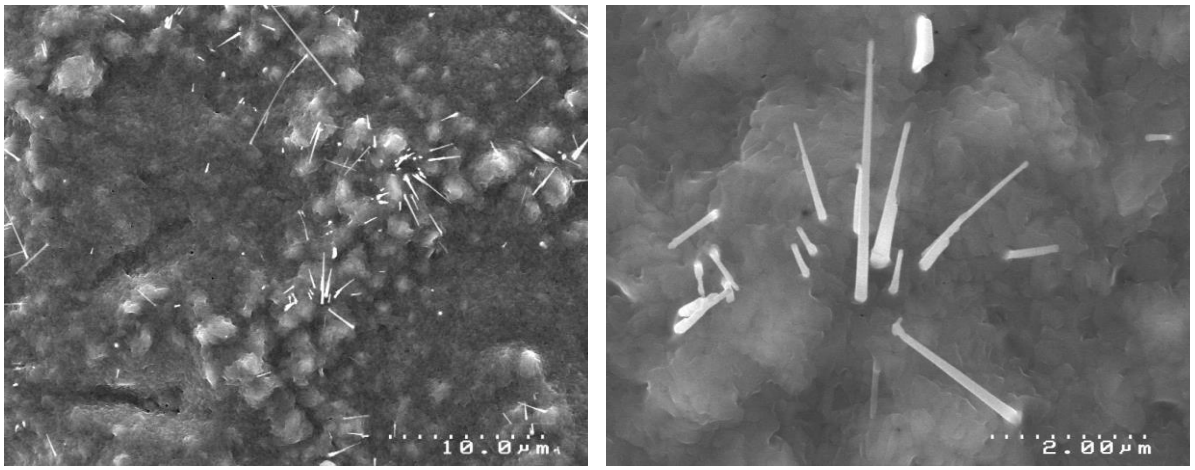

Figure 4.21 – SEI SEM images of 347HFG inner surface topography after oxidation in air for 250 hours at 600 °C showing slightly porous iron rich outer oxide covered surface and occasional whiskers.

a) b)

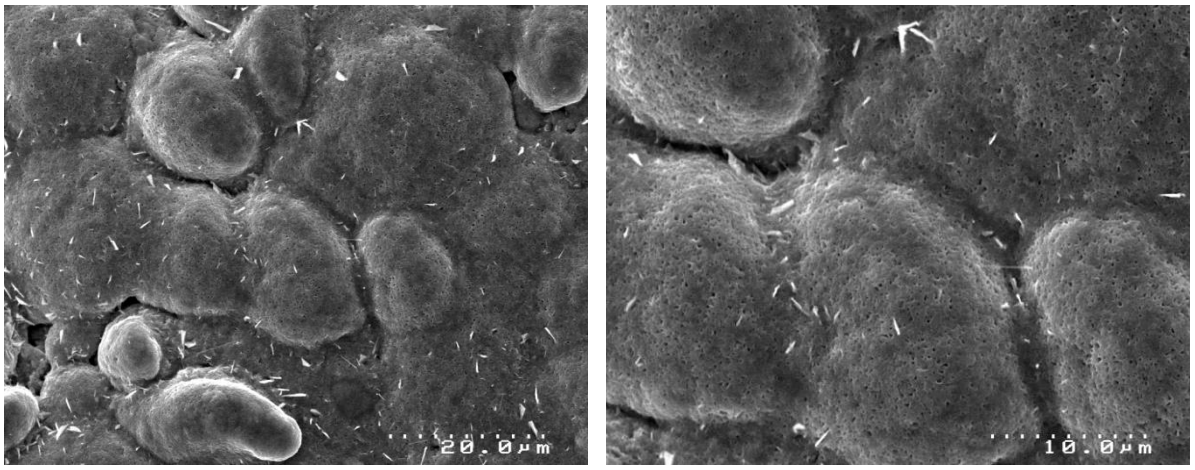

Figure 4.22 – SEI SEM images of 347HFG inner surface topography after oxidation in air for 1000 hours at 600 °C showing porous iron rich outer oxide and occasional whiskers

a) b)

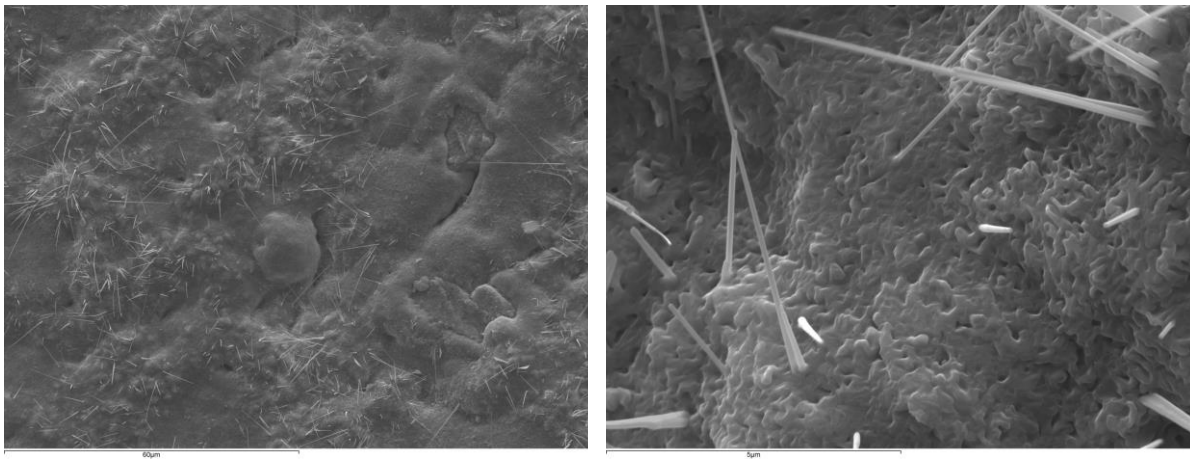

Figure 4.23 – SEI SEM images of 347HFG inner surface topography after oxidation in air for 2000 hours at 600 °C showing iron rich oxide with abundance of whiskers.

At 650 °C whiskers were largely replaced with platelets (Figure 4.24). The bulk oxide resembled that of oxidation at 600 °C.

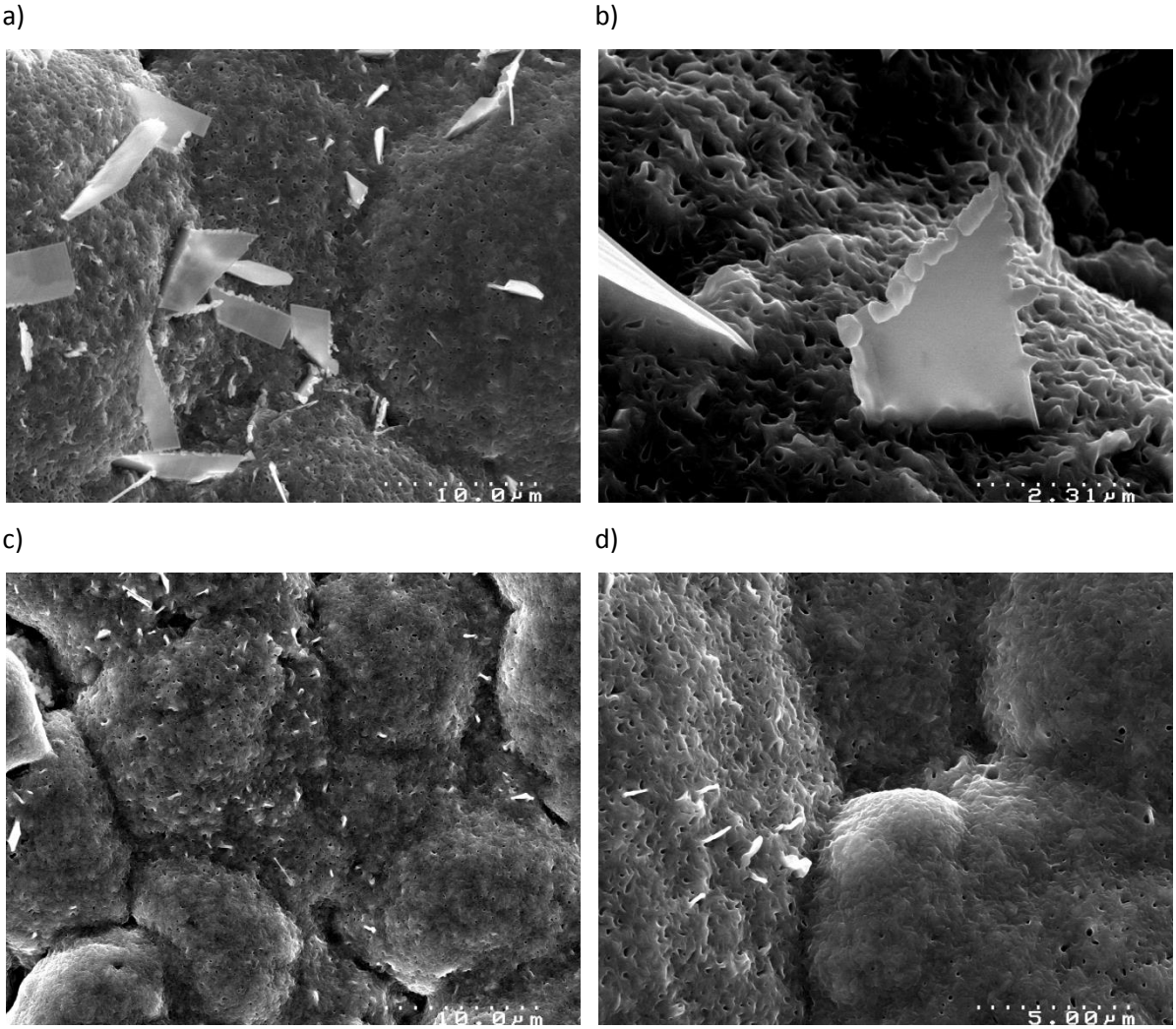

Figure 4.24 – SEI SEM images of 347HFG inner surface topography after oxidation in air for 2000 hours at 650 °C. Platelets largely replaced whiskers compared with oxidation at 600 °C.

At 700 °C platelets were observed in a seemingly random distribution across the oxide surfaces. These were thicker but shorter in height at the higher temperature as shown in Figure 4.25 and Figure 4.26.

a) b)

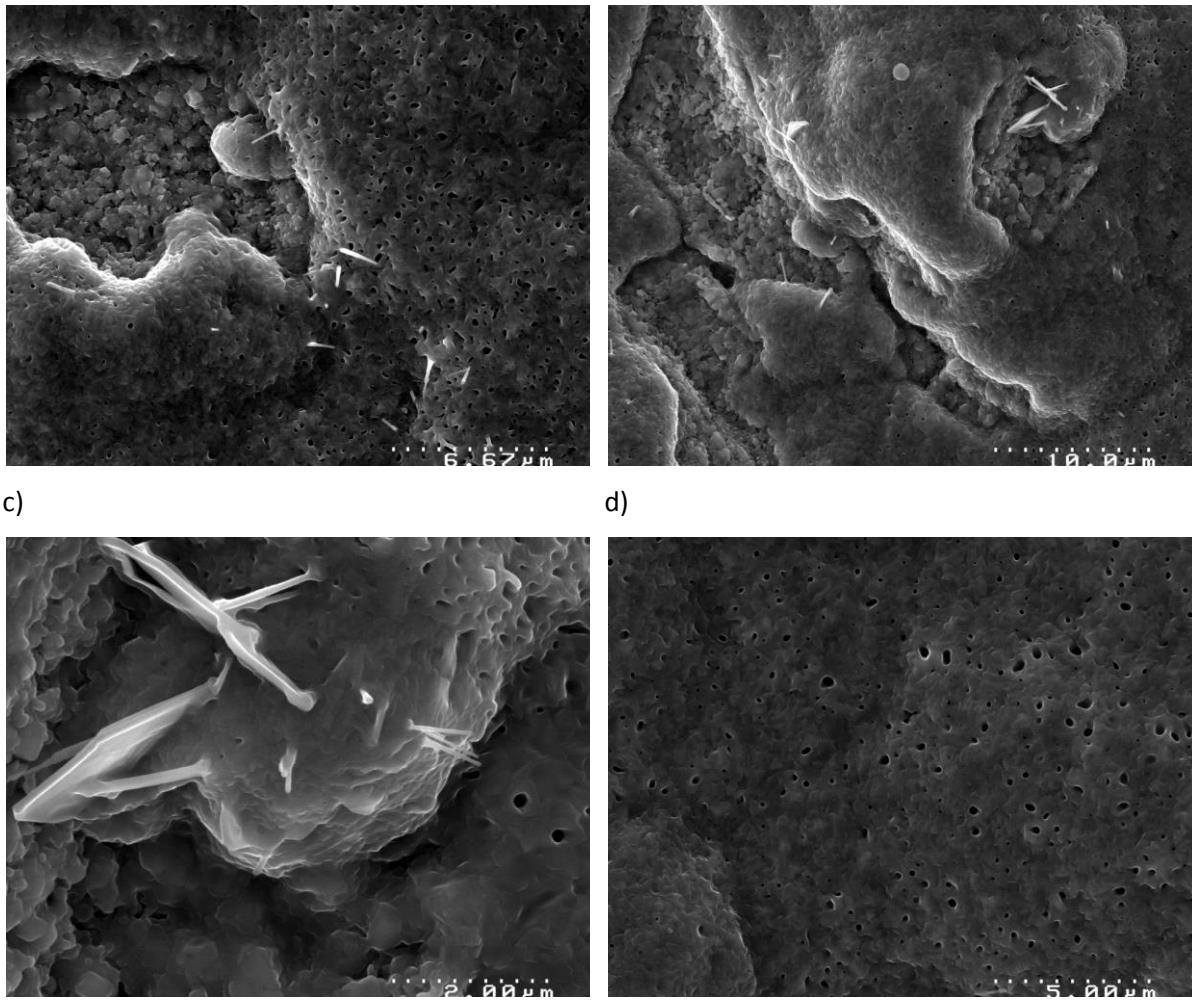

c) d)

Figure 4.25 – SEI SEM images of 347HFG inner surface topography after oxidation in air for 250 hours at 700 °C showing porous oxide compared to 600 °C and 650 °C. Fewer platelets were observed than after oxidation at 650 °C.

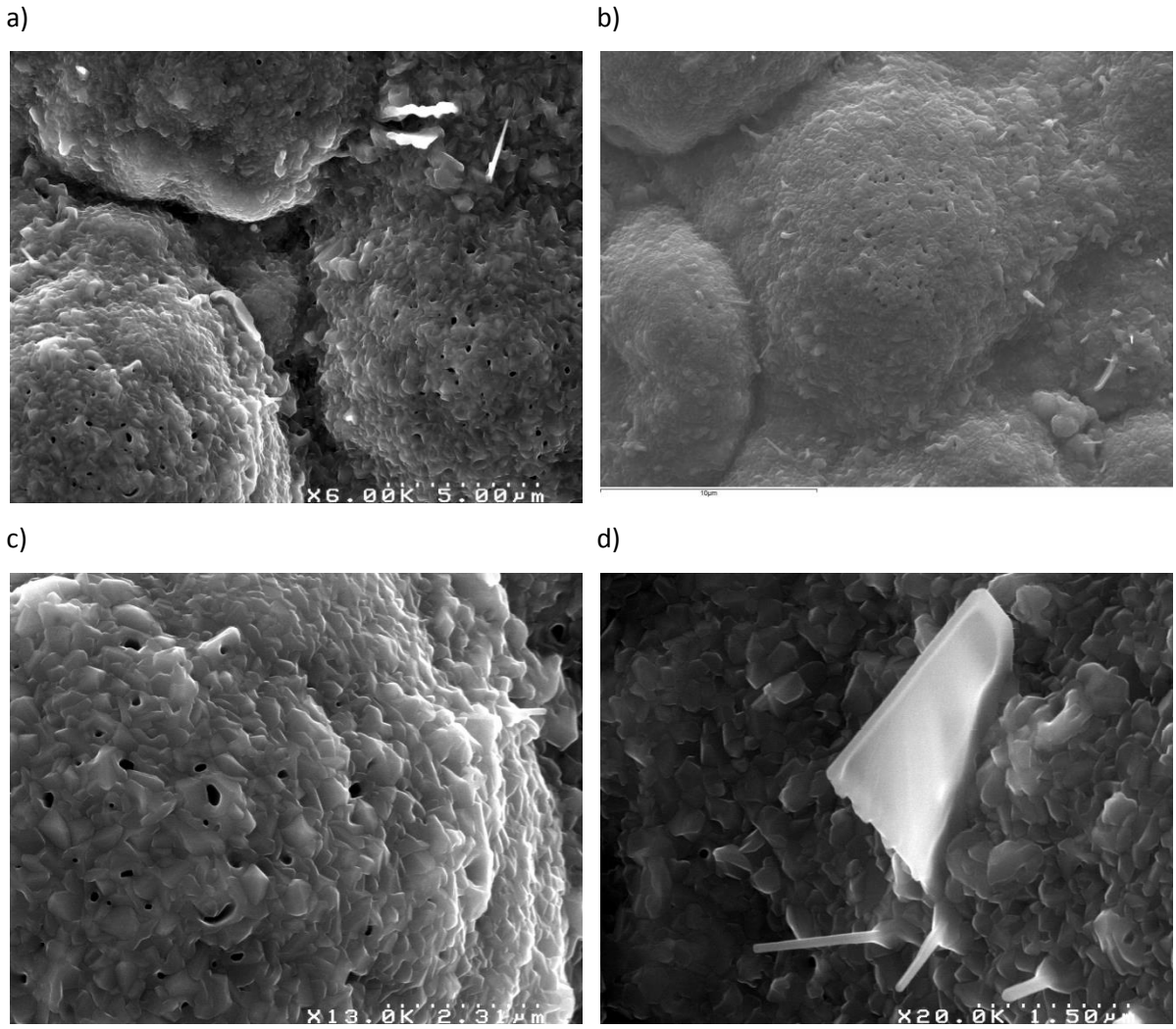

Figure 4.26 – SEI SEM images of 347HFG inner surface topography after oxidation in air for 2000 hours at 700 °C. Fewer platelets were observed than at 650 °C.

4.3.2.1.3 Oxide Cross-Section Morphology of 347HFG as a Function of Time and Temperature after Oxidation in Laboratory Air

The morphology of 347HFG oxidised in air varied little with time and temperature. A continuous duplex scale was formed under all conditions. The thickness of the scale tended to increase with time and temperature, as shown by the oxide thickness measurements. The slightly nodular appearance of the spinel at lower times and temperatures suggested it had formed from a nodular oxide that had coalesced into a continuous duplex scale.

The duplex oxide consisted of an outer iron rich oxide and inner spinel type oxide consisting of iron, chromium, nickel and sometimes a small concentration of manganese. The concentration of chromium in the spinel tended to increase towards the metal/oxide interface. This structure was the same for all oxidation temperatures.

Thickness measurements for individual oxide layers were not taken. However, from analysis of the cross-sectional micrographs the outer oxide was approximately twice as thick as the spinel for most exposures. This contrasts with oxidation in steam, where the spinel and outer oxide thicknesses remained more even until the longer exposures (Section 4.4.1.2).

SEM micrographs of the cross sections for oxidation times of 100, 250, 500 and 1000 hours and temperatures of 600, 650 and 700 °C are shown in Figure 4.27, Figure 4.28 and Figure 4.29.

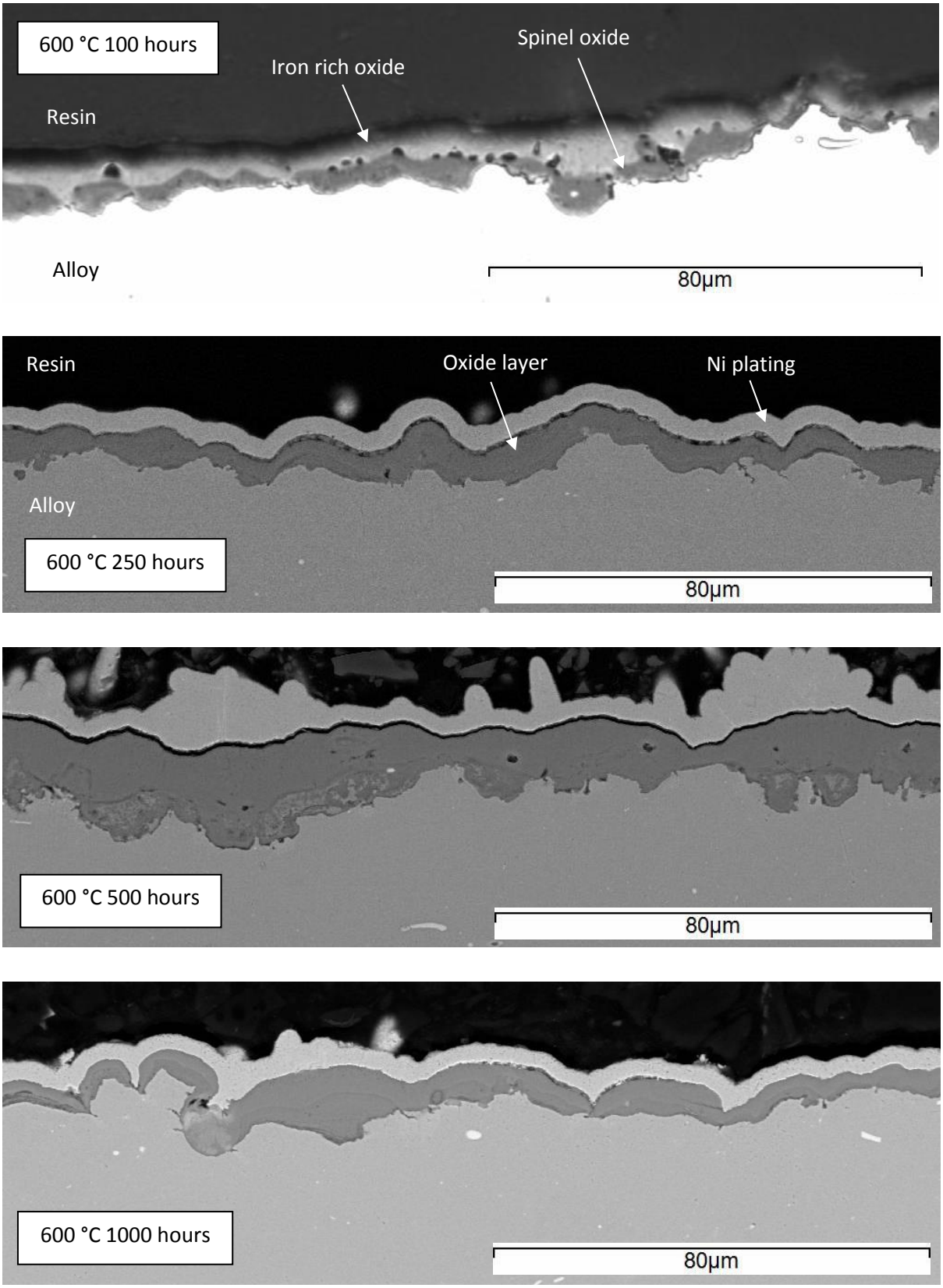

Figure 4.27 – BSE SEM micrographs of oxide formed on 347HFG oxidised in air at 600 °C. A duplex oxide was formed after every duration. After 100 hours the spinel oxide appeared slightly nodular.

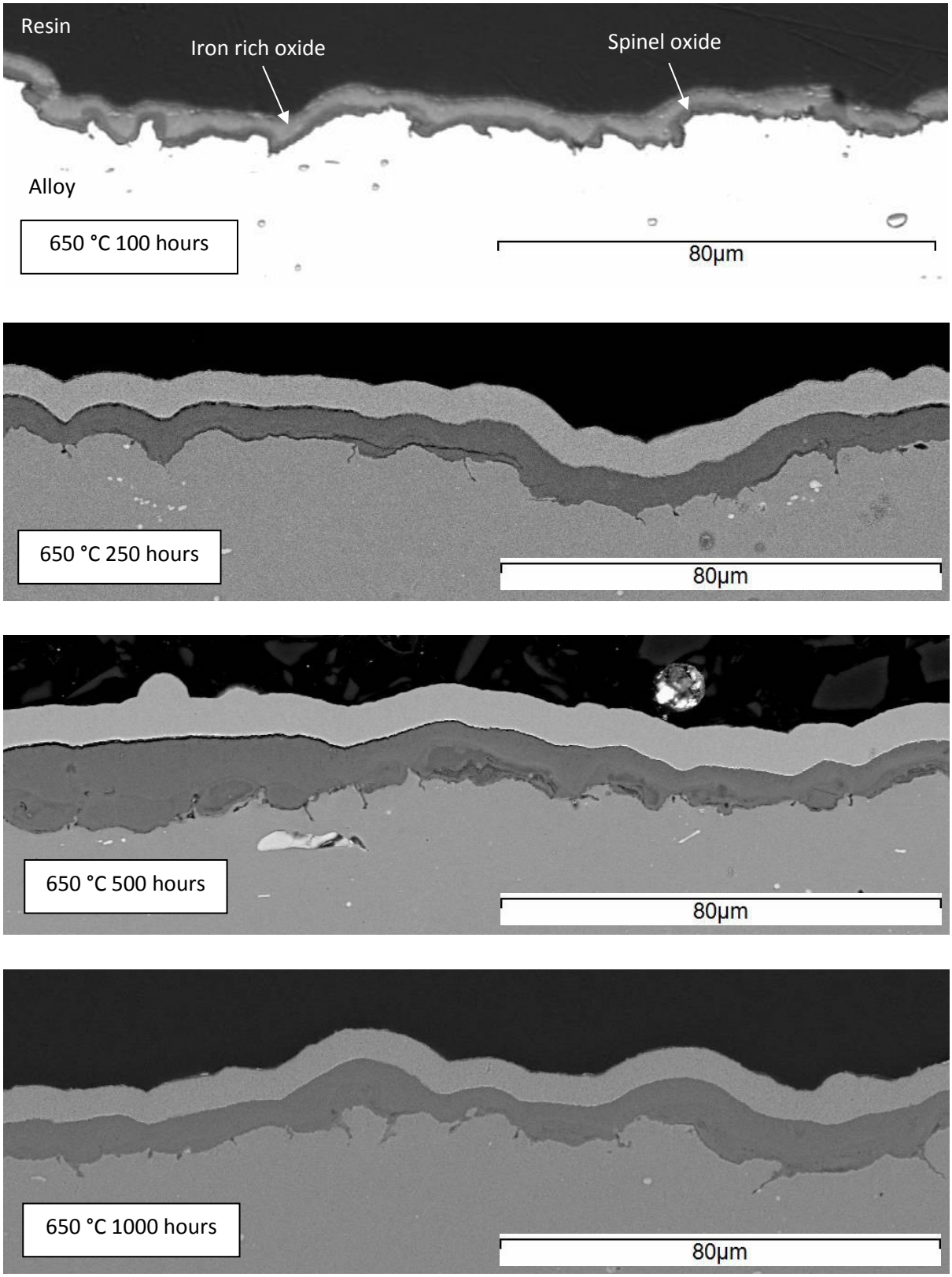

Figure 4.28 – BSE SEM micrographs of oxide formed on 347HFG oxidised in air at 650 °C. A thicker and more uniform duplex oxide grew compared with oxidation at 600 °C. After 100 hours a uniform spinel oxide had formed.

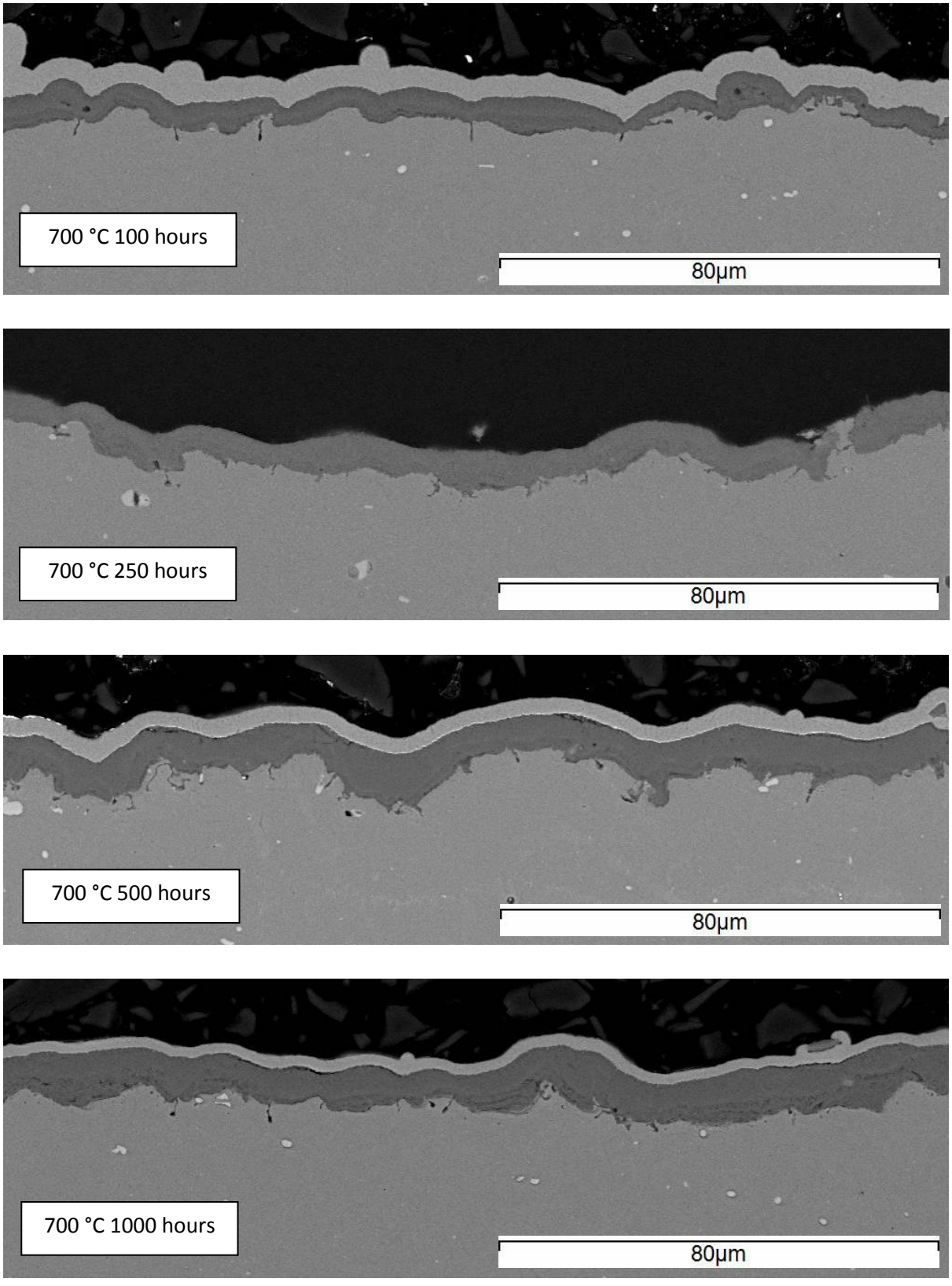

Figure 4.29 – BSE SEM micrographs of oxide formed on 347HFG oxidised in air at 700 °C. Oxide morphology was similar to that at other temperatures albeit a thicker duplex oxide had formed.

4.3.2.1.4 Oxide Area Maps of 347HFG after Oxidation in Laboratory Air

EDX mapping of the oxide formed on 347HFG after oxidation in air for 1000 hours at 650 °C was performed for qualitative analysis. The map in Figure 4.30 shows two distinct regions of oxide, an outer iron rich oxide and inner mixed oxide containing concentrations of iron, chromium, nickel and manganese. A slight depletion of chromium is visible in the substrate subjacent to the spinel oxide. A corresponding enrichment in nickel is visible. Depletion was rare on samples oxidised at 600 °C and extensive in alloys oxidised at 700 °C. Areas with the highest depletion of chromium and manganese corresponded to where alloy grain boundaries reached the surface.

4.3.2.1.5 EDX Analysis of 347HFG after Oxidation in Laboratory Air

EDX spot analysis provided quantitative information regarding the composition of the oxide formed on 347HFG after 1000 hours at 650 °C. EDX spots 2-5 correspond to the inner oxide as identified in the area maps in the previous section. Table 4.1 shows an enrichment in chromium in these areas, relative to iron and nickel.

Cr_2O_3 is the preferred protective oxide for stainless steels at high temperature. However, on the pickled surface this rarely passivates as a complete and protective layer. Figure 4.31 shows a duplex oxide (which had covered the complete surface of the alloy) after oxidation at 650 °C for 1000 hours. If a Cr-rich protective oxide were present, it would be in the form of a thin dark line contouring the alloy/oxide interface, as Cr-rich oxide is dark when viewed through SEM BSE. Such a feature is absent from Figure 4.31, and the inner oxide appears to be propagating into the alloy. Furthermore, the internal oxidation front has not reached such a thickness that it has consumed entire austenite grains. In steam, it has been shown to promote growth of a Cr-rich protective oxide or “healing layer” along the grain boundary (see for example Figure 4.79 in Section 4.4.2.1.3).

Spot locations 2 – 4 on Figure 4.31 correspond to the inner oxide. Quantitative EDX analyses on spots 4 and 5 show element distributions of roughly a 2:1 ratio of oxygen to metal (Table 4.2). It is likely that the EDX analysis is over-representing the oxygen content, which is an inherent limitation of EDX. It is difficult to identify the exact phases present in the inner oxide, but a spinel of Fe-Cr-Ni is likely if nickel is present within the oxide, or a Fe-Cr spinel in a metallic nickel matrix.

EDX spots 2 and 3 show an enrichment of Cr. If the oxide in these areas was Cr_2O_3, the EDX composition would be expected to be 40 at.% Cr and 60 at.% O, with no traces of other elements. The measured Cr content is 17 – 20 at.%, suggesting this is not the case. It more likely exists as part of the spinel oxide $(Fe_{3-x}Cr_x)_3O_4$ where ‘x’ ranges from 1 at the inner/outer oxide interface to 2 at the base of the spinel. Spots 2 and 3 also show enrichments in manganese and silicon. Manganese has a similar

affinity to oxygen as chromium and could exist in the form Cr_2MnO_4 or be incorporated into the Fe-Cr-Ni spinel. Silicon has the greatest affinity to oxygen and is often found at the alloy/oxide interface in the form SiO_2.

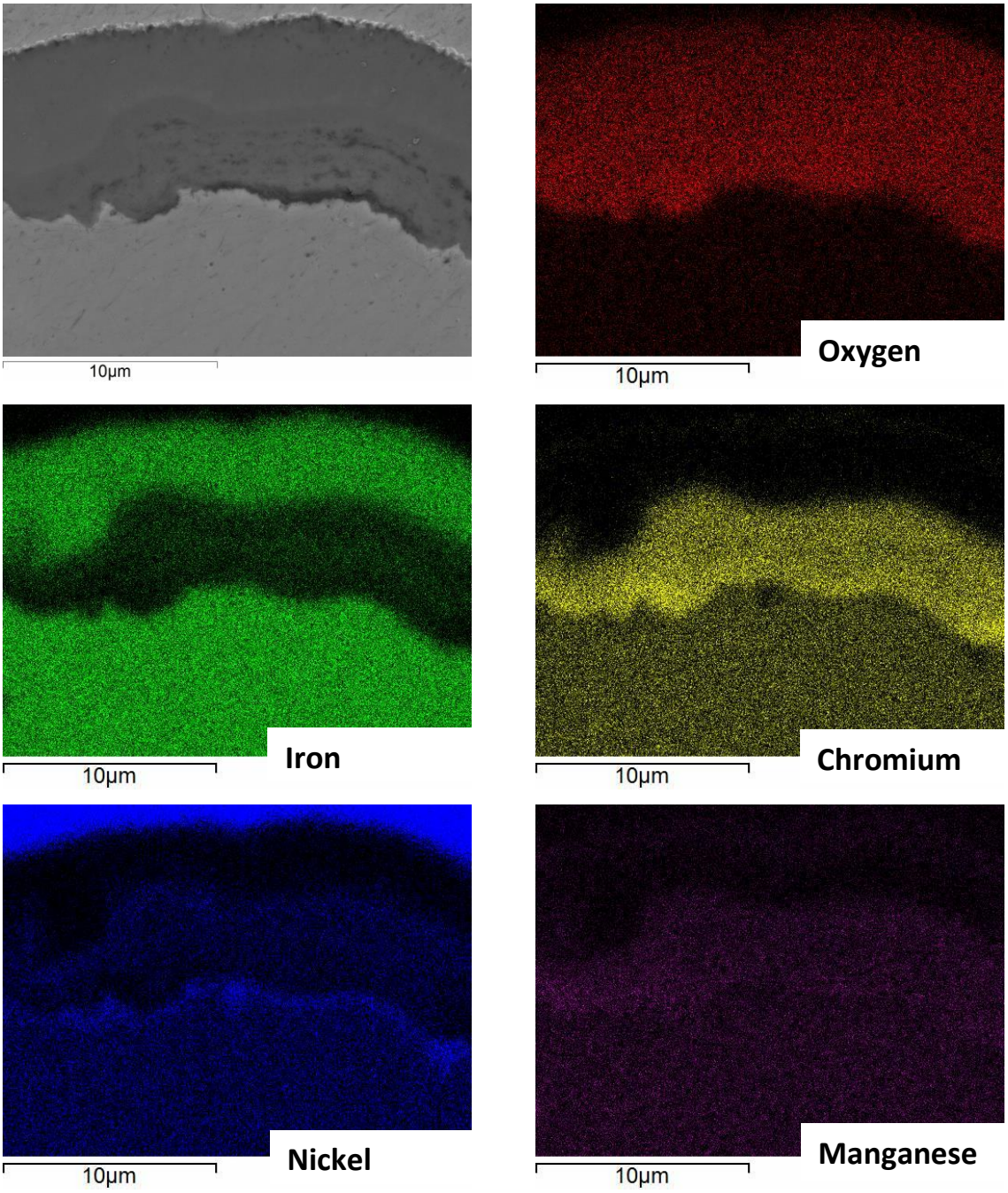

Figure 4.30 – EDX element area map for a cross-section of 347HFG oxidised in air after 1000 hours at 650 °C. Sample has been nickel plated. Element maps show the presence of an outer iron rich oxide and inner spinel oxide containing iron, chromium, nickel and manganese. At the base of the oxide is a slight chromium enrichment and corresponding depletion of nickel and iron. This composition is reversed in the subjacent alloy.

It should be noted that the EDX spot analysis will detect elements within an approximate <5 µm diameter. Therefore, it is likely spots 2 and 3 are picking up traces of elements from the underlying alloy, and further out into the inner oxide. The area maps in Figure 4.31 show a depletion of nickel in the oxide at the alloy/oxide interface, and corresponding enrichment in the alloy immediately subjacent to the oxide. Conversely, chromium and manganese are enriched in the oxide at the alloy/oxide interface and depleted in the subjacent alloy. It is therefore likely that the EDX analysis is limited by resolution, and the true oxide composition at spots 2 and 3 contain a higher fraction of chromium, manganese, and oxygen, and a lower fraction of iron and nickel.

The outer oxide (spots 6 and 7) was purely iron rich (save for trace amounts of chromium and nickel). A limitation of EDX analysis is the accurate quantification of lighter elements such as oxygen. It was therefore difficult to determine whether the outer oxides grown in both air and steam were composed of haematite, magnetite, or both. EDX analysis of Fe_2O_3 should report 40 at.% Fe and 60 % O. Fe_3O_4 should return 42.9 at.% Cr and 57.1 at.% O – a marginal difference. Spots 6 and 7 on Figure 4.31 reported 68.4 and 67.1 at.% O, respectively. This is far above the value expected for Fe_2O_3, and does not correspond to any expected oxide growth on 347HFG. EDX could therefore not be used to accurately determine the phases present within the outer oxide.

Comparing the EDX results from oxidation in air and oxidation in deoxygenated steam yields an interesting observation. The oxygen concentrations in the outer oxide layer following oxidation in air were 68.4, and 67.1 at.% O for 347HFG (Table 4.1), and 65.9, 65.1, and 63.9, at.% O for Super 304H (Table 4.2). In deoxygenated steam the concentrations were 59.4, and 61.8 at.% O for 347HFG (Table 4.8), and 58.3 at.% O for Super 304H (Table 4.9). The lower oxygen concentrations found in the outer oxide after oxidation in deoxygenated steam could suggest magnetite forms in this atmosphere, whereas haematite is preferred in an air atmosphere. Optical microscopy and XRD analysis were used to further investigate the phases present in the outer oxides of 347HFG and Super 304H in both atmospheres and support this theory.

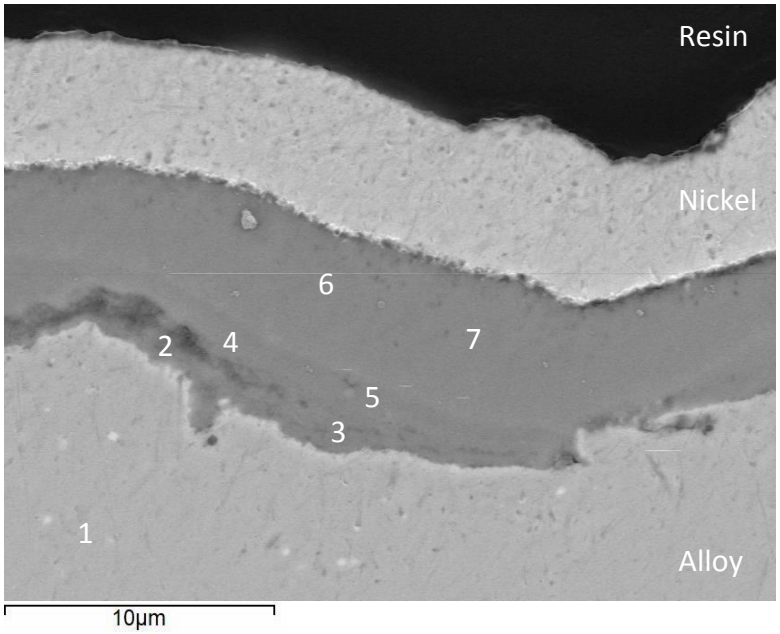

Figure 4.31 – BSE-SEM micrograph of oxide grown on 347HFG in air at 650 °C for 1000 hours. Numbers mark areas of EDX analysis. Spots 2-5 are located on spinel oxide, and 6-7 on the iron rich oxide.

Table 4.1 – Composition in at. % from EDX analysis of oxide grown on 347HFG in air at 650 °C for 1000 hours. The spinel oxide contains iron, chromium, and nickel, along with minor element additions. The outer oxide is iron rich, with trace amounts of other elements.

Spot	Oxygen	Iron	Chromium	Nickel	Manganese	Silicon
1	-	66.7	21.0	10.6	1.5	0.3
2	58.8	13.0	20.8	5.3	0.9	1.1
3	61.1	13.9	17.7	5.2	1.2	0.9
4	64.8	14.3	15.8	4.6	0.5	-
5	64.9	13.4	16.8	4.5	0.5	-
6	68.4	29.8	1.0	0.9	-	-
7	67.1	28.7	2.1	1.5	0.6	-

4.3.2.1.6 Optical Microscopy of 347HFG after Oxidation in Laboratory Air

Optical microscopy was used throughout the study to identify the iron oxide phases magnetite and haematite that could not be differentiated using EDX. Through an optical microscope haematite appears lighter than magnetite. In addition, the spinel layer appears slightly darker than magnetite. Visual analysis was performed on many optical micrographs during the project from samples oxidised in air, deoxygenated steam, and air saturated steam. The outer oxide on samples oxidised in air saturated steam (and a small number oxidised in deoxygenated steam) often consisted of two phases – haematite and magnetite. It was apparent from optical analysis of the scale formed on 347HFG after oxidation in air (Figure 4.32) that the outer iron rich layer consisted of only one phase. From comparison of the contrast between oxides on many other micrographs, findings of other researchers

in the literature, and supported by XRD analysis (Section 4.3.2.1.7), the iron rich outer oxide phase was determined to be haematite.

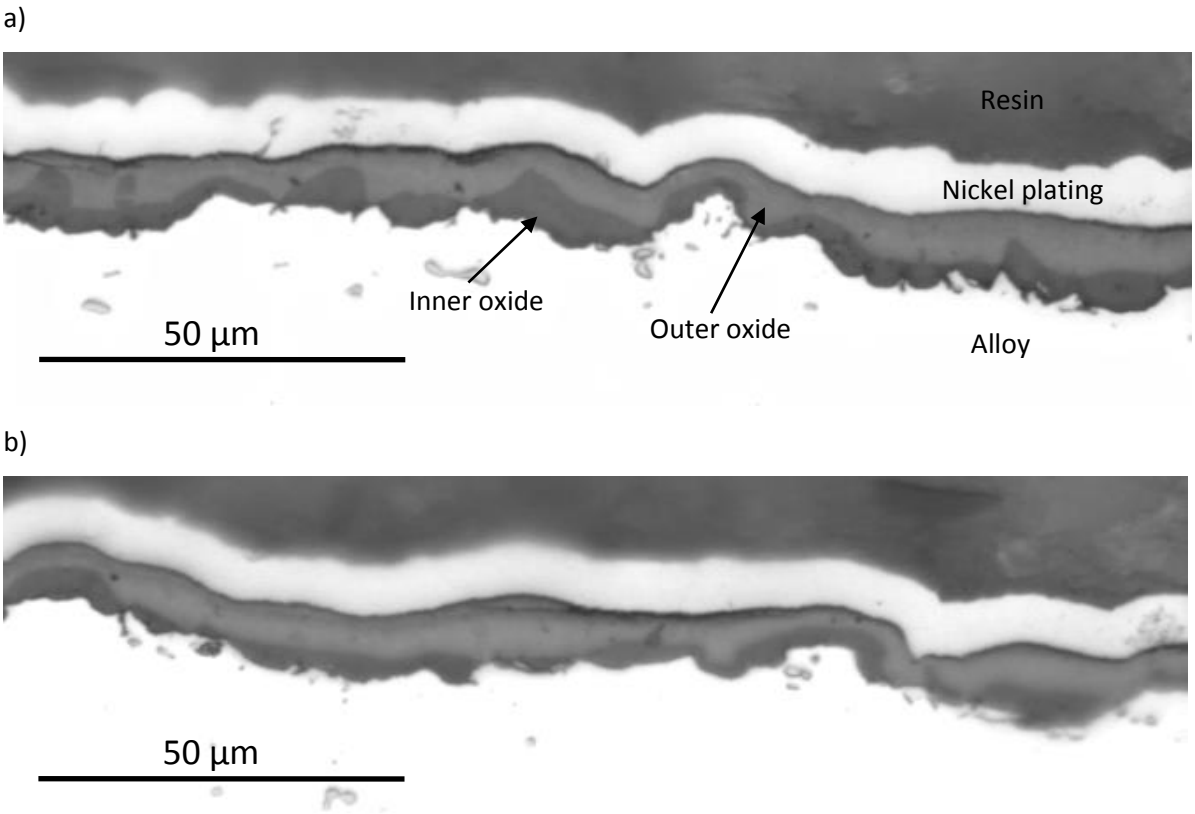

Figure 4.32 – Optical images of the oxide formed on 347HFG after exposure to laboratory air at 650 °C for 500 hours. Inner spinel oxide is covered by an iron oxide of only one phase, suggested to be haematite.

4.3.2.1.7 XRD Analysis of 347HFG after Oxidation in Laboratory Air

XRD analysis was performed on the inner surface of a sample of 347HFG oxidised in air at 650 °C for 100 hours, as presented in Figure 4.33. The aim of XRD analysis was to determine whether the outer oxide grown on 347HFG in air was magnetite or haematite. X'Pert Highscore software was used to correlate the peak trace to known peak lists. Peak lists for haematite (blue, second from bottom) and magnetite (red, bottom) are included in the figure for reference. XRD analysis was also performed on the inner surface of an un-oxidised, as-received sample of 347HFG, such that peaks in the oxidised sample that corresponded to the underlying alloy could be identified. The trace for as-received 347HFG is included in the figure in yellow (second from top).

X'Pert Highscore software calculated a strong correlation to haematite. There were also significant peaks that corresponded to the underlying alloy. Unfortunately, the strongest magnetite reference peaks overlap either haematite or the alloy making it difficult to determine whether magnetite phase was present. The magnetite peaks may also be attributed to the underlying spinel as Fe_3O_4 and $FeCr_2O_4$ form a complete solid solution. The peak trace can be compared to that of spalled oxide from a sample

of 347HFG oxidised in steam at 650 °C for 100 hours in Figure 4.117. The spalled oxide contained a large fraction of magnetite, and the magnetite peaks are considerably stronger in relation to haematite peaks in that figure. In conclusion, as the outer oxide on 347HFG oxidised in air was formed of only one phase, this is suggested to be haematite. This finding is in agreement with that of other researchers for the outer oxide layer grown on 347HFG in air [80].

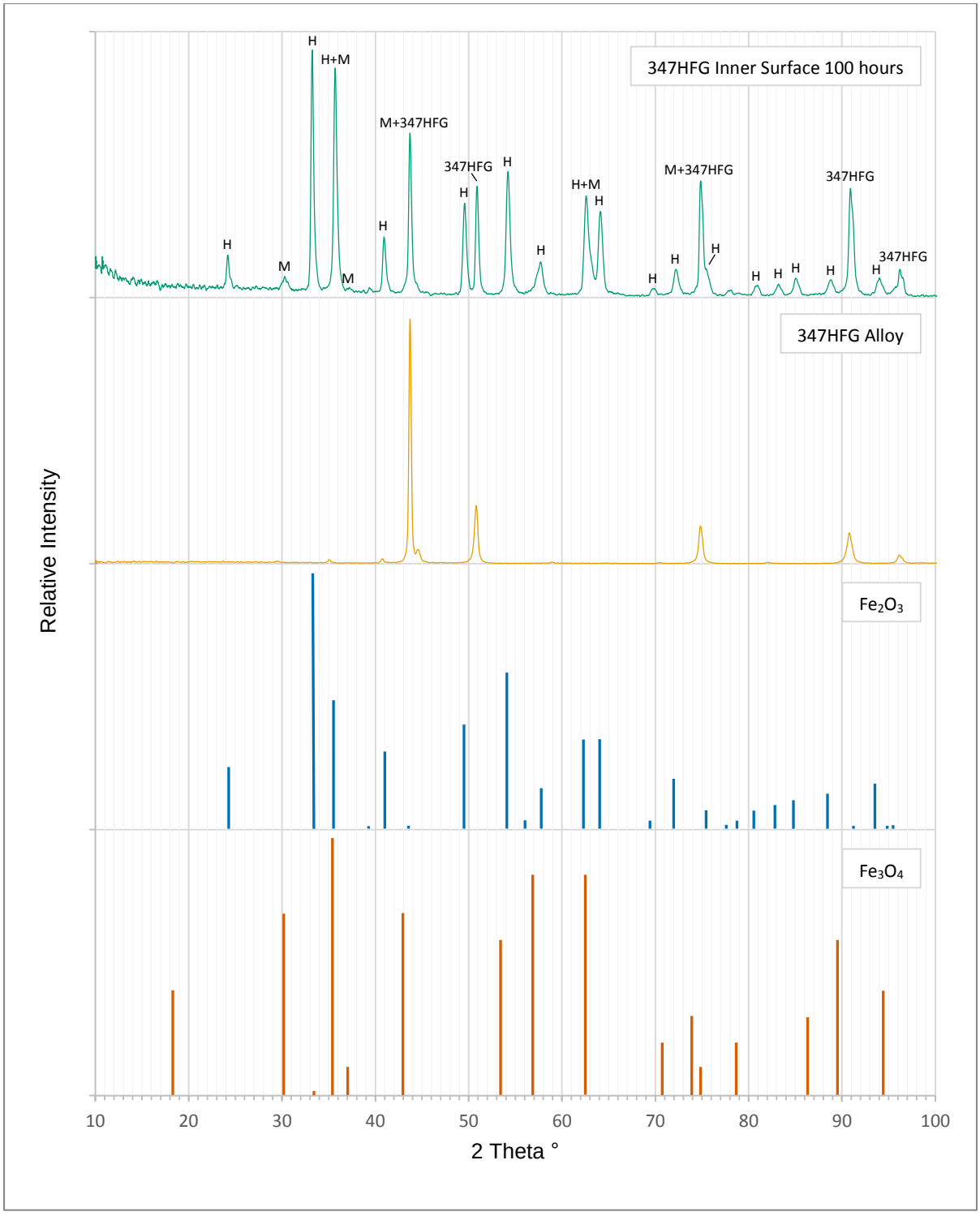

Figure 4.33 – XRD analysis of the inner surface of 347HFG oxidised in laboratory air at 650 °C for 100 hours (top), and the inner surface of a sample of unoxidised as-received 347HFG alloy (second from top). The measured peaks of the oxide are compared with reference peaks for haematite (third from top) and magnetite (bottom), and show a stronger correlation to haematite over magnetite.

4.3.2.2 Super 304H

4.3.2.2.1 Visual Observations of Super 304H after Oxidation in Laboratory Air

Super 304H samples oxidised in air were matt grey in appearance. The axial surface defects were visible on all samples, i.e. they were not fully engulfed in oxide. No observable spallation was apparent on any sample. Optical images of the sample surfaces are shown in Figure 4.34 and Figure 4.35.

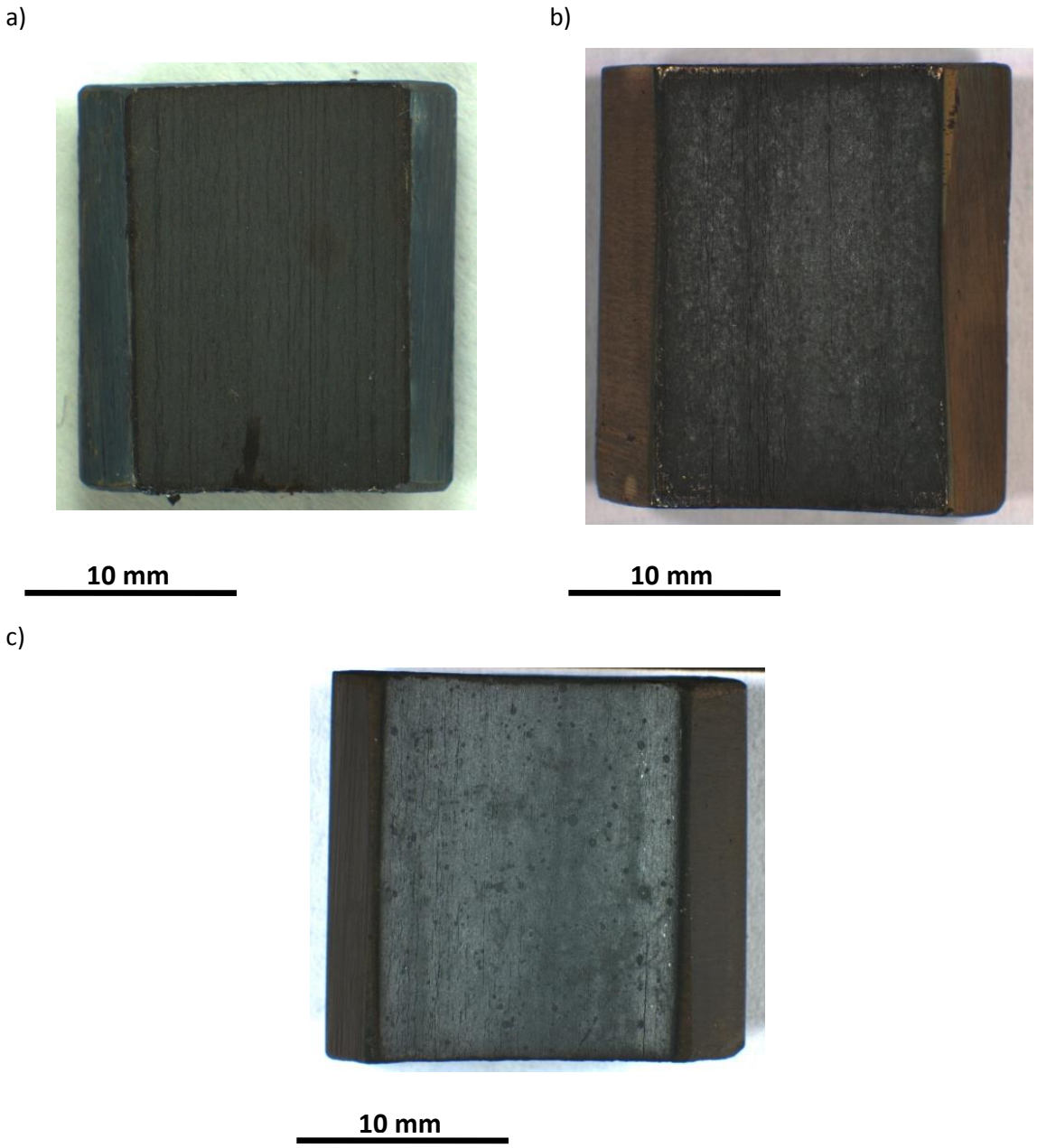

Figure 4.34 – Macro images of air oxidised Super 304H inner surface after 100 hours at a) 600 °C, b) 650 °C, c) 700 °C. The inner surface was often dull grey in appearance. There was no evidence of spallation from any sample.

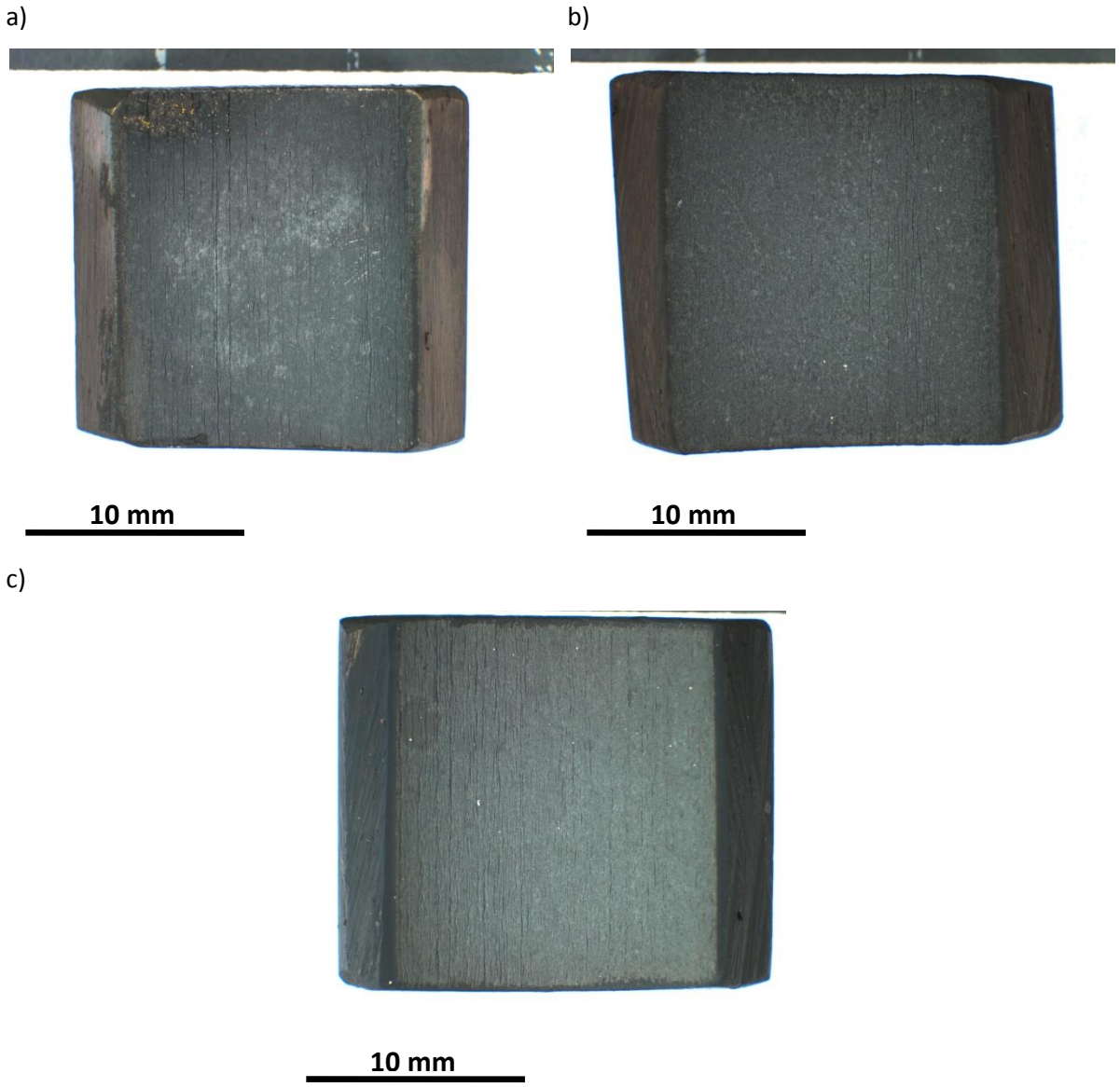

Figure 4.35 – Macro images of air oxidised Super 304H inner surface after 1000 hours at a) 600 °C, b) 650 °C, c) 700 °C. Inner surfaces were dull grey in appearance with no evidence of spallation.

4.3.2.2.2 SEM Surface Analysis of Super 304H after Oxidation in Laboratory Air

The outer scale of Super 304H had a level of porosity similar to that found on 347HFG. The magnitude of porosity tended to be constant within a nodule, but vary between not at all porous and highly porous between oxide nodules. Whiskers and platelets were not found on Super 304H in air as shown in Figure 4.36, Figure 4.37 and Figure 4.38

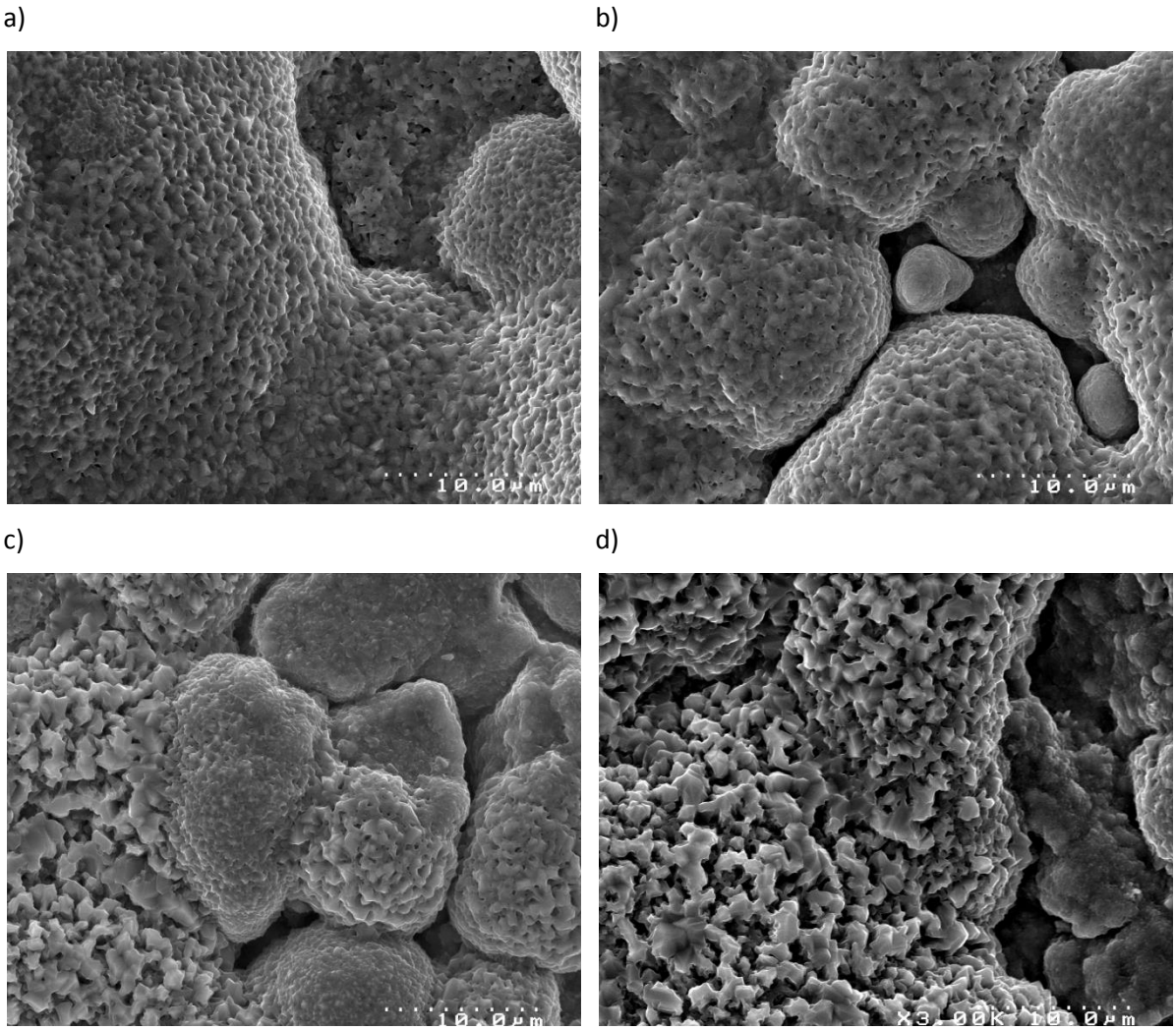

Figure 4.36 – SEI SEM images of Super 304H inner surface topography after oxidation in air at 600 °C after a) 250 hours, b) 1000 hours, c) 2000 hours, d) 3000 hours. Porous and non-porous oxides were identified at all durations.

a) b)

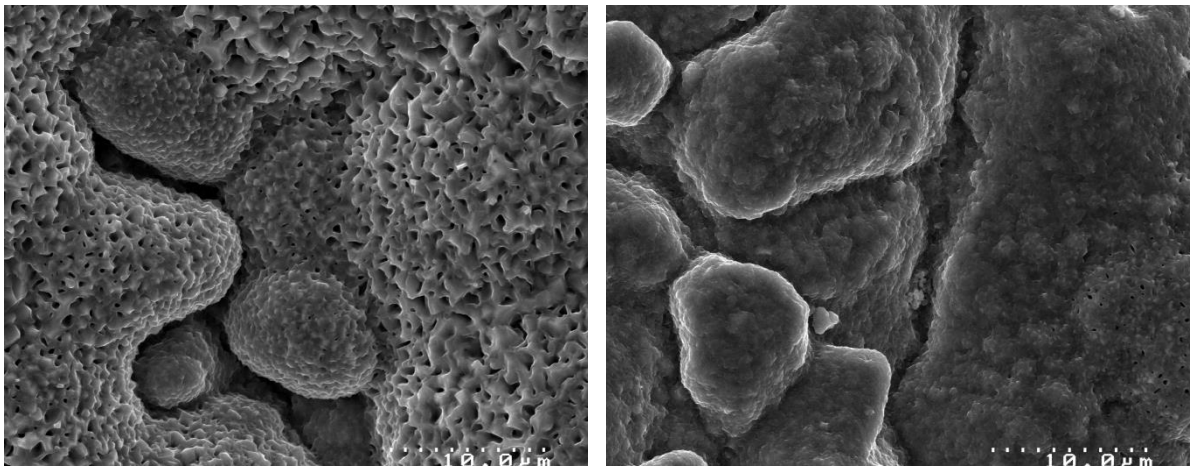

Figure 4.37 – SEI SEM images of Super 304H inner surface topography after oxidation in air at 650 °C after a), b) 2000 hours.

a) b)

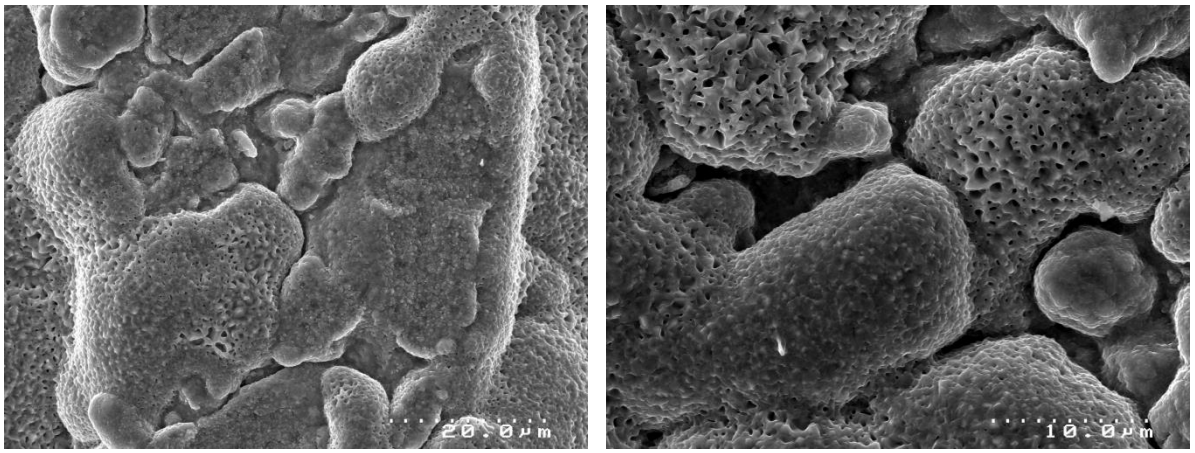

c) d)

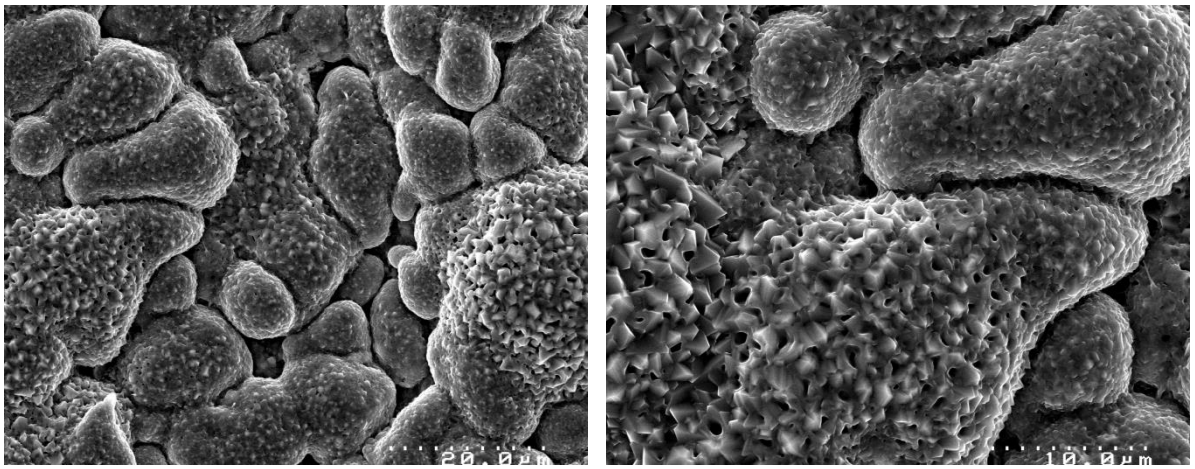

Figure 4.38 – SEI SEM images of Super 304H inner surface topography after oxidation in air at 700 °C after a), b) 250 hours, c), d) 2000 hours.

4.3.2.2.3 Oxide Cross-Sectional Morphology of Super 304H as a Function of Time and Temperature after Oxidation in Laboratory Air

The morphology of the oxide grown on Super 304H in air initially consisted of an array of oxide nodules that developed into a continuous duplex scale as oxidation time increased. The time it took to form a continuous scale decreased with increasing temperature. At 600 °C a continuous layer formed after 1000 hours (Figure 4.39). At 650 and 700 °C a continuous layer was formed after 500 hours (Figure 4.40 and Figure 4.41).

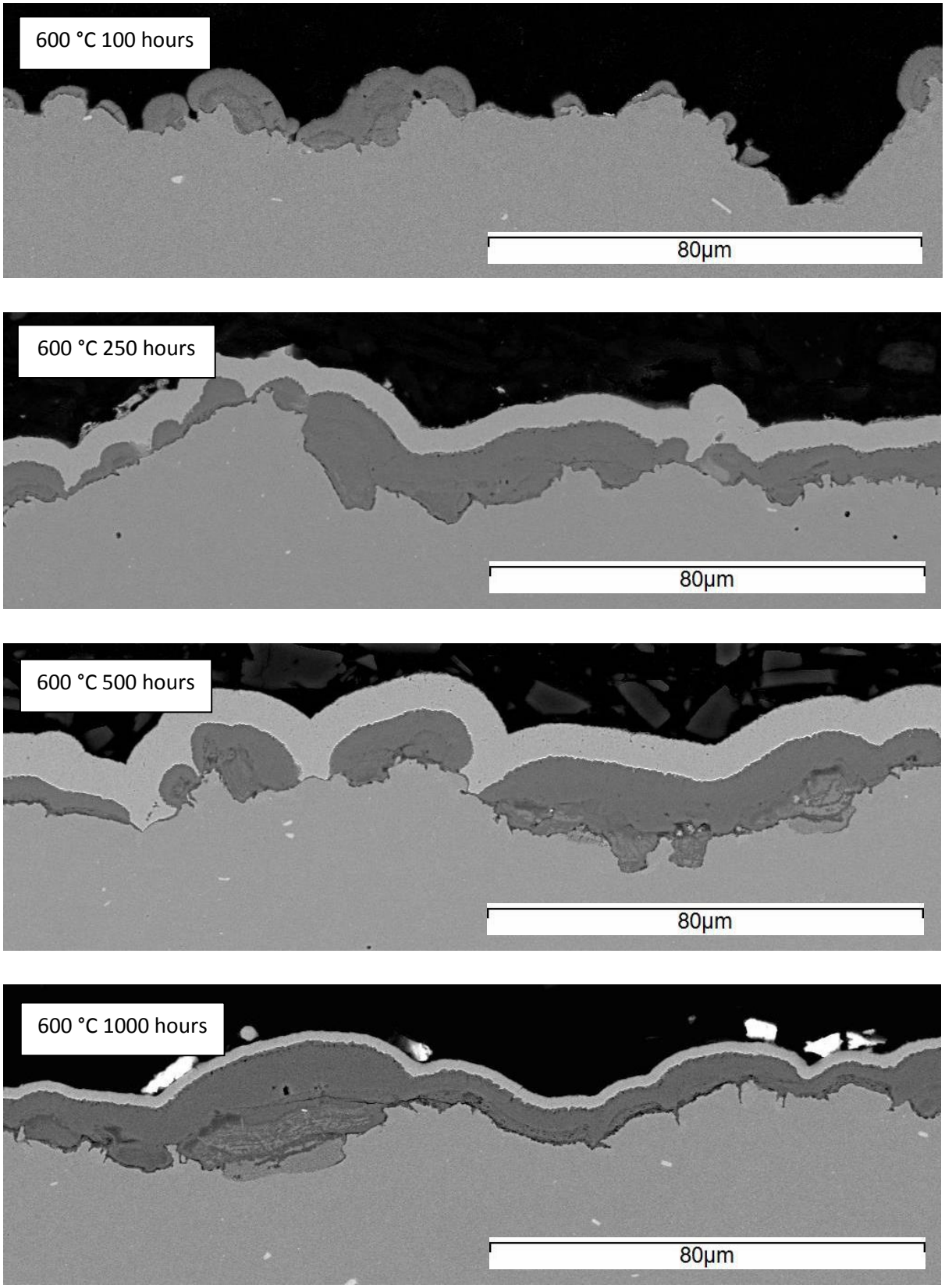

Figure 4.39 – BSE SEM micrographs of oxide formed on Super 304H oxidised in air at 600 °C showing nodular oxide growth evolving into complete duplex oxide coverage after longer periods.

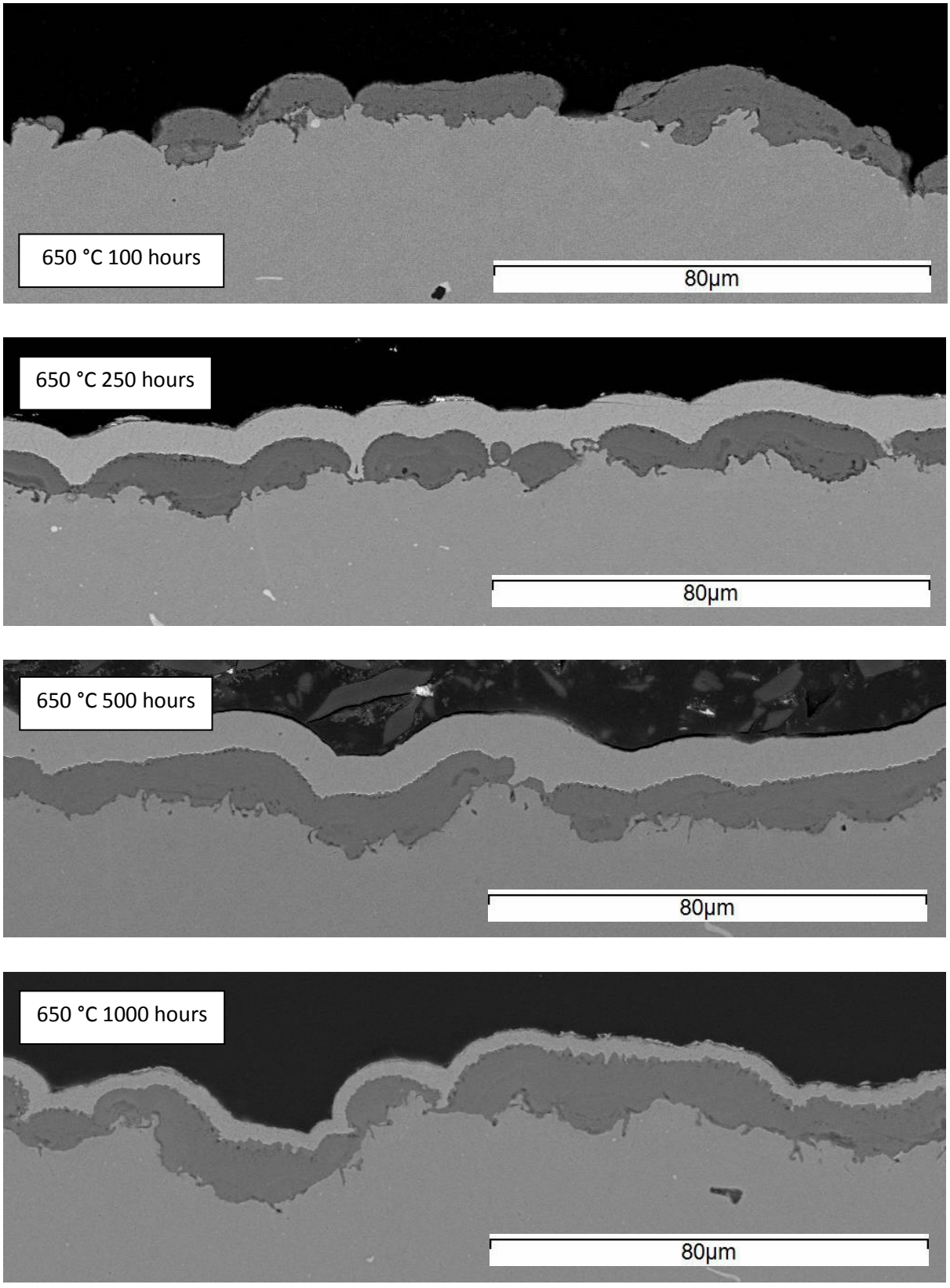

Figure 4.40 – BSE SEM micrographs of oxide formed on Super 304H oxidised in air at 650 °C. Complete duplex oxide coverage was observed after 500 hours.

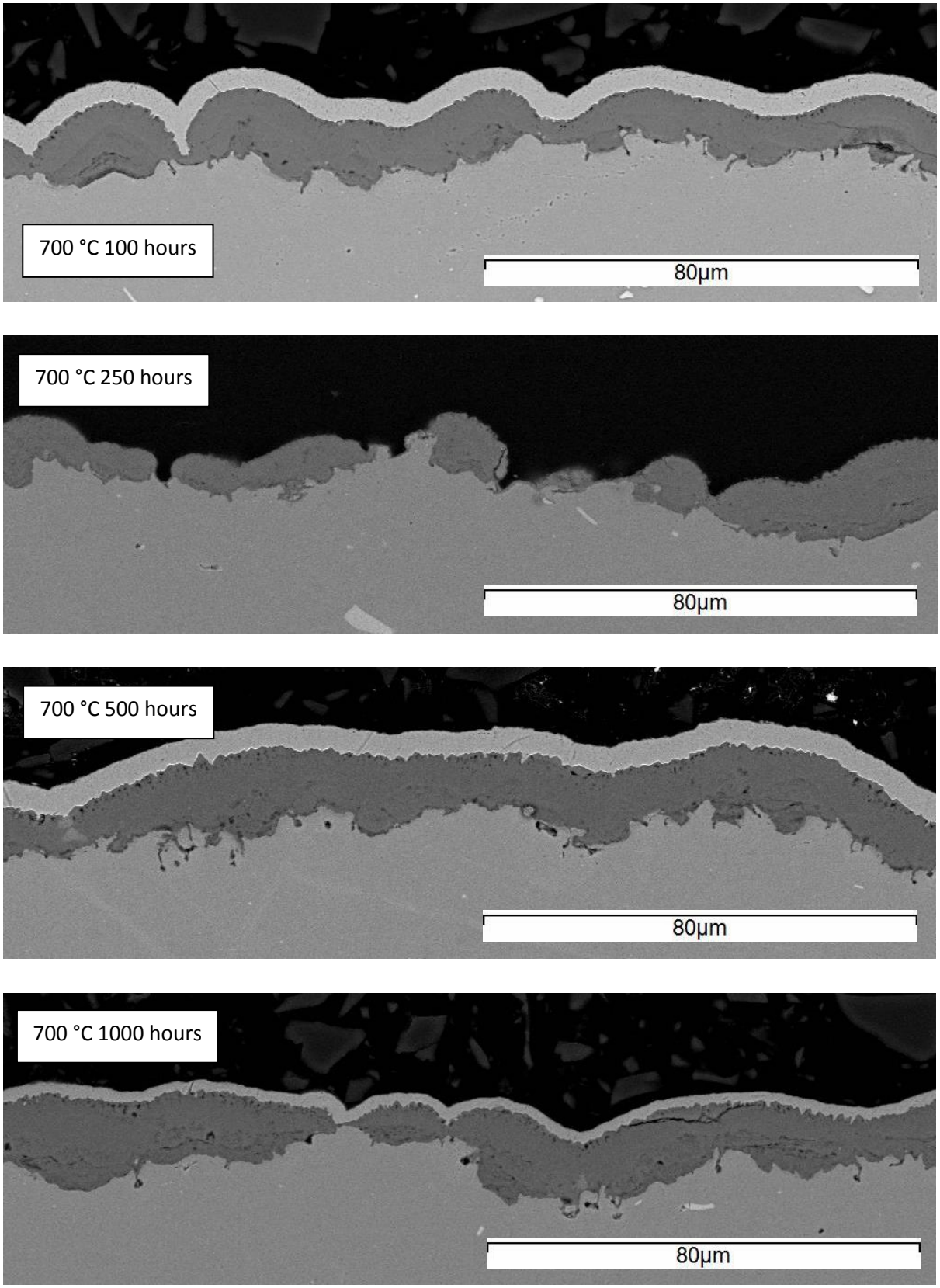

Figure 4.41 – BSE SEM micrographs of oxide formed on Super 304H oxidised in air at 700 °C showing almost complete duplex oxide coverage after only 100 hours oxidation.

4.3.2.2.4 Oxide Area Maps of Super 304H after Oxidation in Laboratory Air

Area EDX maps of S304H oxidised in air are shown in Figure 4.42 and Figure 4.43. There were areas of chromium depletion in the alloy beneath the spinel at 650 °C and 700 °C. Increasing oxidation time increased the depth of depletion and the concentration gradient. Chromium depleted areas were primarily found where grain boundaries met the alloy surface. In areas of chromium depletion manganese was also found to be depleted and an enrichment of nickel was found.

Copper, probably in metallic form, was often found in small concentrations within the spinel layer. At 700 °C the element was found in higher concentrations towards the top of the spinel, and was even detected in the Fe-rich outer layer at the oxide/gas interface. Kim et al. [84] suggested the most likely mechanism to explain the outer oxide enrichment is for bulk diffusion of copper through haematite grains. This is thought to occur as a result of the Gibbs free energy reduction of copper spinel solid solution formation in hematite at high oxygen partial pressure. This is a reasonable hypothesis given the similar standard Gibbs free energy of formation above 600 °C.

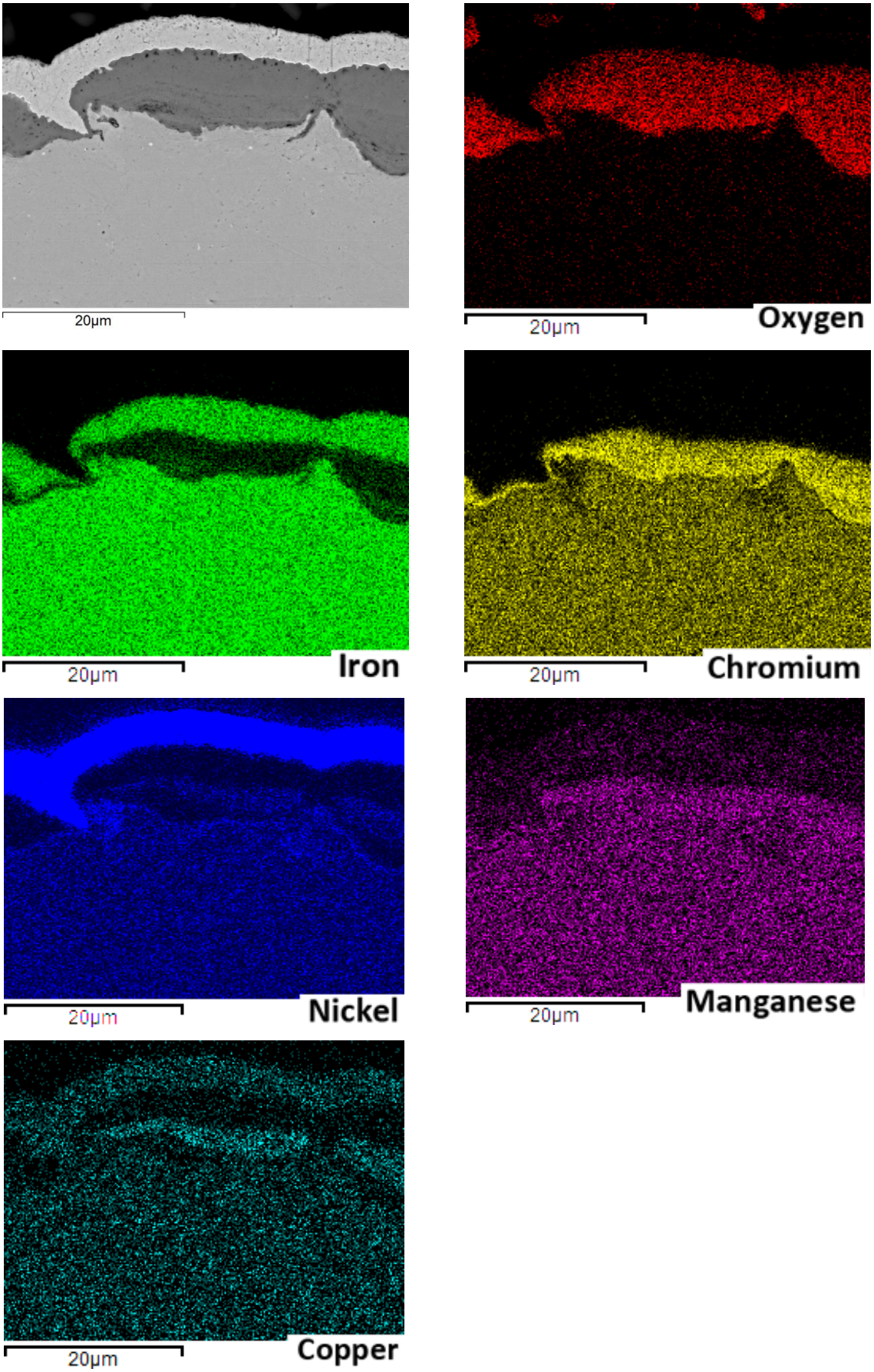

Figure 4.42 – EDX element area map for a cross-section of Super 304H oxidised in air after 100 hours at 700 °C. Sample has been nickel plated. In addition to iron, chromium, nickel and manganese, the spinel oxide also contained copper.

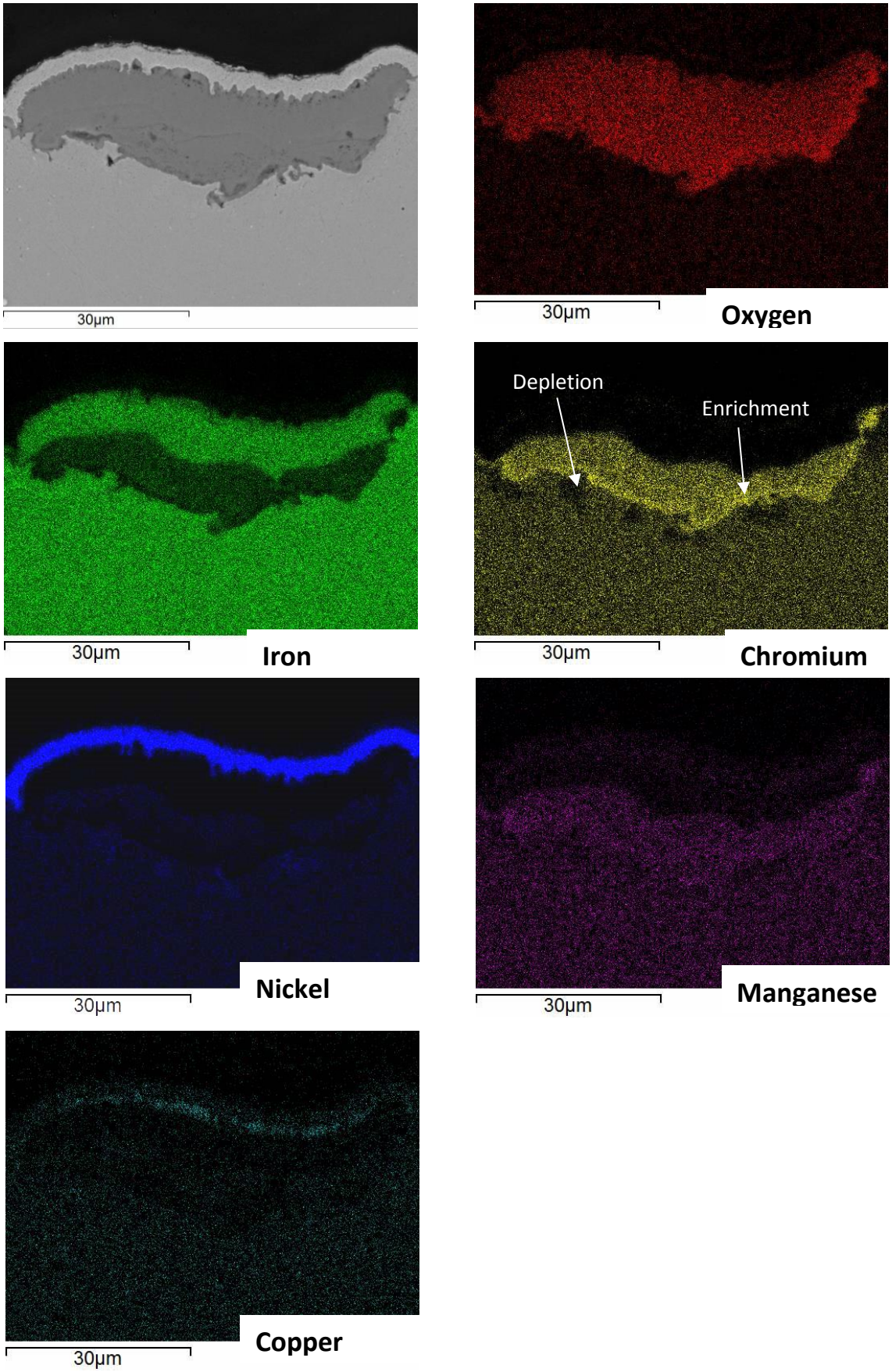

Figure 4.43 – EDX element area map for a cross-section of Super 304H oxidised in air after 1000 hours at 650 °C. Sample has been nickel plated. The outer oxide appears to consist almost exclusively of iron, whereas the spinel contains concentrations of each element. Copper appears to have accumulated within the iron rich layer at the scale/gas interface.

4.3.2.2.5 EDX Analysis of Super 304H after Oxidation in Laboratory Air

Quantitative analysis of the oxide grown on Super 304H after oxidation at 650 °C for 1000 hours. Figure 4.44 shows a similar duplex morphology to that found on 347HFG, although Super 304H retained a nodular composition for longer than 347HFG. A Cr-rich protective oxide had not formed at the internal oxidation front. However, the two nodules in the figure are separated by a small area of thin oxide.

EDX spots 1 and 4 have the highest concentration of chromium, although, interestingly, copper was detected at 3.0 at. % in the oxide at spot 1. As with 347HFG, EDX analysis at spot 1 is suggested to be influenced by the alloy and bulk inner oxide, and the true concentrations of chromium and manganese are expected to be higher. The oxides at spots 1 and 4 are suggested to be mixed spinels of Fe-Cr-Ni, or Fe-Cr spinel in a metallic matrix of nickel. Table 4.2 shows the quantification from the EDX spots shown in Figure 4.44.

Spots 2, 3, and 5 correspond to outer Fe-rich oxide. As with 347HFG, EDX is unable to determine the phase of the outer oxide. However, it is likely to the same as 347HFG – Fe_2O_3. Spots 1 and 4 show a lower oxygen content than spots 2, 3, and 5. This could be an indication that the nickel in the inner oxide at these locations is in metallic form, or it could indicate that the inner oxide is a spinel of the form M_3O_4, while the outer oxide is of the form M_2O_3.

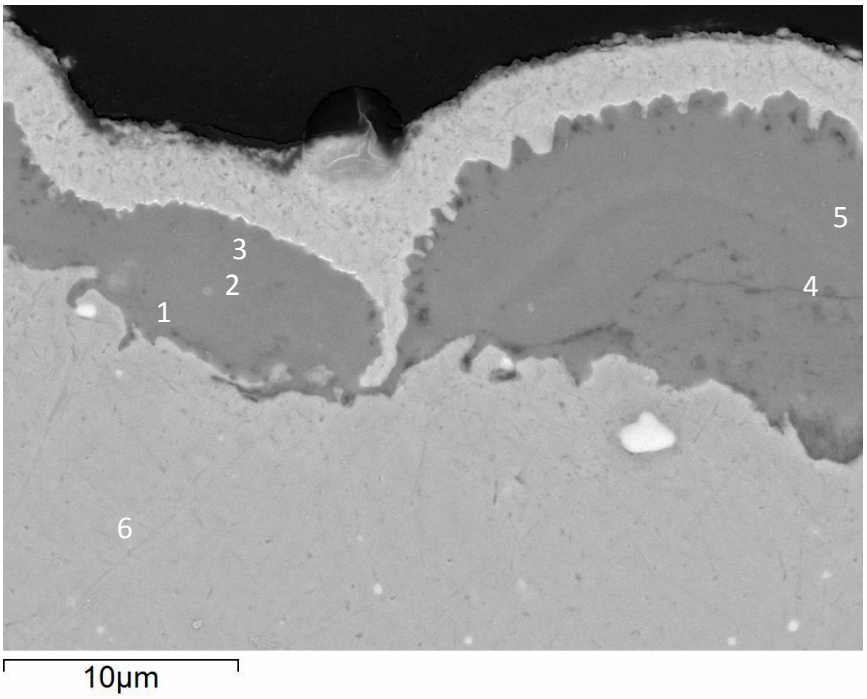

Figure 4.44 – BSE-SEM micrograph of oxide grown on Super 304H in air at 650 °C for 1000 hours. Numbers mark areas of EDX analysis.

Table 4.2 – Composition in at. % from EDX analysis of oxide grown on Super 304H in air at 650 °C for 1000 hours. The outer iron rich layer contains small amounts of minor element additions. The inner spinel oxide contains iron, chromium and nickel, along with manganese and copper.

Spot	Oxygen	Iron	Chromium	Nickel	Manganese	Copper
1	59.1	14.5	17.5	5.3	0.7	3.0
2	65.1	30.5	1.3	1.8	0.2	1.2
3	65.9	31.1	0.6	1.5	0.5	0.4
4	59.6	14.0	21.1	4.2	0.3	0.9
5	63.9	32.7	1.7	1.0	0.3	0.4
6	-	68.0	20.7	8.1	1.0	2.3

4.3.2.2.6 Optical Microscopy of Super 304H after Oxidation in Laboratory Air

Figure 4.45 and Figure 4.46 are optical micrographs of the oxide grown on Super 304H in air after 250 and 500 hours at 650 °C, respectively. On inspection of the exposed grain structure in the alloys it was found that oxide nodules tended to grow on bulk alloy grains, and where grain boundaries reached the surface, only a thin oxide film was visible. Oxide nodules were duplex in morphology and as oxidation time and temperature increased, the outer oxide of each nodule joined eventually forming a thick, continuous oxide layer. As oxidation time and temperature further increased the inner spinel oxide also formed a continuous layer, as with 347HFG. In comparison with the scale grown in steam, the outer oxide exhibited only one phase, suggested to be haematite.

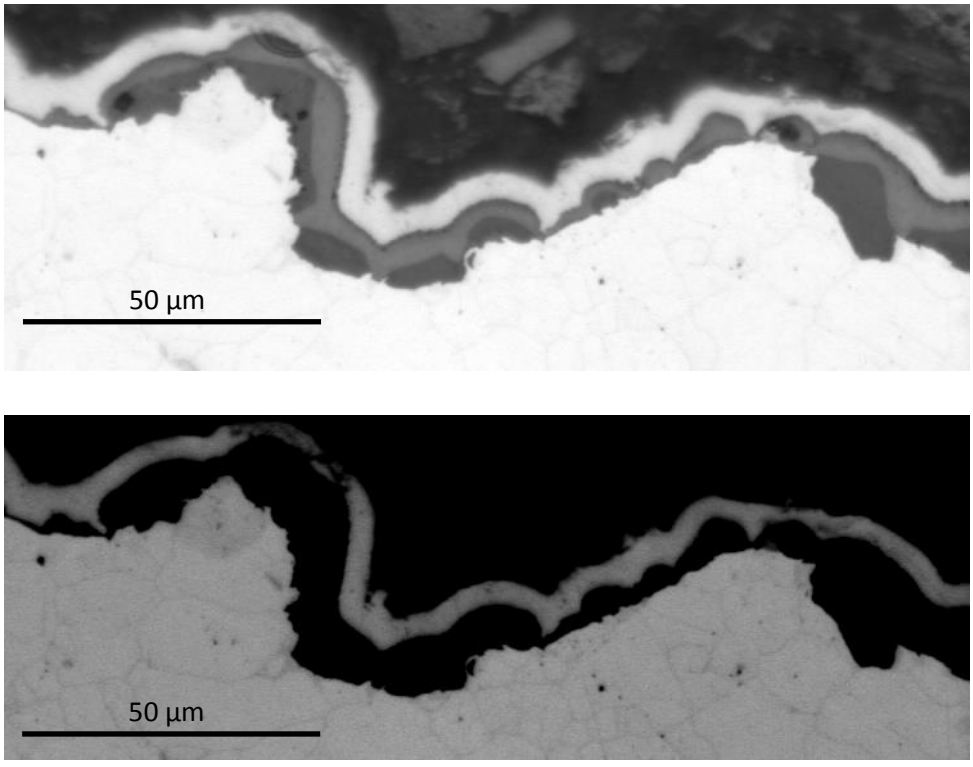

Figure 4.45 – Optical micrograph of grain boundary location at surface, corresponding to nodule location. Super 304H after oxidation in air for 250 hours at 600 °C. Spinel nodules often grew from the centre of austenite grains.

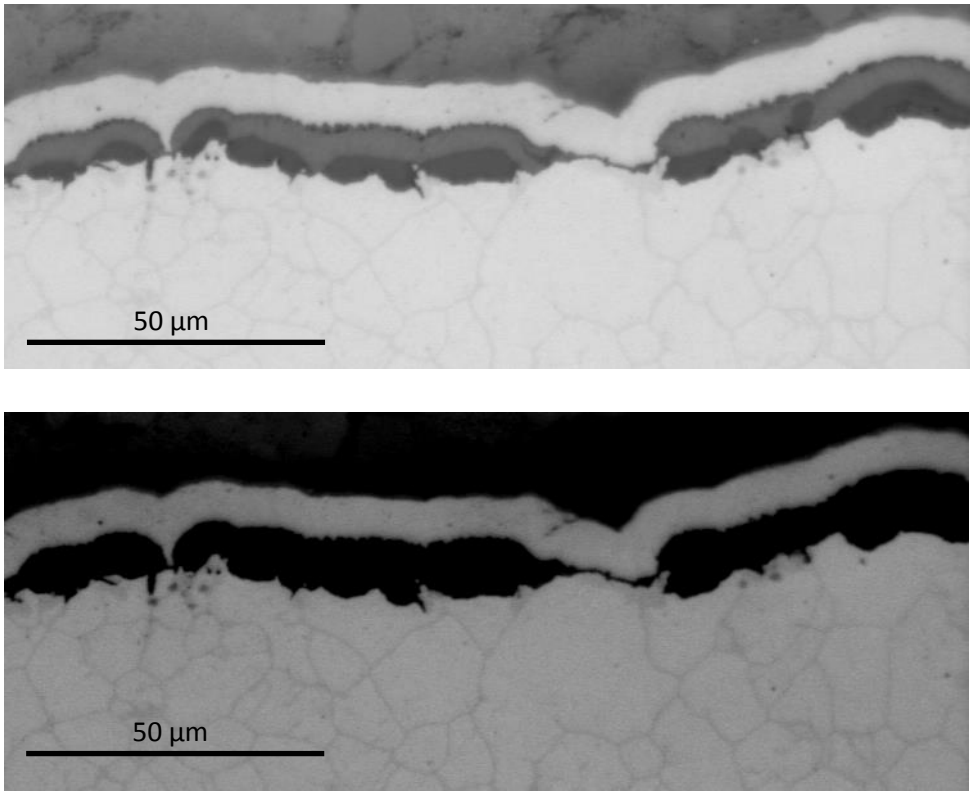

Figure 4.46 – Optical micrograph of grain boundary location at surface, corresponding to nodule location. Super 304H after oxidation in air for 500 hours at 650 °C. Spinel nodules often grew from the centre of austenite grains.

4.3.2.3 Shot Peened Super 304H

4.3.2.3.1 Visual Observations of Shot Peened Super 304H after Oxidation in Laboratory Air

The inner surface of S304HSP appeared shiny at 600 °C up to 3000 hours and 650 °C up to 500 hours. After longer durations at 650 °C and all durations at 700 °C the surface appeared a darker matt grey. These are shown in Figure 4.47 and Figure 4.48.

4.3.2.3.2 SEM Surface Analysis of Shot Peened Super 304H after Oxidation in Laboratory Air

The topography of S304HSP oxidised in air as imaged with an SEM featured a variety of oxide formations that appeared to be determined by the peening process in any given area. In relatively flat areas a non-porous base oxide provided a foundation for crystallites scattered over the surface. The majority of crystallites, believed to be chromium rich, were under 1 micron in length but were occasionally larger and increased in size and number as oxidation time and temperature increased.

On the macro scale, where long surface defects, similar to those found on pickled Super 304H, had not been fully exposed to shot peening, substantial oxide growth occurred from which an abundance

of platelets grew. Thicker oxide and platelets were also found in areas of substrate deformation caused by uneven shot peening. Micrographs of the surface morphology are shown in Figure 4.49, Figure 4.50 and Figure 4.51.

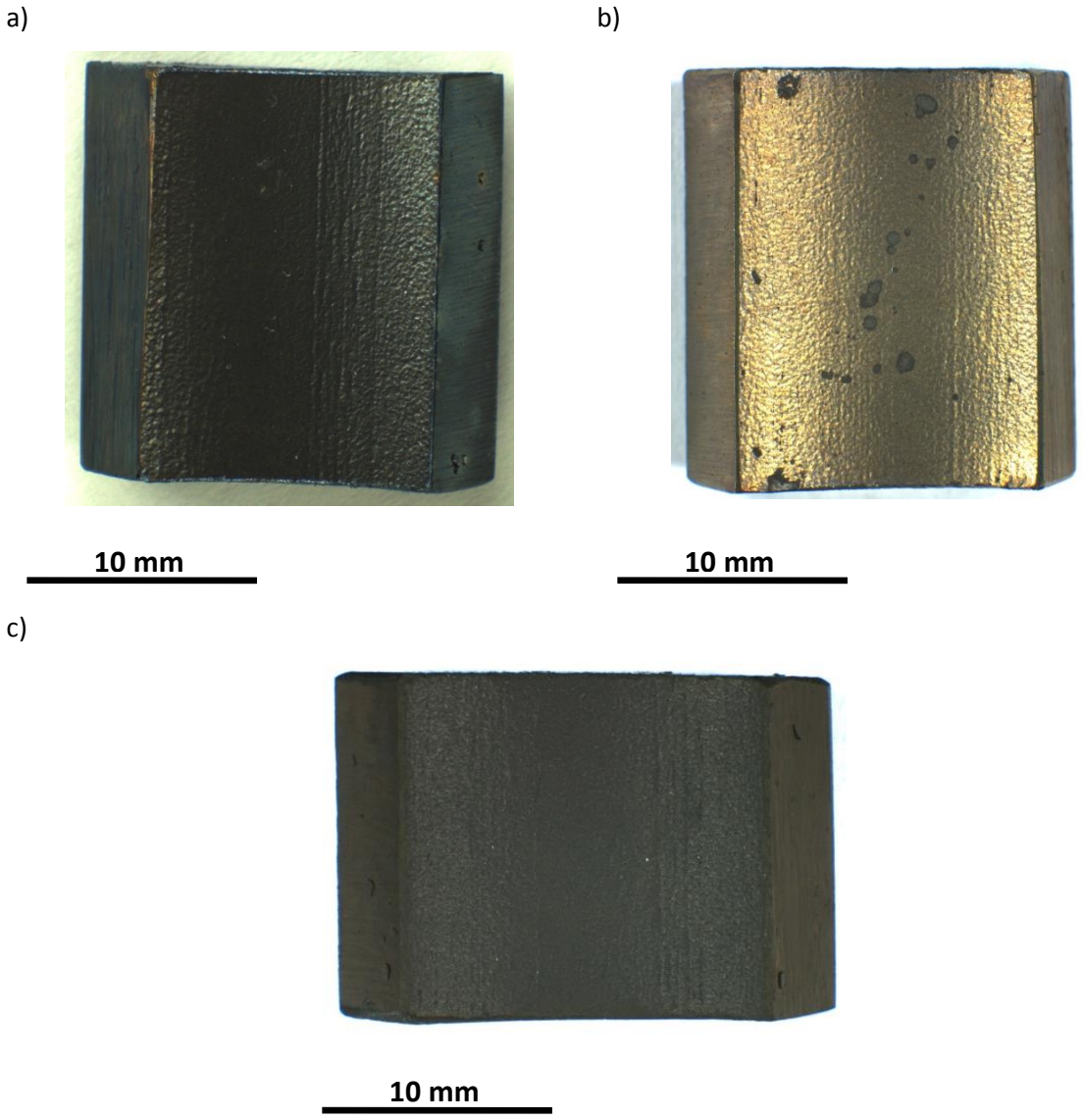

Figure 4.47 – Macro images of air oxidised shot peened Super 304H inner surface after 100 hours at a) 600 °C, b) 650 °C, c) 700 °C. At 600 and 650 °C the inner surface was slightly shiny, compared to a matt appearance at 700 °C.

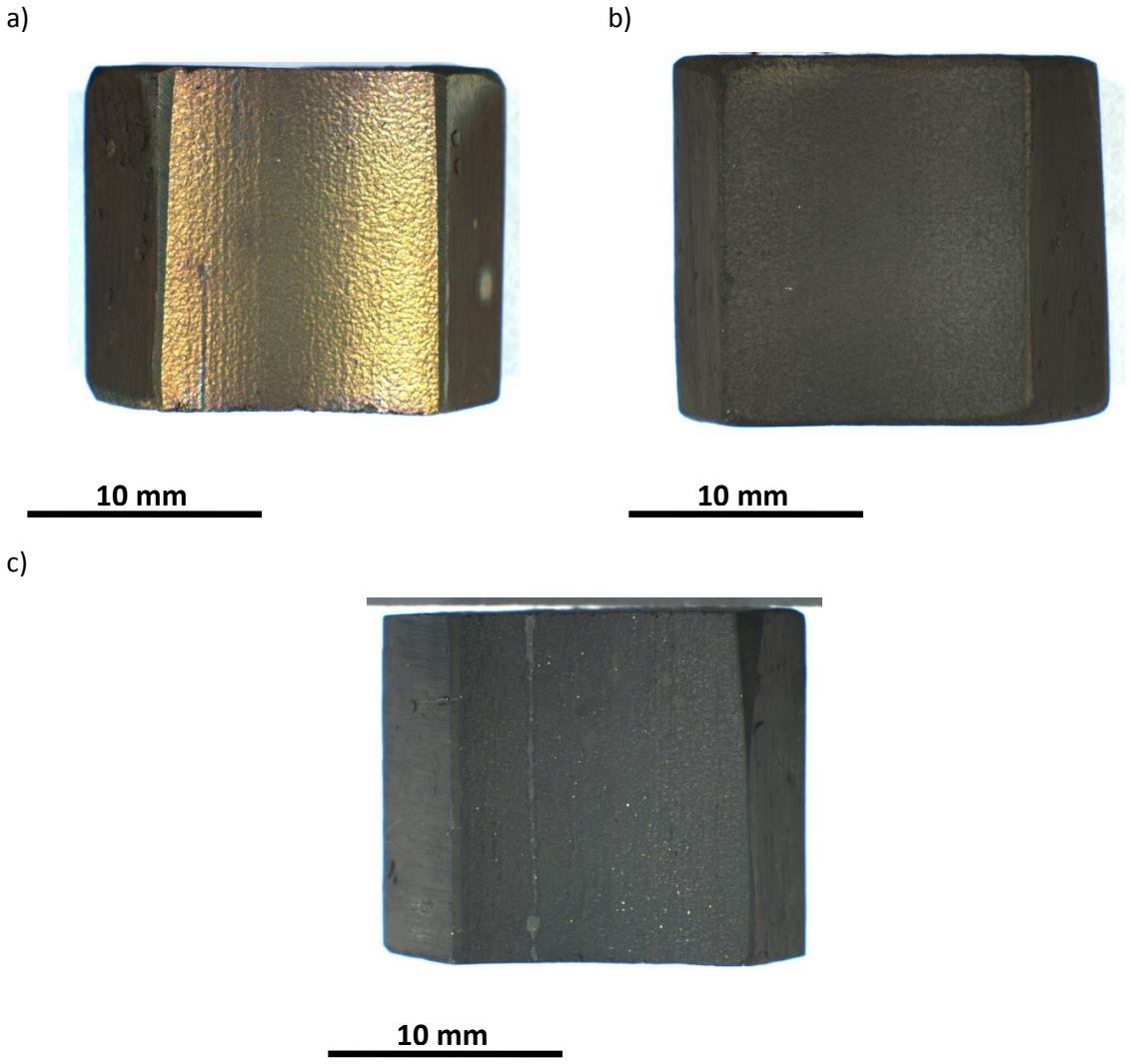

Figure 4.48 – Macro images of air oxidised shot peened Super 304H inner surface after 1000 hours at a) 600 °C, b) 650 °C, c) 700 °C. After 1000 hours the inner surface at 600 °C remained shiny compared to the dark matt appearance at 650 and 700 °C.

a)

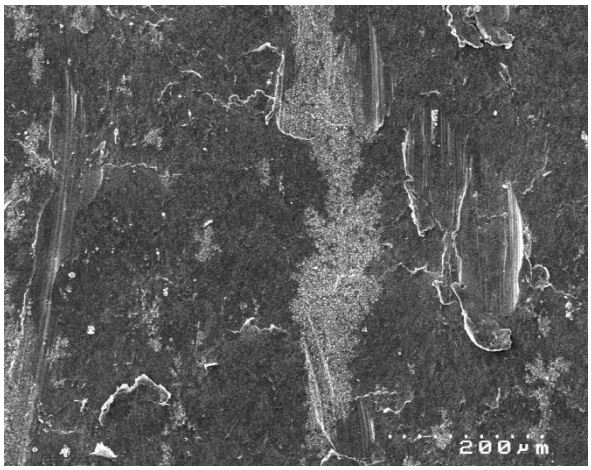

b)

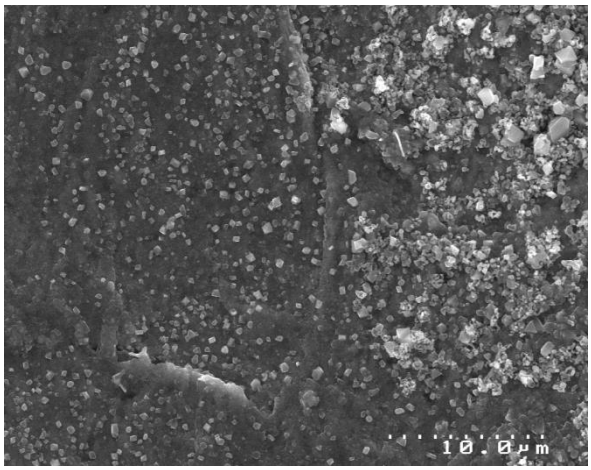

c)

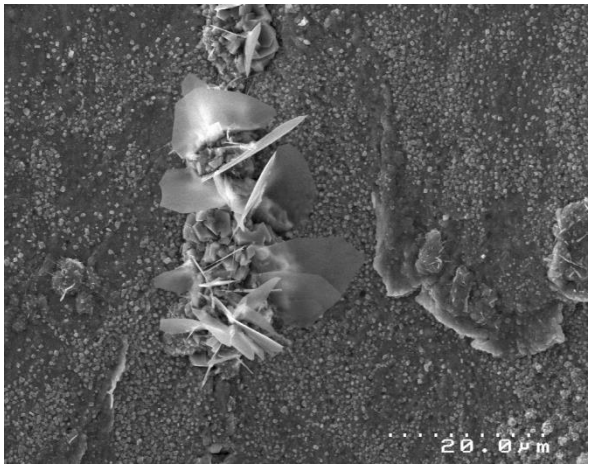

d)

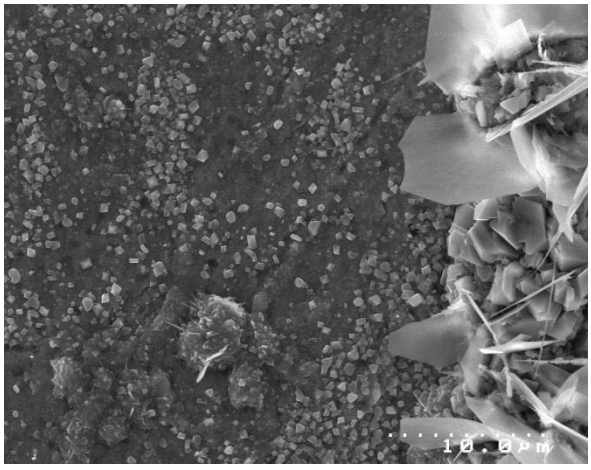

e)

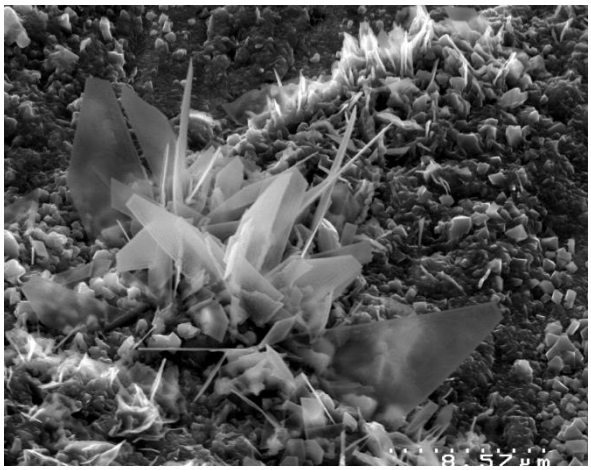

f)

g) h)

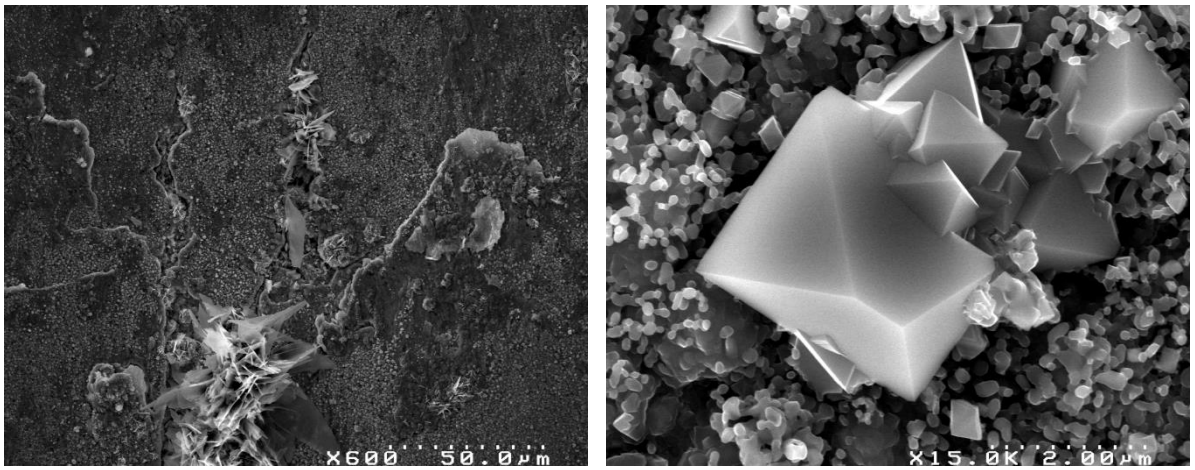

Figure 4.49 – SEI SEM images of shot peened Super 304H inner surface topography after oxidation in air at 600 °C after a), b) 250 hours, c), d) 1000 hours, e), f) 2000 hours, g), h) 3000 hours. Areas in c), d), e) and h) are of interesting features and are not representative of the bulk oxide, which is generally free from platelets large oxide clusters. In f), the peening treatment is considered to have formed the lifted section.

a) b)

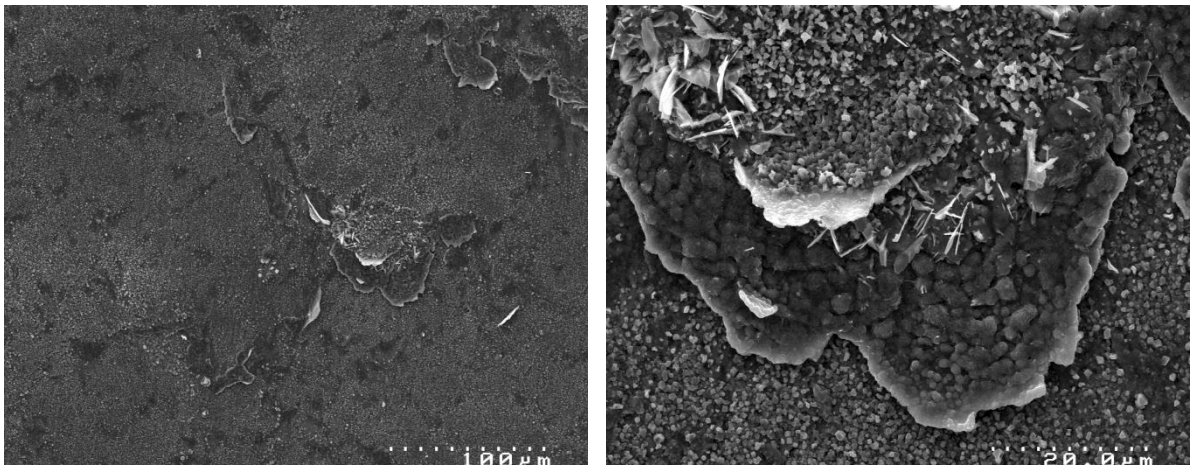

Figure 4.50 – SEI SEM images of shot peened Super 304H inner surface topography after oxidation in air at 650 °C after a), b) 2000 hours. The bulk oxide was scattered with small oxide crystallites and areas deformed during the shot peening process as in b).

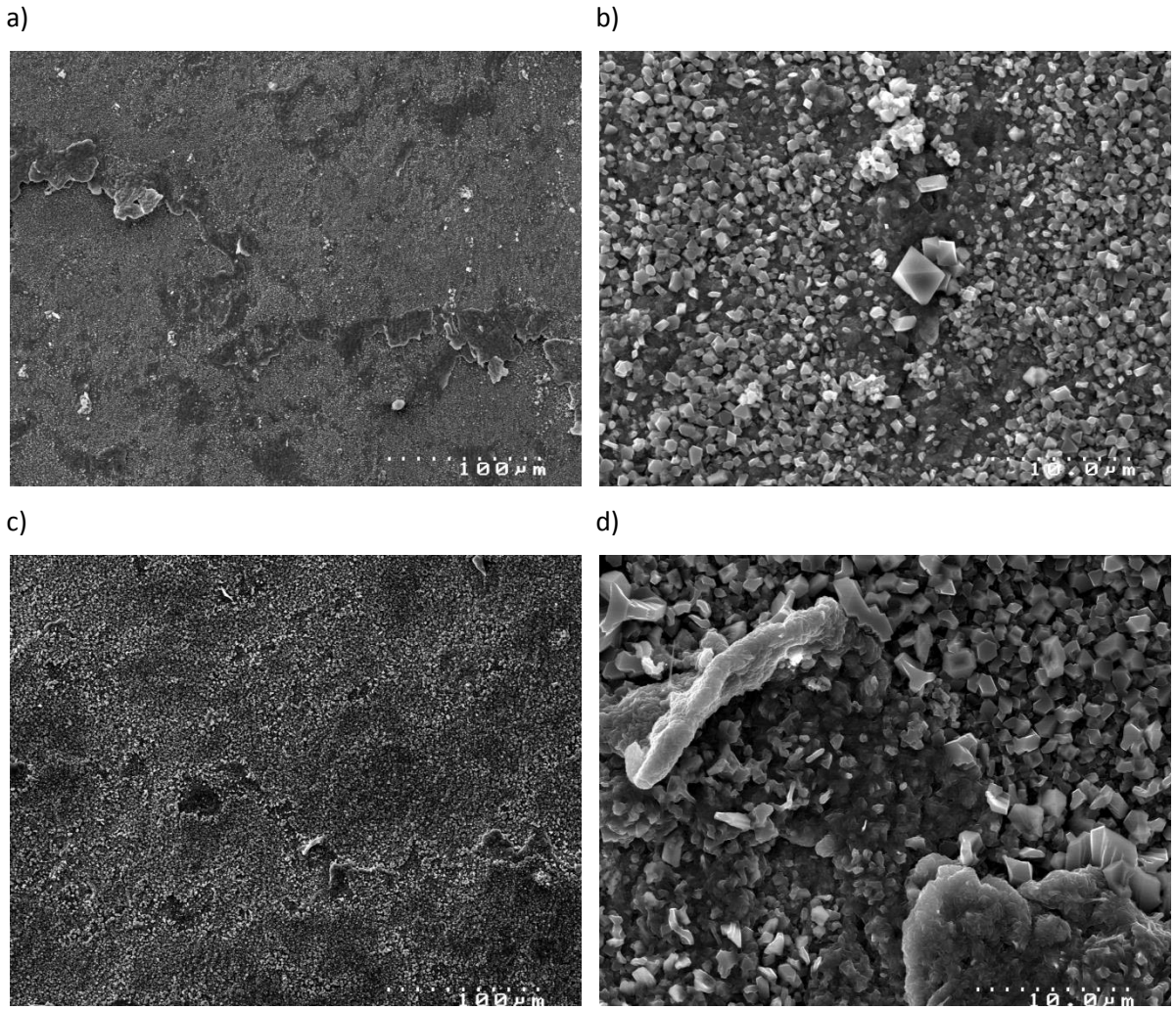

Figure 4.51 – SEI SEM images of shot peened Super 304H inner surface topography after oxidation in air at 700 °C after a), b) 250 hours, c), d) 2000 hours. At the higher temperature, the inner surface appeared more densely covered by crystallites.

4.3.2.3.3 EDX Analysis of Shot Peened Super 304H after Oxidation in Laboratory Air

Quantitative analysis was performed on the topography of Super 304H SP oxidised in air for 2000 hours at 650 °C. In Figure 4.52, spots 1-3 correspond to areas that covered the majority of the oxide surface. The compositions as listed in Table 4.3 indicate high concentrations of iron and chromium in these regions and higher than bulk concentrations of manganese. Due to the thin nature of the oxide, it is expected that quantitative information from the alloy bulk interfered with that from the oxide and the actual iron content of the scale is lower than recorded.

The central feature in Figure 4.52 is not representative of the bulk surface and probably arose from a breakdown in the protective oxide. Spots 4-6 on the figure indicate that the nodule is iron rich with concentrations of chromium present, probably towards the base of the nodule. However, no other alloying elements were detected characteristic of the spinel oxides formed on the pickled variant of Super 304H. The nodule is likely to have the form of the variable $(Fe_{1-x}Cr_x)_2O_3$ corundum-type oxide

where Cr decreases in concentration from the alloy/oxide interface to the oxide/gas interface. Fe_2O_3 may be present at the surface.

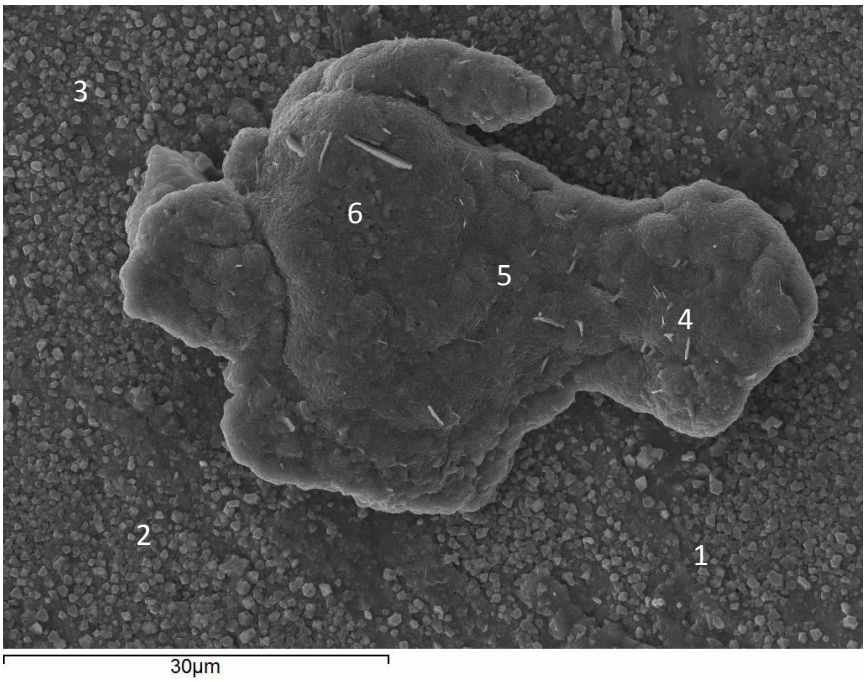

Figure 4.52 - SEM micrograph of oxide grown on shot peened Super 304H in air at 650 °C for 2000 hours. Numbers mark areas of EDX analysis. Central feature is iron rich oxide nodule and not representative of bulk oxide.

Table 4.3 – Composition in at. % from EDX analysis of oxide grown on shot peened Super 304H in air at 650 °C for 2000 hours. In spots 1-3, the composition of the bulk alloy substrate is thought to contribute to the high iron concentration in the chromium rich oxide.

Spot	Oxygen	Iron	Chromium	Nickel	Manganese	Copper
1	50.9	24.0	18.4	2.3	4.4	-
2	39.5	34.0	18.0	4.2	1.8	2.5
3	31.1	43.8	18.6	4.9	1.7	-
4	53.7	37.0	9.3	-	-	-
5	64.6	28.2	7.2	-	-	-
6	67.1	23.3	9.7	-	-	-

A higher magnification image of an area of protective oxide is shown in Figure 4.53. Spots 4-6 are in good agreement with the compositions of spots 1-3 in Figure 4.52. Spots 1-3 were placed on the octahedral crystallites. The compositions in Table 4.4 show very high concentrations of manganese present in these crystallites. The concentrations of elements in Table 4.4 point to a $MnCr_2O_4$ spinel, assuming the Fe concentration was picked up from the underlying alloy. Copper is found in these areas at up to 3 wt.% although it is unclear as to whether it is present in oxide form or as metallic deposits. Botella et al. [44] observed a similar oxide morphology on Type 304 austenitic steel after oxidation in air at 700 °C for 80 hours and reported the octahedral crystals they observed to be a spinel of the form $(Cr_{1.8}Al_{0.1}Fe_{0.1})(Mn_{0.8}Cu_{0.2})O_4$, thereby suggesting copper was incorporated into the spinel oxide.

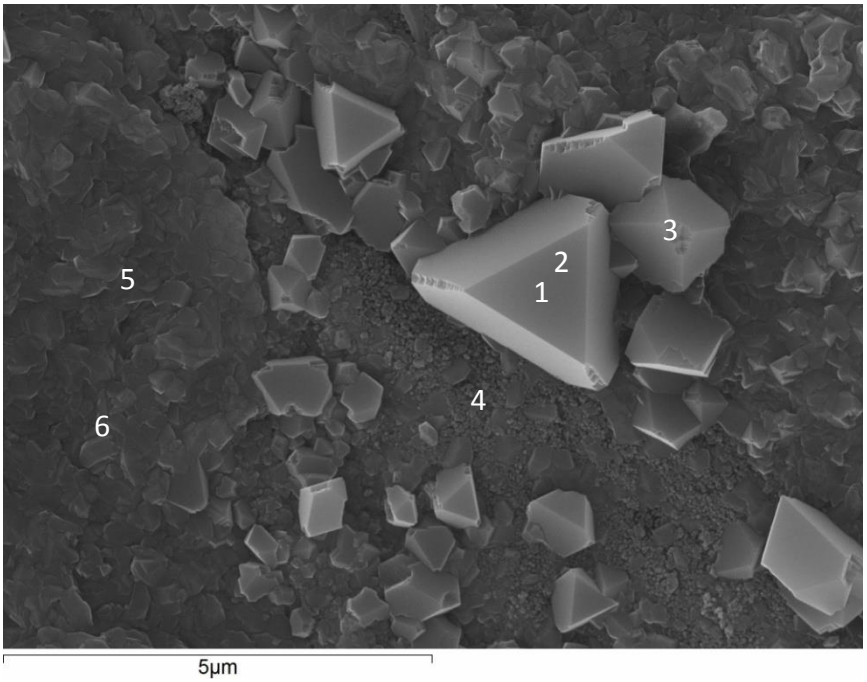

Figure 4.53 – SEM micrograph of oxide grown on shot peened Super 304H in air at 650 °C for 2000 hours. Numbers mark areas of EDX analysis. Area is typical region of bulk, protective oxide, aside from the larger than average crystallite. The crystallites are high in chromium and manganese. Copper is also detected in these areas but in an unknown form. The high concentration of iron in spots 4-6 may have been picked up from the substrate.

Table 4.4 – Composition in at. % from EDX analysis of oxide grown on shot peened Super 304H in air at 650 °C for 2000 hours.

Spot	Oxygen	Iron	Chromium	Nickel	Manganese	Copper
1	65.0	5.8	14.6	-	11.6	3.1
2	68.1	6.1	13.3	-	9.9	2.6
3	68.6	7.9	13.2	-	8.4	1.8
4	39.8	36.0	18.4	3.5	2.3	-
5	56.8	20.7	18.2	1.5	2.8	-
6	50.0	27.3	16.2	3.0	3.5	-

4.3.2.3.4 SEM Cross-Sectional Analysis of Shot Peened Super 304H after Oxidation in Laboratory Air

Cross-section analysis of the oxide grown on Super 304H SP in air revealed a morphology significantly different to those found on the alloys which had a pickled surface finish. A thin, protective oxide film was found to cover the majority of the surface of Super 304H SP oxidised in air ss illustrated in Figure 4.54,. From this film crystallites had grown. In areas where the peening process had left the alloy deformed and protruding from the surface, thicker oxide was present (Figure 4.55). Additionally, oxides were found beneath the surface, where it appeared the peening process had deformed the alloy surface such that it had folded over onto itself, leaving apparent cracks that were attacked by oxidation (Figure 4.55 a)).

a)

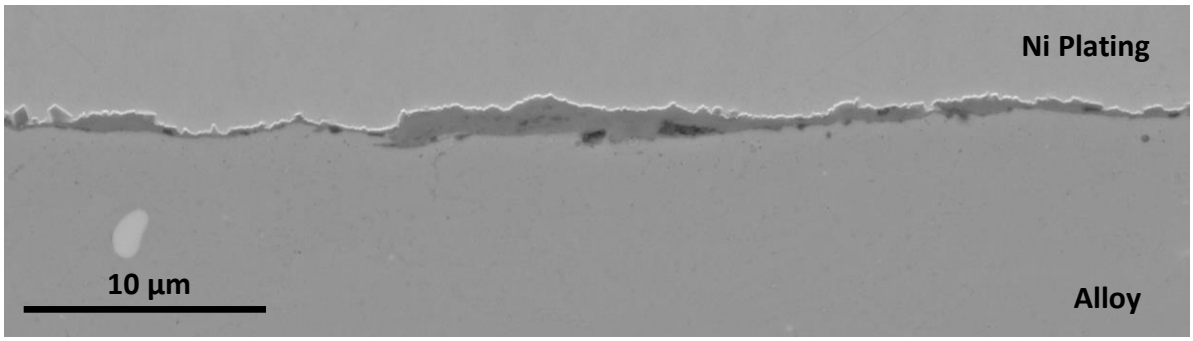

b)

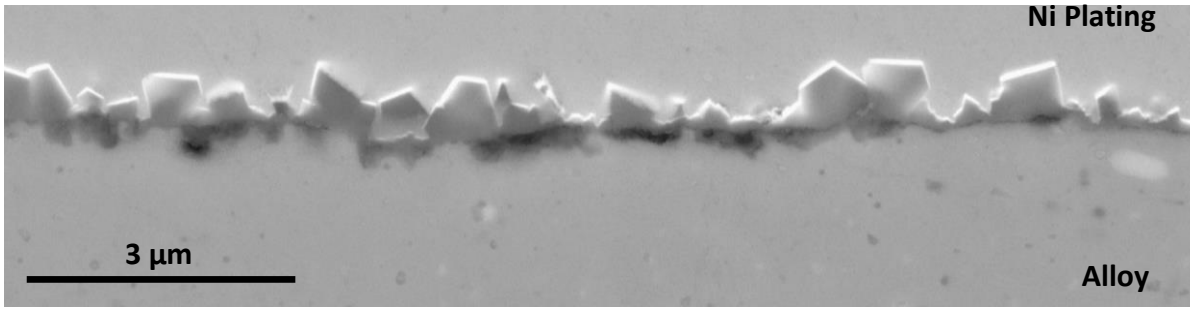

Figure 4.54 - BSE SEM micrographs of typical shot peened Super 304H oxide morphology after oxidation in air for 500 hours at 650 °C. a) Across the majority of shot peened surface a thin, semi protective oxide film had formed. b) The thin oxide layer often consisted of many oxide crystallites, in agreement with topographical observations.

Deformation as a result of the peening process was occasionally observed to cause internal oxidation of the form found in Figure 4.55 a). In this atypical region of oxide the alloy has been deformed in such a way that it has folded back onto itself, allowing oxidation to occur between the two surfaces. Figure 4.55 b) is a high resolution micrograph showing what appears to be oxide crystallites on top of a thin oxide layer. This morphology was found frequently on the surface of shot peened samples oxidised in air.

a)

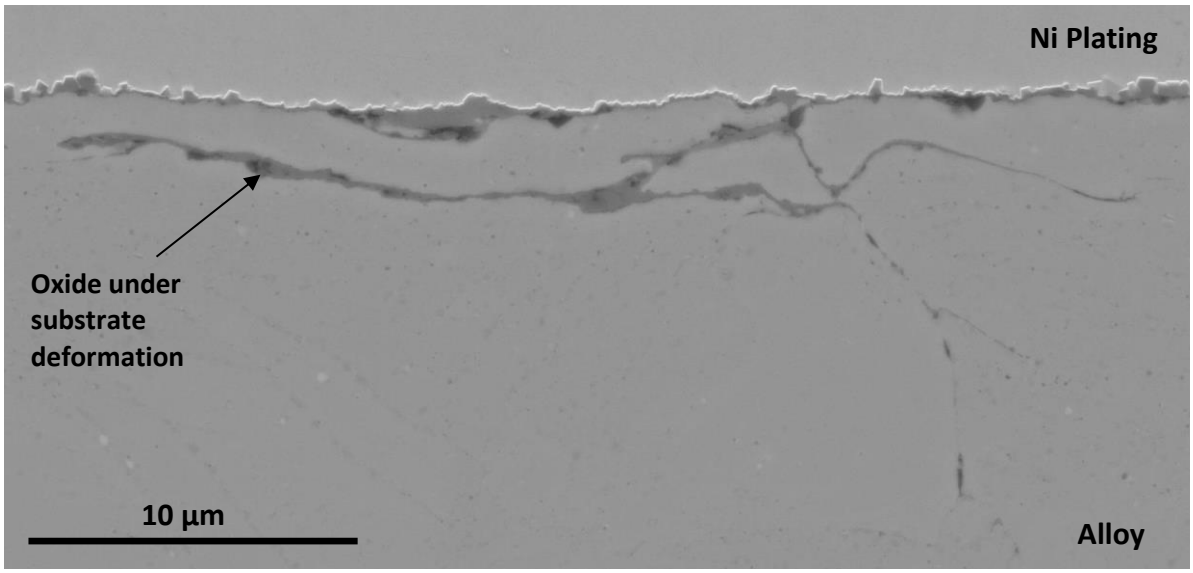

b)

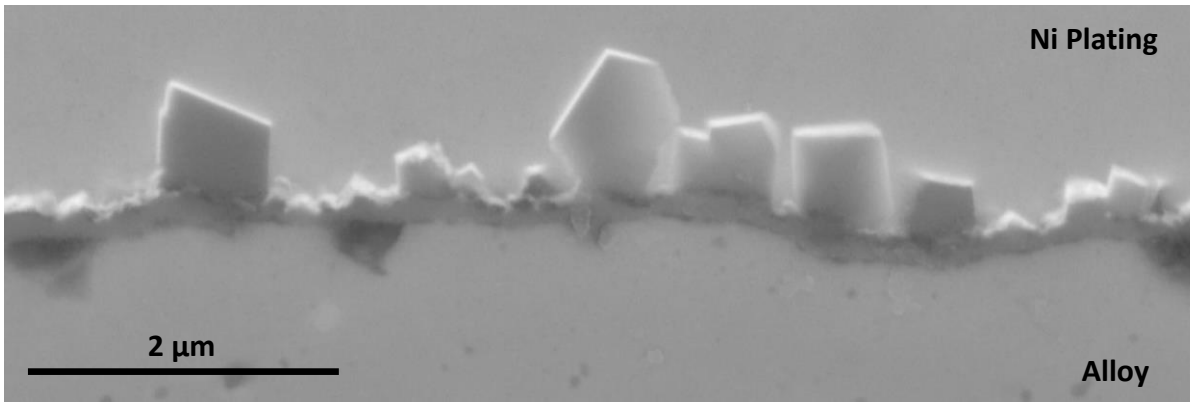

Figure 4.55 – BSE SEM micrograph of shot peened Super 304H oxide morphology after oxidation in air for 500 hours at 650 °C. A) atypical region of internal oxidation caused by deformation of the alloy during the peening process. B) Typical region where crystallites have grown atop a thin oxide layer.

The morphology of the oxide grown on S304HSP in air ranged from sub-micron thick chromium rich films where crystalline growth occurred, to iron and chromium rich layers of a few microns, the latter favoured at higher temperature and longer durations. In areas where the peening process had left an uneven surface deformation thicker scale was found.

4.3.2.3.5 EDX Analysis of Shot Peened Super 304H after Oxidation in Laboratory Air

Accurate compositional analysis of the protective oxide film proved difficult because of its thickness. However, EDX quantitative analysis as found in Figure 4.56/Table 4.5 and Figure 4.57/Table 4.6 indicated the base film was chromium rich with an increased amount of manganese within the layer at around 2-4 at.%. Spots placed on individual crystallites found a higher concentration of manganese of between 4-10 at.%. Similar concentrations of iron, chromium and manganese in these crystallites

suggested they may be composed of a mixed spinel of the three elements, or, if the reported iron content is exaggerated due to the crystallites' proximity to the alloy substrate, a Cr-Mn spinel of the form $MnCr_2O_4$ is likely. Unfortunately, the necessity of nickel plating used in sample preparation means that the reported concentrations of nickel in Table 4.5 are highly exaggerated and therefore speculation to the involvement of this element within the oxide layer cannot be made accurately.

Spots 1, 2, and 3 in Figure 4.56 are suggested to be a mixture of Cr_2O_3 and Cr-Mn spinel (spot 1 a Cr-Mn-Cu spinel). The Fe and Ni reported at these locations is considered to be due to the alloy and nickel plating. Spot 4, however, is a thicker oxide and has a higher concentration of Fe, suggesting a Fe-Cr spinel formed at this location (most likely on top of a Cr,Mn-rich spinel).

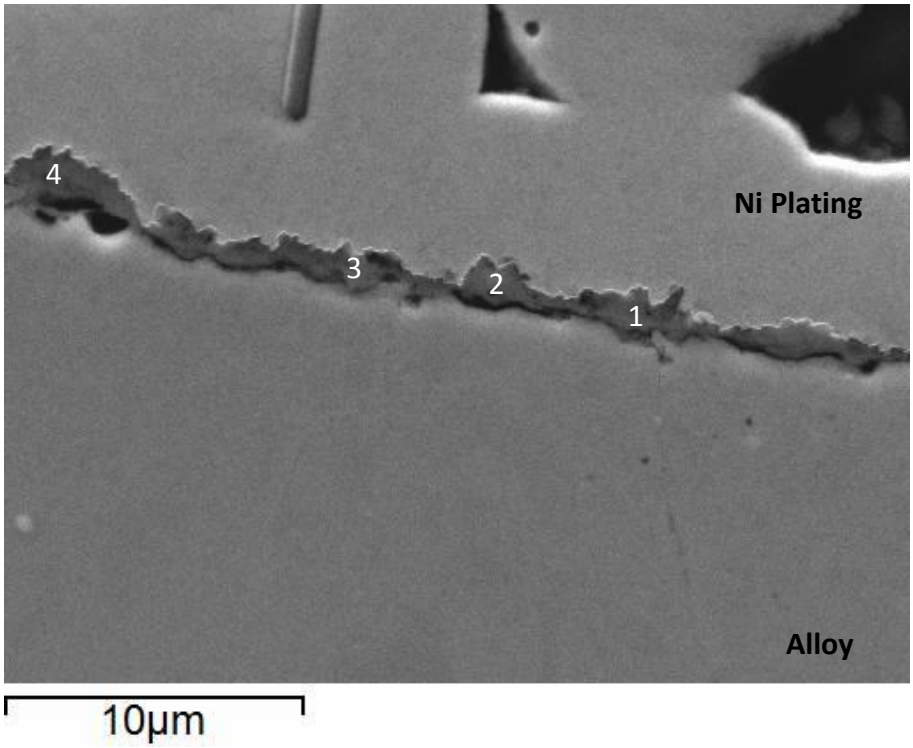

Figure 4.56 – BSE-SEM micrograph of oxide grown on shot peened Super 304H in air at 650 °C for 500 hours. Numbers mark areas of EDX analysis. Because of the thickness of the oxide, and protective nickel plating, concentration values should be considered with caution.

Table 4.5 – Composition in at. % from EDX analysis of oxide grown on shot peened Super 304H in air at 650 °C for 500 hours.

Spot	Oxygen	Iron	Chromium	Nickel	Manganese	Copper
1	52.7	10.1	20.1	11.0	4.0	1.9
2	56.4	9.6	24.4	7.3	2.2	0.2
3	49.8	6.0	18.3	21.7	3.7	0.6
4	57.0	23.5	13.7	5.0	0.8	0.0

EDX analysis of the oxide crystallites formed on S304HSP samples oxidised in air confirm the high Mn content as reported in Table 4.6. Cu is also visibly enriched at these sites. Fe and Ni concentrations are considered to be erroneously high due to proximity to the alloy interface and nickel plating.

Crystallites of this form have been observed by other researchers [75] on fine grained Type 310 steel foils exposed to CO_2. They reported the crystallites to comprise ~95 wt.% Mn cation content. Given their proximity to the nickel plating, Cr-rich protective oxide, and Fe-rich substrate, the crystallites in Figure 4.57 could exhibit similar composition. It should be noted that Type 310 austenitic steel has up to twice the Mn content than Super 304H.

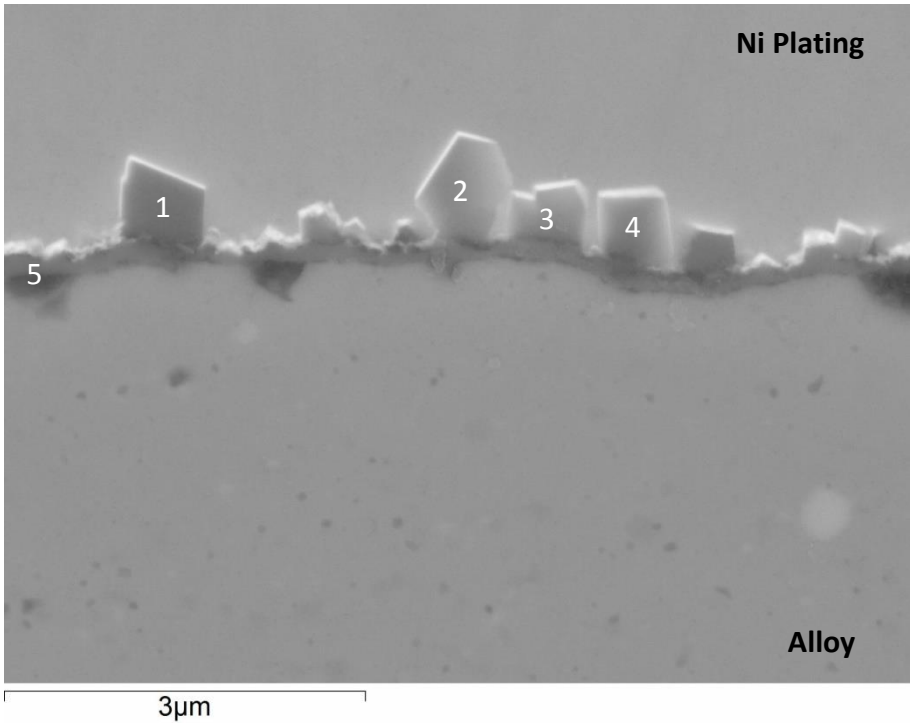

Figure 4.57 – BSE-SEM micrograph of oxide grown on shot peened Super 304H in air at 650 °C for 500 hours. Numbers mark areas of EDX analysis. The reader should note that nickel surrounding each crystallite will have led to a higher than expected registered concentration of nickel.

Table 4.6 – Composition in at. % from EDX analysis of oxide grown on shot peened Super 304H in air at 650 °C for 500 hours.

Spot	Oxygen	Iron	Chromium	Nickel	Manganese	Copper
1	40.8	8.8	12.6	27.1	8.0	3.1
2	39.1	4.0	5.7	46.1	3.6	1.5
3	40.5	11.2	11.5	30.5	4.7	1.6
4	36.0	10.2	2.2	34.2	5.8	2.2
5	31.5	36.8	13.7	15.3	1.3	1.4

4.3.2.4 HR3C

4.3.2.4.1 Visual Observations of HR3C after Oxidation in Laboratory Air

As with the 18-8 austenitic steels, the inner surfaces of HR3C samples oxidised in air were a dull matt grey colour at all temperatures and durations. No spallation was observed on any samples. Photos of these samples are shown in Figure 4.58 and Figure 4.59.

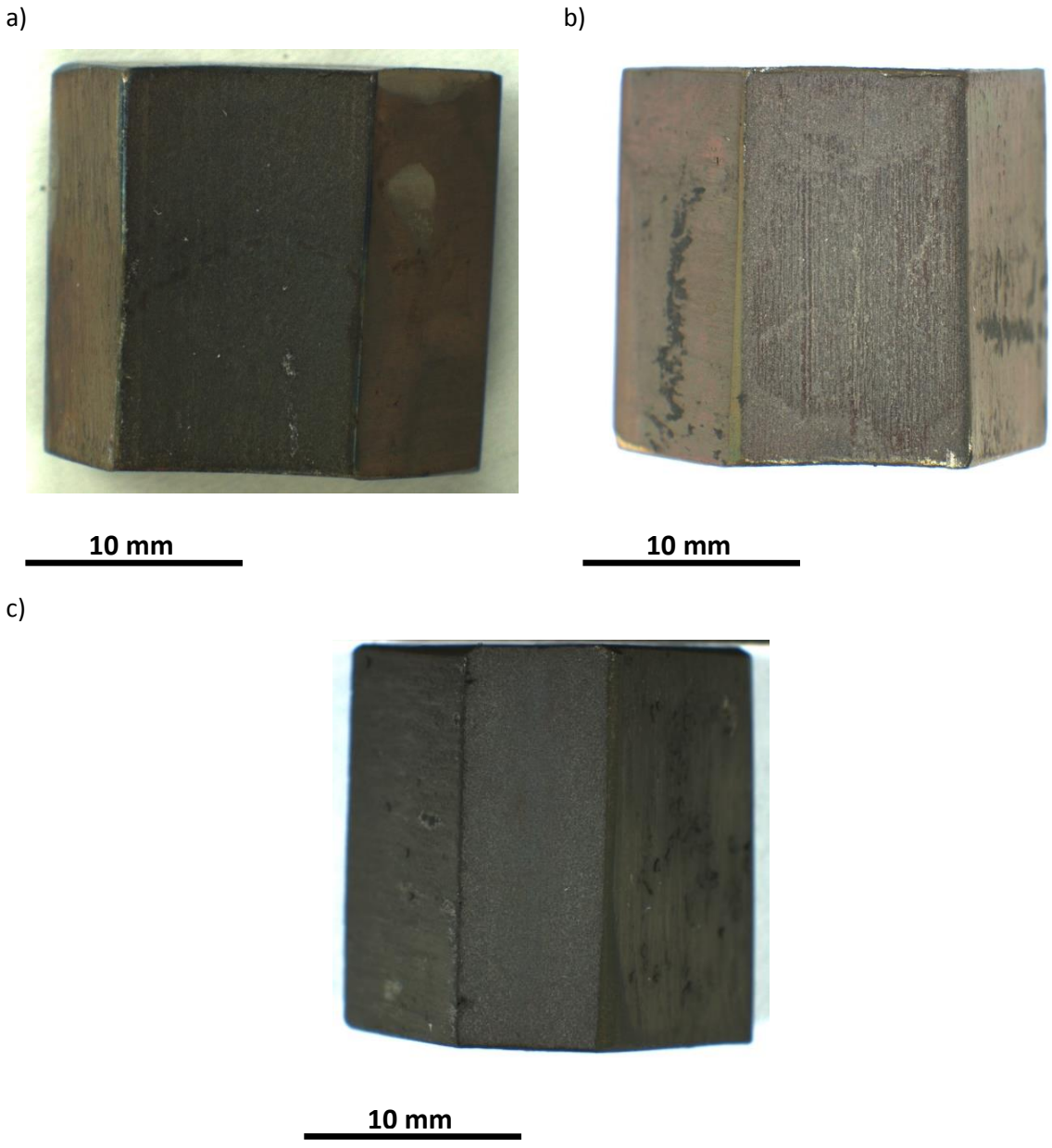

Figure 4.58 – Macro images of air oxidised HR3C inner surface after 100 hours at a) 600 °C, b) 650 °C, c) 700 °C. The inner surfaces were matt grey in colour.

After 1000 hours oxidation, the inner surface morphology appeared very similar to oxidation for only 100 hours.

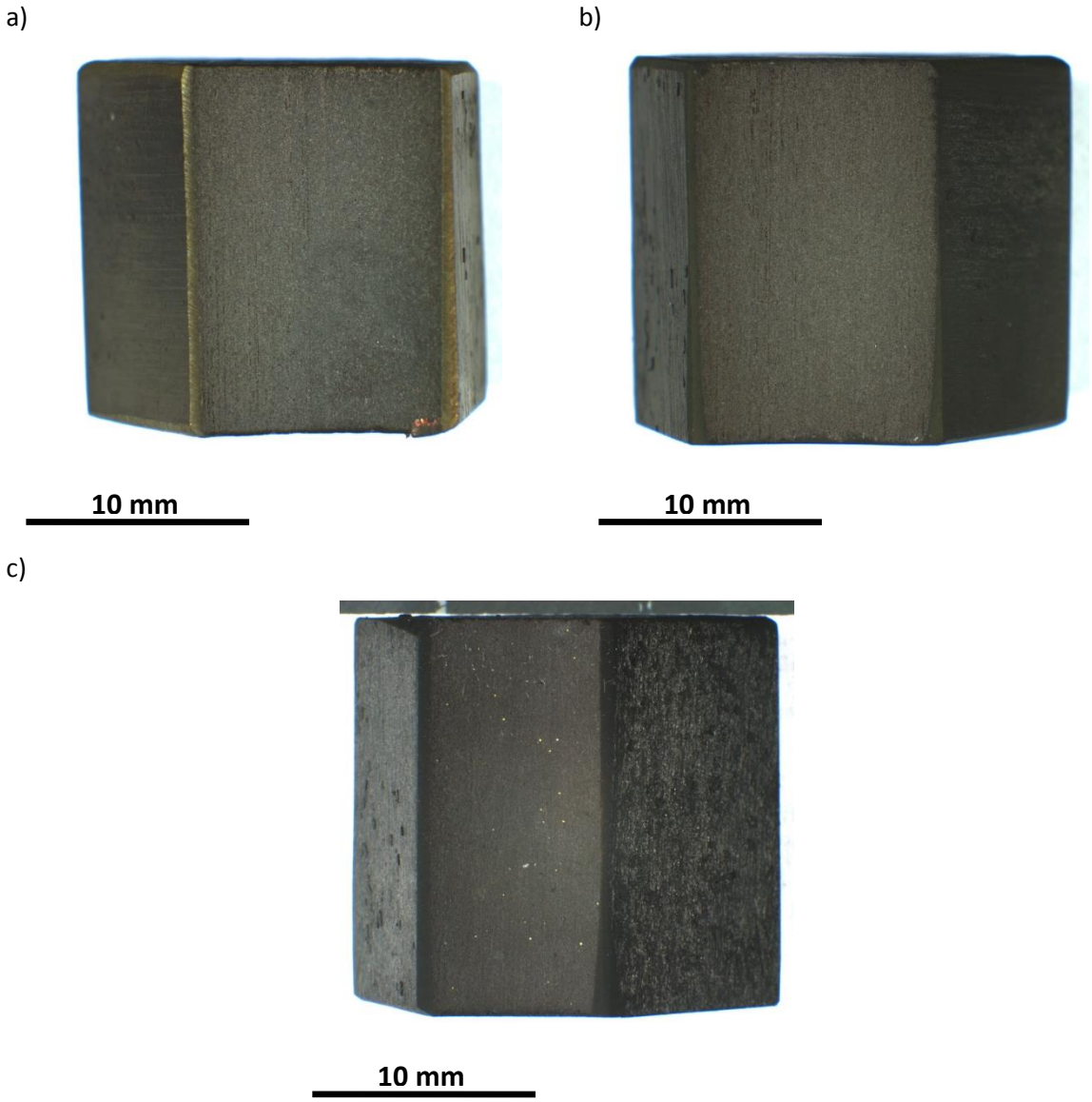

Figure 4.59 – Macro images of air oxidised HR3C inner surface after 1000 hours at a) 600 °C, b) 650 °C, c) 700 °C. The inner surfaces remained matt grey in colour.

4.3.2.4.2 SEM Surface Analysis of HR3C after Oxidation in Laboratory Air

Oxide grown on HR3C oxidised in air appeared to take two forms. Slightly porous oxide nodules that tended to grow on raised areas of the substrate defined by the pickling process, and a non-porous oxide that resided within the pickled grains. The alloy grain structure was visible after oxidation at all temperatures suggesting the oxide layer in areas absent from nodules was particularly thin. Whiskers and platelets grew from the porous oxide. Whisker growth was favoured at lower temperatures. The porous oxide grew as nodules, which increased in size with temperature and oxidation time. SEM micrographs of the sample morphology are shown in Figure 4.60, Figure 4.61 and Figure 4.62.

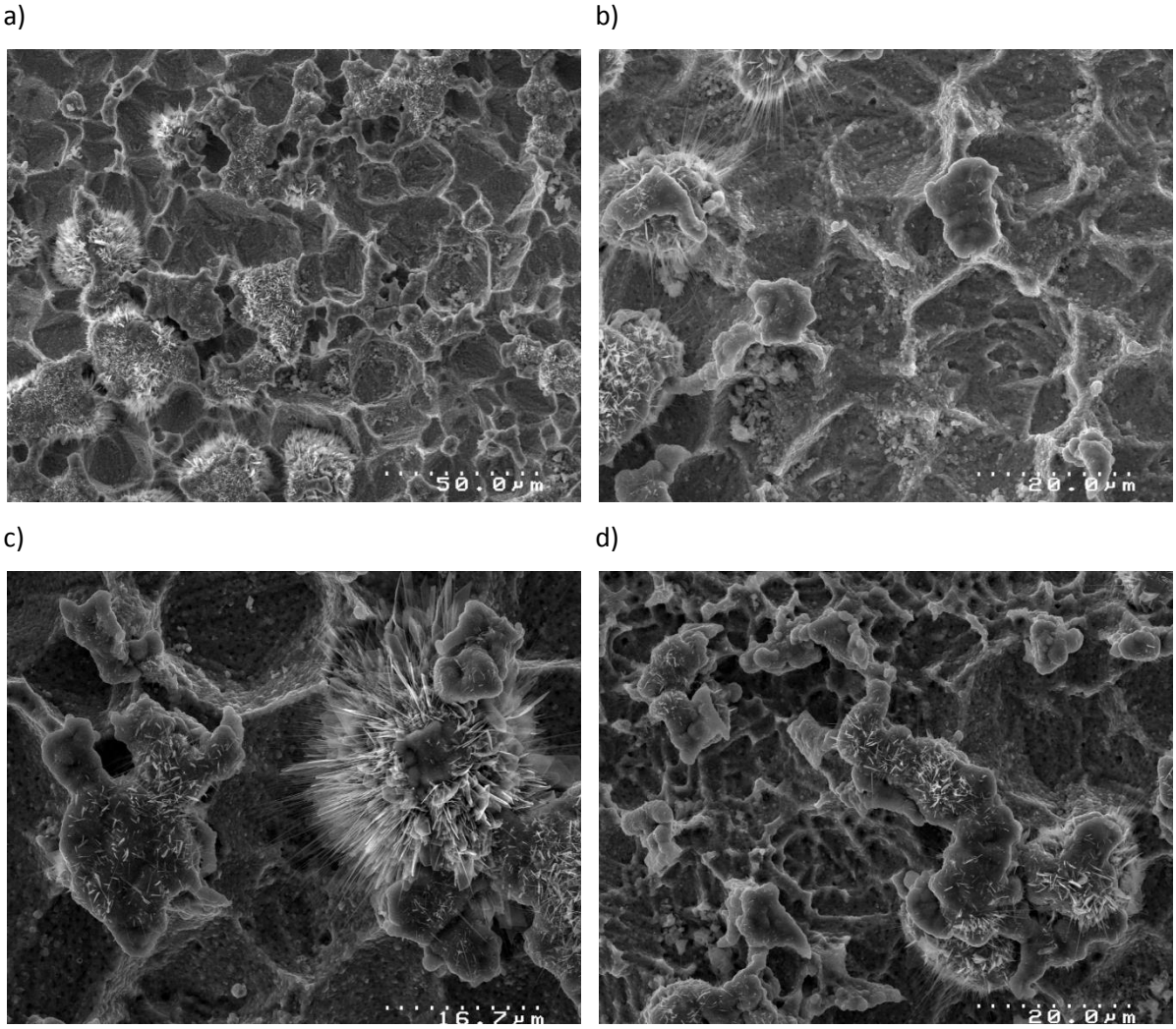

Figure 4.60 – SEI SEM images of HR3C inner surface topography after oxidation in air at 600 °C after a) 250 hours, b), 1000 hours, c) 2000 hours and d) 3000 hours.

At 650 °C notably thicker oxide covered the inner surface concealing the grain structure left by the pickling process.

a) b)

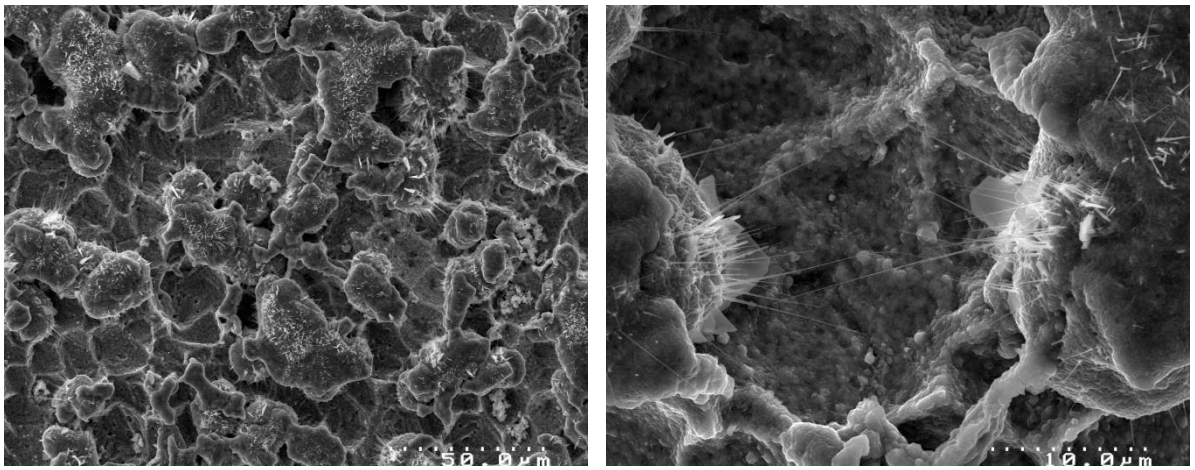

Figure 4.61 – SEI SEM images of HR3C inner surface topography after oxidation in air at 650 °C after a), b) 2000 hours.

At 700 °C there was an abundance of smaller whiskers covering oxide nodules.

a) b)

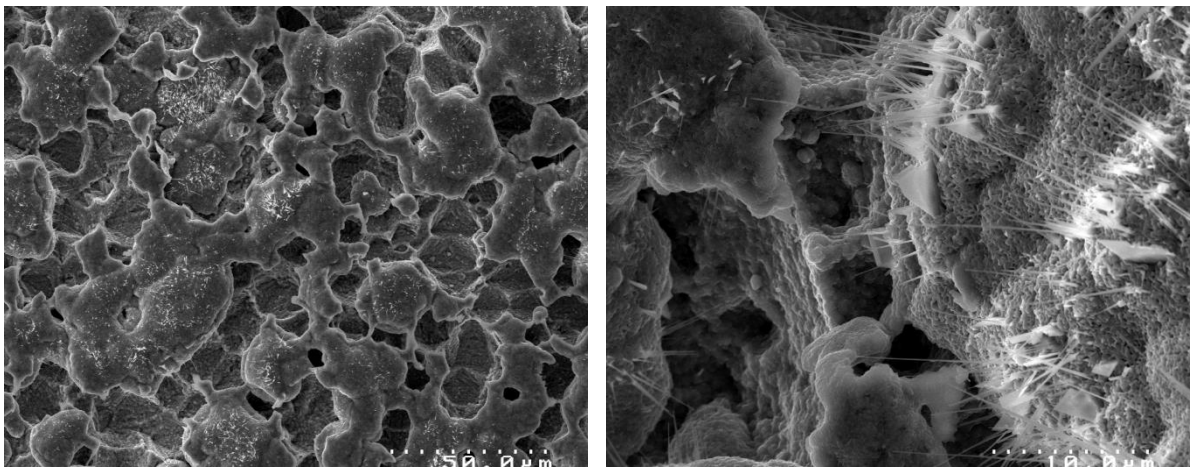

c) d)

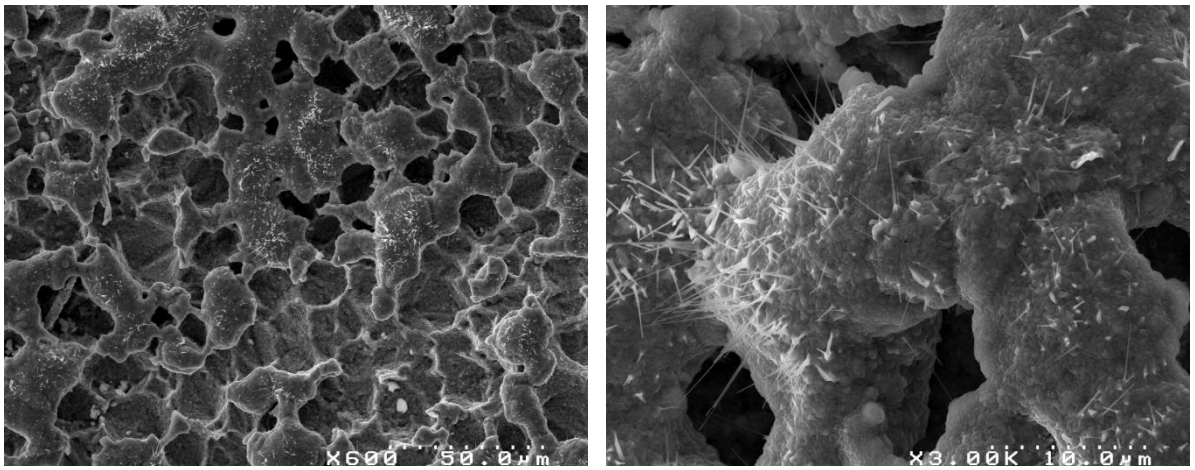

Figure 4.62 – SEI SEM images of HR3C inner surface topography after oxidation in air at 700 °C after a), b) 250 hours, c), d) 2000 hours.

4.3.2.4.3 Oxide Cross-Sectional Morphology of HR3C as a Function of Time and Temperature after Oxidation in Laboratory Air

The morphology of the oxide grown on HR3C in air differed to that grown on Super 304H and 347HFG. Two distinct oxides were identified at all temperatures and durations. Covering the entire alloy surface was a thin, protective oxide film, similar to that grown on shot peened Super 304H. Large, duplex oxide nodules then scattered the surface, increasing in population as time and temperature increased. Nodules almost exclusively nucleated on raised ridges of the pickled surface. After 1000 hours at 700 °C, over 50% of the inner surface had been consumed by duplex oxide, and resembled the oxide formed on Super 304H after oxidation in air for 100 hours at 600 °C.

The inner spinel on average contained larger amounts of chromium and nickel than the spinels found on 347HFG and Super 304H oxidised in air, likely as a result of the high bulk concentrations of these elements. An interesting observation was the formation of an iron and nickel rich intermediate phase within the outer oxide adjacent to the spinel. Evidence that this phase was present in the outer oxide was that the cross-section outline of the spinel oxide matched that of the unoxidised alloy cross-section. The iron-nickel rich intermediate phase exhibited a hemispherical shape suggesting outward growth from the prior substrate surface.

SEM micrographs of the cross sections for oxidation times of 100, 250, 500 and 1000 hours and temperatures of 600, 650 and 700 °C are shown in Figure 4.63, Figure 4.64 and Figure 4.65.

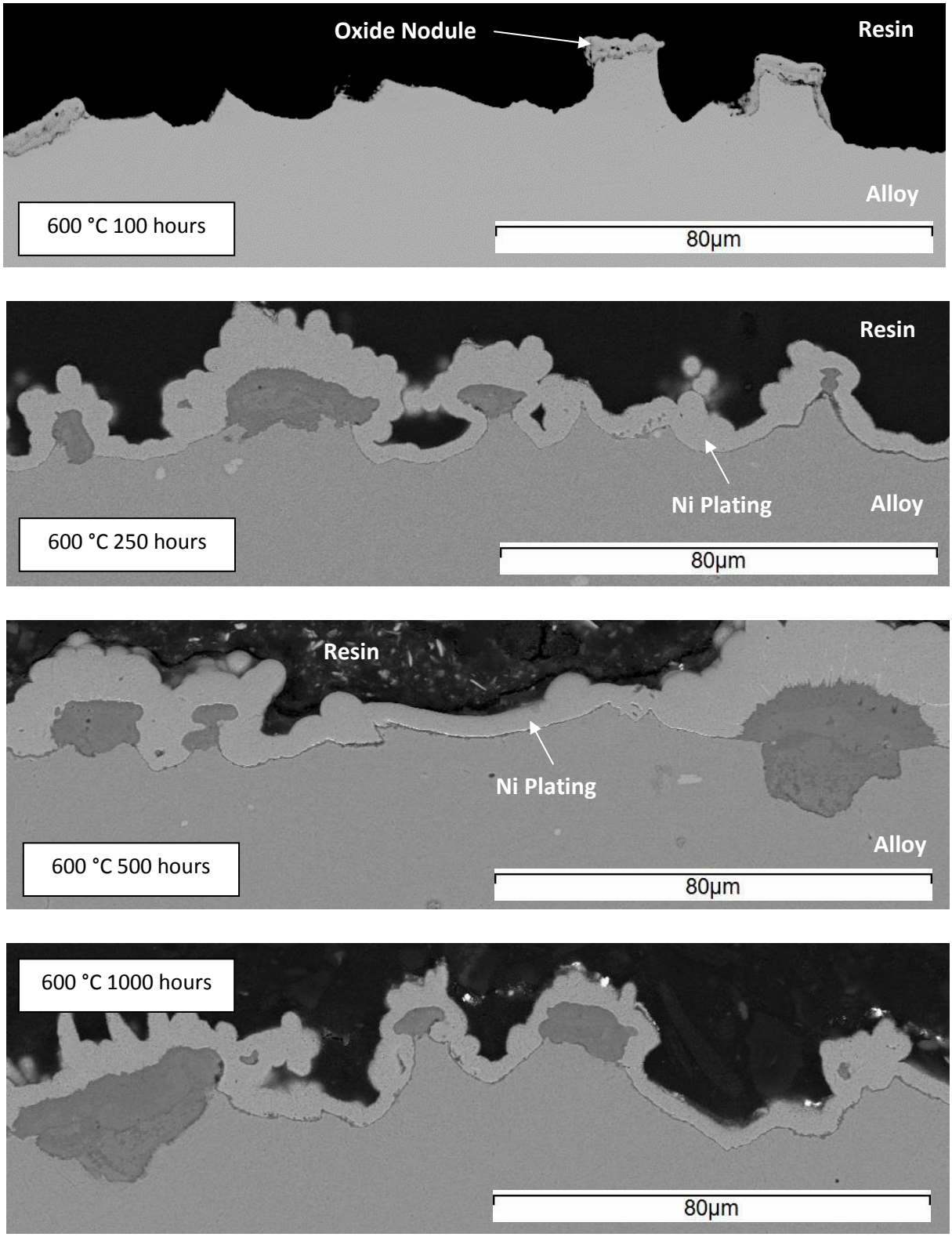

Figure 4.63 – BSE SEM micrographs of the oxide formed on HR3C following oxidation in air at 600 °C. In contrast to the 18-8 austenitic steels, HR3C grew a thin protective oxide film along with distinguished, duplex oxide nodules.

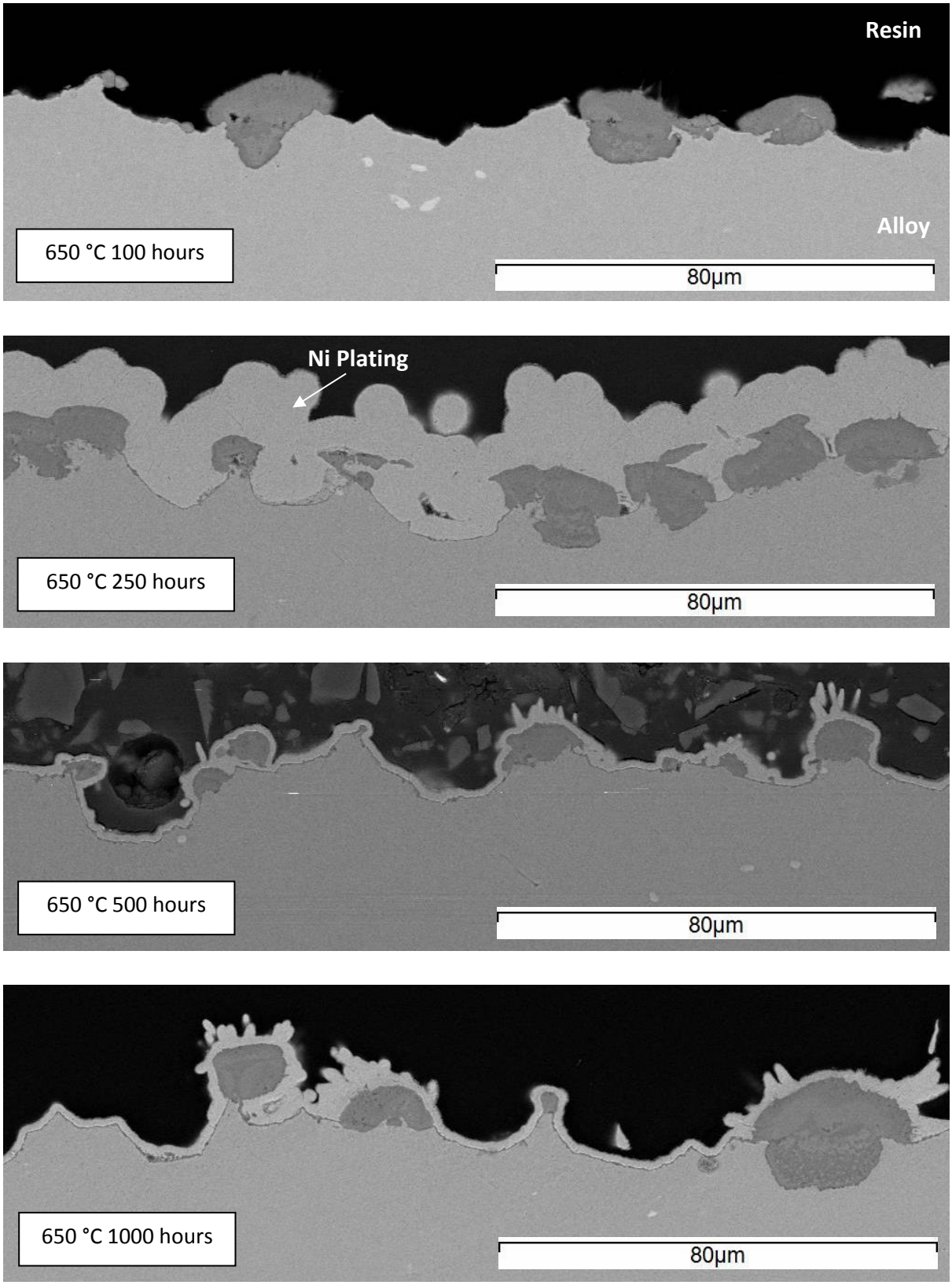

Figure 4.64 – BSE SEM micrographs of the oxide formed on HR3C following oxidation in air at 650 °C. In contrast to the 18-8 austenitic steels, HR3C grew a thin protective oxide film along with distinguished, duplex oxide nodules. More and larger nodules were present that at 600 °C.

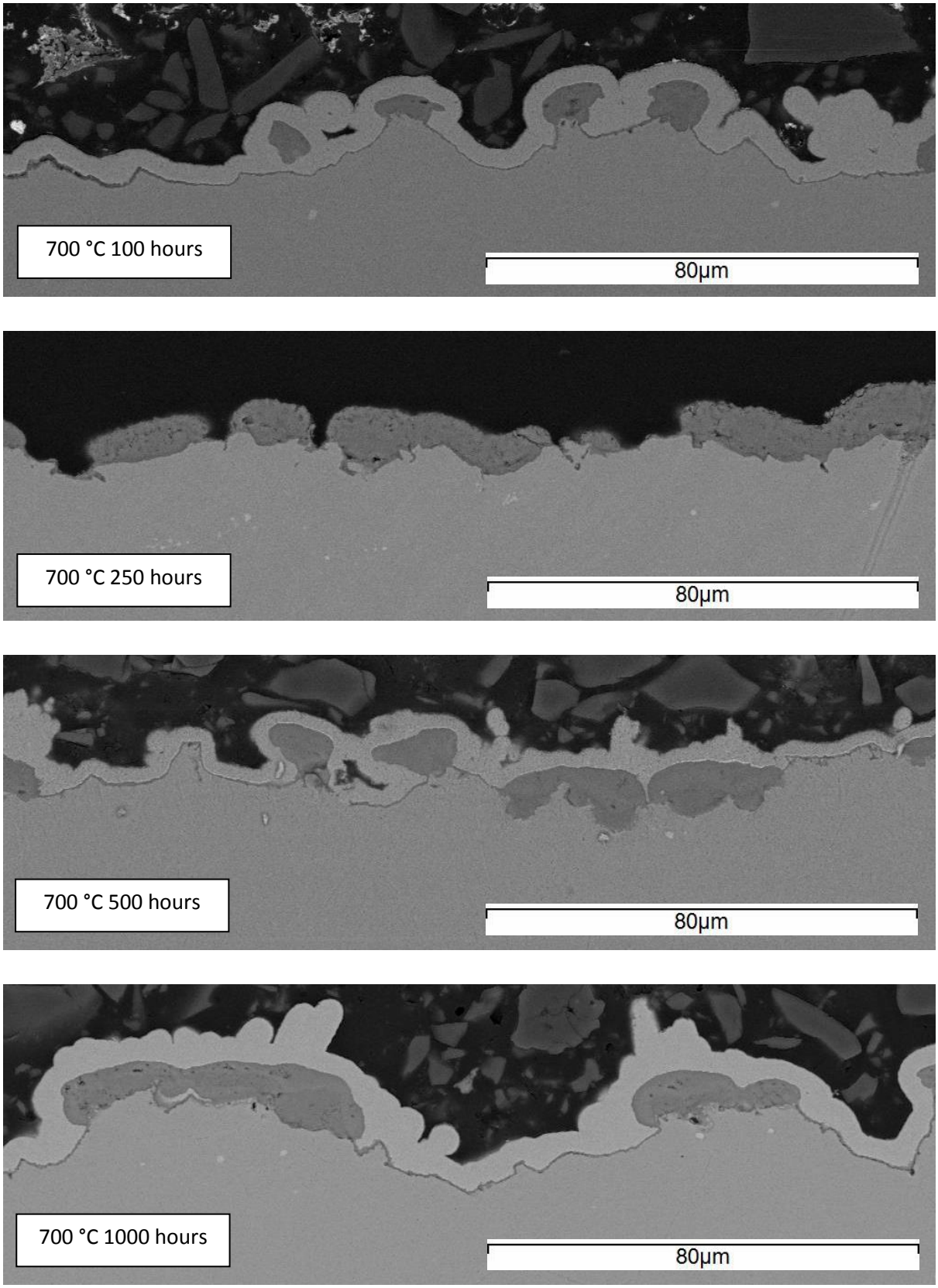

Figure 4.65 – BSE SEM micrographs of the oxide formed on HR3C following oxidation in air at 700 °C. In contrast to the 18-8 austenitic steels, HR3C grew a thin protective oxide film along with distinguished, duplex oxide nodules. At 700 °C the oxide nodules started to coalesce to form a thick, duplex oxide layer.

4.3.2.4.4 Oxide Area Maps of HR3C after Oxidation in Laboratory Air

An EDX area map of HR3C oxidised in air for 1000 hours at 700 °C is shown in Figure 4.66, focusing on nodular morphology. The outline of alloy grains is highlighted by increases or decreases in element concentrations within the alloy grain boundaries indicating where grain boundaries reach the surface. In these locations protective oxide appears to have formed, whereas nodules had formed furthest away from these locations.

The morphology of the large nodule is as follows. The alloy subjacent to the spinel oxide was slightly depleted in chromium and manganese. Nickel was enriched in these areas. The spinel contained iron, chromium, nickel and manganese. A concentration gradient of chromium indicates this element was enriched towards the alloy/oxide interface. The outer oxide consisted of a lower iron-nickel rich region and an upper iron rich region. This was different to the morphology of the outer oxide on 347HFG and Super 304H oxidised in air, which exhibited only an iron rich phase. Alloy grain boundaries near to the alloy surface were enriched in chromium and manganese, and depleted of iron. It is proposed that a protective Cr,Mn-rich oxide, possibly Cr_2MnO_4, initially forms on the surface of the alloy, before breaking down into duplex nodules at the centre of where austenite grains reach the surface. A slight enrichment of oxygen suggests oxidation may have occurred within the grain boundaries. Unusually, a thin band of chromium and manganese is present within the outer oxide at the scale/gas interface.

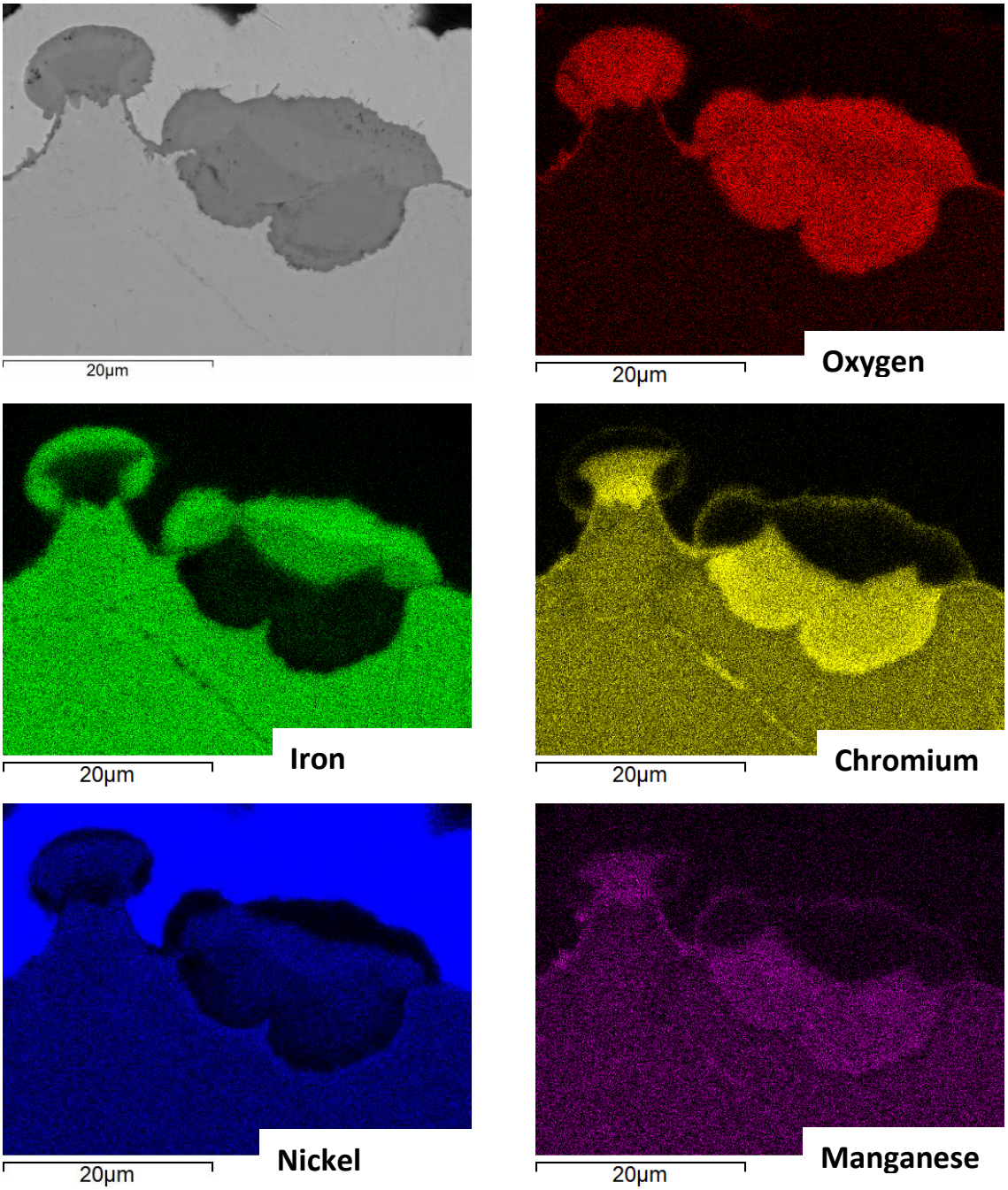

Figure 4.66 – EDX element area map for a cross-section of HR3C oxidised in air after 1000 hours at 700 °C. Sample has been nickel plated. Region of interest has been selected to specifically analyse morphology of nodular oxide. Above the spinel oxide, which contains iron, chromium, nickel and manganese, the iron rich layer appears to be split into an outer layer containing exclusively iron, and an inner layer with the addition of nickel. This morphology was found to be exclusive to HR3C. At the scale/gas interface there appears to be a thin layer enriched in chromium and manganese.

4.3.2.4.5 EDX Analysis of HR3C after Oxidation in Laboratory Air

EDX quantitative analysis was performed on an oxide nodule following oxidation for 1000 hours at 650 °C, the results of which are shown in Table 4.7. Oxide nodules often facilitated whisker and platelet growth as identified by the hairline oxides emerging from the surface of the nodule in Figure 4.67. The reader should note that this area was chosen specifically to characterise an oxide nodule and is not representative of the entire alloy surface. The vast majority of oxide nodules had the morphology of those shown in the area map in Figure 4.66. The spots placed in Figure 4.67 for a nodule grown for 1000 hours at 650 °C revealed the spinel to vary in composition, but consistently have higher concentrations of chromium and nickel than the spinels of Super 304H and 347HFG. Lighter areas, as indicated by spot 3, contained a higher concentration of nickel than darker areas. The concentrations of iron and chromium were decreased in light areas of the spinel. A similar amount of nickel as the light areas of the inner spinel oxide was found in the intermediate iron-nickel rich layer. The outermost layer was iron rich.

The oxide at spot 6 is suggested to be Fe_2O_3, as with the 18Cr8Ni alloys. The oxide at spot 5 contains a high amount of nickel. Outward diffusion of Ni must have occurred in this location as the prior austenite surface is likely to be at the inner oxide/Ni-rich outer oxide interface because the Ni-rich intermediate oxide is devoid of the substrate's minor elements. The oxygen partial pressure will be higher in this oxide than the inner spinel, so it is likely that spot 5 relates to a spinel oxide of the form $(Fe,Ni)_3O_4$, in agreement with the cation ratio of the EDX spot. Spots 3 and 4 are suggested to be either $(Fe,Cr)_3O_4$ spinels in a metallic nickel matrix, or $(Fe,Cr,Ni)_3O_4$ spinel. The spinel is suggested to have variable composition with a higher Cr content in darker areas (spot 4), and higher Ni content in lighter areas (spot 3). The oxygen content of spot 3 is lower compared to spot 4, which could suggest that nickel is present in metallic form.

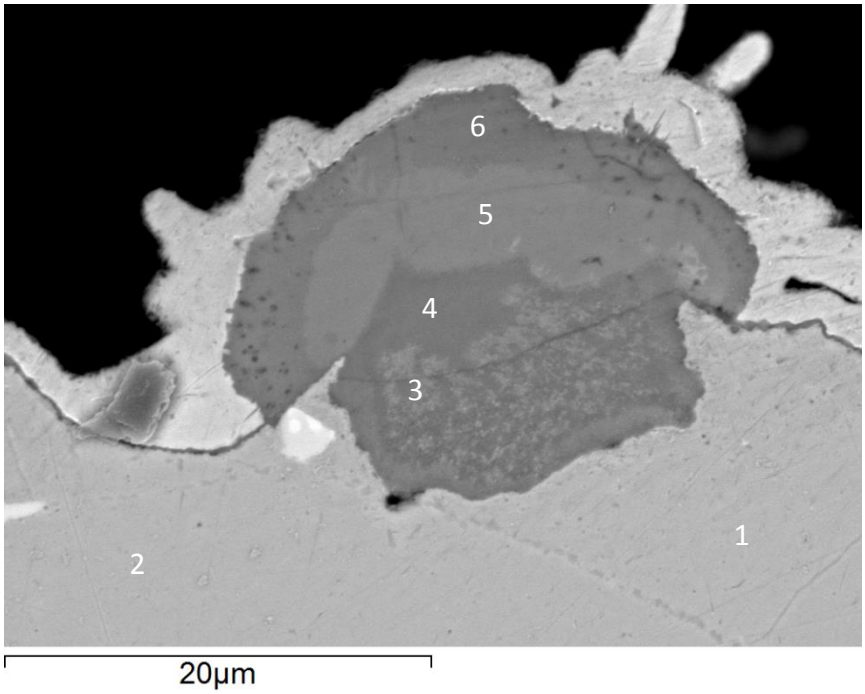

Figure 4.67 – BSE-SEM micrograph of oxide grown on HR3C in air at 650 °C for 1000 hours indicating the presence of an iron-nickel intermediate layer between the inner spinel oxide and outer iron rich oxide. Numbers mark areas of EDX analysis. Region focuses on oxide nodule and is not representative of entire oxide surface.

Table 4.7 – Composition in at. % from EDX analysis of oxide grown on HR3C in air at 600 °C for 500 hours.

Spot	Oxygen	Iron	Chromium	Nickel	Manganese
1	-	51.9	28.3	18.4	1.6
2	-	52.3	27.8	18.2	1.6
3	57.1	7.3	23.2	11.2	1.3
4	60.6	8.8	23.7	7.0	-
5	62.4	24.2	1.2	12.2	-
6	68.1	29.3	1.6	1.0	-

4.3.3 Summary of Oxidation of Austenitic Steels in Laboratory Air

Austenitic steels 347HFG, Super 304H, shot peened Super 304H, and HR3C were oxidised in static laboratory air at 600, 650 and 700 °C for up to 3000 hours, in order to characterise the oxidation behaviour of the inner (steamside) tube surface. The results are summarised below.

- 347HFG and Super 304H exhibited the largest mass gain and oxide thickness of all four alloys. The oxidation rate reduced with time, and was initially rapid, before reducing in what appeared to be a change of oxidation rate. The oxidation time at which the change in oxidation rate occurred decreased as oxidation temperature increased, and was more pronounced on 347HFG than Super 304H.
- HR3C and shot peened Super 304H recorded similar mass gains. However, oxide thickness measurements revealed a much thinner oxide on shot peened Super 304H. This was a result

of the non shot peened outer tube surface on shot peened Super 304H samples growing a thick duplex oxide that contributed to mass gain measurements.

- The oxide morphology on HR3C retained a bimodal distribution throughout air oxidation, skewing mean oxide thicknesses. The oxide thickness of the Cr-rich layer was calculated separately, and found to be similar in thickness to the oxide layer grown on shot peened Super 304H at 700 °C, suggesting similar composition.
- A change in oxidation rate was observed, but to a lesser extent on HR3C than the 18Cr alloys, and was attributed to the formation of a protective Cr-rich oxide. Oxide thickness measurements of shot peened Super 304H suggested a single kinetic regime was followed for this alloy.
- The effect of increasing oxidation temperature was to accelerate oxide growth initially, and decrease the time taken for the oxidation rate to reduce.
- 347HFG and Super 304H initially formed nodular duplex oxides separated by a thin Cr-rich oxide. The nodules coalesced eventually forming a thick duplex oxide over the entire surface with increasing time and temperature. The oxide grown on HR3C remained nodular over the full scope of testing.
- The duplex oxide was formed from an outer Fe-rich oxide and inner spinel. The outer oxide was identified as Fe_2O_3, suggesting equilibrium conditions were reached at the oxide/gas interface. The inner oxide was a spinel containing contains the constituent elements of the underlying alloy. However, the anion/cation ratios measured by EDX suggested nickel may have remained in metallic form. On HR3C, a Ni-Fe-rich intermediate layer grew between the outer oxide and inner spinel. Shot peened Super 304H grew a thin protective oxide thought to comprise a mixture of Cr_2O_3, $MnCr_2O_4$, and $(Fe_{1-x}Cr_x)_2O_3$.
- Areas of Cr and Mn depletion were found in the alloy at the alloy/oxide interface on all alloys. These were most pronounced at higher temperatures and corresponded with an enrichment in Ni.
- Copper was found to accumulate at the outer oxide/gas interface on Super 304H after oxidation at 700 °C.
- No spallation was observed on austenitic steels oxidised in laboratory air.

4.4 Oxidation of Austenitic Stainless Steels in Deoxygenated Steam

Early oxidation experiments in deoxygenated steam resulted in spallation of the steam-side surface oxide on a small number of Super 304H and 347HFG samples. These experiments marked the initial commissioning of the atmospheric steam oxidation rig, and lacked the flow rate control and oxygen monitoring equipment that was retrospectively fitted for the majority of steam oxidation experiments. A number of samples in these early experiments exhibited spallation. The results of the early experiments are presented separately in Section 4.5 as the steam parameters of these early experiments could not be verified,

The current section presents the results of oxidation experiments conducted after a number of upgrades were made to the steam oxidation facility and correspond to stages 3 and 4 of development. These stages allowed for in-situ temperature monitoring, accurate flow control utilising a dosing pump, and feed-water oxygen content monitoring. Full details of the development of the steam oxidation facility can be found in (Section 3.4).

Experiments in flowing deoxygenated steam were undertaken on 347HFG, Super 304H, shot peened Super 304H, and HR3C. Experiments were conducted at 600, 650, and 700 °C for up to 1300 hours.

4.4.1 Oxidation Kinetics after Oxidation in Deoxygenated Steam

The following section reports the kinetic data for austenitic steels oxidised in flowing deoxygenated steam. No samples oxidised in effectively deoxygenated steam spalled. Kinetic data for samples oxidised in ineffectively deoxygenated steam that did exhibit spallation can be found in Section 4.5.1. Mass gain data is reported in the following section for 347HFG, Super 304H, shot peened Super 304H, and HR3C. Oxide thickness data is reported in Section 4.4.1.2 for 347HFG and Super 304H only. Thicknesses measurements are reported for the outer oxide, spinel oxide, and chromium rich oxide in order to obtain rate constants and activation energies for individual layers. Measuring the oxide thickness of individual layers was also used when calculating the stress and strain energy in individual layers in the Discussion chapter.

4.4.1.1 Mass Gain Measurements after Oxidation in Deoxygenated Steam

Mass gain data for austenitic steels exposed to deoxygenated steam can be found in Figure 4.68 - Figure 4.71. Note that 347HFG was tested at 650 °C for up to 1300 hours. For comparison between graphs, Figure 4.69 considers data up to 600 hours and the reader is referred to Figure 4.70 for the

full range of mass gain data for 347HFG at 650 °C. Mass gain in deoxygenated steam was higher than in air for all alloys at all temperatures and appeared to be more temperature dependent than oxidation in air. The largest increase in mass gain was from 600 °C to 650 °C for all 347HFG and Super 304H, both of which showed the largest mass gain. There was a marked increase in the mass gain of Super 304H SP compared to HR3C at 650 °C and 700 °C that was not observed in air. 700 °C saw the largest difference. HR3C showed the least mass gain of all alloys tested. Mass gain of HR3C increased from 600 °C to 650 °C but exhibited a slight decrease at 700 °C compared with 650 °C. This may be a result of earlier formation of a protective oxide film.

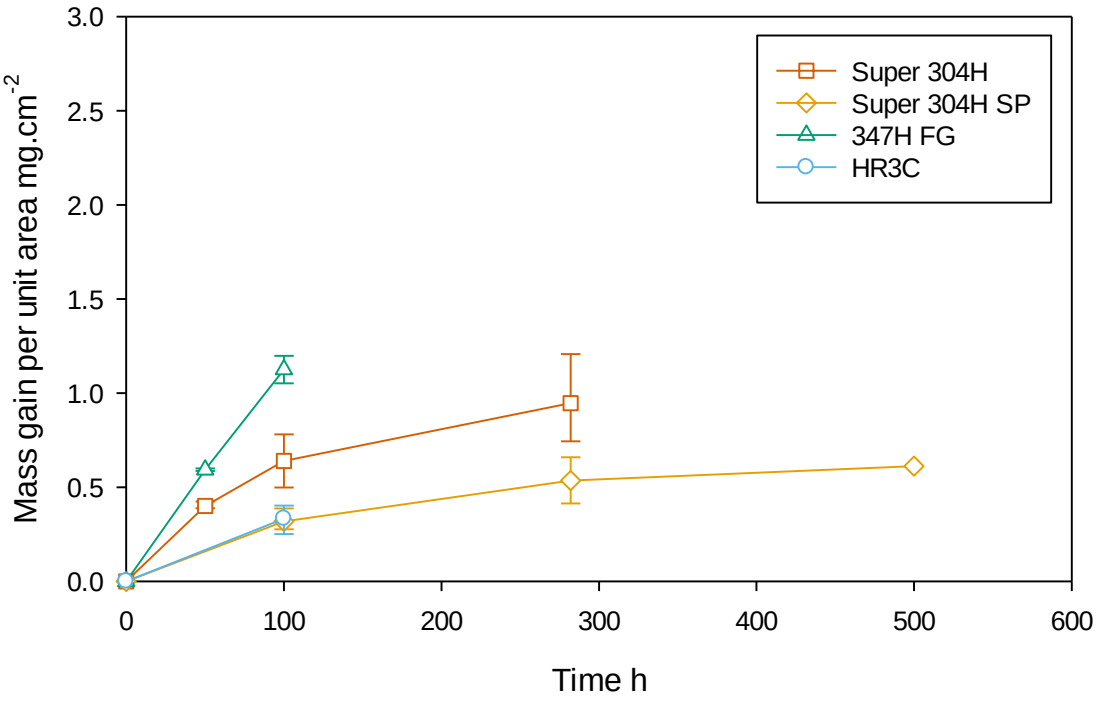

Figure 4.68 – Mass gain data for austenitic steels oxidised in deoxygenated steam at 600 °C. The mass gain of each steel was a factor of 3 higher than after oxidation in air after 100 hours. Error bars show the range where multiple experiments were undertaken.

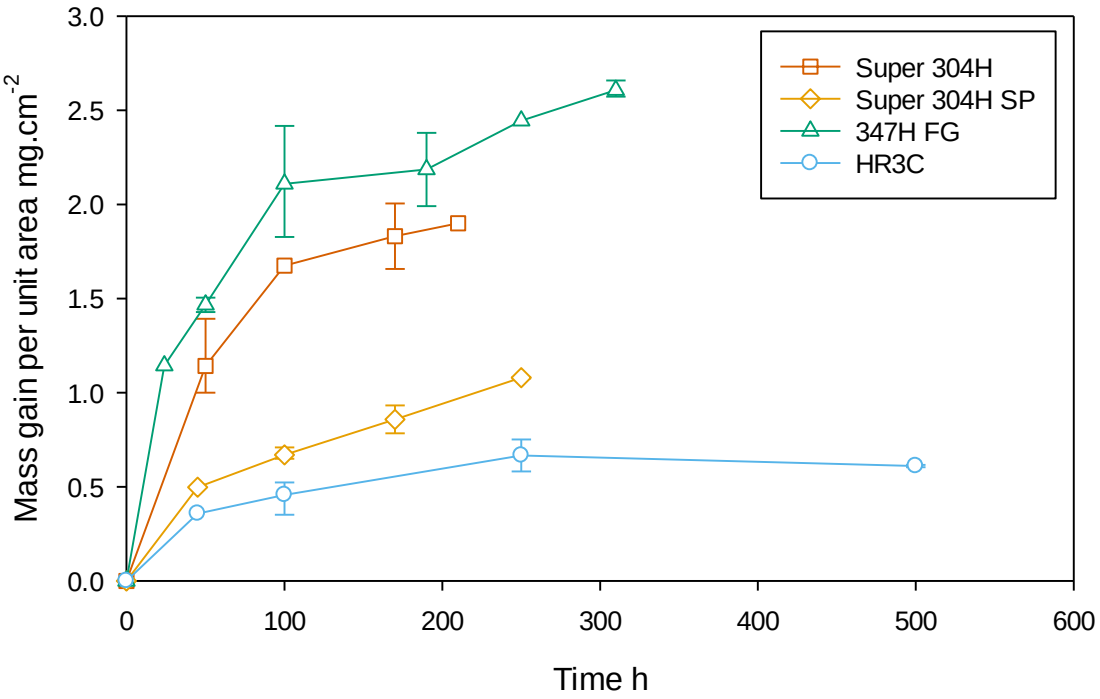

Figure 4.69 – Mass gain data for austenitic steels oxidised in deoxygenated steam at 650 °C up to 500 hours oxidation. Shot peened Super 304H and HR3C gained less mass than 18-8 austenitics, as found in air. Error bars show the range where multiple experiments were undertaken.

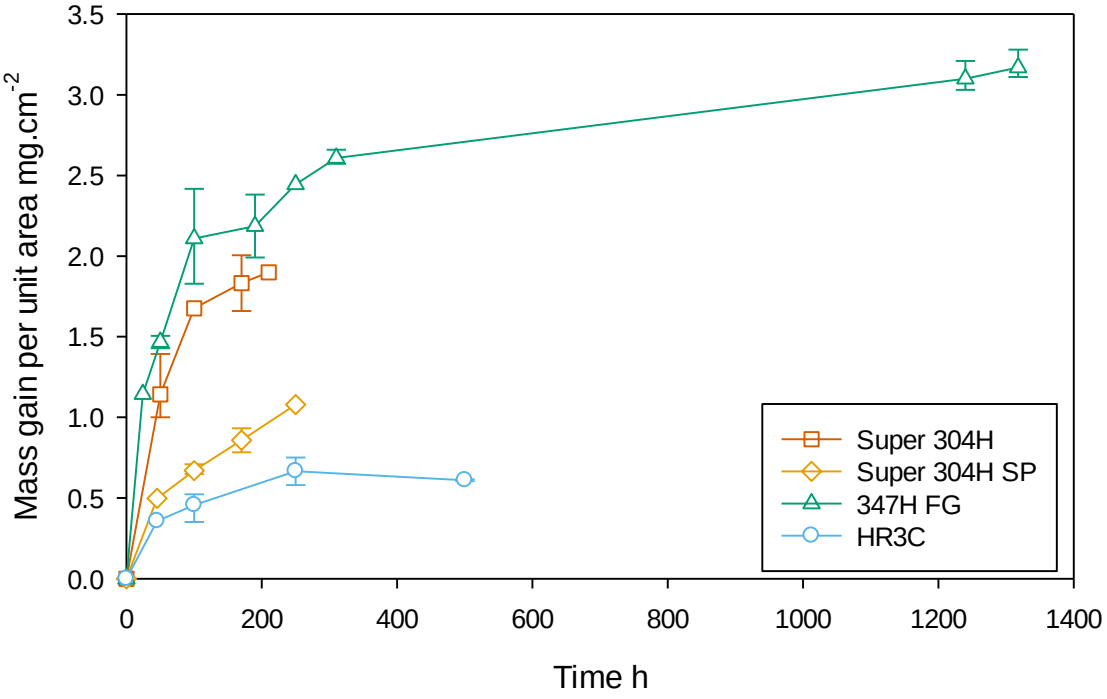

Figure 4.70 – Mass gain data for austenitic steels oxidised in deoxygenated steam at 650 °C for up to 1300 hours oxidation. Error bars show the range where multiple experiments were undertaken.

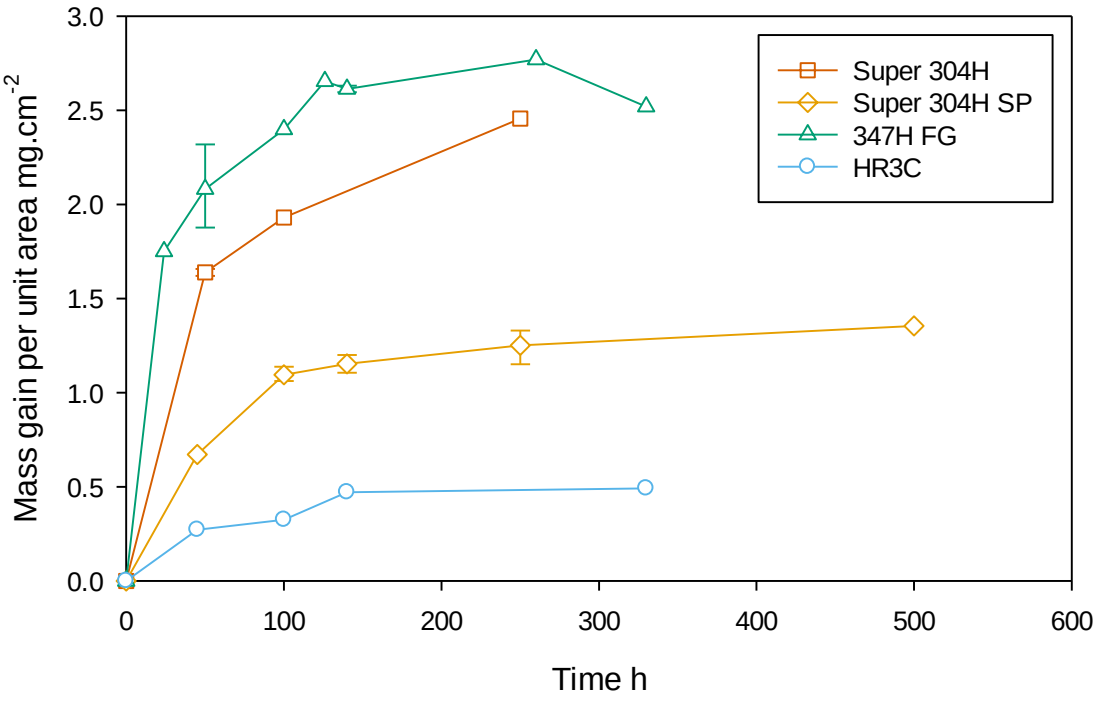

Figure 4.71 – Mass gain data for austenitic steels oxidised in deoxygenated steam at 700 °C. Unlike oxidation in air, shot peened Super 304H displayed larger mass gain than HR3C at 700 °C. Error bars show the range where multiple experiments were undertaken.

4.4.1.2 Oxide Thickness Measurements after Oxidation in Deoxygenated Steam

Oxide thickness measurements were taken of the three identified oxide layers grown in steam on 347HFG and Super 304H. These were the outer iron rich oxide, the inner spinel oxide, and the thin chromium rich base layer. The results from each temperature can be found in Figure 4.72. Note that for comparison purpose, 347HFG thickness data for oxidation times above 300 hours at 650 °C has been removed from the figure. The full set of data, accompanied by a graph for Super 304H of equivalent scale can be found in Figure 4.73. The total thickness measurement was calculated from the sum of the thicknesses of the three individual layers. Super 304H recorded slightly lower total oxide thicknesses than 347HFG at all temperatures. There were differences in the temperature and time dependences of the spinel and outer oxide layers for both 347HFG and Super 304H. At 600 °C the thickness of both layers was approximately equal for all oxidation times for both alloys. At higher temperatures the outer layers had larger thicknesses than the spinel layers. This effect was slightly more noticeable at 700 °C and also increased with oxidation time. A chromium rich base oxide was absent from exposures of 50 hours at 600 °C for both 347HFG and Super 304H, and largely absent after longer periods at the same temperature resulting in a very low average thickness.

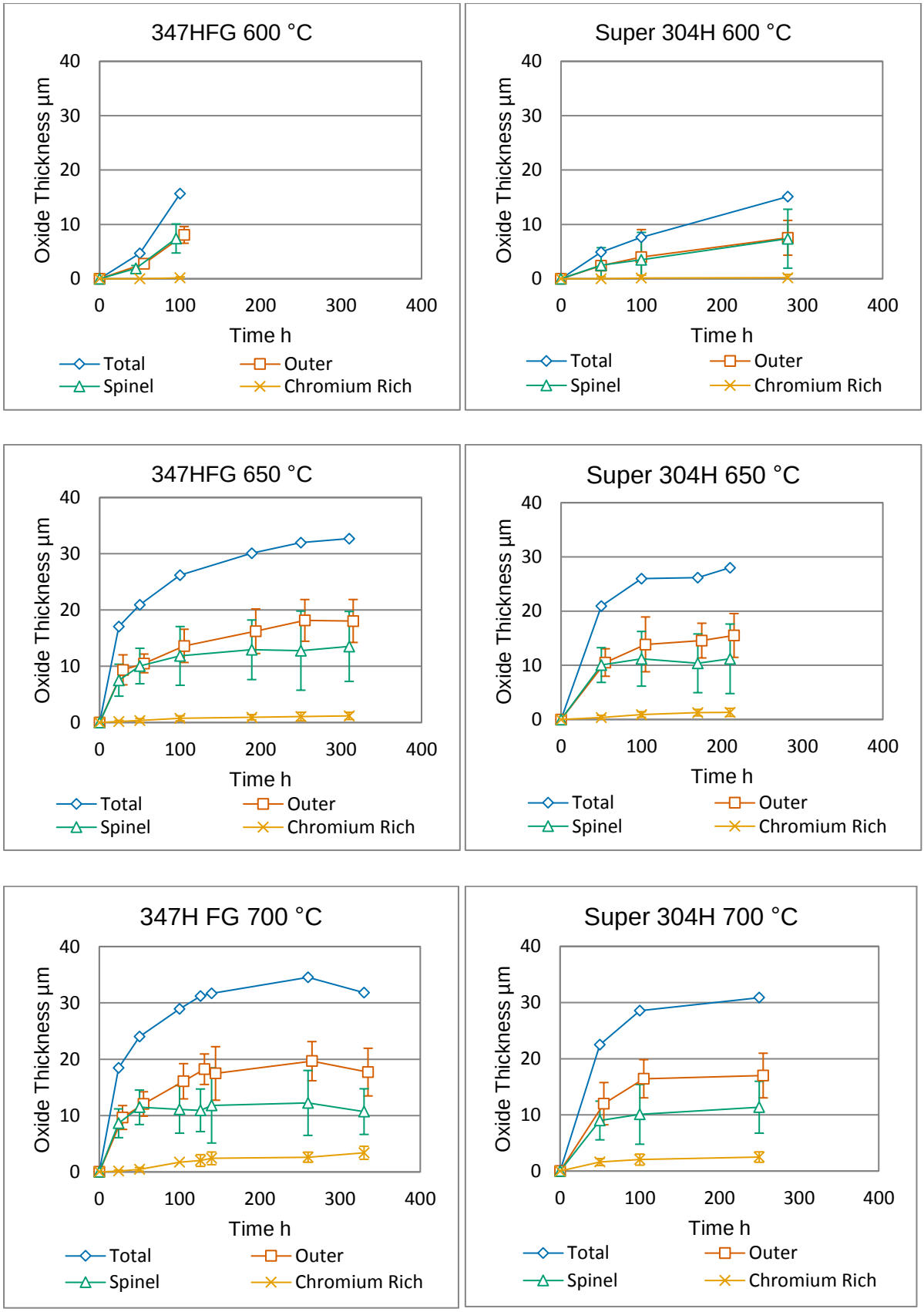

Figure 4.72 – Oxide thickness measurements for 347HFG and Super 304H oxidised in deoxygenated steam. Data for the total thickness was taken from the sum of the individual layer thicknesses. >1000 hours thickness data for 347HFG has been omitted for comparison purposes and can be found in Figure 4.73. At 650 and 700 °C, the outer oxide grows at a slightly faster rate than the spinel oxide on both steels.

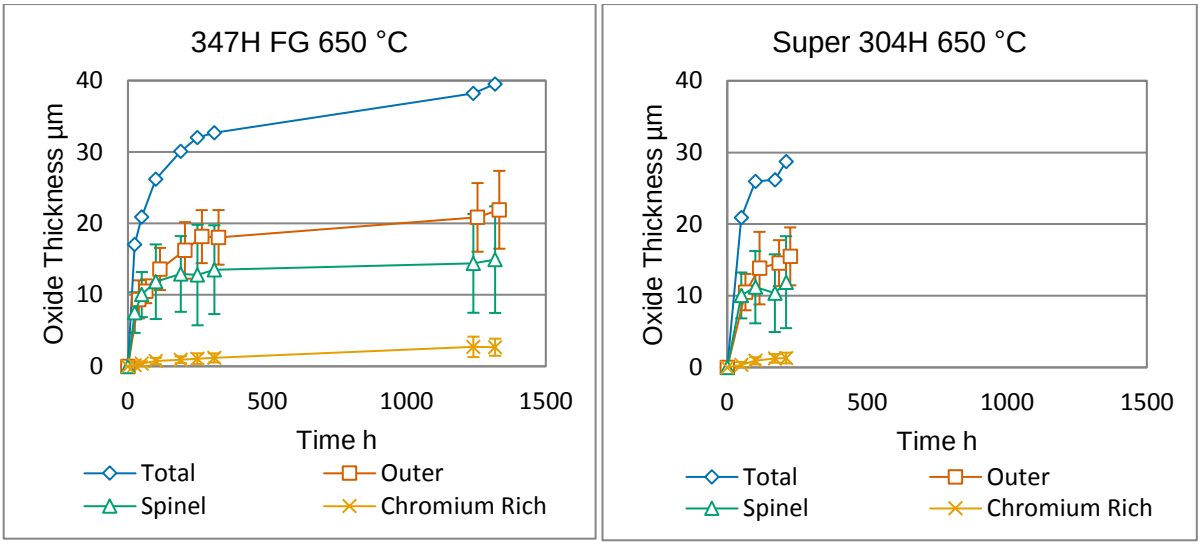

Figure 4.73 – Oxide thickness measurements of 347HFG and Super 304H oxidised in deoxygenated steam for up to 1300 hours at 650 °C. Data for the total thickness was taken from the sum of the individual layer thicknesses.

4.4.2 Oxide Morphology after Oxidation in Deoxygenated Steam

4.4.2.1 347HFG

4.4.2.1.1 Visual Observations of 347HFG after Oxidation in Deoxygenated Steam

The inner surface of 347HFG after oxidation in deoxygenated steam appeared a lighter grey than was common after oxidation in air. The surface was generally matt and occasionally slightly glossy. The reader is reminded that the samples in the current section did not spall. Samples that exhibited spallation following oxidation in what was considered to be improperly deoxygenated steam can be found in Section 1.6. Photos of the sample surfaces are shown in Figure 4.74 and Figure 4.75.

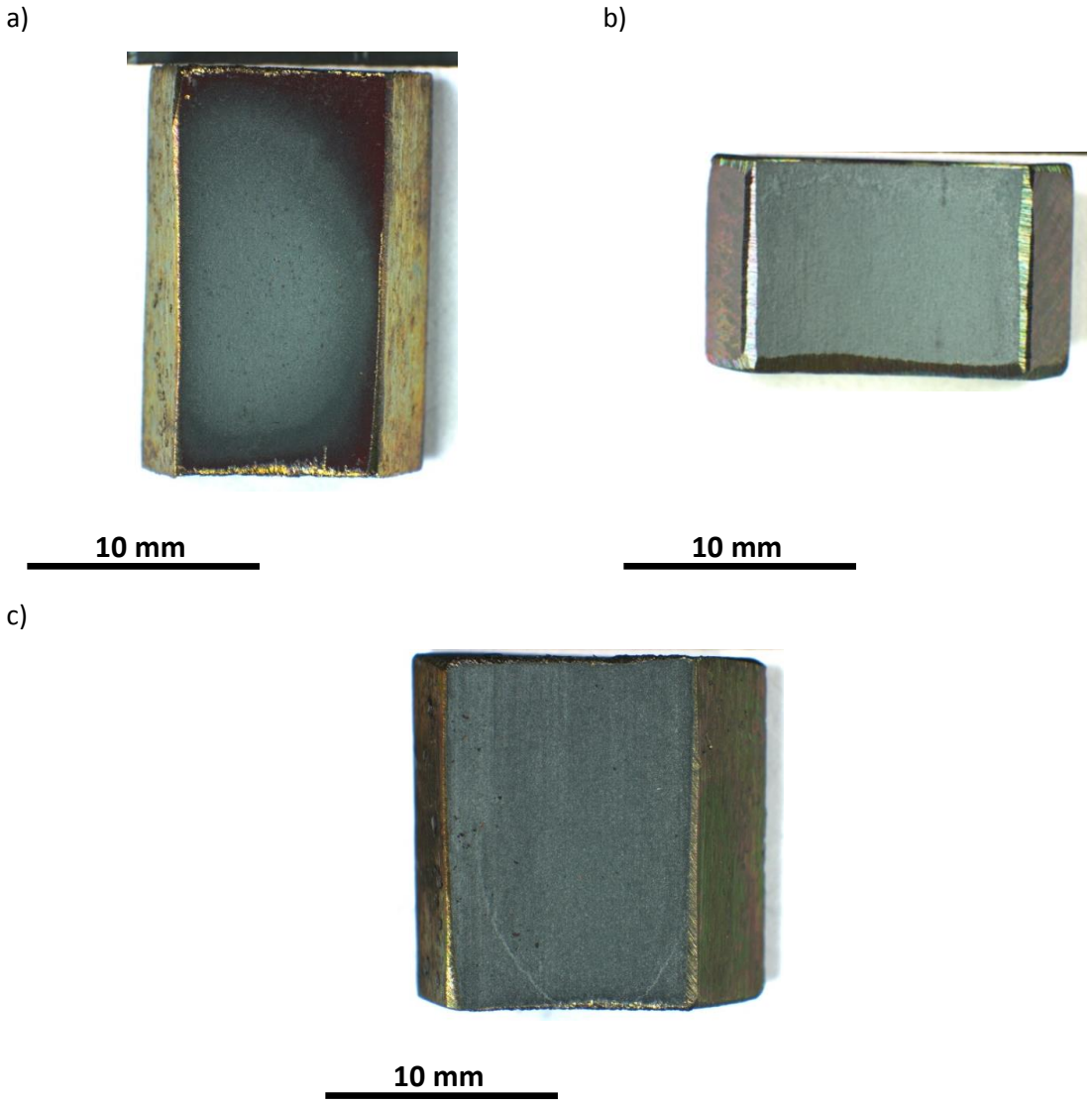

Figure 4.74 – Macro images of 347HFG inner surface after oxidation in deoxygenated steam for 100 hours at a) 600 °C, b) 650 °C, c) 700 °C.

The morphology of the inner surface did not notably change after oxidation in deoxygenated steam for longer periods, as illustrated by Figure 4.75.

a) b)

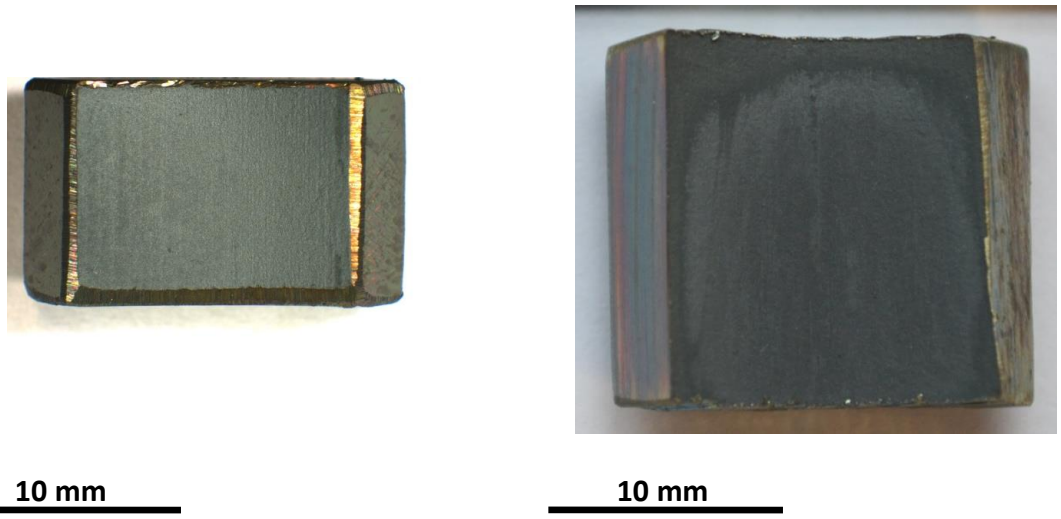

Figure 4.75 – Macro images of 347HFG inner surface after oxidation in deoxygenated steam for a) 310 hours at 650 °C, b) 260 hours at 700 °C.

4.4.2.1.2 SEM Surface Analysis of 347HFG after Oxidation in Deoxygenated Steam

The inner surface topography of 347HFG oxidised in deoxygenated steam as imaged using an SEM exhibited variable morphology as shown by Figure 4.76, Figure 4.77 and Figure 4.78.

a)

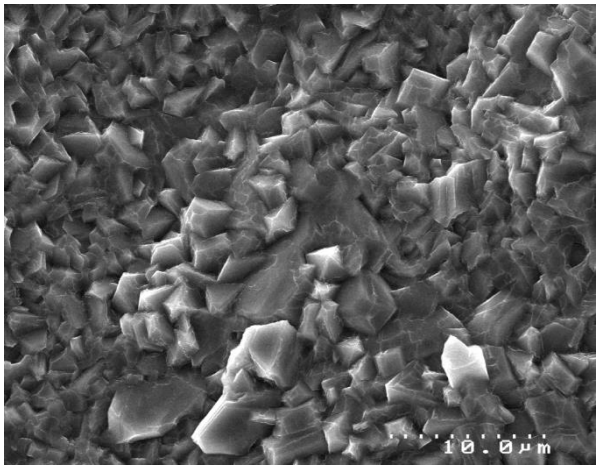

Figure 4.76 – SEI SEM image of 347HFG inner surface topography after oxidation in deoxygenated steam at 600 °C for 100 hours.

a)

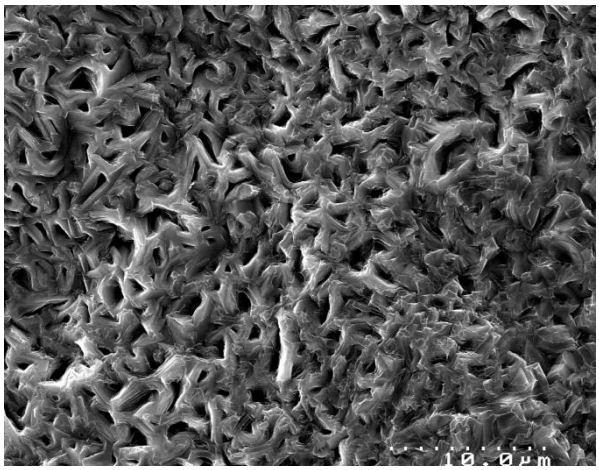

Figure 4.77 – SEI SEM images of 347HFG inner surface topography after oxidation in deoxygenated steam at 650 °C for 100 hours.

a)

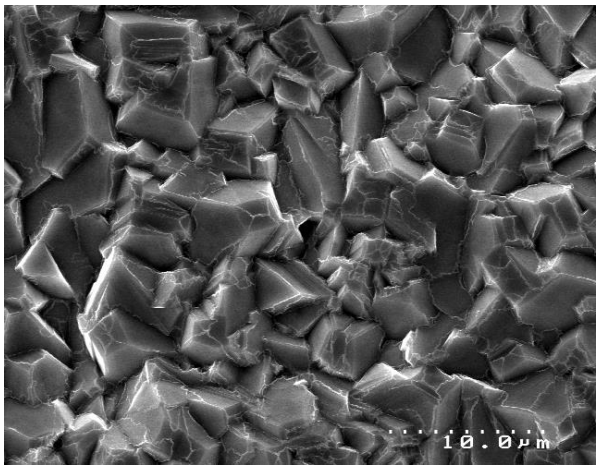

Figure 4.78 – SEI SEM images of 347HFG inner surface topography after oxidation in deoxygenated steam at 700 °C for 50 hours.

4.4.2.1.3 SEM Cross-Section Analysis of 347HFG after Oxidation in Deoxygenated Steam

BSE SEM cross-section micrographs showed an increase in scale thickness with increasing time and temperature. The scale at all temperatures was duplex. Porosity was apparent in the outer oxide at all temperatures and oxidation times, in contrast with little outer oxide porosity after oxidation in air. Porosity was generally spread evenly throughout the outer oxide, sometimes concentrating towards the middle of the layer. The distribution and extent of porosity did not seem to be temperature or time dependent. The spinel oxide grew to consume alloy grains. At 600 °C alloy grains at the surface were only partially consumed by the oxidation front. This was evident by the absence of the thin, dark chromium rich oxide film that was present where alloy grain boundaries were in contact with the oxidation front. At 650 and 700 °C after 100 hours or more, a chromium rich film was present as a

boundary between oxidised grains and the unoxidised alloy, impeding further internal oxidation. With increasing time and temperature the oxidation front had, in places, continued into subjacent grains leading to spinel morphology that consisted of two or more prior austenite grains encompassed by a chromium rich film as illustrated by Figure 4.79 d) and f). The chromium rich layer increased in thickness with time and temperature. On samples with thicker oxides, hairline cracks that ran parallel with the surface were visible within the spinel layer towards the spinel/outer oxide interface. These often intercepted the base of the outer oxide layer between spinel oxide of prior austenite grains.

4.4.2.1.4 Oxide Area Maps of 347HFG after Oxidation in Deoxygenated Steam

Figure 4.80 provides qualitative analysis of the oxide grown on 347HFG in deoxygenated steam. The sample, after oxidation for 1300 hours at 650 °C, consisted of a porous iron rich outer oxide and inner spinel which had consumed more than one austenite grain during oxidation. From the elemental EDX maps there is evidence of chromium and manganese depletion in the alloy below the chromium rich oxide. Nickel was enriched in these areas. Lighter precipitates appear between oxidised grains in the spinel layer. The element maps of nickel and oxygen suggest these are areas with a high concentration of metallic nickel. The chromium rich oxide corresponds to areas of nickel depletion. Manganese is enriched in these areas.

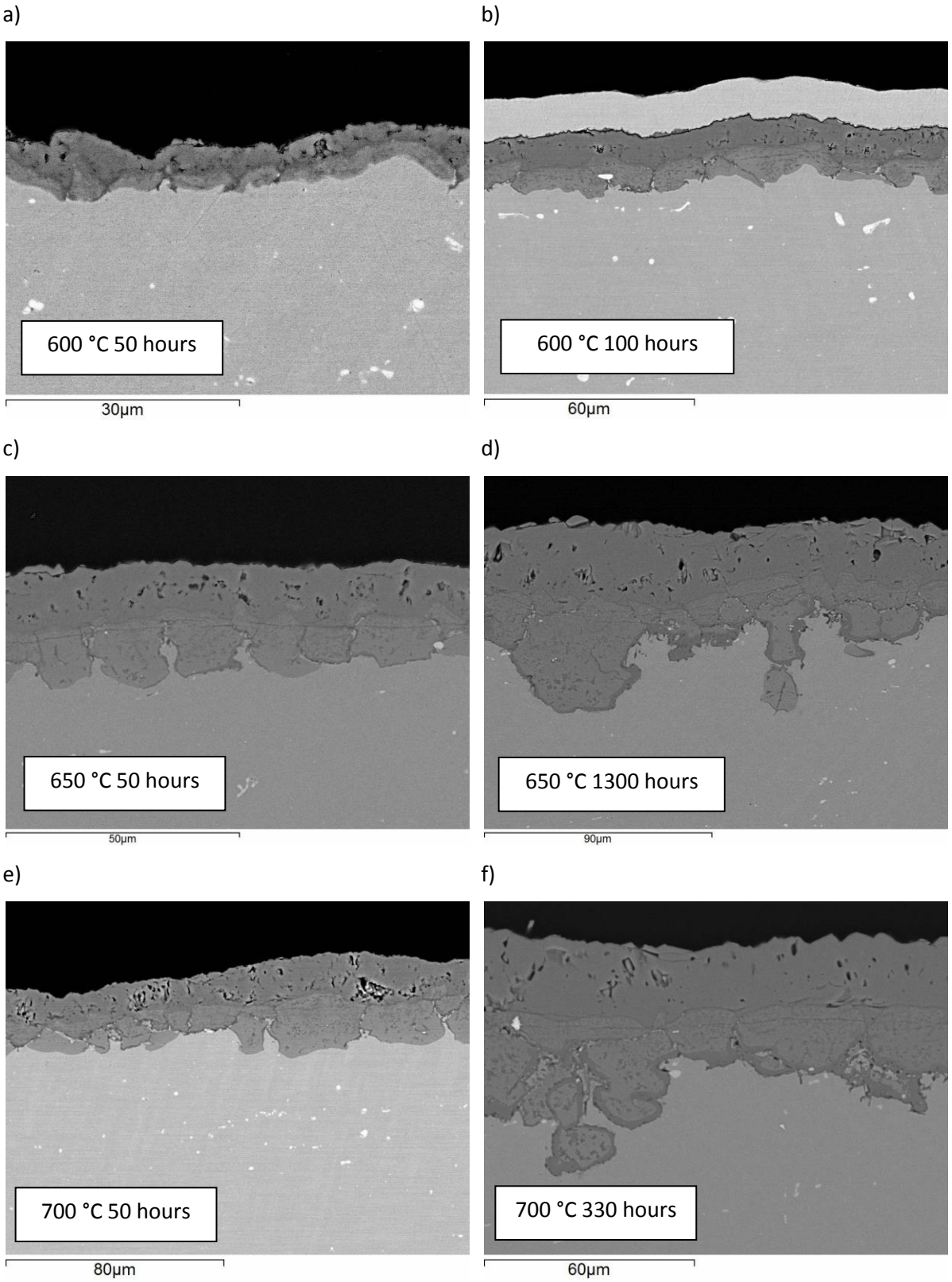

Figure 4.79 – Backscatter SEM images of 347HFG oxide morphology. The outer oxide formed during oxidation in deoxygenated steam was often porous. Where internal oxidation had consumed entire prior austenite grains (650, 700 °C >50 hours), a dark protected film had developed, inhibiting further internal oxidation.

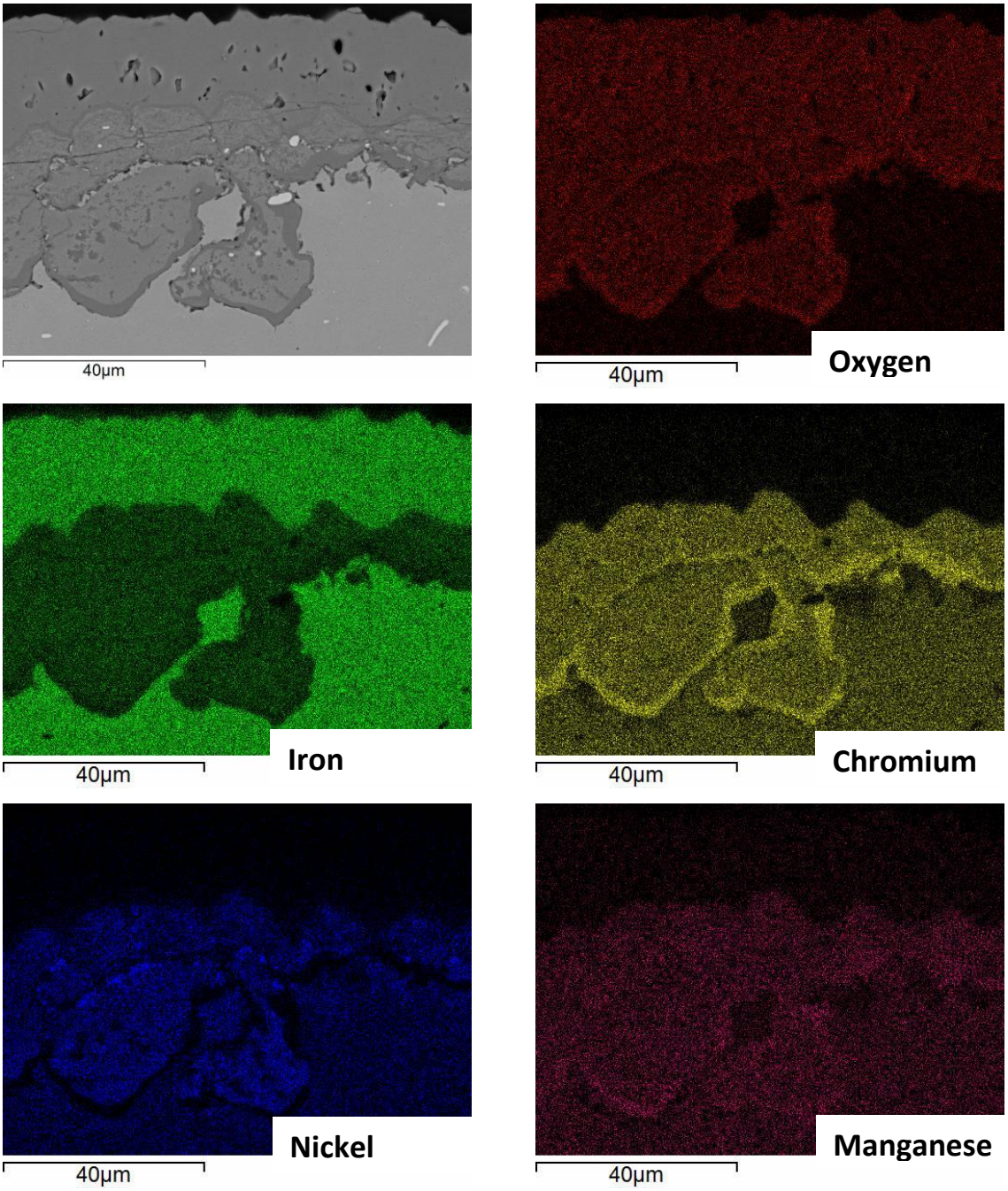

Figure 4.80 – EDX element area map for a cross-section of 347HFG oxidised in deoxygenated steam for 1300 hours at 650 °C. Defined chromium and manganese enrichment is visible at the base of the oxide and corresponding depletion of nickel and iron. Chromium and manganese are depleted below these areas. The spinel contains iron, chromium, nickel and manganese and the outer oxide exclusively iron.

4.4.2.1.5 EDX Analysis of 347HFG after Oxidation in Deoxygenated Steam

Spot analysis was conducted on the oxide grown after 260 hours at 700 °C. Spots 5 and 6 relate to the outer iron rich oxide. The cation / anion ratio in Table 4.8 falls in between that expected for either Fe_2O_3 or Fe_3O_4 growth. As explained in Section 4.3.2.1.5, EDX analysis struggles with accurate measurement of lighter elements such as oxygen. Comparisons were made between the oxygen content of the outer oxide grown in air and deoxygenated steam, and the oxide in air consistently

reported a higher oxygen content. Complimentary techniques (XRD and optical analysis) were also employed, and the outer iron rich oxide grown on 347H FG and Super 304H in deoxygenated steam was determined to be formed of >90% Fe_3O_4.

Spots 1 and 2 show the dark oxide film at the alloy/oxide grain boundary to be rich in chromium. The ratio of elements in Table 4.8 suggest the most likely oxide is a corundum of the form $(Fe,Cr)_2O_3$. However, because of EDX accuracy, and considering the outer oxide has a similar ratio of anions and cations, but is suggested to be magnetite, it is likely that the chromium rich film is $FeCr_2O_4$. Manganese is also slightly enriched at these locations, and the areas maps show it to be enriched along the oxide film, so a $(Fe,Cr,Mn)_3O_4$ spinel is also likely.

Spots 3 and 4 contain a lower oxygen content than the spots on the outer oxide and protective film oxide. This suggests that nickel is (at least partially) in metallic form, and the oxide is likely to be a $(Fe,Cr,Mn)_3O_4$ spinel within a metallic nickel matrix, with a higher fraction of Fe than in the protective oxide film. This would align with the findings of previous researchers [100, 111], where the oxidation of nickel appears to be sensitive to the pO_2 of the carrier gas.

Spots 7 and 8 relate to areas of unoxidised substrate (the oxygen in spot 8 being picked up from the surrounding spinel). Spot 7 shows a depletion of Cr and Mn, and an enrichment of Fe and Ni. This is similar to that found after oxidation in air, but to a greater degree. Spot 8 is thought to be a metallic nickel precipitate resulting from selective oxidation of Fe, Cr, and Mn.

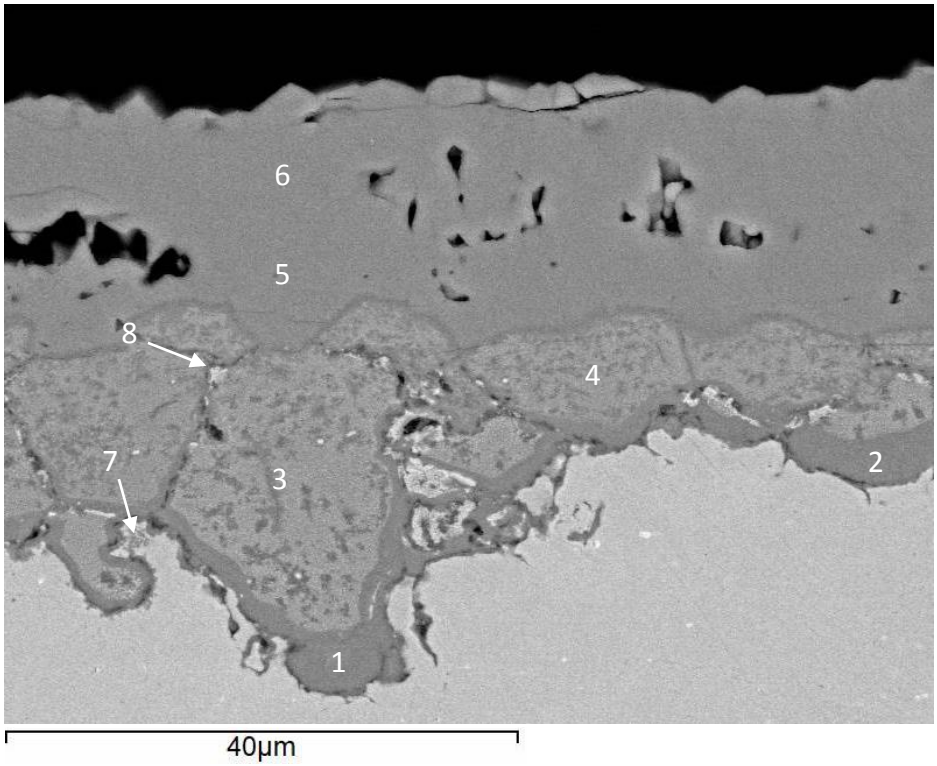

Figure 4.81 – BSE-SEM micrograph of oxide grown on 347HFG in deoxygenated steam at 700 °C for 260 hours. Numbers mark areas of EDX analysis. The dark oxide at the alloy/scale interface contains the highest concentration of chromium and coincides with a depletion of nickel. The alloy immediately subjacent to the oxide is partially depleted of chromium as shown by spot 7.

Table 4.8 – Composition in at. % from EDX analysis of oxide grown on 347HFG in deoxygenated steam at 700 °C for 260 hours.

Spot	Oxygen	Iron	Chromium	Nickel	Manganese
1	59.8	12.2	23.3	0.4	1.3
2	62.0	11.1	24.9	0.8	1.2
3	51.5	20.3	17.2	9.6	1.4
4	53.7	18.7	17.2	9.7	0.7
5	59.4	39.5	0.7	0.4	-
6	61.8	37.8	0.4	-	-
7	-	72.9	12.47	14.3	0.3
8	38.8	19.4	8.6	32.8	0.4

4.4.2.1.6 Porosity and oxide pull out in 347HFG after Oxidation in Deoxygenated Steam

During sample preparation, the presence of a porous outer oxide sometimes resulted in oxide pull out localised around pores. Figure 4.82 a) illustrates the occurrence of oxide pull out in a porous area of the oxide. Close inspection of the voids suggested that oxide, connecting nearby pores, had been removed during the polishing stage. In Figure 4.82 b) there is very little pull out.

a) b)

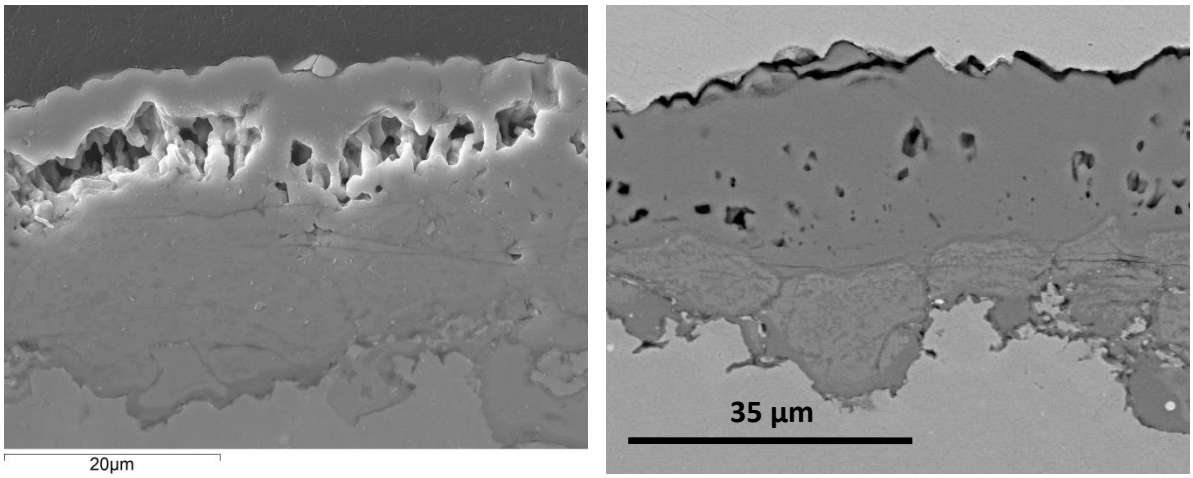

Figure 4.82 – Examples of porous outer oxide condition on 347HFG oxidised in deoxygenated steam. a) 190 hours at 650 °C showing oxide pull out in porous region, b) 1200 hours at 650 °C showing porous oxide visibly free of pull out.

4.4.2.1.7 Optical Microscopy of 347HFG after Oxidation in Deoxygenated Steam

Different oxide phases in the outer oxide were identified through optical microscopy as illustrated in Figure 4.83. The outer oxide consisted almost exclusively of the darker phase, believed to be magnetite. Small patches of a phase that appeared light grey in colour, believed to be haematite was occasionally found within the magnetite layer. The haematite phase tended to outline pores within the layer. The thickness at a given point of the phase was of the order of a micron. Haematite around the perimeter of pores was evidence that pores were formed during oxidation and were not a result of oxide pull out.

After oxidation in effectively deoxygenated steam, the outer oxide never contained more than approximately 10% haematite. The dissociation pressure of haematite at 600 °C is approximately 7 x 10^{-16}, well below the pO_2 of approximately 1 x 10^{-8} of deoxygenated steam. Thermodynamically Fe_2O_3 is expected to form at the oxide/gas interface. The outer oxide formed in deoxygenated steam was over 90% Fe_3O_4 (usually 100%), suggesting equilibrium was not reached at the oxide/gas interface during the duration of the experiments.

a)

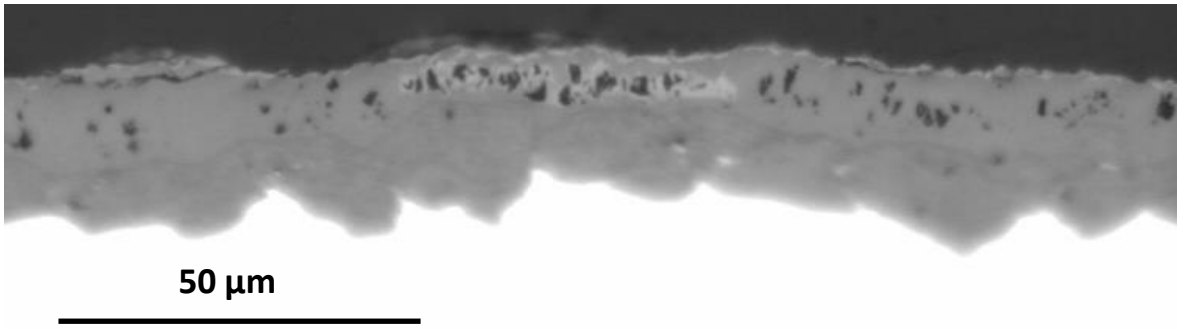

b)

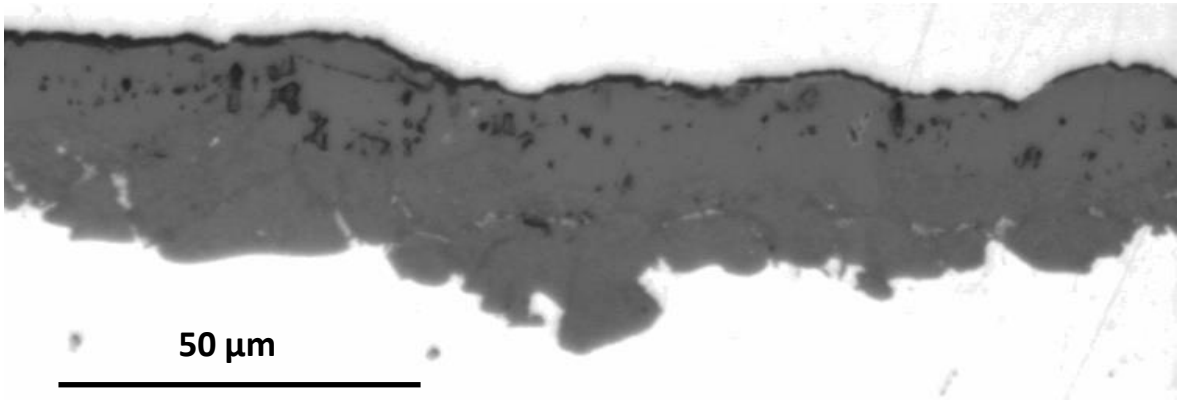

Figure 4.83 – Optical micrographs of oxide on 347HFG oxidised in effectively deoxygenated steam showing slight haematite fraction in the outer layer (lighter grey phase). a) 50 hours at 650 °C, b) 120 hours at 650 °C. No more than 10% haematite was present within the outer oxide of samples oxidised in effectively deoxygenated steam.

4.4.2.2 Super 304H

4.4.2.2.1 Visual Observations of Super 304H after Oxidation in Deoxygenated Steam

The reader is reminded that the samples in the current section did not spall. Samples that exhibited spallation following oxidation in what was considered to be improperly deoxygenated steam can be found in Section 4.5. The inner surfaces of Super 304H samples oxidised in deoxygenated steam were dull or light grey in colour, similar to 347HFG. Vertical defects on this alloy were still visible following oxidation. Photos of the sample surface are shown in Figure 4.84 and Figure 4.85.

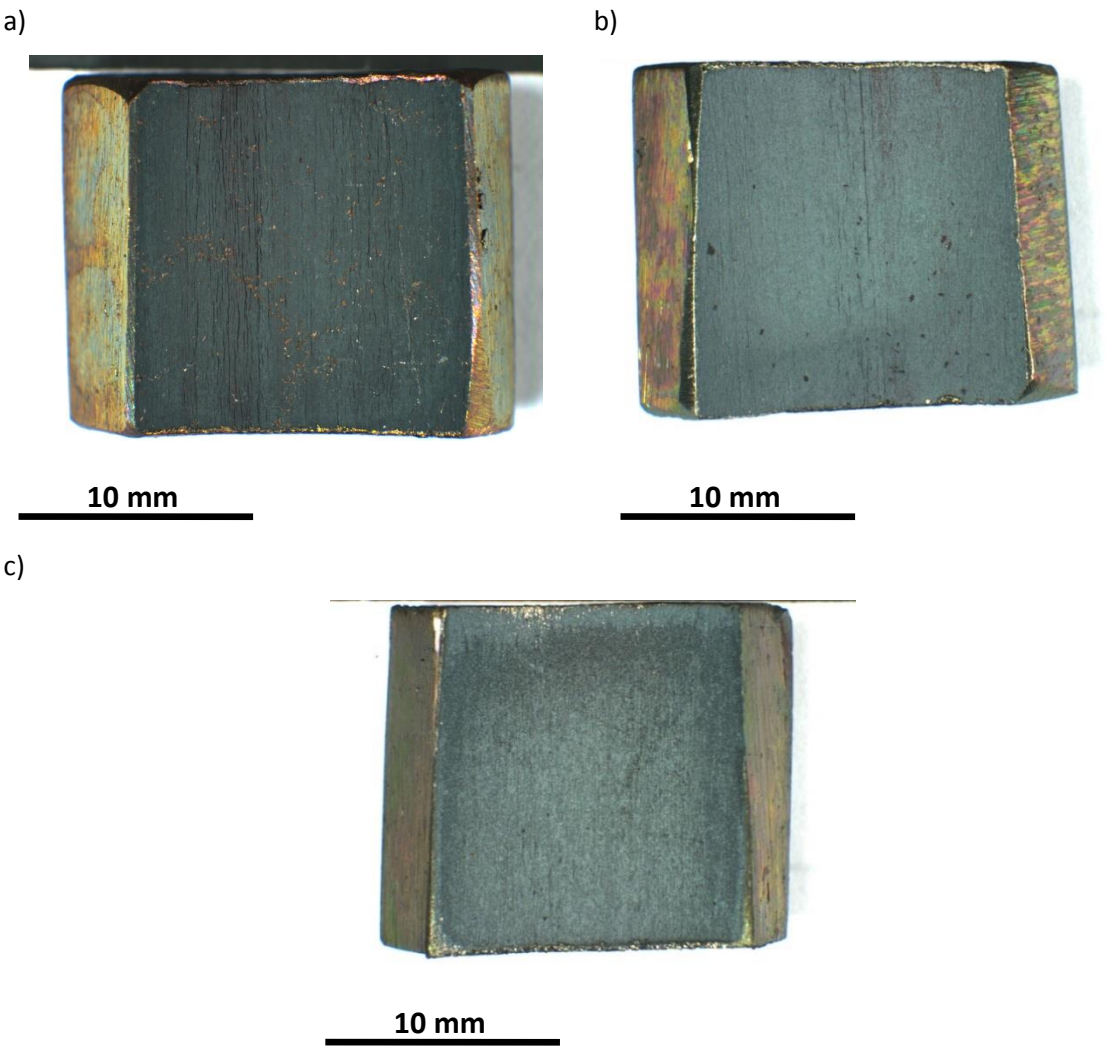

Figure 4.84 – Macro images of Super 304H inner surface after oxidation in deoxygenated steam for 100 hours at a) 600 °C, b) 650 °C, c) 700 °C. Inner surfaces were dull or light grey in appearance, similar to 347HFG. Vertical defects on this alloy were still visible following oxidation.

a)

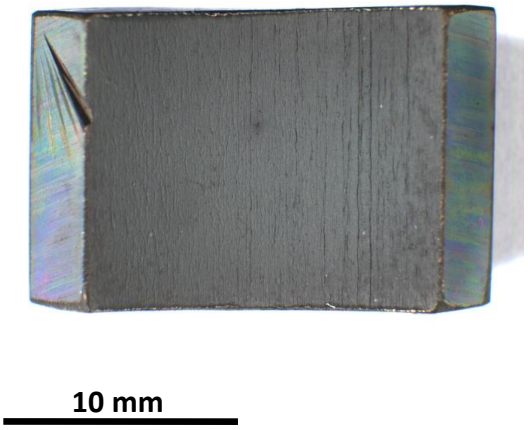

Figure 4.85 – Macro images of Super 304H inner surface after oxidation in deoxygenated steam for 170 hours at a) 650 °C. Inner surfaces were dull or light grey in appearance, similar to 347HFG. Vertical defects on this alloy were still visible following oxidation.

4.4.2.2.2 SEM Surface Analysis of Super 304H after Oxidation in Deoxygenated Steam

The inner surface topography of 304H oxidised in deoxygenated steam as imaged using an SEM exhibited variable morphology as shown by Figure 4.86 and Figure 4.87.

a)

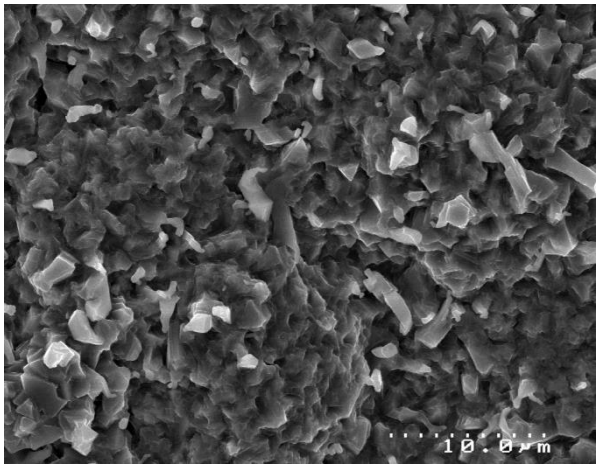

Figure 4.86 – SEI SEM images of Super 304H inner surface topography after oxidation in deoxygenated steam at 600 °C for 100 hours.

a)

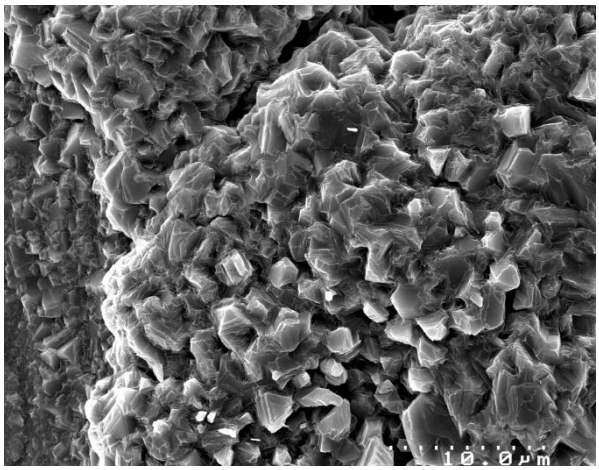

Figure 4.87 – SEI SEM images of Super 304H inner surface topography after oxidation in deoxygenated steam at 650 °C for 50 hours.

4.4.2.2.3 SEM Cross-Section Analysis of Super 304H after Oxidation in Deoxygenated Steam

The oxide grown on Super 304H oxidised in deoxygenated steam was duplex and increased with time and temperature. The largest increase in thickness was found between 600 and 650 °C. The outer oxide exhibited porosity at every exposure. Pores were distributed evenly throughout the outer layer and sometimes collected within the centre of the layer. This was the case except for oxidation after 50 hours at 600 °C, where the thin outer oxide exhibited porosity at the spinel/outer oxide interface. The pore fraction in the outer layer appeared slightly larger at the highest temperature, but this could have been a result of oxide pull out during sample preparation. At the interface between the alloy and spinel oxide dark chromium rich film had formed on samples oxidised for 100 hours or more at 650 °C and from 50 hours at 700 °C. The chromium rich layer was not present where the spinel oxide had not reached alloy grain boundaries, notably after oxidation at 600 °C. As with 347HFG, hairline cracks were visible within the spinel oxide. These cracks did not appear to increase in frequency or size significantly as oxidation time and temperature increased. Backscatter SEM images of Super 304H oxide morphology at various oxidation times and temperatures are shown in Figure 4.88.

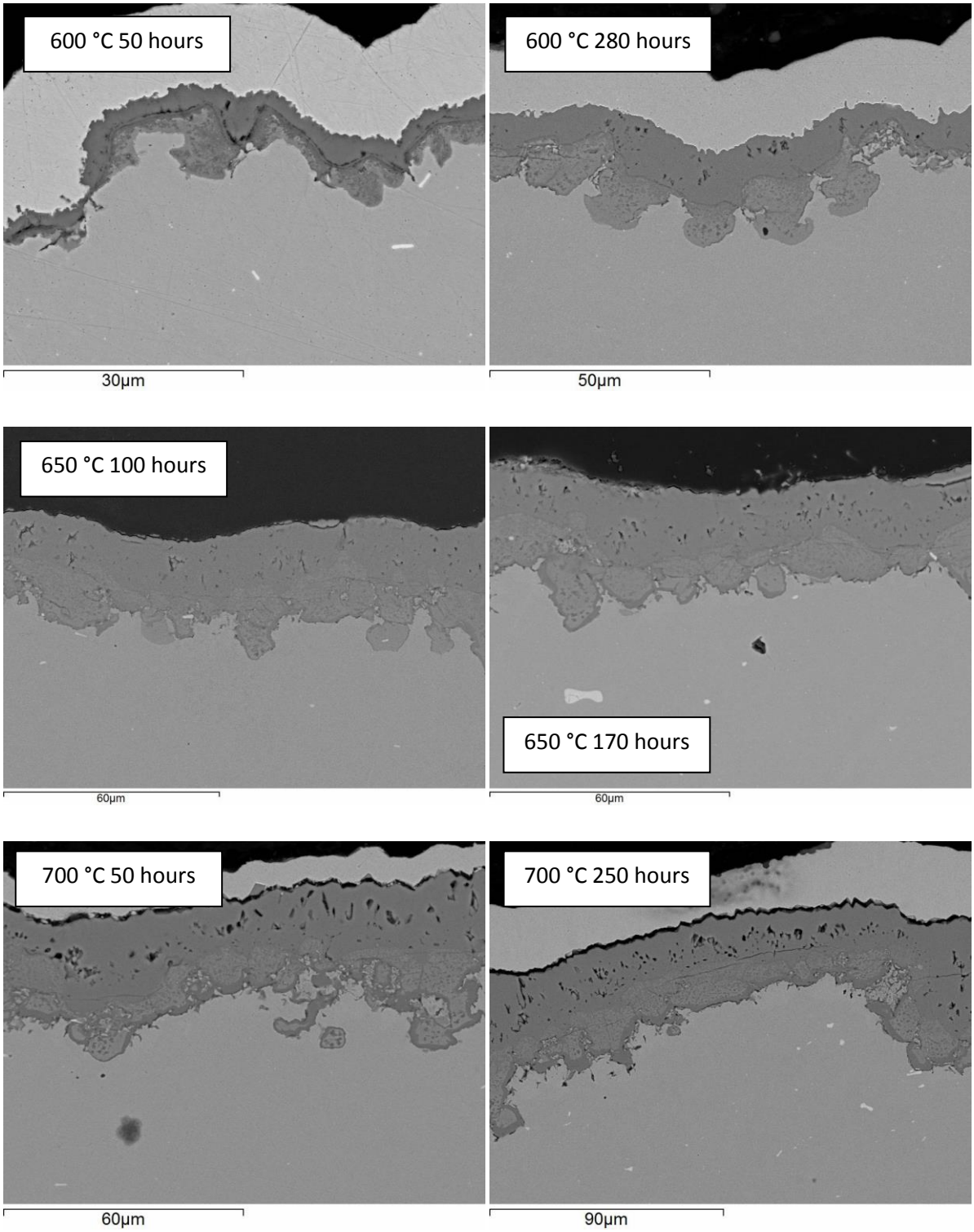

Figure 4.88 – Backscatter SEM images of Super 304H oxide morphology. As with 347HFG, a dark oxide film formed at the base of internally oxidised grains. The outer oxide was consistently porous.

4.4.2.2.4 Oxide Area Maps of Super 304H after Oxidation in Deoxygenated Steam

An EDX area map of the oxide grown on Super 304H after oxidation in deoxygenated steam for 100 hours at 700 °C is displayed in Figure 4.89. The element map shows there was a similar distribution of elements as found in the oxide of 347HFG in deoxygenated steam. There is a pronounced depletion in chromium and manganese within the substrate along the alloy/oxide interface. The depth of depletion is higher where alloy grain boundaries met the surface. In areas of chromium and manganese depletion, nickel was enriched. Light grey areas between oxidised grains in the spinel oxide were enriched in nickel and iron and depleted in chromium. It was unclear as to whether these were metallic precipitates or oxide. The outer oxide appeared to be exclusively iron oxide. Copper was present in the spinel oxide, the highest concentration was towards the inner/outer oxide interface.

4.4.2.2.5 EDX Analysis of Super 304H after Oxidation in Deoxygenated Steam

Quantitative analysis showed similar results to that of 347HFG oxidised in deoxygenated steam. An SEM micrograph of the sample surface with numbered analysis points is shown in Figure 4.90 and elemental quantification is shown in Table 4.9. Spots 1 and 2 correspond to a Cr-rich healing layer that appears to have formed at prior austenite grain boundaries. Copper is depleted in these areas and the oxide likely comprises of a mixture of $FeCr_2O_4$ and $(Fe,Cr,Mn)_3O_4$ spinel.

Spots 3 and 4 correspond to the inner oxide. The lower oxygen fraction in these areas suggest the oxide is a $(Fe,Cr,Mn)_3O_4$ spinel interspersed with metallic nickel. Copper is present in a similar quantity to the bulk alloy, and most likely remains the least mobile and in metallic form.

Spot 5 corresponds to the outer iron rich oxide, and as with 347HFG, is considered to be formed from >90% Fe_3O_4.

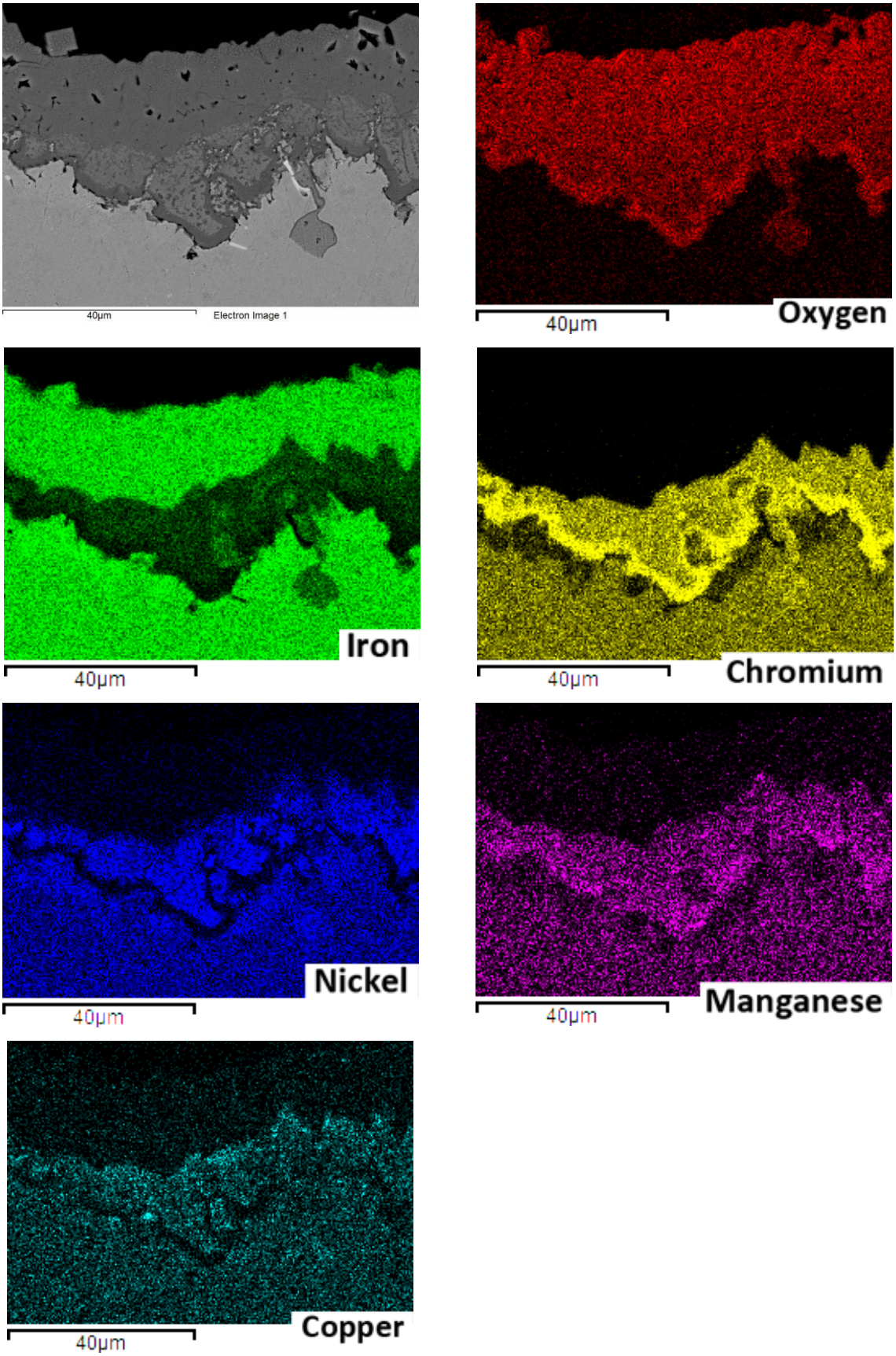

Figure 4.89 – EDX area map of Super 304H after oxidation in deoxygenated steam for 100 hours at 700 °C. The duplex oxide consists of an iron rich outer layer and internal spinel containing iron, chromium, nickel, manganese and copper. At the base of the spinel chromium and manganese are enriched, and nickel is depleted. In the alloy directly beneath this, chromium and manganese are depleted, and nickel is enriched.

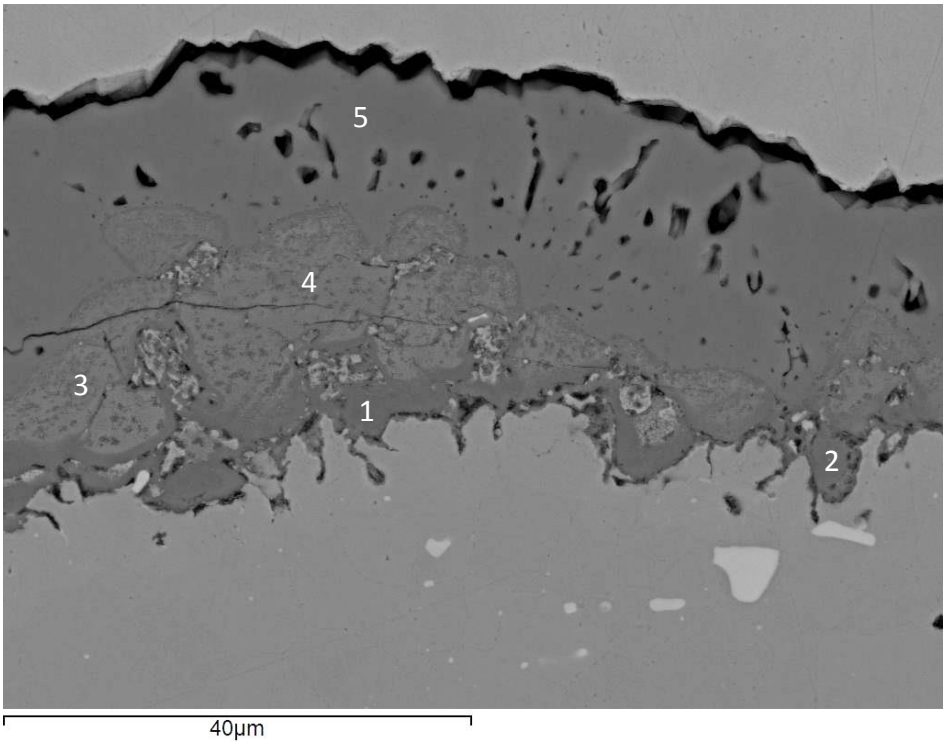

Figure 4.90 – BSE-SEM micrograph of oxide grown on Super 304H in deoxygenated steam at 700 °C for 250 hours. Numbers mark areas of EDX analysis. The dark oxide at the alloy/scale interface contains the highest concentration of chromium and coincides with a depletion of nickel.

Table 4.9 – Composition in at. % from EDX analysis of oxide grown on Super 304H in deoxygenated steam at 700 °C for 250 hours.

Spot	Oxygen	Iron	Chromium	Nickel	Copper	Manganese
1	56.7	12.9	28.2	1.1	0.3	0.8
2	57.7	13.6	26.6	0.8	0.5	0.9
3	46.7	20.0	19.3	10.5	2.5	1.0
4	48.8	18.9	18.4	10.3	2.7	0.8
5	58.3	41.7	-	-	-	

4.4.2.3 Shot Peened Super 304H

4.4.2.3.1 Visual Observations of Shot Peened Super 304H after Oxidation in Deoxygenated Steam

Exposure in deoxygenated steam resulted in an oxide layer that was light grey/orange in colour and shiny. The dimpled surface finish from the peening process was clearly visible. Axial ridges partially concealed by the peening process were visible and the oxide formed did not visually differ from regions where shot peening had covered the surface effectively. No spallation was observed from samples of Super 304H SP oxidised in deoxygenated steam. Photos of the sample surface are shown in Figure 4.91 and Figure 4.92.

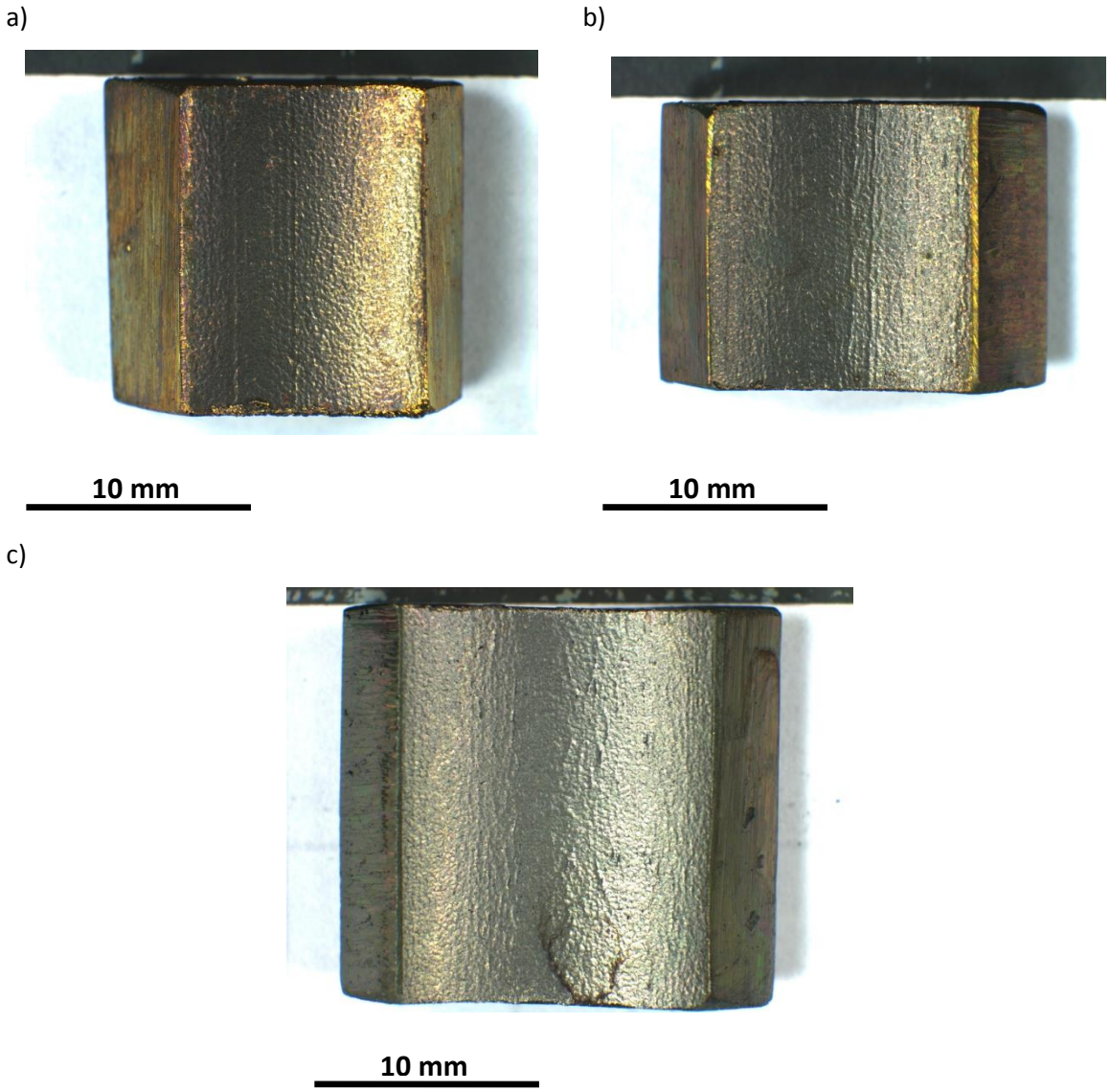

Figure 4.91 – Macro images of shot peened Super 304H inner surface after oxidation in deoxygenated steam for 100 hours at a) 600 °C, b) 650 °C, c) 700 °C. In contrast to the sometimes matt appearance of the alloy when oxidised in air, the inner surface after oxidation in deoxygenated steam was light grey/orange in colour and shiny following every exposure.

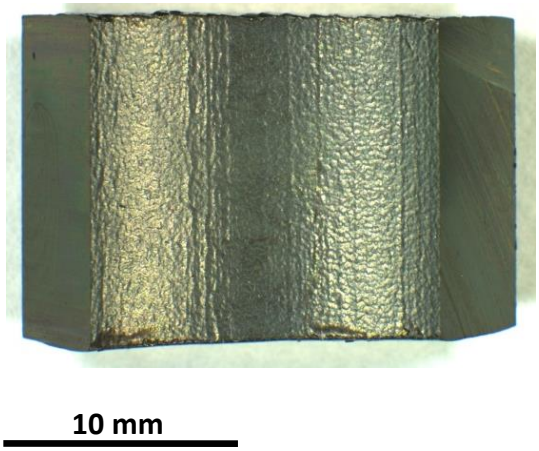

Figure 4.92 – Macro images of shot peened Super 304H inner surface after oxidation in deoxygenated steam for 250 hours at 650 °C. In contrast to the sometimes matt appearance of the alloy when oxidised in air, the inner surface after oxidation in deoxygenated steam was light grey/orange in colour and shiny following every exposure.

4.4.2.3.2 SEM Surface Analysis of Shot Peened Super 304H after Oxidation in Deoxygenated Steam

The inner surface morphology differed depending on the prior substrate deformation. In smooth regions, which occupied the majority of the inner surface, a dark and non-porous oxide had grown. Where the peening process had left ridges of metal protruding from the surface, thicker oxides had grown. This oxide became slightly porous at the tips of ridges. Thick oxide protruded from axial surface defects. The oxide in these areas was porous and scattered with small, thick whiskers. Small, thick platelets were sometimes found in clusters or scattered around the surface. The effect of increasing oxidation temperature was to produce a more uniform oxide in areas of properly peened surface. At 600 °C, the oxide was less uniform and speckled in a light grey, perhaps where crystallites had begun to form as with oxidation in air, but that a less protective oxide had covered. This is shown in the SEM micrographs in Figure 4.93. Figure 4.94 shows the small platelets and whiskers formed on areas of deformation caused by peening and the smoother oxide than that formed during air oxidation.

a) b)

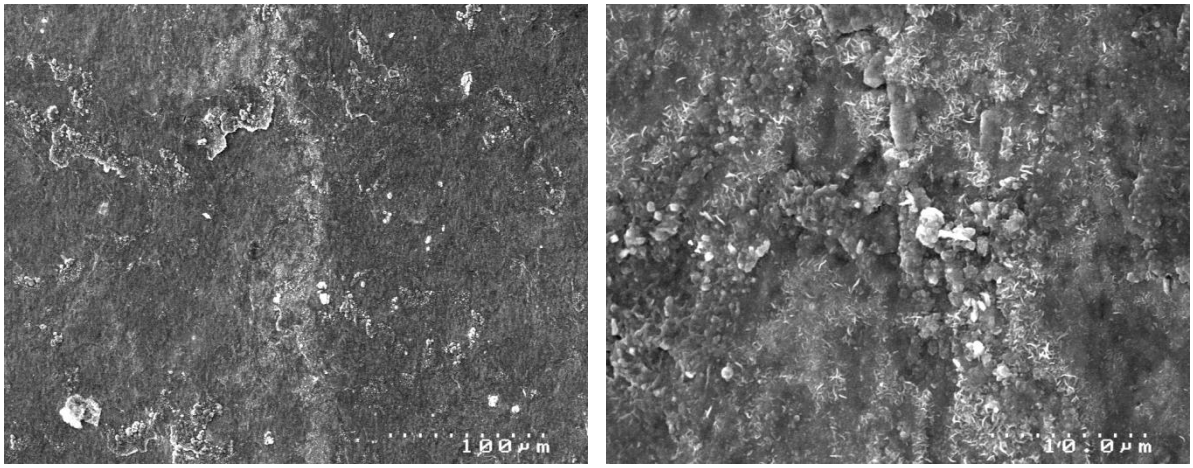

Figure 4.93 – SEI SEM images of shot peened Super 304H inner surface topography after oxidation in deoxygenated steam at 600 °C for; a), b) 100 hours. The oxide appeared thicker in deoxygenated steam, with less defined crystallites than in air.

a) b)

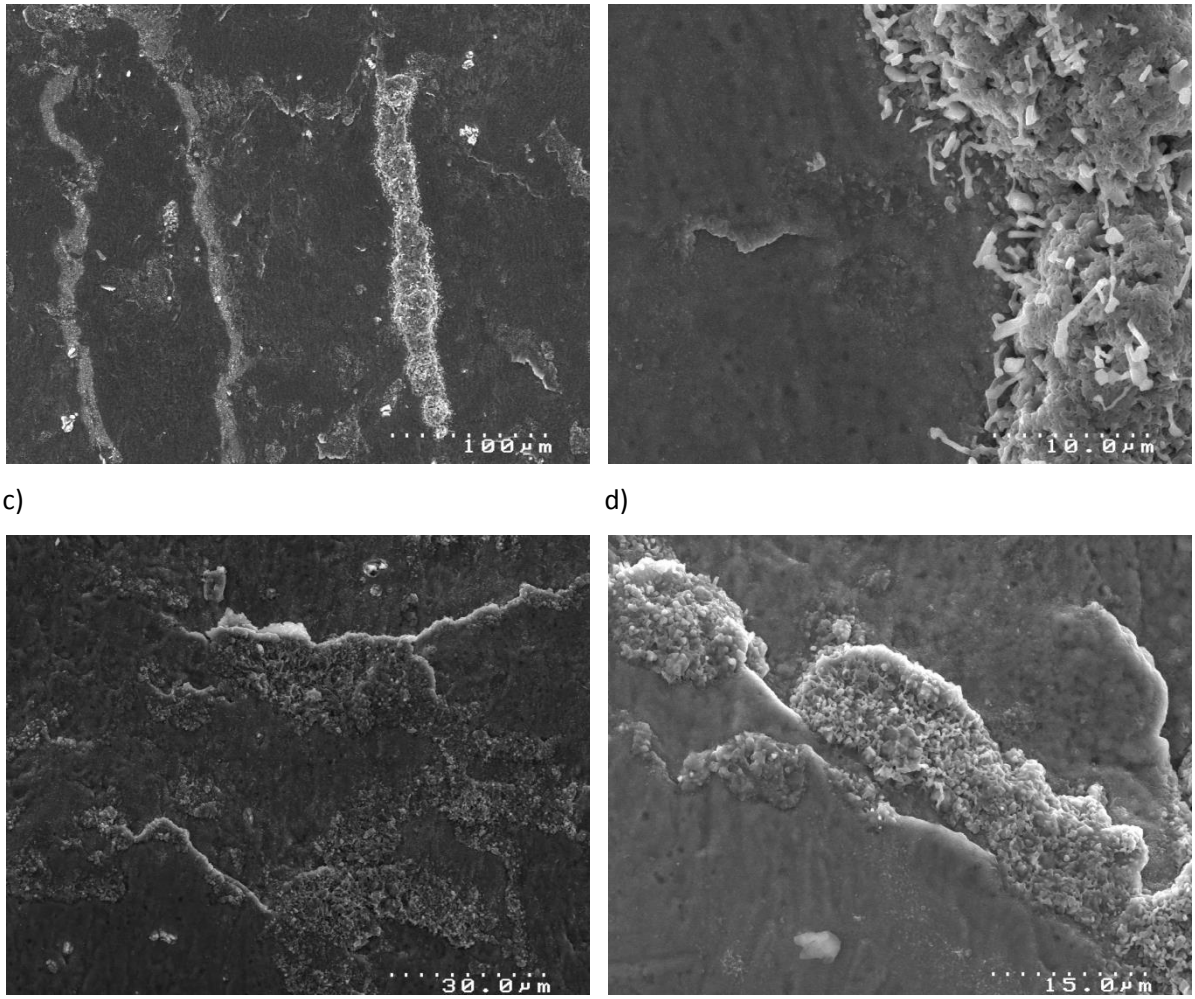

c) d)

Figure 4.94 – SEI SEM images of shot peened Super 304H inner surface topography after oxidation in deoxygenated steam at 650 °C for; a), b) 100 hours. Small platelets and whiskers formed on areas of deformation caused by peening. A smoother oxide than that formed during air oxidation covered the bulk after oxidation in deoxygenated steam.

4.4.2.3.3 SEM Cross-Section Analysis of Shot Peened Super 304H after Oxidation in Deoxygenated Steam

A thin oxide, thicker than that formed in air, covered the surface of Super 304H SP oxidised in deoxygenated steam. In areas where the film was particularly thin it appeared as a single layer. Where the scale was thicker two layers could be distinguished. It was unclear as to the growth direction of the inner layer. Thick oxide was located where axial defects had not been effectively removed by the peening process as in Figure 4.95 a).

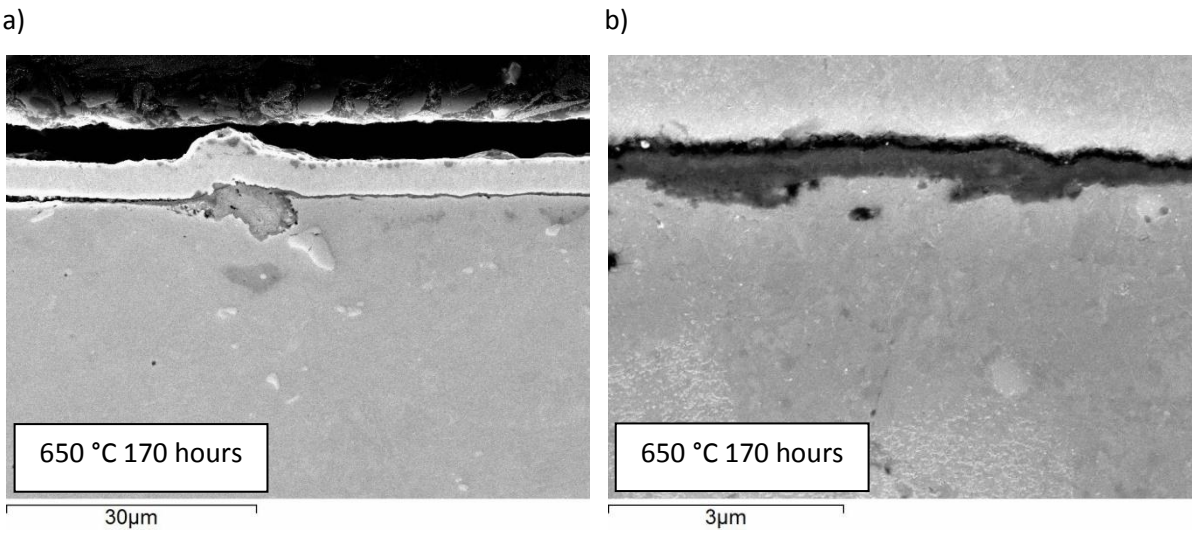

Figure 4.95 – Backscatter SEM images of shot peened Super 304H oxide morphology. a) ineffective shot peening left the alloy vulnerable to non-protective oxide growth (note, region is not representative of majority of surface). b) thicker oxide than found after oxidation in air was present after oxidation in deoxygenated steam.

4.4.2.3.4 Element Linescans of Shot Peened Super 304H after Oxidation in Deoxygenated Steam

The low thickness of the oxide grown on shot peened Super 304H in deoxygenated steam prevented accurate quantitative elemental analysis within the scale. An element linescan of a duplex area of oxide is shown in Figure 4.96 for Super 304H SP oxidised for 170 hours at 650 °C. The linescan provides a qualitative analysis of the oxide layers formed.

Considering the thickness of the oxide layer, it is likely that the composition is a mixture of Fe-Cr-Mn spinels, with concentration gradients changing from the alloy/oxide to oxide/gas surface. Nickel appears to be absent from the oxide layer, and the rising concentration towards the nickel plating is assumed to be due to erroneous detection from the nickel plating. However, the linescan does suggests three discrete layers, marked 1, 2, and 3 on the linescan.

Suggested oxide phases for each layer are as follows. Layer 1 has a higher oxygen content than layers 2 and 3, and is suggested to consist of Cr_2O_3 and $MnCr_2O_4$. Silicon is not shown on the linescan.

However, this is expected to have formed a thin film at the alloy/oxide interface. Layer 2 is suggested to be a (Fe,Mn)Cr_2O_4 spinel, where the Cr content decreases further away from the alloy surface, and Fe content increases away from the alloy surface. Layer 3 is suggested to be Fe_3O_4.

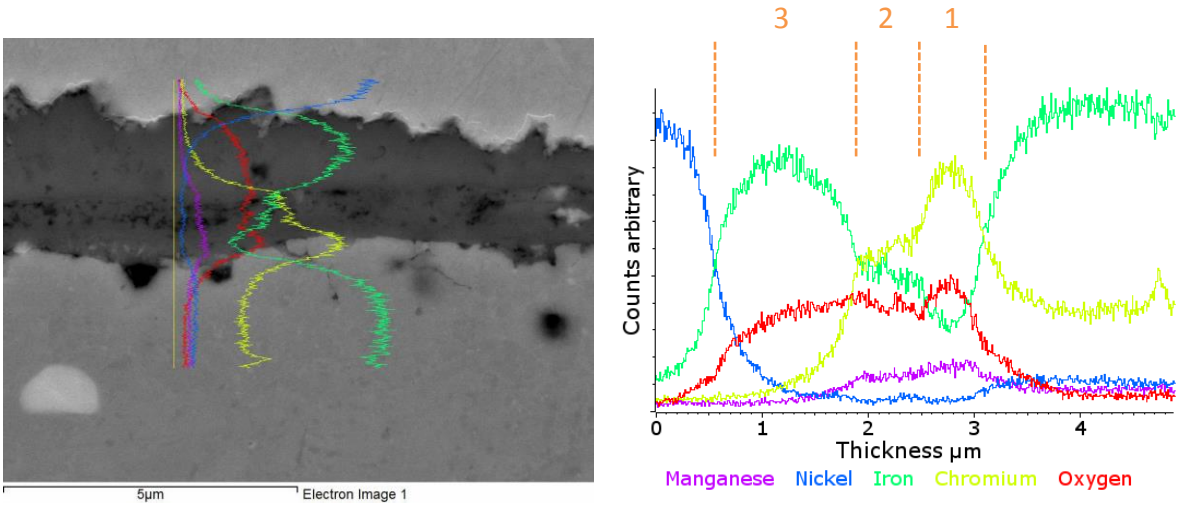

Figure 4.96 – EDX linescan of oxide grown on Super 304H SP after 170 hours at 650 °C showing duplex oxide, thicker than that grown in air.

4.4.2.4 HR3C

4.4.2.4.1 Visual Observations of HR3C after Oxidation in Deoxygenated Steam

No HR3C samples exhibited spallation throughout oxidation in deoxygenated steam. The inner surface of oxidised samples was either light or dark matt grey in appearance. Photos of the sample surface are shown in Figure 4.97 and Figure 4.98.

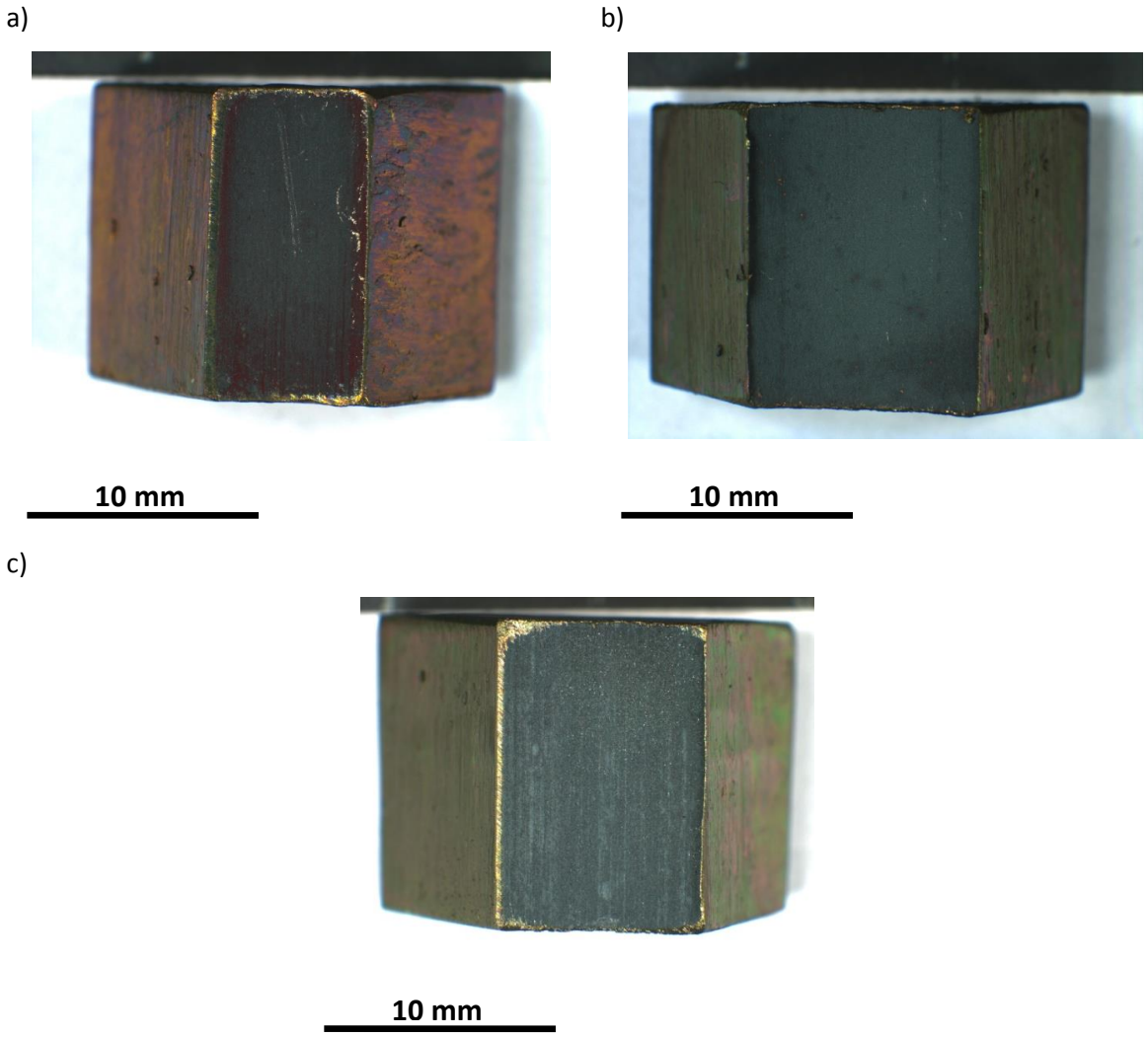

Figure 4.97 – Macro images of HR3C inner surface after oxidation in deoxygenated steam for 100 hours at a) 600 °C, b) 650 °C, c) 700 °C. The inner surface of HR3C resembled the matt grey appearance of the 18-8 austenitics.

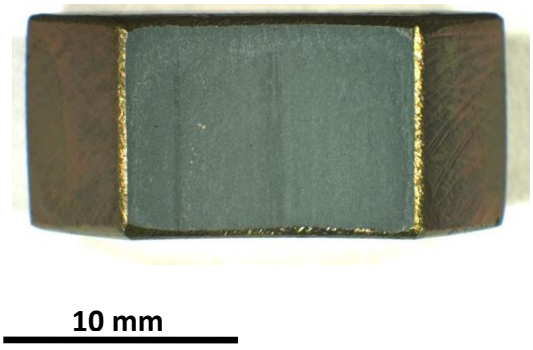

Figure 4.98 – Macro images of HR3C inner surface after oxidation in deoxygenated steam for 250 hours at 650 °C. The inner surface of HR3C resembled the matt grey appearance of the 18-8 austenitics.

4.4.2.4.2 SEM Surface Analysis of HR3C after Oxidation in Deoxygenated Steam

The alloy grain structure was less visible on deoxygenated steam oxidised samples of HR3C than air oxidised samples, indicating a thicker oxide exists on steam oxidised samples. At 600 °C, a porous oxide covered the surface and short, thick whiskers were scattered throughout the oxide between nodules as shown in Figure 4.99. At higher temperatures whiskers were absent and a continuous slightly porous oxide covered the surface as shown in Figure 4.100.

a) b)

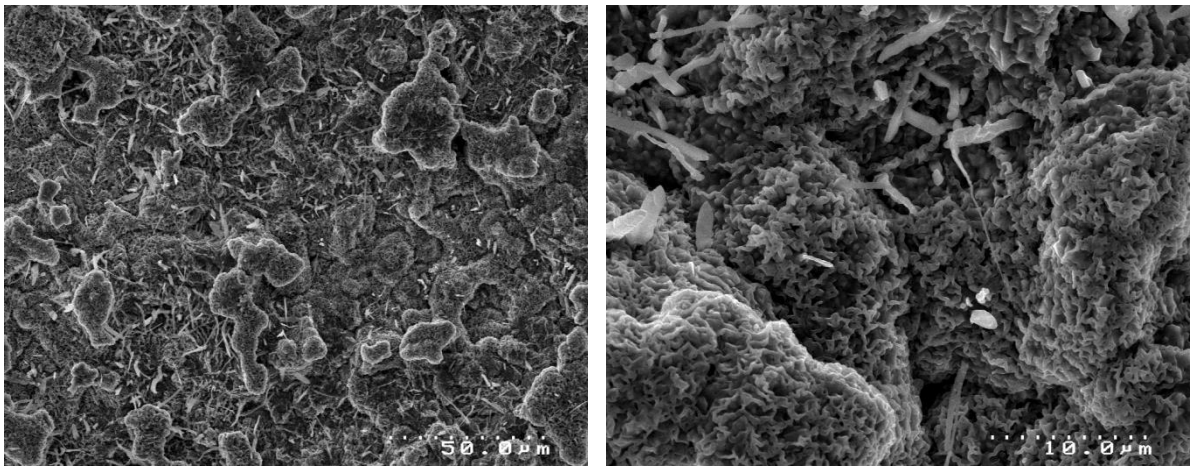

Figure 4.99 – SEI SEM images of HR3C inner surface topography after oxidation in deoxygenated steam at 600 °C for a), b) 100 hours. Short thick whiskers could be found that were absent at higher temperatures.

a) b)

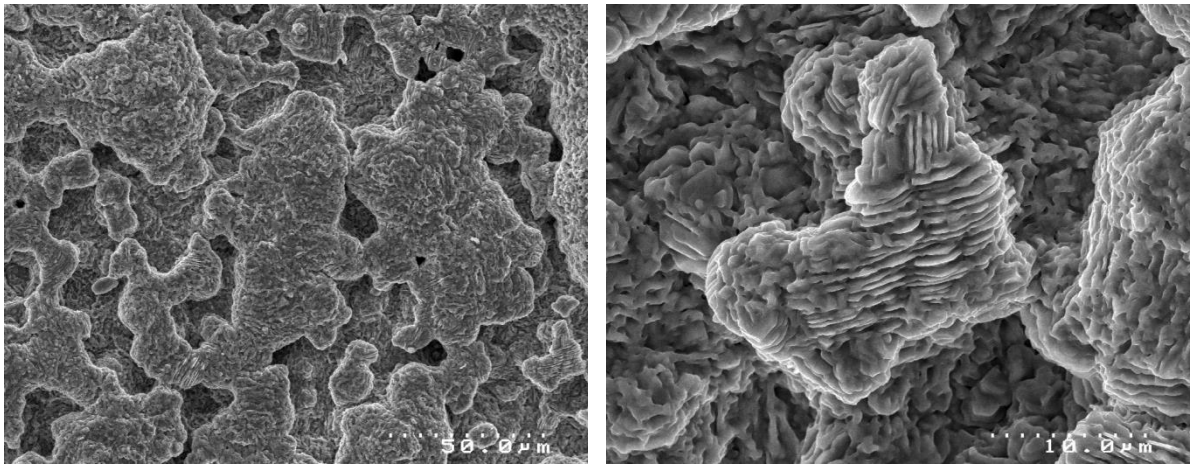

Figure 4.100 – SEI SEM images of HR3C inner surface topography after oxidation in deoxygenated steam at 650 °C after a), b) 100 hours. A slightly porous oxide covered the surface at 650 and 700 °C that sometimes featured repetition as in b).

4.4.2.4.3 SEM Cross-Section Analysis of HR3C after Oxidation in Deoxygenated Steam

A nodular, duplex oxide was found to grow on HR3C in deoxygenated steam. The oxide connecting nodules was thicker than that grown in air and had two observable layers. The outer oxide that existed

over large spinel nodules, and the thin spinel layer found between nodules, was porous. Porosity was concentrated at the spinel/outer oxide interface for outer oxide layers of small thickness. In thicker scales, pores were distributed evenly throughout the lower half of the outer oxide. This could indicate the presence of more than one iron rich oxide phase in the outer oxide. A chromium rich protective oxide film was present for all tests. Backscatter SEM images of Super HR3C oxide morphology at various oxidation times and temperatures after oxidation in deoxygenated steam are shown in Figure 4.101.

4.4.2.4.4 Oxide Area Maps of HR3C after Oxidation in Deoxygenated Steam

Area EDX maps for the oxidation of HR3C in deoxygenated steam for 500 hours at 650 °C and 100 hours at 700 °C can be found in Figure 4.102 and Figure 4.103. The outer oxide was iron rich, however, mapping was unable to identify the presence of more than one outer oxide phase in Figure 4.102, as found following oxidation in air. The spinel oxide consisted of light and dark grey areas. The dark area had a higher concentration of chromium and manganese and a lower concentration of nickel. Light grey areas were enriched in nickel and had lower concentrations of chromium and manganese. Enrichment of chromium and manganese and corresponding depletion in nickel was apparent at the base of both oxides, and the reverse true for the subjacent alloy.

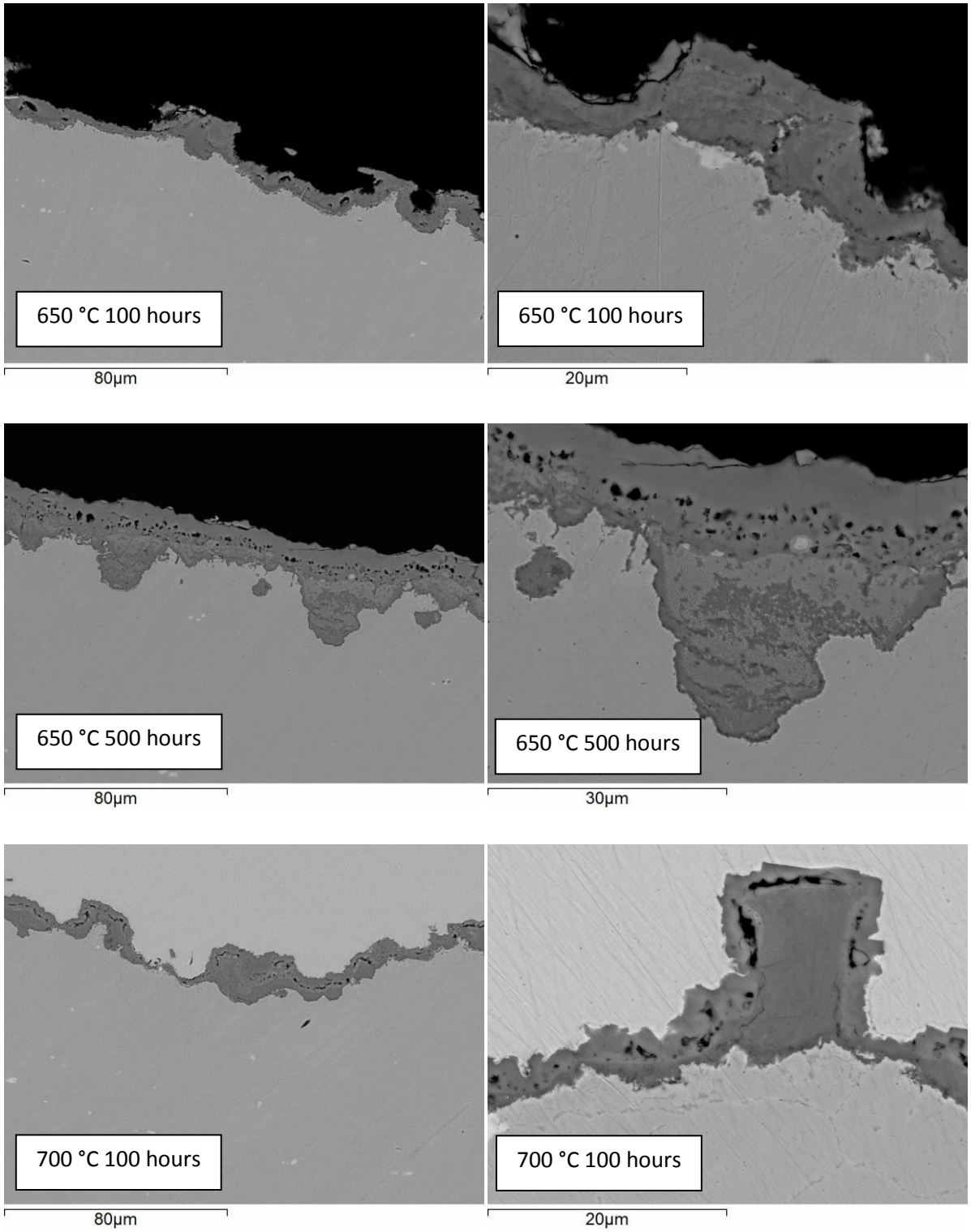

Figure 4.101 – Backscatter SEM images of HR3C oxide morphology after oxidation in deoxygenated steam. After short exposure times, thin, duplex oxide connected thick oxide nodules. After longer exposures a thick, duplex oxide, similar to that found on 347HFG and Super 304H had formed. Porosity was present in the lower half of the outer oxide layer.

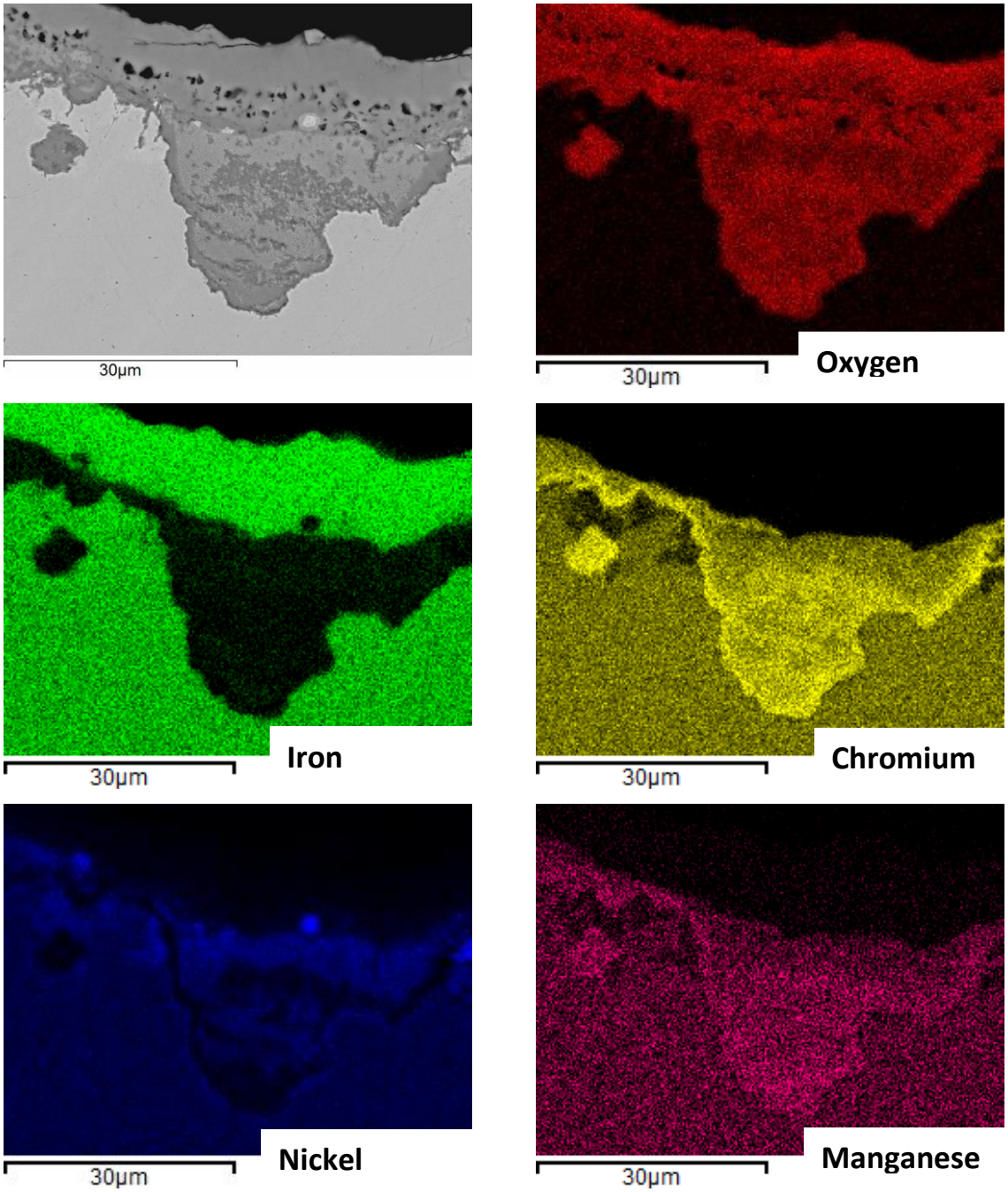

Figure 4.102 – EDX area map of oxide grown on HR3C after oxidation in deoxygenated steam at 650 °C for 500 hours. A single iron rich phase could be distinguished in the map, unlike the iron rich, and iron-nickel rich layers found on air oxidised samples. At the base of the spinel oxide chromium and manganese are enriched and nickel is depleted. The reverse is true in the immediately subjacent alloy. The selected region was selected for characterisation of a nodule and is unrepresentative of the oxide on a whole.

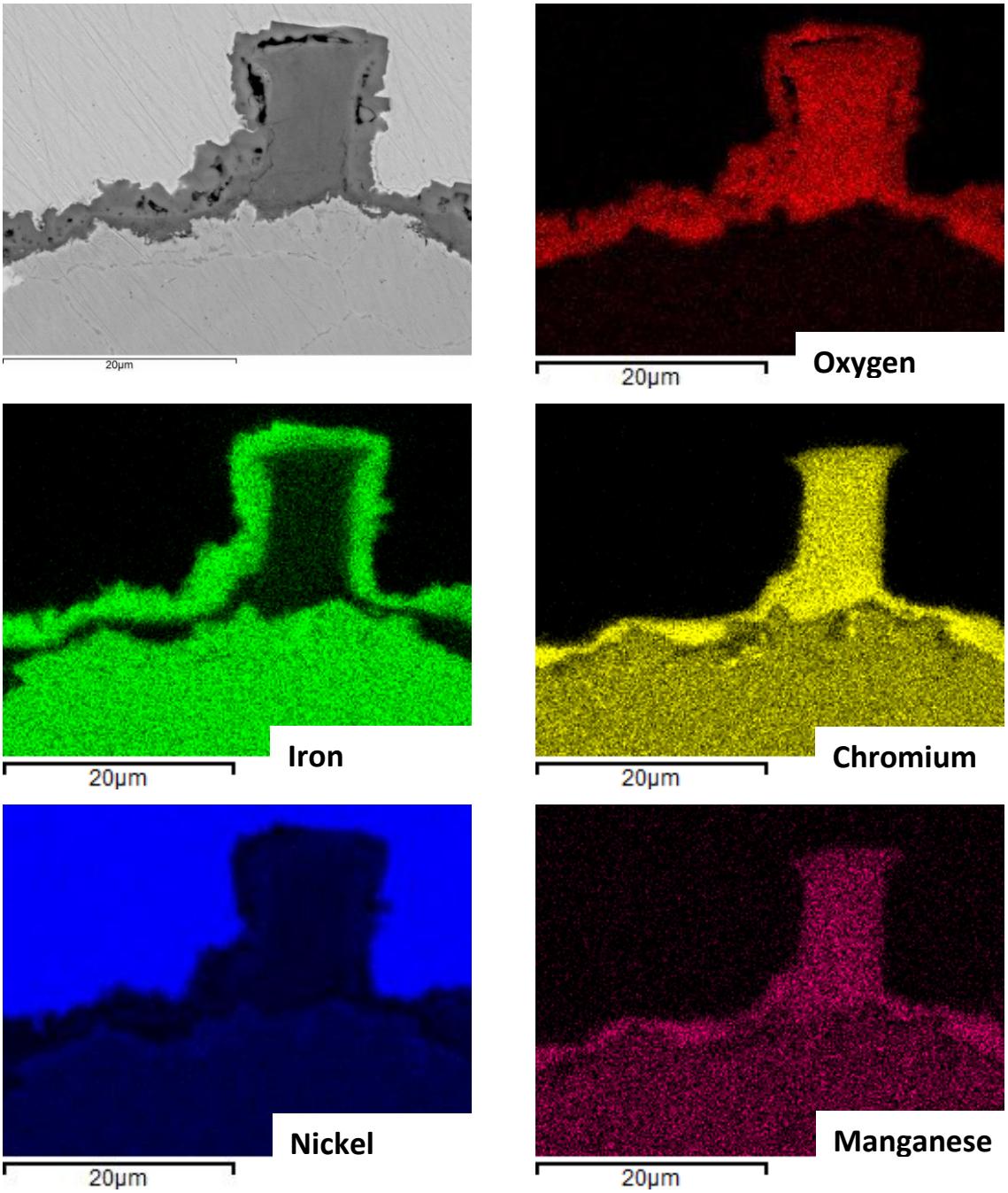

Figure 4.103 – EDX element area map for a cross-section of HR3C oxidised in deoxygenated steam after 100 hours at 700 °C. Sample has been nickel plated. The thin oxide either side of the nodule consists of an outer iron rich oxide and inner spinel. The nodule itself shows evidence of containing an intermediate iron-nickel rich oxide between the spinel and iron rich outer oxide, as found after oxidation in air. The selected region was selected for characterisation of a nodule and is unrepresentative of the oxide on a whole.

4.4.2.4.5 EDX Analysis of HR3C after Oxidation in Deoxygenated Steam

EDX analysis was performed on a section of HR3C that had experienced significant internal oxidation. The size of the inner oxide layer was substantially larger than that found on 347HFG or Super 340H alloys. Spots 2 and 3 in Figure 4.104 show a similar fraction of Cr to the protective oxide layers on 347HFG and Super 304H. Given the higher Cr content of the alloy, it may have been expected for the oxide film to show a higher Cr concentration. However, this does suggest that oxide of the same

composition had formed, suggested to be a mixture of $FeCr_2O_4$ and $(Fe,Cr,Mn)_3O_4$ spinel. Table 4.10 shows the elemental quantification from the EDX spots shown in Figure 4.104.

The higher bulk Cr content in HR3C was represented within the inner oxide layer. The layer appears to comprise two phases – a lighter coloured phase that has a concentration higher in Ni and lower in Cr (spots 4 and 6), and a darker phase that is higher in Cr and lower in Ni (spot 5). As with 347HFG and Super304H, the form of nickel could not be determined, and may be a $FeCr_2O_4$ spinel within a metallic nickel matrix, or a $(Fe,Cr,Ni)_3O_4$.

A Fe-Ni-rich intermediate layer between the outer and inner oxide layers was not observed on HR3C oxidised in deoxygenated steam. Spot 7 would be the location, but the Ni concentration is too low and considered to be picked up from the inner oxide layer. The area map in Figure 4.102 supports this observation. The outer oxide was therefore entirely Fe-rich. Spot 9 reports a higher oxygen content that spot 8. This could be because of in ability of EDX analysis to accurately quantify oxygen. However, the outer oxide adjacent to the inner oxide was observed to be porous, whereas the oxide at the oxide/gas interface was not. From analysis of the oxides presented in Sections 4.5 and 4.6, Fe_3O_4 tends to exhibit more porosity than Fe_2O_3, so this could be an indication that both phases were present on HR3C oxidised in deoxygenated steam. Unfortunately, it was not possible to undertake complimentary techniques for verification.

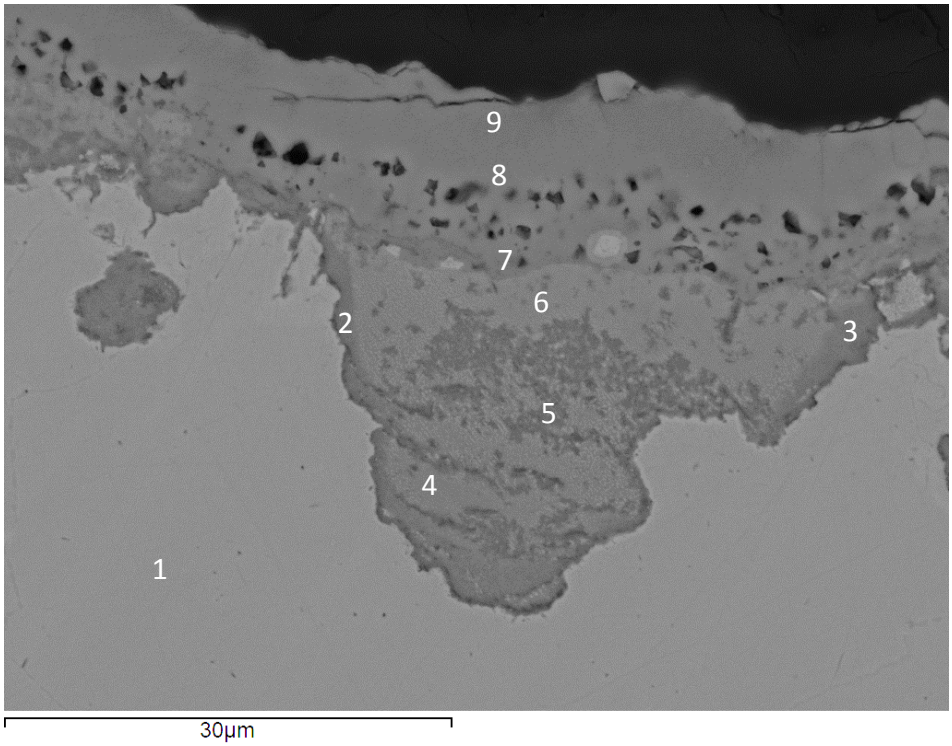

Figure 4.104 – BSE-SEM micrograph of oxide grown on HR3C in deoxygenated steam at 650 °C for 500 hours. Numbers mark areas of EDX analysis. The dark oxide at the alloy/scale interface contains the highest concentration of chromium and coincides with a depletion of nickel.

Table 4.10 – Composition in at. % from EDX analysis of oxide grown on HR3C in deoxygenated steam at 650 °C for 500 hours.

Spot	Oxygen	Iron	Chromium	Nickel	Manganese	Niobium	Silicon
1	-	52.4	27.3	18.2	1.2	0.2	0.7
2	60.6	10.5	23.9	3.3	1.1	-	0.6
3	63.1	8.8	23.3	3.4	1.0	-	0.5
4	59.1	8.9	19.8	10.4	1.1	-	0.7
5	61.2	7.4	23.8	5.6	1.0	0.1	0.9
6	56.5	9.0	16.4	17.3	0.4	-	0.4
7	63.9	29.1	2.2	4.8	-	-	-
8	63.9	34.1	0.5	1.5	-	-	-
9	69.8	29.8	0.4	-	-	-	-

4.4.3 Summary of Oxidation of Austenitic Steels in Deoxygenated Steam

Austenitic steels 347HFG, Super 304H, Super 304H SP and HR3C were oxidised in deoxygenated steam at 600, 650 and 700 °C for up to 1300 hours. Experiments were undertaken in stages 3 and 4 of development of the steam oxidation facility. The findings are summarised below.

- The steam oxidising atmosphere was detrimental to the oxidation resistance of all alloys. The mass gain of each alloy was approximately 3-4 times that recorded in air at all temperatures.
- The oxidation rate of all alloys decreased with increasing time, at all temperatures. An increase in oxidation temperature corresponded with an increase in initial oxidation rate, which decreased at longer oxidation times.
- 347HFG and Super 304H recorded higher mass gain than shot peened Super 304H and HR3C. 347HFG recorded consistently higher mass gain than Super 304H in steam.
- HR3C showed the lowest mass gain in steam. However, the oxide thickness of shot peened Super 304H was clearly lower than that of HR3C. This is attributed to the outer non shot peened surface contributing to mass gain. Unfortunately, because of issues with sample preparation, oxide thickness measurements were not taken for shot peened Super 304H in steam.
- 347HFG and Super 304H formed complete duplex oxide coverage at all times and temperatures. It is postulated that nodular oxide formed initially, as with oxidation in air, but full coverage had already occurred at the minimum test duration (24 hours at 650 °C).
- The outer Fe-rich oxide formed in deoxygenated steam was found to be Fe_3O_4, in contrast to Fe_2O_3 found in air. This suggests that either equilibrium was not reached at the oxide/gas interface, or that the local pO_2 at the oxide/gas interface was lower than that of bulk steam. This could be explained by the evolution of H_2 gas from oxidation reactions, effectively reducing the pO_2 at the oxide/gas interface.
- The inner oxide contained elements from the bulk alloy in similar concentration to that of the bulk alloy, save for Fe, which was lower. The exact composition of the inner oxide could not be determined using the analytical methods employed. However, the cation/anion ratio recorded by EDX was higher than expected for M_3O_4 phase. Therefore, it is suggested that at least a portion of nickel remained in the metallic phase. The oxide is suggested to be primarily a $FeCr_2O_4$ spinel within a metallic nickel matrix. Manganese and a small amount of nickel are also expected to be incorporated into the spinel oxide.

- Unlike in air, the internal oxidation front in steam consumed entire grains. This was accelerated with increasing temperature. A Cr-rich “healing layer” was observed to form on all pickled alloys at grain boundaries. This was most obvious on the 18Cr alloys, as few entire grains were consumed on HR3C.
- The Cr-rich healing layer was suggested to be primarily FeCr2O4, on top of a thin layer of Cr_2O_3 at the alloy/oxide interface. Area maps also showed an enrichment in Mr in these areas, so incorporation of a spinel of the form $MnCr_2O_4$ is likely. The Cr-rich healing layer corresponded with a depletion in Cr and Mn in the subjacent alloy. The depletion was greater than observed in air.
- No spallation occurred on samples oxidised in effectively deoxygenated steam. However, during early steam oxidation facility trials samples exposed to what was thought to be deoxygenated steam, but later postulated to be ineffectively deoxygenated steam, did exhibit spallation. The results of oxidation of these samples are presented in the following section.

4.5 Spallation of Austenitic Steels in "Deoxygenated Steam"

A number of early oxidation experiments in deoxygenated steam resulted in spallation from 347HFG and Super 304H samples. Subsequent analysis of the samples and further oxidation testing in an environment containing a high pO_2 led to the conclusion that effective oxygen removal by degassing did not take place for the affected experiments and therefore the pO_2 during these early experiments was likely much higher than 10 pbb (the approximate pO_2 of feedwater effectively deoxygenated using N_2). Therefore, the term "deoxygenated steam" will be used to describe the ineffectively deoxygenated steam atmosphere in which these early tests took place in.

The results in this section are presented exclusively for tests on Super 304H and 347HFG that exhibited spallation during oxidation in "deoxygenated steam" (shot peened Super 304H and HR3C were included in these early tests but did not exhibit spallation, and will not be considered in this chapter).

Please note that although the pO_2 during oxidation of the affected tests was not known it has been accepted that it was most likely higher than that of the effectively deoxygenated tests. It follows that the oxidising atmospheres for tests that saw a spallation event were likely variable, the evidence for this being the large variance in the fraction of haematite present in the outer oxide layer, and corresponding variance in the quantities of spall evolved from the inner surface of different samples. This variance is reflected in the differences in net and gross mass gain between samples.

4.5.1 Oxidation Kinetics of Spalled Samples after Oxidation in "Deoxygenated Steam"

Mass gain data and individual layer oxide thickness data for 347HFG and Super 304H were recorded and are presented below. Spalled oxide from individual samples was collected and weighed with the sample and recorded as the gross mass gain. The sample was then re-weighed without spalled oxide to find the net mass gain. The gross and net mass gain data for spalled samples can be found in Figure 4.105 and Figure 4.106 for oxidation at 650 and 700 °C, respectively. No spallation was observed to occur on any samples at 600 °C. To identify individual samples, brackets are used in the figures to connect corresponding gross and net mass gain values. Oxide thicknesses for individual layers were recorded as they were for non-spalled samples. The "Total Outer" thickness values are the sum of attached and detached outer oxide values. Decohesion was only observed to occur within the outer oxide layer or at the spinel/outer oxide interface. In addition to individual layer thicknesses, the total

outer oxide thickness was plotted against the thickness of detached oxide to determine the fraction of the outer layer thickness that had spalled for each sample.

4.5.1.1 Mass Gain Data of Spalled Samples after Oxidation in "Deoxygenated Steam"

Mass gain data are shown in Figure 4.105 and Figure 4.106 for 347HFG and Super 304H samples that spalled in early oxidation tests in "deoxygenated" steam. No spallation was observed at 600 °C and no spallation was observed on shot peened Super 304H or HR3C at any temperature. For samples that were weighed with and without spall (gross and net), brackets identify individual samples. Kinetic rate laws were not calculated from mass gain data and trends over time and temperature were not considered for the current samples for the following reasons:

1. There is a strong possibility that the oxygen content in the steam atmosphere during oxidation varied greatly between tests, this could have affected the growth kinetics of the scales by preferential formation of a particular phase.
2. It was difficult to collect 100% of the spalled oxide from each sample to obtain gross mass gain measurements because of the nature of spallation. Therefore, the gross mass gain of each sample may be underestimated.

Mass gain for 347HFG and Super 304H was higher at 700 °C than 650 °C. It can be seen from the difference between net and gross mass gain that the quantity of spallation varied considerably.

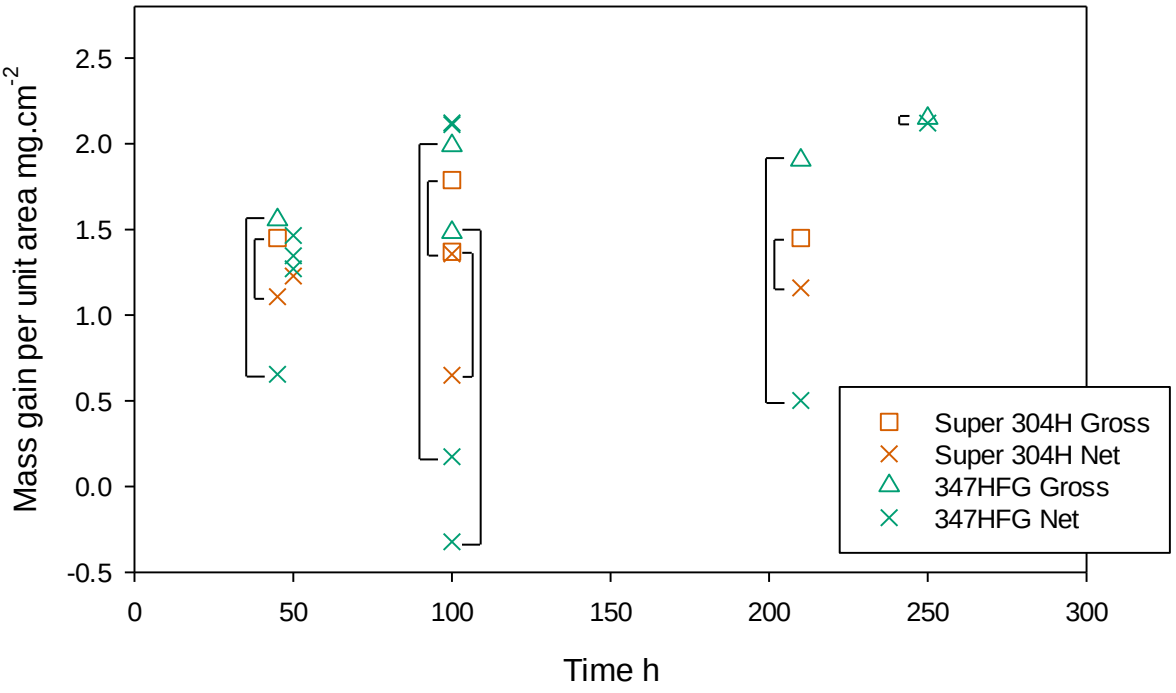

Figure 4.105 – Mass gain data for Super 304H and 347HFG oxidised in deoxygenated steam at 650 °C that exhibited spallation. Brackets indicate gross and net mass gains of individual samples. No spallation was observed from HR3C or shot peened Super 304H. The large scatter in gross and net mass highlight the large variance in quantity of spallation between samples.

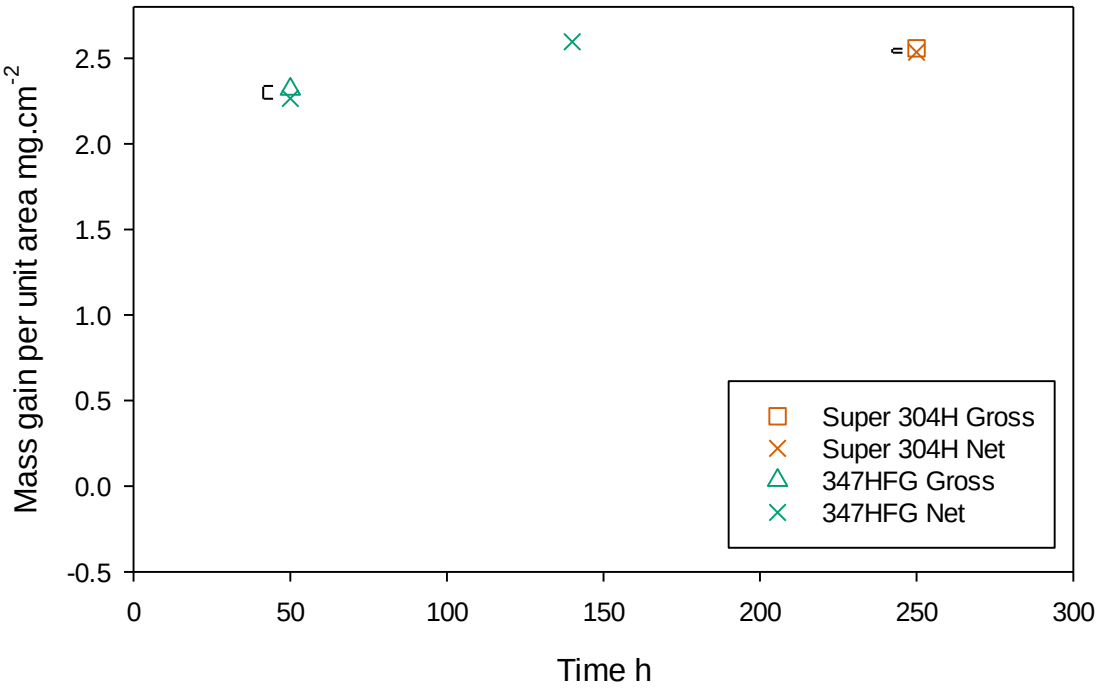

Figure 4.106 – Mass gain data for Super 304H and 347HFG oxidised in deoxygenated steam at 700 °C that exhibited spallation. Brackets indicate gross and net mass gains of individual samples. No spallation was observed from HR3C or shot peened Super 304H. The gross mass gain was higher for samples oxidised at 700 °C than at 650 °C, however the quantity of spallation was less, as indicated by the small variance in gross and net mass gain.

4.5.1.2 Oxide Thickness of Spalled Samples after Oxidation in "Deoxygenated Steam"

The outer oxide layer was thicker than the spinel oxide for the majority of samples as with samples oxidised in deoxygenated steam that did not spall. Samples that spalled did not display as clear a trend towards increasing outer oxide thickness compared with spinel thickness as seen with samples that did not spall. The total oxide thicknesses of samples that exhibited spallation differed from those that did not spall. 347HFG exhibited lower total oxide thicknesses after 100 hours at 650 and 700 °C. The total oxide thicknesses of samples of Super 304H that spalled were lower than those that did not spall after all durations at 650 and 700 °C. There are two reasons why lower oxide thicknesses may have been recorded for samples that spalled. Either the change of environment from effectively deoxygenated steam promoted different growth kinetics/oxide morphology causing the growth of thinner scales, or, the surface roughness profile at the spallation interface caused by decohesion and residual porosity led to measurement errors in the thickness of the adherent and unadherent components of the outer oxide.

In Figure 4.107 Figure 4.108 b) and d), total oxide thicknesses are plotted with unadherent oxide thicknesses, labelled "Spalled"[7]. From the figures it is possible to visualise the thickness fraction of the outer oxide layer that spalled during cooling. The figures show that the thickness fraction of outer oxide spalled during cooling varies with oxidation time. At 650 °C there is a large variation in spall fraction for up to 100 hours oxidation time for 347HFG. The largest fraction of outer oxide that spalled was 80% after 100 hours at 650 °C. The spallation interface for these samples was within the outer oxide. For oxidation times over 100 hours, 100% of the outer oxide was found to spall on 347HFG at both 650 °C and 700 °C. The spallation interface for these samples was the spinel/outer oxide interface.

The data point indicated by a red arrow in Figure 4.107 b) corresponds to the unadherent oxide of a sample whose outer oxide morphology was unlike other samples of 347HFG oxidised in "deoxygenated steam" that exhibited spallation. The spallation interface for this sample was closer to the oxide/gas interface than other samples, and appeared to reside within a porous interface towards the top of the outer oxide. It is unclear as to why the oxide exhibited this morphology. As the pO_2 of the test steam was unknown, this may have been a contributory factor.

The spallation interface on Super 304H shows a similar trend to 347HFG at 650 °C. Approximately 65% of the thickness of the outer oxide spalled after 50 and 100 hours oxidation. After 210 hours, 100% of the thickness of the outer oxide layer spalled. Unlike 347HFG, however, at 700 °C only 70% of the thickness of the outer layer had spalled after 250 hours oxidation. To summarise, although the oxidising atmosphere most likely varied between oxidation tests, there is a clear trend towards total outer oxide layer detachment from partial outer oxide layer detachment as oxidation time increases for both 347HFG and Super 304H.

[7] Where the full thickness of the outer oxide layer had spalled catastrophically, leaving no spalled oxide in close proximity to the surface for measurements of spalled oxide thickness, the thickness of the adherent outer oxide layer was used.

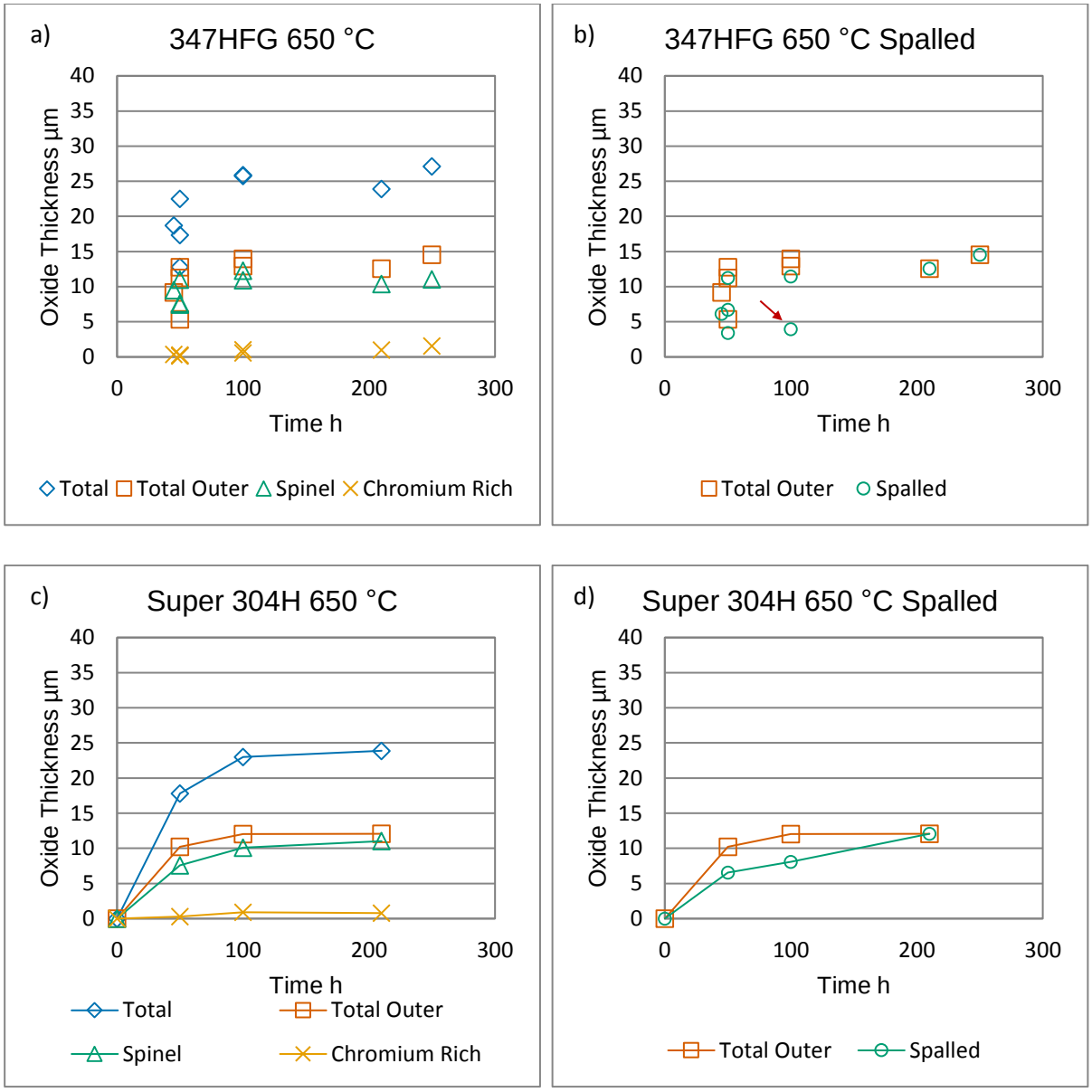

Figure 4.107 – Oxide thickness measurements for samples of 347HFG and Super 304H oxidised in deoxygenated steam at 650 °C that exhibited spallation. Data for the total thickness was taken from the sum of the individual layer thicknesses. Outer oxide thicknesses were taken as the sum of adherent and unadherent oxide thicknesses in areas where spallation occurred. Spallation from the sample indicated by the red arrow is thought to have occurred via a blistering mechanism, not a decohesion mechanism. Figures b) and d) indicate that the spallation interface was located within the outer oxide layer, and that the fraction of outer layer released increased with oxidation time up to 100 % outer layer spallation (spallation interface the spinel/outer oxide interface). For clarity of illustration, the data for 347HFG are not joined with a connecting line.

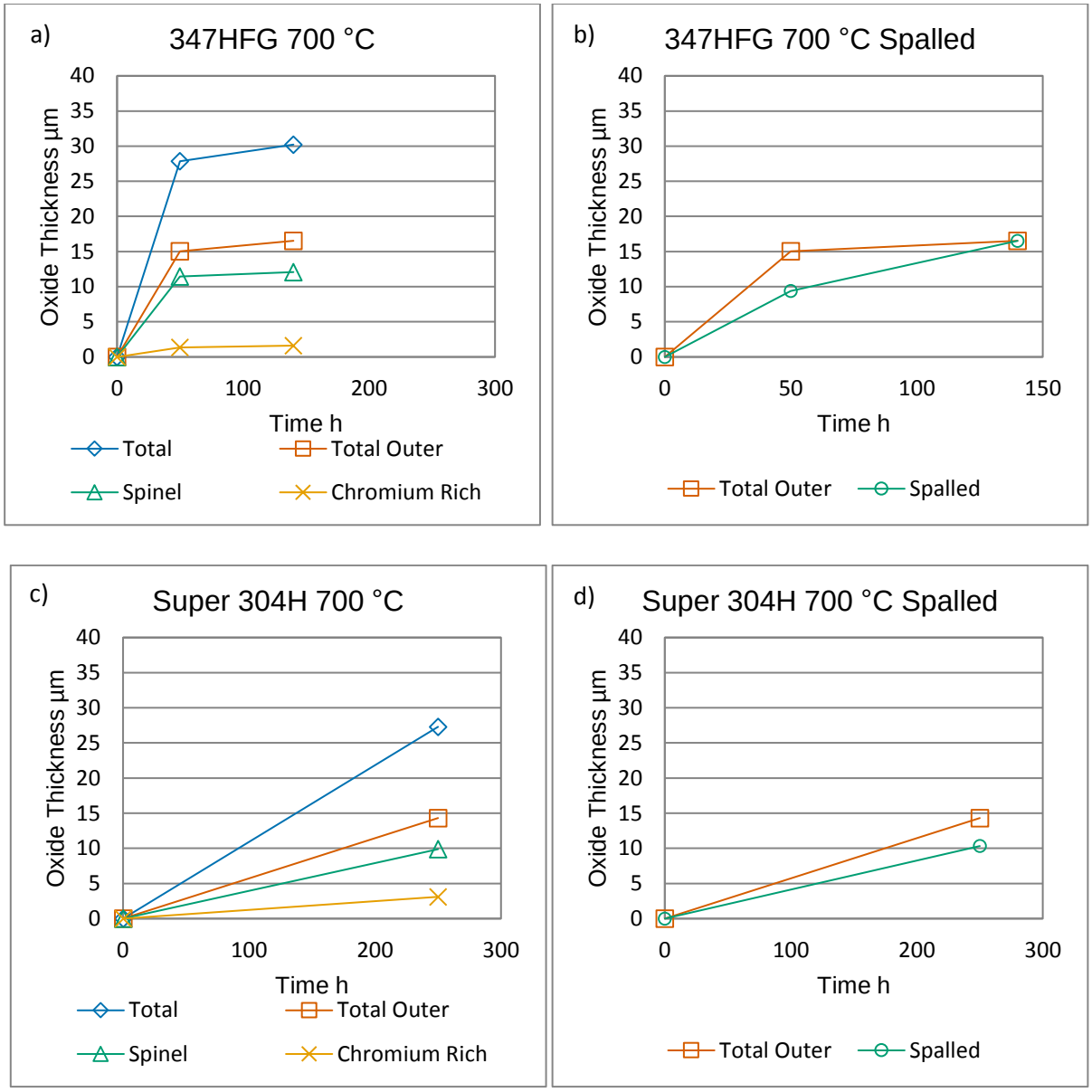

Figure 4.108 – Oxide thickness measurements for samples of 347HFG and Super 304H oxidised in deoxygenated steam at 700 °C that exhibited spallation. Data for the total thickness was taken from the sum of the individual layer thicknesses. Outer oxide thicknesses were taken as the sum of adherent and unadherent oxide thicknesses in areas where spallation occurred. Figures b) and d) indicate that the spallation interface was located within the outer oxide layer, and that the fraction of outer layer released increases with oxidation time up to 100 % outer layer spallation (spallation interface the spinel/outer oxide interface).

4.5.2 Oxide Morphology of Spalled Samples after Oxidation in "Deoxygenated Steam"

4.5.2.1 347HFG

A total of twelve samples of 347HFG oxidised in deoxygenated steam exhibited spallation: ten at 650 °C and two at 700 °C.

4.5.2.1.1 Visual Observations of 347HFG after Oxidation in "Deoxygenated Steam"

Spallation was observed from both the inner and outer surfaces of 347HFG during cooling. The fraction of spallation from the inner surfaces varied between samples, as did the size of spallation particles. There was no clear trend in surface spallation fraction with time and temperature, however, the least spallation was observed from a sample oxidised for 50 hours at 650 °C and a sample oxidised for 250 hours at 700 °C. The largest spallation fraction was observed on a sample oxidised for 100 hours at 650 °C. Photos of the sample surfaces are shown in Figure 4.109, Figure 4.110 and Figure 4.111.

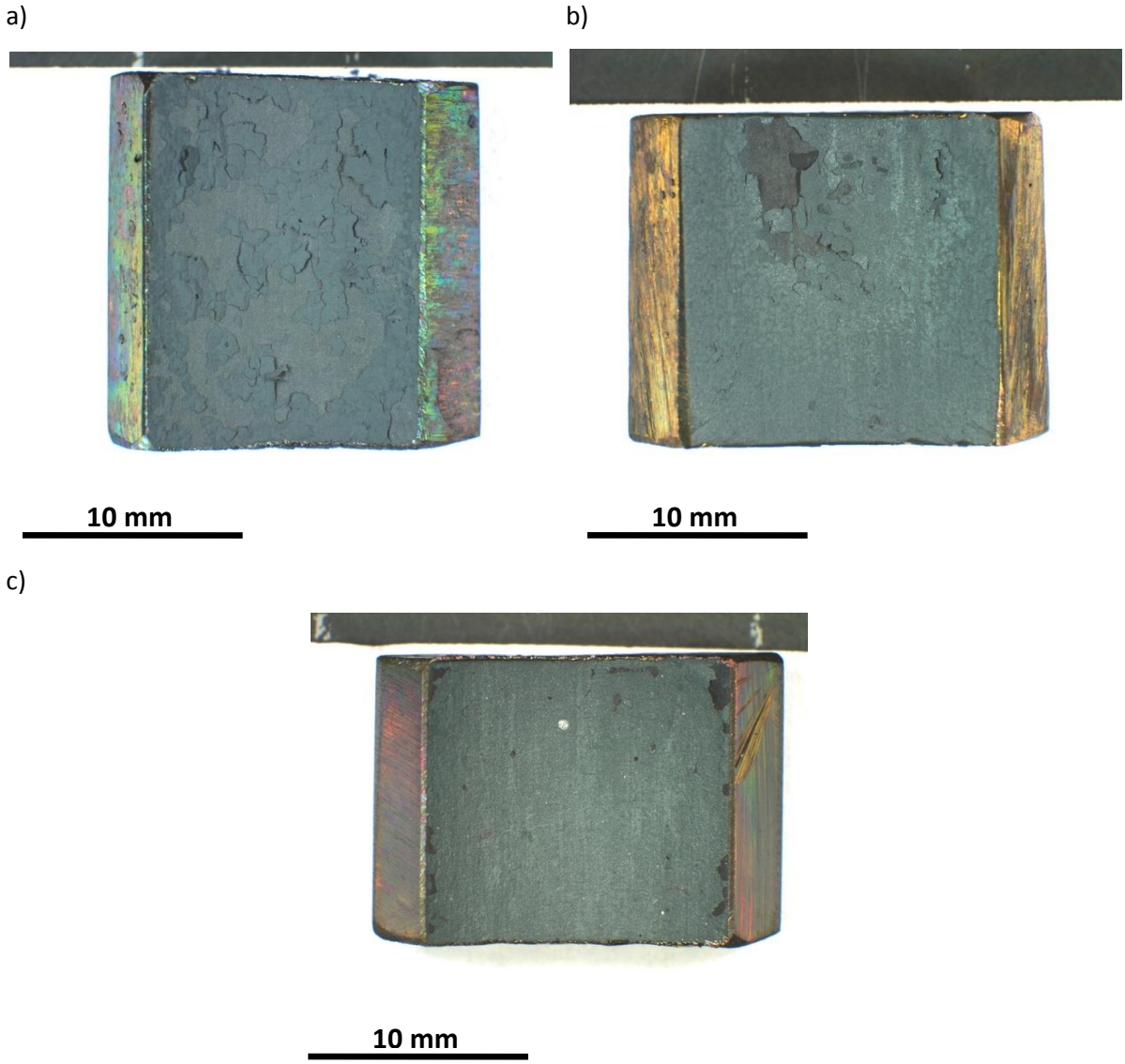

Figure 4.109 – Macro images of 347HFG inner surface after oxidation in deoxygenated steam at 650 °C for a) 45 hours, b), c) 50 hours. Quantity of spallation and size of spallation particles varied greatly between samples.

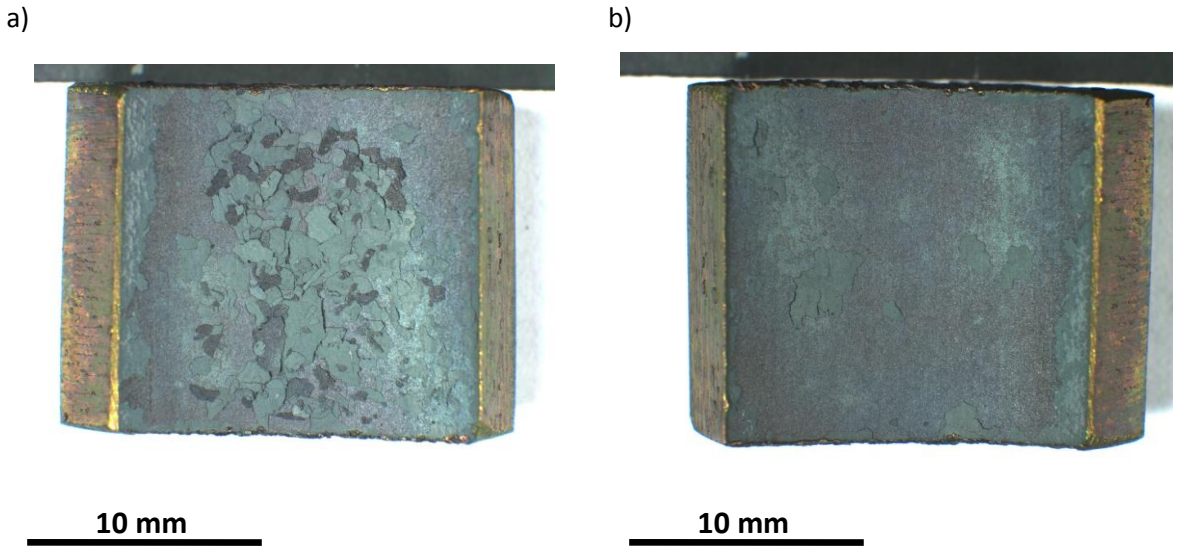

Figure 4.110 – Macro images of 347HFG inner surface after oxidation in deoxygenated steam at 650 °C 100 hours. Quantity of spallation and size of spallation particles varied greatly between samples. Figure a) is shown with spallation particles. Nearly 100% of the inner surface has spalled.

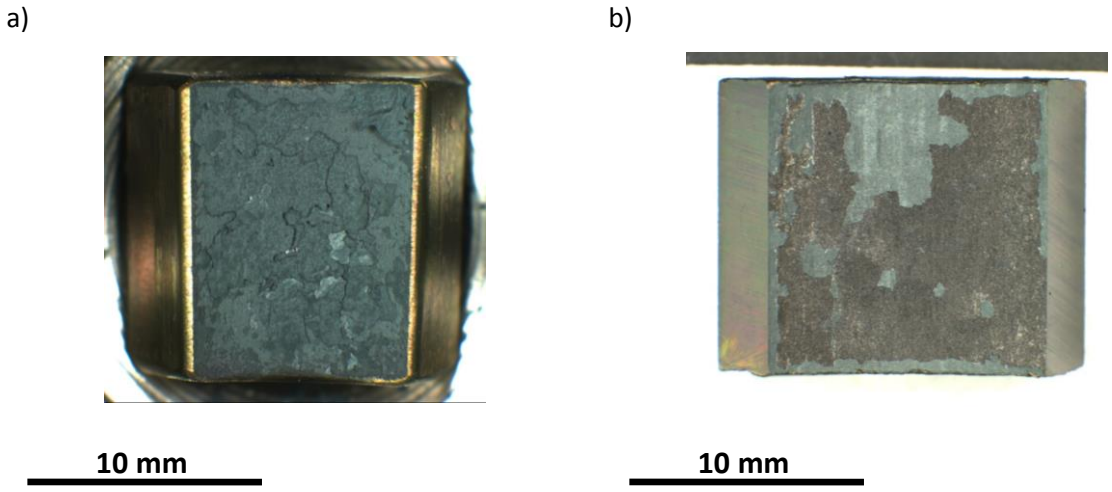

Figure 4.111 – Macro images of 347HFG inner surface after oxidation in deoxygenated steam at 650 °C a) 210 hours, b) 250 hours. Quantity of spallation and size of spallation particles varied greatly between samples. Figure a) is shown with spallation particles.

4.5.2.1.2 SEM Surface Analysis of 347HFG after Oxidation in "Deoxygenated Steam"

The surface of samples that exhibited spallation displayed several different oxide morphologies. Figure 4.112 illustrates spalled and unspalled regions of oxide on a sample of 347HFG oxidised for 100 hours at 650 °C. In Figure 4.112 a) the unspalled outer oxide has a porous structure. Cross-section analysis of this sample revealed a continuous layer of haematite at the oxide/gas interface and magnetite present at the spinel/outer oxide interface. Figure 4.112 b) and c) show fracture surfaces where the entire outer oxide had spalled from the spinel oxide. Fracture surfaces in the outer oxide are visible where spall particles have been released. The outer oxide cross-section in these areas shows the bulk

of the outer oxide layer to have low porosity. Prior austenite grains are visible as non-porous spinel oxide in b), c) and d), along with residual outer oxide between spinel nodules.

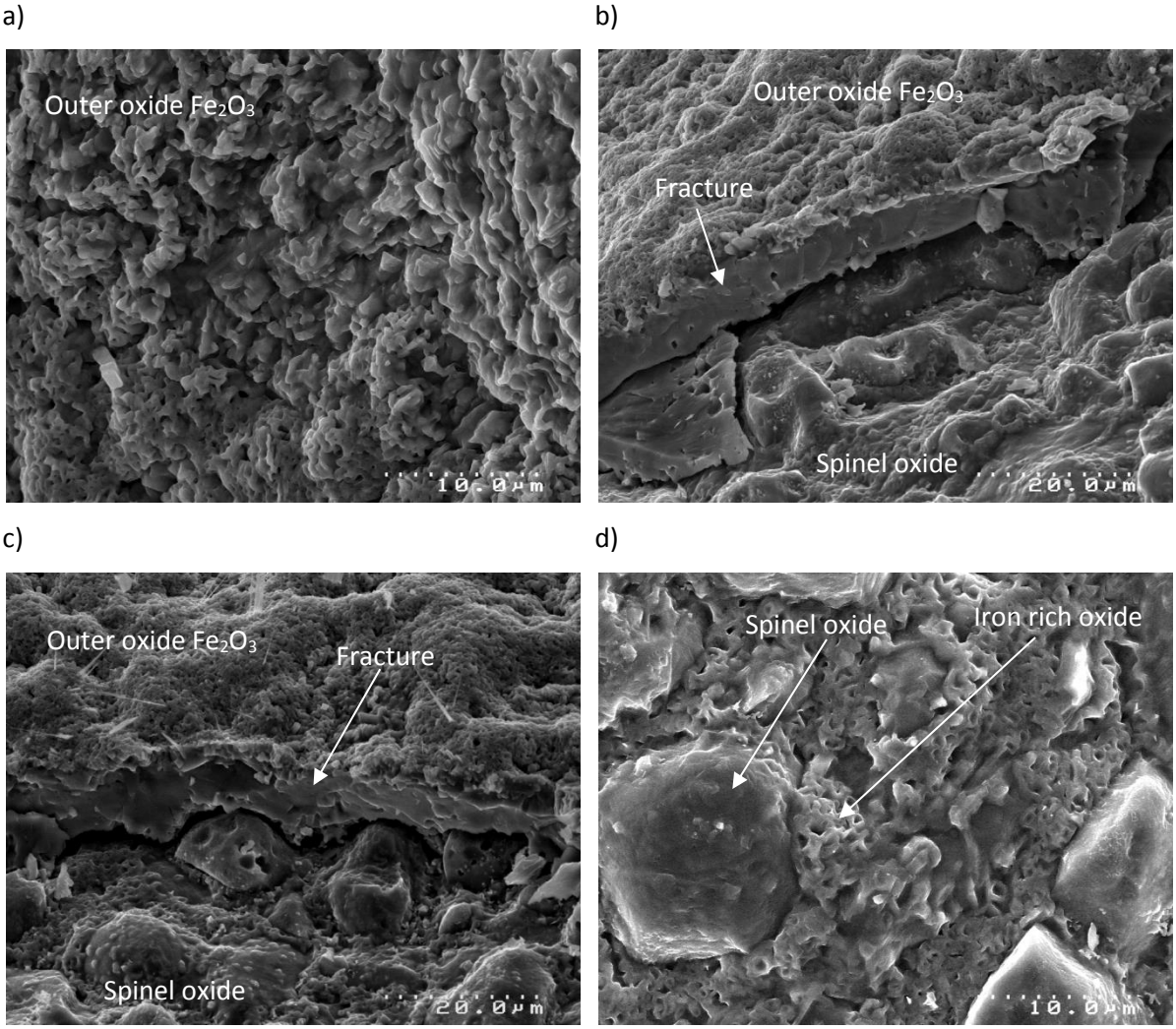

Figure 4.112 – 347HFG after oxidation in "deoxygenated steam" for 100 hours at 650 °C. Topography of a) unspalled area, b), c) fracture surface, d) spinel oxide following spallation.

Figure 4.113 shows regions of oxide from a sample of 347HFG that has been oxidised for 50 hours at 700 °C. The spallation interface was porous, and within the outer oxide layer, as illustrated in Figure 4.113 a). From analysis of the cross-section, there was 10% haematite in the outer oxide of this sample and this was usually located in small regions surrounding pores or at the scale/gas interface, possibly taking the form illustrated in Figure 4.113 b). Figure 4.113 c) shows a region of unspalled oxide to the left of the figure and the spallation interface to the right following the release of a spall particle. The spallation interface, also shown in Figure 4.113 d), was extremely porous. In the top right had corner of c) and d), the entire outer oxide layer appears to have spalled, leaving non-porous spinel oxide.

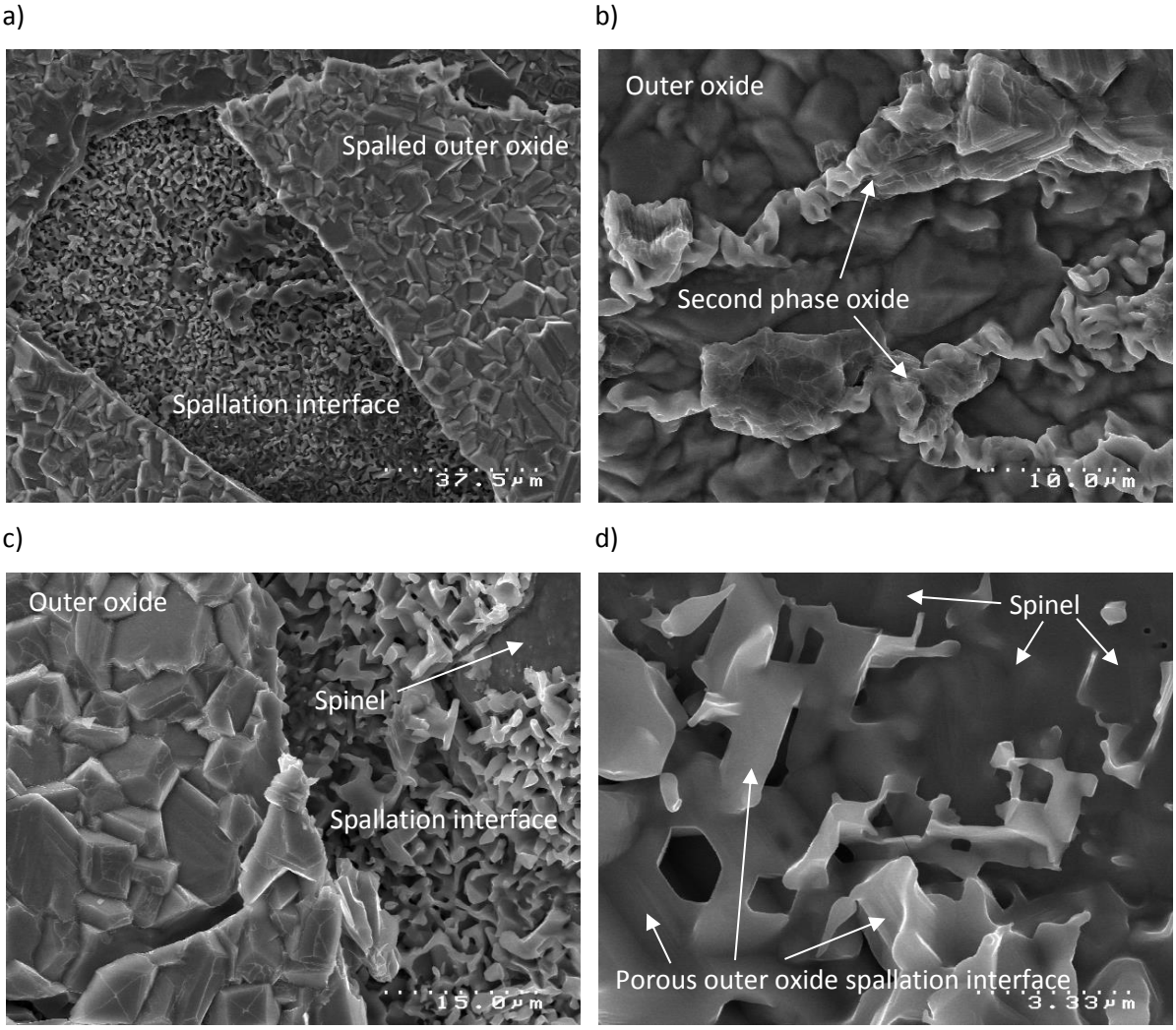

Figure 4.113 – 347HFG after oxidation in "deoxygenated steam" for 50 hours at 700 °C. Topography showing; a) Disconnected spall particle revealing porous spallation interface, b) unspalled region featuring two distinct outer oxide morphologies, c) fracture surface showing unspalled outer oxide and porous spallation interface (within outer oxide), d) fracture surface showing porous spallation interface and underlying spinel oxide.

4.5.2.1.3 SEM Cross-Section Analysis of 347HFG after Oxidation in "Deoxygenated Steam"

Cross-section analysis of the 347HFG samples whose oxide had buckled, lifted, or had spalled completely, permitted investigation into the spallation mechanisms and morphology of the oxide involved in spallation. The spinel oxide did not appear to differ to that formed on samples that did not spall. The internal oxidation front had not consumed the majority of austenite grains at the alloy surface or formed a chromium rich film before 100 hours oxidation at 650 °C. A continuous chromium rich film was present at the base of the spinel oxide from 50 hours oxidation at 700 °C. Porosity in the outer oxide varied between individual samples. At 650 °C the majority of spalled oxide was largely non-porous, save for micro porosity at the oxide/gas interface on some samples that diminished approximately 5 µm into the scale. One sample oxidised for 50 hours, and one sample oxidised for 250

hours contained a high level of porosity in the outer oxide, the entirety of which had detached (the spallation interface for these samples was the spinel/outer oxide interface). Within the outer oxide, a higher concentration of pores had accumulated at the spinel/outer oxide interface on these samples, and this reduced to zero porosity at the outer oxide/gas interface. The sample oxidised for 45 hours spalled within the outer oxide. On this sample the adherent oxide was free of pores. However, the surface roughness profiles of both spallation interfaces, indicated that spallation may have occurred along a thin porous interface within the outer oxide. A similar morphology was found on two samples oxidised for 50 hours. Figure 4.114 f) shows evidence of a thin porous interface within the outer oxide that had acted as the spallation interface as can be seen on the left hand side of the micrograph. The spallation interface on one sample oxidised for 100 hours at 650 °C was within the outer oxide layer and close to the spinel/outer oxide interface (Figure 4.114 j) and k)). Both attached and detached parts of the outer oxide were free of pores apart from a small amount of micro porosity towards the surface of the detached outer oxide. The spinel/outer oxide itself appeared as though it may have a thin porous interface along which spallation occurred. A similar morphology was found on the sample oxidised for 210 hours (Figure 4.114 l), m), n)). Over the majority of the surface of this sample, 100% of the outer layer had spalled. In areas where a fraction of outer oxide had remained adherent (up to 20%), this was sometimes found to be porous. In areas where spallation had not occurred, there was evidence of cracks and a possible thin layer of porosity along the interface that spallation would be expected to occur (Figure 4.114 m)).

a) b)

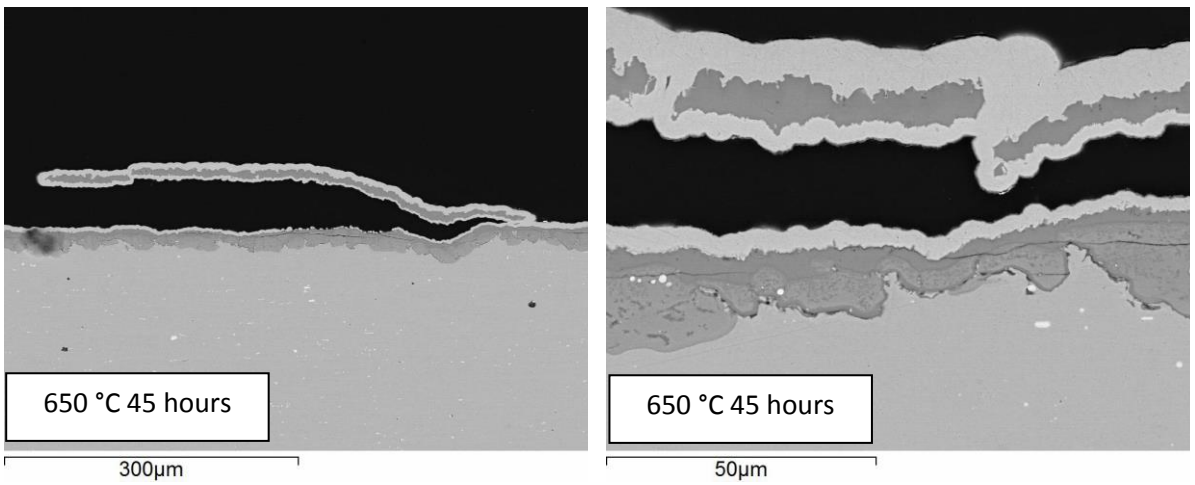

c)

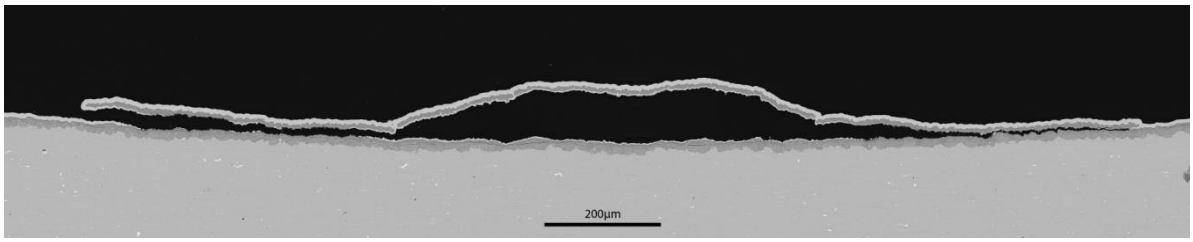
200µm

d)

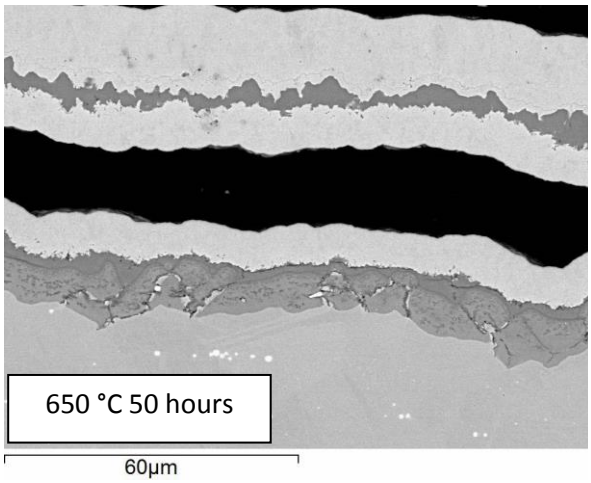
650 °C 50 hours
60µm

e)

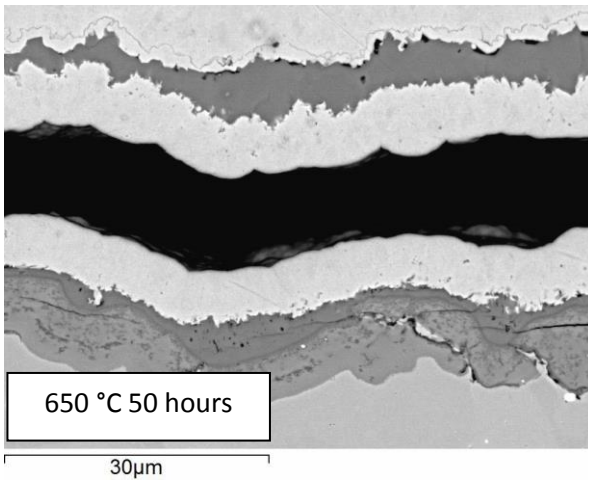
650 °C 50 hours
30µm

f)

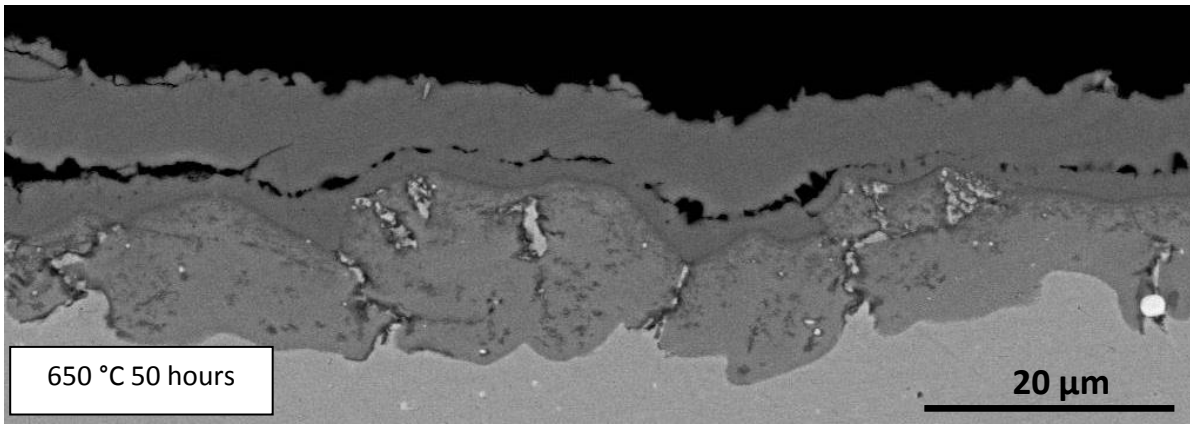
650 °C 50 hours
20 µm

g)

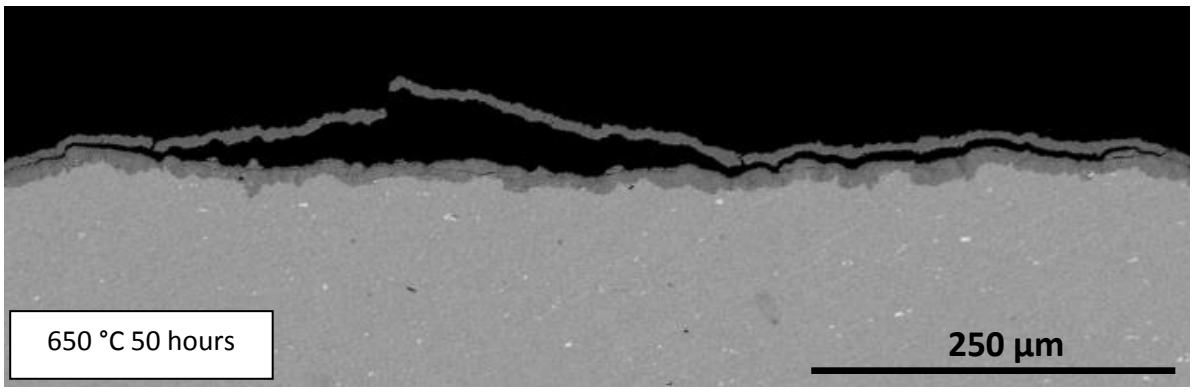
650 °C 50 hours
250 µm

h)

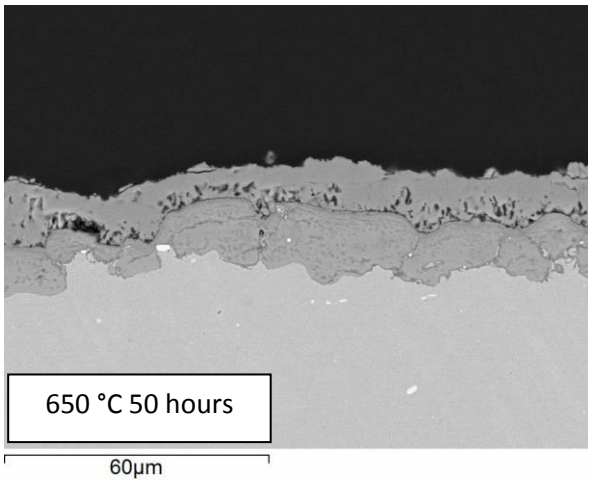
650 °C 50 hours
60µm

i)

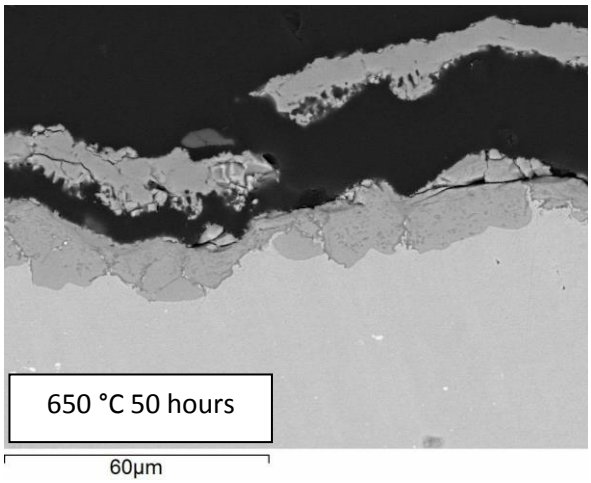
650 °C 50 hours
60µm

j)

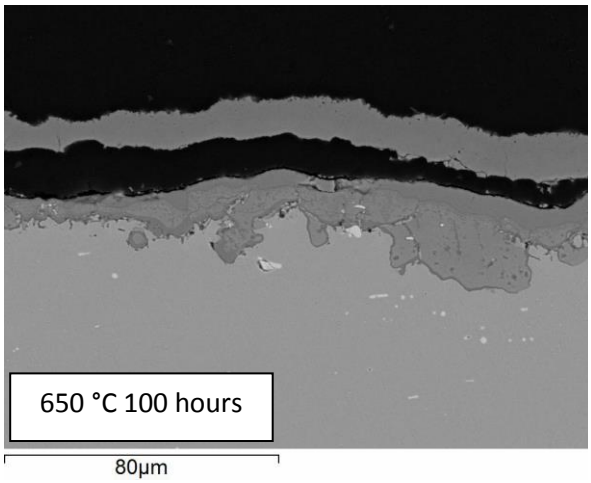
650 °C 100 hours
80µm

k)

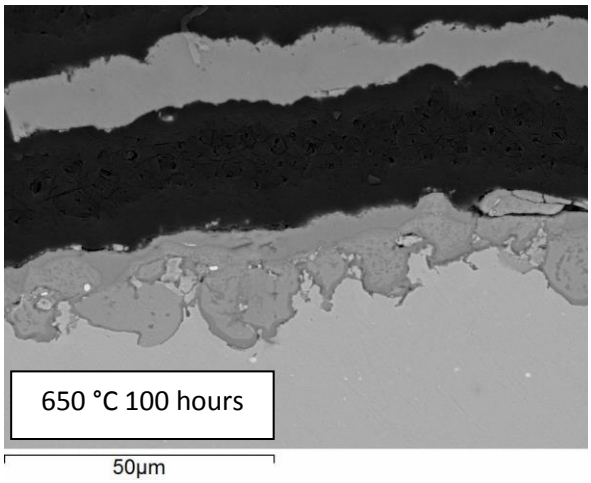
650 °C 100 hours
50µm

l)

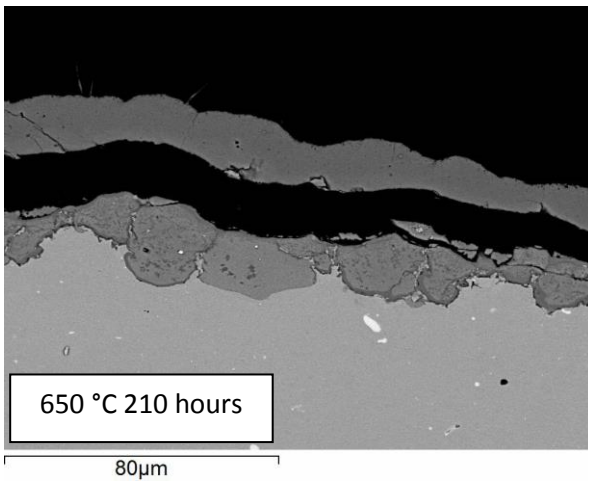
650 °C 210 hours
80µm

m)

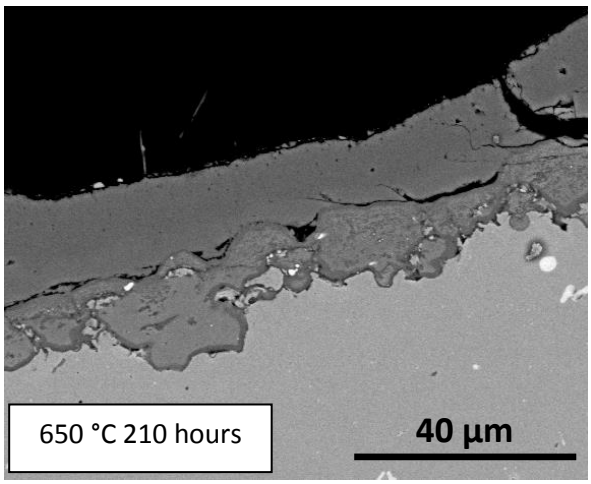
650 °C 210 hours
40 µm

n)

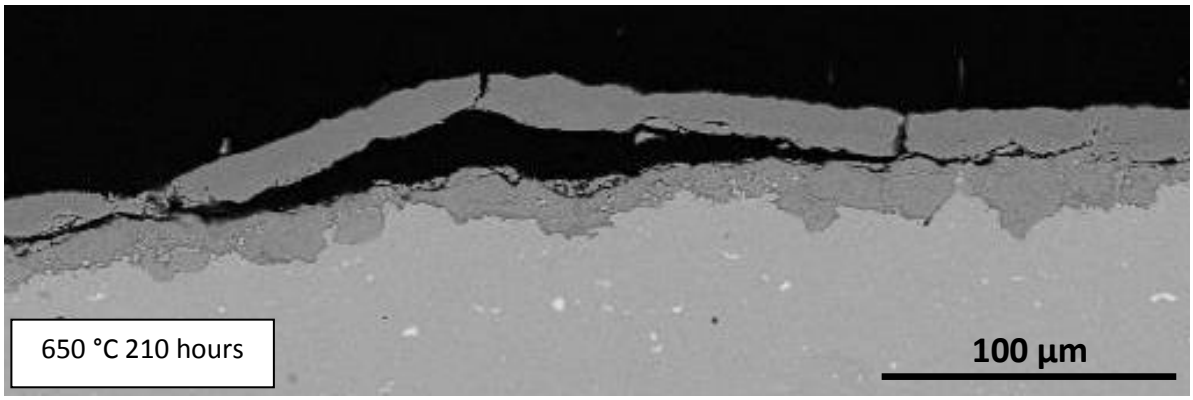

o)

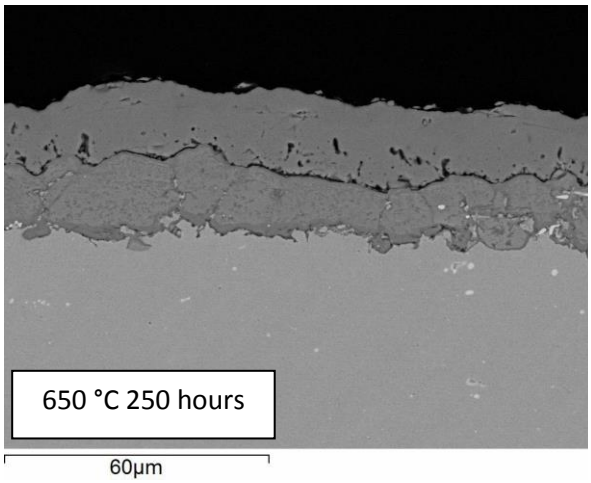

p)

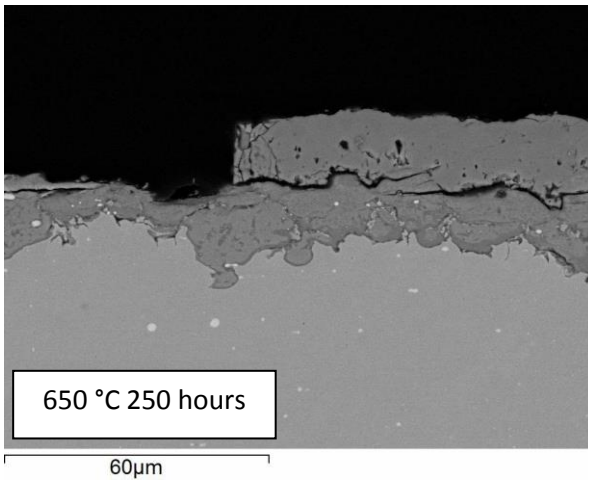

Figure 4.114 – BSE SEM cross-section micrographs of oxide grown on 347HFG after oxidation in deoxygenated steam at 650 °C. Samples exhibited spallation.

Porosity within the outer oxide layer was higher at 700 °C than at 650 °C, as shown by Figure 4.115. The sample oxidised for 50 hours showed a thick band of porosity concentrated slightly towards the spinel/outer oxide interface. Spallation occurred within this porous band. The sample oxidised for 250 hours had less porosity in the outer scale than after 50 hours. Where spallation occurred, porosity was again concentrated towards the spinel/outer oxide interface or at the spinel/outer oxide interface. Decohesion occurred where porosity was at its highest, detaching either the entire outer layer or a fraction of the outer layer thickness.

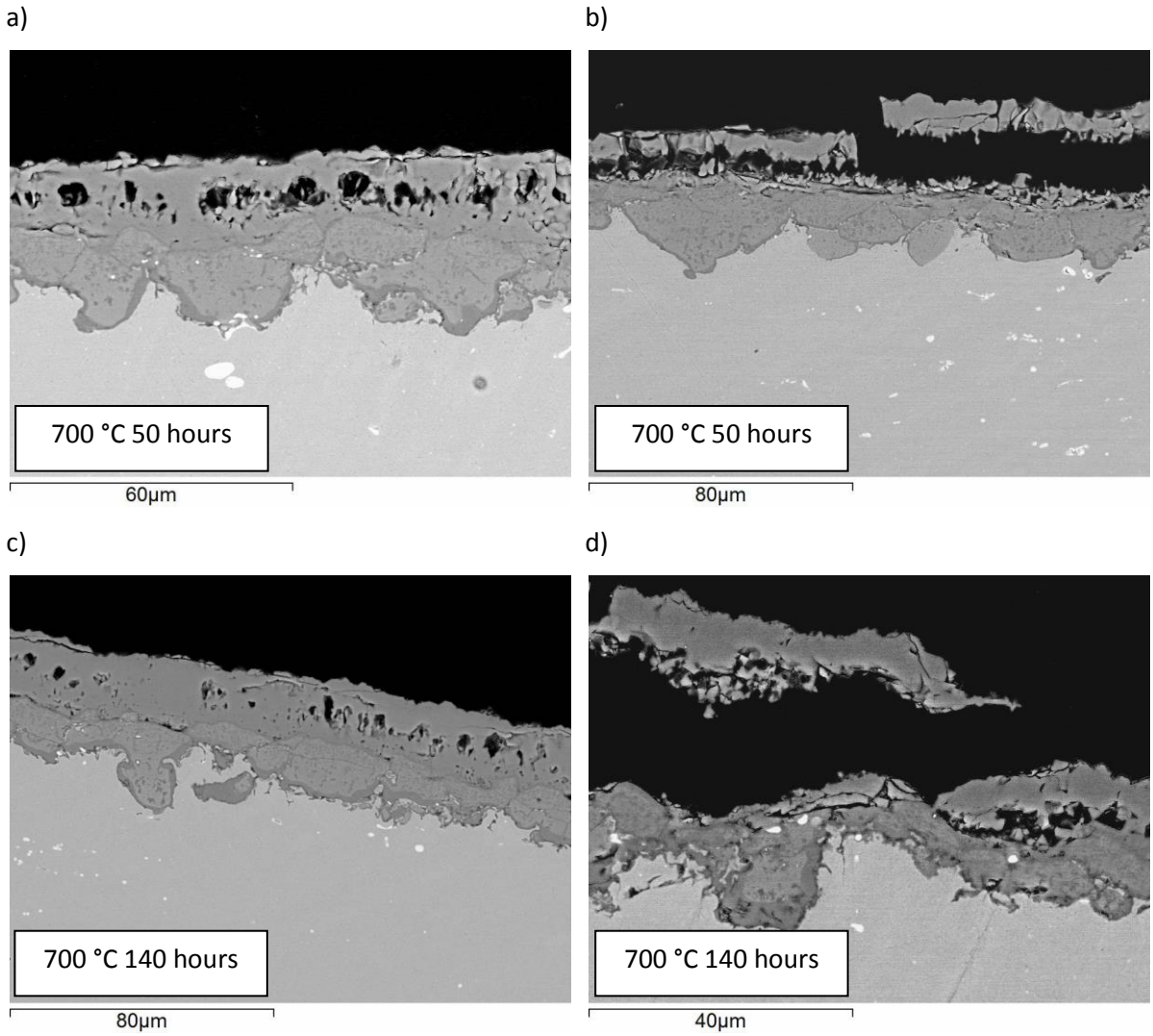

Figure 4.115 – Backscatter SEM images of 347HFG oxide morphology.

4.5.2.1.4 Optical Microscopy of 347HFG after Oxidation in "Deoxygenated Steam"

Optical microscopy was used to determine the haematite fraction in the outer oxide layer. In contrast to unspalled samples, which were observed to contain little or no haematite within the outer layer, the haematite fraction within the outer oxide of spalled samples varied largely between samples and ranged from 10% to 70%. Figure 4.116 illustrates the varying degree of haematite presence within the outer layer on samples of 347HFG oxidised in deoxygenated steam that spalled. The location of haematite was not consistent between samples. Figure 4.116 a)-d) show areas of haematite distributed randomly throughout the detached outer oxide. Where the haematite fraction was large, a solid layer of haematite tended to form in the detached outer oxide at the oxide/gas interface as in Figure 4.116 e) and f). From observation of optical micrographs, it was clear that the spallation interface very rarely corresponded with the haematite/magnetite phase boundary within the outer oxide layer (where there was a clear two layered outer oxide as in Figure 4.116 e) and f)). This phase boundary was not porous on any sample that spalled (aside from general porosity within the outer

oxide on certain samples). In areas of porous magnetite, haematite was sometimes found surrounding pores. This was also found, albeit to a lesser extent, on the outer oxide of samples that did not spall. Haematite was sometimes present at the spallation interface of detached oxide, suggesting the spallation interface may have been located along a seam of pores on many samples.

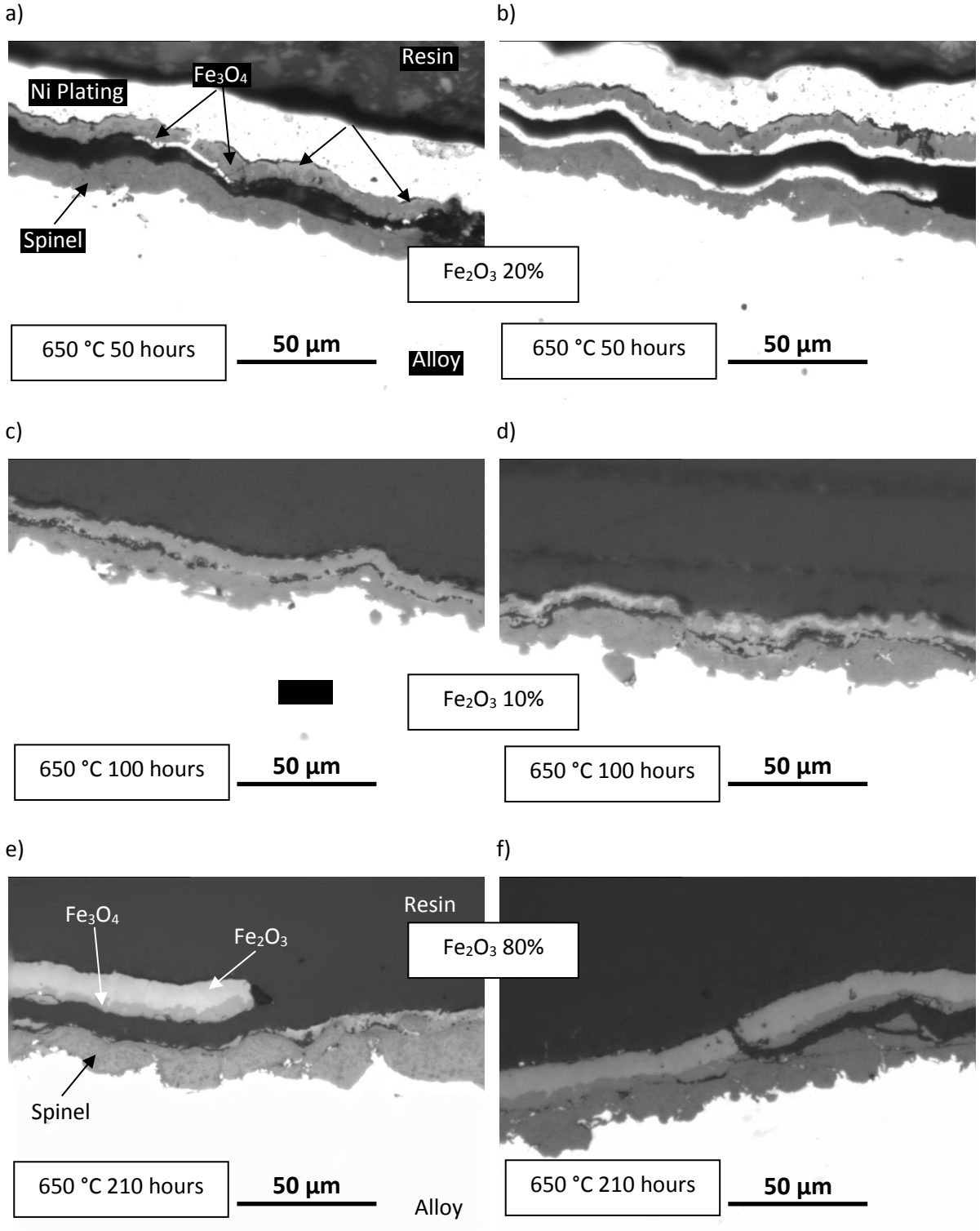

Figure 4.116 – Optical micrographs of 347HFG oxide oxidised in "deoxygenated steam". Haematite was found within the outer oxide on all samples that exhibited spallation.

4.5.2.1.5 XRD Analysis of 347HFG after Oxidation in "Deoxygenated Steam"

XRD analysis was performed separately on spalled oxide from two 347HFG samples oxidised in "deoxygenated steam" at 650 °C to determine the composition. Cross-sectional analysis revealed that only the outer iron-rich oxide contributed to spallation, and optical microscopy revealed two distinct phases in detached oxide, suggested to be magnetite and haematite.

Figure 4.117 presents the results of XRD analysis for 210 hours (top) and 100 hours (second from top) oxidation. Referring to the optical microscopy analysis, the spalled oxide of the 210 hours sample (Figure 4.116 e) and f)) contained a higher fraction of lighter (in colour) oxide than the 100 hours sample (Figure 4.116 c) and d)). The lighter oxide is suggested to be haematite as it was more frequently found at the oxide/gas interface, which is the thermodynamically preferred location.

X'Pert HighScore software calculated a high correlation to reference peaks for haematite and magnetite, and these are reproduced in the same figure. Comparing the two patterns, it can be seen that peaks that correspond to magnetite are higher on the 100 hour sample, indicating a higher fraction of magnetite in the sample. This is in agreement with the measurements of haematite fraction for the samples, which was 10% haematite for the 100 hour sample and 80% haematite for the 210 hour sample.

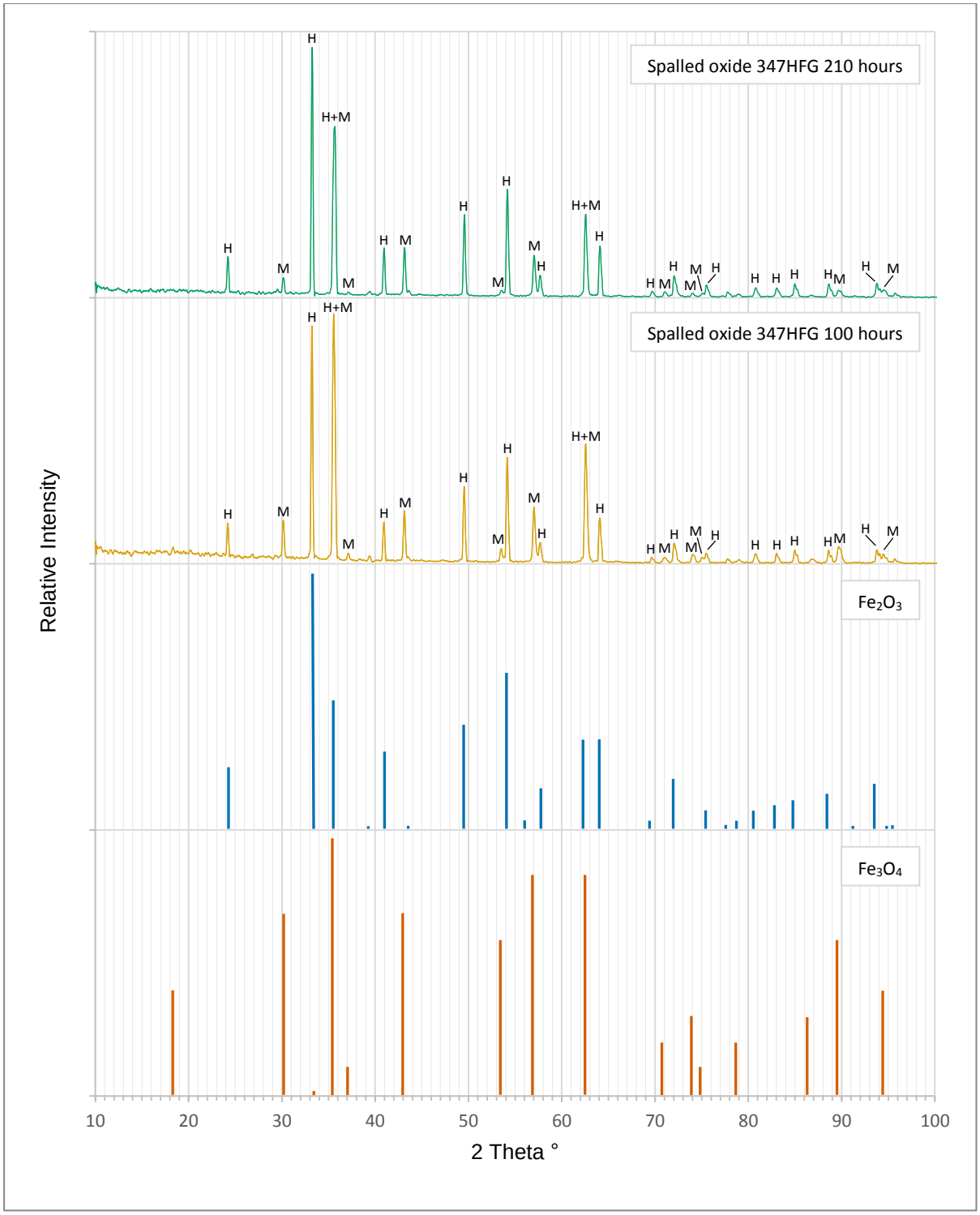

Figure 4.117 – XRD analysis of spalled oxide from samples of 347HFG oxidised in "deoxygenated steam" at 650 °C for 210 (top) and 100 (second from top) hours. Comparing the peak intensity of each spectrum with those of haematite (third from top) and magnetite (bottom), the spalled oxide after oxidation for 210 hours appears to contain a larger haematite fraction than the spalled oxide oxidised for 100 hours, in agreement with optical microscopy analysis.

4.5.2.2 Super 304H

4.5.2.2.1 Visual Observations of Super 304H after Oxidation in "Deoxygenated Steam"

Spallation was observed from both the inner and outer surfaces of Super 304H during cooling. The fraction of spallation from the inner surfaces varied between samples. At 650 °C the least spallation was observed on samples oxidised for 50 hours. The sample oxidised for 45 hours spalled partially over the whole inner surface and was slightly concentrated towards one corner. The sample oxidised for 50 hours showed more localised spallation. Samples oxidised at 650 °C for 100 and 210 hours showed a similar amount of spallation evenly distributed across the sample surface. Compared with 347HFG, a lot more partially adherent oxide was visible on the inner surface of samples. Where decohesion tended to lead to release of a spall particle on 347HFG, on Super 304H there was a large fraction of partially adherent oxide on the inner surface. Photos of the sample surface are shown in Figure 4.118.

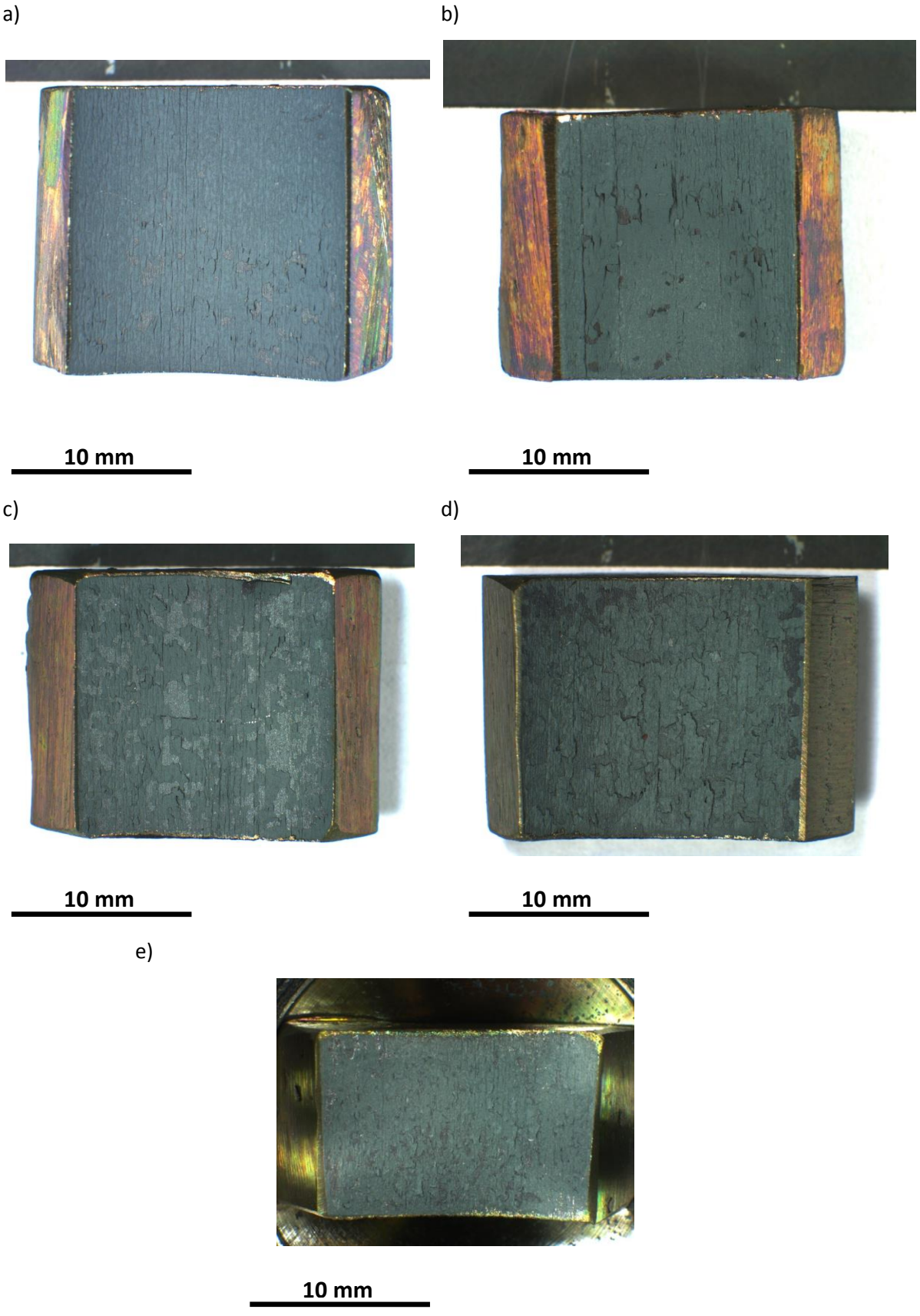

Figure 4.118 – Macro images of Super 304H inner surface after oxidation in deoxygenated steam for 650 °C after a) 45 hours, b) 50 hours, c), d) 100 hours, e) 210 hours.

4.5.2.2.2 SEM Surface Analysis of Super 304H after Oxidation in "Deoxygenated Steam"

Figure 4.119 and Figure 4.120 show BSE SEM micrographs of the surfaces of two samples of Super 304H oxidised for 100 hours at 650 °C that spalled. The locations of cracks in the scale were influenced by the surface defects that ran in the axial direction of the sample's inner surface (Figure 4.119 a), b), Figure 4.120 a)). Cracks often ran adjacent and parallel to these defects. The oxide within these defects was usually secure, such that two of these defects acted as boundaries for two sides of a spall particle, which was formed by cracking of the oxide nearby and parallel to these defects. An example of axial defects anchoring the outer oxide is shown in Figure 4.120 a). In Figure 4.119 c) and d) oxide morphologies are shown for an area of oxide from which a spall particle had been released, and an area of outer oxide that had partially come away from the bulk of the oxide and substrate.

The morphology of the detached oxide (in focus in Figure 4.119 c)), which had been directly exposed to the steam environment during oxidation, was less jagged than the underlying oxide, and a small amount of porosity could be detected. This may have resulted from the surface profile growing outwards and creating small voids. The underlying oxide surface (in focus in Figure 4.119 d)) was formed by detachment of the spalled outer oxide. The surface is rough suggesting the spallation interface was within the outer oxide in this case (there were no outlines or morphology changes characteristic of spinel oxide visible).

Occasionally, there were whisker like features believed to be pillars of oxide connecting the bulk oxide with the oxide that spalled. These oxide pillars suggest that the oxide was porous in these areas. In contrast, the spallation interface of the sample in Figure 4.120 was the spinel/outer oxide interface. Evidence for this is the morphology of the underlying oxide in Figure 4.120 c), d) and e). Non-porous oxidised prior austenite grains are visible. The grains do not appear to have been fractured suggesting the spallation interface ran along the contours of the original alloy surface at the spinel/outer oxide interface.

The outer oxide surface that had been exposed to the steam environment during oxidation resembled that of the oxide in Figure 4.119 and also that of the outer oxide of the sample of 347HFG shown in Figure 4.112 that was exposed for 100 hours at 650 °C. In Figure 4.120 d) and e) the fracture surface of the spalled oxide cross-section is visible. On close inspection there were two types of porosity visible. Pores over 1 μm in diameter on average were visible in the lower half of the spalled cross-section. However, these were infrequent and porosity overall was very low. Reaching the upper oxide surface and penetrating up to a few microns deep into the oxide were collections of sub-micron in diameter micro pores. It was difficult to characterise these pores due to the uneven fracture surface.

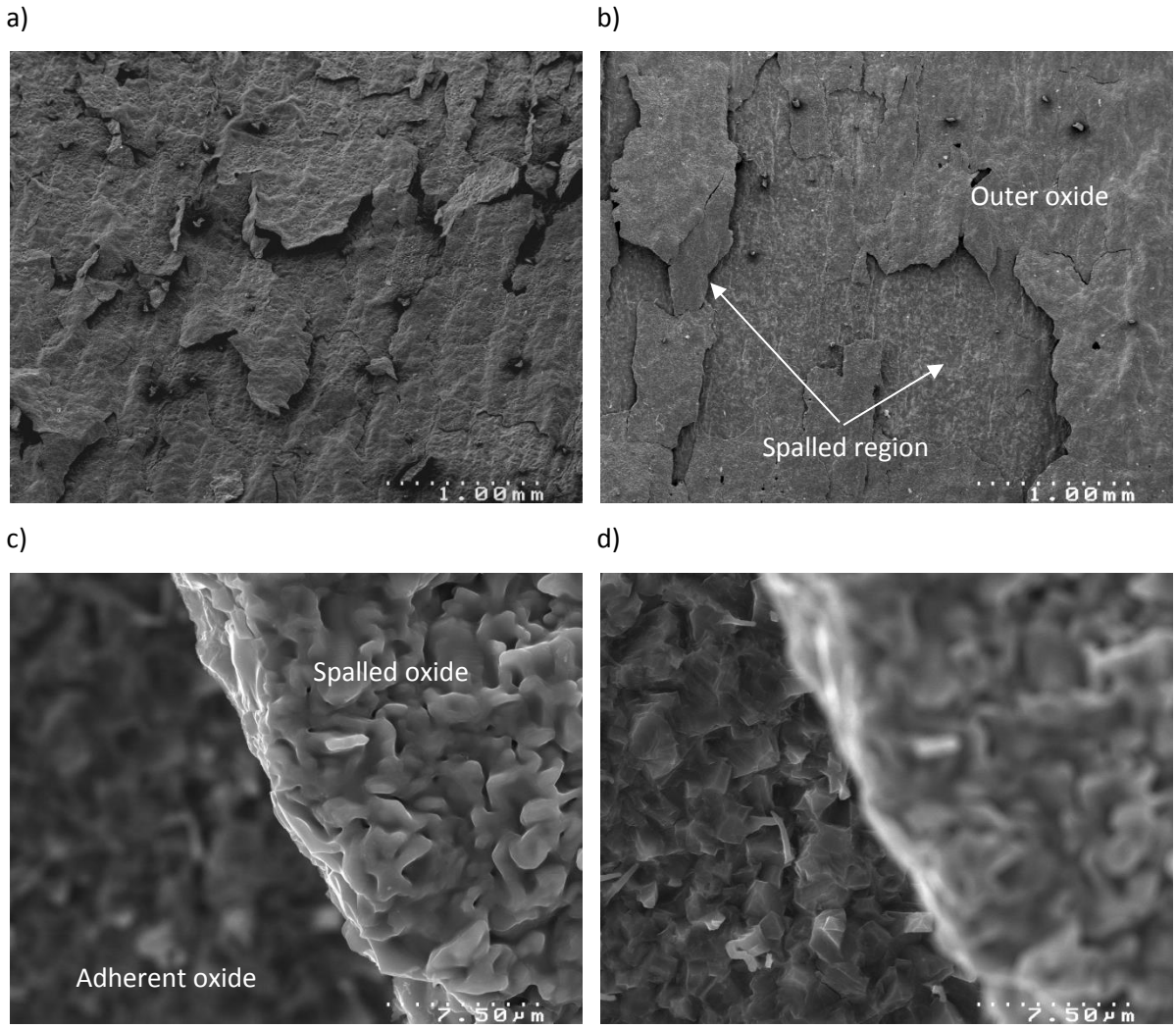

Figure 4.119 – SEI SEM micrographs of oxide formed on Super 304H after oxidation in deoxygenated steam for 100 hours at 650 °C.

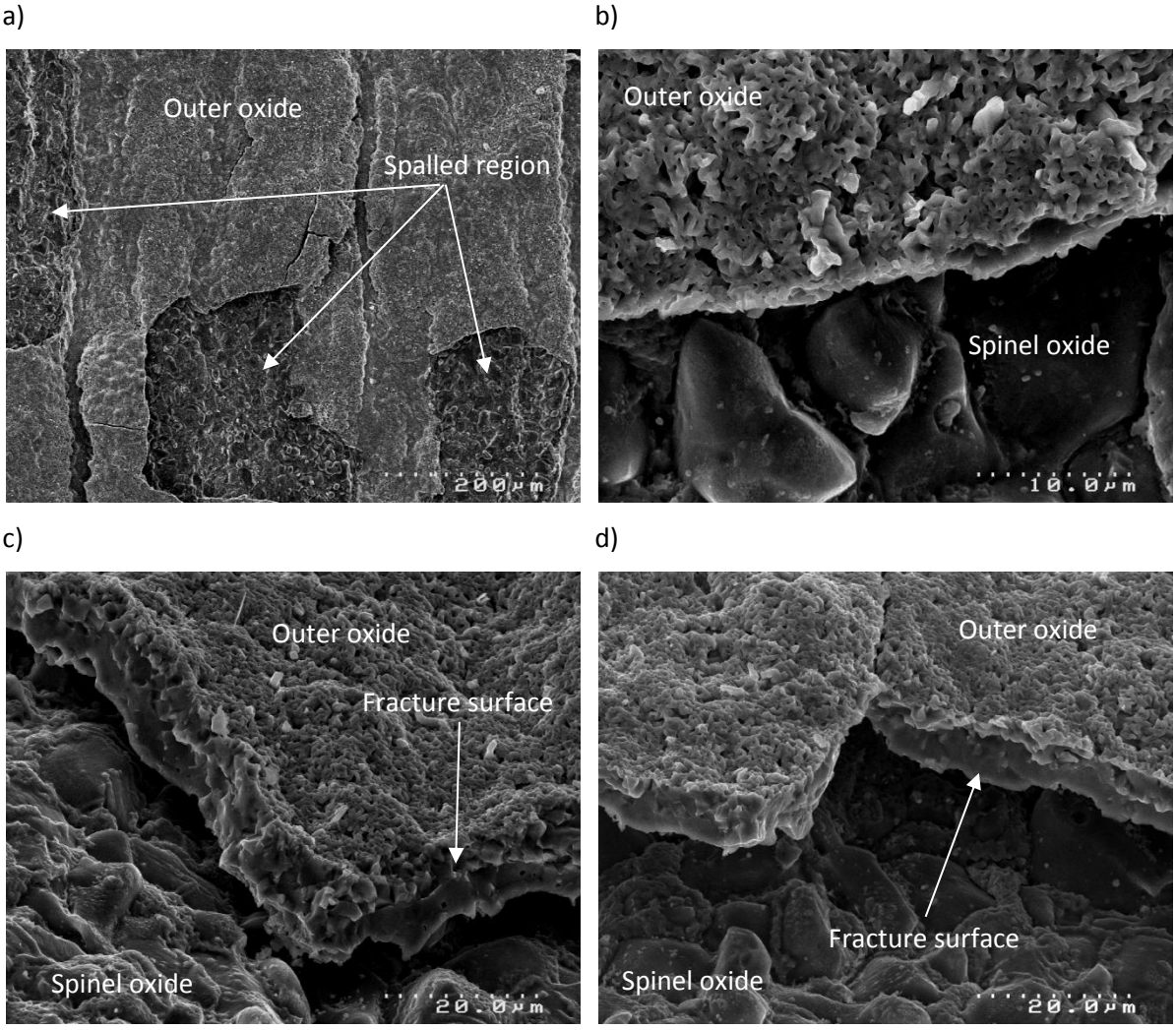

Figure 4.120 – SEI SEM micrographs of oxide formed on Super 304H after oxidation in deoxygenated steam for 100 hours at 650 °C.

4.5.2.2.3 SEM Cross-Section Analysis of Super 304H after Oxidation in "Deoxygenated Steam"

SEM cross-section analysis revealed the morphology of the inner and outer oxide on Super 304H as well as the spallation interface and location of porosity in the scale. The spallation interface was within the outer oxide layer for every sample of Super 304H that spalled after oxidation in deoxygenated steam and contained between 70 and 90% of the total outer oxide thickness. Porosity in the outer layer was variable. At 650 °C, after 50 hours there was very little porosity throughout as shown in Figure 4.121. It was unclear whether decohesion had initiated along a thin porous interface. On one sample exposed for 100 hours, a small concentration of pores had accumulated towards the spinel/outer oxide interface. Detachment of the oxide appeared to be from this porous interface. Another sample oxidised for 100 hours had less porosity and it was unclear whether spallation

occurred along a porous interface. The spallation interface on the sample oxidised for 210 hours was within the porous interface within the outer oxide, towards the spinel/outer oxide interface.

a)

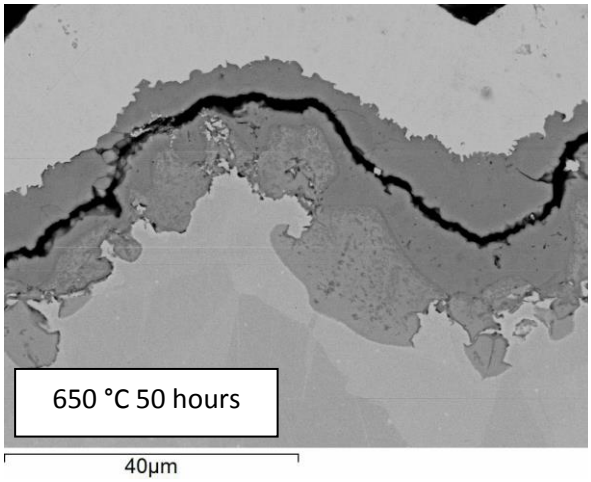

b)

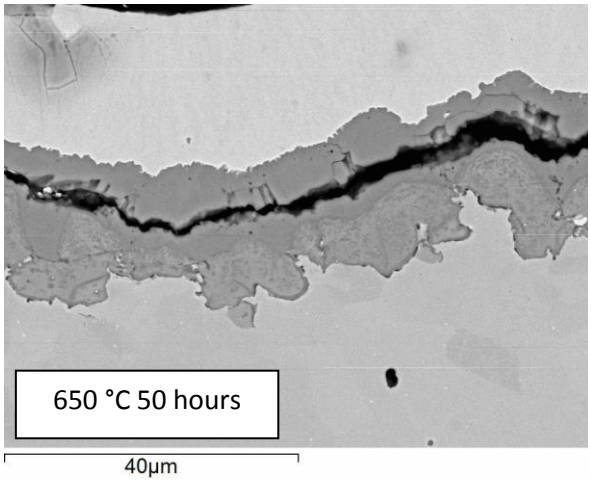

c)

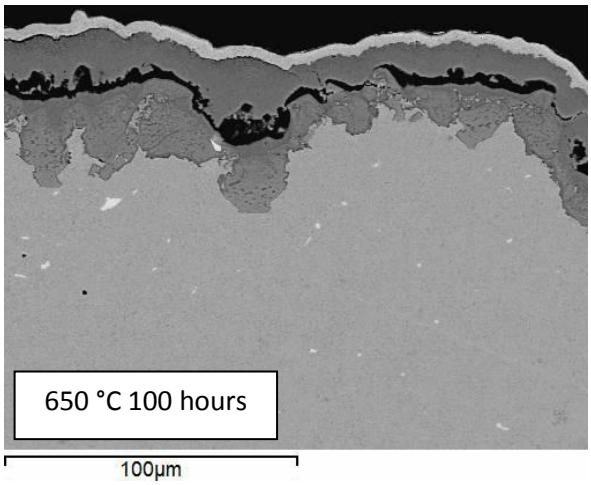

d)

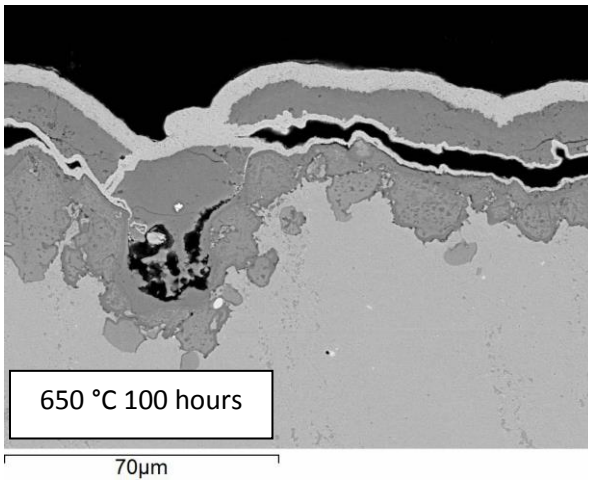

e)

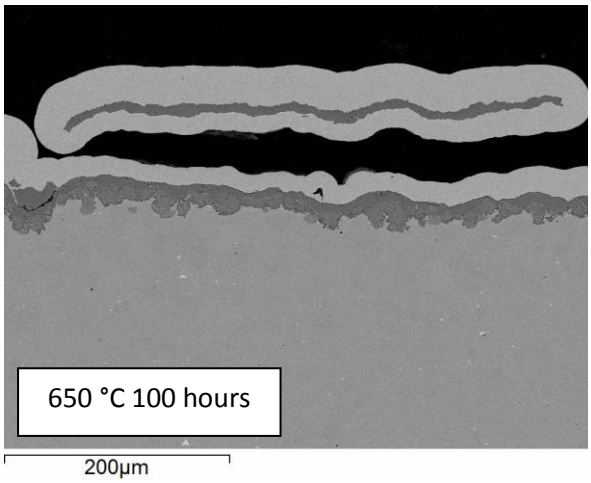

f)

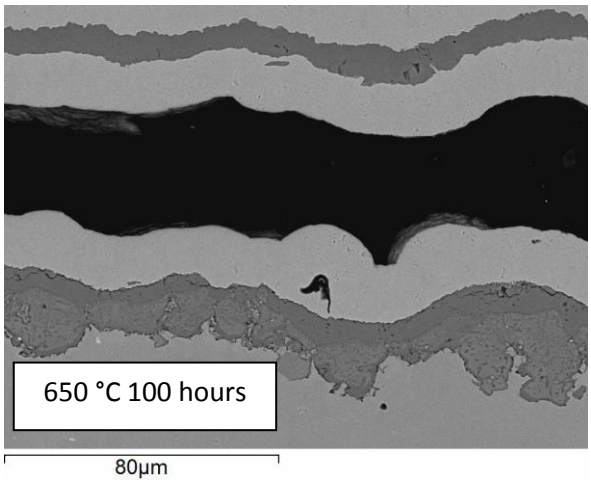

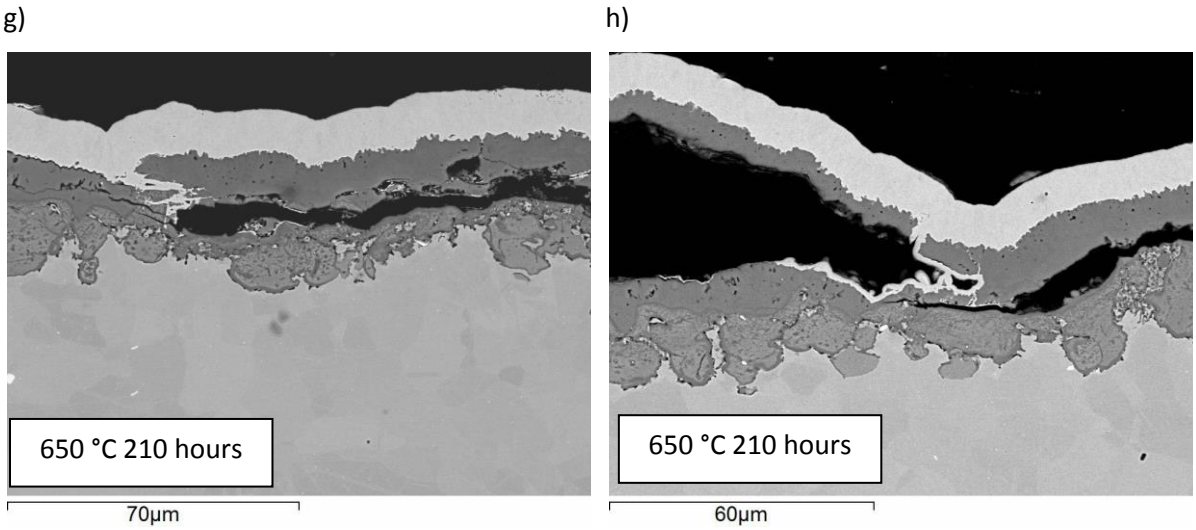

Figure 4.121 – BSE SEM cross-section micrographs of spallation on Super 304H oxidised in deoxygenated steam at 650 °C.

One sample oxidised at 700 °C spalled. The sample, oxidised for 250 hours is shown in Figure 4.122. The outer oxide had a high level of porosity, which was distributed either throughout the outer oxide or more heavily concentrated towards the spinel/outer oxide interface. Spallation always occurred along the porous interface. The morphology of the inner oxide was similar to that of samples oxidised at the same temperature for the same duration that did not spall. The sample in Figure 4.122 had a thicker chromium rich film than the equivalent sample that did not spall. Figure 4.122 c) shows a buckle in the outer oxide of the same sample.

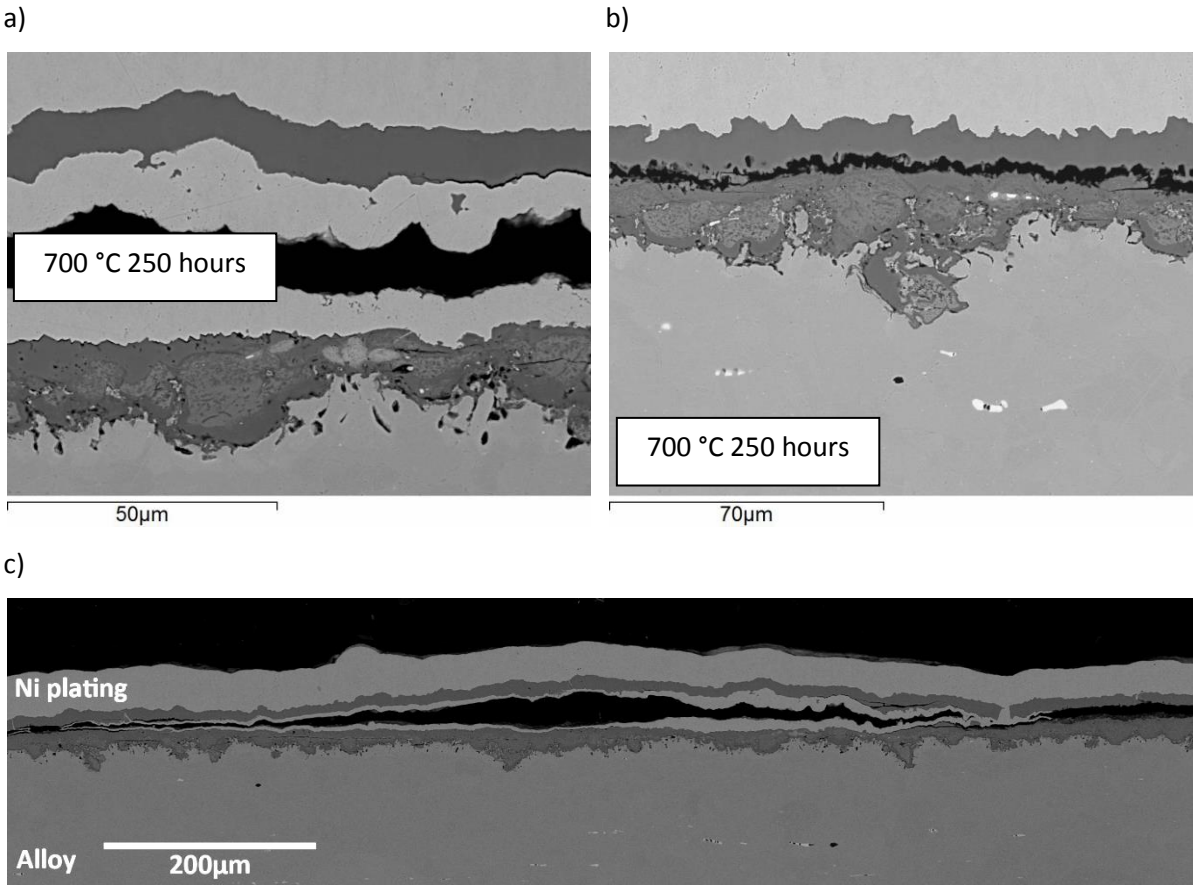

Figure 4.122 – BSE-SEM micrograph of spallation of oxide on Super 304H oxidised in deoxygenated steam at 700 °C for 250 hours.

4.5.2.2.4 Oxide Area Maps of Super 304H after Oxidation in "Deoxygenated Steam"

An EDX area map of adherent and unadherent oxide on the sample of 347HFG oxidised for 250 hours at 700 °C is shown in Figure 4.123. The element maps confirm spalled oxide is purely iron rich oxide. The spinel oxide is surrounded by a thick chromium rich oxide where iron, nickel and copper are depleted. Here, manganese is enriched. In the subjacent alloy there is a thick band of chromium and manganese depletion, which corresponds with nickel and iron enrichment. Copper appears to be enriched slightly in areas at the top of the spinel oxide and also largely enriched in small areas between consumed austenite grains in the spinel oxide, presumably as metal particles.

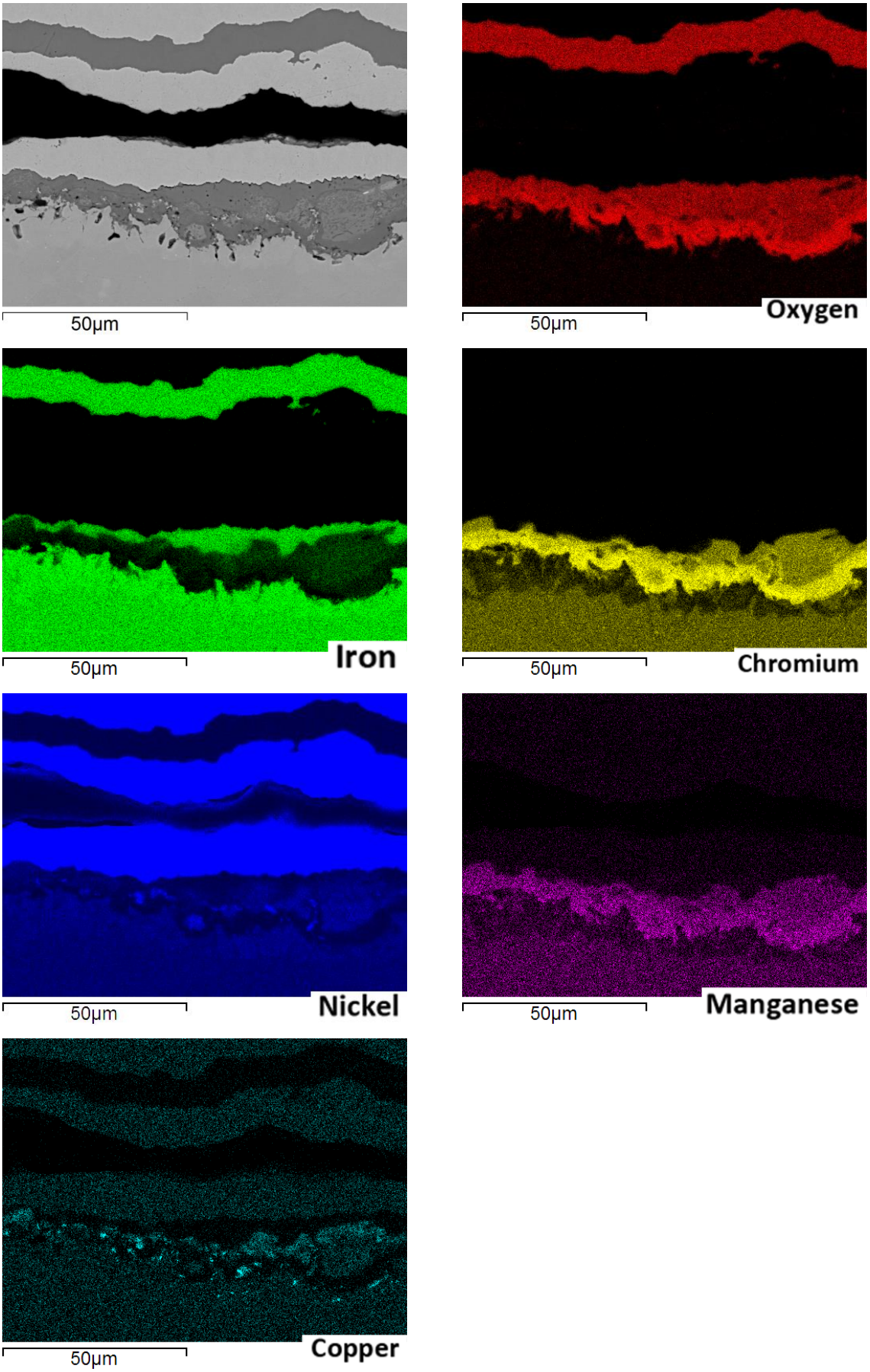

Figure 4.123 – EDX area map of buckle in oxide of Super 304H oxidised in deoxygenated steam at 700 °C for 250 hours.

4.5.2.2.5 Optical Microscopy of Super 304H after Oxidation in "Deoxygenated Steam"

The fraction of haematite in the outer oxide layer of samples of Super 304H oxidised in deoxygenated steam that spalled varied between 10 – 100%. Where the haematite fraction was low as shown in Figure 4.124 a)), it did not tend to form a uniform layer at the top of the oxide. Instead it formed in patches throughout the fraction of outer oxide that had spalled. In no cases was haematite found in the attached oxide where the above oxide had spalled. On samples where the haematite content was above approximately 40% of the spalled oxide, the haematite was present as a distinct layer between magnetite and the outer oxide/gas interface as in Figure 4.124 c), d)).

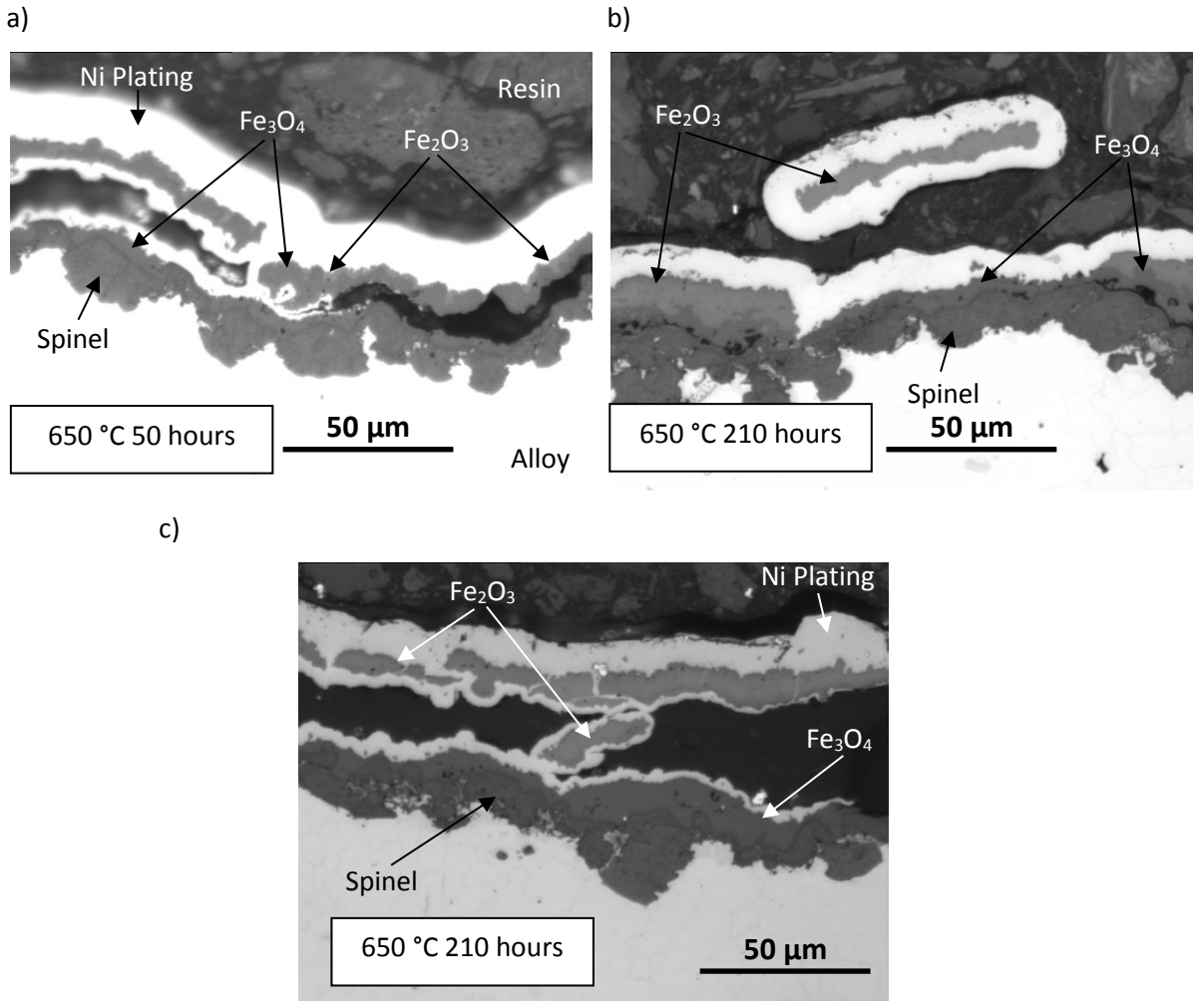

Figure 4.124 – Optical micrograph of oxide on Super 304H.

4.5.2.2.6 XRD Analysis of Super 304H after Oxidation in "Deoxygenated Steam"

Super 304H sample showed stronger haematite peaks and weaker magnetite peaks compared with oxide spalled from 347HFG. From optical microscopy analysis in Figure 4.124 c), it appeared as if the

oxide that was detached from the surface was homogeneous in phase. That is, between 90 and 100% of the detached oxide was the lighter (in colour) of the two outer oxide phases. Comparison between the XRD trace for 347HFG oxidised for 100 hours in Figure 4.117, magnetite appears weaker in the oxide spalled from the Super 304H sample, suggesting the dominant phase observed in detached oxide through the optical microscope is haematite. The peak heights of the 210 hour Super 304H spalled oxide sample closely resemble those of the 210 hour 347HFG sample, which contained approximately 80% haematite in the outer oxide.

Note that because of the limited oxide spall from the Super 304H sample available to analyse, and the mounting method employing a sticky carbon tag, a large amount of background noise was picked up during the scan. The majority of this was removed by the background removal algorithm in X'Pert Highscore. However, it did not completely remove the background noise, which remains present as a broad peak on the left side of the scan in Figure 4.125.

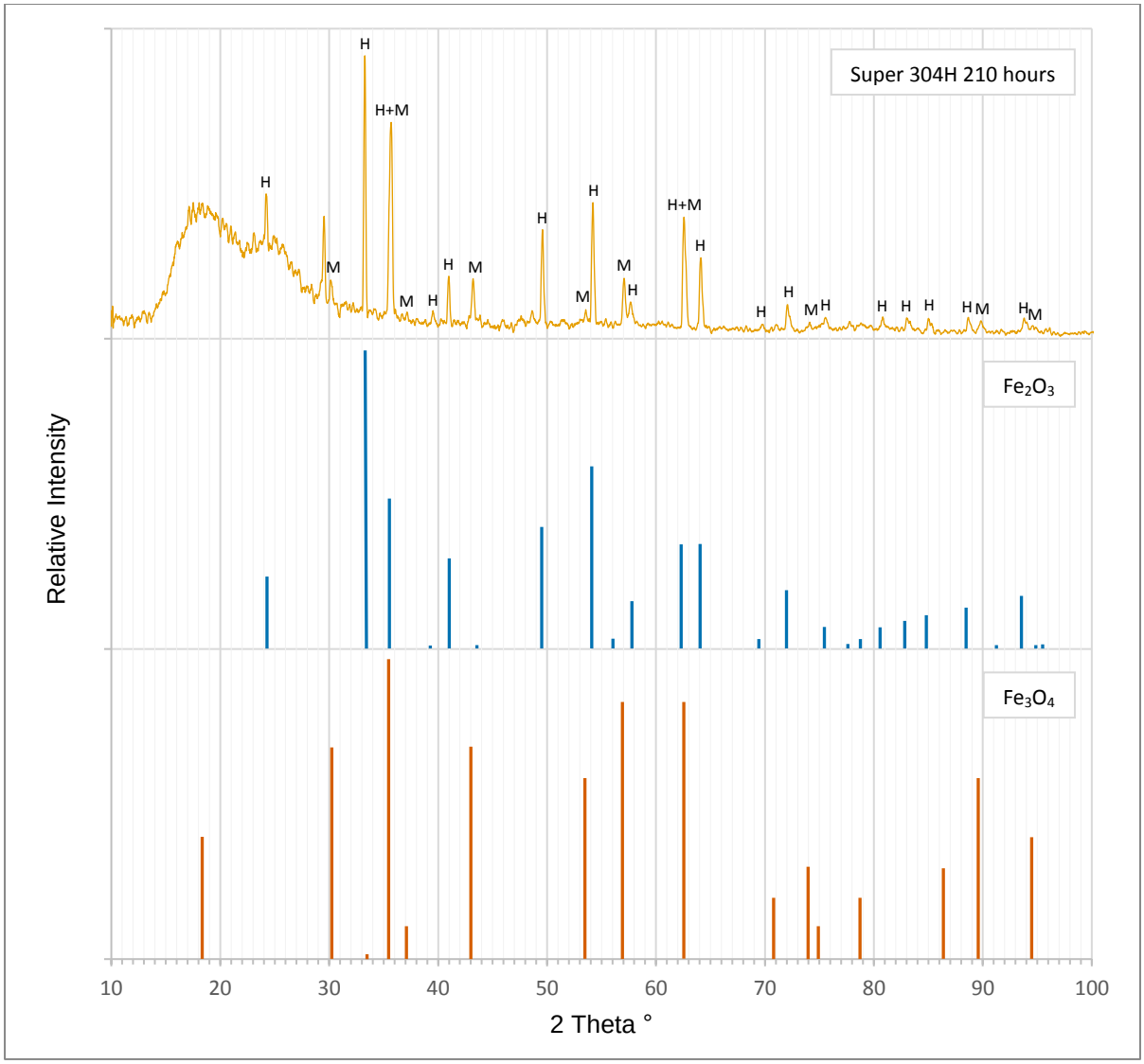

Figure 4.125 – XRD analysis of spalled oxide from a sample of Super 304H oxidised in "deoxygenated steam" at 650 °C for 210 (top) hours. Comparing the peak intensity of each spectrum with those of haematite (second from top) and magnetite (bottom), the spalled oxide after oxidation for 210 hours appears to contain a larger haematite fraction than the spalled oxide oxidised for 100 hours, in agreement with optical microscopy analysis.

4.5.3 Summary of Spallation of Austenitic Steels in "Deoxygenated Steam"

This section summarises the results of steam oxidation experiments on samples of 347HFG and Super 304H that exhibited spallation during stage 1 and 2 development of the steam oxidation facility. The results of these experiments are included as they provide insight into the cause for spallation and associated mechanisms.

During the early stages of development, the conclusion was drawn that the feedwater was not effectively deoxygenated prior to oxidation experiments being undertaken, leading to a high pO_2 oxidising atmosphere. The following conclusions were drawn following analysis of spalled samples.

- Spallation from early flowing steam oxidation experiments was observed from the inner surfaces of 347HFG and Super 304H samples after oxidation at 650 and 700 °C. No spallation was observed on HR3C or the inner surfaces of Super 304H SP samples.
- XRD detected both haematite and magnetite in samples of spalled oxide, suggesting the spallation interface was not at the magnetite/haematite interface. This was confirmed by cross-sectional analysis.
- A fraction of between 10 and 80% haematite was recorded in the outer oxide of spalled samples. The conclusion was drawn that the pO_2 of the oxidising atmosphere must have been higher for these experiments than for those where the oxygen content of the water was verified below 10 ppb.
- Haematite in the outer oxide showed little porosity whereas magnetite showed highly variable porosity.
- The spallation interface was either within the outer oxide layer or at the spinel/outer oxide interface.
- The spallation interface usually ran through a porous band in the outer oxide layer.

4.6 Air Saturated Steam: Investigation into the Spallation Behaviour of 347HFG

Oxidation of austenitic steels in deoxygenated steam showed that under steam flow conditions where the pO_2 was less than 10 ppb, no spallation was observed from any of the steels tested (Section 4.4). Spallation was observed to occur on a number of samples of 347HFG and Super 304H that were tested before installation of the molecular oxygen content monitoring equipment in stage 4 of development of the steam oxidation facility (see Section 3.4.5). Analysis of the oxides grown on all steels exposed to steam revealed that spallation occurred only on samples when the outer oxide contained more than 10% haematite. Haematite growth, although thermodynamically stable in pure steam at the temperatures investigated, is favoured at increased pO_2 leading to the consideration that the pO_2 of the steam exposed to the samples that exhibited spallation during early steam oxidation trials, may have been somewhat higher than 10 ppb.

To investigate the effect of oxygen partial pressure on oxidation and spallation behaviour, the oxygen free nitrogen gas cylinders were replaced with BOC air cylinders as the feedwater degassing medium. Samples of 347HFG (which had previously shown a spallation tendency) were oxidised in flowing air saturated steam for 50, 100, 250 and 500 hours at 650 °C. The morphology and spallation behaviour of the oxides grown were investigated and compared to those grown on samples oxidised in deoxygenated steam.

All samples of 347HFG exhibited spallation. The fraction of the oxide on the sample inner surface that spalled varied between samples and generally increased with oxidation time. No visible spallation was found to have already occurred on sample boat removal from the furnace. The time to first spallation of the inner surface oxide was recorded from removal of the sample boat from the furnace. The time to spallation for 347HFG varied between 6 and 12 minutes and decreased with increased oxidation time.

4.6.1 Oxidation Kinetics of 347HFG after oxidation in Air Saturated Steam

4.6.1.1 Mass Gain Measurements of 347HFG after oxidation in Air Saturated Steam

Samples were weighed without spall as spallation in the boat could not be associated with a particular sample.

Mass gain data for 347HFG oxidised in air saturated steam can be found in Figure 4.126. With the exception of the data point at 500 hours (identified with an arrow), there is a clear negative trend in mass gain as oxidation time increases. The reason for this is the increase in spallation after longer exposures. The identified data point corresponds to a sample that must have slipped on entering the furnace and was found resting against a sample of P92 in the alumina boat on removal from the furnace (air saturated steam oxidation experiments included samples of P92, which are not reported on in the project). P92 samples were larger than 347HFG samples and so steam flow across the surface of the 347HFG sample may have been restricted, which may have affected the oxide growth and spallation of the sample.

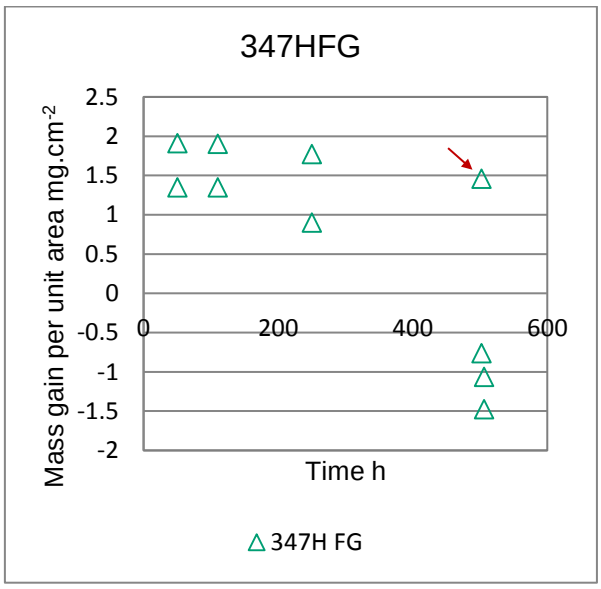

Figure 4.126 – Mass gain data for 347HFG oxidised in air saturated steam at 650 °C.

4.6.1.2 Oxide Thickness Measurements of 347HFG after oxidation in Air Saturated Steam

Oxide thickness measurements for the chromium rich, spinel, outer and total oxide layer thicknesses are shown in Figure 4.127 a). The outer oxide data points are a sum of attached and detached oxide

thicknesses to obtain the total outer oxide thickness. The total oxide thickness data points are a sum of the individual layer thicknesses. In agreement with oxidation in deoxygenated steam, the thickness of the individual layers increases with increasing oxidation time. The detached oxide thicknesses are plotted with total oxide thicknesses in Figure 4.127 b).

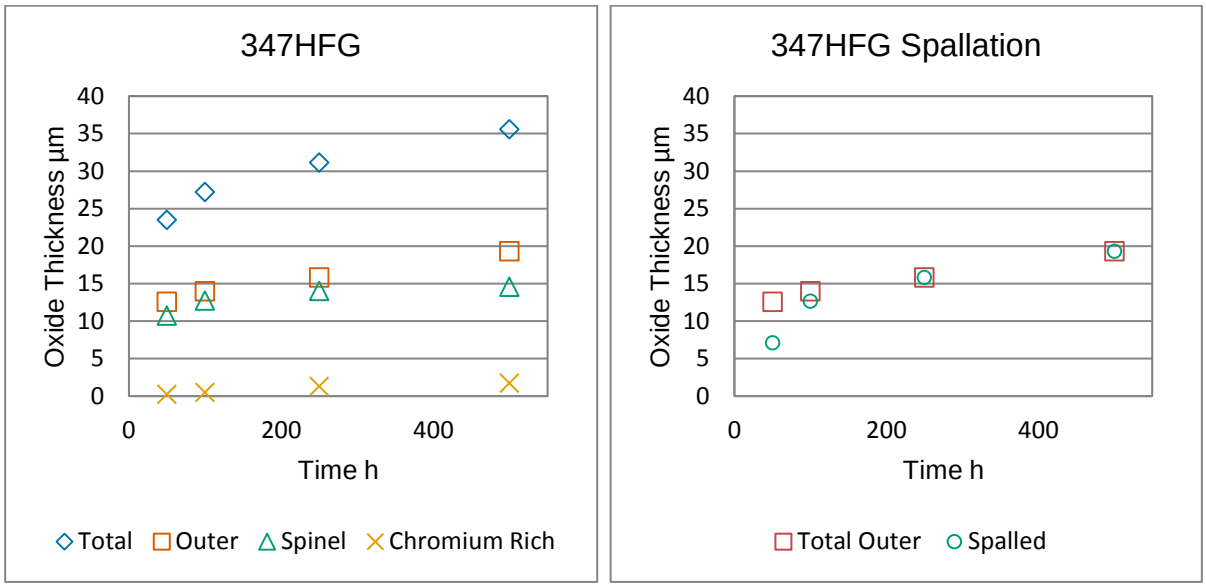

Figure 4.127 – Oxide thickness data for 347HFG oxidised in air saturated steam at 650 °C. a) Individual oxide layer thicknesses, note "Outer" refers to the sum of adherent and spalled thicknesses, b) Comparison of total outer oxide thickness and spalled outer oxide thickness.

4.6.2 Oxide Morphology of 347HFG after oxidation in Air Saturated Steam

4.6.2.1 Visual Observations of 347HFG after oxidation in Air Saturated Steam

Samples of 347HFG showed varying amounts of spallation on their inner surface. The fraction of inner surface that had spalled increased with increasing oxidation time. Unspalled areas were matt grey in appearance and spalled areas were either dark grey and matt or grey and reflective. Reflective areas were not found after 50 hours and formed only a small fraction of the spalled area after 100 hours. After 250 and 500 hours the majority of the spalled area was of the reflective kind. The inner surfaces of 347HFG samples are shown in Figure 4.128.

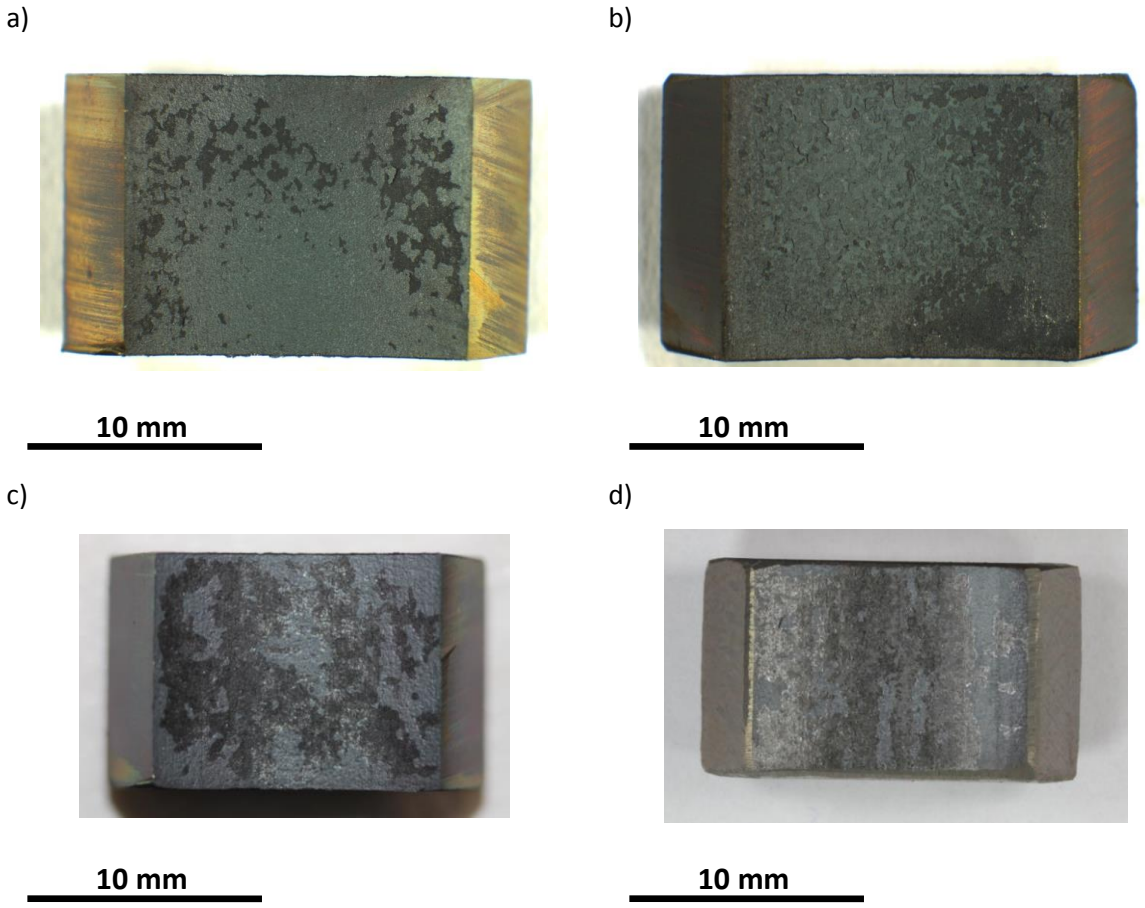

Figure 4.128 – Macro images of 347HFG inner surface after oxidation in air saturated steam at 650 °C for a) 50 hours, b) 100 hours, c) 250 hours, d) 500 hours.

4.6.2.2 SEM Analysis of 347HFG after Oxidation in Air Saturated Steam

The morphology of the inner surface of 347HFG after oxidation in air saturated steam differed between areas of adherent oxide and areas where spallation had occurred. In areas where the entire oxide remained adherent, as in Figure 4.129 a), the scale consisted of porous haematite, from which platelets and a small number of whiskers had grown. The base haematite oxide was consistent across unspalled regions of the inner surface, however, in areas where blisters had formed during oxidation (see below), whiskers and platelets were largely absent. It was occasionally difficult to differentiate between oxide phases in areas where spallation had occurred because of the destructive nature of a spallation event. This was particularly true around the parameter of spalled regions, where through thickness cracking had led to the release of a spalled particle. Nevertheless, it was clear from inspection of the inner surfaces that there existed two defined oxide morphologies in spallation regions that corresponded to two distinct spallation interfaces: spallation of the entire outer oxide layer (haematite, and magnetite where present) leaving spinel oxide exposed (Figure 4.129 b)); and spallation within the outer oxide leaving areas of adherent iron oxide (Figure 4.129 c)). EDX analysis of different spallation regions confirmed the locations of iron rich oxide and spinel oxide.

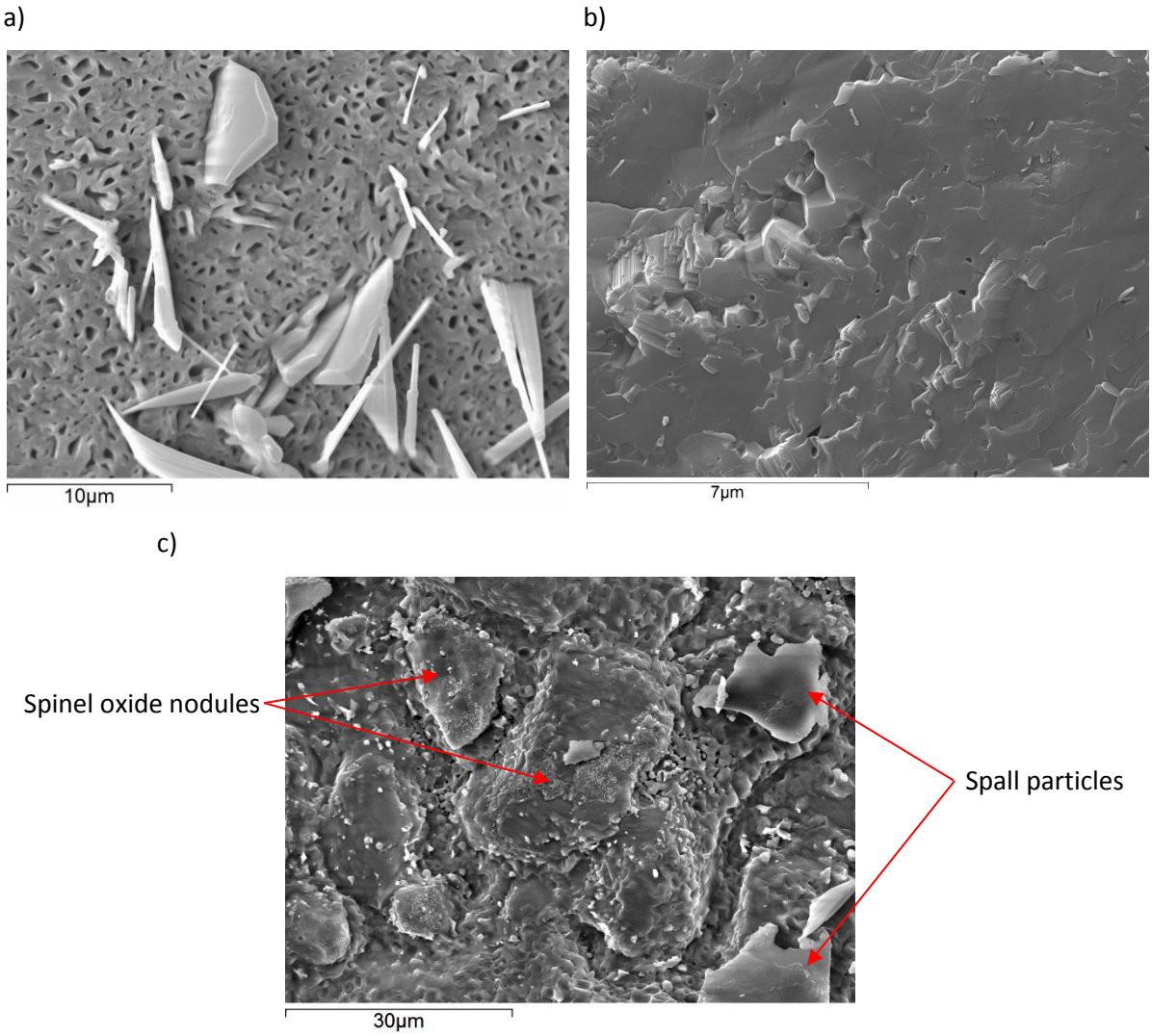

Figure 4.129 – Oxide morphology of the inner surface of 347HFG after oxidation in air saturated steam for 500 hours at 650 °C. a) unspalled region, b) region where spallation had occurred within the outer layer, c) region where spallation had occurred at the inner/outer oxide interface.

Cross-section analysis revealed oxide morphology similar to that formed in deoxygenated steam. The outer oxide exhibited variable porosity. Through inspection under the optical microscope, it was possible to differentiate between magnetite and haematite layers, in that haematite appeared as a lighter grey. Haematite was identified as an individual layer at the oxide gas interface (Figure 4.130) and not dispersed in patches throughout the magnetite layer as was occasionally the case for samples that exhibited spallation after oxidation in deoxygenated steam. The haematite fraction in the outer layer increased with oxidation time from an average of 75% after 50 hours to an average of 90% after 500 hours. On close inspection of the haematite layer, micro pores, around 0.5 µm in diameter could be identified at the oxide/gas interface, to a depth of around 5 µm, other than these, the haematite layer could be considered free of pores. Generally, the magnetite layer exhibited a high level of porosity. Pores were either distributed evenly throughout the magnetite or had accumulated with a

bias towards the spinel/outer oxide interface (Figure 4.130 a) and c)). Pores in the magnetite layer were sometimes found to be lined with a sub-micron thick layer of haematite.

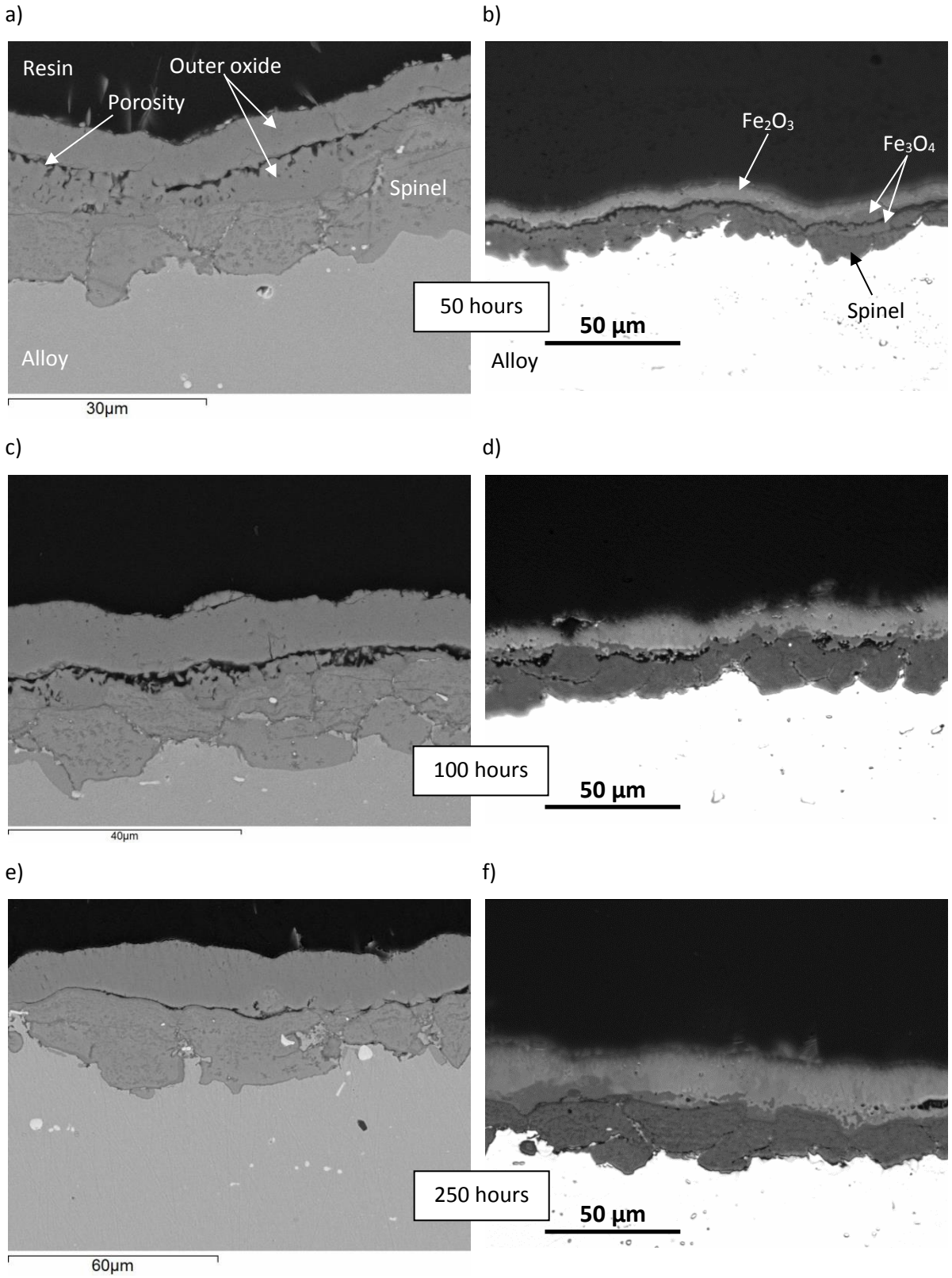

Figure 4.130 – a), c), e) BSE SEM cross-section micrographs and b), d), f) optical cross-section micrographs of fully adherent regions of oxide formed on 347HFG after oxidation in air saturated steam for 50, 100 and 250 hours at 650 °C.

4.6.2.3 Spallation Morphology of 347HFG Oxidised in Air Saturated Steam

Two forms of spallation were identified on samples of 347HFG oxidised in air saturated steam: spallation involving the majority or the entire outer oxide layer, and spallation of very thin layers of haematite, which took the form of oxide "blisters". The latter will be addressed in the following section, but first, the more familiar form will be considered.

Spallation of the outer oxide occurred on all samples. The fraction of spallation of the inner tube surface increased as oxidation time increased. Figure 4.131 is an SEM topographical view of a region of spallation on the inner surface of 347HFG after oxidation in air saturated steam for 500 hours at 650 °C. Spallation of both the entire outer oxide layer, revealing the underlying spinel, and of a fraction of the outer oxide layer occurred, as indicated in Figure 4.131 b). In Figure 4.131 e) the fracture surface extends from the outer oxide surface to within the outer oxide layer revealing the distribution of pores from the surface to the depth from which spallation occurred. The pores are over 1 µm in diameter just below the oxide surface and decrease in size to sub-micron as depth increases. The pore volume fraction decreases into the oxide suggesting the porous surface only reaches a few microns into the oxide layer, in agreement with analysis of oxide cross-sections containing an outer layer of haematite. In areas absent of spallation, the oxide surface was scattered with platelets and occasionally whiskers, as shown in Figure 4.131 d), e) and f). Pores are visible in the oxide fracture surface in Figure 4.131 e) and f). The porosity is highest where the fracture reaches the surface, and decreases with fracture depth.

The composition of the spalled particles, as identified by optical microscopy in Figure 4.132 and Figure 4.133, often consisted of both magnetite and haematite. The spallation interface was often within a porous region of magnetite, or, where the entire outer oxide layer was identified as haematite, at the spinel/haematite interface. After 50 hours oxidation the mode of failure was identified as buckling. The buckle in Figure 4.132 was formed from approximately 80 – 90% of the outer oxide thickness, and contained approximately 80% haematite in the form of layer at the oxide/gas interface. The failure mode was less obvious after longer periods of oxidation as there were no obvious buckles identified on samples oxidised for 250 and 500 hours. However, the area of decohesion in Figure 4.131 b) (approximately 400 µm) is large enough to have permitted buckling there, assuming that the area corresponds to a single spallation event.

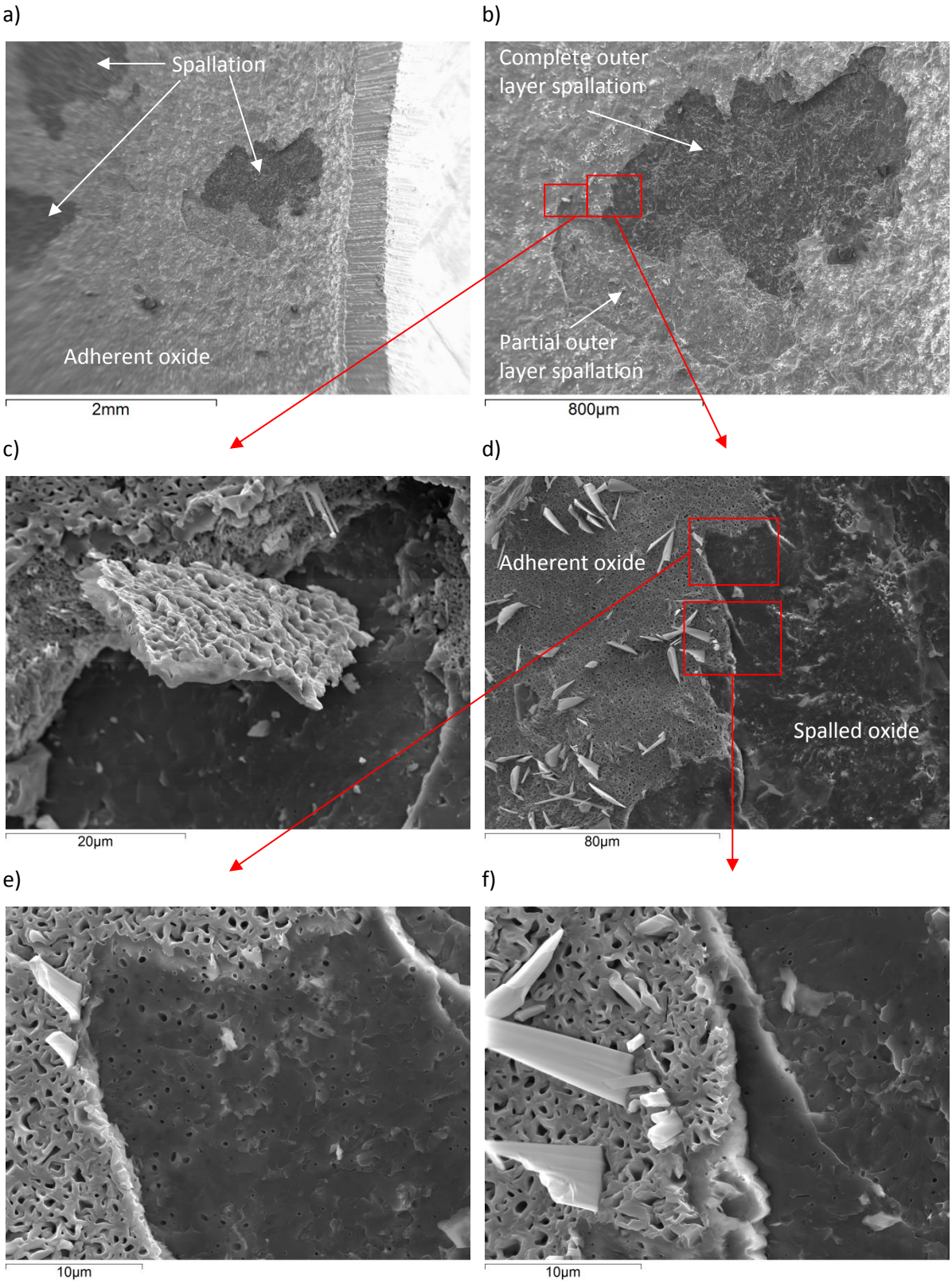

Figure 4.131 – SEI SEM micrographs of inner surface of 347HFG after oxidation in air saturated steam for 500 hours at 650 °C. a) low magnification image of inner surface showing areas of spallation, b) area of spallation, c) loose spallation particle on sample surface, d), e), f) spallation fracture surfaces showing areas of adherent oxide and areas where spallation has occurred.

a)

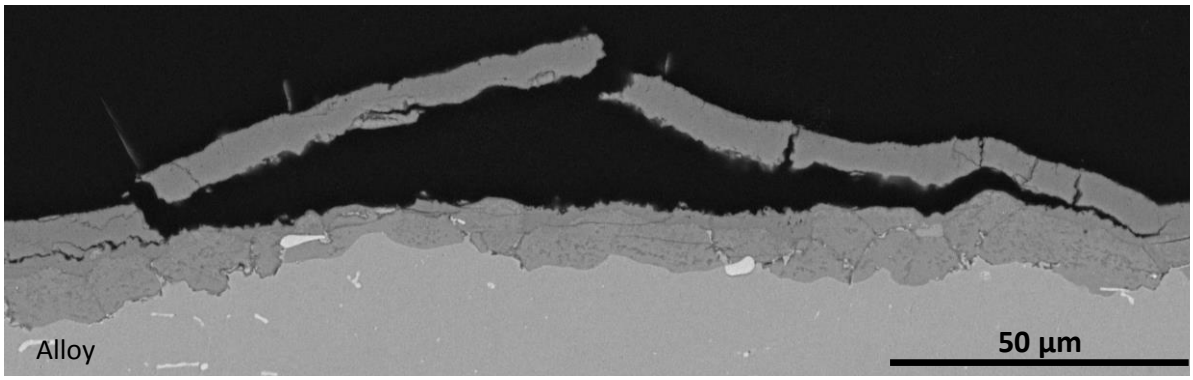

b)

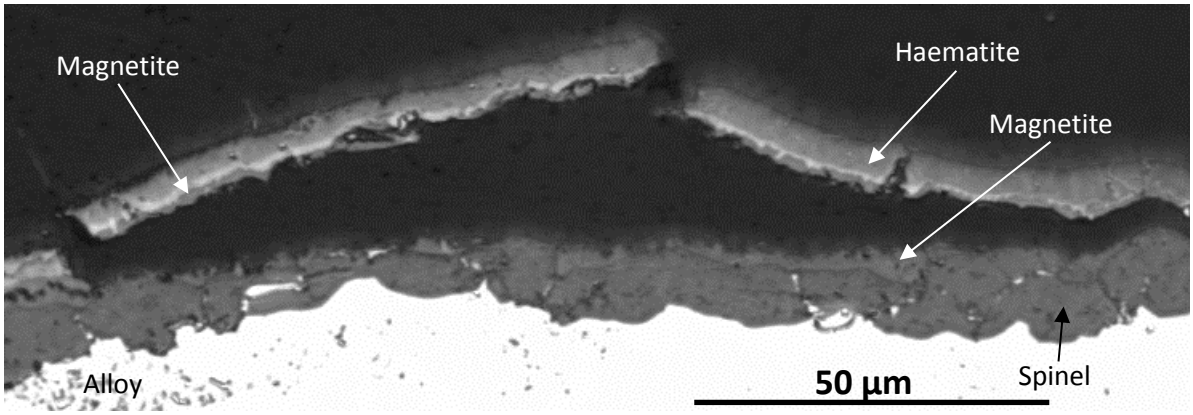

c)

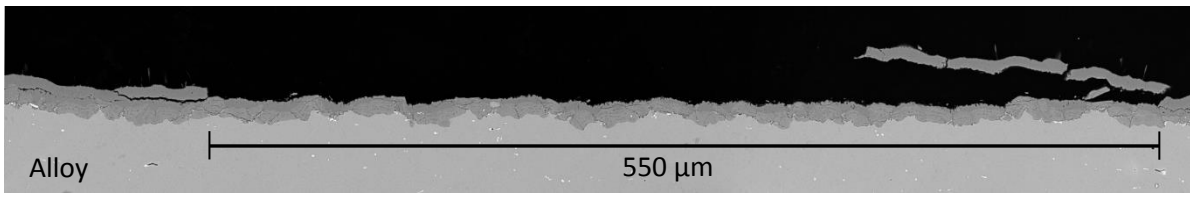

Figure 4.132 – a), b) oxide buckle and c) spallation after oxidation for 50 hours at 650 °C.

Figure 4.133 shows varying amounts of haematite in the outer oxide of samples of 347HFG oxidised for 100 and 250 hours. The spallation interface varied between the spinel/outer oxide interface and within the magnetite layer.

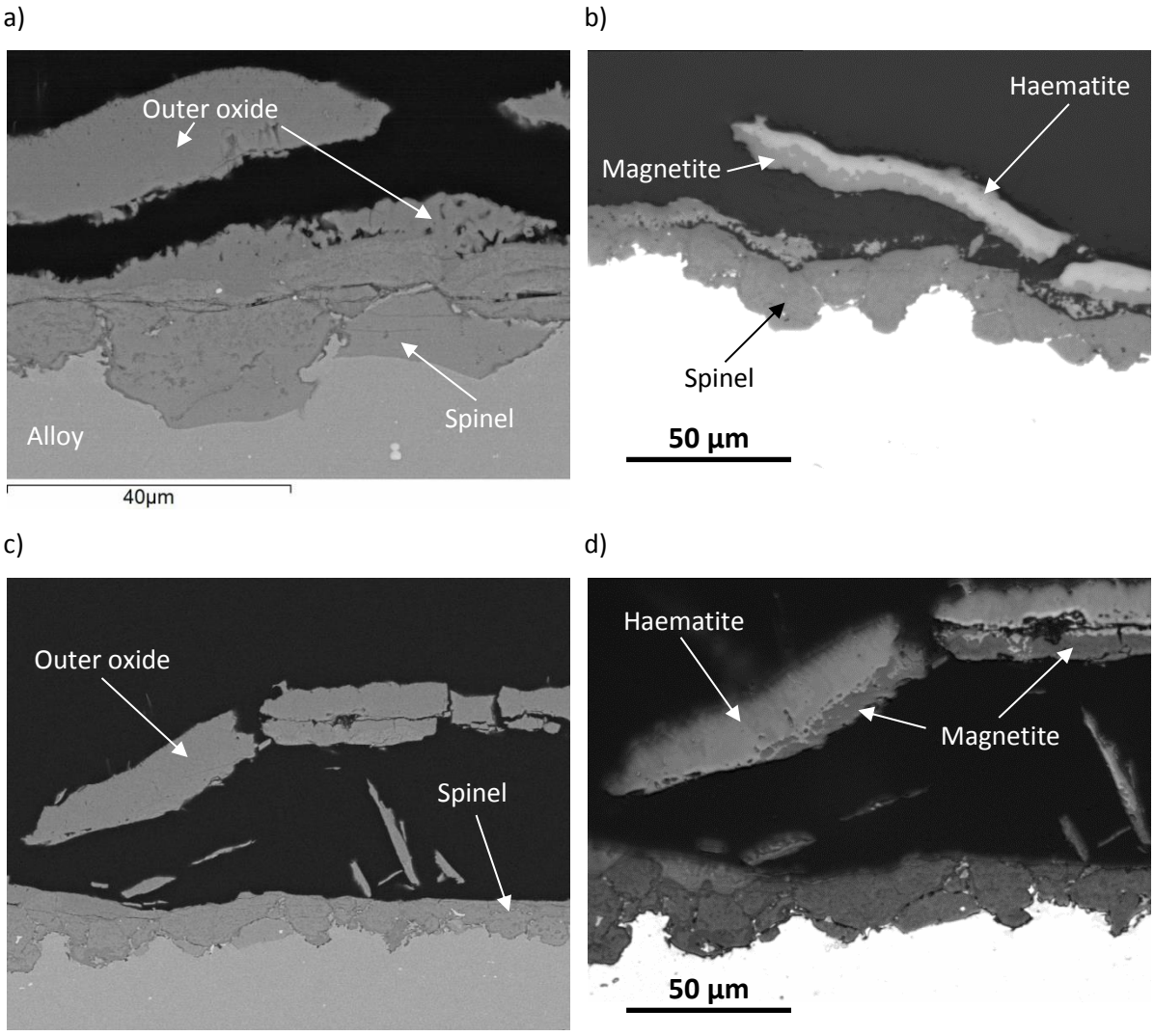

Figure 4.133 – a), c), BSE SEM cross-section micrographs and b), d), optical cross-section micrographs of spallation regions of oxide formed on 347HFG after oxidation in air saturated steam for a), b) 100 hours and c), d) 250 hours at 650 °C.

The second form of spallation was that from blistered oxide, which was found intermittently on all samples oxidised in air saturated steam. Oxide blisters resembled oxide buckles (that are considered to initiate over an area of decohesion during cooling). The morphology of the oxide blisters suggests they would have buckled on cooling, however, there is evidence to suggest that they are formed *during* oxidation. The following evidence is listed:

1) Thickness of detached oxide

The thickness of spalled oxide from samples that exhibited spallation in "deoxygenated steam" was relatively consistent for each sample. On samples oxidised in air saturated steam, there were two clearly different oxide thicknesses for unadherent oxide: unadherent oxide that resembled that of the unadherent oxide on "deoxygenated steam" samples (Figure 4.132), and a much thinner oxide that appeared to have only ever been connected to the bulk oxide at the perimeter

of the buckle. This is illustrated in Figure 4.134 for a sample of 347HFG oxidised for 100 hours and 250 hours.

a)

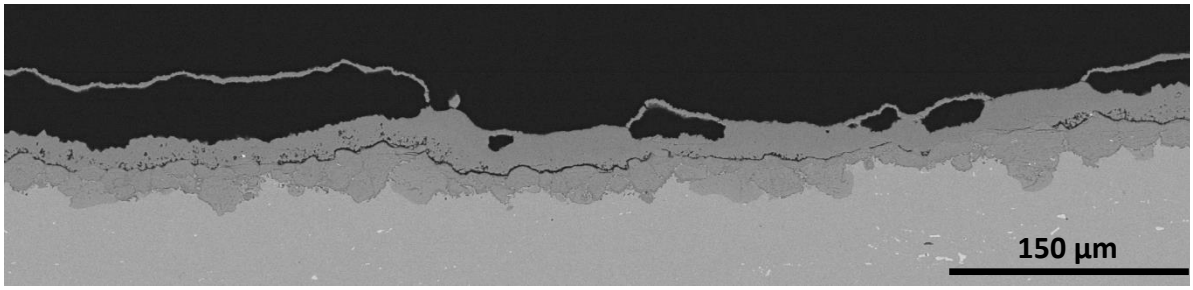

b)

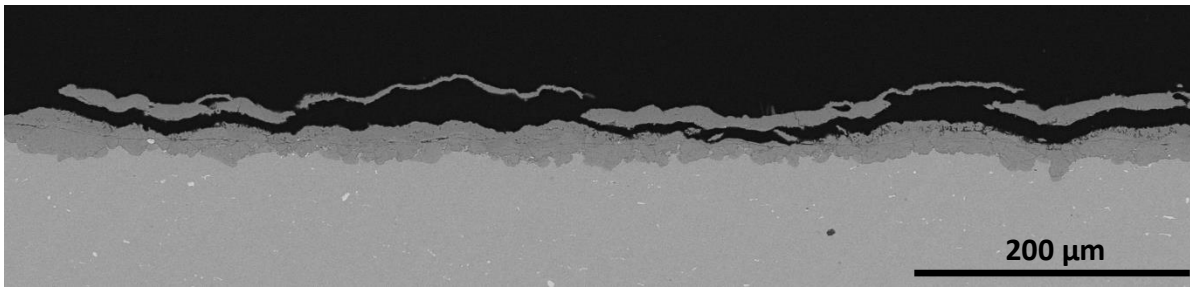

Figure 4.134 – Oxide blisters on samples of 347HFG oxidised in air saturated steam for a) 250 hours and b) 100 hours. Note in that in b), the surrounding outer oxide has become unadherent from the rest of the oxide.

2) Strain in detached oxide

The strain in the unadherent oxide in Figure 4.135 is a factor of 2 larger than is expected (-1.067% compared to -0.417%), had the oxide originally been in contact with the bulk oxide. This suggests the oxide became decoherent, and expanded, during oxidation.

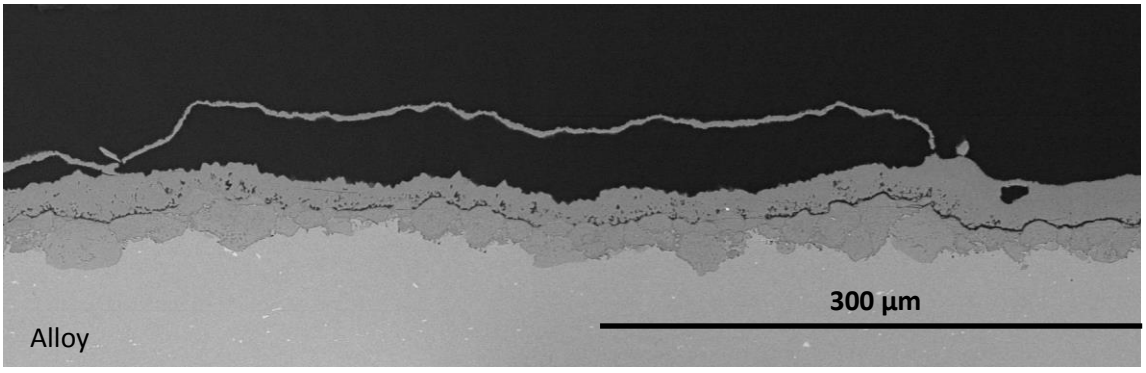

Figure 4.135 – Unadherent oxide on 347HFG oxidised for 250 hours at 650 °C in air saturated steam. The unadherent oxide is longer than would be expected had it been in contact with the bulk oxide at the oxidation temperature, suggesting the oxide was in the form of a blister during oxidation.

3) Composition of oxide beneath blister

The composition of the oxide beneath areas of thin, unadherent oxide was different to other areas of the oxide. Under blisters, the outer oxide was composed almost entirely of magnetite after 50 and 100 hours, and a small fraction of haematite after 250 and 500 hours – much less than the bulk fraction of between 75% and 90% haematite in the outer oxide. The presence of magnetite increased the porosity of the oxide beneath blisters. This is illustrated by the two oxide blisters in Figure 4.136, following 100 hours oxidation at 650 °C.

a)

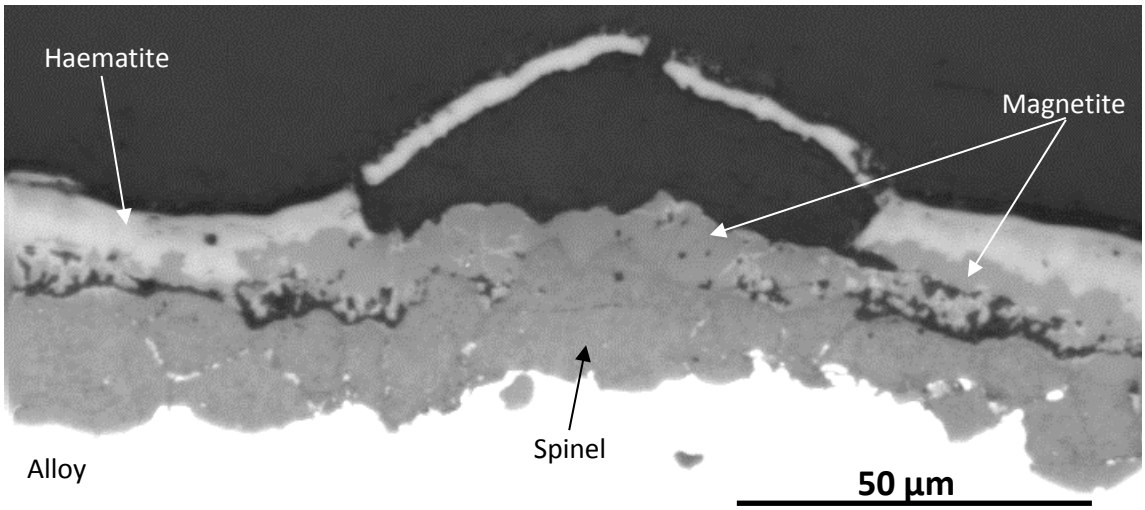

b)

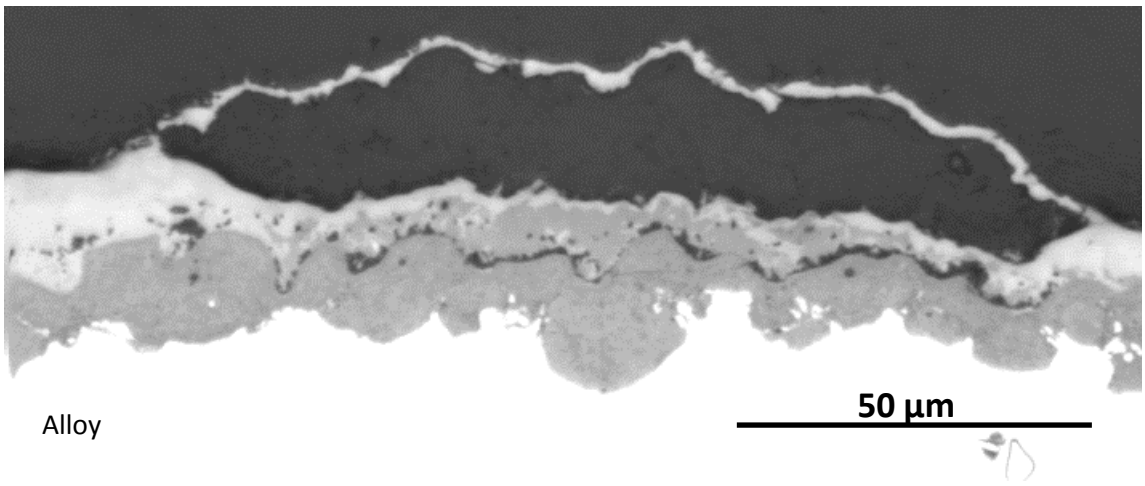

Figure 4.136 – Unadherent oxide on 347HFG oxidised in air saturated steam for 100 hours at 650 °C. In locations of unadherent oxide, the underlying outer oxide contains less haematite than surrounding areas. After 50 and 100 hours, the underlying outer oxide was composed almost entirely of magnetite.

4) Perimeter of blisters

Whereas buckling of the oxide because of cooling resulted in the perimeter of such buckles converging into a point, where tensile crack growth caused lateral propagation of the buckle (See Figure 4.132 a), Figure 4.114, Figure 4.116), the perimeter of the oxide blisters were not observed

to have formed tensile cracks at all. In fact, at the perimeter of an oxide blister, the thin blistered oxide had usually formed at the edge of a much thicker region of outer oxide, as shown in Figure 4.137.

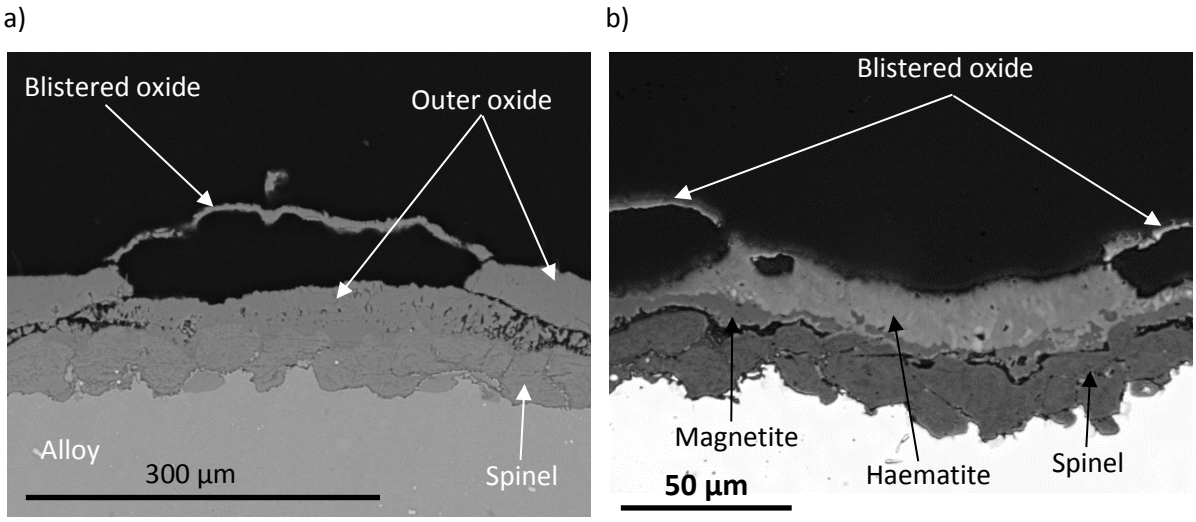

Figure 4.137 – a) BSE SEM micrograph and b) optical image of blistered oxide on 347HFG after a) 100 and b) 250 hours of oxidation in air saturated steam at 650 °C showing absence of tensile cracks at the perimeter of the blisters.

5) Surface morphology within blisters

BSE SEM topography micrographs of the inner surface of 347HFG after oxidation in air saturated steam for 500 hours at 650 °C are shown in Figure 4.138. The micrographs show two distinct areas of spallation: to the right of each micrograph, spallation of the entire outer oxide has revealed the fracture surface and spinel oxide. In the centre of the micrographs, the outer layer of the oxide blisters has spalled, revealing a morphology that resembles the outer oxide of unspalled regions of the surface. Had the overlying oxide spalled via a decohesion process, the underlying oxide within the spalled blisters would resemble a fracture surface.

Further verification of the oxide morphology inside blisters can be found in Figure 4.139 and Figure 4.140. Figure 4.139 shows the similarities between oxide morphologies within an oxide blister to that of adherent bulk oxide. In contrast, the fracture surface from a spallation event of the bulk oxide looks completely different. The surface oxide in unspalled regions appeared porous. In Figure 4.140 spallation of the bulk oxide has revealed the depth to which pores at the surface penetrate to. Surface pores were around 0.5 µm in diameter – smaller than those found in the magnetite layer, and decreased in number from the surface until the oxide was pore-free at approximately 5 µm depth. In agreement with cross-sectional analysis (see Figure 4.130) the pore morphology would suggest that this oxide phase is haematite.

a)

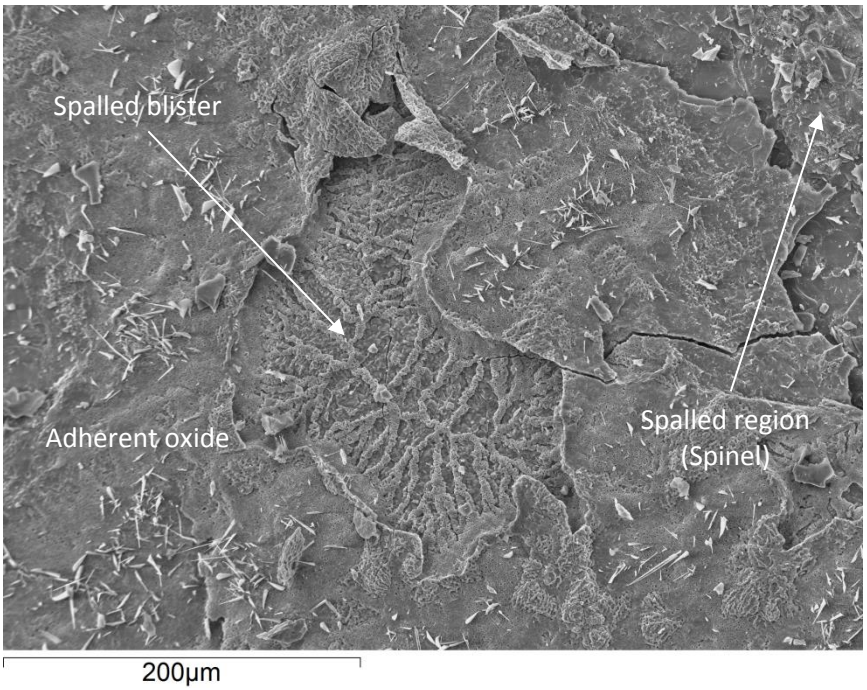

b)

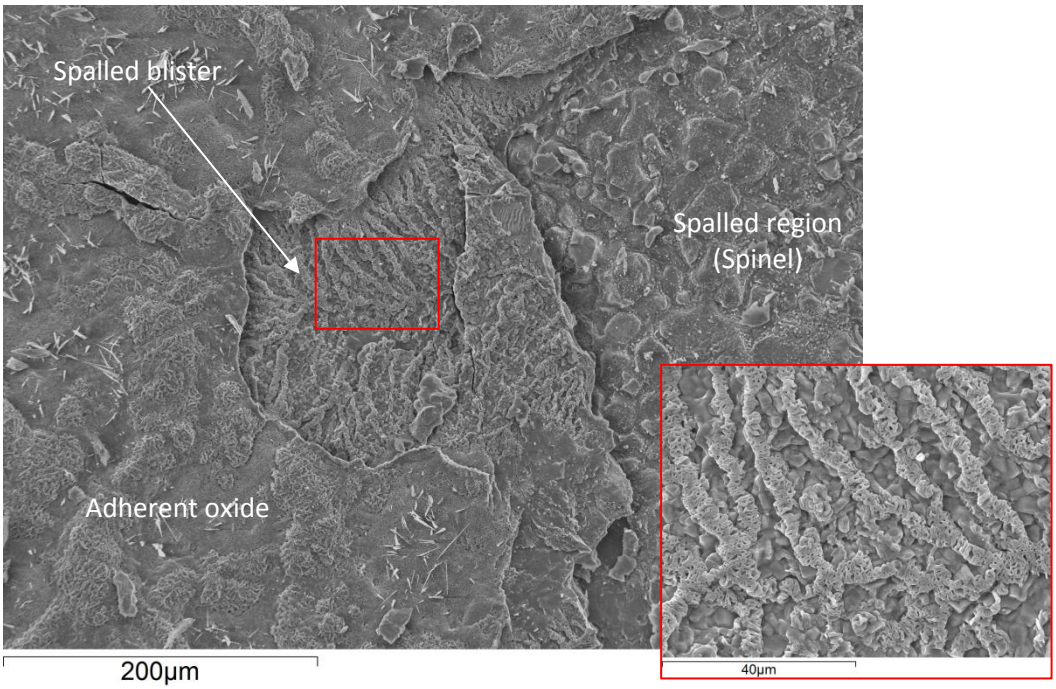

Figure 4.138 – SEI SEM micrographs of the inner surface of 347HFG after oxidation in air saturated steam for 500 hours at 650 °C illustrating areas where the top oxides of oxide blisters have spalled off leaving the underlying oxide exposed.

Figure 4.141 is an example of a fracture surface after spallation of the outer oxide of a sample oxidised for 500 hours at 650 °C. A band of pores runs through the micrograph in Figure 4.141 a) and on closer inspection (Figure 4.141 b)) the oxide in is faceted. The pores are larger, and deeper within the oxide than in Figure 4.140 suggesting the oxide may be magnetite.

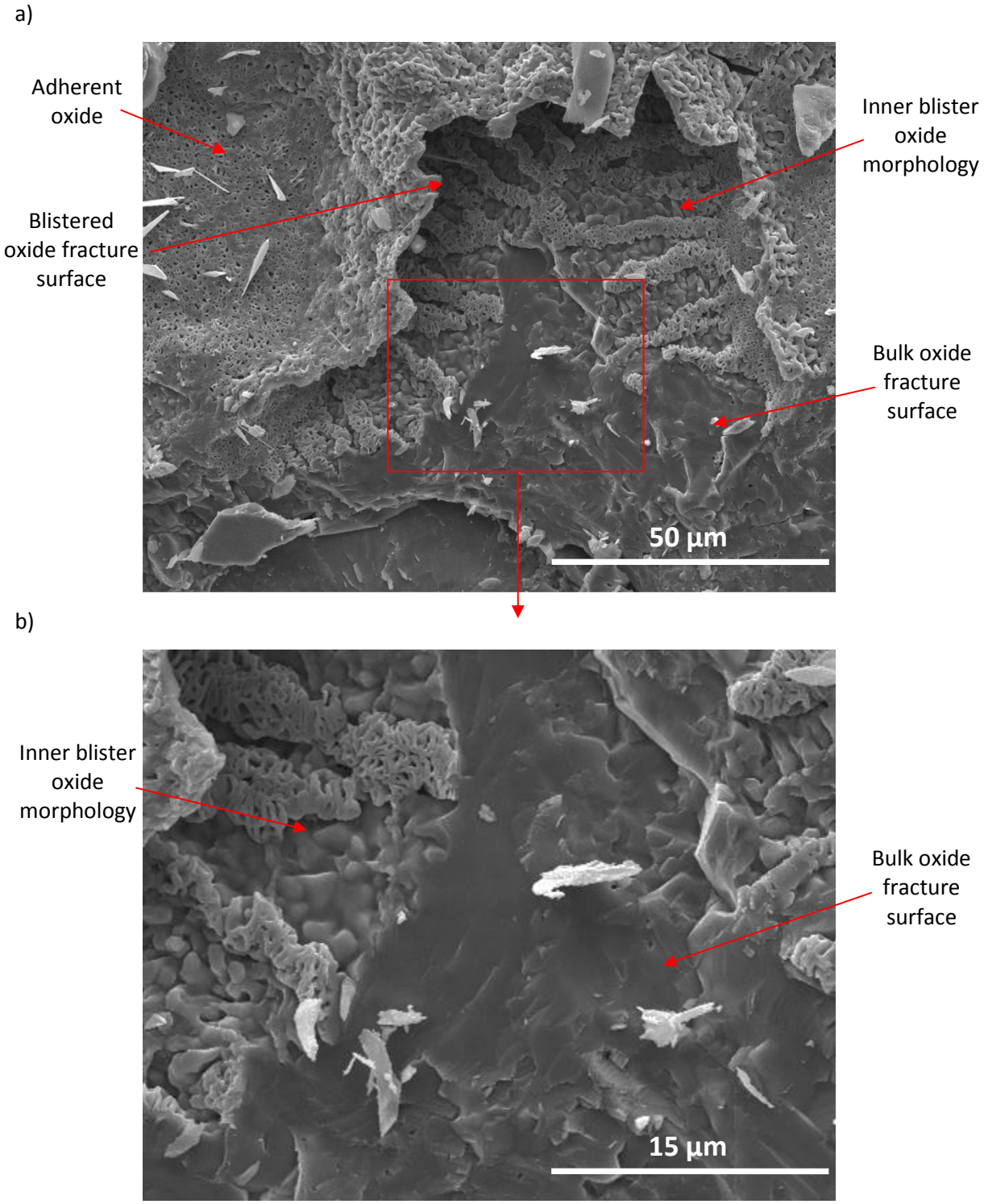

Figure 4.139 – SEI SEM micrographs of the inner surface of 347HFG after oxidation in air saturated steam for 500 hours at 650 °C. a) area where the outer layer of a blister, along with a portion of underlying oxide has spalled, b) high magnification of fracture surface notably revealing non-porous morphology of haematite oxide directly below the surface.

Oxide spallation where blistering was frequent sometimes involved decohesion of a large thickness fraction of the outer oxide, constrained lengthways by two oxide blisters (Figure 4.134 b)). The thin layer of oxide forming the dome of the blister would then be removed along with the bulk oxide either

side of the blister, leaving only the underlying adherent magnetite where the blister used to be, and the spinel oxide.

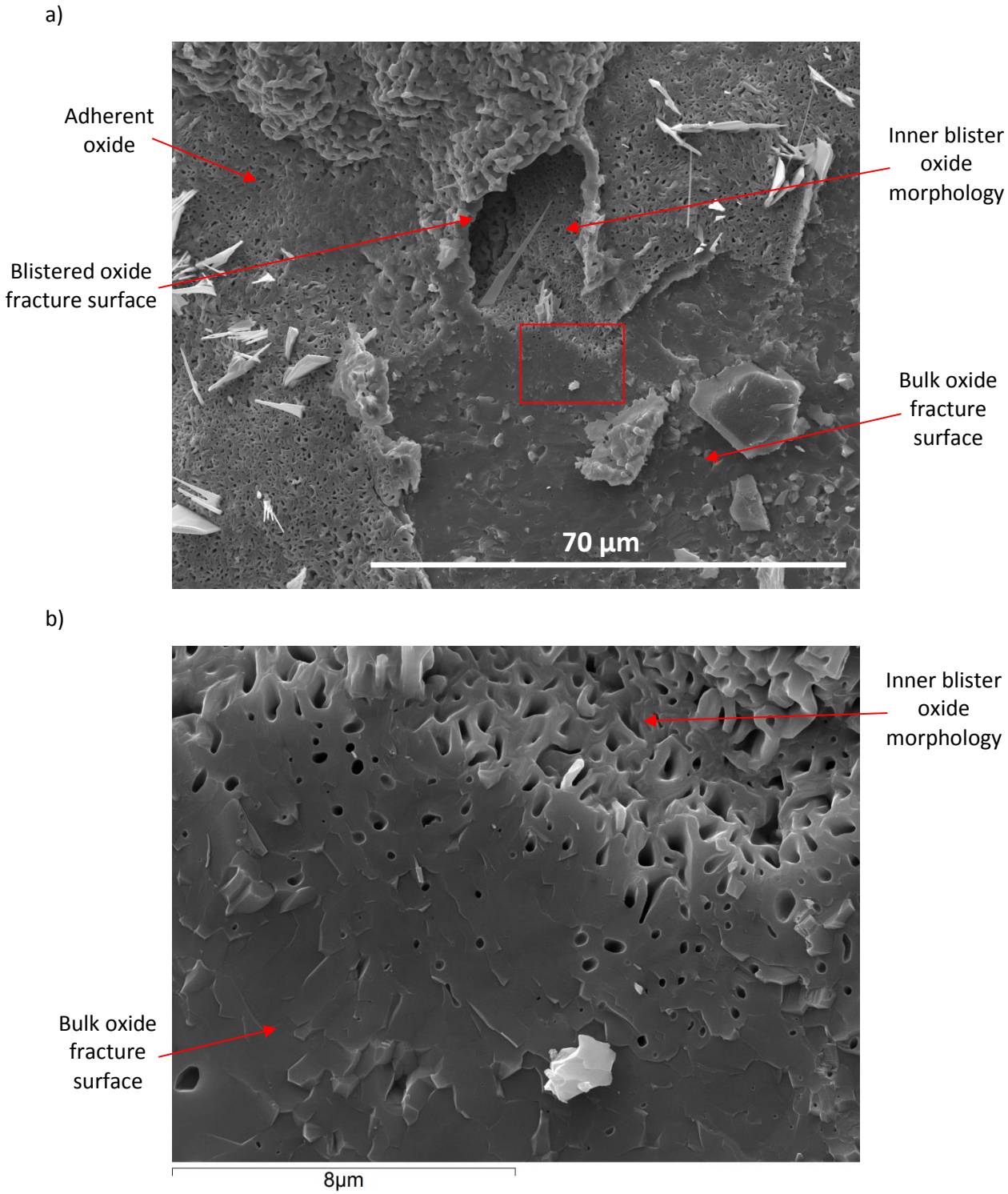

Figure 4.140 - SEI SEM micrographs of the inner surface of 347HFG after oxidation in air saturated steam for 500 hours at 650 °C. a) area where the outer layer of a blister, along with a portion of underlying oxide has spalled, b) high magnification of fracture surface notably revealing non-porous morphology of haematite oxide directly below the surface.

After 250 and 500 hours, the fraction of haematite in the adherent oxide within blisters increased to as much as 50% and spallation of both the oxide away from blisters, and the outer oxide within blisters

spalled. Oxide blisters most likely buckled during cooling, leading to spallation of the blistered oxide. However, because of the mechanism of formation and failure, they are treated separately to other forms of spallation in the Discussion chapter.

a)

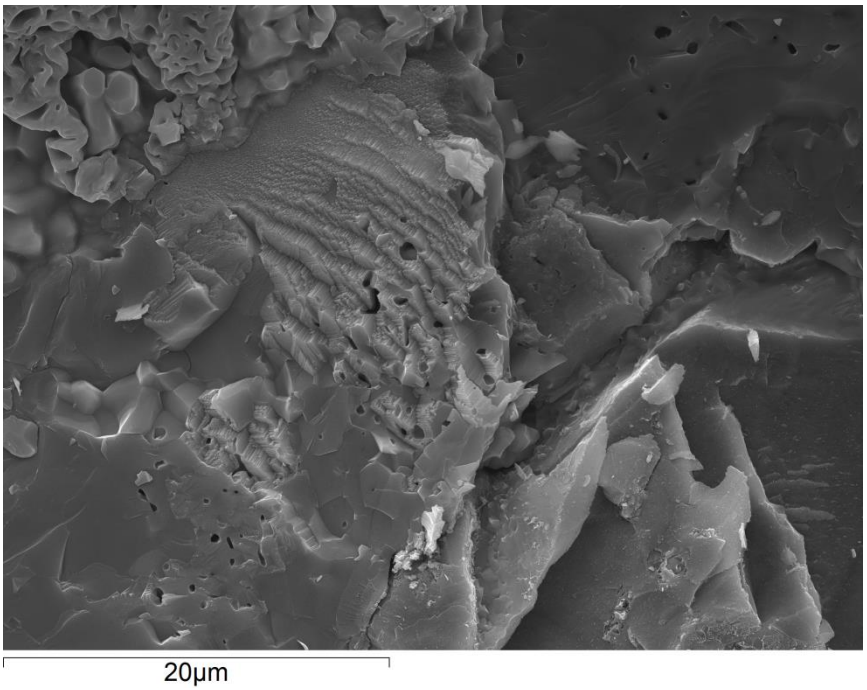

b)

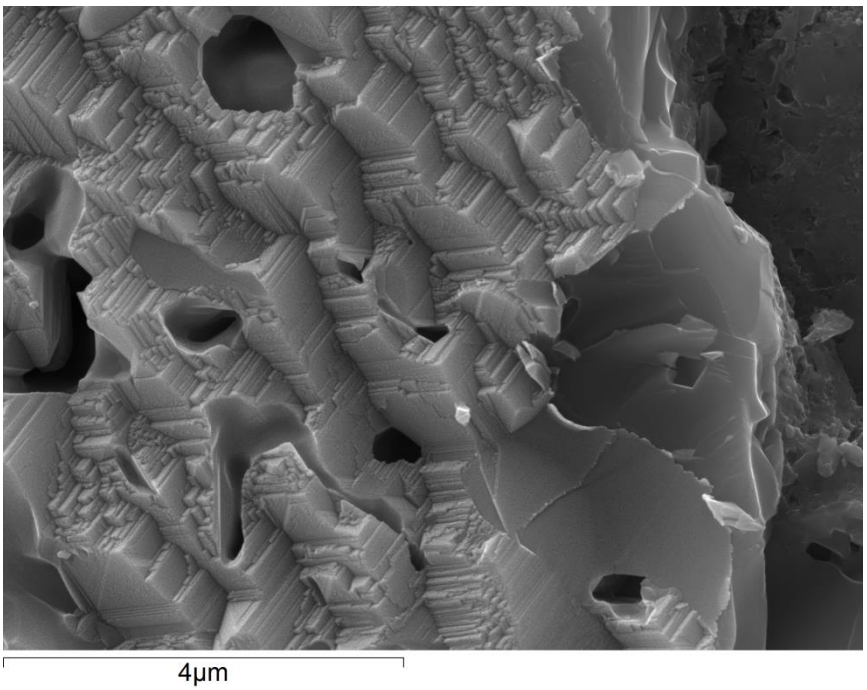

Figure 4.141 – Fracture surface following spallation of the outer oxide on a sample of 347HFG oxidised in air saturated steam for 500 hours at 650 °C showing porosity within the layer.

4.6.3 Summary of Oxidation and Spallation in Air Saturated Steam

347HFG grew thicker scales in air saturated steam than in deoxygenated steam. The oxide grown is duplex, with an inner spinel oxide and outer iron rich oxide. A chromium rich base layer is sometimes grown. Optical microscopy revealed two distinct phases in the outer oxide – magnetite and haematite. Haematite formed at the oxide/gas interface and its thickness increased with exposure time. Consequently, the thickness of magnetite decreased with exposure time, leading to the assumption that magnetite is first formed and then converted, from the oxide/gas interface down, to haematite. After 500 hours exposure, approximately 90% of the outer oxide layer was haematite. Haematite oxide was largely free of pores. However, micro pores were present at the surface to a depth of around 5 μm where there was an absence of oxide blistering. The magnetite layer appeared more porous, with porosity either evenly spread throughout the layer, accumulating below the perimeter of oxide blisters, or accumulating at the magnetite/haematite interface. The accumulation of pores is believed to be favourable for spallation to occur.

SEM and optical analysis of both the topography and cross-section micrographs of the oxide formed on 347HFG led to a number of observations regarding the spallation behaviour of 347HFG in air saturated steam.

- All samples of 347HFG oxidised in air saturated steam exhibited spallation.
- The fraction of inner tube surface area that was subject to spallation increased with oxidation time.
- Spallation occurred exclusively after removal from the furnace.
- Spallation primarily occurred either at the inner/outer oxide interface or within the outer oxide, at the magnetite/haematite phase boundary.
- Thin sections of outer oxide that appeared as buckles in cross-section micrographs were identified as oxide growth blisters and did not form from the decohesion of adherent oxide during sample cooling.
- The top oxide of many blisters had spalled, fracturing at the perimeter of the buckle.
- The oxide beneath oxide blisters was primarily magnetite up to 250 hours oxidation. After 500 hours oxidation the underlying oxide of around 50% of oxide blisters consisted of approximately 40% haematite, which was located at the oxide/gas interface.

4.7 Summary of Experimental Results

The oxidation and spallation behaviour of the inner (steam-side) surface of austenitic steel tubing has been investigated experimentally as a function of the following parameters;

- **Temperature**
  - 600 °C;
  - 650 °C;
  - 700 °C.
- **Alloy composition**
  - Alloy 347HFG (18Cr11Ni, fine grained);
  - Super 304H (18Cr8Ni3Cu, fine grained);
  - Alloy HR3C (25Cr20Ni, course grained).
- **Surface treatment**
  - Inner surface pickled (347HFG, Super 304H, HR3C);
  - Inner surface shot peened (Super 304H).
- **Oxidising atmosphere**
  - Static laboratory air;
  - Flowing deoxygenated steam;
  - Flowing air saturated steam.

Additionally, in order to facilitate high temperature oxidation experiments in flowing steam, an atmospheric steam oxidation facility was built, commissioned, and improved as part of this research programme.

The findings of this study are summarised below.

Temperature

- Oxide morphology showed little variation over the temperature range explored on all alloys in all oxidising atmospheres. The main influence of temperature was to accelerate the oxide growth. For example, the morphology of an oxide after 500 hours at 600 °C may have appeared similar to an oxide grown after 100 hours at 700 °C.
- For the pickled 18Cr alloys in air, oxidation kinetics tended to proceed at an initially rapid rate until duplex oxide covered the entire surface, at which point the oxidation rate decreased. This occurred after a shorter oxidation time as temperature increased. A faster initial

oxidation rate was observed for HR3C. However, this was to a lesser extent, and was thought to correspond to formation of a Cr-rich protective oxide, rather than complete duplex coverage. A steady increase in oxidation kinetics with increasing temperature were observed on shot peened Super 304H in air.

- In steam, a fast initial oxidation rate was observed, followed by a reduced rate, as with oxidation in air. However, in steam the rate reduction was attributed to the internal oxidation front consuming the first layer of prior austenite grains, where a Cr-rich healing layer was established, reducing ion diffusion and oxide growth rate. Increasing the oxidation temperature decreased the time it took for the oxidation rate to decrease.

Alloy Composition

- The effect of alloy composition was mainly attributed Cr content. 18Cr alloys 347HFG and Super 304H behaved similarly in all atmospheres. In air they formed a nodular oxide that coalesced into full duplex coverage. HR3C retained a nodular oxide in air, with limited coalescence after longer durations. This was attributed to the formation of a more protective Cr-rich film, with possibly higher Cr_2O_3 content, which took longer to break down than on the 18Cr alloys.
- In steam, HR3C gave way to a duplex oxide, albeit of much smaller thickness than 18Cr alloys. The composition of the inner spinel oxide contained more Cr and Ni than the 18Cr alloys. Interestingly, where the oxidation front did propagate into the alloy, a number of much larger pits were observed compared with the 18Cr alloys. This was attributed to the larger grain size of HR3C, and proved that even with the higher Cr content, grain boundary diffusion plays a big role in formation of a healing layer.

Surface Treatment

- Shot peening provided a huge improvement in oxidation resistance of Super 304H compared to the pickled surface. In air, the oxide generally took two forms: a thin, Cr,Mn-rich protective oxide, upon which Mn-rich crystallites formed, or a Cr,Mn-rich protective oxide with a thin Fe-rich outer oxide. The shot peening treatment left a smooth but clearly worked finish, with micro-features and burrs, which sometimes acted as nucleation sites for rare oxide nodules to grow. The oxide morphology appeared similar in a steam environment, albeit slightly thicker. Shot peening proved to be a more effective method at resisting oxidation than raising Cr content on a pickled alloy (HR3C). Unfortunately, because of difficulty with sample

preparation, in-depth cross-sectional analysis of shot peened Super 304H could not be undertaken.

Oxidising Atmosphere

- The effect of steam on oxidation of the pickled alloys was to accelerate oxidation, and promote formation of a thick duplex oxide, in comparison to the nodular oxide formed in air.
- A combination of EDX, XRD, and optical microscopy were used to identify the Fe-rich outer phase in each atmosphere. This was found to be Fe_2O_3 in air, Fe_3O_4 in deoxygenated steam, and a combination of Fe_2O_3 and Fe_3O_4 in air saturated steam. Although Fe_2O_3 is stable at the oxygen partial pressure of all atmospheres, it was believed to be suppressed in deoxygenated steam due to a local reduction of pO2 at the oxide/gas interface. Porosity in the outer oxide tended to coincide with the presence of Fe_3O_4. It follows that the outer oxide was found to be significantly porous in deoxygenated steam, and non-porous in air.
- The inner oxide contained the elements found in the bulk alloy. EDX analysis on the oxide cross section was not able to determine the form of nickel within the layer. The composition of the spinel oxide was suggested to be either a $(Fe,Cr,Ni)_3O_4$ spinel, or a $(Fe,Cr)_3O_4$ spinel within a metallic nickel matrix. The ratio of anions to cations reported by EDX was broadly higher on samples oxidised in air than deoxygenated steam, indicating that a higher fraction of nickel may have oxidised in air atmosphere. EDX analysis was not performed on samples oxidised in air saturated steam.
- The formation of a Cr-rich healing layer only occurred in atmospheres containing steam, and was found to correspond to the internal oxidation front reaching prior austenite grain boundaries. This occurred on the 18Cr alloys at all temperatures. The Cr-rich healing layer effectively reduced the internal oxidation rate, and once formed, the inner/outer oxide layer thickness ratio began to decrease, suggesting that Fe ions were continuing to diffuse to the oxide/gas interface, but anion diffusion through the healing layer was limited.
- The presence of steam caused sporadic heavy pitting of HR3C. It is postulated that the large grain size allowed deeper propagation of the internal oxidation front than the 18Cr fine grained alloys, until a prior austenite grain boundary was reached.

Spallation

- Spallation was only observed on pickled 347HFG and Super 304H samples.
- Spallation was not observed on any sample oxidised in laboratory air.
- Spallation was not observed on any sample oxidised in effectively deoxygenated steam.

- Spallation was observed on all samples of 347HFG oxidised in air saturated steam (347HFG was the only austenitic alloy subjected to air saturated steam experiments).
- Spallation was observed on a small number of pickled 347HFG and Super 304H samples during early trials of the steam oxidation facility. Examination of the oxide scales suggests that the feedwater was ineffectively deoxygenated, and this promoted the formation of Fe_2O_3 on these samples.
- Cross-sectional analysis of samples that exhibited spallation revealed that spallation was directly linked to the presence of haematite in the outer oxide layer.
- The spallation interface was found to be either the inner/outer oxide interface, or within the outer oxide.
- Spallation tended to occur along a porous interface, suggesting porosity influences spallation behaviour.

Wright & Dooley [42] propose a similar mechanism where spallation of the outer oxide occurs after the formation of a healing layer facilitates the formation of haematite in the outer layer. However, laboratory tests of much shorter durations [115] have shown exfoliation to occur on Super 304H without a complete base layer or large haematite fraction present. The work also found decohesion to occur at both the inner/outer oxide interface and within the outer oxide [115], in contrast to the mechanism proposed by Wright & Dooley, which assumes the decohesion interface to be the inner/outer oxide interface only.

Chapter 5 Discussion

5.1 Introduction

Increasing the steam parameters within plant boilers facilitates the need for new materials that can withstand higher temperatures and pressures than materials currently in use. The superheater and reheater experience the highest temperatures and pressures. It is these that require the most advanced materials such as fine grained TP347HFG and Super 304H, and alloys whose chromium contents are above 20 wt .% (HR3C). Increasing steam parameters results in faster steam side oxidation increasing the frequency and quantity of spallation within steam tubes. The resulting tube failures are extremely costly. Therefore, it is necessary to characterise the behaviour of each material in a steam oxidising environment in order to more accurately predict when scheduled maintenance should be undertaken and to avoid unexpected plant shut downs.

In support of these aims, experiments were conducted to investigate the oxidation and spallation behaviour of Super 304H, 347HFG and HR3C advanced austenitic steals in a flowing steam environment. The experimental results are presented in the previous chapter.

The alloys were oxidised in deoxygenated steam for up to 1300 hours at atmospheric pressure at 600, 650 and 700 °C. The surface of interest was the inner, pickled tube surface that would be in contact with flowing steam in plant. The effect of surface finish was investigated by the inclusion of Super 304H tube that had been shot peened on the inner surface. Oxidation experiments were also conducted in static laboratory air at the same temperatures for comparison.

The spallation behaviour of the alloys tested was of great interest and further experiments on 347HFG were undertaken at 650 °C in air saturated steam to promote spallation of the inner surface oxide.

This chapter is presented in three sections as follows:

- Section 5.2 compares the morphology of oxide grown on each alloy in air, deoxygenated steam, and air saturated steam, and proposes oxidation mechanisms for each alloy and surface finish type;

- Section 5.3 explores the oxidation kinetics of the three austenitic alloys in each of the oxidising atmospheres, and calculates predicted oxide growth using derived models; and
- Section 5.4 investigates the spallation behaviour of 347HFG in air saturated steam.

5.2 Oxide Morphology

The oxidation experiments conducted in this research programme revealed that oxidation behaviour of austenitic steels is influenced by alloy composition (primarily Cr content), oxidising atmosphere, and surface finish. Mechanisms for oxide growth on each alloy in each atmosphere are proposed. Oxidation experiments were conducted at 600, 650, and 700 °C. Oxide morphology generally showed minor temperature dependence in this temperature range. Other researchers have noted that Cr_2O_3 growth on 347HFG in steam is only observed above 585 °C [111] . Above 700 °C, Cr volatilisation begins to have a significant detrimental effect on oxidation behaviour [97, 98], and near-surface recrystallisation reduces the effectiveness of shot peening [27].

The effect of increasing the oxidation temperature in the current programme was to increase the speed at which the longer term oxidation products grew. For example, in air, the oxide on Super 304H remained nodular for a longer period of time at 600 °C than at 700 °C. However, as oxidation time increased, the oxide tended towards a uniform duplex oxide at both temperatures (meaning both complete coverage over the alloy surface and approximately even thickness), albeit at a smaller thickness for a given oxidation time at 600 °C.

5.2.1 Oxidation in Air

A proposed mechanism for oxide growth on pickled 18Cr alloys 347HFG and Super 304H (which oxidise in a similar fashion) in static air is presented in Figure 5.1. A thin layer of Cr,Mn-rich oxide forms on the alloy surface in the initial stages of oxidation. This is enriched where austenite grain boundaries meet the alloy surface. On the 18Cr alloys this is likely to be primarily $FeCr_2O_4$ and $MnCr_2O_4$, with a small quantity of Cr_2O_3 [30]. This rapidly breaks down and gives way to the growth of duplex oxide nodules. These nucleate in the centre of grains, away from grain boundaries. The oxide nodules are duplex in structure. They have an outer Fe rich oxide that grows via outward cation transport (mainly as Fe^{2+} and/or Fe^{3+}), and an inner spinel type oxide that grows via inward anion transport (O^-).

The oxide nodules extend laterally across the surface. This results in a faster growth rate in the early stages of oxidation. The main difference observed between 347HFG and Super 304H was that 347HFG

formed a continuous duplex oxide in as little as 50 hours, whereas Super 304H took over 500 hours at 600 °C. This is reflected in the kinetics of both alloys. The oxidation rate appears to greatly reduce once a continuous duplex oxide is fully formed.

The outer oxide is Fe_2O_3 (see Section 4.3.2.1.7) and grows via outward cation transport (mainly as Fe^{2+} and/or Fe^{3+}). Vacancy condensation due to rapid ion diffusion does not take place as it does in steam. The result is in an outer layer that is free of pores. It is suggested that the slower rate of reaction allows equilibrium to be achieved at the oxide/gas interface, resulting in a fully Fe_2O_3 outer oxide. Cu was occasionally observed on Super 304H within the outer oxide of nodules at the oxide/gas interface (not shown in Figure 5.1). Similar observations have been made by Naraparaju et al., who reported the Cu to be present as CuO oxide [37], and Kim et al., who reported Cu to be present in the form of the spinel Fe_2CuO_4 [84].

The inner oxide grows via inward anion transport (O^{2-}). This is proposed to be either a Fe-Cr-Ni spinel, or Fe-Cr spinel embedded within a metallic Ni matrix. Cr concentration decreases towards the inner/outer oxide interface. Cross-sectional analysis suggests that the internal oxidation front does not consume the majority of austenite grains at the alloy/gas interface. No evidence of healing layer growth at the alloy/spinel interface was observed. However, Cr and Mn were enriched at the base of the spinel at the higher temperatures, and could be present in the form $MnCr_2O_4$.

Figure 5.2 presents a proposed mechanism for the oxidation of pickled HR3C in air between 600 and 700 °C. The effect of increasing Cr content is to promote the formation of a more protective Cr-rich external oxide. This is proposed to be a thin layer of Cr_2O_3 overlaid with a mix of $FeCr_2O_4$ and $MnCr_2O_4$ spinels (shown collectively as 'Cr-rich oxide' in Figure 5.2). However, 25 wt.% Cr was not high enough to prevent the growth of nodules, which nucleate at the centre of austenite grains at the alloy surface. Nodule growth continues, but full coalescence into a uniform duplex oxide does not occur (up to 1000 hours at 700 °C). Oxide nodules were generally smaller than those grown on 18Cr austenitics, with the exception of a few large nodules, facilitated by the larger grain size of HR3C.

The higher Ni content of HR3C (20 wt.% Ni) results in a stratified spinel, with regions of high Ni and low Cr, or low Ni and high Cr (not shown in Figure 5.2). Additionally, a Fe-Ni oxide grows via outward cation diffusion at the spinel/outer oxide interface. Hansson et al. and Jianmin et al. both reported the presence of Fe_2NiO_4 spinel beneath the outer Fe_3O_4 oxide after plant trials on 347HFG between 7720 and 57554 hours [111, 117] in steam. This outwardly growing oxide was absent from the 18Cr alloys and HR3C oxidised in steam in the current study, and was only observed on the scale grown on HR3C in air.

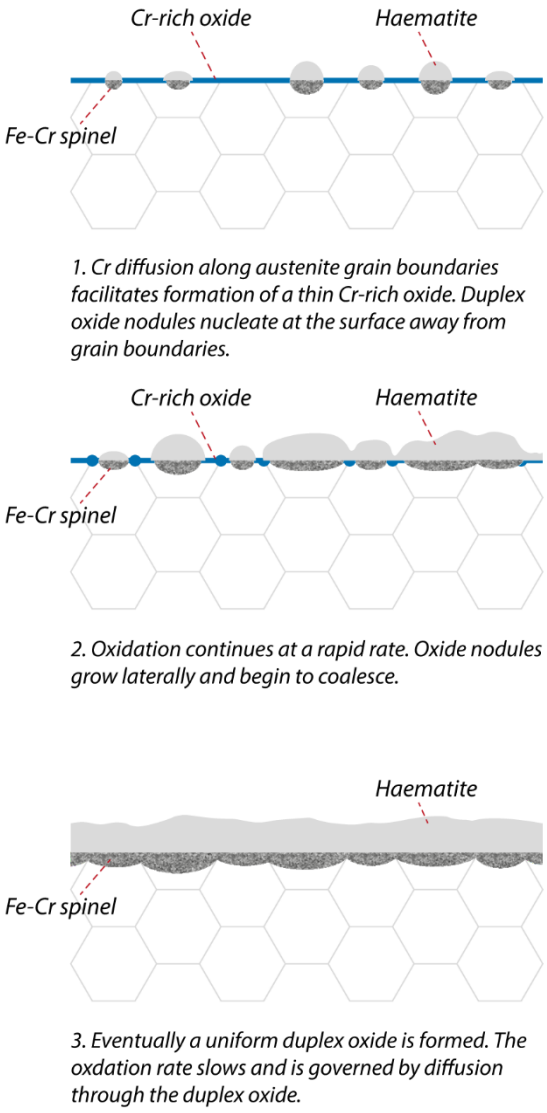

Figure 5.1 – Schematic representation of oxide growth on pickled 18Cr austenitic alloys in air for up to 1000 hours between 600 and 700 °C.

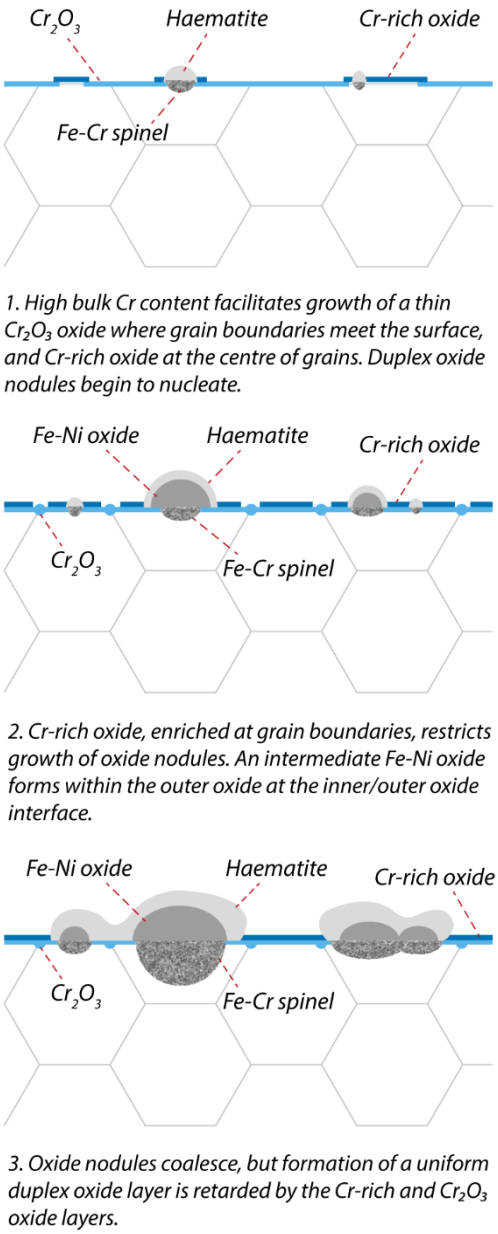

Figure 5.2 – Schematic representation of oxide growth on pickled HR3C austenitic alloy in air for up to 1000 hours between 600 and 700 °C.

5.2.2 Oxidation in Steam

Steam was detrimental to the oxidation resistance of all alloys, producing thicker, less protective oxides.

The following mechanism is proposed for isothermal oxidation of pickled Super 304H and 347HFG in deoxygenated steam (Figure 5.3 a)). Initially, Cr-rich oxide is formed at the steel surface, enriched where austenite grain boundaries meet the steel surface [147]. This is suggested to be a mix of (Fe, Mn)Cr_2O_4 spinels and a small amount of Cr_2O_3 [148]. The available Cr dips below that required to sustain a protective film. Oxide nodules can then nucleate at the centre of gains on the alloy surface.

Unlike in air, the nodules rapidly form a continuous layer of duplex oxide. The original metal surface is considered to lie at the inner/outer oxide interface [30, 116]. A uniform duplex oxide had formed on 347HFG after as little as 24 hours at 650 °C in deoxygenated steam.

The outer oxide was found to be Fe_3O_4, in contrast to the Fe_2O_3 phase found following oxidation in air. It is suggested that rapid inward diffusion of OH^-, coupled with a dissociation mechanism at the inner/outer oxide interface creates the porous morphology. This also stops equilibrium from being reached at the oxide/gas interface. Additionally, it is possible that hydrogen evolution from oxidation reduces the local oxygen partial pressure at the oxide/gas interface. Other researchers have found the outer oxide phase to be sensitive to oxygen partial pressure [148].

The internal oxidation front is channelled by prior austenite grain boundaries. It continues to consume the bulk of the austenite grain at a rapid rate because of the low bulk diffusion coefficient of chromium. This continues until the grain boundary at the base of the prior austenite grain is reached and the supply of chromium is sufficient enough to form a protective oxide that acts as a barrier to further ion transport [111]. External oxidation of this layer is favoured [116].

The inner oxide is an Fe-Cr spinel. Some researchers have found Ni to be oxidised, forming a Fe-Ni-Cr spinel [100, 116-118], while others have reported the Fe-Cr spinel to exist within a metallic Ni matrix [111, 148]. It is likely that the oxidation of Ni is sensitive to the pO_2 of the carrier gas.

Iron supply to the outer oxide/gas interface is either provided by the alloy involving diffusion through the protective Cr-rich film, or by dissociation of the spinel and outer iron rich oxides (giving rise to pores). The depletion of chromium and manganese directly beneath the Cr-rich rich film and the corresponding enrichment of iron and nickel in Section 4.4.2.1.4, suggests that diffusion through the Cr-rich layer is largely restricted to these elements. Substrate depletion of these elements, and corresponding enrichment in nickel, has also been reported elsewhere [80, 96, 100]. The porosity in the outer iron oxide also suggests a dissociation mechanism.

Eventually, breakthrough of the Cr-rich healing layer occurs by oxidation of the Cr-rich oxide into a less protective spinel. This allows penetration of the layer by oxidant species and rapid oxidation of the grain beneath [116] (see Figure 5.3 a) stage 3). Other researchers have found this to occur on 347HFG [80, 117].

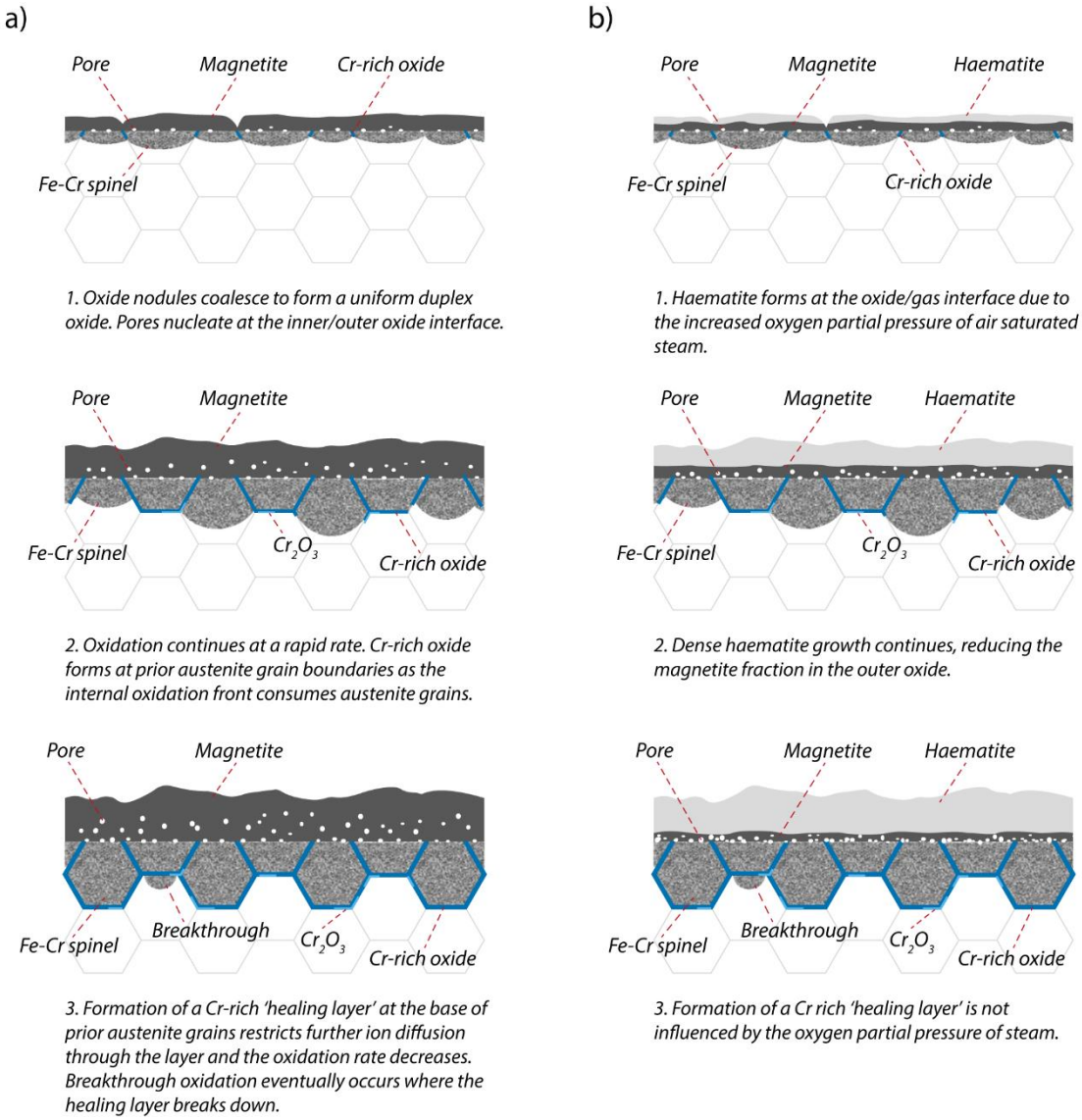

Figure 5.3 – Schematic representation of the oxidation of 347HFG and Super 304H austenitic steels in deoxygenated steam between 600 and 700 °C.

The effect of oxygen partial pressure on oxidation behaviour was investigated by oxidising 347HFG in air saturated steam at 650 °C for up to 500 hours. The only significant difference to deoxygenated steam in the oxide morphology was the formation of Fe_2O_3 at the oxide/gas interface. The Fe_2O_3 fraction increased with oxidation time. After 250 and 500 hours over 90% of the outer oxide was observed to be non-porous Fe_2O_3 above a porous band of Fe_3O_4. A proposed mechanism for oxidation in air saturated steam is given in Figure 5.3 b). The oxide was found to be slightly thicker on samples oxidised in air saturated steam.

A schematic representation of the oxidation of HR3C in deoxygenated steam is provided in Figure 5.4. HR3C formed a uniform duplex oxide that was thinner and more protective than that formed on the 18Cr steels. An enrichment in Cr and Mn was present at the internal oxidation front, even away from

grain boundaries. This is marked as a dashed blue line in Figure 5.4. This is to indicate that it was not as protective as the healing layer that forms at grain boundaries on 18Cr steels. Although the average oxidation rate is lower than 18Cr steels, deep pits began to form after longer oxidation times because of the large grain size of HR3C. A small amount of Cr_2O_3 is suggested to be present at the base of the Cr-rich oxide at grain boundaries.

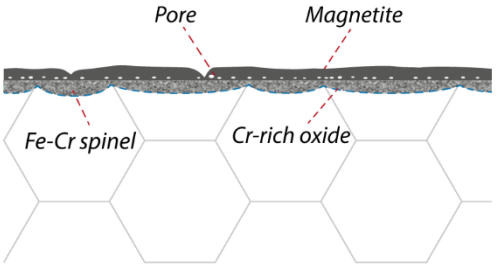

1. A slow growing duplex oxide forms across the entire alloy surface. Cr and Mn are enriched at the internal oxidation front.

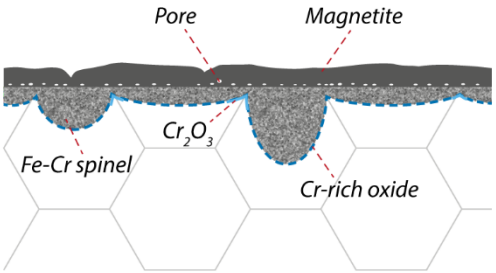

2. The internal oxidation rate through the bulk alloy is generally lower than observed on 18Cr austenitics. Deep internal oxidation pits form at the centre of grains. Cr and Mn continue to be enriched at the internal oxidation front.

Figure 5.4 – Schematic representation of the sequence of events for oxidation of pickled HR3C austenitic steel in deoxygenated steam between 600 and 700 °C.

5.2.3 The Effect of Shot Peening on the Oxidation Behaviour of Super 304H

Shot peening mechanically works the surface of an alloy, increasing the grain boundary and dislocation density. This improves the oxidation resistance of austenitic alloys by facilitating the formation of protective Cr-rich oxides such as Cr_2O_3. This is achieved through 'short circuit' diffusion along grain boundaries and dislocation defects, through which Cr diffuses faster than Fe. The greater affinity to oxygen of Cr allows for, in theory, a dense, passivating layer to form before less protective Fe oxides accelerate oxidation.

A proposed mechanism for the oxidation of shot peened Super 304H in air between 600 and 700 °C is shown in Figure 5.5 a). Shot peening greatly improved the oxidation resistance of Super 304H in both air and deoxygenated steam environments. In air, a thin, passivating oxide layer covered the entire surface. EDX analysis revealed the oxide layer to comprise of multiple oxide phases, rather than pure Cr_2O_3, as found by some workers [36]. The oxide was enriched in Cr and Mn, and it is proposed that a combination of Cr_2O_3, $FeCr_2O_4$, and $MnCr_2O_4$ initially form (shown as 'Cr-rich oxide' in Figure 5.5), before segregating into discrete layers. Mn diffusion through Cr_2O_3 is faster than Cr and it is likely that Cr_2O_3 and $FeCr_2O_4$ form at the base of the oxide, and a thicker layer of $MnCr_2O_4$ forms at the oxide/gas interface [75, 149]. Crystallites, rich in Mn, were scattered across the surface. Cu was occasionally found to be enriched in these areas. Other researchers have suggested Cu to exist as metallic precipitates in similar oxide configurations [54]. In other areas, Fe was enriched towards the oxide/gas interface, suggesting the presence of $(Fe,Cr)_2O_3$ or Fe_2O_3, as found on non shot peened Super 304H in air. It is proposed that Fe-rich oxide forms in the first stage of oxidation, before a Cr_2O_3 layer is fully established and further outward Fe ion diffusion is reduced. This mechanism is supported by the sub-parabolic kinetics observed in air. SiO_2 (not shown in the figure) is expected to be present in small quantities at the alloy/oxide interface.

Switching the oxidation atmosphere to deoxygenated steam was detrimental to the oxidation resistance of shot peened Super 304H, although the oxide was still significantly thinner the oxide grown on pickled Super 304H in steam. Figure 5.5 b) outlines the proposed sequence of events. The outer oxide was consistently thicker in air, and is proposed to be Fe_3O_4. Mn-rich crystallites were rarely observed in steam. Growth of a thin duplex oxide continues with time. Limited success with metallographic sample preparation, coupled with the thickness of the scale made it difficult to determine whether the porosity of the oxide.

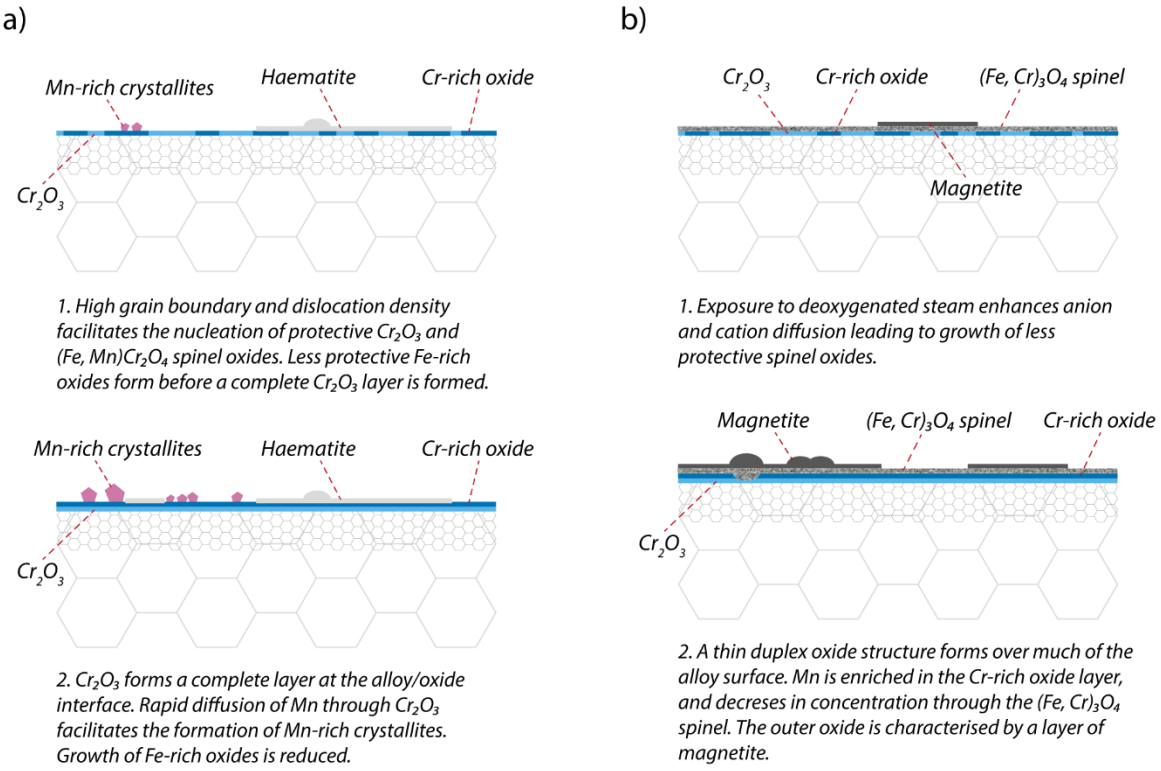

Figure 5.5 – Schematic representation of oxide growth on shot peened Super 304H in a) air and b) deoxygenated steam between 600 and 700 °C.

5.2.4 Haematite in the Outer Oxide Layer

A combination of EDX, XRD, and optical microscopy were used to differentiate between Fe_2O_3 and Fe_3O_4 in the outer Fe-rich oxide of samples oxidised in laboratory air, deoxygenated steam, and air saturated steam. Analysis of the oxide cross-section through optical microscopy revealed a contrast difference, indicating the presence of two distinct layers. The lighter grey of these layers was determined to be Fe_2O_3.

The presence of Fe_2O_3 in the outer oxide has also been reported by Zhong et al. [150], who observed a contrast difference in the outer oxide layer of T91 through optical microscopy, following oxidation in steam. The presence of Fe_2O_3 at the oxide/gas interface was confirmed by Ramen spectroscopy.

The outer oxide layer grown on austenitic steels in deoxygenated steam consisted of over 90% magnetite. This is illustrated in Figure 5.6 a) for a sample of 347HFG oxidised for 50 hours at 650 °C. In contrast, Figure 5.6 b) shows a sample of 347HFG oxidised for 50 hours at 650 °C in air saturated steam where spallation occurred on removal from the furnace. The effect of haematite on the spallation tendency in steam is discussed in Section 5.4.

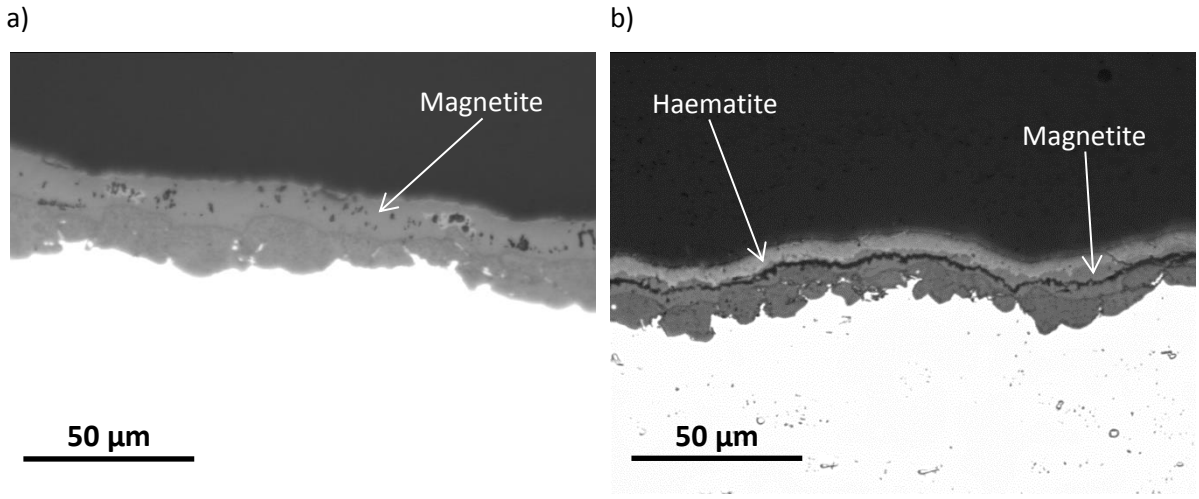

Figure 5.6 – Optical images illustrating a) magnetite outer iron oxide on sample of 347HFG oxidised in deoxygenated steam at 650 °C for 50 hours, and b) haematite presence in the outer oxide of a sample of 347HFG after oxidation in air saturated steam at 650 °C for 50 hours.

A mechanism for haematite growth within the outer oxide of 300-series austenitic steels has been proposed by Write and Dooley [96]. In their mechanism, magnetite initially forms as an outer oxide via cation transport to the oxide/gas interface, until the internal oxidation front reaches internal austenite grain boundaries and a healing layer is formed. The healing layer restricts iron diffusion from the substrate to the oxide/gas interface effectively increasing the oxygen partial pressure and oxidising magnetite at the oxide/gas interface to haematite. This transformation, in addition to the formation of a porous network at the spinel/outer oxide interface, causes the outer oxide layer to spall on cooling.

In the current work this mechanism is not strictly followed. Haematite was found in the outer oxide of 347HFG oxidised in air saturated steam. However, 75% of the outer oxide layer after only 50 hours oxidation was found to be haematite. This is significant because after 50 hours in air saturated steam, a healing layer had not yet formed at the base of the spinel oxide. In addition, 347HFG oxidised for 1300 hours in deoxygenated steam was (virtually) free of haematite in the outer oxide layer despite an extensive oxidation period at which a healing layer had fully formed. This does not discount the Wright and Dooley mechanism which considers long term service. The basic principle by which haematite formation is sensitive to an increase in oxygen partial pressure at the oxide/gas interface is in agreement with the findings in the current work. Verification that iron transport is restricted following the growth of a healing layer is provided by the marked change in kinetics discussed in Section 5.3.1. Longer term tests would be required to determine whether the outer magnetite oxide would eventually transform to haematite using deoxygenated steam in the laboratory. The sensitivity

of the haematite fraction in the outer oxide to the spallation tendency is significant and discussed further in Section 5.4.

There is a need for further work regarding the sensitivity of haematite formation in flowing steam. The oxygen partial pressure purely from the dissociation of H_2O at 600 – 700 °C is higher than that of the dissociation partial pressure of haematite, indicating that equilibrium is not reached at the oxide/gas interface when the outer oxide remains as magnetite during oxidation. Hydrogen evolution has been reported to decrease the effective partial pressure of oxygen at the oxide/gas interface during steam oxidation [40]. This effect that can be reduced by increasing the steam flow rate to remove evolved hydrogen gas away from the oxide surface [76].

5.2.5 Oxide Blistering

Oxide blisters were found to have grown on samples of 347HFG after oxidation in air saturated steam. Oxide blistering is well documented [151] on low alloy steels oxidised in dry environments. However, it is uncommon on austenitic steels oxidised in steam and the morphology could be mistaken for that of an oxide buckle produced during a temperature transient. Section 4.6.2.3 lists the differences between the two. A typical blister configuration is shown for 347HFG in Figure 5.7. The mechanism of formation of oxide blisters is unclear, but several researchers have suggested possible growth mechanisms.

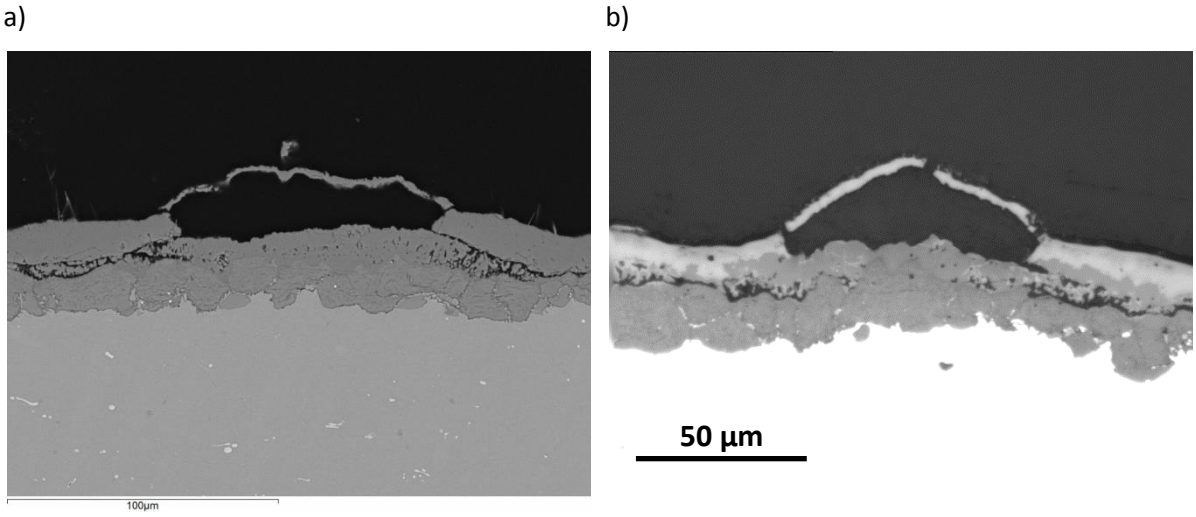

Figure 5.7 – Typical blister morphology formed on 347HFG during oxidation in air saturated steam for 50 hours at 650 °C. Oxide blisters are considered to form during oxidation, and not as a result of decohesion on cooling.

Evans [58], suggests that blistering is expected during oxide growth when cohesion within an oxide layer is high and adhesion is low. Other researchers [152] have reported blistering as a rare mode of failure on low carbon steel when oxidised in air between 800 and 1100 °C. Kondo et. al [153]

investigated the effect of blistering on the surface of carbon steel and found blisters to initiate after as little as 14 seconds when exposed to air at 950 °C. Stress generation within the oxide layer has been suggested as a possible mechanism for blister nucleation and growth. However, they found that the stress generated during the formation of the initial FeO on carbon steel was largely reduced as Fe_3O_4 and Fe_2O_3 grew. In addition, blistering only initiated when a multi-phase scale was present. These findings led to the proposal that gas pressure from CO, CO_2 and N_2, generated at the alloy/scale interface, was responsible for blister nucleation and growth, and that haematite acted as an effective diffusion barrier to evolved gas [154]. N_2 gas was found to promote blister growth from within the substrate when the sample was held in a N_2 atmosphere prior to oxidation, rather than a vacuum [155]. Griffiths [156], reported blistering to be suppressed in pure oxygen or moist atmospheres. A finding that is in contradiction to the current body of work and to that of Stott and Wei [157], who found blistering to occur on 310 and 321 austenitic steels oxidised in a pure oxygen environment between 800 and 1000 °C.

It might be expected that oxygen may exist within oxide blisters given the atmosphere in which blistering was found in the current work. The oxide morphology of the outer oxide layer *within* a blister was mainly magnetite. This suggests that the pO_2 of the gas inside the blister is lower than the dissociation pressure of haematite. If the gas inside the blister is assumed to be relatively static in relation to the steam flow, even a slight increase of pO_2 above the dissociation pressure of haematite would be expected to cause transformation from magnetite. A more satisfying mechanism, with regards to that proposed by Kondo et. al [154], is that rapid haematite formation in air saturated steam acts as a diffusion barrier for escaping gases beneath the oxide, leading to nucleation and growth of the blister. It is unclear as to the composition of such gases assuming this mechanism is correct. However, hydrogen from steam oxidation reactions is likely and would explain the suppression of haematite transformation within the blister (although the blistered oxide was entirely haematite). Haematite *is* formed under blisters as oxidation time increases. This leads to speculation that the composition of the entrapped gas changes with time, or, that rupture of the blister because of stresses imposed by the entrapped gas allow for ingress of the air saturated steam. The latter was found to have caused oxidation of the interior of ruptured blisters on 310 steel and 321 steel [157]. Further work is required to characterise the nucleation and growth of blisters in moist atmospheres.

It is unknown whether blisters formed in the current body of work ruptured during oxidation or buckled as a result of cooling from the oxidation temperature. However, the mode of failure is not considered to relate to that of the spallation of thicker oxides, and will not be considered in the analysis of spallation in Section 5.4.

5.3 Oxidation Kinetics

Mass gain and oxide thickness measurements confirmed that oxidation in steam was detrimental to the oxidation resistance of the alloys examined in this body of work. At 600 °C each alloy gained approximately 3x the mass of the alloys after oxidation in laboratory air. At 650 °C the mass gain in deoxygenated steam was 4x that of oxidation in air, except for HR3C, which gained approximately 3x the mass. At 700 °C 347HFG and Super 304H gained 4x, Super 304H SP gained 3x and HR3C gained 2x the mass after oxidation in deoxygenated steam than after oxidation in air.

The oxidation kinetics as determined by oxide thickness for Super 304H SP were much slower than when calculated from mass gain. Super 304H has a factor of approximately 1.7x the average mass gain to that of Super 304H SP in laboratory air, compared to a factor 12x the oxide thickness. This difference is because the shot peening surface treatment is only applied to the inner tube surface. Therefore, mass gain measurements erroneously include the mass gain of the outer 'as-received' tube surface. This grew a thick duplex oxide. (see section 2.2.2.2 of the Literature Review). The lower average mass gain and oxide thickness of HR3C compared to that of 347HFG and Super 304H can be attributed to the higher chromium content of HR3C (see section 2.3.3.5 of the Literature Review).

A common procedure to compare the oxide thickness of austenitic steels is to compare the thickness of the inner layer only. Measurements are conducted in this way as spallation of the outer oxide layer is frequent for these steels. The inner layer thicknesses of 347HFG oxidised in deoxygenated steam in the current work was compared with inner layer thicknesses of 347HFG oxidised for 1000 hours at 600, 650 and 700 °C under laboratory conditions in steam with an oxygen content of less than 0.2 ppm by Matsuo et al. [27]. They reported the thickness to be between 6 and 12 µm at 650 °C and 5 and 20 µm at 700 °C. This is in agreement with the current work. The oxidation of Super 304H in steam has been studied by Sato et al. [158]. After 1000 hours exposure, the inner layer thickness at 600, 650 and 700 °C was reported to be 21 µm, 26 µm and 30 µm respectively. This is somewhat higher than the measured thicknesses in the current work. No data regarding the steam conditions or sample preparation were available for the Sato et al. Report.

5.3.1 Oxidation Kinetics in Air

A common assumption is that austenitic steels oxidise with parabolic kinetics between 600 and 700 °C in air and steam. This assumption is typically based on long term experimental data, and is it often 'assumed' in order to allow comparison of the parabolic rate constant. The mechanistic theory behind this assumption is that oxide growth is governed by ion diffusion through a uniform dense oxide layer.

This then acts as the rate limiting step for oxidation at the surface of the scale (see Appendix A). The main issue with this assumption is that initial oxidation of a bare metal surface usually results in a transient oxidation period before establishment of a uniform oxide layer. Furthermore, processes such as formation of different oxide phases, or grain recrystallisation can occur, influencing the oxidation rate. The current study has shown that the formation of a Cr-rich 'healing layer' on austenitic steels oxidised in steam influences the oxidation behaviour. One aim for the current research is to extrapolate short term laboratory data in order to predict oxide growth throughout life of the subject alloys. It is therefore important to accurately model the oxidation kinetics so as not to over or under-predict long term growth rates. This section explores the isothermal oxidation kinetics of experiments conducted in air and steam as part of this research project.

For an initial analysis in-line with convention, mass gain data for samples oxidised in air were forced to a parabolic relationship according to

$$\Delta m^2 = k_p t + c \qquad \textbf{(5-1)}$$

where Δm^2 is the mass gain in mgcm^{-2}, k_p is the parabolic rate constant in mg^{2}cm^{-4}s^{-1}, t is time in s, and the integration constant, c, is given in mg^{2}cm^{-4}. No prior high temperature oxidation had taken place and so the integration constant, c, was forced to zero, assuming Δm^2 = 0 mgcm^{-2} at t = 0 s. Figure 5.8 illustrates the fit to parabolic kinetics at 600 °C.

The R^2 value relates to how well the experimental data is described by the trendline, and is one way of measuring goodness of fit. A tight, linear correlation of experimental data to the trendline would be expected for oxidation that followed parabolic kinetics. For comparison, data more accurately described by sub-parabolic kinetics would appear as a curve of decreasing rate against the trendline.

Figure 5.8 presents the fit of mass gain squared verses time to a linear relationship for pickled 347HFG, Super 304, and HR3C, and shot peened Super 304H. k_p is given by the gradient of the trendline. Pickled 347HFG and Super 304H both contain 18 wt.% Cr and are expected to oxidise in a similar fashion. Super 304H shows a higher confidence in fit than 347HFG at 600 °C. One explanation for this is that Super 304H retained a nodular oxide up to 1000 hours at 600 °C, whereas 347HFG formed a uniform duplex oxide from as little as 100 hours (see Section 4.3.2.1.3). It is suggested that in the initial stages of oxidation, duplex nodules nucleate and propagate laterally until uniform coverage is established (see Figure 5.1). Further oxidation is then governed by diffusion through the duplex oxide at a slower rate. This transition was observed to occur sooner on 347HFG, leading to a more pronounced decrease in oxidation rate.

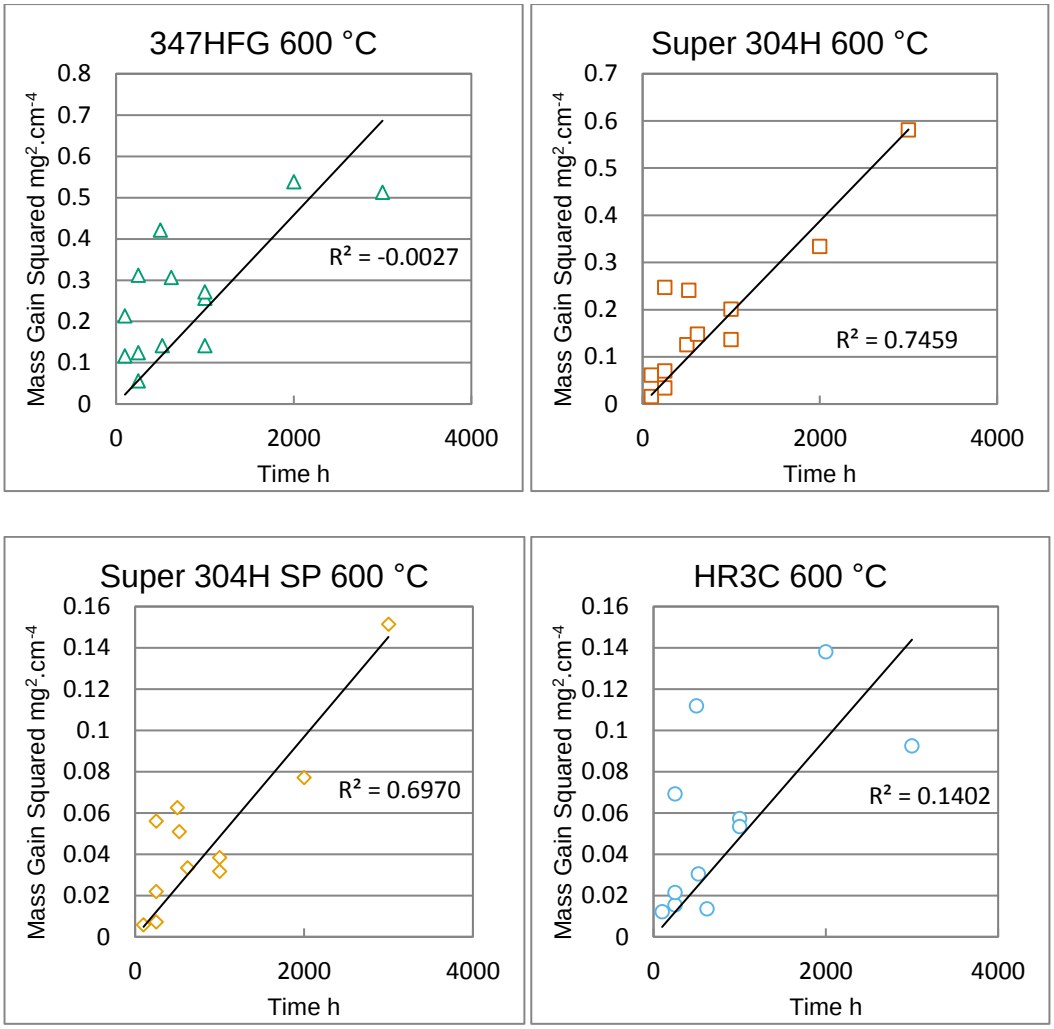

Figure 5.8 – Forced parabolic kinetics

Shot peened Super 304H shows a similar confidence to pickled Super 304H. The experimental results show a thin, Cr-rich oxide to grow on the shot peened surface. This has been shown to grow with parabolic kinetics in air by other researchers. Accordingly, the parabolic rate constant for shot peened Super 304H is lower than pickled Super 304H. The higher than expected k_p is because of the growth of thick duplex oxide on the outer tube surface. This highlights a limitation when calculating oxidation kinetics from mass gain using samples with non-homogenised surfaces.

The R^2 value for HR3C is low. It should be noted that R^2 is a measure of variance from the trendline, and on its own cannot determine whether a regression model is adequate. There is a lot of scatter in the HR3C data, but it appears to fit a parabolic relationship quite well. The k_p of 1.33 x10^{-8} $mg^2cm^{-4}s^{-1}$ is similar to that of shot peened Super 304H (1.34 x10^{-8} $mg^2cm^{-4}s^{-1}$) for growth at 600 °C.

To assess the deviation from parabolic growth, the natural log of mass gain was plotted against the natural log of time (Figure 5.9). The order of reaction, n, was calculated from the reciprocal of the

gradient in equation (3-3). An order of reaction greater than 2 suggests that the kinetics can be more accurately described by sub-parabolic growth.

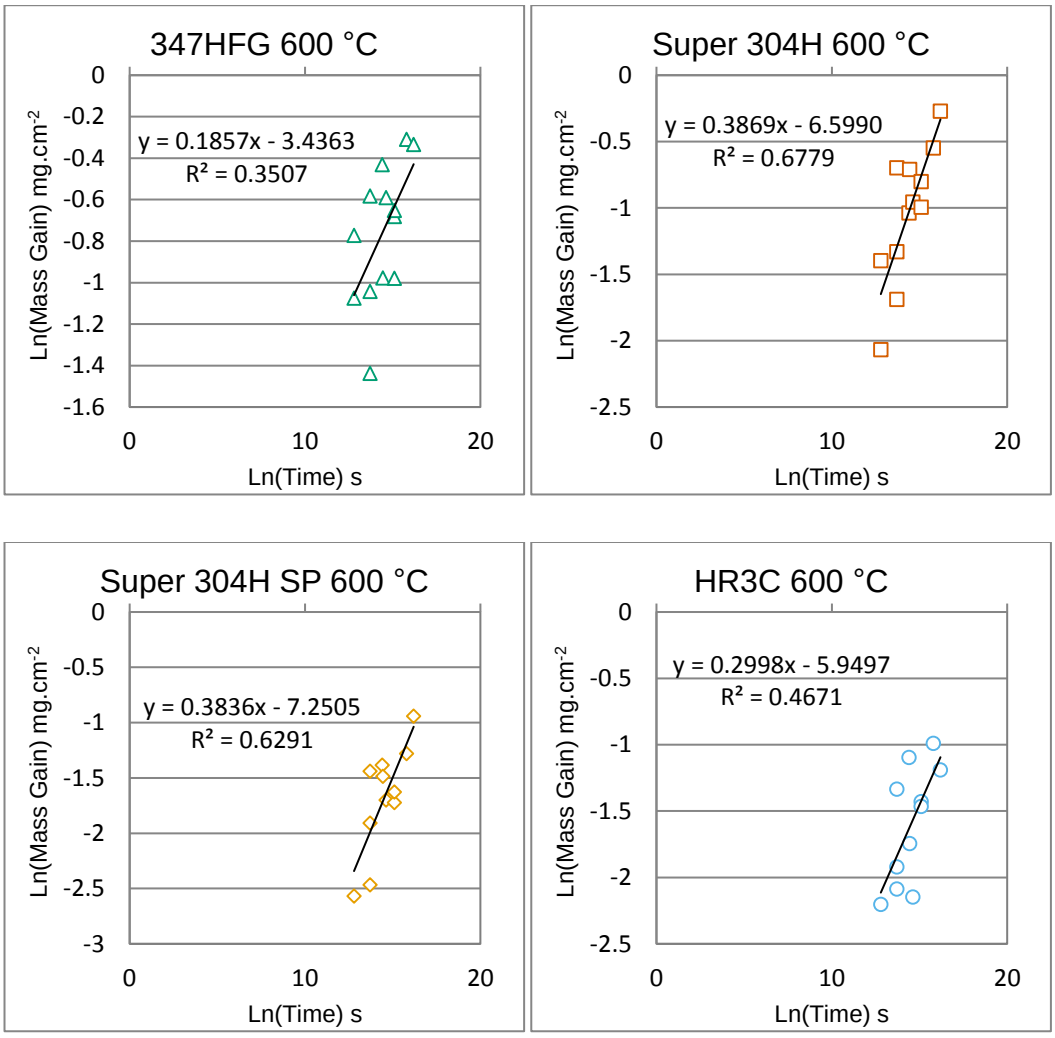

Figure 5.9 – Plots of Ln(mass gain) verses Ln(time) used to determine the order of reaction at 600 °C in air.

The oxidation kinetics of each alloy at 600 °C were recalculated using the calculated order of reaction, n. The mass gain^n verses time plots are presented in Figure 5.10. The R^2 for 347HFG significantly improved, suggesting that fitting a parabolic relationship from t = 0 s produced a poor fit for the data. Pickled Super 304H and shot peened Super 304H saw a slightly improved fit at 600 °C. These alloys represented the closest fit to parabolic kinetics in air at all temperatures. The R^2 for HR3C improved but the scatter in data remained.

Kinetic data calculated from mass gain for all three oxidising temperatures is presented in Table 5.1. n increased with temperature and increased dramatically at 700 °C for pickled 347HFG and Super 304H. This is highlighted in Figure 5.11, which plots mass gain squared verses time at 700 °C. The figure illustrates an initial rapid oxidation period followed by a greatly reduced mass gain. This is most

noticeable for Super 304H when compared with oxidation at 600 °C in Figure 5.8. Super 304H formed a uniform oxide in as little as 100 hours at 700 °C (see Section 4.3.2.2.3). This provides evidence that the rate limiting step for further oxidation changes, once a duplex oxide fully forms on the surface of these alloys.

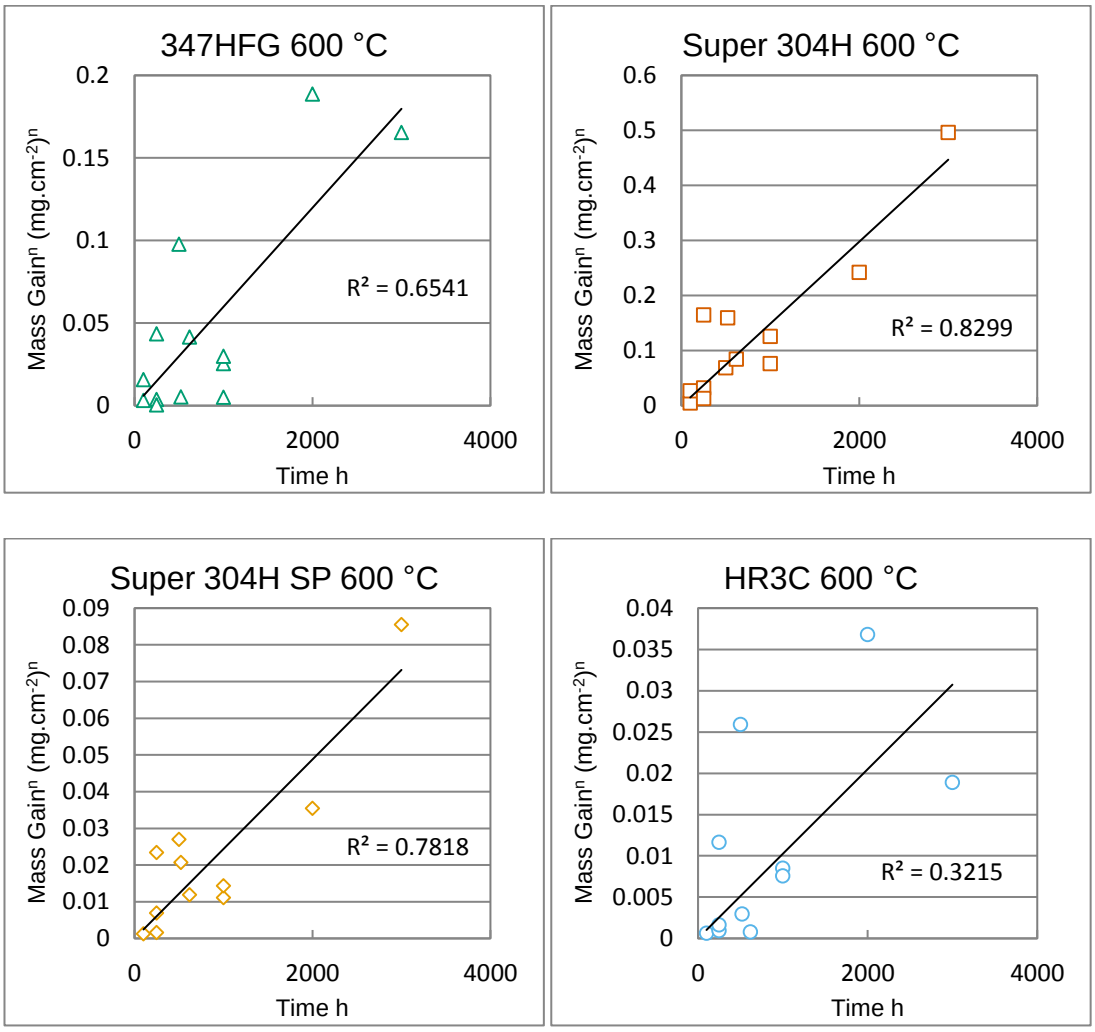

Figure 5.10 – Mass gainⁿ verses time for oxidation of austenitic alloys in air at 600 °C.

The value of n for HR3C at 700 °C is much lower than for the 18Cr steels, and varied the least across all three oxidation temperatures. HR3C was shown to grow a more protective oxide, in which the oxide nodules did not coalesce into a uniform duplex oxide for up to 3000 hours in air. Table 5.1 also illustrates how forcing parabolic kinetics becomes more misleading as n increases. The calculated parabolic rate constants remain within one order of magnitude between 600 and 700 °C for each alloy, whereas the constant k_n changes more readily with n.

Table 5.1 – Rate constants calculated from mass gain for the oxidation of austenitic steels in static laboratory air for up to 3000 hours.

Alloy	Oxidation Temperature (°C)	Parabolic Rate Constant, k_p ($mg^2cm^{-4}s^{-1}$)	Order, n	Rate Constant, k_n $((mgcm^{-2})^n s^{-1})$
347HFG	600	1.66×10^{-8}	5.39	6.35×10^{-8}
347HFG	650	5.93×10^{-8}	6.28	2.18×10^{-8}
347HFG	700	5.37×10^{-8}	20.48	2.10×10^{-11}
Super 304H	600	4.137×10^{-8}	2.58	5.39×10^{-8}
Super 304H	650	6.16×10^{-8}	4.89	1.34×10^{-8}
Super 304H	700	6.86×10^{-8}	18.57	2.50×10^{-10}
Super 304H SP	600	1.34×10^{-8}	2.61	6.77×10^{-9}
Super 304H SP	650	1.60×10^{-8}	5.79	3.38×10^{-10}
Super 304H SP	700	2.45×10^{-8}	13.65	1.62×10^{-12}
HR3C	600	1.33×10^{-8}	3.34	2.85×10^{-8}
HR3C	650	1.17×10^{-8}	8.74	3.96×10^{-12}
HR3C	700	2.66×10^{-8}	6.99	4.32×10^{-10}

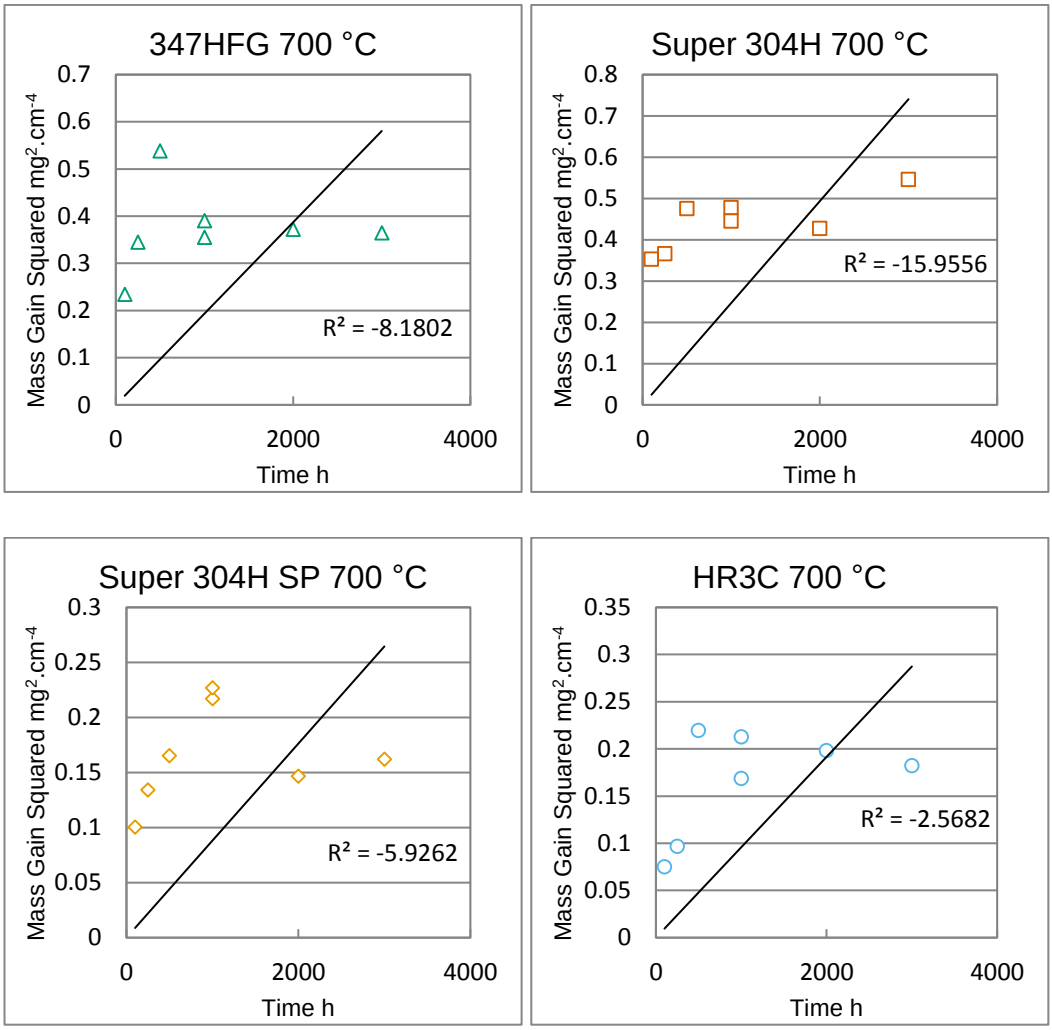

Figure 5.11 – Plots of mass gain squared verses time for austenitic alloys oxidised in laboratory air at 700 °C.

Shot peened Super 304H exhibited a similar initial rapid increase in mass gain to pickled Super 304H at 700 °C. This was due to the outer surface of the sample forming a thick duplex oxide. This again highlights the limitations of calculating oxidation kinetics from mass gain. In order to more accurately determine the oxidation kinetics of the inner surface of the shot peened alloy, oxidation kinetics were calculated from oxide thickness.

Figure 5.12 illustrates the difference in inner oxide thickness between pickled and shot peened Super 304H. The calculated k_p of 1.26 x10^{-19} m^2s^{-1} is two orders of magnitude smaller than that of pickled Super 304H (1.96 x10^{-17} m^2s^{-1}). It should be noted that the R^2 values for all alloys are low, and clearly demonstrate sub-parabolic kinetics. There is, however, a less defined rate change for shot peened Super 304H when analysing the oxide thickness measurements in comparison to mass gain. This was expected as duplex oxide formation on the outer surface of shot peened Super 304H did not influence the inner surface oxide thickness measurements.

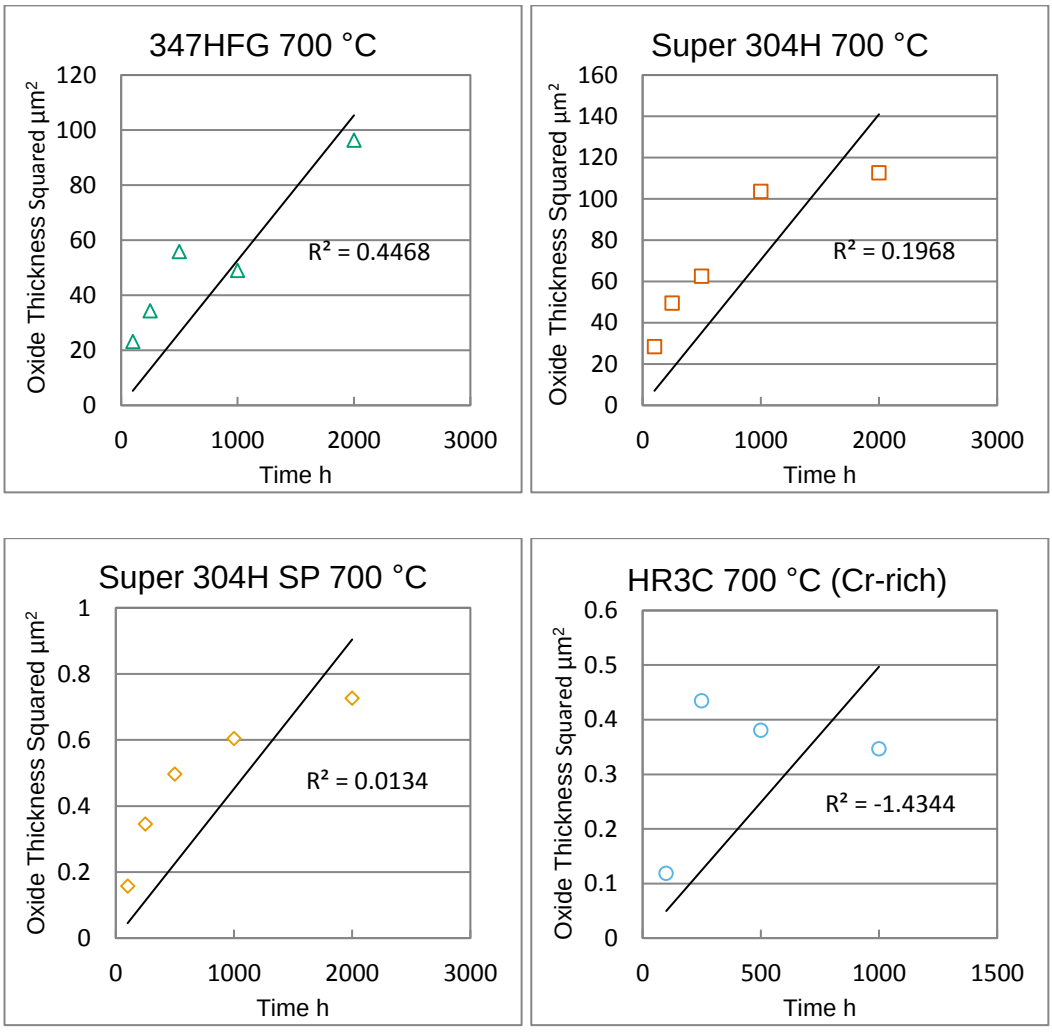

Figure 5.12 – Plots of oxide thickness squared verses time for austenitic alloys oxidised in laboratory air at 700 °C.

Cross-sectional analysis revealed shot peened Super 304H to grow a thin Cr-rich oxide in air that was overlaid with Mn-rich crystallites and Fe-rich oxide. The sub-parabolic kinetics suggest that growth of the faster, less protective Fe-rich oxide may have initially grown at a faster rate before a Cr-rich healing layer fully formed. Nevertheless, the value of k_p can be compared with the literature. In the literature review, Figure 2.10 shows k_p values for Cr_2O_3 growth in dry atmospheres, compiled by Taylor et al [60]. At 700 °C k_p values range from approximately 8 x 10^{-20} to 3 x 10^{-19} m^2s^{-1}. This is in good agreement with the k_p value for oxide growth on shot peened Super 304H.

The kinetic parameters calculated from oxide thickness at 700 °C are presented in Table 5.2. n was calculated to be above 4 for all alloys. The values of n are lower than those calculated from oxidation in air. This is likely because of oxide thickness measurements only being recorded up to 1000 hours oxidation compared with 3000 hours for mass gain. The sub-parabolic kinetics calculated from t = 0 s would be expected to return a higher value for n as oxidation time increases.

Table 5.2 – Rate constants calculated from oxide thickness for the oxidation of austenitic steels in static laboratory air. Rate constants are calculated for up to 1000 hours for HR3C, and for up to 2000 hours for shot peened Super 304H, and pickled Super 304H and 347HFG. The regression lines for the parabolic rate constants are forced through the origin.

Alloy	Oxidation Temperature (°C)	Parabolic Rate Constant, k_p (m^2s^{-1})	Order, n	Rate Constant, k_n (m^ns^{-1})
347HFG	700	1.46 x10^{-17}	4.60	1.20 x10^{-30}
Super 304H	700	1.96 x10^{-17}	4.21	1.87 x10^{-28}
Super 304H SP	700	1.26 x10^{-19}	4.10	7.05 x10^{-32}
HR3C (Cr-rich)	700	1.38 x10^{-19}	4.59	1.03 x10^{-35}

In order to improve the calculated oxidation rates for pickled 347HFG and Super 304H, consideration was given to two distinct oxidation regimes, before and after formation of a uniform duplex oxide. At 700 °C this had occurred by 100 hours for both alloys. The parabolic rate constants were calculated again from oxide thickness measurements, but this time were not forced through the origin. This method evaluates all data points from $t \geq 100$ hours while discounting the transient oxidation period of nodule growth and coalescence up to t = 100 hours. This is considered reasonable because once duplex coverage is complete, the rate limiting step is expected to change to anion and cation diffusion through the thick duplex oxide layer. It is acknowledged that in reality this change will occur gradually, as more of the alloy surface is covered in duplex oxide. However, over the timescales involved and with the data available, taking t = 100 hours as the point from which to calculate oxidation kinetics of duplex oxide growth is reasonable.

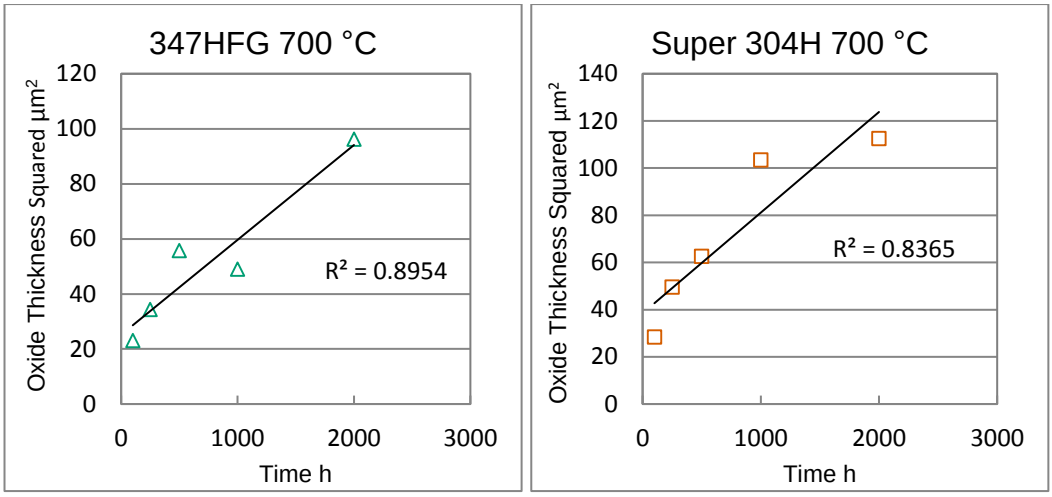

Figure 5.13 – Oxide thickness squared verses time plot for duplex oxide growth on pickled 347HFG and Super 304H. Trendline not forced through origin.

The R^2 fit for both alloys has significantly improved in comparison to Figure 5.12, and indicate that the oxidation kinetics begin to approach parabolic following the formation of a uniform duplex oxide layer. k_p was calculated as 9.57 x 10^{-18} m^2s^{-1} for 347HFG and 1.18 x 10^{-17} m^2s^{-1} for Super 304H. These are slightly lower than the values presented in Table 5.2, where the intercept was forced through the origin, and corresponds to slower growth of the established duplex oxide layer. These k_p values are still higher than the k_p calculated for shot peened Super 304H, indicating, as expected, that the duplex oxide is less protective than the Cr-rich oxide grown on shot peened surface.

The parabolic rate constants calculated above are presented in Table 5.3 along with corresponding k_ps at 600 and 650 °C. It should be noted that 347HFG formed a uniform duplex oxide from as little as 100 hours at both 600 and 650 °C. The duplex oxide formed on Super 304H had not fully coalesced until 1000 hours at 600 °C and 500 hours at 650 °C. However, because of the lack of long term oxide thickness data, the k_ps were calculated from 100 hours. This improved the fit in comparison to forcing the regression through the origin, but the reader should be aware that the k_ps calculated for Super 304H at the lower temperatures are likely to be erroneously high. This is discussed further at the end of Section 5.3.2.

Table 5.3 – Rate constants calculated from oxide thickness for the oxidation of pickled Super 304H and 347HFG in static laboratory air. The regression lines were not forced through the origin. The parabolic rate constants reflect the oxidation rate once a uniform duplex oxide layer had fully formed. Note that Super 304H had not formed a uniform duplex oxide by 100 hours at 600 and 650 °C. Therefore the parabolic rate constants are considered to be erroneously high. They are included for comparison and due to lack of longer term data.

Alloy	Oxidation Temperature (°C)	Oxidation Period (hours)	Parabolic Rate Constant, k_p (m^2s^{-1})	Integration Constant, c (m^2)
347HFG	600	100 – 1000	2.37×10^{-18}	4.67×10^{-11}
347HFG	650	100 – 1000	1.37×10^{-17}	2.78×10^{-11}
347HFG	700	100 – 2000	9.57×10^{-18}	2.52×10^{-11}
Super 304H	600	100 – 1000	1.31×10^{-17}	2.20×10^{-11}
Super 304H	650	100 – 1000	1.03×10^{-17}	3.46×10^{-11}
Super 304H	700	100 – 2000	1.18×10^{-17}	3.85×10^{-11}

It should be noted that on pickled 347HFG and Super 304H the internal oxidation front had not entirely consumed the first layer of austenite grains by 2000 hours (the longest period for which cross-sectional analysis was undertaken). Therefore, unlike in steam, a Cr-rich healing layer had not formed at the base of prior austenite grains. This would be expected to further reduce the oxidation rate, and so if oxidised for a long enough time period, another change of rate may be observed for these alloys.

Furthermore, shot peened Super 304H was not observed to have such a defined rate-change. Shot peened Super 304H grew a thin oxide. This did not appear to change in morphology significantly with time, and did not form an oxide layer that visibly coalesced like the duplex oxide on the pickled alloys, which caused the oxidation rate change in those alloys. Therefore, no attempt was made to calculate second stage parabolic oxide growth for this alloy. Over the oxidation time-range, the alloy is considered to exhibit sub-parabolic kinetics.

The oxidation kinetics for HR3C were calculated from measurements of the Cr-rich oxide layer only, and the fit is presented in Figure 5.12. This was achieved by filtering out larger oxide thicknesses from the full population that reflected duplex nodule growth (see Section 4.3.1.2). The k_p value of 1.38×10^{-19} m^2s^{-1} is similar to that of shot peened Super 304H, suggesting growth of a similarly protective Cr-rich oxide. The nodular oxide on HR3C did not coalesce into a uniform layer over the maximum oxidation period of 3000 hours, and so no attempt was made to calculate a second regime oxidation rate for this alloy.

5.3.2 Oxidation Kinetics in Steam

One of the objectives of this research project was to offer a predictive tool for oxide growth on the inner surface of austenitic steels in a steam atmosphere. To achieve this, the oxidation kinetics for 347HFG oxidised in deoxygenated steam at 650 °C were calculated. This was because experiments for

this alloy and temperature were conducted for the longest duration – up to 1300 hours. The longest possible duration was preferred as the previous section showed how an initial transient period of oxidation can affect the oxidation kinetics for austenitic alloys.

Wright & Dooley used data from laboratory and field data to calculate predicted oxide thicknesses for different alloys up to 40 Kh. The total oxide thickness grown on 347HFG at 650 °C was calculated to be 116 µm. It should be noted that this thickness was calculated from thickness data of the inner oxide layer only. The inner thickness was multiplied by 2 to reach the total thickness of 116 µm. Oxide thickness can also be derived from parabolic rate constants, where provided. Muramatsu compiled parabolic rate constants for a range of boiler steels [108]. The k_p for Super 304H at 650 °C was approximately 1.4 x 10^{-16} m^2s^{-1}, which relates to a total oxide thickness of approximately 142 µm after 40 Kh. It should be noted that Muramatsu states that the use of k_p is based on the assumption that the alloys oxidise with parabolic kinetics.

In order to investigate the oxidation kinetics of 347HFG in steam in the current study, k_p was initially fit to the full range of data, and forced through the origin, assuming ξ = 0 µm at t = 0 s. Regression analysis of Figure 5.14 a) shows a poor fit to parabolic kinetics. The curve clearly indicates sub-parabolic kinetics. k_p was calculated as 3.77 x 10^{-16} m^2s^{-1}, which is higher than that calculated by Muramatsu. Although both calculations assume parabolic kinetics, it is likely that the k_p in the Muramatsu report was calculated from longer term data. This would be expected (and is seen here) to lead to a lower value of k_p as it would be less influenced by any initial transient oxidation period.

The total oxide thickness at 40 Kh using the k_p value of 3.77 x 10^{-16} m^2s^{-1}, was calculated to be 233 µm. This value is significantly higher than both the Wright & Dooley value of 116 µm and Muramatsu value of 142 µm. Although the two literature values are also extrapolations, they are likely calculated from longer term experimental data, and therefore considered more reliable.

The order of reaction, n, was calculated for the full time range to be 5.0. Figure 5.14 b) plots oxide thickness^n verses time for comparison to the parabolic fit in Figure 5.14 a). The R^2 value improves significantly, indicating a good fit to sub-parabolic kinetics. k_n was calculated to be 2.17 x 10^{-29} m^ns^{-1}.

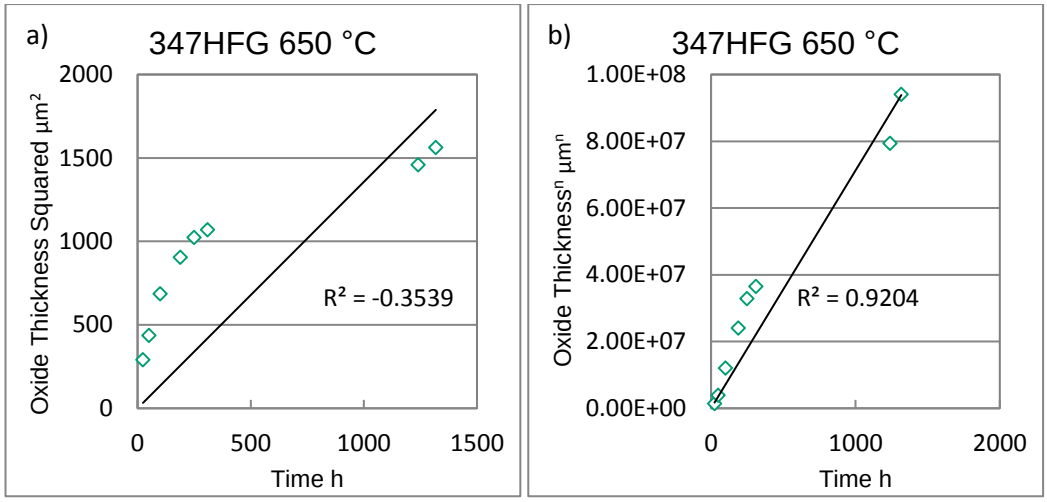

Figure 5.14 – Oxidation kinetics for pickled 347HFG oxidised in deoxygenated steam at 650 °C. a) Oxide thickness squared verses time forced through the origin, b) Oxide thickness^n verses time forced through the origin, illustrating sub-parabolic kinetics over the full time range.

The oxide thickness at 40 Kh calculated from k_n was 78 µm. This value is lower than both literature values, and suggests that the use of a single kinetic regime to describe the experimental data has limited use in predicting future oxide growth.

The rate constants calculated for the full oxidation period assuming a single oxidation regime are presented in Table 5.4. Included along with 347HFG are the rate constants calculated for pickled Super 304H. Calculations are made for oxidation temperatures of 650 and 700 °C.

Table 5.4 – Rate constants for single regime kinetics calculated for pickled 347HFG and Super 304H oxidised in deoxygenated steam.

Alloy	Oxide Layer	Temp (°C)	Oxidation Period (hours)	Parabolic Rate Constant, k_p (m^2s^{-1})	Rate Constant, k_n (m^ns^{-1})	Order, n
347HFG	Total	650	0 – 1300	3.77×10^{-16}	2.17×10^{-29}	4.99
347HFG	Total	700	0 – 330	3.77×10^{-15}	1.28×10^{-26}	4.45
347HFG	Inner	650	0 – 1300	5.59×10^{-17}	2.48×10^{-40}	6.82
Super 304H	Total	650	0 – 210	1.20×10^{-15}	5.37×10^{-31}	5.36
Super 304H	Total	700	0 – 250	1.28×10^{-15}	2.48×10^{-30}	5.25

Fine grained 18Cr austenitic steels such as 347HFG and Super 304H tend to oxidise at an initially rapid rate in steam. During this first stage of growth, the internal oxidation front progressively oxidises the elements in the bulk austenite grain primarily via O^{2-} and OH^- anion diffusion [148]. The literature suggests that the alloy in the bulk of the grain oxidises to an Fe-Cr spinel, with Ni and minor element additions either incorporated into the spinel or forming metallic precipitates [148]. Cr diffusion in the bulk alloy is slow, and although it has a high affinity to oxygen, is below the critical concentration to facilitate growth of a complete Cr-rich oxide layer (ideally Cr_2O_3). The oxidation rate in this first stage

of oxidation is therefore governed for the inner oxide by inward anion diffusion through the duplex oxide to the internal oxidation front, and via outward cation diffusion for the outer oxide [66].

As the internal oxidation front continues to consume the first layer of austenite grains at the alloy surface it encounters grain boundaries. These act as short circuit diffusion paths where Cr diffusion is greatly enhanced. The increased Cr mobility facilitates the formation of a protective Cr-rich film. Ion diffusion through this oxide layer is lower than that in the bulk grain and so the internal oxidation front is effectively 'channelled' by the grain boundaries. Internal oxidation continues until the entire gain has been oxidised and is surrounded by a Cr-rich oxide at the former grain boundary. At this point, further oxidation would be entirely governed by diffusion through the protective Cr-rich 'healing layer', and correspond to a rate change in the oxidation kinetics. In a model scenario this would occur for the first layer of austenite grains at the same time, and correspond to a sharp decline in oxidation rate at a time, t_i. This has been modelled by other researchers [67, 69]. In reality a more subtle rate change is expected as austenite grains of different sizes are consumed one by one, and are influenced by local variations in oxidation behaviour. Nevertheless, a number of researchers have reported the oxidation rate to effectively stop once a healing layer had formed [67].

Cr-rich healing layer formation was observed on pickled 347HFG and Super 304H oxidised in steam at 650 and 700 °C. At 600 °C the oxidation front had not fully consumed the first layer of austenite grains after the maximum experimental oxidation time of 280 hours. The time, t_i, at which the Cr-rich healing layer became a complete layer varied between alloy and temperature. A combination of cross-sectional analysis and oxide thickness verses time plots were used to determine t_i. For 347HFG oxidised in deoxygenated steam at 650 °C, this was identified to be approximately 100 hours. Accuracy in determining t_i was limited by the number of oxidation tests performed.

Figure 5.15 illustrates the formation of a complete healing layer between 50 and 100 hours oxidation for 347HFG oxidised at 650 °C. After 50 hours, a Cr-rich film oxide had begun to form at grain boundaries but the oxidation front had not consumed the entirety of many austenite grains. Where grain boundaries had not been reached, no Cr-rich oxide existed, meaning the rate of oxidation was not yet dictated by diffusion through the protective layer. After 100 hours, the vast majority of internally oxidised austenite grains were encompassed by a chromium rich oxide film.

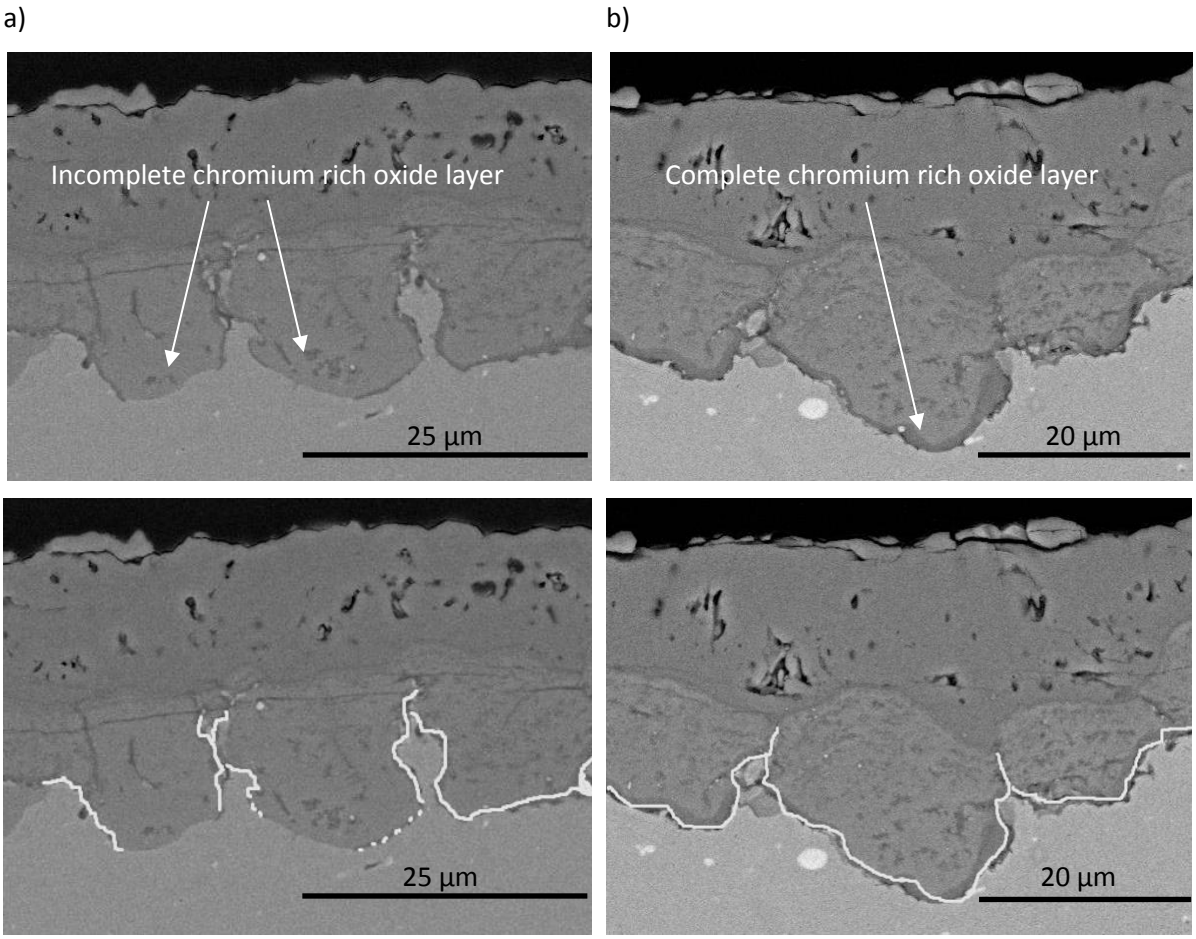

Figure 5.15 – BSE SEM micrographs of a) partially formed and b) fully formed chromium rich protective oxide layer on 347HFG after oxidation at 650 °C for a) 50 hours and b) 100 hours, illustrating point of kinetic regime change. The bottom micrographs are marked up to illustrate where the chromium rich protective oxide has formed.

In order to improve the fit to experimental data, the oxidation kinetics were split into two regimes; before and after the formation of a complete healing layer. The second regime parabolic rate constant was calculated according to:

$$\xi^2 = k_p t + c \qquad \textbf{(5-2)}$$

where the integration constant, c, is oxide thickness squared at t = 0 hours, and unlike the first oxidation regime, was not forced through the origin. It should be noted that for the second oxidation regime this equation is only valid after a time t_i, which corresponds to the point at which a complete Cr-rich healing layer forms at the base of the inner oxide. Between $t = 0$ and $t = t_i$, the oxidation rate will be governed by ion diffusion through the duplex oxide layer, and the first oxidation regime.

Figure 5.16 illustrates the fit to experimental data for the two oxidation regimes. t_i was taken as t_i = 100 hours. Trendlines are fitted to the first and second regimes between 0 ≤ t ≤ 100 hours and 100 ≤ t ≤ 1300 hours, respectively. The integration constant, c, was set to c = 0 µm for the first regime,

assuming ξ = 0 µm at t = 0 hours. The R^2 values for both regimes see a significant improvement over Figure 5.14 a).

The parabolic rate constant for the second regime, valid for oxidation times of $t \geq 100$ hours, was calculated to be k_p= 1.60 x 10^{-16} m^2s^{-1}. The integration constant was calculated to be c = 7.92 x 10^{-10} m^2. Using these values, the oxide thickness at 40 Kh was calculated to be 154 µm. This is a lot closer to the value of 142 µm calculated from the parabolic rate constant in the Muramatsu report [108]. It is considered to be a more accurate prediction than the thickness of 233 µm calculated from the k_p that covered the full range of data. It should be noted that the Muramatsu value of 142 µm is calculated for Super 304H rather than 347HFG. Parabolic rate constants compiled from several sources by Wright & Dooley using mass gain data suggest that Super 304H is slightly more oxidation resistant than 347HFG in steam. This is supported by the mass gain results in the current work.

The present calculated value of 154 µm is larger than the Wright & Dooley value of 116 µm. This could be due to the Wright & Dooley value being calculated from an inner oxide thickness of 58 µm, which was doubled to reach a total oxide thickness of 116 µm. To investigate the validity of this method, the oxidation kinetics for the inner and outer oxide layers were calculated.

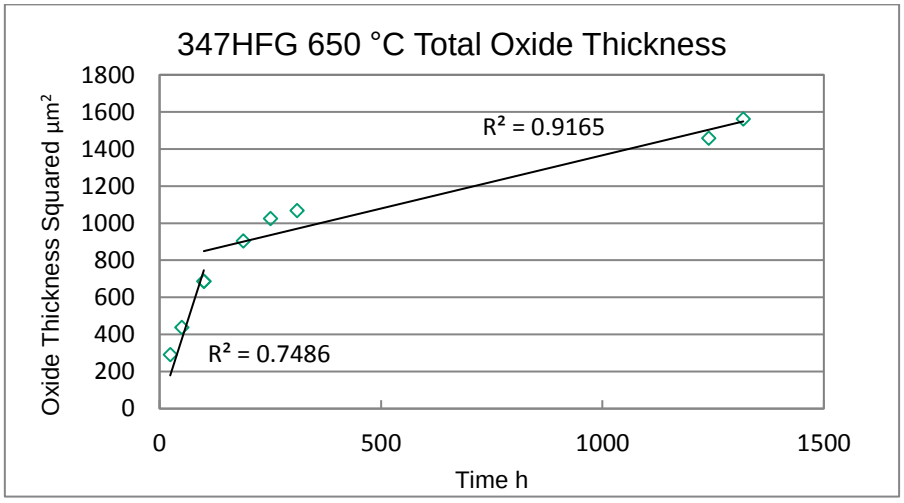

Figure 5.16 – Total oxide thickness squared verses time for 347HFG oxidised in deoxygenated steam at 650 °C. Trendlines are fitted to the first and second oxidation regimes, for between 0 ≤ t ≤ 100 hours and 100 ≤ t ≤ 1300 hours, respectively.

Figure 5.17 and Figure 5.18 show the parabolic fits for inner and outer oxides, respectively. Parabolic rate constants were calculated for two oxidation regimes with t_i = 100 hours. Fitting the data to two regimes dramatically improves the fit. Interestingly, the inner oxide appears to have a more distinct rate change than the outer oxide. It appears that once a healing layer forms, further internal oxidation is constrained by the healing layer, whereas the outer oxide is more freely able to grow at the outer oxide/gas interface.

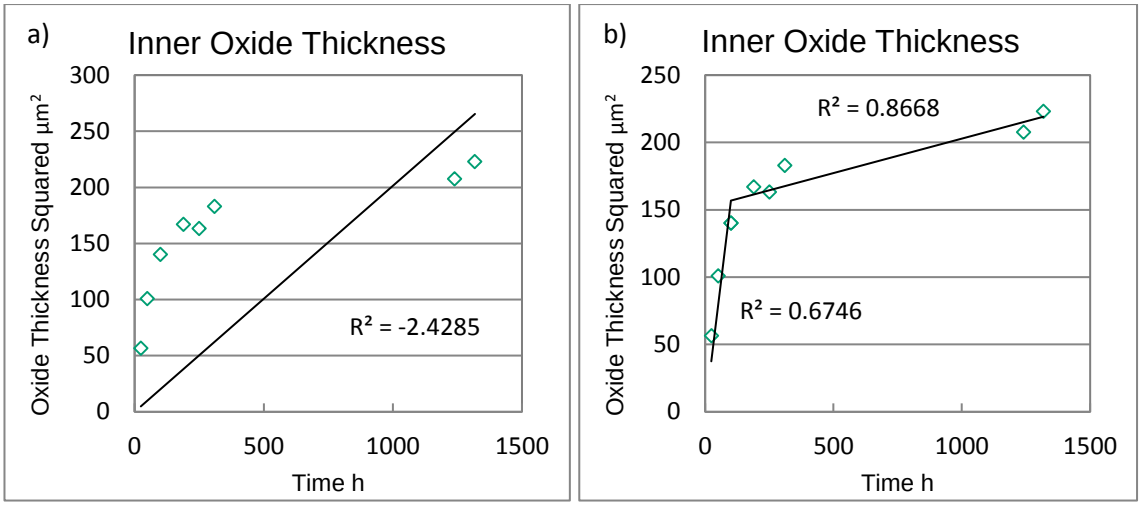

Figure 5.17 – Inner oxide thickness squared verses time for 347HFG oxidised in deoxygenated steam at 650 °C. a) single regime, and b) dual regimes for between 0 ≤ t ≤ 100 hours and 100 ≤ t ≤ 1300 hours, respectively.

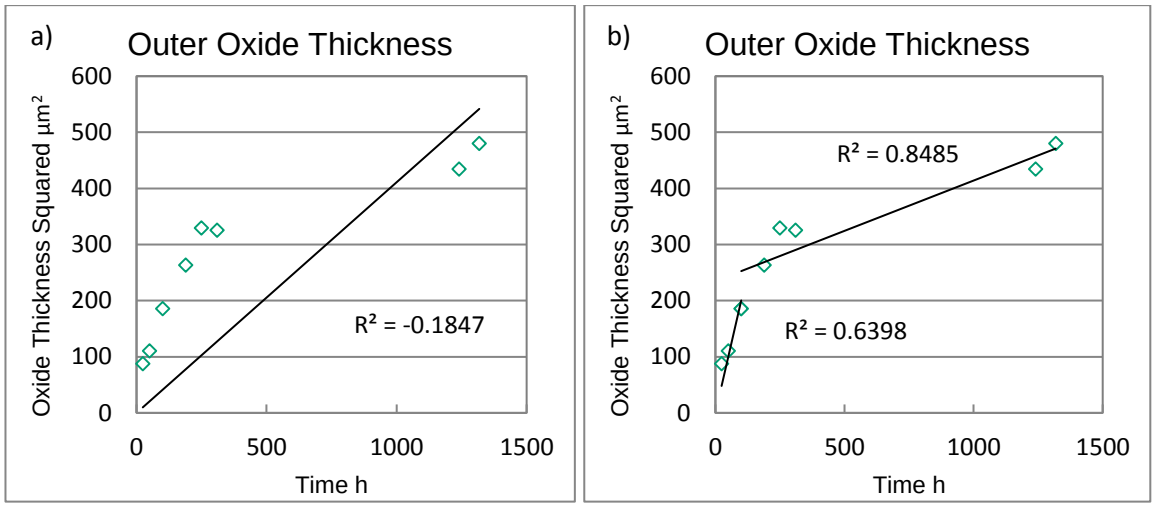

Figure 5.18 – Outer oxide thickness squared verses time for 347HFG oxidised in deoxygenated steam at 650 °C. a) single regime, and b) dual regimes for between 0 ≤ t ≤ 100 hours and 100 ≤ t ≤ 1300 hours, respectively.

The k_p value for the second regime of inner oxide growth was calculated to be k_p= 1.42 x 10^{-17} m^2s^{-1}. The integration constant was calculated to be c = 1.52 x 10^{-10} m^2. The equivalent k_p and c for outer oxide growth were calculated to be k_p= 4.98 x 10^{-17} m^2s^{-1} and c = 2.35 x 10^{-10} m^2. These results indicate that the outer oxide grows at a faster rate than the inner oxide, even after formation of a Cr-rich healing layer. This result is significant as the total oxide thickness after 40 Kh, calculated using the Wright & Dooley method of multiplying the inner oxide thickness by 2 gives ξ = 47 x 2 = 94 µm. This is well below the value calculated using the total oxide thickness, and bares more resemblance to the Wright & Dooley value of 116 µm, albeit is still lower. This suggests that Wright & Dooley are likely underestimating the predicted total oxide thickness when multiplying the inner oxide thickness by 2. Their value is also lower than that of Muramatsu.

In summary, three methods were used to model the oxidation kinetics of pickled 347HFG oxidised in deoxygenated steam at 650 °C. These were:

1. Assuming a single parabolic oxidation regime for the entire oxidation period;
2. Calculating the rate constant, k_n, from the calculated order of reaction, n; and
3. Accounting for healing layer growth by calculating two distinct parabolic oxidation regimes.

The third, dual-regime method is considered the most accurate for use as an oxide thickness prediction tool for lifing purposes. This was confirmed using a combination of regression analysis and comparison with long term oxide thickness literature values.

Table 5.5 presents the oxidation parameters for second regime oxide growth for pickled 347HFG oxidised in deoxygenated steam at 650 °C. Included in the table for completeness are oxidation parameters calculated for 347HFG at 700 °C, and pickled Super 304H at both 650 and 700 °C. Additionally, the rate constants for total oxide growth on 347HFG oxidised in air saturated steam are included. The rate constant is higher than that found in deoxygenated steam. This suggests that the oxygen partial pressure of steam has a small influence on oxidation kinetics, in agreement with other researchers findings [55].

Table 5.6 summarises the calculated oxide thickness at 40 Kh for each alloy and temperature using the rate constants in Table 5.5. For both alloys and both temperatures, calculating the oxide thickness using the second regime method returns a thickness in between the single regime k_p and single regime k_n values, which are considered to be over and under estimations, respectively.

It should be noted that the oxidation period varied between alloys and temperatures. This likely influenced the value of k_p for each alloy and temperature. For example, the k_p for Super 304H at 650 °C was calculated for between 100 and 210 hours, shorter than the duration of 100 to 1300 hours calculated for 347HFG. This has resulted in a high k_p value, despite Super 304H having slightly lower mass gain and oxide thickness at equivalent time compared to 347HFG in steam. The higher k_p has resulted in a thicker predicted oxide at 40 Kh of 192 µm. This is considered to be an over estimation because of the lack of oxide thickness data at longer time periods.

Table 5.5 – Oxidation parameters for parabolic growth in deoxygenated steam after formation of a Cr-rich healing layer.

Alloy	Oxide Layer	Temp (°C)	Oxidation Period, t_i – t (hours)	Parabolic Rate Constant, k_p (m^2s^{-1})	Integration Constant, c (m^2)	Activation Energy, Q ($KJmol^{-1}$)
347HFG	Total	650	100 – 1300	1.60×10^{-16}	7.92×10^{-10}	-140
347HFG	Total	700	50 – 330	4.07×10^{-16}	6.87×10^{-10}	
347HFG	Inner	650	100 – 1300	1.42×10^{-17}	1.52×10^{-10}	N/A

347HFG	Outer	650	100 – 1300	4.98 x10^{-17}	2.35 x 10^{-10}	N/A
Super 304H	Total	650	100 – 210	2.51 x10^{-16}	5.70 x 10^{-10}	-113
Super 304H	Total	700	50 – 250	5.35 x10^{-16}	5.02 x 10^{-10}	
347HFG*	Total	650	100 – 500	3.62 x10^{-16}	6.23 x 10^{-10}	N/A

*Oxidised in air saturated steam

Table 5.6 – Oxide thickness at 40 Kh, calculated using different kinetic regimes for steam oxidation.

Alloy	Oxide Layer	Temp (°C)	Calculated Oxide Thickness at 40 Kh (µm)		
			k_p, (Full Range)	k_n, (Full Range)	k_p, (2nd Regime)
347HFG	Total	650	233	78	154
347HFG	Total	700	428	103	244
347HFG	Inner x 2*	650	179	79	94
Super 304H	Total	650	416	75	192
Super 304H	Total	700	429	82	278

*Total oxide thickness calculated by multiplying the inner layer by 2

Smith et al. [67] modelled the oxidation kinetics of 18/8 stainless steels that form a healing layer, and concluded that oxidation exposures at least three times t_i (the time at which a rate change due to complete healing layer formation is observed) must be evaluated in order to calculate the second parabolic regime with confidence. Applying this theory to the current data, the oxidation period, t_i – t, of 100 – 1300 hours for 347HFG oxidised at 650 °C meets this requirement. The oxidation period of 100 – 210 hours for Super 304H at 700 °C does not.

The activation energies for second regime oxide growth were calculated according to:

$$k_p = k_0 e^{\left(-Q/RT\right)} \qquad \textbf{(5-3)}$$

where T is the absolute temperature in K and R is the ideal gas constant. Q is given in Jmol^{-1} so R is given as 8.314 JK^{-1}mol^{-1}. k_0 is the activation constant. The natural log of k_p is plotted against 10,000/T in Figure 5.9. The activation energy for secondary regime oxide growth of 347HFG in deoxygenated steam between 650 and 700 °C was calculated to be -140 KJMol^{-1}. This is in quite good agreement to the activation energy derived from the Murumatsu report for Super 304H between 500 and 775 °C of -156 KJmol^{-1} [108]. The value of Q calculated for Super 304H was -113 KJmol^{-1}. As previously stated, the k_p for Super 304H oxide growth at 650 °C was conducted over the shortest time frame, and additional data would be expected to reduce the k_p. The effect of this would be to make the activation energy more negative, tending towards the value presented in the literature.

It should be noted that the calculated activation energies are for total oxide growth of 347HFG and Super 304H after the formation of Cr-rich healing layer, and do not represent growth of a single oxide

phase. Additionally, they were only calculated using two data points relating to growth at 650 and 700 °C. Data at either end of the scale would support refining the values. A second oxidation regime was not calculated for 600 °C because a healing layer was not observed to have formed by the maximum oxidation period of 280 hours. Otsuka et al. [59] oxidised coarse and fine grained steels in steam between 590 and 900 °C. The authors observed a diversion in the gradients of oxide thickness verses time between the two at 600 °C. This shows that above 600 °C a rate change is realised in the fine grained material, and suggests there is a lower limit of 1000 hours for a healing layer to fully form on fine grained austenitics at 600 °C.

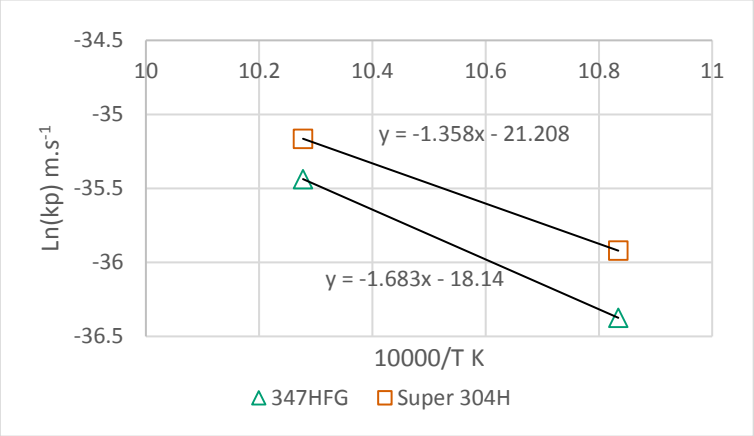

Figure 5.19 – Arrhenius

The oxidation rate constants were calculated from t = 0 to $t = t_i$ for both alloys, corresponding to the first stage of growth. Here, the regression lines for both k_p and k_n were forced through the origin assuming ξ = 0 µm at t = 0 s. The initial rate of growth is defined by diffusion through the duplex oxide up until such a time as a Cr-rich healing layer has fully formed. This rate is expected to be significantly higher than second stage growth. Table 5.7 presents the rate constants calculated for 600, 650, and 700 °C. The rate constants calculated for the first oxidation regime are factors of between 8 and 12 higher than those of the second oxidation regime in Table 5.5. There were few oxide thickness measurements in the first regime with which to calculate the oxidation kinetics, and this is reflected in the calculated n values, also in Table 5.7.

Coarse grained austenitic steels tend to struggle forming a Cr-rich healing layer at the base of prior austenite grains during oxidation in steam at 600 °C [96]. Therefore, it could be hypothesised that the long term oxidation rate should be similar to the first regime growth of fine grained austenitics. This was explored by calculating the oxide thickness of 347HFG at 40 Kh, and comparing with literature data. The oxide thicknesses calculated from the parabolic rate constants at 650 and 700 °C were 546 and 694 µm, respectively. Wright & Dooley calculated predicted oxide thickness after 40 Kh from mass

gain data and for 650 and 675 °C arrived at values of 380 and 550 µm, respectively [42], both lower than the calculated values. The oxide thicknesses calculated using the k_n values were 159 and 261 µm. These are a lot lower than the literature values for coarse grained alloys. Rather than draw any conclusions from the results it is suggested that more data is required between t = 0 to $t = t_i$ to further understand the oxidation kinetics in this short time period. Doing so would allow for a more critical analysis and comparison of the oxidation behaviour of coarse and fine grained austenitics prior to the formation of a Cr-rich healing layer. Activation energies for first regime growth were calculated as -126 KJmol^{-1} and -184 KJmol^{-1}, for 347HFG and Super 304H, respectively.

Table 5.7 – Parabolic rate constants for iron rich outer oxide and spinel oxide growth in deoxygenated steam.

Alloy	Oxide Layer	Oxidation Temp (°C)	Time Period (hours)	Parabolic Rate Constant, k_p (m^2s^{-1})	Order, n	Rate Constant, k_n (m^ns^{-1})	Activation Energy, Q (KJmol^{-1})
347HFG	Total	600	0 – 100	5.69 x10^{-16}	0.57	4.82 x10^{-9}	-126
347HFG	Total	650	0 – 100	2.07 x10^{-15}	3.32	1.64 x10^{-21}	
347HFG	Total	700	0 – 50	3.34 x10^{-15}	2.80	6.45 x10^{-19}	
Super 304H	Total	600	0 – 280	2.16 x10^{-16}	1.54	3.88 x10^{-14}	-184
Super 304H	Total	650	0 – 100	1.99 x10^{-15}	3.2	5.58 x10^{-21}	
Super 304H	Total	700	0 – 50	5.69 x10^{-15}	-	-	

It is of interest to explore the protectiveness of the Cr-rich healing layer in comparison to pure Cr_2O_3. Calculating an oxidation rate constant for the Cr-rich healing layer must be done only after complete formation of the layer. Prior to complete formation, growth will continue laterally, and will not be governed by diffusion through the layer.

Using equation *(5-2)*, the parabolic rate constant for Cr-rich protective film growth on 347HFG after oxidation in deoxygenated steam at 650 °C was calculated for between 100 and 1300 to be 1.63 x10^{-18} m^2s^{-1}. This value is considered correct for protective film growth once a complete film has been established. As the k_p for the protective film relates to a second stage oxidation regime, the regression was not forced through the origin. Parabolic rate constants for protective film growth on 347HFG and Super 304H in deoxygenated steam were calculated for 650 and 700 °C and are presented in Table 5.8. The order of reaction was calculated for each test and the activation energy for each alloy from the parabolic rate constants for growth at 650 and 700 °C. The time period for which these calculations were made is also listed.

Table 5.8 – Parabolic rate constants for chromium rich oxide growth in deoxygenated steam following formation of a complete Cr-rich healing layer.

Alloy	Oxidation Temperature (°C)	Time Period (hours)	Parabolic Rate Constant, k_p (m^2s^{-1})	Order, n	Activation Energy ($KJmol^{-1}$)
347HFG	650	100 – 1300	1.63×10^{-18}	1.89	-267
347HFG	700	50 – 330	9.71×10^{-18}	2.07	
Super 304H	650	100 – 210	2.29×10^{-18}	1.69	-154
Super 304H	700	50 – 250	8.18×10^{-18}	3.04	

In the current steam oxidation work on the pickled alloys, the oxidation front was observed to have occasionally penetrated the Cr-rich oxide at the base of the spinel oxide, resulting in rapid oxidation of the subjacent grain. This may be expected if the supply of chromium to the chromium rich film decreases below a critical value [49, 51]. This is illustrated in Figure 5.20, where the oxidation front has penetrated the Cr-rich film and partially oxidised the subjacent austenite grain. As Figure 5.20 is a cross-sectional micrograph, the identified breakthrough oxidation could be a small section of a larger grain that reached the alloy surface, rather than breakthrough. However, breakthrough is proposed based on the number of similar occurrences increasing as time and temperature were increased, and is supported by similar observations in the literature [111, 148].

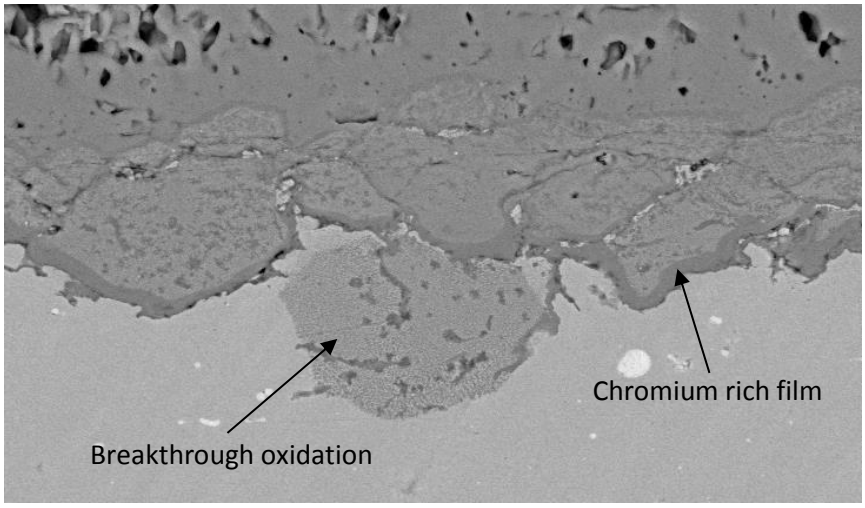

Figure 5.20 – Breakthrough oxidation of austenite grain beneath the chromium rich film on 347HFG after oxidation in deoxygenated steam for 1250 hours at 650 °C. The protection offered by the chromium rich film has failed in one area, resulting in rapid oxidation of the grain below.

This does indicate, however, that following the formation of a protective film, spinel growth is stunted compared to the continued growth of the outer iron oxide (albeit at a slower rate) via cation diffusion [59].

5.3.3 Summary of Oxidation Kinetics

Figure 5.21 presents a selection of the most relevant parabolic rate constants calculated using oxide thickness in the previous section. Forcing parabolic kinetics is useful to compare between data. However, as discussed throughout this section, the oxidation kinetics did not always fit to a parabolic regime with high confidence. For example, the oxidation kinetics calculated for shot peened Super 304H and the Cr-rich oxide grown on HR3C in air both exhibit an order of reaction, n, larger than 4, indicating sub-parabolic growth. Other researchers have found ground 18Cr samples to oxidise with cubic kinetics in steam at 800 °C [116]. Likewise, first regime oxidation of 347HFG and Super 304H in deoxygenated steam exhibit values of n between 0.57 and 3.32. Further data in this oxidation period would greatly support accurate analysis of the initial oxidation kinetics of these alloys in steam.

Oxidation of the pickled 18Cr alloys in steam was characterised by the formation of a Cr-rich healing layer that produced a step change in the oxidation rate. Calculating the oxidation kinetics for second regime growth significantly improved the confidence in fit to parabolic kinetics. Similarly, oxidation in air on the same alloys was characterised by an initial rapid oxidation period in which duplex oxide nodules rapidly coalesced into a uniform duplex oxide. Discounting this transient oxidation period in the kinetic calculations had a similar improvement to the parabolic regression. The exception to this was in fitting a parabolic relationship to Super 304H in air at 600 and 650 °C, where there were not enough long term data to discount the first 500 or 250 hours (respectively). The oxide grown on Super 304H remained nodular up to these oxidation times, and additional data at longer durations would have allowed these data to be discounted when calculating the oxidation kinetics. The effect this had was to erroneously increase the k_p for Super 304H in air, and is most noticeable at the data point corresponding to growth at 600 °C in Figure 5.21. 347HFG formed a uniform duplex oxide from as little as 100 hours at 600 °C, and this is reflected the lower k_p for 347HFG at 600 °C. This anomaly does, however, support the hypothesis that the oxidation rate is influenced by the formation of a uniform duplex oxide for these alloys in air.

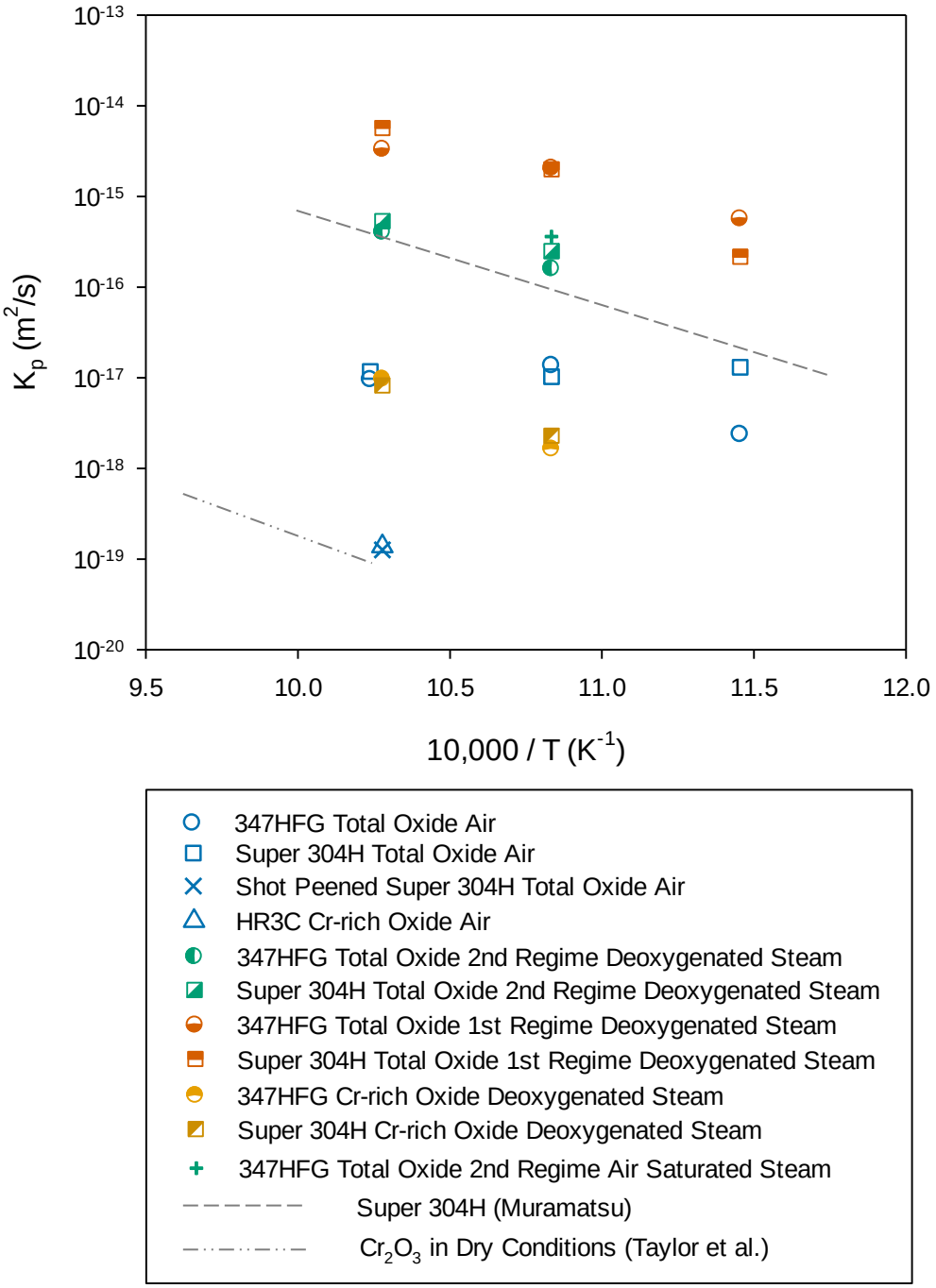

Figure 5.21 – Parabolic rate constants for the studied austenitic stainless steels in air, deoxygenated steam, and air saturated steam environments. The k_ps for oxidation of pickled 347HFG and Super 304H in air were calculated after formation of a uniform duplex oxide layer. The k_p for HR3C refers to the Cr-rich layer and does not take into account oxide nodules. k_ps for the 1st and 2nd oxidation regimes are plotted, referring to before and after formation of a complete Cr-rich healing layer. Also included is the k_p for the total oxide grown on 347HFG in air saturated steam. Included in the figure is the trendline for Cr_2O_3 growth in dry atmospheres, after Taylor et al. [60]. Included in the figure is the trendline for the oxide grown on Super 304H in steam, after Muramatsu [108]. For clarity of illustration, the markers for 347 Total Oxide Air and Super 304H Total Oxide Air at 700 °C have been slightly offset in the x-axis.

Despite these considerations, Figure 5.21 illustrates clear trends and differences in the oxidation kinetics of each configuration. The Cr-rich layer that grows on 18-8 austenitic steels is designed to be

a slow growing, protective oxide barrier. Ideally a dense layer of pure chromia would provide the greatest protection for these alloys, and is preferred. The thin oxide grown on shot peened Super 304H in air at 700 °C closely aligns with the trendline for Cr_2O_3 growth in dry atmospheres. This trendline was calculated from the data presented in Figure 2.10, which was compiled by Taylor et al. [60]. This result suggests that the oxide grown on shot peened Super 304H has a high Cr content. This was confirmed by cross-sectional analysis, although concentrations in Fe and Mn were also identified. It is suggested that a combination of multiple oxides form on this alloy, such as Cr_2O_3, $FeCr_2O_4$, and $MnCr_2O_4$.

The Cr-rich oxide grown on HR3C was similarly as protective as that formed on shot peened Super 304H. This suggests that the bulk Cr concentration was above that required to form a passivation layer on this alloy in these locations. It should be noted, however, that HR3C formed a nodular oxide, and so the k_p calculated for Cr-rich oxide growth does not fully reflect the oxidation kinetics of HR3C. Including the oxide nodules in the calculation would act to increase the value of k_p. This suggests that the shot peening treatment on 18Cr steel is more effective at resisting oxidation than increasing the Cr content of the alloy.

An interesting result is that pickled Super 304H and 347HFG appear to oxidise at a similar rate to the Cr-rich oxide grown on the same alloys in deoxygenated steam at 700 °C. The most accurate data for calculation of the Cr-rich oxide growth in steam was for 347HFG at 650 °C. There were fewer long term data available at 700 °C. Additional data may act to further reduce the calculated k_p, reducing it below those calculated for oxide growth in air. Additionally, the air data at 700 °C was calculated using longer term data than available at 600 and 650 °C. This may have a similar effect of slightly reducing the k_ps at these temperatures.

A humid environment is known to reduce the oxidation resistance of alloys. The Cr-rich healing layer grown on pickled Super 304H in deoxygenated steam at 700 °C is shown to grow at a factor of 65 times faster than the Cr-rich oxide grown on shot peened Super 304H in air at 700 °C. This suggests that less protective oxides form in steam, and would be in agreement with the literature [148]. Findings in the current work report the Cr-rich protective layer that grows on 18-8 austenitic steels in humid conditions to contain manganese in addition to chromium, possibly in the form of $FeCr_2O_4$, and $MnCr_2O_4$ spinels. Hansson et al. [148] reported the protective layer formed on 347HFG oxidised at 700 °C in humid conditions to contain iron in addition to chromium and manganese, and feature occasional particles of Cr_2O_3 between the protective spinel layer and substrate. Manganese has also been found enriched at the base of the spinel oxide following long term steam oxidation tests of 347HFG [117]. The equipment used for analysis of oxides in the current project was unsuitable to

determine the exact composition of the protective film. Oxidation in air of the pickled alloys was not conducted for a suitably long time period to promote the growth of a protective film. However, it has been suggested that chromia forms along the prior austenite grain boundaries of these alloys oxidised in air at the temperatures of consideration [30].

Included in Figure 5.21 are k_ps for second regime oxide growth for pickled Super 304H and 347HFG. These align well with the trendline for oxidation of Super 304H in steam taken from Muramatsu [108]. k_ps for first regime growth are also included and confirm that a rate change occurs on formation of a Cr-rich healing layer. The larger values for k_p are suggested to more closely represent those for coarse grained 18Cr austenitic steels.

5.4 Oxide Spallation

As reported in the Results chapter, oxide spallation of the inner tube surface was only found on samples exposed to flowing steam (See sections 4.5 and Chapter 5). The oxide morphology of all samples suggested that the presence of 10% or more haematite in the outer oxide was a prerequisite for oxide spallation. A number of samples of Super 304H and 347HFG were found to have spalled following oxidation in "deoxygenated steam"[8]. It was later found that the outer oxide of these samples contained a significant amount of haematite, leading to the conclusion that the steam used during oxidation of these samples had been ineffectively deoxygenated. Subsequent oxidation tests were performed on 347HFG austenitic steel in flowing air saturated steam, resulting in spallation on all 347HFG samples. Spallation of all samples occurred on cooling shortly after removal from the furnace.

Several approaches have been taken to explain the mechanisms governing spallation on engineering alloys. The spallation diagram developed by Armitt et al. [119] in 1978 (Figure 2.42) has been used by several researchers to predict the strain at which spallation of the oxide on boiler steels occurs. This approach has been used semi-successfully as a predictive tool [34, 159], and has been refined since is was originally development [145, 160]. However, it is limited in applicability because of the complex nature of the oxide exfoliation problem.

An alternative approach is to consider the stored energy within the oxide. Oxide spallation is driven by the release of strain energy held within the oxide layer. The strain energy criterion predicts that spallation will occur when the stored energy within the oxide layer exceeds that of the shear fracture

[8] "Deoxygenated steam" (in quotation marks) relates to the steam used in experiments where spallation was found to occur. The term is placed in quotation marks to denote the ineffectiveness of oxygen removal during these tests and differentiate between effectively deoxygenated steam where no spallation was found to occur.

surface energy. By following either a buckling route or wedging route a spall particle is released. As outlined in the Literature Review, two common sources of stress are that of oxide growth and thermal transients. For the austenitic-oxide system, creep of the substrate likely relaxes growth stresses to such an extent that stresses associated with temperature transients dominate [140].

The stress an oxide is exposed to on cooling is sensitive to the thermal expansion coefficients of the oxide and substrate. The alloys tested in the current study have a tube wall thickness an order of 1000 larger than the thickness of the oxides, and so the assumption is made that all oxide layers will conform to the substrate's dimensions during changes in temperature, according to the thin film approximation [140]. Assuming all stresses are equal and biaxial, the in-plane stress in an oxide layer is then given by:

$$\sigma_{ox} = -\frac{E_{ox}\Delta T(\propto_m - \propto_{ox})}{(1-v)} \qquad \textbf{(5-4)}$$

and the strain:

$$\epsilon_r = -\frac{(\alpha_m - \alpha_{ox})\Delta T}{(1-v)} \qquad \textbf{(5-5)}$$

If the thin film approximation approach is not employed, as by some researchers [96], the stress and strain in the outer oxide layer would be calculated according to the difference in thermal expansion coefficients between the spinel and outer oxide, leading to larger or smaller values for the calculations of stress and strain. Figure 5.22 shows the curves used to calculate the thermal expansion coefficients of the outer oxides and alloy during samples cooling following removal from the furnace. For magnetite, the curve presented by Armitt et al. [119] in EPRI report FP 686 was used with reasonable confidence. However, as outlined in the Literature Review chapter, more meticulous measurements around the peak at 580 °C would be desirable, and limited reliable data is available above 650 °C. The thermal expansion coefficient of haematite is consistently lower than that of 347HFG, causing this oxide phase to remain in compression throughout cooling to room temperature. The spike in the thermal expansion coefficient of magnetite causes magnetite to undergo tensile stress during cooling between approximately 550 and 420 °C, before returning to compression down to room temperature. It can be appreciated from Figure 5.22 that an outer oxide on 347HFG formed from haematite will have a larger Δα than an oxide composed entirely of magnetite, resulting in larger cooling stresses in the oxide. This has implications on the overall strain energy of the oxide, which will increase if a large fraction of the outer oxide is composed of haematite.

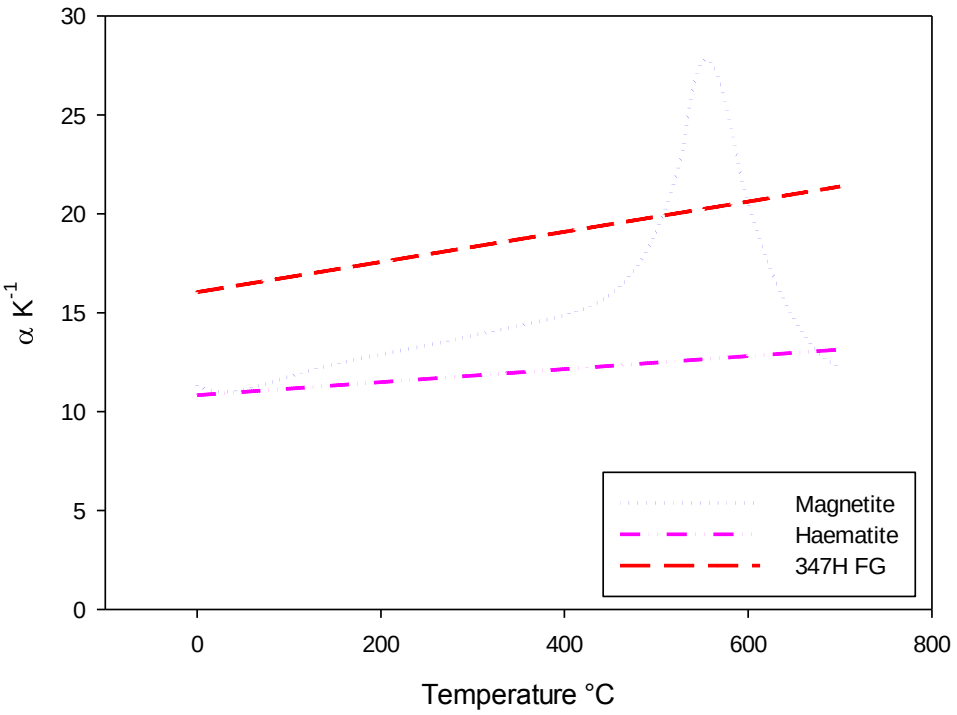

Figure 5.22 – True thermal expansion coefficient curves used in stress and strain energy calculations [119, 129, 133].

In calculating the stresses, strains and strain energies within the oxide layers in this study, a number of assumptions have been made in order to reduce the complexity of calculations. Firstly, all deformation is assumed to be elastic. When performing calculations on a single oxide layer, the system is modelled as a two layered oxide-alloy composite of infinite length under equal elastic biaxial stress. This negates any shear stresses that may be active towards the edge of the inner surface of tested samples, and also the curvature of the inner surface. Neglecting all other sources of stress, the mismatch in thermal expansion coefficients between the metal and oxide will contribute to the oxide strain energy, W*, of each oxide layer, given by:

$$W^* = (\Delta T)^2 \xi E_{ox} (\propto_m - \propto_{ox})^2 (1 - \upsilon_{ox}) \qquad \textbf{(5-6)}$$

As the Young's modulus and the thermal expansion coefficients of the metal, $\propto_m$, and oxide, $\propto_{ox}$, are temperature dependent, values and were integrated between the oxidation temperature and temperature at which spallation first occurred on cooling, T_c, (or to 25 °C for samples that did not exhibit spallation) according to Equation (5-7). This was especially important for magnetite, where the oxide may be under compression or tension depending on the magnitude of the temperature drop. The Young's modulus of the oxide, E_{ox}, is also temperature dependent. However, because of the lack of data on the temperature dependence of the parameter, constants were used. For

magnetite a value of E_{mag} = 225.8 GPa was used [161], and for haematite E_{hae} = 230 GPa was used [162]. A value of v = 0.3 was used for Poisson's ratio for all calculations. The method of integration of the thermal expansion coefficients can be found in Appendix . The strain energy, W*, was then calculated according to:

$$W^* = (\Delta T)^2 \xi E_{ox} \left(\int_{T_{spall}}^{T_{ox}} \propto_m dT - \int_{T_{spall}}^{T_{ox}} \propto_{ox} dT \right)^2 (1 - v_{ox}) \qquad \textbf{(5-7)}$$

For samples that exhibited spallation, the strain energy, W*, was calculated for the thickness of oxide spalled, over the temperature drop at which spallation was first observed from the inner sample surface[9]. For example, a sample of 347HFG that was oxidised at 650 °C, spalled at 500 °C, that had an outer oxide thickness of 20 µm, 15 µm of which spalled, ΔT_c would be taken as 150 °C and ξ as 15 µm. The significance of these values is that the strain energy of interest is that required to produce the first particle of spallation from the inner tube surface, assumed to reside within the thickness of the spallation particle. This gives the effective fracture energy to initiate spallation. It must be stated at this stage that the outer oxides of samples that spalled were composed of both magnetite and haematite. This is important to note as although the spallation interface was principally within the magnetite layer, the sum of the contributions to the strain energy from both the haematite and magnetite phases must be used. This is because it is the strain energy within the thickness of oxide spalled that is released via a failure mechanism. The haematite phase within the outer oxide was not always found to form a uniform layer at the oxide/gas interface, however. For the current analysis it was assumed to be located at the oxide/gas interface and uniform for all samples. Therefore, contributions to the strain energy were calculated for the proportional thickness of each layer and summed to give a total strain energy value. This method has been used previously for the scales grown on Type 316 steel [119].

For 347HFG oxidised in air saturated steam for 50 hours at 650 °C, where ΔT_c was 575 °C and spalled oxide thickness of 7.1 µm, the strain energies from the haematite (75%) and magnetite (25%) components of the spalled oxide were calculated to be $W_h^* = 13.06\, Jm^{-2}$ and $W_m^* = 0.73\, Jm^{-2}$ respectively, giving a total strain energy of $W^* = 13.79\, Jm^{-2}$. For this temperature drop the values of the expansion coefficients used were $\propto_m = 18.8\, K^{-1}$, $\propto_{mag} = 16.0\, K^{-1}$ and $\propto_{hae} = 12.0\, K^{-1}$. In comparison, the strain energy of 347HFG oxidised in deoxygenated steam for 50 hours at 650 °C whose outer oxide remained adherent, and was composed entirely of magnetite, was $W^* = 5.8\, Jm^{-2}$

[9] A cooling profile for 347HFG was used to relate the time at which spallation initiated, to the temperature drop. The cooling profile can be found in Appendix .

(ΔT = 625 °C, $\propto_m = 18.6\ K^{-1}$, $\propto_{mag} = 15.6\ K^{-1}$, $\xi = 10.5\ \mu m$). It can therefore be appreciated that the presence of haematite in the outer oxide increases the stored energy within the oxide, satisfying the strain energy criterion and causing it to spall on cooling.

For samples oxidised in air saturated steam, the time to first spallation was recorded, and found to decrease with increasing oxide thickness and haematite content. Furthermore, there was strong evidence that the majority of the samples failed via a buckling mechanism. A spallation map for haematite growth on 347HFG, similar to that constructed by Evans [125] for chromia growth, is presented in Figure 5.23. The diagram is constructed from two lines: one that represents the fracture energy, γ', of the interface at which spallation occurs, to the right of which the strain energy criterion is satisfied and failure via a wedging mechanism is expected. The second is a buckling line, to the left of which buckling of a pre-existing defect, having a buckling radius *R*, is expected to occur, and initiate spallation via tensile cracks at the edge of the buckle. It is important to note that for the strain energy criterion to apply to oxides that fall within the buckling regime, they must fall within the area at the top of the map enclosed by both the buckling and wedging lines. In this region, a buckle will propagate laterally via tensile crack growth along the spallation interface, or alternatively fail via wedging. The wedging boundary in Figure 5.23, as outlined in section 2.4.4.2 of the Literature Review was calculated using Equation (5-8) [139]:

$$\Delta T_c = \left(\frac{\gamma_F}{\xi E_{ox}(\propto_m - \propto_{ox})^2(1 - v_{ox})}\right)^{1/2} \qquad \textbf{(5-8)}$$

and the buckling boundary using Equation (5-9) [125]:

$$\Delta T_b = \frac{1.22}{\Delta\alpha(1 - v^2)}\left(\frac{\xi}{R}\right)^2 \qquad \textbf{(5-9)}$$

As previous explained, the temperature dependent variables (α_m, α_{ox}) were integrated between the oxidation temperature and temperature at which spallation was first observed, ΔT_c (in Figure 5.23 for a temperature drop from 650 °C). Defining values for the effective fracture energy, γ', and defect radius, *R*, that fit well with experimental observations requires multiple data that a line can be fit to with reasonable confidence.

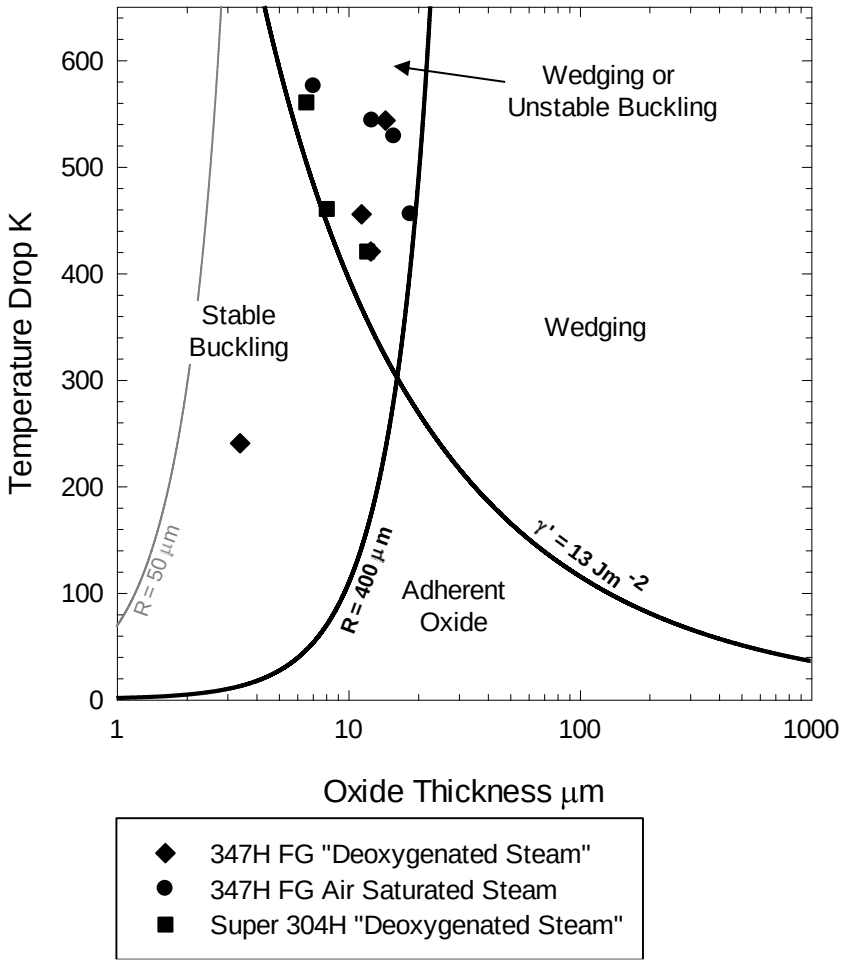

Figure 5.23 – Spallation map for haematite growth on 18-8 austenitic steel cooled from 650 °C. The black line labelled "R = 400 μm" indicates the boundary to the left of which stable buckling is expected where the defect radius is 400 μm. To the right of the line labelled "γ' = 13 Jm^{-2}" failure via wedging is expected. In the upper area encompassed by the two black lines, either wedging or unstable buckling is expected. The lines correspond to boundary conditions of varying defect size and fracture surface energies. Data is included for samples of 347HFG and Super 304H that exhibited spallation following oxidation in improperly "deoxygenated steam" and for 347HFG oxidised in air saturated steam. Maps corresponding to the correct fraction of magnetite in the outer scale of each sample can be found below.

For the wedging boundary, Evans and Lobb [143] reported an effective fracture energy of 6 Jm^{-2} for chromia growth on a 20Cr-25Ni-Nb stainless steel. In the current work, the boundary condition was chosen from calculations of the strain energies of samples of 347HFG oxidised in air saturated steam listed in Table 5.9. A value of $\gamma' = 13Jm^{-2}$ was chosen and this represents a lower limit to the effective fracture energy calculated for experimental data. The critical temperature drops for samples of 347HFG and Super 304H oxidised in "deoxygenated steam" are also plotted on Figure 5.23. The unreliability of the testing procedures and unknown pO_2 of the steam used in testing of these samples resulted in their strain energy values (listed in Table 5.10), which drop as low as $\gamma' = 7.68Jm^{-2}$, not being considered when defining the boundary conditions in Figure 5.23. A justification for a minimum effective fracture energy of $\gamma' = 13Jm^{-2}$ comes from the strain energies of samples oxidised in

effectively deoxygenated steam that did not exhibit spallation. A second spallation map, this time for magnetite growth on 347HFG, was constructed to present the data from samples that did not exhibit spallation and whose outer oxides are composed almost entirely of magnetite. It can be seen from the magnetite spallation map presented in Figure 5.24, that the strain energy within the oxides of these samples reaches as high as W* = 12.1 Jm^{-2} without spallation of the oxide. As the spallation interface was usually found to be within the magnetite layer, an effective fracture energy of $\gamma' = 13Jm^{-2}$ is acceptable. Calculated strain energy data can be found in Table 5.9 for 347HFG oxidised in air saturated steam, and Table 5.10 for 347HFG and Super 304H oxidised in "deoxygenated steam".

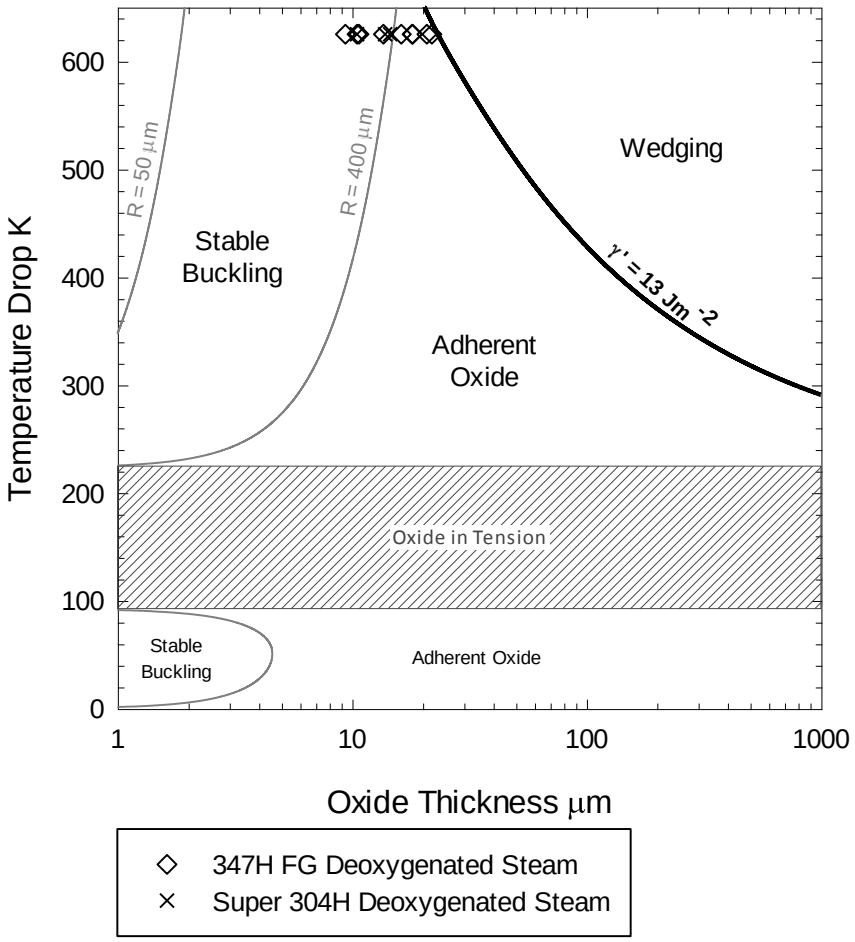

Figure 5.24 – Spallation map for magnetite growth on 18-8 austenitic steel cooled from 650 °C. To the right of the black line labelled "γ' = 13 Jm^{-2}" failure via wedging is expected. The buckling line corresponding to a defect radius of "R = 400 μm" is in grey due to the absence of buckling on the plotted data, suggesting that this may not be a regime followed by pure magnetite growth. For a temperature drop from 650 °C the lines do not intersect to create a region of unstable buckling or wedging, as with the haematite map. Data for 347HFG and Super 304H are included. Note that these data represent samples that did not spall.

Table 5.9 – Calculated strain energies for spalled oxides on 347HFG oxidised in air saturated steam at 650 °C

Alloy	Oxidation Time (h)	ΔT_c (°C)	Spalled Oxide Thickness (μm)	Fraction Fe_2O_3 in Spalled Oxide (%)	Strain Energy in Fe_2O_3 (Jm^{-2})	Strain Energy in Fe_3O_4 (Jm^{-2})	Total Strain Energy (Jm^{-2})
347HFG	50	575	7.1	75	13.06	0.73	13.79
347HFG	100	543	12.7	80	22.67	0.85	23.52
347HFG	250	528	15.8	90	30.29	0.95	31.24
347HFG	500	455	18.6	95	29.42	0.16	29.40

Table 5.10 – Calculated strain energies for spalled oxides on 347HFG oxidised in "deoxygenated steam" at 650 °C.

Alloy	Oxidation Time (h)	ΔT_c (°C)	Spalled Oxide Thickness (μm)	Fraction Fe_2O_3 in Spalled Oxide (%)	Strain Energy in Fe_2O_3 (Jm^{-2})	Strain Energy in Fe_3O_4 (Jm^{-2})	Total Strain Energy (Jm^{-2})
347HFG	50	240	3.4	30	0.54	0.00	0.54
347HFG	100	455	11.5	40	7.58	1.15	8.73
347HFG	210	420	12.5	80	14.45	0.30	14.75
347HFG	250	543	14.5	30	9.73	3.40	13.13
Super 304H	50	560	6.6	40	6.20	1.48	7.68
Super 304H	100	460	8.1	60	8.20	0.57	8.76
Super 304H	210	420	12.1	70	12.20	0.43	12.63

For the buckling boundary, the defect radius, *R*, relates to the area of decohesion required to initiate buckling of the oxide above it. If in the region enclosed by both the buckling and wedging boundaries, tensile stresses at the edge of the buckle may initiate lateral propagation of the buckle resulting in spallation. It is difficult to determine a value for *R* from analysis of the oxide post-spallation where the spallation interface is particularly porous. Initial observations of cross-section micrographs indicated that defects in the form of cracks in the oxide layer of around 50 µm existed and could be used for *R*. However, on calculating the minimum defect size for spalled samples, it was found that *R* ranged between 130 and 360 µm for air saturated steam samples, and 150 and 310 µm for "deoxygenated steam" samples. These minimum defect size values are much larger than 50 µm, suggesting that the initial area of decohesion comprises more than a single defect. This can be understood by envisioning that the stress fields of individual defects that are within close proximity, interact with each other, effectively allowing them to be treated as one larger composite defect. This has been addressed by Hancock and Nicholls [141], who outline a model for estimating the composite defect size in oxides based on the size, location and shape of individual defects within an oxide. For two coplanar embedded defects, the distance, *S*, between them must be shorter than the average length, *l*, of the defects for them to be considered as one composite defect, as shown in Figure 5.25.

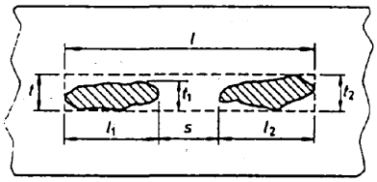

$$s \leqslant \frac{l_1 + l_2}{2}$$

Figure 5.25 – Schematic illustration of the conditions of interaction between two embedded defects [141].

The high level of porosity found within the outer oxide, or at the spinel/outer oxide interface of steam oxidised samples increases the effective value of *R*. This allows for buckling of the outer oxide. Figure 5.26 illustrates a large area of spallation produced via buckling.

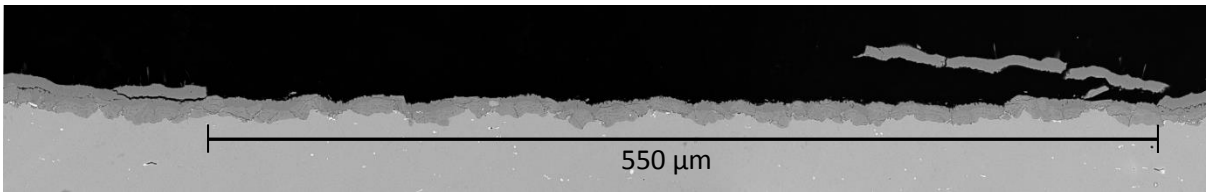

Figure 5.26 – Large area of decohesion on sample of 347HFG oxidised for 50 hours at 650 °C.

The same boundary conditions are used for the magnetite spallation map in Figure 5.24. However, the data plotted on the map are for samples of 347HFG and Super 304H that did not spall. Generally, porosity was found to be lower in the oxides of samples that did not exhibit spallation, leading to

composite defect radii smaller than 400 μm. This would explain the lack of buckling on samples within the buckling boundary on the magnetite spallation map. The buckling line is coloured grey because of the uncertainty of buckling as a relaxation mechanism for pure magnetite on 347HFG.

Considering the spallation data in Figure 5.23, both the air saturated steam data and the data for samples oxidised in "deoxygenated steam" fit into the upper region where spallation is expected via unstable propagation of a buckle or wedging (with the exception of one sample of 347HFG located towards the bottom left corner). Observations of oxide micrographs confirm that buckling is the primary failure mechanism for the thinner scales. For the thickest scales, the failure mode is less obvious, and for the air saturated steam samples after 250 and 500 hours, wedging appears more likely than buckling. Some of the data in Figure 5.23 fall to the right of the wedging boundary line despite having a strain energy value of less than 10 Jm^{-2}. This is because the contribution to the strain energy from the magnetite phase is small compared with the contribution from the haematite phase (see Table 5.9 and Table 5.10). A 3D spallation map was constructed that is able to place data according to the percentage of magnetite in the scale, along with temperature drop and oxide thickness. The spallation map, shown in Figure 5.27, provides a visual representation of the fraction of magnetite in the outer oxide of each spalled sample. Data for unspalled samples is included, and located at 100% magnetite.

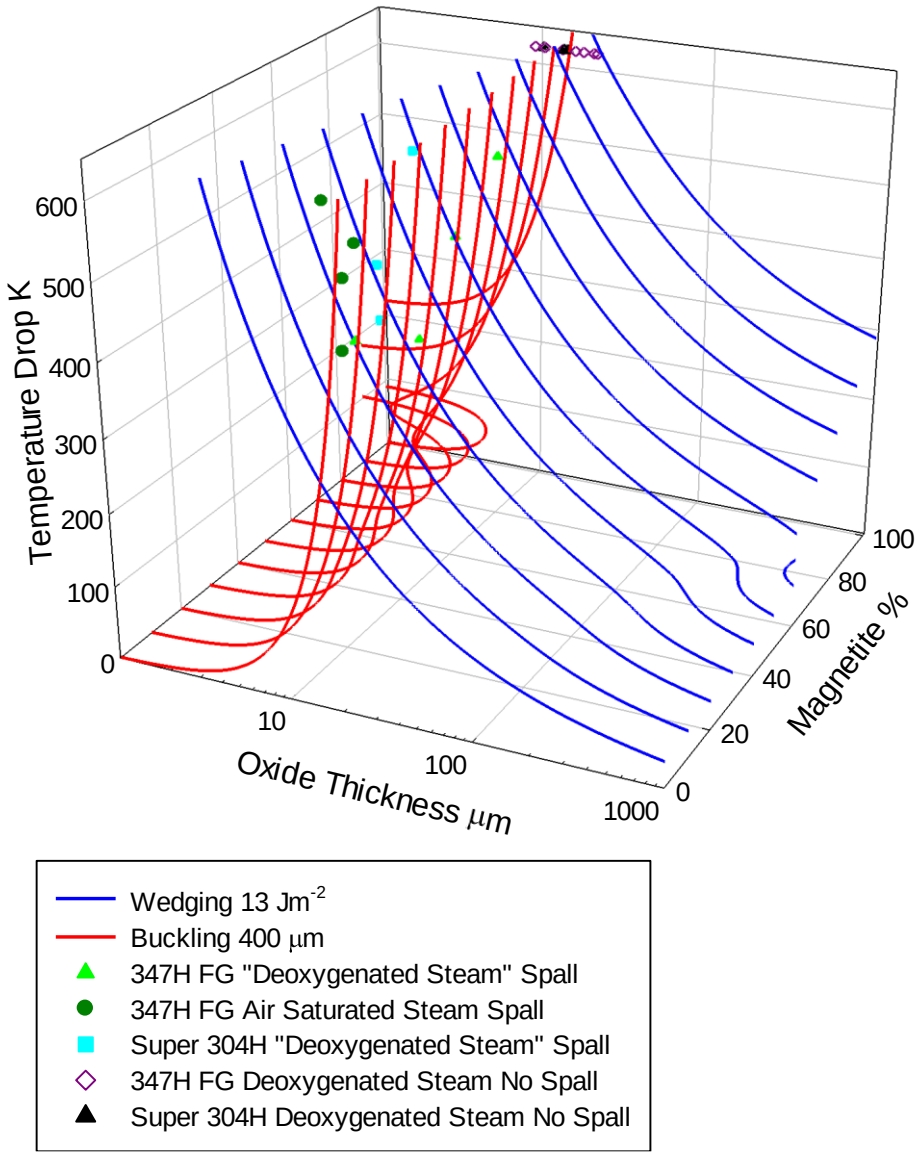

Figure 5.27 – 3D spallation map for haematite with varying fraction of magnetite growth on 18-8 austenitic steel cooled from 650 °C. Spallation data for 347HFG oxidised and "deoxygenated steam" and air saturated steam are included at the correct magnetite percentage. Note that the air saturated steam data are all closer towards 0% magnetite than the "deoxygenated steam" samples. Also included are data for the oxidation of Super 304H and 347HFG in deoxygenated steam. These data correspond to samples that did not spall and are positioned at magnetite % = 100, correctly indicating the absence of haematite in the outer oxides of these samples.

Concerning the low strain energies of the "deoxygenated steam" samples, the oxygen partial pressure of these early tests was unknown. This should not have direct relevance to the tendency to spallation. However, there seemed to be no trend in the location of the spallation interface, fraction of haematite, and porosity of these samples. Furthermore, temperature monitoring was not performed in situ of these early experiments, and may have risen above 650 °C. Calculating the strain energy of

these samples assuming a higher oxidation temperature would increase the strain energy towards a value of 13 Jm^{-2}. Nevertheless, the data show that the critical strain energy criterion does apply for oxide growth on 347HFG and Super 304H, and that a value of 13 Jm^{-2} is a realistic effective fracture energy to initiate spallation. Armitt et al. [119] proposed a lower limit of around 6 Jm^{-2} for magnetite, and calculated a value of 11.5 Jm^{-2} for the outer oxide on Type-316 steel by measuring the mean outer oxide thickness, haematite fraction, extent of spalling and fraction of interfacial porosity. $\gamma' = 11.5Jm^{-2}$ was taken as an average value. This was deduced from the value of the strain energy at room temperature when 50% of the oxide from the inner surface of analysed 316 tubes had spalled. The premise was that stress relaxation in the partially spalled oxide layer will reduce the strain energy in the remaining adherent oxide[10]. This is shown in Figure 5.28 a), along with a similar graph in Figure 5.28 b) for data compiled in the current work.

The reader should be aware that calculating the fraction of spallation from the inner tube surface may have differed between the current work and literature. In the current work, areas of oxide that were obviously lifted from the surface, but had not spalled completely, were included in the spalled fraction. The difficulty in determining exactly how much oxide had lifted as a result of a failure mode would give rise to an uncertainty in the measurement. In addition, for the air saturated steam samples, it was difficult to differentiate between areas of oxide that had spalled according to the critical strain energy criterion, and areas where oxide blisters had spalled. For oxidation times of 250 and 500 hours, this distinction was less relevant because of the spallation interface favouring the spinel/outer oxide interface. Consequently, all measurements of the spalled oxide fraction should be treated as rough estimates.

With that in mind, the initial observation is that spallation in the current work continues until a much higher fraction of the surface has spalled. This would suggest that relaxation processes operating as spallation continued were less effective for 347HFG. Additionally, for the air saturated steam data, there does not appear to be a defined strain energy at which the fraction of spalled oxide increases dramatically, as with the data in Figure 5.28 a). The reason for this may be related to the size of the spalled particles, which were generally much larger on samples of 347HFG oxidised in “deoxygenated steam” than those oxidised in air saturated steam. It is proposed that the change in oxide morphology, to that of magnetite, beneath oxide blisters limits the particle size in air saturated steam samples. The more homogeneous morphology of “deoxygenated steam” samples of 347HFG allows a buckle to propagate further, resulting in a larger spallation particle size. This restriction applies less to the

[10] The statistical nature of oxide spallation is covered in further detail by Evans [107]

samples oxidised for 250 and 500 hours in air saturated steam, as the oxide beneath blisters contained a high fraction of haematite and spalled with areas free from blisters.

A similar mechanism is thought to occur on Super 304H, where the axial defects on these samples is likely to limit the spallation particle size[11], resulting in a lower spalled fraction than 347HFG. If the data from 347HFG and Super 304H oxidised in "deoxygenated steam" are treated separately from each other, it is possible to speculate strain energies at which, the fraction of spalled oxide rapidly increases to a maximum value (for Super 304H ~50% and for 347HFG ~80%). Then, a value of approximately $\gamma' = 15Jm^{-2}$ would correspond to the strain energy at which massive scale loss occurs. This value is relatively close to that obtained by Armitt et al. [119], however, the extent of porosity was not measured in the current study, and for 316 steel was not divulged. The reader is reminded that these values are speculative, and further work is clearly needed to refine the trend and explain the discrepancy between air saturated steam and "deoxygenated steam" due to the lack of data.

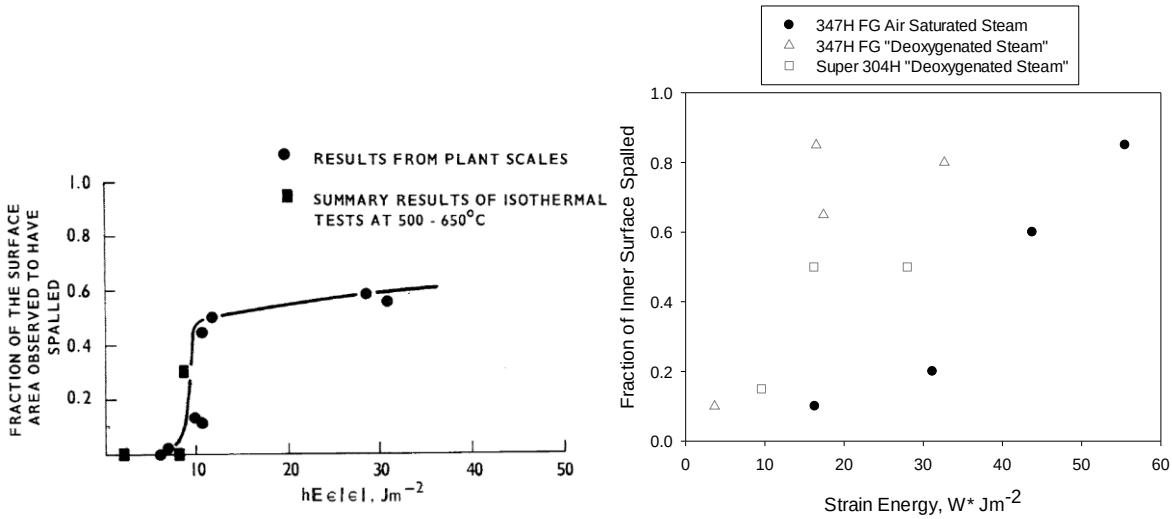

Figure 5.28 – Fraction of inner surface oxide spalled as a function of strain energy in spalled oxide thickness at room temperature. a) data for Type-316 steel after Armitt et al. , b) spallation samples in the current work, oxidised in steam at 650 ℃.

[11] See Figure 4.119 and Figure 4.120.

Chapter 6 Conclusions

For the first time, an atmospheric steam oxidation facility was built and commissioned at the University of Birmingham. Oxidation experiments in flowing deoxygenated steam were conducted on advanced austenitic steels 347HFG, Super 304H, and HR3C for up to 1300 hours. Oxidation temperatures were 600, 650, and 700 °C. Experiments were carried out on samples cut from production tubing. The surface of interest was the pickled inner steamside surface. Additionally, samples of shot peened Super 304H tubing were included to investigate the effect of surface finish on the oxidation behaviour.

Oxidation experiments were also carried out in static laboratory air for up to 3000 hours to provide a baseline comparison to the deoxygenated steam environment.

Finally, 347HFG was oxidised in flowing air saturated steam for up to 500 hours to investigate the spallation behaviour of the alloy at 650 °C.

The following conclusions were drawn with respect to oxide morphology, oxidation kinetics, and oxide spallation behaviour.

6.1 Oxide Morphology

- In air, pickled 347HFG and Super 304H initially grow oxide nodules, which coalesce with time into a uniform duplex oxide. 18 wt.%Cr is therefore below the threshold required to form a complete Cr-rich protective film on pickled fine grained austenitic alloys in air.
- In air, pickled HR3C forms a Cr-rich protective film over much of its surface. Oxide nodules form and increase in size and frequency as oxidation time and temperature increase. However, nodules covered no more than 50% of the alloy surface after 1000 hours at 700 °C. Therefore, 25 wt.%Cr is below the threshold required to form a complete Cr-rich protective film on pickled course grained austenitic alloys in air.
- HR3C exhibited consistently lower weight gain and oxide thickness to pickled 347HFG and Super 304H in all atmospheres.
- The outer oxide grown on HR3C in air differs from the 18Cr alloys in that an intermediate Fe,Ni-rich oxide is formed at the spinel/outer oxide interface. This intermediate layer is absent following oxidation in deoxygenated steam.

- Deoxygenated steam has a detrimental effect on the oxidation resistance of all alloys. 347HFG and Super 304H grow thick duplex oxides. The oxide grown on HR3C consists of a uniform porous Fe-rich outer layer and inner spinel. The spinel tends to be thinner than that grown on 18Cr alloys, but as oxidation time increases deep pits begin to form away from austenite grain boundaries, due to the large grain size.
- In air, the outer oxide of 347HFG and Super 304H is non-porous Fe_2O_3, suggesting that equilibrium is achieved at the oxide/gas interface. In deoxygenated steam the outer oxide is almost entirely formed of porous Fe_3O_4. The oxygen partial pressure of deoxygenated steam is above the dissociation pressure of Fe_2O_3, suggesting that equilibrium is not reached at the oxide/gas interface. Enhanced ion transport mechanisms in steam are proposed to be responsible for this.
- Changing the carrier gas to air saturated steam promotes the formation of Fe_2O_3 in the outer layer. The total oxide thickness showed a slight increase in air saturated steam compared with deoxygenated steam.
- A Cr-rich 'healing layer' forms at prior austenite grain boundaries on 347HFG and Super 304H in steam atmospheres, which significantly reduces further oxidation into the alloy. The layer is enriched in Mn and depleted in Fe and Ni.
- Shot peening greatly improves oxidation resistance in all atmospheres. The high near-surface grain boundary and dislocation density promotes the formation of Cr_2O_3 and Cr,Mn-rich crystallites in air. Quantities of Mn and Fe in the oxide grown in air suggest that a complete layer of pure Cr_2O_3 does not grow in air. In steam, small quantities of Fe-rich oxide overlay a thin Cr,Mn-rich oxide layer. The oxide thickness of shot peened Super 304H was a factor of 10 smaller than that of pickled Super 304H after 2000 hours at 700 °C in air.
- Increasing temperature does not significantly change the morphology of the oxides grown on all alloys between 600 and 700 °C.
-

6.2 Kinetics

- Oxidation kinetics were calculated from both mass gain and oxide thickness measurements in air and steam. The kinetics calculated from mass gain were influenced by the different surface finishes on each side of the sample surface. For this reason, analysing the oxidation kinetics calculated from oxide thickness measurements was preferred. Retaining the inner pickled or shot peened surface was of high importance in the current programme to ensure the oxidation behaviour observed would be an accurate reflection to that seen in plant. This differentiates the programme from many existing laboratory studies that conduct oxidation experiments on ground coupons.
- The oxidation performance of austenitic steels can be increased by increasing the Cr content or shot peening the alloy surface.
- In air, all alloys oxidised with sub-parabolic kinetics from t = 0 s. The order of reaction, n, was calculated to fall between 4.10 and 4.60 for all alloys, as calculated using oxide thickness measurements. The order of reaction was found to be higher on 347HFG as this alloy formed a uniform duplex oxide in a shorter time period to Super 304H.
- For pickled 347HFG and Super 304H the sub-parabolic kinetics are attributed to an initial period of rapid nodule growth and coalescence, followed by a reduced oxidation rate once a

uniform duplex oxide layer is established. Once a uniform duplex oxide is established the kinetics fir with a high confidence to a parabolic regime. Parabolic rate constants for growth at 700 °C following the formation of a uniform duplex oxide layer were 1.46 $x10^{-17}$ for 347HFG and 1.96 $x10^{-17}$ for Super 304H.

- The Cr-rich protective oxide grown on HR3C in air grows at a similar rate to shot peened Super 304H at 700 °C. A defined rate change was not observed for these alloys. The parabolic rate constants for growth from t = 0 s were calculated to be 1.26 $x10^{-19}$ m^2s^{-1} for shot peened Super 304H and 1.38 $x10^{-19}$ m^2s^{-1} for the Cr-rich oxide grown on HR3C.
- The parabolic rate constant for shot peened Super 304H agrees with literature values for chromia growth in dry conditions.
- In deoxygenated steam pickled 347HFG and Super 304H follow two distinct kinetic regimes. The first regime can be explained by an initial rapid growth of uniform duplex oxide. This continues until the internal oxidation front consumes the first layer of austenite grains and a complete Cr-rich healing layer is formed. At this point the oxidation rate significantly reduces. The rate limiting step for further oxide growth is considered to be ion diffusion across the Cr-rich healing layer, which is much slower than through spinel and Fe oxides due to its highly stoichiometric structure.
- Parabolic rate constants for growth before healing layer formation between 600 and 700 °C were calculated to be between 2.07 $x10^{-15}$ m^2s^{-1} and 5.69 $x10^{-16}$ m^2s^{-1} for 347HFG and between 1.99 $x10^{-15}$ m^2s^{-1} and 2.16 $x10^{-16}$ m^2s^{-1} for Super 304H. This Cr-rich oxide layer was found to be less protective than the Cr-rich oxide layer grown in air.
- Following the formation of a Cr-rich healing layer, second regime parabolic rate constants were calculated for 650 and 700 °C. These were calculated to be between 1.63 $x10^{-18}$ m^2s^{-1} and 9.71 $x10^{-18}$ m^2s^{-1} for 347HFG and between 2.29 $x10^{-18}$ m^2s^{-1} and 8.18 x 10^{-18} m^2s^{-1} for Super 304H.
- The oxide thickness at 40 Kh for 347HFG was calculated by extrapolating oxide thickness data using three methods. The first was to assume a single parabolic regime. The second was using the calculated order of reaction and the rate constant K_n. The third was using the second regime parabolic rate constant. The third method was considered to be most representative and matched literature values. The calculated oxide thickness of 154 µm matched the literature value of 142 µm well.
- The second regime oxidation rate of the outer oxide on the pickled 18Cr alloys was found to be higher than the inner oxide. This is a significant finding as researchers sometimes assume total oxide thickness to be two times inner layer thickness. This is calculated in this way when the outer oxide has spalled off leaving only the inner layer thickness. The results of the current work showed that calculating oxide thickness at 40 Kh by this method underestimated the oxide thickness.
- The effect of increasing oxidation temperature was to increase the oxidation rate of all alloys in all atmospheres.

6.3 Spallation

- No alloys exhibited spallation when oxidised in deoxygenated steam.
- Only 347HFG and pickled Super 304H exhibited spallation.

- A pre-requisite for spallation to occur was the presence of at least 10% Fe_2O_3 in the outer oxide scale.
- Fe_2O_3 was only observed above 10% in the outer scale when oxidised in air saturated steam.
- Spallation was only observed on sample removal from furnace. This provides evidence that spallation results from a build-up of stress caused by the miss-match in thermal expansion coefficients between the alloy and oxide layer.
- Evidence of failure via a buckling mechanism was found. At longer durations a wedging mechanism may have occurred.
- The strain energies within the grown scales of 347HFG oxidised in air saturated steam were calculated and a lower limit for the effective fracture energy of $\gamma' = 13Jm^{-2}$ was reported for the initiation of spallation of the outer oxide of 347HFG. The same value was calculated as an upper limit for the adherence of pure magnetite on 347HFG, based on the strain energies of the oxidation tests performed in the current study. The porous nature of the spallation interface was thought to decrease the effective fracture energy of the spallation interface.
- A spallation map for haematite was constructed and spallation data was found to fall inside the region of expected failure via wedging or unstable buckling. Observation of unadherent regions of oxide led to the conclusion that buckling was the principal mode of failure for the samples tested, however, the thickest oxides may have spalled via a wedging mechanism.

Chapter 7 Future Work

The focus of the current study was to investigate the effect of steam on the oxidation and spallation properties of austenitic stainless steels. Spallation only occurred when more than 20% of the outer oxide composed of haematite, which was facilitated by a high oxygen partial pressure in the steam flow. The current study dealt with two extremes: deoxygenated steam, where the feed water was purged with oxygen free nitrogen to reduce the level of oxygen in the feed water to under 10 ppb, and air saturated steam, where bottled air was purged through the feed water to increase the oxygen partial pressure to 24%. These two extremes had the effect of: reducing the outer oxide haematite fraction to less that 10% (in the case of deoxygenated steam), or increasing the outer oxide haematite fraction to above 75% (in the case of air saturated steam)[12]. Further work is needed to determine the feed water pO_2 that is in equilibrium with haematite during oxidation in flowing steam. Hydrogen evolution is thought to reduce the oxygen partial pressure at the oxide/gas interface, so the effect of steam flow rate should be included in this experiment [40, 55].

A number of assumptions were made to calculate the strain energies of spalled and unspalled oxides. Further investigation into the refinement of the parameters used is required. Particular attention should be placed on the effect of porosity on the effective fracture energy of the spallation interface. The porosity issue has been addressed by simply scaling the magnitude of the strain energy with the area fraction of pores at the spallation interface by Armitt et al. [119], and more thorough analysis has been made by other researchers [145], including the characterisation of porous oxides [163]. Knowledge of how porosity affects spallation is critical to obtaining accurate fracture energies.

The radius of decohesion, *R*, was assumed in this body of work to incorporate porosity in the oxide layer for the initiation of buckling. A more accurate analysis of buckling and critical decohesion area sizes is required to gain a better understanding of the spallation problem.

As indicated in the literature review, the thermal expansion coefficient of magnetite requires refinement around the peak at 580 °C. The magnitude above this temperature also varies between

[12] For the samples that exhibited spallation after oxidation in ineffectively deoxygenated steam, the oxygen content of the feed water was unknown.

researchers. This is desirable as the stresses and strains imposed on engineering alloys on which the oxide grows are sensitive to the thermal expansion of the oxide.

Finally blistering was a phenomenon found on samples oxidised in air saturated steam. There is little documentation of these features in the literature, and none applying to the current system. The causes and mechanisms of blister growth needs to be investigated.

No spallation was found to occur from the inner surface of any sample oxidised in laboratory air, for the oxidation periods investigated (up to 3000 hours). Longer term oxidation tests in laboratory air should be undertaken to investigate the spallation tendency of the oxides grown on austenitic steels. The outer

Chapter 8 Appendices

8.1 Appendix A – Fundamentals of Steel Metallurgy and High Temperature Oxidation

8.1.1 Introduction

The oxidation of boiler components is a major concern in plant. As plant steam parameters increase tubes are designed with higher chromium contents to resist oxidation by forming a dense, protective oxide film that reduces the oxidation rate of the base metal iron. Without preferential oxidation of minor element additions thick scales would form and lead to rupture of the heat exchanger tube. It is the thermodynamics of these elements along with oxygen that allow reactions to take place and so a great effort is made to reduce the molecular oxygen content of boiler steam. The following section provides an overview of the mechanisms involved in high temperature oxidation in air and steam, and reviews research into the high temperature oxidation of metals, with particular attention placed on the steam oxidation of engineering alloys employed in the boiler sections in plant.

8.1.2 Structure of Steel

Covalent and ionic bonding, unlike metallic bonding usually give rise to materials that exhibit poor thermal and electrical conductivity due to the outer electrons interaction in the bond restricting the freedom of movement within the material. In contrast, in a metal the valence electrons of each atom are free to move throughout the material and the metallic bond is caused by the attraction of these electrons with the positive metal ions. When describing a metal on a macroscopic scale it can be said that a metal comprises of an arrangement of positive metal ions surrounded by a “cloud” of delocalised electrons. It is the freedom of movement of these electrons that give rise to a metal’s high thermal and electrical conductivity [164].

Ions in a metal repel one another leading to an arrangement of ions that are bounded by the attractive force of delocalised electrons and separated by the repulsive force of adjacent ions. The ions arrange

themselves in a configuration that gives the lowest entropy and so one can begin to see that the energetically favourable arrangement of ions in different metals gives rise to the different atomic structures observed. In a crystal, the atomic structure is defined by a repeating unit of pattern known as the unit cell which, when regularly repeated, defines the position of all the ions in the metal crystal.

Three common crystal structures for metals are shown in Figure 8.1. Face centred cubic (fcc) and hexagonal close packed (hcp) are two configurations of closely packed ions. Body centred cubic (bcc) is also a common configuration amongst metals [164].

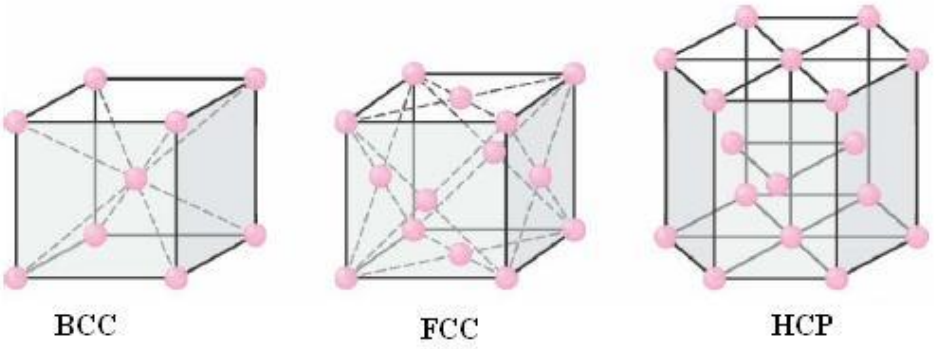

Figure 8.1 – Common metallic crystal structures.

8.1.2.1 Iron and Primitive Steel

Pure iron is allotropic and may exist in more than one crystal structure depending on temperature. The three phases of pure iron include: alpha iron (ferrite), which has a bcc structure and is stable up to a temperature of 912°C, gamma iron (austenite), which has an fcc structure and is stable between 913°C and 1394°C, and delta iron (delta ferrite), which is stable between 1394°C and the melting point of pure iron, and has a bcc structure [165].

Iron in its pure form has little engineering significance, and is generally known for its mechanical properties when alloyed with carbon and other elements to form steel (<2 wt.% C) or cast iron (>2 wt.% C). Combining other elements with iron has the effect of shifting the phase boundaries of the alloy.

Figure 8.2 shows the iron-carbon phase diagram for carbon contents up to 5 wt.% carbon. The far left hand side of the diagram denotes the phase boundaries for pure iron. The phase diagram illustrates the effect of increasing amounts of carbon on the phase fields of the system under equilibrium, and is

only valid for a pressure of one atmosphere, as variations in pressure cause shifts in the phase boundaries and even give rise to new phases [166].

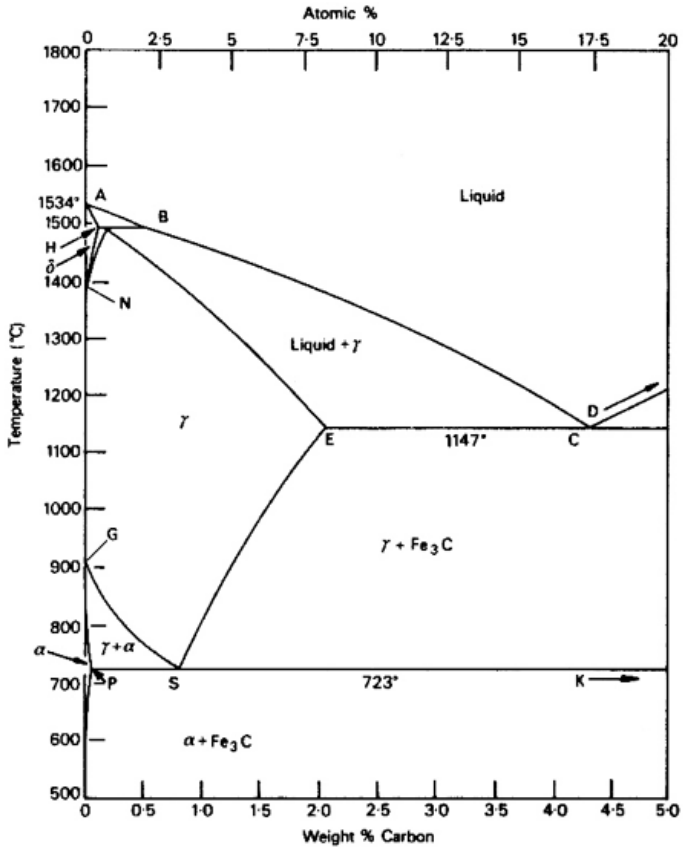

Figure 8.2 – Iron carbon phase diagram.

The addition of carbon to iron to make steel is the oldest and most common way of improving the strength of iron. Carbon enters iron at interstitial sites and has different solubilities in alpha and gamma iron. In ferrite a maximum of 0.1 at% (0.02 wt%) carbon is soluble at a temperature of 723 °C and <0.00012 at.% <0.00005 wt.% at room temperature. Austenite can hold as much as 8.8 at.% 2.04 wt.% carbon at a temperature of 1150 °C and 3.6 at.% 0.8 wt.% at 723°C. The reason for the difference in solubility is the packing of the iron atoms in the lattice and available interstitial sites. There are tetragonal and octahedral interstitial sites in alpha and gamma iron and in alpha iron carbon enters the smaller octahedral sites as these are preferred for the relief of strain on the atomic microstructure. Although the fcc structure has closer packing than the bcc structure, the octahedral sites in austenite are larger than those of ferrite and so carbon is more soluble in austenite than ferrite. When the solubility limit of carbon in iron is reached excess carbon forms cementite (Fe_3C) which, below 723 °C forms a eutectoid with alpha ferrite known as pearlite [165]. As with carbon, other

element additions can be used to control which phases are stable over temperature ranges for specific applications.

8.1.2.2 Martensitic Stainless Steel

Alpha ferrite can hold less than 0.00012 at.% (0.00005 wt.%) carbon in solution at room temperature. This increases to 0.095 at.% (0.02 wt.%) at 723 °C but to increase the solubility further the metal must be heated to the austenitic phase where the maximum solubility is 8.8 at.% (2.04 wt.%) carbon in solution at 1150 °C. On slow cooling into the ferrite phase field, excess carbon precipitates out of solution in the form of Fe_3C cementite and forms the alpha/Fe_3C pearlite eutectoid familiar as ferritic steel. This process occurs via diffusion of iron ions into the new bcc structure. If the austenite is rapidly quenched however, excess carbon does not have time to precipitate out of the iron matrix and a diffusionless shear transformation takes place transforming the lattice from the austenitic fcc structure to a body-centred tetragonal one referred to as martensite [165]. Laths or plates are formed during the transformation in order to minimize the strain energy due to the deformation and these are heavily dislocated in as-quenched form. The martensite transformation may not be a complete one and the resulting fraction of martensite is determined by the quenching medium (e.g. water or oil), the martensite start and finish temperatures, the geometry of the component and the composition of the metal. Alloying elements can be added to control the martensite start and finish temperatures and can determine the fraction of martensite achieved on quenching. As-quenched martensite is extremely hard and fairly brittle. It has a high dislocation density and as the carbon content of original austenite from which it is formed is increased so does the frequency of twins. Martensite in this form is often too brittle for use in industrial applications and so is tempered to increase the toughness at the expense of hardness. Tempering is performed by holding the metal at an intermediate temperature typically in the range 150 – 700 °C depending upon the alloy composition. At the lower end of this temperature range carbon precipitates out and forms carbides. As the temperature increases and more carbon precipitates the martensite begins to lose its tetragonal form and eventually returns to essentially bcc ferrite. At higher temperatures the martensite lath boundaries are replaced by ferrite grain boundaries until the overall structure of the alloy resembles that of a largely ferrite grain structure with carbide precipitates dispersed mainly but not exclusively on grain boundaries.

8.1.2.3 Austenitic Stainless Steel

Certain alloying elements expand the gamma phase field to room temperature, allowing steel to retain the austenite structure in a stable or meta-stable condition at room temperature. The stable condition

defined as that when the martensite start temperature is below room temperature. Austenitic steels have several benefits as engineering materials over ferritic steels; they are more ductile and do not undergo a ductile/brittle transition, allowing for easy fabrication, and the oxidation/corrosion resistance is vastly improved due to the high chromium content. The disadvantages over ferritic steels are mostly related to cost, however, certain applications call for properties (such as high thermal conductivity of boiler tubes) to which ferritics are favoured.The addition of chromium to low carbon steel reduces the size of the gamma phase field. To stabilise austenite at room temperature, the addition of as little as 8% nickel to 18%Cr steel is sufficient. If the chromium content is reduced or increased from this amount, more nickel is needed to retain the austenitic structure. This effect leads to the common 18Cr8Ni group of austenitic steels. Other elements, such as manganese are austenite stabilisers but are less effective than nickel. In the absence of nickel approximately 12-15%Cr and 12-15%Mn are required for room temperature stability [165]. Carbon and nitrogen are strong austenite formers, however, excessive carbon content causes carbide precipitation issues at elevated temperature. The solubility of carbon increases to 0.5 wt.% at 1100 °C and rapid cooling leads to a supersaturated solid solution at room temperature. Issues arise when the alloy is heated to an intermediate temperature, when carbon precipitates out often forming carbides with chromium in the form of $Cr_{23}C_6$. These carbides preferentially form at alloy grain boundaries decreasing low temperature ductility and most importantly depleting the alloy bulk of chromium, reducing corrosion protection. $Cr_{23}C_6$ Can form at very low carbon contents (<0.05 wt.%). Carbide precipitation may lead to sensitisation – a depletion of chromium usually at, or near grain boundaries, and can be avoided by reducing the carbon content or through the use of strong carbide formers such as niobium and titanium, which act preferentially over chromium to combine with carbon in the form of NbC/TiC.

8.1.3 Effects of Minor Element Additions

Elemental additions to pure metals are essential for achieving the required properties of engineering materials. Boiler tubes operate at high temperatures and pressures, and are subject to corrosive environments therefore alloying additions are chosen that improve high temperature strength and corrosion resistance. The following is a summary of the effect common alloying elements have on boiler tube steels.

8.1.3.1 Carbon

Carbon is often found in alloys at around 0.10 wt.% for ferritic and martensitic steels and around 0.08 wt.% for austenitics. Low carbon content prevents sensitisation of the alloy during welding. Interstitial carbon atoms strengthen the steel via solid solution strengthening and excess carbon precipitates out

in the form of Fe_3C cementite strengthening the alloy via precipitation hardening. Each of these methods restrains the movement of dislocations through the lattice, increasing the creep and room temperature strength.

8.1.3.2 Nitrogen

Nitrogen is an austenite stabiliser and contributes to tensile strength through solid solution strengthening. Over long periods of service however, nitrogen may precipitate out of the austenite matrix reducing this effect. Nitrogen is more soluble than carbon so its contribution to sensitisation is limited. The addition of nitrogen reduces the onset of carbide precipitation [167]. Nitrogen forms carbonitride precipitates particularly with vanadium that improve the creep strength of the material.

8.1.3.3 Nickel

Nickel is the major element responsible for stabilising the austenitic phase to room temperature. In stainless steel, where 18 wt.% chromium is added for corrosion resistance, nickel is added at around 8 wt.%, the minimum required to retain the austenite phase. These alloys are known as the popular 18Cr8Ni series of austenitic steels. In other, high strength steels nickel may be found at up to 35 wt.%.

8.1.3.4 Chromium

Chromium is the major element offering oxidation protection to boiler tube steels [15]. Chromium forms a single oxide, chromia (Cr_2O_3), and offers the greatest level of oxidation protection up to around 900 °C, above which, the volatilisation of chromium species renders the level of protection provided by chromia inferior to that of alumina. Alumina, a highly protective oxide, grows too slowly at low temperatures to offer a fully protective oxide film. When present in high enough concentrations, chromium forms a thin, slow growing layer of dense, highly stoichiometric Cr_2O_3 oxide. Steels that are able to form a base layer of Cr_2O_3 usually oxidise with parabolic kinetics, whereas those with too low a chromium concentration exhibit a more linear regime. Chromium reduces the size of the austenitic phase field. In austenitic steels, chromium may form complex carbides of the composition $Cr_{23}C_6$, often along grain boundaries where carbon and chromium diffusion is fastest. The detrimental effect of this precipitate is one of martensitic transformation in the affected area and reduced oxidation resistance, as the area surrounding the precipitate will be depleted of chromium [167]. In order to minimise chromium carbide precipitation and increase creep strength, stronger carbide formers such as niobium and vanadium are added in small concentrations.

8.1.3.5 Manganese

Manganese, along with nickel is an important austenite stabilising element and in some alloys is used to ensure an austenitic structure to room temperature. This also helps in the formation of martensite where the rate of cooling required for martensitic transformation is reduced allowing the steel to be quenched in oil or air instead of water. The formation of manganese sulphides aid machinability and reduce formation of iron sulphides which cause cracking during steel fabrication. Manganese content is often balanced with carbon content to strengthen and harden an alloy and can be used to promote pearlite formation as an alternative to increasing the carbon content which may have an adverse effect on weldability. Manganese also increases strength through solid solution and grain refinement effects, as with aluminium [165]. Regarding the effects on oxidation of alloys, manganese appears to be detrimental in the formation of a protective oxide layer [149]. Manganese tends to diffuse through protective Cr_2O_3 to form the spinels $MnCr_2O_3$ or Mn_2CrO_4 at the surface [168, 169]. In steels that form a duplex iron-rich outer/spinel inner layer oxide, Mn can be found throughout the spinel layer [170] and within the chromium rich base layer [52].

8.1.3.6 Niobium

Niobium (along with vanadium and titanium) forms stable carbides at low concentrations (typically less than 0.1 wt.%) which reduce dislocation movement and therefore increase creep strength. This property is also used as a grain refiner, locking austenite grain boundaries and allowing finer ferrite grain sizes to be achieved on transformation from austenite[165].

8.1.3.7 Molybdenum

Molybdenum is added to ferritic steels with chromium to allow operation above 500 °C, improving the strength and oxidation resistance of plain carbon steels. Initially commercial products such as T11 were replaced with T22, then martensitic T9 each with higher quantities of chromium and molybdenum. From T9, T91 was developed with 9Cr1Mo and is currently one of the most widely used materials in boilers. Molybdenum additions contribute to solid solution strengthening and one researcher has found that substituting an amount of Mo for W can increase the creep strength of the alloy by up to 30%, albeit at the expense of oxidation resistance [3]. This alloy, designated P92 can be used, from a creep perspective up to 593 °C, from 565 °C of T91. The replacement of Mo by W also reduces the cost of the alloy [11].

8.1.3.8 Copper

Copper was historically added to austenitic steels to prevent corrosion in sulphuric acid environments [167]. Copper increases strength without decreasing toughness. In an effort to increase the creep strength of alloys used in high temperature areas of plant, Super 304H was developed. The "Super" refers to the addition of copper to 304H, which increases the creep strength via precipitation of a copper rich phase [132]. The copper rich phase primarily precipitates within grains and contributes the largest volume fraction of precipitates present in Super 304H [1]. Tensile strength is also improved with adjusted amounts of carbon, nitrogen and niobium allowing the alloy to be suitable for service temperatures of up to 650 °C. Calculations have shown that the addition of only 1 wt.% copper would be insufficient to form the strengthening precipitate at 650 °C in Super 304H. However, to remain coherent with the austenite matrix, the copper rich precipitates should not be larger than 30nm diameter, for this reason a maximum of 3 wt.% copper to used [132]. Aging tests performed on Super 304H at 650 °C [1] have revealed copper rich phase precipitates to grow from 1.5 nm in radius after 1 hour of treatment to 35 nm after 10000 hours while remaining coherent with the austenite matrix throughout aging. There is little research into the effects of copper on the oxidation of steel, although the high thermal stability of the element would suggest any concentrations to be in metallic form at the temperatures reached in service.

8.1.3.9 Silicon

Silicon forms the thermodynamically stable oxide silica, SiO_2, which tends to form subscales between the substrate and Cr_2O_3 layer. A thin, continuous film offers the most effective protection, however, incomplete layers formed from additions of as little as 0.05 wt.% have been shown to decrease the oxidation rate of a Co-25Cr alloy [171]. The work of Henry et al. [48] reported a delay in the onset of breakaway oxidation on 15Cr steels as the silicon concentration was increased up to 1 wt.%. Evans et al. [172] and Lobb et al. [173] reported the influence of between 0-2.25 wt.% silicon on the oxidation of 20Cr25NiNb steels in CO_2 atmospheres and found scale growth to be a minimum of between 0.5 & 1.0 wt.% Si at 850 °C and 900 °C, respectively. This is in contrast to the work of Kumar and Douglas [174], who found a silicon concentration of 4 wt.% in a Fe14Cr14Ni steel was required to reduce the oxide growth rate, when compared to lower silicon concentrations. Increased silicon content has been found, however, to correlate to increased scale spallation [172, 173], reported for work undertaken on 20Cr25NiNb steels [173], to be the result of a change in the mode of spallation, from a buckling regime to a wedging one, due to increased thickness of the silica interlayer. Mechanisms of spallation will be discussed in detail in section 2.4.

8.1.4 Diffusion

The process of a species diffusing down a concentration gradient is described by Fick's first law of diffusion

$$J = -D\frac{dc}{dx} \qquad \textit{(8-1)}$$

Where J is the flux of the diffusing species, c is the concentration of the species in the system and D is the diffusion coefficient. Fick's first law applies to both liquids and solids.

For crystalline solids bulk diffusion can occur via two mechanisms. Interstitial diffusion (e.g. H, C, O and N) occurs at a faster rate than vacancy diffusion (e.g. Mg, Ni, Cr, Cu), which requires a vacancy to be present adjacent to the diffusing atom. Vacancy diffusion is the most common mechanism in bulk solids but diffusion may be increased by the presence of dislocations or grain boundaries which act as fast diffusion paths for atoms. A grain boundary acts as a channel of approximately two atom widths and a dislocation core a wire of $(2b)^2$ cross-section where b is the atom size, through which diffusion can be as much as 10^6 times greater than in the bulk lattice. The contribution to overall diffusion of coarse depends on the volume fraction of grain boundaries and dislocations.

8.1.5 Thermodynamics

The general equation for the oxidation of a pure metal is

$$aM + \frac{b}{2}O_2 \rightarrow M_aO_b \qquad \textit{(8-2)}$$

Whether or not a reaction occurs is determined by the second law of thermodynamics, which states that in any cyclic process the entropy will either stay the same or decrease. The second law may be written in terms of the Gibbs free energy

$$G = H - TS \qquad \textit{(8-3)}$$

The change in Gibbs free energy can be thought of as the driving force for a reaction. The entropy *S*, of a reaction must overcome the enthalpy *H*, the heat energy of the system, at a given temperature *T*, for a reaction to take place. Therefore if the Gibbs free energy change $\Delta G < 0$, a spontaneous reaction

is expected. If $\Delta G > 0$, a reaction is thermodynamically impossible, and if $\Delta G = 0$, the reaction is in equilibrium.

For a reaction between a pure metal and oxygen (1-a), ΔG is expressed as

$$\Delta G = \Delta G^0 + RT \ln\left(\frac{a_{M_aO_b}}{a_M^a a_{O_2}^{b/2}}\right) \qquad \textbf{(8-4)}$$

Where ΔG^0 is the free energy change when all species are present in their standard states, *R* is the molar gas constant and $a_x = \frac{p_x}{p_x^\circ}$ is the thermodynamic activity, which describes the deviation from the standard state of a given species, where p_x is the vapour pressure over a condensed species or the partial pressure over a gaseous species and p_x° the same quantity corresponding to the standard state of *x* [17]. In a closed system the reaction will proceed down a concentration gradient as the concentration of reactants decreases until equilibrium is reached at $\Delta G = 0$. ΔG^0 can then be expressed as

$$\Delta G^0 = -RT \ln\left(\frac{a_{M_aO_b}}{a_M^a a_{O_2}^{b/2}}\right)_{equilibrium} = -RT \ln K_p \qquad \textbf{(8-5)}$$

where K_p is the reaction's equilibrium constant at constant pressure. K_p is useful for determining the standard free energy change for different reactions and is related to the partial pressure of the reacting gas as follows

$$K_p = \frac{a_{M_aO_b}}{a_M^a a_{O_2}^{b/2}} \qquad \textbf{(8-6)}$$

For a metal/oxygen reaction this can be written

$$K_p = \frac{1}{P_{O_2}^{b/2}} \qquad \textbf{(8-7)}$$

because the bulk activities of metal and oxide can be taken as unity. The equilibrium oxygen partial pressure can then be written in terms of the Gibbs free energy

$$P_{O_2}^{b/2} = exp\frac{\Delta G^0}{RT} \quad \textit{(8-8)}$$

The equilibrium partial pressure, also known as the dissociation pressure, is the oxygen partial pressure below which an oxide will be reduced to its metal. In a closed system this reaction will continue until either all oxide has been reduced to metal or the oxygen partial pressure has increased to equilibrium.

8.1.5.1 The Ellingham Diagram

The Ellingham diagram plots Gibbs free energy against temperature for reactions often involving metal and its oxide. The diagram is useful for determining the feasibility of a metal oxidising and comparing the stabilities of different metal oxides. For a given reaction the standard Gibbs free energy change is

$$\Delta G^0 = \Delta H^0 - T\Delta S^0 \quad \textit{(8-9)}$$

Where ΔH^0 and ΔS^0 are approximately constant with temperature. ΔG^0 plotted against temperature then gives the line representative of the reaction between the reacting species. Reactions between metals and their oxides usually involve the elimination of the gas phase and since gases have higher entropy than liquids and solids ΔS for the reaction is negative. This drives ΔG^0 higher (ie. less negative) for increasing T and so the slope of most metal/oxide reactions is positive. The standard entropy of the reaction dictates the gradient of the line

$$\frac{\partial \Delta G^0}{\partial T} = -\Delta S^0 \quad \textit{(8-10)}$$

and the intercept at 0 K gives the standard enthalpy change of the reaction

$$\Delta G^0|_{0\,K} = \Delta H^0 \quad \textit{(8-11)}$$

A lower standard enthalpy of reaction relates to a lower Gibbs free energy of reaction and a higher driving force for the oxidation of a metal to its oxide. Generally, this means that the further down the Ellingham diagram a metal/oxide reaction is - the more stable its oxide. As can be seen in Figure 8.3, the protective engineering oxides Cr_2O_3, Al_2O_3 and SiO_2 are low down in the figure. Positioning on the Ellingham diagram does not dictate growth rate of an oxide however, other factors such as defect structure influence the growth rate of an oxide. For example, titanium oxide has a much higher rate of growth than silicon oxide yet is further down in the diagram.

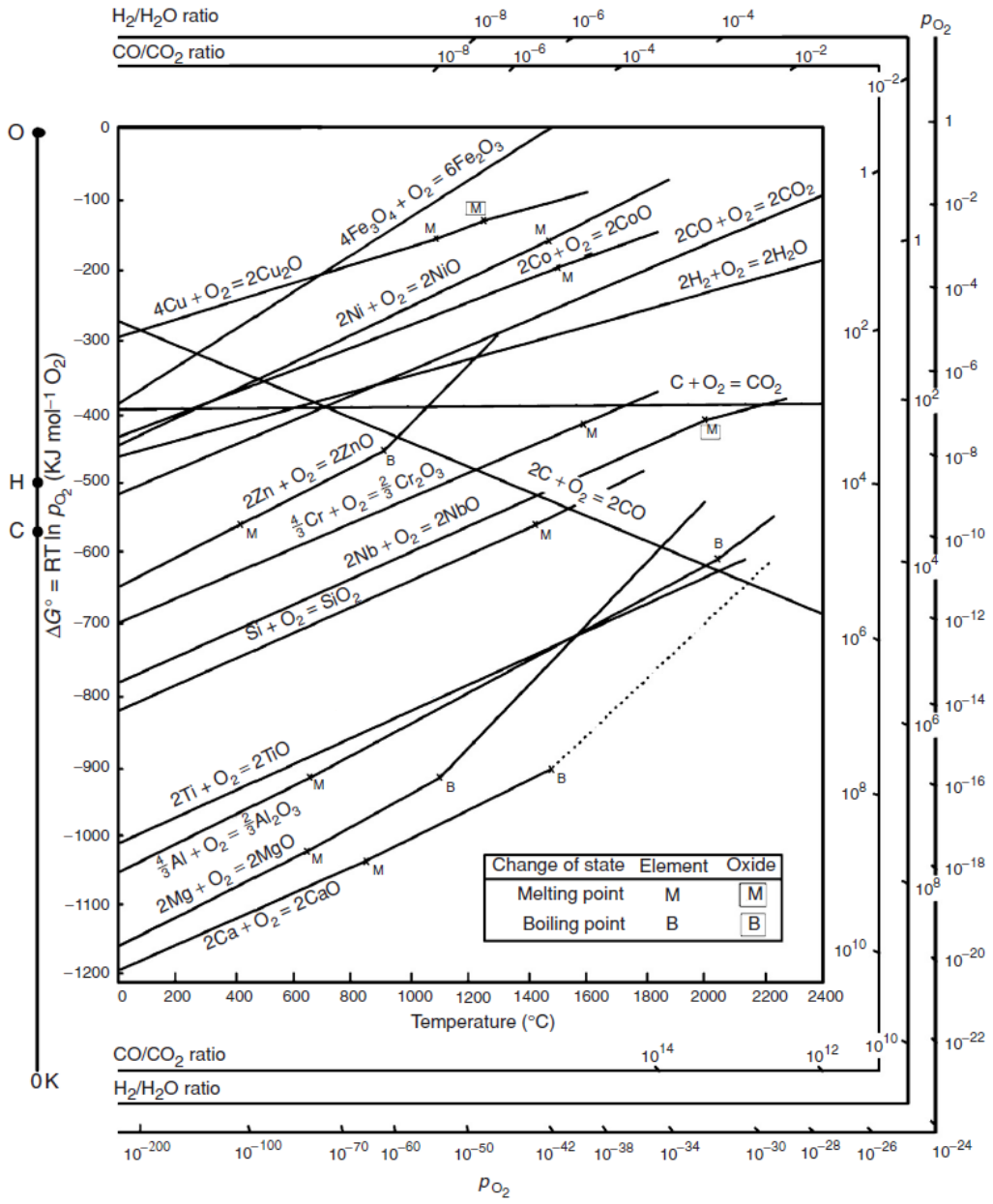

Figure 8.3 – Standard free energy of formation of oxides as a function of temperature [17].

The dissociation pressure of each metal/oxide system can be read by connecting a line between the "O" point on the left hand side of the Ellingham diagram to the point on the reaction line of interesting at the required temperature. The dissociation pressure can be read from the where the line crosses the pO_2 scale to the right of the Ellingham diagram. Similarly, equilibrium pressure ratios can be read for CO/CO_2 and H_2/H_2O if the carrier gas is not oxygen.

8.1.6 Mechanisms of Oxidation

During its service life the vast majority of the oxidation of a component will be most likely be governed by the factors affecting the diffusion of cationic and anionic species through existing scale, be it a thick

scale resulting from many hours of high temperature service or a very thin scale grown in the hours proceeding the manufacture of the component. In its simplest form the equation describing the oxidation of a metal gives little in way of explanation of how it may proceed and a variety of mechanisms exist which vary with alloy composition, oxidising environment, surface condition and alloy microstructure.

$$aM + \frac{b}{2}O_2 \rightarrow M_aO_b \qquad \textit{(8-12)}$$

The following section explores the factors that govern the oxidation of metal from initial adsorption of oxygen to diffusion controlled oxidation in air and steam.

8.1.6.1 Initial Oxidation of Metals

Although the first phase of oxidation of a component whose service life may exceed 100,000 hours may be relatively short lived it is still essential to understand how it proceeds.

The initial oxidation step involves the adsorption of gas on the metal surface, and as shown in the previous chapter this must be associated with a decrease in free energy. Two types of adsorption are possible. Physical adsorption (physisorption) involves the gas binding to the surface of the metal via van der Vaals forces whereas the chemical adsorption (chemisorption) of gas to the metal surface involves a chemical reaction requiring the transfer of electrons. The two processes differ in that, along with the method of binding, physisorption may occur on any surface and with little required activation energy and therefore is often found at low temperatures. Chemisorption on the other hand generally occurs at high temperatures and has a higher associated activation energy. For this reason chemisorption generally occurs at high energy or “active” sites such as surface defects and holes and is influenced by crystal orientation at the metal surface. Chemisorption is considered to continue only until a single molecular layer of gas is formed on the metal surface [85] at which point oxide molecules begin to nucleate at essentially random sites across the surface. This itself continues until a thin continuous oxide layer has been formed on the surface. Given that this layer is dense, further oxidation may only proceed via solid state diffusion through the oxide layer.

8.1.6.2 Oxide Transport Mechanisms

Thermodynamics dictates the presence of defects in any solid of appreciable scale and the defect structure of a solid can be used to predict what oxidation mechanisms predominate. Defect structures can be split into two types: stoichiometric and non-stoichiometric. The most common defects found in stoichiometric solids are Schottky, where a vacancy on either the cation or anion sub-lattice is

complemented by a vacancy on the other lattice, and Frenkel, where a vacancy on either sub-lattice is complemented by the presence of an equivalent ion at an interstitial site. Complementary defects conserve the equivalence between cation and anion atoms as required to keep stoichiometry.

Bulk diffusion necessitates the presence of point defects, however, most compounds deviate from stoichiometry and are classed as semi-conductors. This can be facilitated, in the case of p-type semiconductors in the form of a metal deficit or excess of non-metal, where the charge carriers are electron holes. Likewise, n-type semiconductors exhibit a deficit of non-metal or an excess of metal and electrons are the charge carriers. It is important to note that an oxide will exhibit either positive or negative behaviour and this will dictate at which interface the oxide is formed. For p-type semi-conductors mobile cations will cause oxide growth at the scale/gas interface and for n-type semi-conductors mobile anions will cause oxide growth at the metal/scale interface as in Figure 8.4.

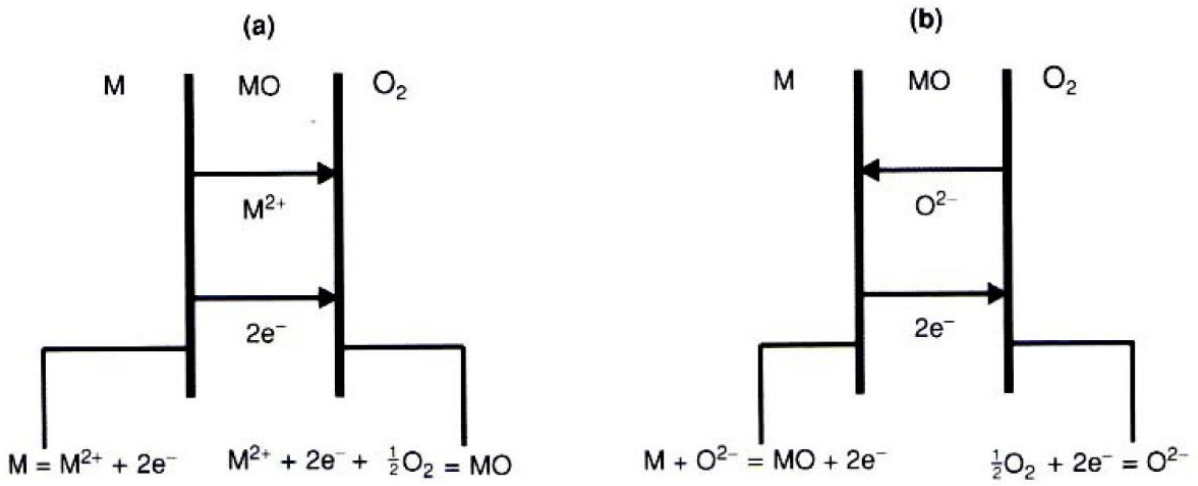

Figure 8.4 – Schematic of a) cation outward diffusion and b) anion inward diffusion across an oxide scale [17].

Line defects such as dislocations play an important role in diffusion controlled oxidation offering fast diffusion pathways for point defects. Surface defects such as twins, free surfaces (e.g. the surfaces of pores) and grain boundaries (facilitated by lattice mismatch between neighbouring grains) also allow for enhanced diffusion. Grain boundary diffusion has a smaller activation energy than lattice diffusion and becomes significant below the Tamman temperature (two-thirds of absolute melting point) [85], often predominating where oxidation takes place at lower temperatures. Grain boundary volume fraction has a large influence on overall diffusion rate and so usually predominates to a lower temperature in oxides where the grain boundary volume fraction is usually a lot higher than the substrate. With regards to the high temperature oxidation resistance, the most protective oxides (such

as α-Al_2O_3, Cr_2O_3 and SiO_2) are those with low concentrations and mobilities of defects such that diffusion is kept to a minimum [18].

8.1.7 Oxidation Kinetics

An alloy undergoing oxidation tends to follow, although not necessarily strictly, one, or more of the kinetic rate laws described below.

The linear rate law is typically relevant during the early stages of oxidation before the scale is at a thickness such that diffusion through the scale becomes the rate determining step [17]. It can be described by the following equation

$$\xi = k_1 t \qquad \textit{(8-13)}$$

where ξ is the scale thickness [m], k_1 represents the linear rate constant [ms^{-1}] and t is the time [s]. Other mechanisms such as breakaway oxidation may take the form of a linear, or near linear rate, along with oxidation at very high temperatures.

At low temperatures typically up to 400 °C an initial rapid reaction that quickly reduces to a low rate has been found to conform to logarithmic rate laws as

$$\xi = k_{log} \log(t + t_0) + A \quad \text{(direct log law)} \qquad \textit{(8-14)}$$

$$1/\xi = B - k_{i1} log t \quad \text{(inverse log law)} \qquad \textit{(8-15)}$$

where A, B, k_{i1}, t_0 and k_{log} are constants at constant temperature [85]. As the processes that conform to logarithmic regimes are usually reactions with a clean metal surface and very early stages of oxidation, difficulties can arise when attempting to measure oxidation rates in this period. Logarithmic kinetics is often superseded by an alternative regime by the time the sample has been heated to testing temperature. To retain a clean metal service to testing temperature, the sample may be heated in an ultra-high vacuum vessel prior to the oxidant being released into the chamber.

For dense, adherent oxides, after the formation of a continuous oxide film, the rate determining step will change to diffusion through the oxide of either the metal or oxygen. Many metals oxidised at high temperature will then follow parabolic kinetics as dictated by

$$\xi^2 = k_p t + c \qquad \textit{(8-16)}$$

where k_p is the parabolic rate constant [m^2s^{-1}] and the y-intercept, c, denotes oxide thickness [m^2] at $t = 0$. Equation (8-16) is often forced through the origin on the assumption that oxidation begins with a clean metal surface. This is a reasonable assumption for engineering alloys that grow thick scales over long oxidation periods. If oxide growth is measured by mass gain the above equation takes the form of

$$\left(\frac{\Delta M}{A}\right)^2 = k_p' t + c \qquad \textbf{(8-17)}$$

where ΔM is the mass change [$mg.cm^{-2}$] and A is the surface area of the oxidation sample [cm^{-2}].

The parabolic rate equation is valid, according to Wagner if the following conditions are satisfied (after [15]):

1) The oxide layer is a compact, perfectly adherent scale.
2) Migration of ions or electrons across the scale is the rate-controlling process.
3) Thermodynamic equilibrium is established at both the metal-scale and scale-gas interfaces.
4) The oxide scale shows only small deviations from stoichiometry and, hence, the ionic fluxes are independent of position within the scale.
5) Thermodynamic equilibrium is established locally throughout the scale.
6) The scale is thick compared with the distances over which space charge effects (electrical double layer) occur.
7) Oxygen solubility in the metal may be neglected.

Wagner's theory of parabolic oxidation deviates from earlier theories in that oxide growth is assumed to occur by the transport of ions and electrons, instead of neutral atoms as assumed by the Tammann-Pilling-Bedworth parabolic law [98]. The free energy change associated with the formation of the oxide from its constitute elements is the driving force for the reaction, and activity gradients for both the metal and non-metal are established across the scale facilitating ion migration. The diffusion coefficients of the cations, anions and electrons are different causing a separation of charge across the scale, which itself creates an electric field across the scale facilitating the transport of electrons to keep charge neutrality. The flux of ions across the scale is proportional to the growth of the scale according to Fick's first law, taking into account diffusion due to both the chemical potential, μ, and the electrical potential, ϕ

$$J_i = -\frac{c_i v_i}{z_i e}\left(\frac{d\mu_i}{d\xi} + z_i e \frac{d\phi}{d\xi}\right) \qquad \textbf{(8-18)}$$

where $d\mu_i/d\xi$ is the chemical potential gradient, $d\phi/d\xi$ is the electric field strength, e is the electric charge, z_i is the valency of the particle, c_i is the particle concentration and v_i is the mobility of the particles [85].

Often, oxidation kinetics deviate from idealised parabolic behaviour, and may even change rate during the oxidation period. Where a single power law regime is followed, the oxidation rate can be determined using

$$\xi^n = k_n t \qquad \textbf{(8-19)}$$

where n denotes the order of the reaction. An order higher than 2 indicates sub-parabolic behaviour, whereas an order lower than 2 indicates a more linear regime.

Isothermal oxidation of engineering alloys, which tend to follow the power law kinetics of equation (2-20) may also experience a change in rate limiting process during the oxidation period. To determine whether this is the case, the log of equation (2-20) can be taken to reach:

$$\ln \xi = \ln k_n + \frac{1}{n} \ln t \qquad \textbf{(8-20)}$$

Plotted on Cartesian axes in the form of $y = mx + c$, the gradient, m, gives the reciprocal of the order of reaction, n. If experimental data fit a linear regression with high confidence over the entire oxidation period, then the oxidation behaviour can be described as following a single kinetic regime. However, if a change in gradient is observed, the oxidation behaviour may be modelled more accurately by two or more rate equations, each valid over a defined time period. The rate constant, k_n, for each kinetic regime can be derived from the y-axis intercept, $\ln k_n$.

Many metals oxidised at high temperature will follow parabolic kinetics as outlined by the line OAD in Figure 8.5 [175]. The rate limiting factor is the diffusion of the element responsible for forming a protective oxide. For stainless steel this is the diffusion of chromium through the oxide layer. Breakaway oxidation (or chemical failure) occurs when the oxidation rate increases and propagates at a rate faster than the tangential parabolic rate at the time breakaway occurs [85], as shown by the line OAE. In the case of mechanical chemical failure the cause of this is often cracking or spallation of the oxide layer exposing the bare metal surface to oxygen. Selective oxidation of chromium depletes

the underlying alloy of the element prohibiting the immediate reformation of a protective oxide [57, 176]. The rate limiting factor then becomes the diffusion of oxygen into the metal and internal oxidation will occur. Oxidation at the faster rate will continue until the concentration of chromium in the alloy subjacent to the oxidation front is high enough to reform a protective scale and return the system to parabolic kinetics (line ABC). This may occur when the oxidation front reaches an internal grain boundary where chromium diffusion is sufficient to grow a protective film. Breakaway oxidation of this kind is problematic for boiler tubes that are subject to cyclic oxidation as thermal stresses often cause spallation of the oxide layer formed.

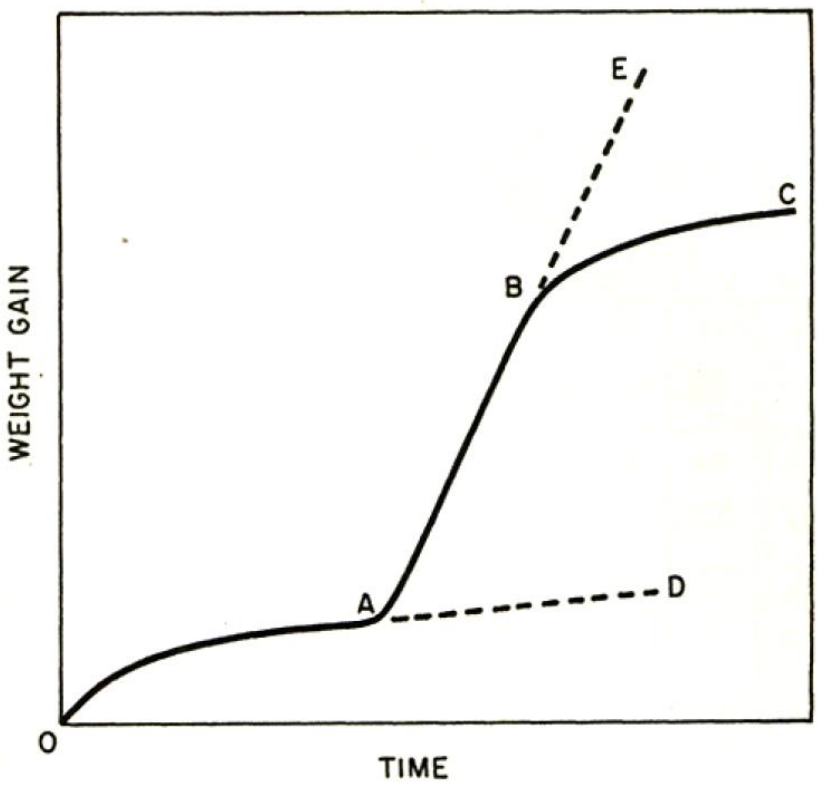

Figure 8.5 – Illustration of oxidation rates followed by a metal undergoing breakaway oxidation. After [175].

On alloys that grow oxides in tension, ie. those whose Pilling-Bedworth ratio is less than unity, through-scale cracking, initiated after a critical oxide thickness has been reached may cause breakaway oxidation. In these cases the faster rate is expected to continue assuming the initiation and propagation of new cracks until the oxide is rebuilt to a new critical thickness, after which the process repeats itself cycling the line ABC in Figure 8.5 [85]. This type of breakaway, where the concentration of protective element at the metal/oxide interface becomes less than that required to form more protective oxide is termed intrinsic chemical failure and is also found to occur on alloys whose oxide

grows in compression, typically at very high temperatures [176]. Other researchers have reported the presence of water vapour to accelerate the onset of breakaway oxidation [38, 88].

8.2 Appendix B – Thermal Expansion Coefficient Calculations

The following equations were integrated and used to calculate the average thermal expansion coefficients of 347HFG alloy, magnetite, and haematite between the oxidation temperature and T_c (for a spallation event) or 25 °C (for a non-spallation event):

347HFG

25 °C to 700 °C:

$$\alpha_m = 0.007625T + 16.045675$$

Magnetite

25 °C to 530 °C:

$$\alpha_{mag} = 2.052 \times 10^{-14}T^6 - 2.931 \times 10^{-11}T^5 + 1.644 \times 10^{-8}T^4 - 4.529 \times 10^{-6}T^3$$

$$+6.189 \times 10^{-4}T^2 - 2.600 \times 10^{-2}T + 11.33$$

530 °C to 593 °C:

$$\alpha_{mag} = 5.30154700 \times 10^{-5}T^3 - 9.43045372 \times 10^{-2}T^2 + 55.6797407T - 10889.5031$$

593 °C to 700 °C:

$$\alpha_{mag} = -8.209 \times 10^{-7}T^3 + 2.281 \times 10^{-3}T^2 - 2.006T + 580.3$$

Haematite

25 °C to 700 °C:

$$\alpha_{hae} = 0.0032958479T + 10.82822187$$

8.3 Appendix C – Sample Cooling Curve

In order to accurately calculate the critical stress to spallation and strain energy within a particular oxide layer the temperature at which spallation occurs must be known. Because of the complexity of attaching a thermocouple to each sample surface, and unreliability of an infrared method, a cooling profile for a single sample of 347HFG was recorded and used as reference for oxidation tests. For most oxidation tests, the time after removal from the furnace to spallation was recorded and the corresponding inner surface temperature can be extracted from Figure 8.6. Table 8.1 lists a number of minutes after removal from furnace and corresponding inner surface temperatures.

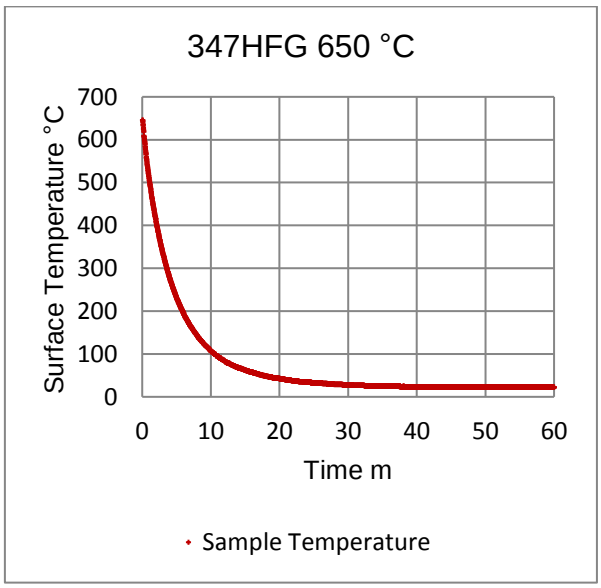

Figure 8.6 – Cooling profile for 347HFG from oxidation temperature of 650 °C.

Table 8.1 – Surface temperature values as a function of time for 347HFG sample removed from furnace at 650 °C.

Time (mins)	Surface Temperature (°C)	ΔT from 650 °C (°C)
2	410	240
4	275	375
6	195	455
8	143	507
10	107	543
15	62	588
34	25	625
55	22	628

Chapter 9 References

1. Chi, C., H. Yu, and X. Xie, *Advanced Austenitic Heat-Resistant Steels for Ultra-Super-Critical (USC) Fossil Power Plants*, in *Alloy Steel - Properties and Use*, E.V. Morales, Editor. 2011, InTech: Shanghai. p. 270.
2. Zhang, Z., Z. Hu, H.Y. Tu, S. Schmauder, and G. Wu, *Microstructure evolution in HR3C austenitic steel during long-term creep at 650°C.* Materials Science and Engineering: A, 2016. **681**: p. 74-84.
3. Mogire, E.O., R.L. Higginson, A.T. Fry, and R.C. Thomson, *Microstructural characterization of oxide scales formed on steels P91 and P92.* Materials at High Temperatures, 2011. **28**(4): p. 361-368.
4. Masuyama, F., *New Developments in Steels for Power Generation Boilers*, in *Advanced Heat Resistant Steels for Power Generation*, R. Viswanathan and J. Nutting, Editors. 1999, IOM Communication Ltd. p. 33-48.
5. Antoni, L., *Comparison of the Cyclic-oxidation Behavior Between AISI 304 and Low-nickel Austenitic Stainless Steels*, in *High Temperature Corrosion and Protection of Materials 5, Pts 1 and 2*, R. Streiff, et al., Editors. 2001, Trans Tech Publications Ltd: Zurich-Uetikon. p. 345-352.
6. Husemann, R.U. *Advanced (700°C) PF Power Plant: A Clean Coal European Technology*. in *CESI Auditorium*. 2005. Milano, Italy: Babcock – Hitachi Europe.
7. Osgerby, S. *Materials R&D Requirements for Fossil Fuelled Steam Plant*. in *Energy Materials – Meeting the Challenge*. 2008. Loughborough, UK.
8. Viswanathan, R., J.F. Henry, J. Tanzosh, G. Stanko, J. Shingledecker, B. Vitalis, and R. Purgert, *US program on materials technology for ultra-supercritical coal power plants.* Journal of Materials Engineering and Performance, 2005. **14**(3): p. 281-292.
9. Powell, C.A. and B.D. Morreale, *Materials challenges in advanced coal conversion technologies.* MRS Bulletin, 2008. **33**(4): p. 309-315.
10. Teir, S. and A. Kulla, *Steam Boiler Technology*. 2002, Helsinki University of Technology Department of Mechanical Engineering.
11. Viswanathan, R. and W. Bakker, *Materials for ultrasupercritical coal power plants-boiler materials: Part 1.* Journal of Materials Engineering and Performance, 2001. **10**(1): p. 81-95.
12. *Steam: Its Generation and Use*. 41st ed. 2005, The Babcock & Wilcox Company, Barberton, Ohio, U.S.A.: The Babcock & Wilcox Company.
13. Cengel, Y.A. and M.A. Boles, *Thermodynamics: An Engineering Approach*. 5th ed. 2006: McGraw-Hill.
14. *Power Plant Life Management and Performance Improvement* 2011, Cambridge: Woodhead Publishing Limited.
15. Birks , N., G.H. Meier, and F.S. Pettit, *Oxidation of Other Selected Alloys*, in *Introduction to the High-Temperature Oxidation of Metals*. 2006, Cambridge University Press: New York. p. 127.
16. Engell, H.J., *The concentration gradient of iron-ion-vacancies in wüstite scaling films and the mechanism of oxidation of iron.* Acta Metallurgica, 1958. **6**(6): p. 439-445.

17. Birks , N., G.H. Meier, and F.S. Pettit, *Introduction to the High-Temperature Oxidation of Metals*. 2nd ed. 2006, New York: Cambridge University Press.
18. Stott, F.H., *The protective action of oxide scales in gaseous environments at high-temperature.* Reports on Progress in Physics, 1987. **50**(7): p. 861-913.
19. Caplan, D., A. Harvey, and M. Cohen, *Oxidation of chromium at 890–1200°C.* Corrosion Science, 1963. **3**(3): p. 161-175.
20. Gulbransen, E.A. and K.F. Andrew, *Kinetics of the oxidation of chromium.* Journal of the Electrochemical Society, 1957. **104**(6): p. 334-338.
21. Tedmon, C.S., *The effect of oxide volatilization on the oxidation kinetics of Cr and Fe‐Cr alloys.* Journal of the Electrochemical Society, 1966. **113**(8): p. 766-768.
22. Mougin, J., G. Lucazeau, A. Galerie, and M. Dupeux, *Influence of cooling rate and initial surface roughness on the residual stresses in chromia scales thermally grown on pure chromium.* Materials Science and Engineering: A, 2001. **308**(1–2): p. 118-123.
23. Jacob, Y.P., H. Buscail, E. Caudron, R. Cueff, M.F. Stroosnijder, and V.A.C. Haanappel, *Influence of cycling frequency on the adherence of chromia scales formed on pure chromium at high temperature.* Materials Chemistry and Physics, 2003. **77**(2): p. 442-446.
24. Atkinson, A., *Wagner theory and short circuit diffusion.* Materials Science and Technology, 1988. **4**(12): p. 1046-1051.
25. Heuer, A.H., D.B. Hovis, J.L. Smialek, and B. Gleeson, *Alumina scale formation: A new perspective.* Journal of the American Ceramic Society, 2011. **94**: p. 146-153.
26. Quadakkers, W.J., A. Elschner, W. Speier, and H. Nickel, *Composition and growth mechanisms of alumina scales on FeCrAl-based alloys determined by SNMS.* Applied Surface Science, 1991. **52**(4): p. 271-287.
27. Matsuo, H., Y. Nishiyama, and Y. Yamadera, *Steam Oxidation Property of Fine-Grain Steels*, in *Advances in Materials Technology for Fossil Power Plants*, R. Viswanathan, D. Gandy, and K. Coleman, Editors. 2004, ASM International: Hilton Head Island, South Carolina. p. 441-450.
28. Kim, J.H., D.I. Kim, S. Suwas, E. Fleury, and K.W. Yi, *Grain-size effects on the high-temperature oxidation of modified 304 austenitic stainless steel.* Oxidation of Metals, 2013. **79**(3-4): p. 239-247.
29. Kim, J.-H., B.K. Kim, D.-I. Kim, P.-P. Choi, D. Raabe, and K.-W. Yi, *The role of grain boundaries in the initial oxidation behavior of austenitic stainless steel containing alloyed Cu at 700°C for advanced thermal power plant applications.* Corrosion Science, 2015. **96**: p. 52-66.
30. Trindade, V.B., U. Krupp, P.E.-G. Wagenhuber, and H.-J. Christ, *Oxidation mechanisms of Cr-containing steels and Ni-base alloys at high-temperatures - Part I: The different role of alloy grain boundaries.* Materials and Corrosion, 2005. **56**(11): p. 785-790.
31. Holcomb, G.R., *Ultra Supercritical Steam Corrosion*. 2004, Albany Research Center: Albany Research Center, U. S. Department of Energy.
32. Nakagawa, K., Y. Matsunaga, and T. Yanagisawa, *Corrosion behavior of ferritic steels on the air sides of boiler tubes in a steam/air dual environment.* Materials at High Temperatures, 2001. **18**(1): p. 51-56.
33. Wood, G.C., *The oxidation of iron-chromium alloys and stainless steels at high temperatures.* Corrosion Science, 1962. **2**(3): p. 173-196.
34. Wright, I.G., P.F. Tortorelli, M. Schuetze, and R.B. Dooley, *Program on technology innovation: oxide growth and exfoliation on alloys exposed to steam*. 2007, EPRI.
35. Yue, Z., M. Fu, X. Wang, and X. Li, *Effect of shot peening on the oxidation resistance of TP304H and HR3C Steels in water vapor.* Oxidation of Metals, 2012. **77**(1-2): p. 17-26.
36. Naraparaju, R., H.J. Christ, F.U. Renner, and A. Kostka, *Dislocation engineering and its effect on the oxidation behaviour.* Materials at High Temperatures, 2012. **29**(2): p. 116-122.

37. Naraparaju, R., V.B. Trindade, H.J. Christ, and U. Krupp, *Effect of shot peening on high temperature oxidation behaviour of boiler steel: experimental results and simulation.* Corrosion Engineering Science and Technology, 2009. **44**(3): p. 211-217.
38. Peng, X., J. Yan, Y. Zhou, and F. Wang, *Effect of grain refinement on the resistance of 304 stainless steel to breakaway oxidation in wet air.* Acta Materialia, 2005. **53**(19): p. 5079-5088.
39. Yu, H., J.L. Dong, D.H. Yoo, K. Shin, J.S. Jung, Y. Pyoun, and I. Cho, *Effect of ultrasonic and air blast shot peening on the microstructural evolution and mechanical properties of SUS304.* Journal of the Korean Physical Society, 2009. **54**: p. 1161.
40. Zurek, J., M. Michalik, F. Schmitz, T.U. Kern, L. Singheiser, and W.J. Quadakkers, *The effect of water-vapor content and gas flow rate on the oxidation mechanism of a 10%Cr-Ferritic steel in Ar-H2O mixtures.* Oxidation of Metals, 2005. **63**(5-6): p. 401-422.
41. Ostwald, C. and H. Grabke, *Initial oxidation and chromium diffusion. I. Effects of surface working on 9–20% Cr steels.* Corrosion Science, 2004. **46**: p. 1113-1127.
42. Wright, I.G. and R.B. Dooley, *A review of the oxidation behaviour of structural alloys in steam.* International Materials Reviews, 2010. **55**(3): p. 129-167.
43. Allen, G.C., J.M. Dyke, S.J. Harris, and A. Morris, *A surface study of the oxidation of type 304L stainless steel at 600 K in air.* Oxidation of Metals, 1988. **29**(5): p. 391-408.
44. Botella, J., C. Merino, and E. Otero, *A comparison of the high-temperature oxidation of 17Cr-2Ni and 18Cr-8Ni austenitic stainless steels at 973 K.* Oxidation of Metals, 1998. **49**(3): p. 297-324.
45. Dudziak, T., M. Łukaszewicz, N. Simms, and J.R. Nicholls, *Steam oxidation of TP347HFG, Super 304H and HR3C – analysis of significance of steam flowrate and specimen surface finish.* Corrosion Engineering, Science and Technology, 2015. **50**(4): p. 272-282.
46. Jansson, S., W. Hübner, G. Östberg, and M.d. Pourbaix, *Oxidation resistance of some stainless steels and nickel-based alloys in high-temperature water and steam.* British Corrosion Journal, 1969. **4**(1): p. 21-31.
47. Hansson, A.N., J.H. Hattel, K.V. Dahl, and M.A.J. Somers, *Modelling Cr depletion under a growing Cr_2O_3 layer on austenitic stainless steel: the influence of grain boundary diffusion.* Modelling and Simulation in Materials Science and Engineering, 2009. **17**(3): p. 19.
48. Henry, S., A. Galerie, and L. Antoni, *Abnormal Oxidation of Stabilized Ferritic Stainless Steels in Water Vapor*, in *High Temperature Corrosion and Protection of Materials 5, Pts 1 and 2*, R. Streiff, et al., Editors. 2001. p. 353-360.
49. Lobb, R.C. and H.E. Evans, *An evaluation of the effect of surface chromium concentration on the oxidation of a stainless-steel.* Corrosion Science, 1983. **23**(1): p. 55-73.
50. Evans, H.E., D.A. Hilton, R.A. Holm, and S.J. Webster, *The development of localized pits during stainless steel oxidation.* Oxidation of Metals, 1980. **14**(3): p. 235-247.
51. Lobb, R.C. and H.E. Evans, *A determination of the chromium concentration for healing layer formation during the oxidation of chromium-depleted 20Cr-25Ni-Nb stainless-steel.* Corrosion Science, 1984. **24**(5): p. 385-396.
52. Tang, J.E., M. Halvarsson, H. Asteman, and J.E. Svensson, *Microstructure of oxidised 304L steel and the effects of surface roughness on oxidation behaviour*, in *High Temperature Corrosion and Protection of Materials 5, Pts 1 and 2*, R. Streiff, et al., Editors. 2001, Trans Tech Publications Ltd: Zurich-Uetikon. p. 205-214.
53. Záhumenský, P., S. Tuleja, J. Országová, J. Janovec, and V. Siládiová, *Corrosion resistance of 18Cr-12Ni-2,5Mo steelannealed at 500–1050°C.* Corrosion Science, 1999. **41**(7): p. 1305-1322.
54. Swaminathan, S., N.G. Krishna, and D.-I. Kim, *Characteristics of oxide scale formed on Cu-bearing austenitic stainless steel during early stages of high temperature oxidation.* Applied Surface Science, 2015. **353**: p. 29-39.

55. Osgerby, S. and J. Quadakkers. *The Influence of Laboratory Test Procedures on Scale Growth Kinetics and Microstructure During Steam Oxidation Testing*. in *Workshop on Scale Growth and Exfoliation in Steam Plant*. 2003. Teddington, England: Science & Technology Letters.
56. Asteman, H., J.E. Svensson, and L.G. Johansson, *Evidence for chromium evaporation influencing the oxidation of 304L: The effect of temperature and flow rate.* Oxidation of Metals, 2002. **57**(3-4): p. 193-216.
57. Asteman, H., J.E. Svensson, and L.G. Johansson, *Oxidation of 310 steel in H_2O/O_2 mixtures at 600°C: the effect of water-vapour-enhanced chromium evaporation.* Corrosion Science, 2002. **44**(11): p. 2635-2649.
58. Masuyama, F., *History of power plants and progress in heat resistant steels.* Isij International, 2001. **41**(6): p. 612-625.
59. Otsuka, N., Y. Shida, and H. Fujikawa, *Internal-external transition for the oxidation of Fe-Cr-Ni austenitic stainless steels in steam.* Oxidation of Metals, 1989. **32**(1-2): p. 13-45.
60. Taylor, M.P., H.E. Evans, S. Gray, and J.R. Nicholls, *A chromia forming thermal barrier coating system.* Materials and Corrosion, 2011. **62**(7): p. 668-673.
61. Hultquist, G., B. Tveten, and E. Hörnlund, *Hydrogen in chromium: Influence on the high-temperature oxidation kinetics in H_2O, oxide-growth mechanisms, and scale adherence.* Oxidation of Metals, 2000. **54**(1): p. 1-10.
62. Montgomery, M. and A. Karlsson, *Survey of oxidation in steamside conditions.* VGB Kraftwerkstechnik, 1995. **75**(3): p. 235-240.
63. Viswanathan, R., J. Sarver, and J.M. Tanzosh, *Boiler materials for ultra-supercritical coal power plants - steamside oxidation.* Journal of Materials Engineering and Performance, 2006. **15**(3): p. 255-274.
64. Atkinson, A., R.I. Taylor, and A.E. Hughes, *A quantitative demonstration of the grain boundary diffusion mechanism for the oxidation of metals.* Philosophical Magazine A, 1982. **45**(5): p. 823-833.
65. Griess, J.C. and W.A. Maxwell, *The long-term oxidation of selected alloys in superheated steam at 482 and 538°C*. 1981. p. 46.
66. Ericsson, T., *A study of the Cr-depleted surface layers formed on four Cr-Ni steels during oxidation in steam at 600°C and 800°C.* Oxidation of Metals, 1970. **2**(4): p. 401-417.
67. Smith, A.F., M.O. Tucker, and R. Hales, *The kinetics of duplex scale formation on 18/8 type stainless steel.* Oxidation of Metals, 1982. **17**(5): p. 329-343.
68. Otsuka, N. and H. Fujikawa, *Scaling of austenitic stainless steels and nickel-base alloys in high-temperature steam at 973K.* Corrosion, 1991. **47**(4): p. 240-248.
69. Hales, R., *The high temperature oxidation behaviour of austenitic stainless steels.* Materials and Corrosion, 1978. **29**(6): p. 393-399.
70. Karimi, N., F. Riffard, F. Rabaste, S. Perrier, R. Cueff, C. Issartel, and H. Buscail, *Characterization of the oxides formed at 1000° C on the AISI 304 stainless steel by x-ray diffraction and infrared spectroscopy.* Applied Surface Science, 2008. **254**(8): p. 2292-2299.
71. Huntz, A.M., A. Reckmann, C. Haut, C. Sévérac, M. Herbst, F.C.T. Resende, and A.C.S. Sabioni, *Oxidation of AISI 304 and AISI 439 stainless steels.* Materials Science and Engineering: A, 2007. **447**(1): p. 266-276.
72. Monceau, D. and B. Pieraggi, *Determination of parabolic rate constants from a local analysis of mass-gain curves.* Oxidation of Metals, 1998. **50**(5-6): p. 477-493.
73. Moulin, P., A.M. Huntz, and P. Lacombe, *Influence des phenomenes diffusionnels sur le mecanisme d'oxydation des alliages Ni ・ Cr.* Acta Metallurgica, 1980. **28**(6): p. 745-756.
74. Tempest, P.A. and R.K. Wild, *Formation and growth of spinel and Cr_2O_3 oxides on 20% Cr-25% Ni-Nb stainless steel in CO_2 environments.* Oxidation of Metals, 1985. **23**(3): p. 207-235.

75. Garrett, J.C.P., J.T. Crook, S.K. Lister, P.J. Nolan, and J.A. Twelves, *Factors in the oxidation assessment of AISI type 310 steels in high pressure carbon dioxide.* Corrosion Science, 1982. **22**(1): p. 37-50.
76. Lukaszewicz, M., N.J. Simms, T. Dudziak, and J.R. Nicholls, *Effect of steam flow rate and sample orientation on steam oxidation of ferritic and austenitic steels at 650 and 700°C.* Oxidation of Metals, 2013. **79**(5-6): p. 473-483.
77. Dudziak, T., M. Lukaszewicz, N.J. Simms, and J.R. Nicholls, *Impact specimen geometry on T23 and TP347HFG steels behaviour during steam oxidation at harsh conditions.* Corrosion Engineering, Science and Technology, 2017. **52**(1): p. 46-53.
78. Wood, G.C., T. Hodgkiess, and D.P. Whittle, *A comparison of the scaling behaviour of pure iron-chromium and nickel-chromium alloys in oxygen.* Corrosion Science, 1966. **6**(3-4): p. 129-147.
79. Tang, J.E., F. Liu, H. Asteman, J.E. Svensson, L.G. Johansson, and M. Halvarsson, *Investigation of FIB-thinned TEM cross-sections of oxide scales formed on type 310 steel at 600°C in water vapour-containing oxygen atmospheres.* Materials at High Temperatures, 2007. **24**(1): p. 27-55.
80. Hansson, A.N., K. Pantleon, F.B. Grumsen, and M.A.J. Somers, *Microstructure evolution during steam oxidation of a Nb stabilized austenitic stainless steel.* Oxidation of Metals, 2009. **73**(1-2): p. 289-309.
81. Tanabe, T. and S. Imoto, *Surface Oxidation of Type 316 Stainless Steel.* Transactions of the Japan Institute of Metals, 1979. **20**: p. 507-515.
82. Simms, H.G., *Oxidation behaviour of austenitic stainless steels at high temperature in supercritical plant*, in *Metallurgy and Materials*. 2011, University of Birmingham: Birmingham.
83. Tang, J.E., M. Halvarsson, H. Asteman, and J.E. Svensson, *The microstructure of the base oxide on 304L steel.* Micron, 2001. **32**(8): p. 799-805.
84. Kim, J.-H., D.-I. Kim, J.-H. Shim, and K.-W. Yi, *Investigation into the high temperature oxidation of Cu-bearing austenitic stainless steel using simultaneous electron backscatter diffraction-energy dispersive spectroscopy analysis.* Corrosion Science, 2013. **77**: p. 397-402.
85. Kofstad, P., *High-Temperature Oxidation Of Metals*. 1966, New York: John Wiley and Sons, Inc.
86. Fujii, C.T. and R.A. Meussner, *The mechanism of the high-temperature oxidation of iron-chromium alloys in water vapor.* Journal of the Electrochemical Society, 1964. **111**(11): p. 1215-1221.
87. Honda, K., T. Maruyama, T. Atake, and Y. Saito, *Oxidation behavior of sus430 stainless steel in moist atmospheres at 873 K.* Oxidation of Metals, 1992. **38**(5-6): p. 347-363.
88. Monteiro, M.J., S.R.J. Saunders, and F.C. Rizzo, *The effect of water vapour on the oxidation of high speed steel, kinetics and scale adhesion.* Oxidation of Metals, 2011. **75**(1-2): p. 57-76.
89. Ehlers, J., D.J. Young, E.J. Smaardijk, A.K. Tyagi, H.J. Penkalla, L. Singheiser, and W.J. Quadakkers, *Enhanced oxidation of the 9%Cr steel P91 in water vapour containing environments.* Corrosion Science, 2006. **48**(11): p. 3428-3454.
90. Schütze, M., D. Renusch, and M. Schorr, *Parameters determining the breakaway oxidation behaviour of ferritic martensitic 9%Cr steels in environments containing H_2O.* Corrosion Engineering, Science and Technology, 2004. **39**(2): p. 157-166.
91. Ikeda, Y. and K. Nii, *Microcrack generation and its healing in the oxide scale formed on Fe-Cr alloys.* Oxidation of Metals, 1978. **12**(6): p. 487-502.
92. Surman, P.L. and J.E. Castle, *Gas phase transport in the oxidation of Fe and steel.* Corrosion Science, 1969. **9**(10): p. 771-777.
93. Fry, A., S. Osgerby, and M. Wright, *Oxidation of Alloys in Steam Environments – A Review*, in *National Physical Laboratory report*. 2002: Teddington, UK.
94. Galerie, A., Y. Wouters, and M. Caillet. *The Kinetic Behaviour of Metals in Water Vapour at High Temperatures: Can General Rules be Proposed?* in *5th International Symposium on High Temperature Corrosion and Protection of Materials*. 2000. Les Embiez, France.

95. Davies, H. and A. Dinsdale, *Theoretical study of steam grown oxides as a function of temperature, pressure and p(O_2).* Materials at High Temperatures, 2005. **22**(1-2): p. 15-25.
96. Wright, I.G. and R.B. Dooley, *Morphologies of oxide growth and exfoliation in superheater and reheater tubing of steam boilers.* Materials at High Temperatures, 2011. **28**(1): p. 40-57.
97. Asteman, H., J.E. Svensson, L.G. Johansson, and M. Norell, *Indication of chromium oxide hydroxide evaporation during oxidation of 304L at 873 K in the presence of 10% water vapor.* Oxidation of Metals, 1999. **52**(1): p. 95-111.
98. Opila, E.J., D.L. Myers, N.S. Jacobson, I.M.B. Nielsen, D.F. Johnson, J.K. Olminsky, and M.D. Allendorf, *Theoretical and experimental investigation of the thermochemistry of $CrO_2(OH)_2$(g).* Journal of Physical Chemistry A, 2007. **111**(10): p. 1971-1980.
99. Asteman, H., J.E. Svensson, M. Norell, and L.G. Johansson, *Influence of water vapor and flow rate on the high-temperature oxidation of 304L; Effect of chromium oxide hydroxide evaporation.* Oxidation of Metals, 2000. **54**(1-2): p. 11-26.
100. Halvarsson, M., J.E. Tang, H. Asteman, J.E. Svensson, and L.G. Johansson, *Microstructural investigation of the breakdown of the protective oxide scale on a 304 steel in the presence of oxygen and water vapour at 600°C.* Corrosion Science, 2006. **48**(8): p. 2014-2035.
101. Lepingle, V., G. Louis, D. Petelot, B. Lefebvre, and J.C. Vaillant, *High Temperature Corrosion Behaviour of some Boiler Steels in Pure Water Vapour*, in *High Temperature Corrosion and Protection of Materials 5, Pts 1 and 2*, R. Streiff, et al., Editors. 2001, Trans Tech Publications Ltd: Zurich-Uetikon. p. 239-246.
102. Quadakkers, W.J., P.J. Ennis, J. Zurek, and M. Michalik, *Steam oxidation of ferritic steels – laboratory test kinetic data.* Materials at High Temperature, 2005. **22**: p. 47-60.
103. Shibli, A. and F. Starr, *Some aspects of plant and research experience in the use of new high strength martensitic steel P91.* International Journal of Pressure Vessels and Piping, 2007. **84**(1–2): p. 114-122.
104. Nishimura, N., N. Komai, Y. Hirayama, and F. Masuyama. *Japanese Experience with Steam Oxidation of Advanced Heat-resistant Steel Tubes in Power Boilers*. in *Workshop on Scale Growth and Exfoliation in Steam Plant*. 2003. Teddington, England: Science & Technology Letters.
105. Mathiazhagan, P. and A.S. Khanna, *Effect of water vapor on the oxidation behavior of modified low alloy steels at high temperatures.* Arabian Journal for Science and Engineering, 2009. **34**(2C): p. 159-178.
106. Zurek, J., E. Wessel, L. Niewolak, F. Schmitz, T.U. Kern, L. Singheiser, and W.J. Quadakkers, *Anomalous temperature dependence of oxidation kinetics during steam oxidation of ferritic steels in the temperature range 550-650°C.* Corrosion Science, 2004. **46**(9): p. 2301-2317.
107. Wright, I.G., J.Y. Howe, and A.S. Sabau, *Morphological evolution of oxide scales grown on ferritic steels in steam.* Materials at High Temperatures, 2009. **26**(2): p. 105-111.
108. Muramatsu, K. *Development of Ultra-Super Critical Plant in Japan*. in *Advanced Heat Resistant Steels for Power Generation*. 1998. San Sebastian, Spain: Maney Publishing.
109. Kan, T., Y. Sawaragi, Y. Yamadera, and H. Okada. *Properties and Experiences of a New Austenitic Stainless Steel Super 304H (0.1C-18Cr-9Ni-3Cu-Nb-N) for Boiler Tube Application*. in *Materials for Advanced Power Engineering*. 1998. Forschungszentrum Jülich GmbH.
110. *Inspection Certificate Super 304H, Shot Peened Super 304H, 347H FG.* Sumitomo Metal Industries Ltd., 2007.
111. Hansson, A.N., H. Danielsen, F.B. Grumsen, and M. Montgomery, *Microstructural investigation of the oxide formed on TP 347H FG during long-term steam oxidation.* Materials and Corrosion-Werkstoffe Und Korrosion, 2010. **61**(8): p. 665-675.
112. *Inspection Certificate HR3C.* Sumitomo Metal Industries Ltd., 2009.
113. *Inspection Certificate Super 304H (Batch 2), HR3C (Batch 2).* Sumitomo Metal Industries Ltd., 2011.

114. Cisse, S., L. Laffont, B. Tanguy, M.C. Lafont, and E. Andrieu, *Effect of surface preparation on the corrosion of austenitic stainless steel 304L in high temperature steam and simulated PWR primary water.* Corrosion Science, 2012. **56**: p. 209-216.
115. Rosser, J.C., M.I. Bass, C. Cooper, T. Lant, P.D. Brown, B.J. Connolly, and H.E. Evans, *Steam oxidation of Super 304H and shot-peened Super 304H.* Materials at High Temperatures, 2012. **29**(2): p. 95-106.
116. Ericsson, T., *Stratified oxide scale growth on two Cr-Ni steels oxidized in high-pressure steam at 800°C.* Oxidation of Metals, 1970. **2**(2): p. 173-205.
117. Jianmin, J., M. Montgomery, O.H. Larsen, and S.A. Jensen, *Investigation on steam oxidation behaviour of TP347H FG Part 1: Exposure at 256 bar.* Materials and Corrosion-Werkstoffe Und Korrosion, 2005. **56**(7): p. 459-467.
118. Jianmin, J., M. Montgomery, O.H. Larsen, and S.A. Jensen, *Investigation of steam oxidation behaviour of TP347H FG Part 2: Exposure at 91 bar.* Materials and Corrosion-Werkstoffe Und Korrosion, 2005. **56**(8): p. 542-549.
119. Armitt, J., R. Holmes, M.I. Manning, D.B. Meadowcroft, and E. Metcalfe, *The Spalling of Steam-Grown Oxide from Superheater and Reheater Tube Steels*. 1978, Central Electricity Research Laboratories: Surrey.
120. Schutze, M., *Protective Oxide Scales and their Breakdown*. 1st ed. 1997: Wiley.
121. Evans, H.E., *Stress effects in high temperature oxidation of metals.* International Materials Reviews, 1995. **40**(1): p. 1-40.
122. Stringer, J., *Stress generation and relief in growing oxide films.* Corrosion Science, 1970. **10**(7): p. 513-543.
123. Rhines, F.N. and J.S. Wolf, *The role of oxide microstructure and growth stresses in the high-temperature scaling of nickel.* Metallurgical Transactions, 1970. **1**(6): p. 1701-1710.
124. Tien, J.K. and J.M. Davidson, *Oxide Spallation Mechanisms*, in *Stress Effects and the Oxidation of Metals*, J.V. Cathcart, Editor. 1975, AIME: New York. p. 200-219.
125. Evans, H.E., G.P. Mitchell, R.C. Lobb, and D.R.J. Owen, *A numerical analysis of oxide spallation.* Proceedings of the Royal Society A: Mathematical, Physical and Engineering Sciences, 1993. **440**: p. 1-22.
126. Arkharov, V.I., V.N. Bogoslovskii, and E.N. Kuznetsov, *Thermal Expansion of Magnetite.* 1972. **8**: p. 1982.
127. Rigby, G.R., G.H.B. Lowell, and A.T. Green, *Some properties associated with the spinels of some ores.* British Ceramic Society Transactions, 1946. **45**: p. 137.
128. Sharma, S.S., *Thermal expansion of crystals.* Proceedings of the Indian Academy of Sciences - Section A, 1950. **31**(4): p. 261-274.
129. Gorton, A.T., Bitsiane.G, and T.L. Joseph, *Thermal expansion coefficients for iron and its oxides from x-ray diffraction measurements at elevated temperatures.* Transactions of the Metallurgical Society of Aime, 1965. **233**(8): p. 1519-1525.
130. Tylecote, R.F., *Factors influencing the adherence of oxides on metals.* Journal of the Iron and Steel Institute, 1960. **196**: p. 135-141.
131. Robertson, J. and M.I. Manning, *Limits to adherence of oxide scales.* Materials Science and Technology, 1990. **6**(1): p. 81-92.
132. *DMV 304 HCu, Bolier Grade DMV 304 HCu Datasheet.* Salzgitter Mannesmann Stainless Tubes, 2008.
133. *DMV 347H FG Datasheet.* Salzgitter Mannesmann Stainless Tubes, 2008.
134. Levy, D., R. Giustetto, and A. Hoser, *Structure of magnetite (Fe_3O_4) above the Curie temperature: a cation ordering study.* Physics and Chemistry of Minerals, 2012. **39**(2): p. 169-176.

135. Levy, D., G. Artioli, and M. Dapiaggi, *The effect of oxidation and reduction on thermal expansion of magnetite from 298 to 1173 K at different vacuum conditions.* Journal of Solid State Chemistry, 2004. **177**(4-5): p. 1713-1716.
136. Christl, W., A. Rahmel, and M. Schütze, *Behavior of oxide scales on 2.25Cr-1Mo steel during thermal cycling. II. Scales grown in water vapor.* Oxidation of Metals, 1989. **31**(1-2): p. 35-69.
137. Osgerby, S., *Oxide scale damage and spallation in P92 martensitic steel.* Materials at High Temperatures, 2000. **17**(2): p. 307-310.
138. Saunders, S., M. Monteiro, and F. Rizzo, *The oxidation behaviour of metals and alloys at high temperatures in atmospheres containing water vapour: A review.* Progress in Materials Science, 2008. **53**: p. 775-837.
139. Evans, H.E. and R.C. Lobb, *Conditions for the initiation of oxide scale cracking and spallation.* Corrosion Science, 1984. **24**(3): p. 209-222.
140. Evans, H.E., *Spallation models and their relevance to steam-grown oxides.* Materials at High Temperatures, 2005. **22**(1-2): p. 155-166.
141. Hancock, P. and J.R. Nicholls, *Application of fracture mechanics to failure of surface oxide scales.* Materials Science and Technology, 1988. **4**(5): p. 398-406.
142. Schutze, M., *Plasticity of protective oxide scales.* Materials Science and Technology, 1990. **6**(1): p. 32-38.
143. Evans, H.E., *Cracking and spalling of protective oxide layers.* Materials Science and Engineering: A, 1989. **120-121**(Part 1): p. 139-146.
144. Evans, H.E., *Spallation of oxide from stainless steel AGR nuclear fuel cladding - mechanisms and consequences.* Materials Science and Technology, 1988. **4**(5): p. 415-420.
145. Schutze, M., P.F. Tortorelli, and I.G. Wright, *Development of a comprehensive oxide scale failure diagram.* Oxidation of Metals, 2010. **73**(3-4): p. 389-418.
146. Tang, J., M. Halvarsson, H. Asteman, and J. Svensson, *The microstructure of the base oxide on 304L steel.* Micron, 2001. **32**: p. 799-805.
147. Smith, A.F., M.O. Tucker, and R. Hales, *The Kinetics of Duplex Scale Formation on 18/8 Type Stainless Steel.* Oxidation of Metals, 1982. **17**(5-6): p. 329-343.
148. Hansson, A.N., M. Montgomery, and M.A.J. Somers, *Development of the inner oxide zone upon steam oxidation of an austenitic stainless steel.* Materials at High Temperatures, 2009. **26**(1): p. 39-44.
149. Stott, F.H., F.I. Wei, and C.A. Enahoro, *The influence of manganese on the high-temperature oxidation of iron-chromium alloys.* Materials and Corrosion, 1989. **40**(4): p. 198-205.
150. Zhong, X.Y., X.Q. Wu, and E.H. Han, *The characteristic of oxide scales on T91 tube after long-term service in an ultra-supercritical coal power plant.* Journal of Supercritical Fluids, 2012. **72**: p. 68-77.
151. Chen, R.Y. and W.Y.D. Yeun, *Review of the high-temperature oxidation of iron and carbon steels in air or oxygen.* Oxidation of Metals, 2003. **59**(5-6): p. 433-468.
152. Taniguchi, S., T. Furukawa, and T. Shibata, *Failure of scales formed on Cu-containing low carbon steels during cooling.* Isij International, 1997. **37**(3): p. 263-271.
153. Kondo, Y., H. Tanei, N. Suzuki, K. Ushioda, and M. Maeda, *Blistering Behavior during Oxide Scale Formation on Steel Surface.* Isij International, 2011. **51**(10): p. 1696-1702.
154. Kondo, Y., H. Tanei, K. Ushioda, and M. Maeda, *Role of Hematite Formation on Blister Generation during High Temperature Oxidation of Steel.* Isij International, 2012. **52**(12): p. 2254-2259.
155. Kondo, Y., H. Tanei, K. Ushioda, M. Maeda, and Y. Abe, *Effect of Nitrogen on Blister Growth Process of Blistering during High Temperature Oxidation of Steel.* Tetsu to Hagane-Journal of the Iron and Steel Institute of Japan, 2013. **99**(9): p. 559-563.
156. Griffiths, R., *The Blistering of Iron Oxide Scales and the Conditions for the Formation of a Non-Adherent Scale.* The Journal of the Iron and Steel Institute, 1934. **130**(11): p. 377-384.

157. Stott, F.H. and F.I. Wei, *High temperature oxidation of commercial austenitic stainless steels.* Materials Science and Technology, 1989. **5**: p. 1140-1147.
158. Sato, T., Y. Fukuda, K. Mitsuhata, and K. Sakai, *The practical application and long-term experience of new heat resistant steels to large scale USC boilers*, in *Advances for Materials Technology for Fossil Power Plants*, R. Viswanathan, D. Gandy, and K. Coleman, Editors. 2004, ASM International: Hilton Head Island, South Carolina. p. 177-190.
159. Angell, M.G., S.K. Lister, and A. Rudge. *The Effect of Steam Pressure on the Oxidation Behaviour of Annealed 9Cr 1Mo Boiler Tubing Materials*. in *International Conference on the Properties of Water and Steam*. 2008. Berlin.
160. Schutze, M., *Modelling oxide scale fracture.* Materials at High Temperatures, 2005. **22**(1-2): p. 147-154.
161. Kester, E., U. Rabe, L. Presmanes, P. Tailhades, and W. Arnold, *Measurement of Young's modulus of nanocrystalline ferrites with spinel structures by atomic force acoustic microscopy.* Journal of Physics and Chemistry of Solids, 2000. **61**(8): p. 1275-1284.
162. Chicot, D., J. Mendoza, A. Zaoui, G. Louis, V. Lepingle, F. Roudet, and J. Lesage, *Mechanical properties of magnetite (Fe3O4), hematite (alpha-Fe2O3) and goethite (alpha-FeO center dot OH) by instrumented indentation and molecular dynamics analysis.* Materials Chemistry and Physics, 2011. **129**(3): p. 862-870.
163. Schütze, M., S. Ito, W. Przybilla, H. Echsler, and C. Bruns, *Test methods and data on the mechanical properties of protective oxide scales.* Materials at High Temperatures, 2001. **18**(1): p. 39-50.
164. Iorio, L., M. Cortie, and R. Jones, *Technical Note: Solubility of nitrogen in experimental low-nickel austenitic stainless steels.* The Journal of The South African Institute of Mining and Metallurgy, 1994: p. 173 - 177.
165. Honeycombe, R.W.K., *Steels - Microstructure and Properties*. 1981, London: Edward Arnold (Publishers) Ltd.
166. Krauss, G., in *Steels: Heat Treatment and Processing Principles*. 1990, ASM International.
167. McGuire, M., *Stainless Steels for Design Engineers*. 2008, Materials Park, Ohio, 44073-0002: ASM International.
168. Caplan, D. and M. Cohen, *Influence of impurities on oxidation of Fe-26Cr alloys.* Nature, 1965. **205**(4972): p. 690.
169. Jonsson, T., F. Liu, S. Canovic, H. Asteman, J.E. Svensson, L.G. Johansson, and M. Halvarsson, *Influence of $H_2O(g)$ on the oxide microstructure of the stainless steel 353MA at 900°C in oxygen.* Journal of the Electrochemical Society, 2007. **154**(11): p. 603-610.
170. Caplan, D. and M. Cohen, *Scaling of Fe-26Cr alloys at 870-1200°C.* Journal of the Electrochemical Society, 1965. **112**(5): p. 471-477.
171. Jones, D.E. and J. Stringer, *The effect of small amounts of silicon on the oxidation of high-purity Co-25 wt. % Cr at elevated temperatures.* Oxidation of Metals, 1975. **9**(5): p. 409-413.
172. Evans, H.E., D.A. Hilton, R.A. Holm, and S.J. Webster, *Influence of silicon additions on the oxidation resistance of a stainless steel.* Oxidation of Metals, 1983. **19**(1-2): p. 1-18.
173. Lobb, R.C., J.A. Sasse, and H.E. Evans, *Dependence of oxidation behaviour on silicon content of 20Cr austenitic steels.* Materials Science and Technology, 1989. **5**(8): p. 828-834.
174. Kumar, A. and D.L. Douglass, *Modification of the oxidation behavior of high-purity austenitic Fe-14Cr-14Ni by the addition of silicon.* Oxidation of Metals, 1976. **10**(1): p. 1-22.
175. Sedriks, A.J., *Corrosion of Stainless Steels*. 2nd ed. 1996, Canada: John Wiley and Sons, Inc.
176. Evans, H.E., A.T. Donaldson, and T.C. Gilmour, *Mechanisms of breakaway oxidation and application to a chromia-forming steel.* Oxidation of Metals, 1999. **52**(5-6): p. 379-402.